A study of the high temperature oxidation and microstructure of niobium silicide-based alloys with the additions of boron and germanium

Joseph Weeks

Thesis submitted for the Degree of Doctor of Philosophy (PhD)

The Department of Materials Science and Engineering

The University of Sheffield

October 2024

Abstract

Niobium silicide-based alloys are a potential candidate martial to supplant nickel-based super alloys for use in the most demanding parts of aircraft engines. This thesis describes research on the development of boron and germanium containing niobium silicide-based alloys. The combined effect of boron and germanium is assessed with focus on the oxidation resistance and oxide scales. Literature regarding phase equilibria, mechanical properties and oxidation is reviewed.

Four alloys were manufactured; a base alloy to facilitate comparison, KZ5 (Nb-18Si-24Ti-5Cr-5Al), and three novel boron and germanium containing alloys, JW1 (Nb-18Si-24Ti-5Cr-5Al-5Ge-5B), JW2 (Nb-18Si-24Ti-5Cr-5Al-5Ge-10B) and JW3 (Nb-18Si-24Ti-5Cr-5Al-10Ge-5B). As-cast and heat-treated (1300°C/1500°C) states of each alloy were characterised.

In the as-cast condition, solid solution (Nb) was present in all alloys. $D8_8$ ($Nb_5Si_3B_x$) and $NbCr_2$ were stabilised in boron and germanium containing alloys. T2 ($Nb_5(SiB)_3$) was found in JW1 and in small amounts in JW2. NbB was found in JW2 and in small amounts in JW3. Heat-treatments resulted in the conversion of NbB to T2, the partial conversion βNb_5Si_3 to αNb_5Si_3 in KZ5, and the elimination of (Nb) in JW3. The amount of (Nb) was reduced by B and Ge additions. Macrosegregation of the high germanium alloy (JW3) was more severe, and macrosegregation of the high boron alloy (JW2) was less severe, when compared to JW1.

Boron and germanium additions are shown to improve oxidation resistance, with total mass gains decreased by up to 79% and 50% at 1000°C and 1200°C, respectively. At 1000°C, JW series alloys performed better than KZ5. Heat-treatment had a significant influence on oxidation. At 1200°C, KZ5 performed worse than JW alloys, where JW2 and JW3 oxidation resistance was generally equivalent, and superior to JW1. Ge-rich layers were observed, but no borosilicate glassy layers, believed to be due to competing phase stability. Spallation of oxide scale was eliminated by boron and germanium additions. This work provides valuable results to aid future alloy design with a balance of properties through boron and germanium additions.

Acknowledgements

I would firstly like to thank Dr Claire Utton for her support throughout this project. Dr Utton's guidance has been invaluable and her the continued encouragement during supervision has enabled me to succeed. I would also like to thank Dr Russell Goodall for likewise key supervision in which would otherwise have been a difficult time.

I would sincerely like to thank the academic and technical staff that have helped me develop as a researcher; Stuart Creasey-Gray and Dr Jonathan Fellowes for their expertise in EPMA, Dr Robert Moorehead for his continued training on XRD equipment, and Dr Yunus Azakli, Tesoro Monaghan, and Sylwester Mikula for their assistance and skills provided for the manufacturing processes utilised in this work. I am grateful for the opportunities provided throughout this project, with special thanks to Professor Mitarai and co for facilitating the work I was able to complete in Japan.

I would also like to thank my friends in and outside of Sheffield, with special thanks to Jenny Ayling for unlimited patience and kindness throughout the writing process. Finally, I am thankful to my parents, brother and sister for their support and encouragement, who I hope to spend more time with now that this is complete.

Contents

Abstract i
Acknowledgements ii
Contents iii
1 Introduction 2
2 Literature review 5
2.1 Introduction 5
2.2 Phase equilibria 7
2.2.1 Nb – Si 7
2.2.2 Nb-Ti 9
2.2.3 Nb-Si-Ti 10
2.2.4 Nb-Cr 12
2.2.5 Nb-Si-Cr 13
2.2.6 Nb-B 16
2.2.7 Nb-Ti-B 17
2.2.8 Nb-Si-B 19
2.2.9 Nb-Ge 22
2.2.10 Nb-Si-Ge 24
2.3 Mechanical properties 27
2.3.1 Mechanical properties of Nb-Si alloys 27
2.3.2 The effect of alloying additions Ti, Cr, Al, Ge and B on the mechanical properties of Nb-Si alloys 28
2.4 Oxidation 30
2.4.1 Oxidation of niobium silicide-based alloys 30
2.4.2 Oxidation kinetics 30
2.4.3 Pesting phenomena 31
2.4.4 The addition of Ti 31
2.4.5 The addition of Cr 32
2.4.6 The addition of Al 34
2.4.7 The addition of B 34
2.4.8 The addition of Ge 35
3 Experimental procedure 38
3.1 Alloy selection and composition 38
3.2 Ingot manufacture 38

3.3 Metallographic preparation 39
3.4 Heat treatments 40
3.5 X-ray diffraction (XRD) 41
3.5.1 Bulk phases 41
3.5.2 Oxides 41
3.6 Electron probe micro-analysis (EPMA) 41
3.7 Scanning electron microscopy – Backscattered electrons (SEM-BSE) 42
3.8 Electron backscatter diffraction (EBSD) 42
3.9 Thermal analysis 43
3.9.1 Isothermal thermogravimetric analysis (TGA) 43
3.9.2 Differential scanning calorimetry (DSC) 43
4 The effect of boron and germanium additions on the microstructure of as-cast KZ5 (Nb-18Si-24Ti-5Cr-5Al) 45
4.1 Introduction 45
4.2 Results 46
4.2.1 KZ5-AC (Nb-24Ti-18Si-5Cr-5Al) 46
4.2.1.1 XRD 46
4.2.1.2 EBSD 46
4.2.1.3 EPMA 47
4.2.1.4 BSE - SEM Imaging 49
4.2.1.5 Area Fraction 53
4.2.2 JW1-AC (Nb-24Ti-18Si-5Cr-5Al-5Ge-5B) 54
4.2.2.1 XRD 54
4.2.2.2 EBSD 54
4.2.2.3 EPMA 56
4.2.2.4 BSE - SEM Imaging 59
4.2.2.5 Area Fraction 63
4.2.2.6 Macrosegregation 63
4.2.3 JW2-AC (Nb-24Ti-18Si-5Cr-5Al-5Ge-10B) 65
4.2.3.1 XRD 65
4.2.3.2 EBSD 65
4.2.3.3 EPMA 66
4.2.3.4 BSE - SEM Imaging 68
4.2.3.5 Area Fraction 73
4.2.3.6 Macrosegregation 73
4.2.4 JW3-AC (Nb-24Ti-18Si-5Cr-5Al-10Ge-5B) 75

4.2.4.1 XRD 75
4.2.4.2 EBSD 75
4.2.4.3 EPMA 76
4.2.4.4 BSE - SEM Imaging 78
4.2.4.5 Area Fraction 82
4.2.4.6 Macrosegregation 82
4.2.5 Differential scanning calorimetry 83
4.3 Discussion 85
4.3.1 The effect of 5 at.% B and 5 at.% Ge on the microstructure and phases of KZ5 (Nb-24Ti-18Si-5Cr-5Al) 85
4.3.2 The effect of 10 at.% B and 10 at.% Ge on the microstructure and phases of JW1 (Nb-24Ti-18Si-5Cr-5Al-5Ge-5B) 87
4.4 Conclusions 91
5 The effect of heat-treatments on KZ5 (Nb-18Si-24Ti-5Cr-5Al), JW1 (Nb-18Si-24Ti-5Cr-5Al-5Ge-5B), JW2 (Nb-18Si-24Ti-5Cr-5Al-5Ge-10B), JW3 (Nb-18Si-24Ti-5Cr-5Al-10Ge-5B). 93
5.1 Introduction 93
5.2 Results 94
5.2.1 KZ5 (Nb-24Ti-18Si-5Cr-5Al) 94
5.2.1.1 XRD 94
5.2.1.2 EBSD 94
5.2.1.3 EPMA 95
5.2.1.4 BSE – SEM imaging 96
5.2.1.5 Area fraction 98
5.2.2 JW1 (Nb-24Ti-18Si-5Cr-5Al-5Ge-5B) 99
5.2.2.1 XRD 99
5.2.2.2 EBSD 100
5.2.2.3 EPMA 101
5.2.2.4 BSE – SEM imaging 102
5.2.2.5 Area fraction 105
5.2.3 JW2 (Nb-24Ti-18Si-5Cr-5Al-5-Ge-10B) 106
5.2.3.1 XRD 106
5.2.3.2 EBSD 107
5.2.3.3 EPMA 108
5.2.3.4 BSE – SEM imaging 109
5.2.3.5 Area fraction 113
5.2.4 JW3 (Nb-24Ti-18Si-5Cr-5Al-10Ge-5B) 114

5.2.4.1 XRD 114
5.2.4.2 EPMA 115
5.2.4.3 BSE – SEM imaging 116
5.2.4.4 Area fraction 120
5.3 Discussion 121
5.3.1 The effect of heat-treatment on a boron and germanium free alloy (KZ5: Nb-24Ti-18Si-5Cr-5Al) 121
5.3.2 The effect of heat treatment on boron and germanium containing alloys 124
5.4 Conclusions 130
6 The isothermal oxidation behaviour of boron and germanium containing alloys at 1000°C and 1200°C 132
6.1 Introduction 132
6.2 Oxidation at 1000°C 133
6.2.1 Oxidation behaviour 133
6.2.1.1 KZ5 133
6.2.1.2 JW1 134
6.2.1.3 JW2 135
6.2.1.4 JW3 136
6.2.2 Oxide scale 140
6.2.2.1 KZ5 140
6.2.2.2 JW1 150
6.2.2.3 JW2 160
6.2.2.4 JW3 171
6.2.3 Discussion 181
6.2.3.1 The effect of alloy composition on oxidation resistance 181
6.2.3.2 The effects of processing on oxidation resistance 184
6.2.4 Conclusions 189
6.3 Oxidation at 1200°C 190
6.3.1 Oxidation behaviour 190
6.3.1.1 KZ5 190
6.3.1.2 JW1 191
6.3.1.3 JW2 192
6.3.1.4 JW3 194
6.3.2 Oxide scale 198
6.3.2.1 KZ5 198
6.3.2.2 JW1 205

6.3.2.3 JW2 213
6.3.2.4 JW3 221
6.3.3 Discussion 230
6.3.3.1 The effect of alloy composition on oxidation resistance 230
6.3.3.2 The effects of processing on oxidation resistance 234
6.3.4 Conclusion 240
6.4 Oxidation at 800°C 241
7 Conclusions and suggestions for future work 243
7.1 Conclusions 243
7.1.1 Introduction 243
7.1.2 KZ5 (Nb-18Si-24Ti-5Cr-5Al) 243
7.1.3 JW1 (Nb-18Si-24Ti-5Cr-5Al-5Ge-5B) 243
7.1.4 JW2 (Nb-18Si-24Ti-5Cr-5Al-5Ge-10B) 244
7.1.5 JW3 (Nb-18Si-24Ti-5Cr-5Al-10Ge-5B) 245
7.1.6 Limitations 246
7.1.7 Summary 247
7.2 Suggestions for future work 249
8 Appendix 251
References 257

Chapter 1

1 Introduction

The modern turbofan jet engine used in commercial aircraft relies on a Brayton cycle consisting of the compression, combustion, and expansion in the turbine chamber of air and fuel [1]. To increase engine efficiency, the operating temperature of the engine can be raised. Over the better part of a century nickel-based superalloys have been used and continuously developed to push the operating temperature of aircraft engines to new heights.

Alloy composition alterations to raise the melting temperature and microstructural developments such as the transition to single crystal blades have facilitated this, although development in this regard has slowed in recent decades [2][3]. Currently aircraft engines have turbine inlet temperatures exceeding 1800K; greater than the melting temperature of nickel-based super alloys. The majority of improvements recently come from cooling systems and thermal barrier coatings (TBCs), which have been developed for turbine blades to withstand this ultra-high temperature. TBCs are applied to components to create a temperature gradient from the hot gases in the engine to the alloy. Cooling methods involve a portion of the air from the compressor being diverted to the blades to conduct heat away and create thin films of cool air to reduce conductive heat transfer. In terms of alloy melting temperature, nickel-based alloys are approaching the limit for what is possible, and to raise the inlet temperature further would require a more extensive cooling system, which in turn results in more work done by the engine being diverted to cool the turbine components. Past a certain point, the efficiency gains from a higher operating temperature are exceeded by the inefficiency of the cooling system [4].

To further improve the efficiency, a new material with higher melting temperature would need to be developed. Niobium silicide-based alloy is one such candidate that has a high melting temperature (~2200K) and a dual phase Nb_5Si_3 / solid solution that has demonstrated adequate creep resistance at elevated temperature [5]. The main limitations that face niobium silicide-based alloys are the poor oxidation resistance and room temperature fracture toughness, as well as the challenge of maintaining adequate performance for other properties whilst addressing these short comings. The general consensus is a coating system will still be required for niobium silicide-based alloys, but due to the high melting temperature, a more extensive cooling system could potentially be avoided, further improving engine efficiency. The base material must still be resistant to oxidation if catastrophic failure of components is to be avoided.

The work in this thesis seeks to utilise boron as an alloying addition to the niobium silicide-based alloy system to enhance the oxidation resistance, whilst maintaining mechanical properties, through promoting the formation of a borosilicate glassy layer on the alloys' surface during the oxidation process. The layer would be capable of self-healing cracks that form as a result of oxidation through viscous flow. This has been effective in a similar refractory silicon system, molybdenum silicide alloys, but so far has been elusive in the niobium equivalent due to the rapid formation of non-protective Nb_2O_5 before a complete B_2O_3-SiO_2 layer can form [6]. The combined effect of boron and another glass forming element, germanium, is investigated in this work to assess whether GeO_2 can aid in the protective formation as is the case in high silicon content coating materials.

The aims of this work are: to characterise the microstructure of novel B and Ge containing alloys; assess the effect of B and Ge on oxidation resistance at 1000^{o}C and 1200^{o}C; search for evidence of borosilicate layers; assess the effect of heat-treatments on oxidation resistance as a function of microstructure and phase change; and finally, based on microstructure and oxidation data, recommend direction of further researched for a balance of mechanical properties and oxidation resistance.

The thesis is split into 7 chapters. A literature review regarding the phase equilibria, mechanical properties and oxidation of niobium silicide-based alloy is conducted in chapter 2, followed by the experimental procedures used to carry out this work in chapter 3. Results are presented in chapters 4 and 5 where the microstructures in the as-cast and heat-treated states are discussed, respectively, and chapter 6 where a comprehensive investigation into the oxidation resistance and oxide scales of alloys is presented for temperatures 1000^{o}C and 1200^{o}C. The appendix includes supplementary information related to preliminary modelling of certain oxygen driven phase transitions and information relating to phase identification.

Chapter 2

2 Literature review

2.1 Introduction

Alloy development of nickel-based super alloys is summarised in Figure 2.1, where the gradual increase in alloy temperature capabilities and turbine entry temperature are displayed [2][3]. The latter surpasses the former through thermal barrier coatings and cooling systems. Modern aircraft engines have turbine inlet temperatures exceeding 1800K. The melting temperatures, T_m, of nickel-based superalloys are approximately 1580K [7]. The thermal barrier coatings and cooling systems allow for this difference, however nickel-based super alloys still operate at temperatures that are a high proportion of their Tm. Usually an increased temperature results in a degradation of mechanical properties such as creep resistance and yield strength as dislocation movement is promoted. However, nickel-based superalloys possess resistance to dislocation movement at elevated temperature due to the presence of the intermetallic precipitate γ' phase which impedes dislocations [8].

Therefore, to further the goal of improved turbine efficiency, any candidate material to supplant nickel-based super alloys in terms of operating temperature would either have to possess a similar mechanism or have a significantly higher T_m. Currently investigated materials focused on an elevated melting temperature include refractory silicide-based alloys [9][10], refractory high entropy alloys (RHEA) [11], and ceramic matrix composites [12]. Refractory metals have received interest owing to their high melting temperatures and consequent preservation of mechanical properties at high temperature. Efforts have primarily been focused on niobium and molybdenum alloyed with silicon. Niobium has several advantages over molybdenum, including the lowest density of the refractory alloys (Nb, Mo, Ta, W, Re) 8.57 $g.cm^{-3}$ [13] and, despite reported values having a wide range, a lower ductile to brittle transition compared to molybdenum (-120 to -200^oC [9][14][15] compared to 130 to -30^oC [9][14][16]). However, niobium silicide-based alloys are only one such path to be investigated, and there are limitations with the Nb-Si system which will be discussed in the following sections such as poor oxidation resistance.

Over the course of niobium silicide-based alloy development, numerous alloying elements have been used to alter mechanical and oxidation properties. Of relevance to the current work are transition metals Ti and Cr, and sp electron elements Al, B and Ge. The phase equilibria of the relevant binary and ternary systems are laid out in the following section, as alloys currently in development consist of quaternary and higher order systems in the pursuit of achieving a balance of material properties, so the understanding of phase stability of such systems is necessary for future alloy development. Niobium silicide-based alloys are less comprehensively studied compared to nickel-based superalloys, and indeed other alternative candidate materials such as the molybdenum silicide system. The high temperature nature of certain phase transitions and ineffectiveness of heat-treatments in some cases at reaching equilibrium are concerns for these systems, especially those relating to Nb-Si-X ternary systems. This results in conflicting reports of phase stability which is required to be considered for alloy design.

The effect on mechanical properties of the relevant elemental additions are also of interested although not directly investigated in this work, as a material intended for bulk component application must have a balance of properties and not solely improved oxidation resistance. The same elements are assessed in terms of oxidation resistance, with the goal of expanding the knowledge of the role of boron and germanium play in oxidation of niobium silicide-based alloys.

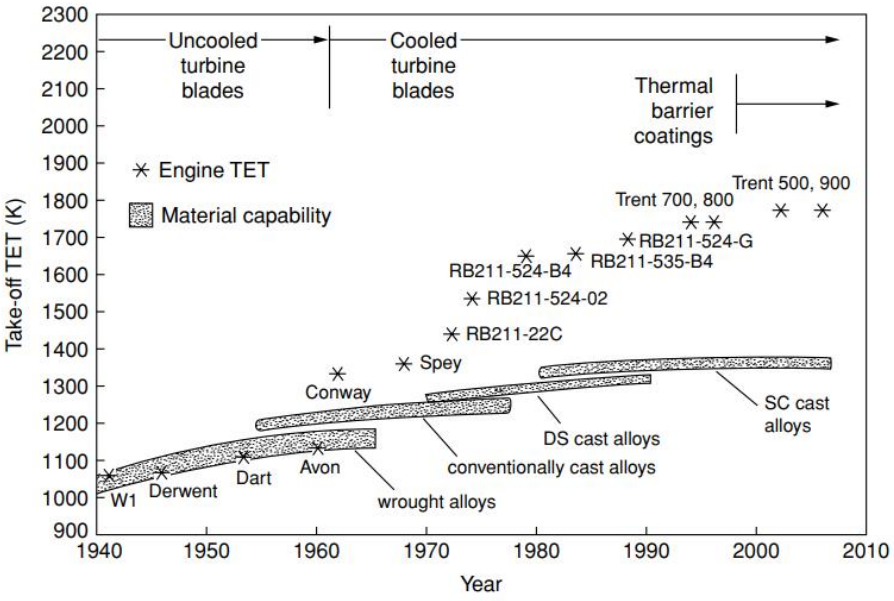

Figure 2.1) The development in material capability and turbine entry temperature of Rolls-Royce commercial aircraft engines over time. From [2] updated by [3].

2.2 Phase equilibria

2.2.1 Nb – Si

The Nb-Si system was described by Schlesinger in 1993 [17]. Six equilibrium solid phases are identified. These are BCC W-type solid solution (Nb), the cubic diamond structure (Si), the tetragonal Ti_3P-type Nb_3Si, the hexagonal $CrSi_2$-type $NbSi_2$ and the two forms of tetragonal Nb_5Si_3; low temperature αNb_5Si_3 with the Cr_5Si_3 prototype structure and high temperature βNb_5Si_3 with the W_5Si_3 prototype structure. The crystal structure data for these phases is given in Table 2.1.

A number of metastable phases are also identified and are referred to as Nb_3Si·m (Pearson symbol: cP8, Prototype: A15), Nb_3Si·m' (cF4, Cu), Nb_3Si·m'' (cP4, $AuCu_3$), Nb_3Si·I (t**, N/A), Nb_4Si (hP*, ϵ-Fe_3N), Nb_7Si (c**, N/A) and γNb_5Si_3 (hP16, Mn_5Si_3). These are likely not relevant to the current study as Nb_7Si and Nb_3Si·m are produced through sputtering onto thin films under low pressure [18], Nb_3Si·m' is produced under high pressures and fast cooling rates [19], Nb_3Si·I is produced under high pressure [20], and Nb_4Si and Nb_3Si·m'' are theorised to form due to impurities from Be compound heating components [21] and lower purity initial elements in [22]. However, the hexagonal structure γNb_5Si_3 should be considered as it is stable in the Nb-Si-B system discussed later. Identified as early as 1954 by Schachner *et al* [23] using a hot press sintering manufacturing technique [24], γNb_5Si_3 was categorised as an impurity-dependant metastable phase by Schlesinger [17] according to accounts from Samsonov *et al* [25] and Knapton [26] of γNb_5Si_3 formation upon the introduction of C impurities to the Nb-Si system. Interestingly, [25] proposes that B, as a light metalloid species, would have the same stabilising effect on γNb_5Si_3 formation.

The eutectic and eutectoid temperatures for reactions $L \rightleftharpoons (Nb) + Nb_3Si$ and $Nb_3Si \rightleftharpoons (Nb) + Nb_5Si_3$ are reported as 1915°C and 1765°C, respectively, in the original Schlesinger Nb-Si phase diagram [17]. These values were lowered by Zhao (2004) to 1880°C and 1700°C based on updated experimental data [27][28]. In fact in [27], the $Nb_3Si \rightleftharpoons (Nb) + Nb_5Si_3$ temperature was actually proposed to be even lower than 1700°C, at 1660-1680°C. The phase transitions in the Nb-Si system are notoriously sluggish. More recent thermodynamic modelling [29][30] utilising the CALPHAD method [31] agrees with this lowered eutectoid but supports the original $L \rightleftharpoons (Nb) + Nb_3Si$ eutectoid at approximately 1915°C proposed by Schlesinger [17]. The version of the Nb-Si system utilised in this work is calculated by Geng *et al* [32] with good agreement to the literature. This version of the Nb-Si phase diagram is presented in Figure 2.2. This follows on from work [29][30] where intermetallic phases are treated as non-stoichiometric, i.e. variable silicon contents, achieved for example with βNb_5Si_3 being modelled as three sub lattices $(Nb)_4(Nb,Si)_1(Si)_3$. The invariant equilibria of the Nb–Si system from [32] are given in Table 2.2.

According to Geng *et al*, the maximum solubility of Si in the (Nb) phase is 3.8 at.% at 1916°C. The original Schlesinger system reported this value to be 3.5 at.% based on the available data at the time [17]. The work that Geng's study is based on presents a range of values from a variety of sources that give the Si solubility in (Nb) at the eutectic temperature between 2.6 and 3.9 at.% [30].

This research will focus on niobium silicide-based alloys intended for structural components such as turbofan jet engine turbine blades and discs. As a result, phases on the niobium side of the phase diagram are of the most interest: (Nb), Nb_3Si, αNb_5Si_3, βNb_5Si_3.

Table 2.1) Nb-Si crystal structure data [17]. *[*1] $P6_222$ and *[*2] Cr_5B_3 *according to* [33]

Phase	Composition (at.% Si)	Pearson symbol	Space group	Prototype structure
(Nb)	0 to 3.5	cI2	$Im\bar{3}m$	W
(Si)	100	cF8	$Fd\bar{3}m$	C (diamond)
Nb_3Si	25	tP32	$P4_2/n$	Ti_3P
$NbSi_2$	64.9 to 69.8	hP9	$P6_422$ *[1]	$CrSi_2$
αNb_5Si_3	36.7 to 69.8	tI32	I4/mcm	Cr_5Si_3 *[2]
βNb_5Si_3	37.5 to 40.5	tI32	I4/mcm	W_5Si_3
γNb_5Si_3	37.5	hP16	$P6_3/mcm$	Mn_5Si_3

Table 2.2) Nb-Si system reaction scheme [32].

Reaction	Composition of respective phases (at.% Si)			Temperature °C	Reaction type
$L \leftrightarrow \beta Nb_5Si_3$		39.0		2526	Melting
$L \leftrightarrow (Nb)$		0		2467	Melting
$L + \beta Nb_5Si_3 \leftrightarrow Nb_3Si$	20.3	37.5	25.0	1977	Peritectic
$L \leftrightarrow NbSi_2$		66.7		1962	Melting
$Nb_3Si + \beta Nb_5Si_3 \leftrightarrow Nb_5Si_3$	25.0	37.5	37.5	1934	Peritectoid
$L \leftrightarrow (Nb) + Nb_3Si$	17.3	3.8	25.0	1916	Eutectic
$L \leftrightarrow \beta Nb_5Si_3 + NbSi_2$	57.7	40.8	66.7	1873	Eutectic
$Nb_3Si \leftrightarrow (Nb) + \alpha Nb_5Si_3$	25.0	2.6	37.5	1673	Eutectoid
$\beta Nb_5Si_3 \leftrightarrow Nb_5Si_3 + NbSi_2$	40.3	66.7	38.2	1648	Eutectoid
$L \leftrightarrow (Si)$		100		1414	Melting
$L \leftrightarrow NbSi_2 + (Si)$	98.3	66.9	100	1407	Eutectic

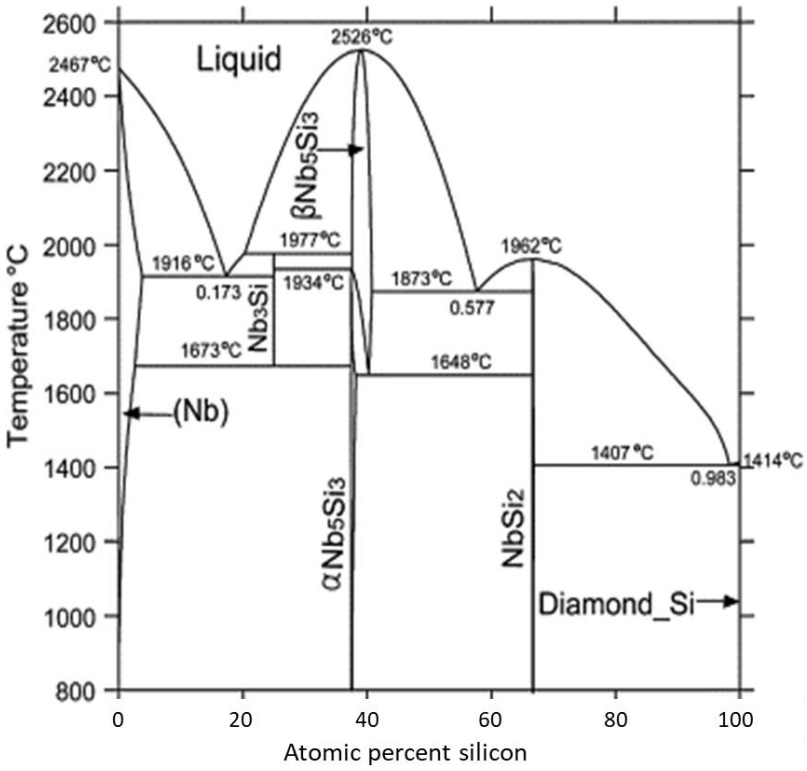

Figure 2.2) The Nb-Si system phase diagram [32]. X axis altered to atomic percent

2.2.2 Nb-Ti

The Nb-Ti phase diagram displayed in (Figure 2.3) consists of three stable phases: the liquid, the hexagonal (αTi) (Pearson symbol: hP2, prototype: Mg) and the BCC solid solution (Nb,βTi) (Table 2.3). Complete miscibility of Ti and Nb in the BCC phase exists above 882°C. Nb has very little solubility in (αTi), approximately 2.5 at.%. A dual phase region between (Nb,βTi) and (αTi) exists at temperatures below 882°C. This is a system where transformation kinetics are sluggish, and where Ti and Nb diffusion through (Nb,βTi) decrease rapidly by orders of magnitude with increasing Nb content [34][35]. Therefore, in ternary Nb-Ti-Si and higher order niobium silicide-based alloys the (αTi) solid solution is generally not seen. This is important to consider when solid solutions with higher Ti contents than Nb contents are encountered in chapter 5. The BCC (Nb,βTi) and HCP (αTi) phases will be referred to as (Nb) and (Ti), respectively, henceforth for simplicity. Where a (Nb) is found that is notably comparatively rich in Ti, this will be indicated with the Ti-rich label.

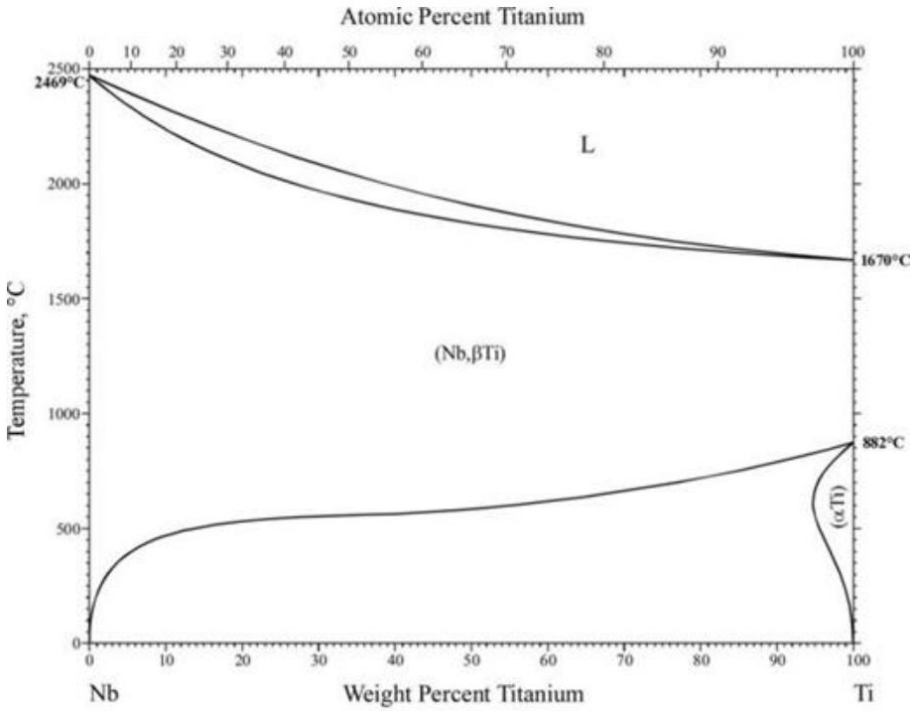

Figure 2.3) The Nb-Ti system phase diagram, with wt.% and at.% displayed at the bottom and top, respectively. [36] redrawn from [34]

Table 2.3) Nb-Ti crystal structure data [33][36]

Phase	Composition (at.% Ti)	Pearson symbol	Space group	Prototype structure
(Nb,βTi)	0 to 100	cI2	$Im\bar{3}m$	W
(αTi)	97 to 100	hP2	$P6_3/mmc$	Mg

2.2.3 Nb-Si-Ti

The phases present in the Nb-Ti-Si system include those listed for the Nb-Si and Nb-Ti binary systems as well several intermetallic phases from the Ti-Si binary system; the orthorhombic FeB-type TiSi, the tetragonal Ti_3P-type Ti_3Si, the orthorhombic $TiSi_2$-type $TiSi_2$, the hexagonal Mn_5Si_3-type Ti_5Si_3 and tetragonal Zr_5Si_4-type Ti_5Si_4 [33]. No ternary phases are found in the system and while substitution of Nb for Ti and vice versa is common in most of the intermetallic phases, only Ti_3Si and Nb_3Si are considered isomorphic. Unless otherwise stated, intermetallic compounds and the BCC solid solution phase (Nb) should be considered to have Ti present on Nb sites, for example Nb_3Si in reality is fully described as $(Nb,Ti)_3Si$ in the ternary system. The addition of Ti to the Nb-Si binary system stabilises Nb_3Si to lower temperatures as well as reduces the temperature of the eutectic reaction L -> (Nb) + Nb_3Si, effectively reducing the melting temperature of the alloy. This eutectic temperature is reduced to a minimum of ~1350°C at approximately 65 at.% Ti where then increased Ti content results in the transition reaction L + Nb_3Si -> (Nb) + Ti_5Si_3 in line with the eutectic reaction L -> (Ti) + Ti_5Si_3 present in the Ti-Si binary system occurring at 1330°C. With both hypereutectic and hypoeutectic Si contents, an increasing Ti content results in a lower melting temperature of the alloy which can be detrimental to mechanical properties at elevated temperature.

The Nb-Ti-Si system has been evaluated by a number of authors [32][37][38][39]. Bewlay *et al* [40] [41] constructed phase diagrams for this system. The Nb and Ti rich portion of the ternary diagram was focused on at several temperatures, three of which are included in Figure 2.4; 1500°C (Figure 2.4a), 1350°C (Figure 2.4b), and 1150°C (Figure 2.4c). The liquidus projection at this composition range is also included (Figure 2.5).

In this phase diagram, displayed in Figure 2.4 and Figure 2.5, no distinction is made between high temperature βNb_5Si_3 and low temperature αNb_5Si_3 in the liquidus projection or isothermal sections. These phases have the same tetragonal crystal structures but have different arrangements of constituent atoms. Later work by Zhao *et al* [37], Xu *et al* [38] and Zhan *et al* [39] acknowledges the existence of both phases but does not label them as such in Nb-Ti-Si isothermal plots at 1000°C/1150°C/1200°C, 1000°C, and 500°C, respectively. It is assumed at this relatively low temperature that αNb_5Si_3 should be the equilibrium phase. Geng [32] assessed the system using the CALPHAD method more recently based on experimental isothermal sections at various temperatures (1000°C -1500°C) [41][37]. Both αNb_5Si_3 and βNb_5Si_3 are included in the liquidus projection with an approximated phase boundary, displayed in Figure 2.6. The evidence for this large area of high temperature stable (up to 2139°C) αNb_5Si_3 is limited and relies on the extrapolation of the thermodynamic parameters of βNb_5Si_3 and observations of experimental data that is yet to be published, so this conclusion is not strongly supported. In contrast a first principles study by Papadimitriou *et al*, suggests that the addition of Ti reduces the transformation temperature between αNb_5Si_3 and βNb_5Si_3 [42]. Evidently knowledge of the Nb-Ti-Si system, particularly at high temperature, is incomplete, however the key points can be considered: no ternary phases are present, there is a reduction of melting temperatures upon the addition of Ti, and there are several two or three phases regions containing intermetallic and the solid solution phases that are desirable for mechanical properties.

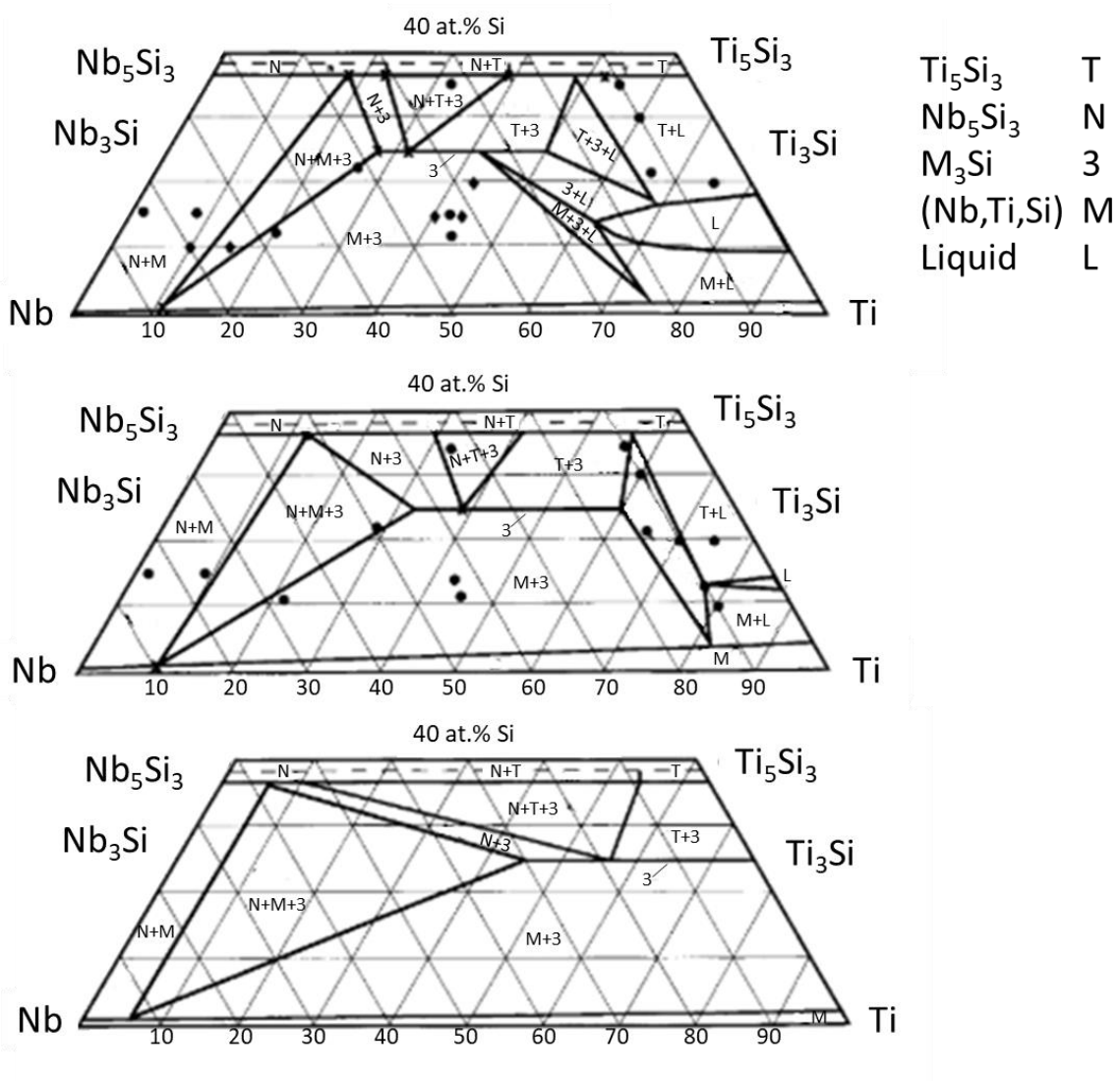

Figure 2.4a-c) The Nb-Ti-Si system ternary phase diagram with <40 at.% Si at a) 1500°C , b) 1350°C, and c) 1150°C [40] (adjusted labels for clarity.)

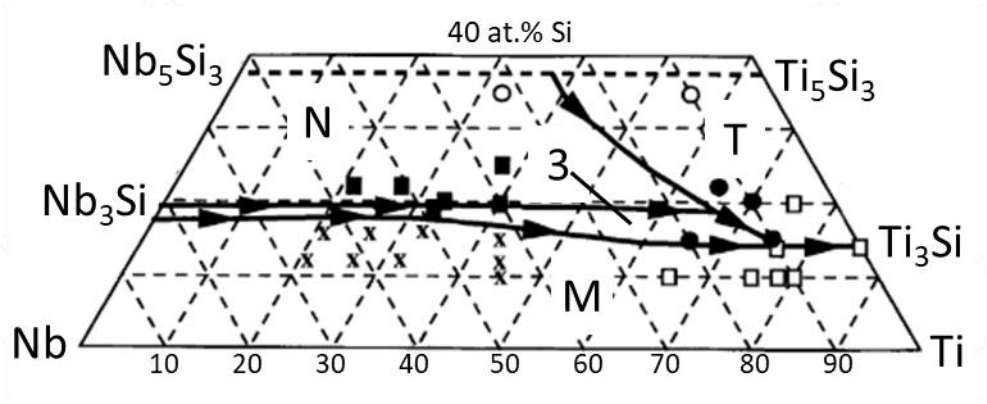

Figure 2.5) The Nb-Ti-Si system liquidus projection diagram with <40 at.% Si, with arrows highlighting the two transition reactions [40]. (adjusted labels for clarity.)

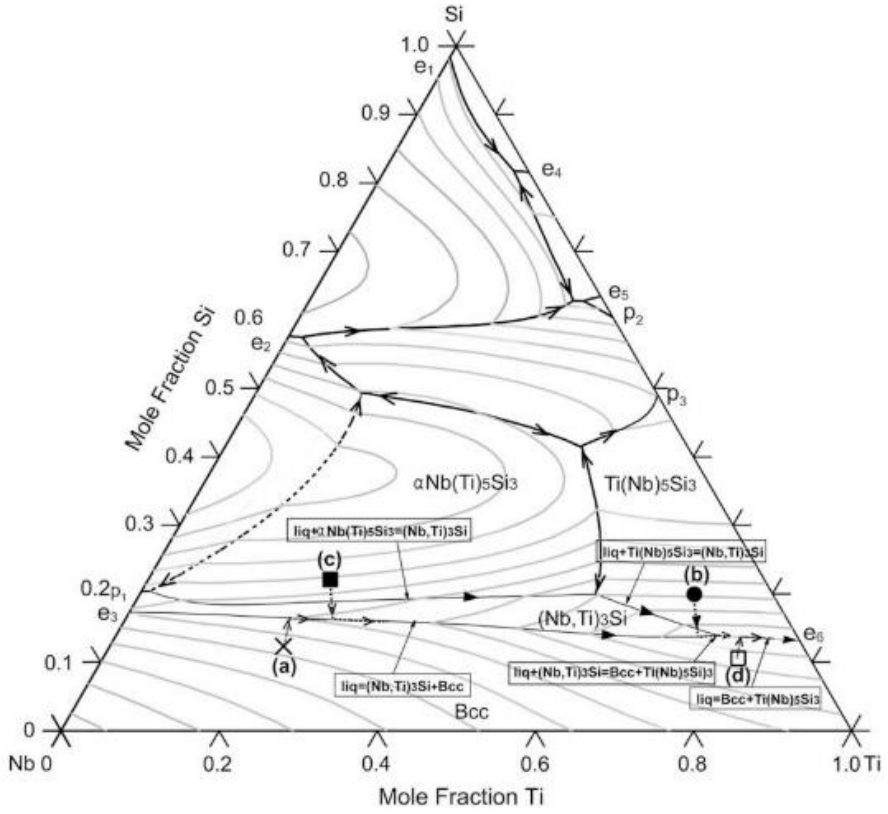

Figure 2.6) The Nb-Ti-Si system liquidus projection diagram, modelled by Geng et al [32]. The dotted arrowed line represents an uncertain approximated boundary of αNb_5Si_3 and unlabelled βNb_5Si_3.

2.2.4 Nb-Cr

The Nb-Cr system by Thoma [43] is given in Figure 2.7 and consists of four solid phases displayed in Table 2.4; the cubic W-type solid solution (Cr), the cubic W-type solid solution (Nb), the hexagonal $MgZn_2$-type Cr_2Nb and the cubic Cu_2Mg-type Cr_2Nb [44] (Table 2.4). The two phases with Cr_2Nb stoichiometry are known as Laves phases, with the hexagonal high temperature Laves phase classed as C14 and the cubic lower temperature Laves phase classed as C15 [45]. The system was reassessed by Thoma [43] based on the previously accepted diagram by Venkatraman [46]. The eutectic compositions as well as solubility limits and solvus boundaries solid solution phases (Nb) and (Cr) were redefined based on EDS data. The maximum solubility of Cr in (Nb) was reported as 24.4 at.% at 1703°C, increased from the previously reported value of ~15 at.%. The eutectic temperatures for the Nb and Cr rich sides of the phase diagram are given as 1703°C and 1668°C, respectively. It is therefore expected that Cr additions to the niobium silicide-based alloys will reduce the melting temperature, considering the Nb-Si eutectic temperature is over 200°C higher.

More recently the existence of the high temperature phase has been disputed in a pure Nb-Cr system [47] based on DTA and High-temperature neutron powder diffraction (HT-NPD). It is proposed that impurities result in metastable C14 formation and that in pure Nb-Cr alloys C15 can be observed as stable until melting, i.e. no C14 ⇌ C15 transition. Whilst this new information has been used to construct C14-absent phase diagrams [48][49][50][51], it is still debated in the literature [52][53][54][55]. In any case, since this present research is concerned with multicomponent alloys, the absence of impurities and therefore the elimination of a C14 will not occur, hence the inclusion of Figure 2.7.

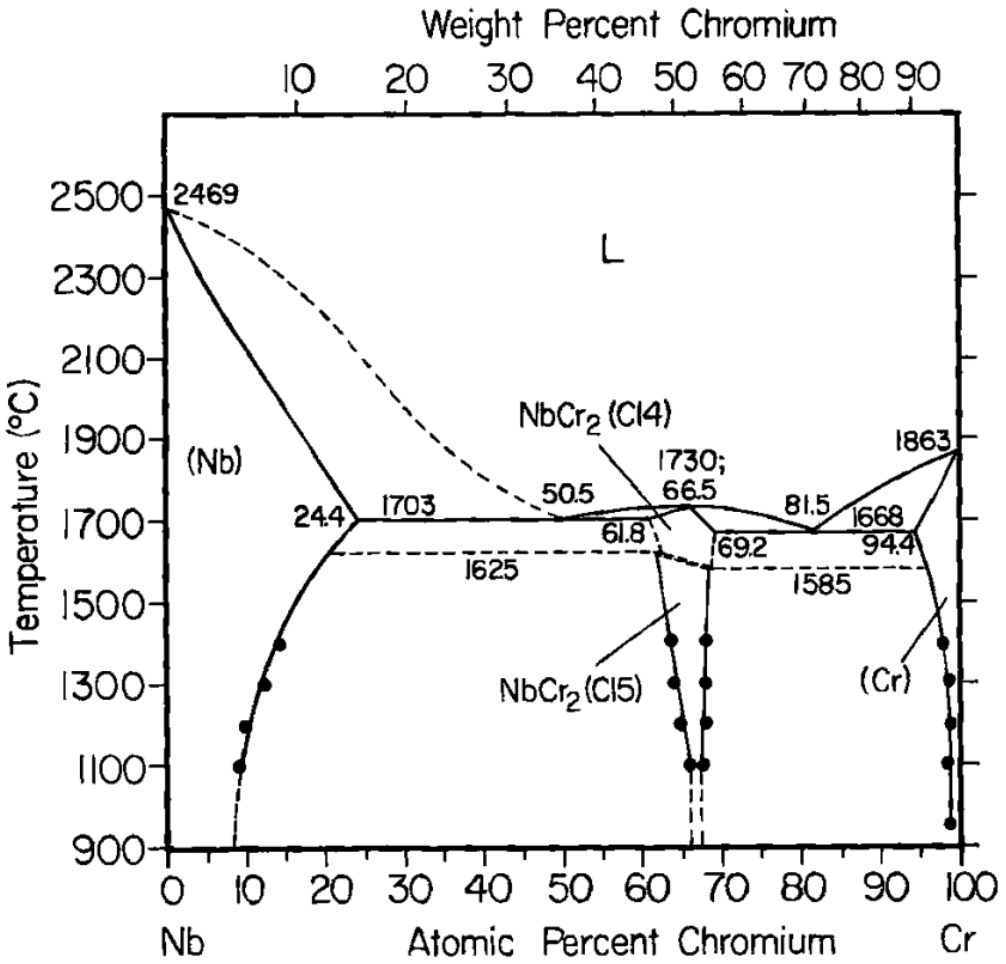

Figure 2.7) The Nb-Cr system phase diagram [43]. It should be noted the (Nb) liquidus is represented by a dotted line as there was insufficient data to make an accurate plot without thermodynamic modelling.

Table 2.4) Nb-Cr crystal structure data [36][43]

Phase	Composition (at.% Cr)	Pearson symbol	Space group	Prototype structure
(Nb)	0 to 24.4	cI2	Imm	W
(Cr)	94.4 to 100	cI2	$Im\bar{3}m$	W
$NbCr_2$ (C14)	61.8 to 69.2	hP12	$P6_3/mmc$	$MgZn_2$
$NbCr_2$ (C15)	61.5 to 69.0	cF24	$Fd\bar{3}m$	$MgCu_2$

2.2.5 Nb-Si-Cr

One of the first ternary phase diagrams constructed of the Nb-Si-Cr system was by Goldschmidt and Brand [56], which was based on experimental data from a number of alloys. The complex system was reported to include five ternary phases, although this included βNb_5Si_3 stabilised to lower temperature by Cr and the hexagonal C14 $NbCr_2$ which is possibly present in the Nb-Cr binary. Further investigation to the system was made by Zhao [57], with the goal of clarifying phases present and phase equilibria with the use of diffusion multiples. However, there is some disagreement with the system as characterised by Zhao, mainly concerning the three-phase fields relevant to the NbCrSi (hP9, $P\bar{6}_2m$) phase above 1000°C as discussed below.

Zhao's diagram has (Nb)-Nb_5Si_3-CrNbSi and (Nb)-C14-CrNbSi three-phase fields, however later investigations, either thermodynamically modelled [58][59] or experimentally investigated through alloy manufacture [60][61], suggest that neither three-phase field exists, as NbCrSi is never in equilibrium with (Nb) in the range of 1000°C to 1500°C. Instead the (Nb)-Nb_5Si_3-C14 three-phase field is seen in the Nb-rich corner, hence the updated diagram by Geng is used in this work (Figure 2.9)[60]. A study by Bewlay *et al* [61] also found an additional ternary phase, $Nb_9(Cr,Si)_5$ (I4/mcm). This has been incorporated into a partial liquidus projection (Figure 2.8), but to the current author's knowledge the complete modelling of the liquidus projection and isothermal sections are yet to be published. Including this phase, four ternary phases are identified, listed in Table 2.5 with additional phases from the Cr-Si binary.

Si added to the Nb-Cr system stabilises the hexagonal version of $NbCr_2$, C14, which can accommodate ~21 at.% Si and result in Cr content as low as ~46 at.% according to the phase diagram. Experimental results show Cr content as low as 45.6 at.% [60], 48.7 at.% [62], and ~41 at.% [57]. The cubic version of $NbCr_2$, C15, has very little Si solubility in the ternary system. Other elements such as Al and Ti can also reduce the Cr content required for $NbCr_2$ formation, as in the ternary systems the C14 and C15 single phase regions extend into the Nb-Metal side of the ternary systems for Al [63] and Ti [64], respectively. The niobium-silicide phases αNb_5Si_3 and βNb_5Si_3 have limited solubility of Cr according to Figure 2.9, and in experimental work Cr content of these phases ranged from 1.9–6.8 at.% [62] and 1.6–3.5 at.% [60]. In the alloys manufactured in this current study Cr is expected to favourably partition to the solid solution phase and $NbCr_2$.

Table 2.5) Nb-Si-Cr crystal structure data [33][58]

Phase	Pearson symbol	Space group	Prototype structure
CrNbSi	hP9	$P\bar{6}_2m$	
$(Cr,Nb)_6Si_5$	oI44	Ibam	
$(Cr,Nb)_{11}Si_8$	oP76	Pnma	
$Nb_9(Cr,Si)_5$		I4/mcm	
Cr_3Si	cP8	$Pm\bar{3}n$	Cr_3Si
βCr_5Si_3	hP16	$P6_3/mcm$	Mn_5Si_3
αCr_5Si_3	TI32	I4/mcm	W_5Si_3
CrSi	cP8	$P2_13$	FeSi
$CrSi_2$	hP9	$P6_222$	$CrSi_2$

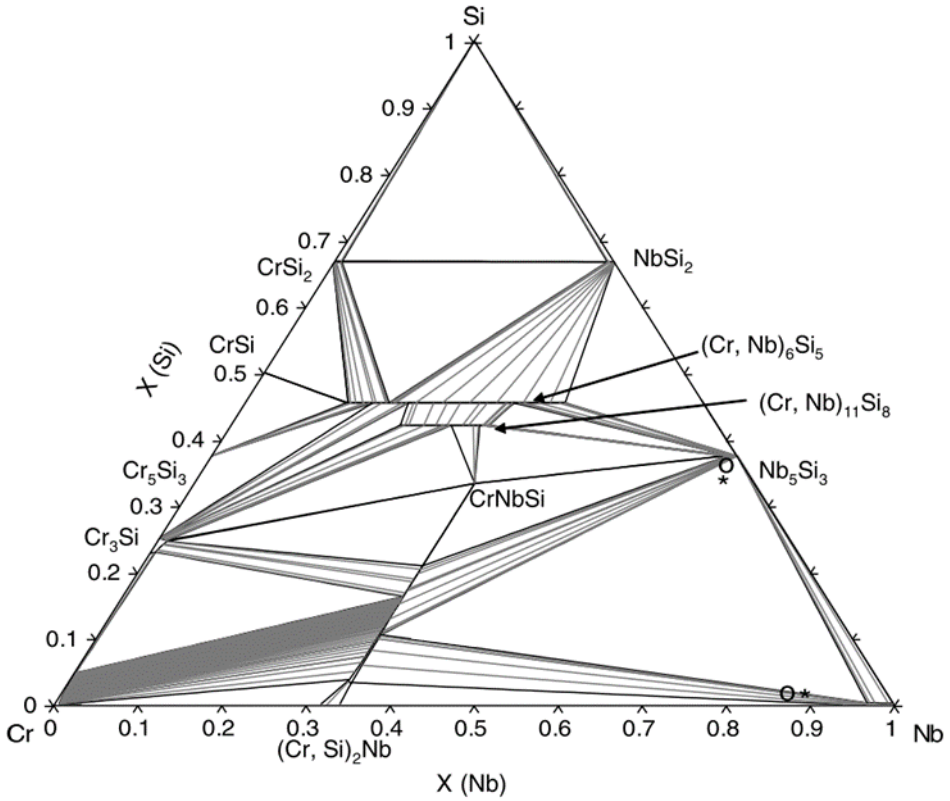

Figure 2.9) Calculated isothermal section of the Nb–Si–Cr system at 1000°C. Altered for clarity form original:[60]

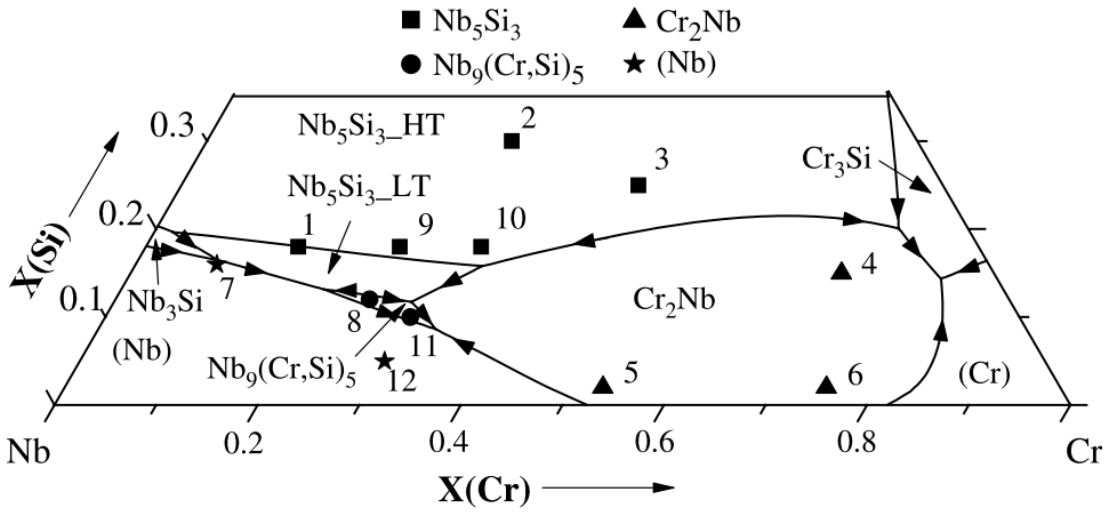

Figure 2.8) Calculated partial liquidus projection with Si at.% <35 of the Nb–Si–Cr system [61]. Symbols represent alloy compositions made by the original authors that had primary solidification phases corresponding to the above key.

2.2.6 Nb-B

The Nb-B binary system has eight solid phases; the cubic W-type Nb solid solution (Nb), the hexagonal elemental boron phase β-B, and a number of niobium borides listed in Table 2.6 [65][66]. Of the niobium borides, only NbB_2 and NbB are reported to have solubility ranges, 29.7-39 at.% and 50-51.2 at.%, respectively. The (Nb) has solubility of B up to 2 at.%, which reduces the solidus temperature of (Nb) from ~2470°C to ~2180°C [65].

In the past the Nb rich side of the phase diagram was reported differently by Massalski [67] and Rudy [68], with the key difference being the existence of the eutectic reaction L -> (Nb) + B_2Nb_3 at ~1600°C versus the eutectic reaction L -> (Nb) + NbB at ~2165°C, respectively. Further examination of the system by Borges [69] supported the original model by Rudy, which has been corroborated by thermodynamic modelling and metallographic and thermal analysis [70][71], but also identified the Nb_5B_6 phase included by Massalski.

Later, several iterations of the Nb-B phase diagram were published. First [72] by consolidating the previous models to include the eutectic reaction L -> (Nb) + NbB and Nb_5B_6 phase. Then thermodynamic modelling by Penchana [70] incorporated more definitive evidence of Nb_5B_6 [73] and the solubility range of B_2Nb [74]. Finally, Witusiewicz *et al* [66] included reports of an additional B_3Nb_2 phase [75] to give the phase diagram displayed in Figure 2.10 (redrawn in [65]), along with crystallographic information in Table 2.6. Evidently it appears the concentrations of B and Nb at the time of solidification will play a key role in which, if any, niobium boride compounds form. These compounds have melting temperatures comparable to phases in the Nb-Si system, so may be the first to form from the melt.

Table 2.6) Nb-B crystal structure data [65]

Phase	Composition (at.% B)	Pearson symbol	Space group	Prototype structure
β-B	99.5 to 100	*hR*108	$R\bar{3}m$	-
B_2Nb	61 to 70.3	*hP*3	*P*6/*mmm*	AlB_2
B_3Nb_2	60	*oC*20	*Cmcm*	B_3V_2
B_4Nb_3	57.1	*oI*14	*Immm*	Ta_3B_4
B_6Nb_5	54.5	*oC**	*Cmmm*	-
NbB	48.8 to 50	*oC*8	*Cmcm*	CrB
B_2Nb_3	40	*tP*10	*P*4/*mbm*	Si_2U_3
(Nb)	0 to 2.0	*cI*2	$Im\bar{3}m$	W

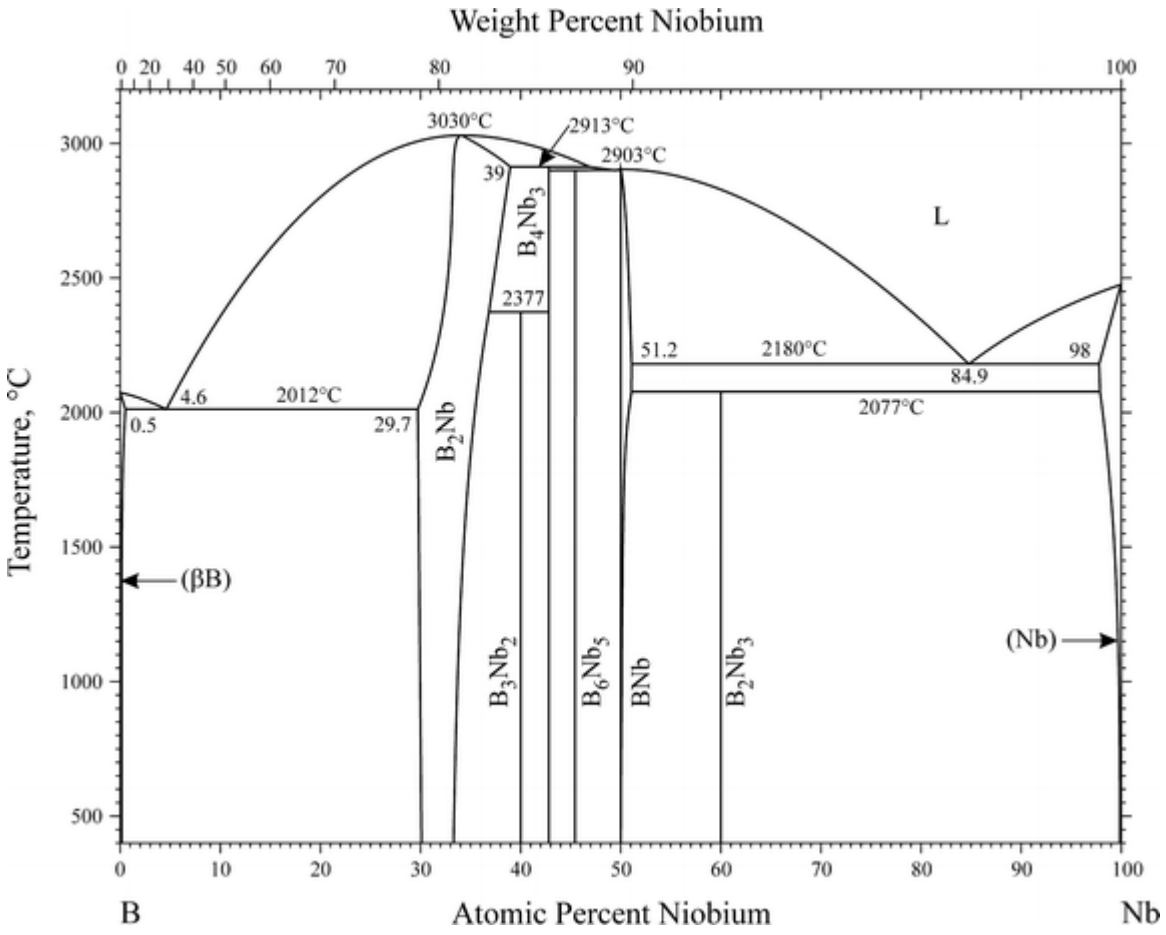

Figure 2.10) The Nb-B system phase diagram [66]. Redrawn by [65].

2.2.7 Nb-Ti-B

Early work on the Nb-Ti-B system performed by Kuz'ma [76] identified through experiments that there were no ternary phases and the two phases TiB_2 and NbB_2 existed in a continuous solid solution. Other phases incorporated into the ternary phase diagram at 1400°C were TiB, Nb_3B_4, NbB and Nb_3B_2. Later work by Borisov *et al* [77] could include phases since found in the binary systems, Nb_5B_6 and Ti_3B_4, for a more compete liquidus projection and <50 at.% B isothermal section at 1400°C, displayed in Figure 2.11 and Figure 2.12, respectively. Another important difference between these two proposed Nb-Ti-B systems is the solubility ranges of TiB and NbB. In [76] maximum solubility of Nb in TiB is given as 5 at.% and Ti in NbB is given as 30 at.%, at 1400°C. In [77] maximum solubility of Nb in TiB is given as 23 at.% and Ti in NbB is given as 15 at.%, at 1400°C. Additionally, the TiB-NbB-(Nb) three phase region is much closer to the Nb-B edge of the phase diagram in [77] to reflect the updated Nb/Ti solubility in TiB/NbB. Thermodynamic modelling [78][79] tends to agree with Borisov *et al*, so the latter values for Nb solubility in TiB and Ti solubility in NbB will be assumed to be approximately 23 at.% and 15 at.%, respectively, although there still exists uncertainty in this regard.

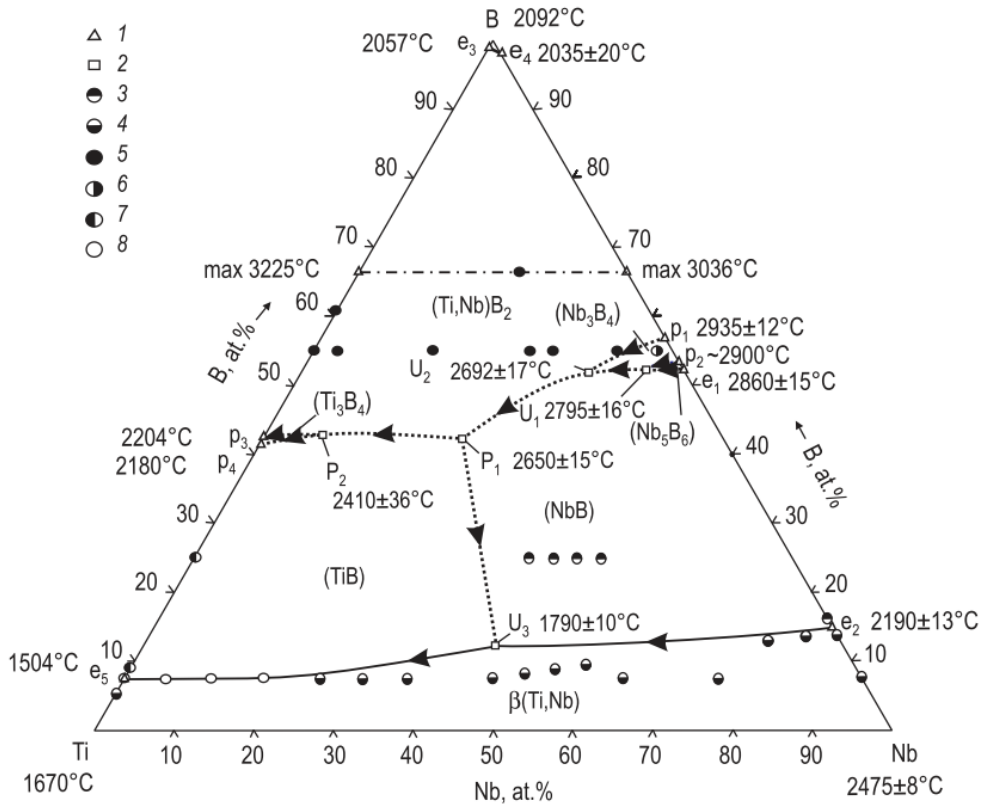

Figure 2.11) Liquidus projection of the Ti – Nb – B ternary system [77]

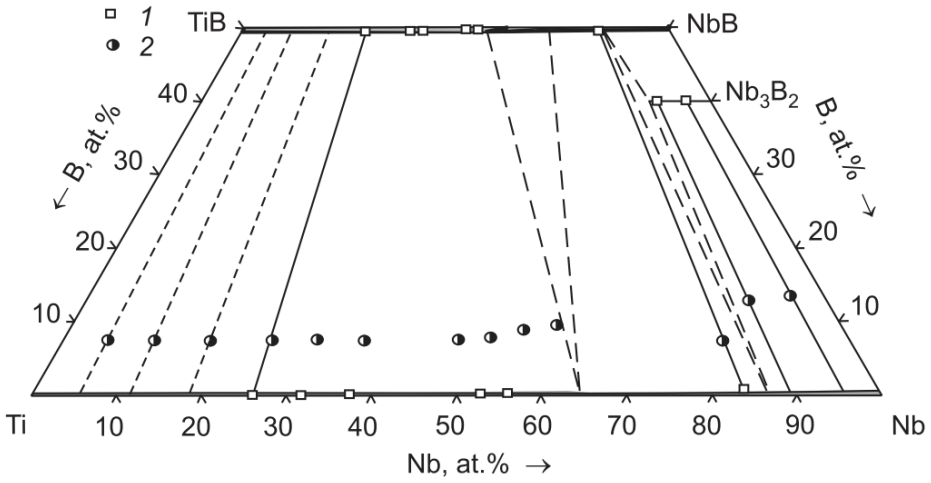

Figure 2.12) Isothermal section of the Ti – Nb – B ternary system at 1400°C [77]

2.2.8 Nb-Si-B

One of the first investigations published on the Nb-Si-B system was by Nowotny [80]. An isothermal projection was constructed at 1600°C based on XRD of powder mixtures (Figure 2.13). Two ternary phases were reported known as T2 and $D8_8$.

$D8_8$ has the hexagonal hP16 Mn_5Si_3-type crystal structure, which has the same crystal structure as meta stable phase γNb_5Si_3 from the Nb-Si binary system (Table 2.1), where B takes positions on interstitial sites; $Nb_5Si_3B_x$. T2 has the same crystal structure as αNb_5Si_3; tetragonal tI32 Cr_5B_3-type [80], and B substitutes for Silicon; $Nb_5(Si,B)_3$. In the case of αNb_5Si_3, the tetragonal tI32 Cr_5B_3-type unit cell is made up of 32 atoms, with 20 Nb atoms and 12 Si atoms. The Si atoms occupy Wyckoff positions 4a and 8h [81][82]. In the case of T2, B atoms substitute onto the 8h positions [83]. If modelled as 4 sublattices, $(Nb)_4(Nb)_1(Si)_2(Si)_1$ after full Si substitution with B on the 8h position would be $(Nb)_4(Nb)_1(B)_2(Si)_1$. T2 is now understood to have a stability range that extends to the Nb-Si edge where it meets αNb_5Si_3 in the Nb-Si binary system but is still conventionally referred to as a ternary phase in the literature. Throughout this current work αNb_5Si_3 will represent a phase absent of B, whereas T2 will refer to the boron containing silicide; $Nb_5(Si,B)_3$.

The 1600°C isothermal section by Nowotny [80] has a number of discrepancies that are now contradicted by the up to date binaries Nb-Si, Nb-B and Si-B . Most notably Nb_4Si has since been confirmed as metastable in the Nb-Si system [21], the existence of Nb_5B_6 and Nb_2B_3 were not known at the time (the latter of which is still not included in the present Nb-Si-B ternary models) and so are not included [73][75], and the phase 'T1' referred to in this current study as βNb_5Si_3 is not stable at 1600°C according to the current understanding of the Nb-Si system where as αNb_5Si_3 should be stable [32].

More recently, a 1700°C isothermal section of the Nb-rich side of the Nb-Si-B system was proposed by Nunes [84] based on experimental results of over 20 alloy compositions. This ternary phase diagram is given in Figure 2.14 and is in broad agreement with thermodynamic modelling by Sun [81] (Figure 2.15a). However Figure 2.14 was constructed based on the $Nb_3Si \rightleftharpoons (Nb) + \alpha Nb_5Si_3$ eutectoid reaction being below 1700°C in the Nb-Si binary, as was the case with the phase diagram presented in Figure 2.2 by Geng *et al* [32]. Whereas Figure 2.15a [81] was based on this reaction occurring at 1700°C or greater, hence the absence of the $(Nb) + Nb_3Si + \alpha Nb_5Si_3$ three phase region in [81]. The (Nb) + T2 region was found to be larger than originally reported by Nowotny and consequently the solubility range of B in T2 is expanded. In [84] its was found to be approximately 25.1% and in [81] its modelled as approximately 24.8 at.% at 1700°C showing good agreement. $D8_8$ is proposed to be a near stoichiometric phase in [84] based on the inability to produce a $D8_8$ single phase alloy. In [81] the $D8_8$ structure is modelled as $(Nb)_5(Si,B)_3(B,Va)$ where B is allowed to substitute onto Si sites, as well as interstitially, so the B range is given as approximately 10.8 at.% to 15.2 at.% (where Va is vacancy). In any case, both $D8_8$ and T2 have smaller Nb compositional ranges if any when compared to the investigation published by Nowotny [80]. The phases present in the 1700°C isothermal sections are given in Table 2.7.

The liquidus projection has been constructed based on experimental work by Pinto Júnior *et al* [85] based on nearly 40 alloys in the as-cast state (Figure 2.16a). The thermodynamic model by Sun *et al* [81] is in good agreement with this work. Six phase fields are reported to exist in the Nb > 60 at.% region: (Nb), NbB, Nb_3Si, βNb_5Si_3, T2 and $D8_8$. T2 does not extend to the Nb-B binary and the minimum amount of B content needed to stabilise this phase to form from the melt is <1 at.%, at Si content of ~19.5 at.%.

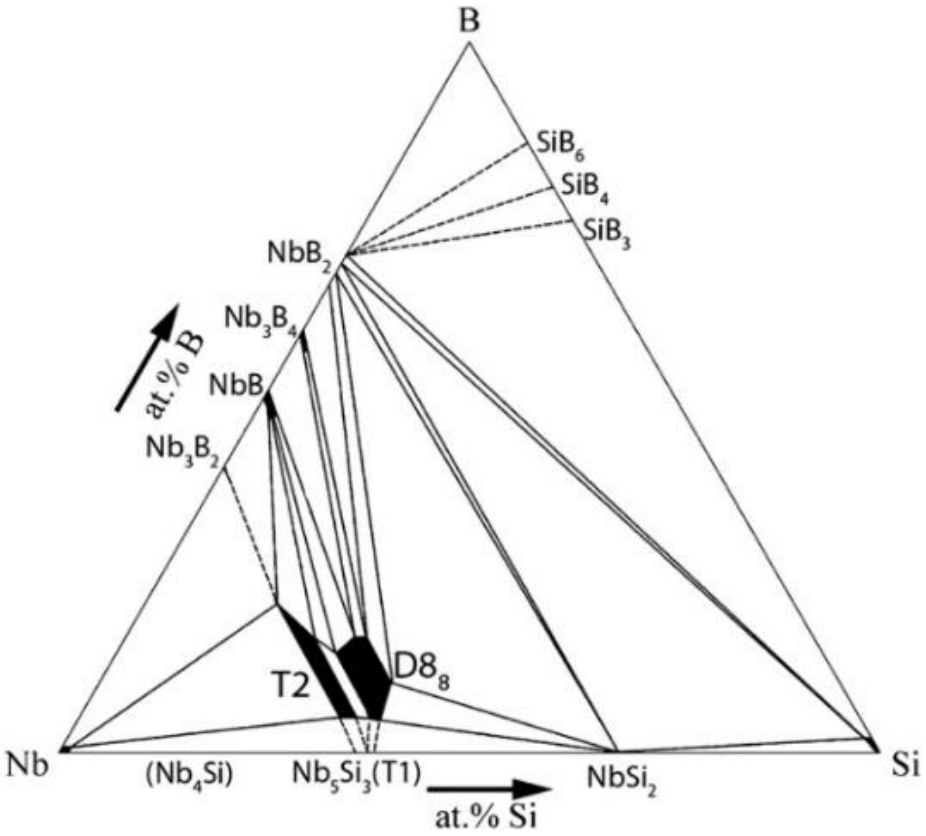

Figure 2.13) The Nb-Si-B system ternary phase diagram at 1600°C. [81] redrawn from [80]

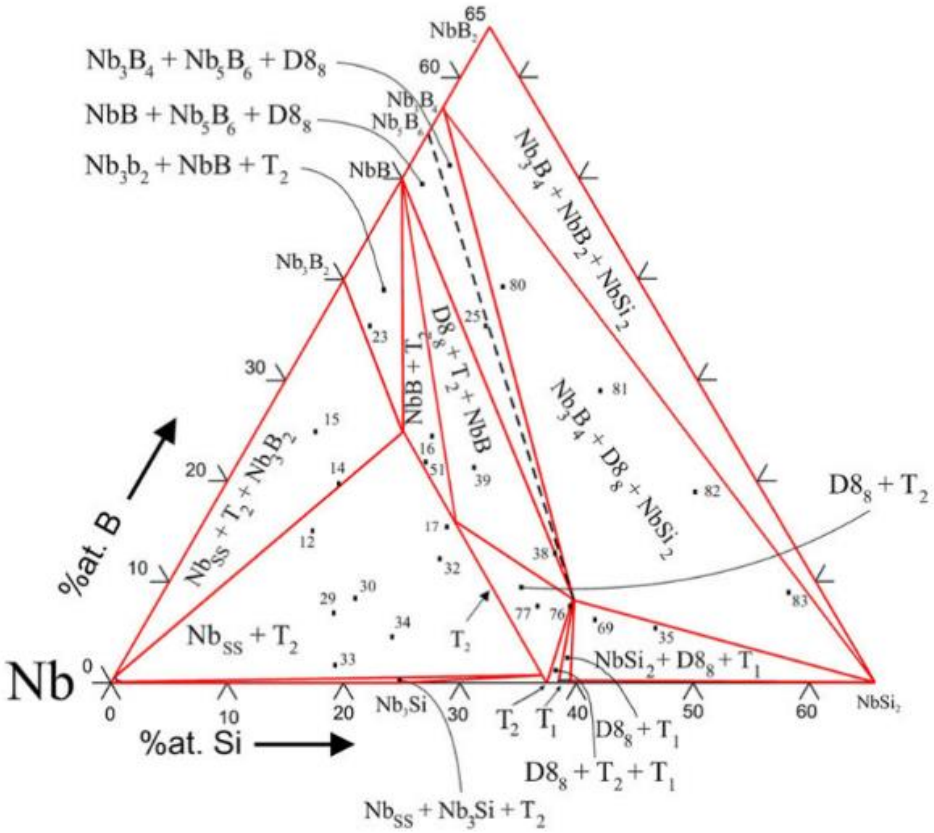

Figure 2.14) The Nb-Si-B system ternary phase diagram for Nb content >65 at.% at 1700°C [84]

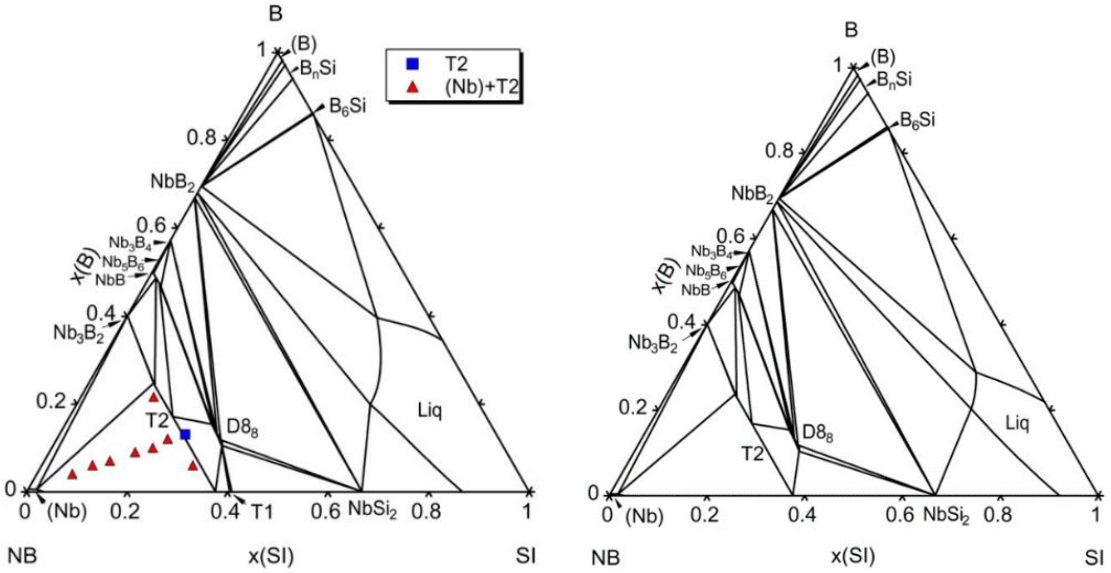

Figure 2.15a and b) The Nb-Si-B system ternary phase diagram at left a) 1700°C and right b) 1600°C [81].

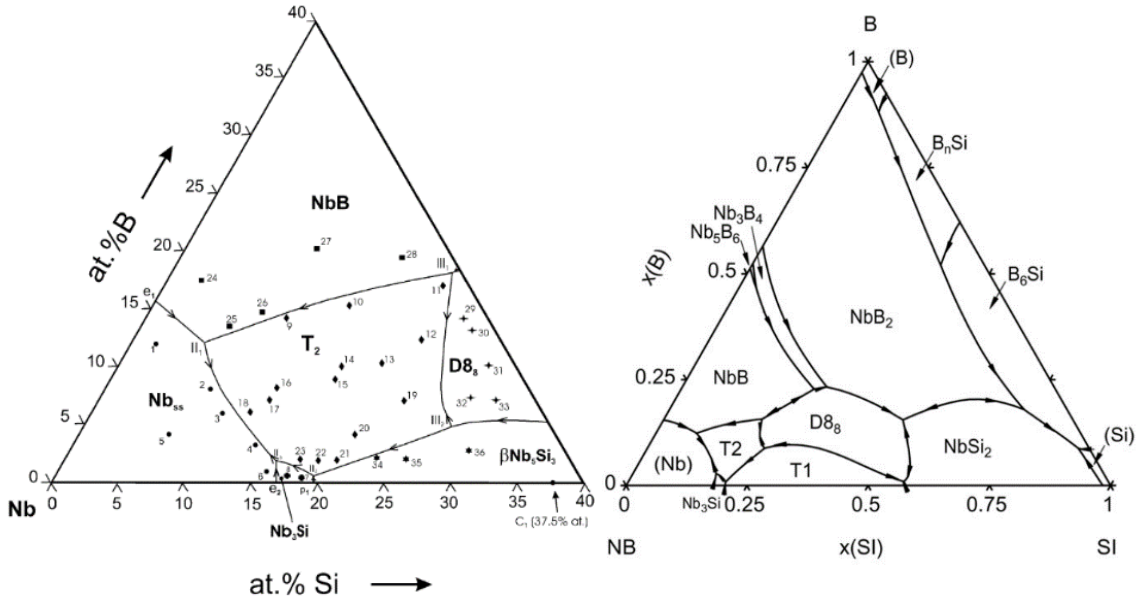

Figure 2.16a and b) The Nb-Si-B system liquidus projection, left a) experimentally constructed of the Nb rich region (Nb>60 at.%) from alloys of compositions marked on the diagram [85] and right b) modelled by [81] for the whole Nb-Si-Si region.

Table 2.7) Nb-Si-B crystal structure data. [17][65] **1 P6222 and *2 Cr_5B_3 according to* [33]

Phase	Pearson symbol	Space group	Prototype structure
(Nb)	cI2	$Im\bar{3}m$	W
T2 – $Nb_5(SiB)_3$	tI32	I4/mcm	Cr_5Si_3 *2
βNb_5Si_3	tI32	I4/mcm	W_5Si_3
$D8_8$ – $Nb_5Si_3B_x$	hP16	$P6_3/mcm$	Mn_5Si_3
$NbSi_2$	hP9	$P6_422$ *1	$CrSi_2$
Nb_3Si	tP32	$P4_2/n$	Ti_3P
Nb_3B_2	*tP*10	*P*4/*mbm*	Si_2U_3
NbB	*oC*8	*Cmcm*	CrB
Nb_5B_6	*oC**	*Cmmm*	-
Nb_3B_4	*oI*14	*Immm*	Ta_3B_4
NbB_2	*hP*3	*P*6/*mmm*	AlB_2

2.2.9 Nb-Ge

The Nb-Ge system consists of 5 solid phases; Cubic Cr_3Si-type Nb_3Ge, tetragonal W_5Si_3-type Nb_5Ge_3 and hexagonal $CrSi_2$-Type $NbGe_2$ intermetallics, as well as BCC W-type solid solution (Nb) and diamond C-type (Ge) [86]. These are listed with their crystal structures in Table 2.8. The maximum solubility of Ge in (Nb) is 11 at.% at 1902°C, considerably larger than that of Si maximum solubility in (Nb) at 3.5 at.%. There is some disagreement in the literature as to whether a) the Nb_5Ge_3 phase has the W_5Si_3 or Cr_5B_3 prototype-structure, and b) there exists a Nb_3Ge_2 phase with the same Mn_5Si_3-type structure as $D8_8$ in the Nb-Si-B ternary system, also known as hexagonal Nb_5Ge_3, $Nb_{10}Ge_7$, $NbGe_{0.67}$ or $Nb_5Ge_{3.5}$, or if this phase is metastable.

The original phase diagram by Pan *et al* [87], as well as the later constructed diagram by Okamoto [88], identifies the tI32 Nb_5Si_3 phase as having prototype structure Cr_5B_3. This structure is also seen in the Nb-Si binary in the low temperature αNb_5Si_3. However other sources list the tI32 Nb_5Si_3 phase as having the W_5Si_3 prototype structure [89][90][91], seen in the Nb-Si binary in the high temperature βNb_5Si_3.

More recently the system has been investigated by Utton *et al* and Papadimitriou *et al* [86][92]. The constructed phase diagram from these studies is given in Figure 2.17. The tI32 Nb_5Ge_3 phase is assessed to have the W_5Si_3 prototype structure based on first-principles calculations, having a more negative enthalpy of formation of −46.63 kJ/mol compared to the calculated value for a Cr_5B_3-type structure equal to −46.53 kJ/mol at 0 K. However, Colinet [93] also calculated enthalpy of formation for the Nb-Ge system later and found the reverse to be true, with the Cr_5B_3-type structure having a lower enthalpy of formation. The difference in calculations is not accounted for in their study, although different calculation parameters and software were used. However, the calculated values for ΔH in both studies are close, which could suggest that phases may be stabilised by impurities, explaining discrepancies in experimental studies. In this current work the W_5Si_3-type structure will be considered to be the stable Nb_5Ge_3 phase as this is in agreement with the Nb-Si-Ge ternary system discussed in the following section.

In regards to the existence of Nb_3Ge_2, both sources [92][93] agree that this is a metastable phase, existing above the convex hull of the enthalpy of formation against composition diagrams, displayed in Figure 2.18 at 500K. Although the original phase diagram presented by Pan *et al* [87] included this phase, experimental work performed after concluded the Mn_5Si_3-type structure of Nb_3Ge_2 is indeed metastable, with which the modelling mentioned previously is in agreement with [94][90]. In this current study Nb_3Ge_2 will be assumed to be metastable in the Nb-Ge binary. However, it should be

noted that the phase may be stabilised by impurities such as boron, carbon and oxygen. Lastly, an argument for the existence of an equilibrium stable Nb_3Ge_2 phase presented in [95] should be noted, in which multiple alloys were manufactured with Nb_3Ge_2 present. In [95] it is proposed that the volatilisation of Ge during heat treatments conducted in other experimental studies of the Nb-Ge binary system results in a shift in composition towards the niobium-rich end of the phase diagram and consequently moving from the Mn_5Si_3-type Nb_3Ge_2 single phase region into the W_5Si_3-type Nb_5Si_3 region. This potential phenomenon may not prove the existence of a stable Nb_3Ge_2 phase as it is contradicted by the studies referenced above, but should be considered in later sections regarding heat treatment of alloys and the Mn_5Si_3-type $D8_8$ phase.

Table 2.8) Nb-Ge crystal structure data [86][88]. ** from* [87].

Phase	Composition (at.% Ge)	Pearson symbol	Space group	Prototype structure
Nb_3Ge	18 to 23	cP8	$Pm\bar{3}n$	Cr_3Si
Nb_5Ge_3	37 to 39	tI32	I4/mcm	W_5Si_3
$NbGe_2$	66 to 67	hP9	$P6_222$	$CrSi_2$
(Nb)	0 to 11	cI2	$Im\bar{3}m$	W
(Ge)	100	cF8	$Fd\bar{3}m$	C (diamond)
Nb_3Ge_2	40-43*	hP16	$P6_3/mcm$	Mn_5Si_3

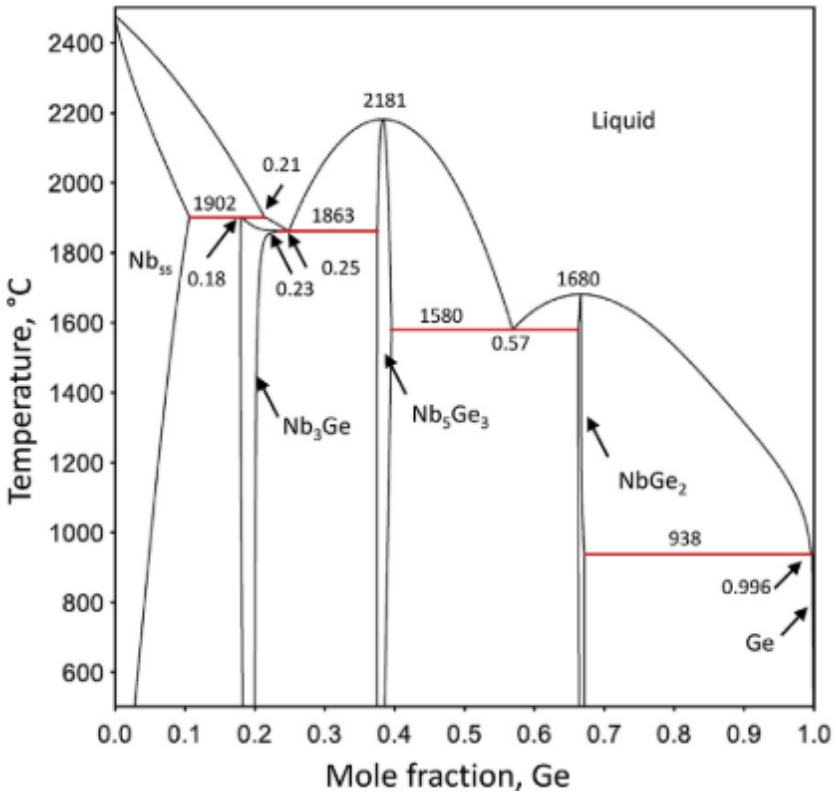

Figure 2.17) The Nb-Ge system phase diagram. [86]

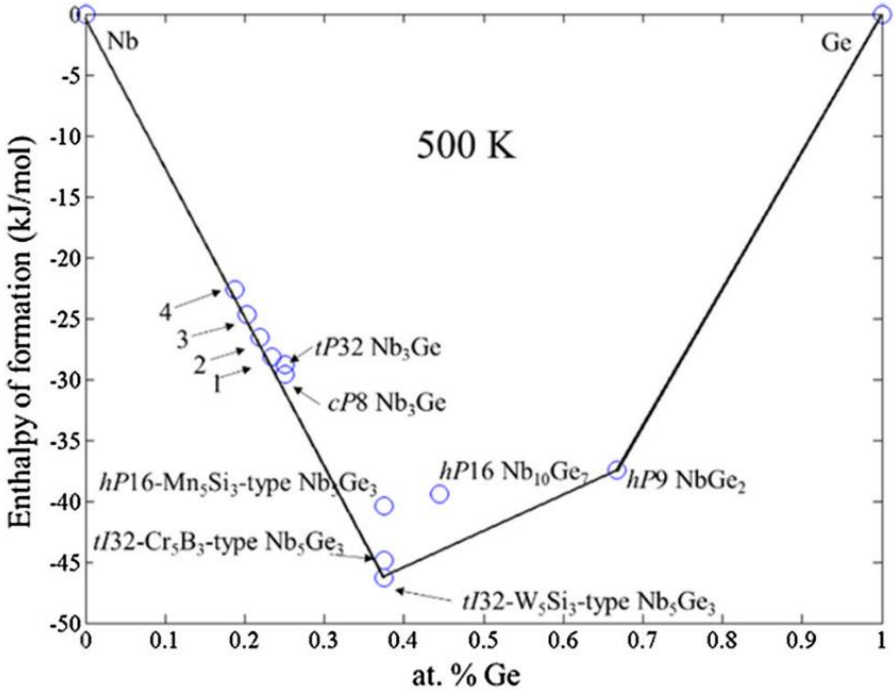

Figure 2.18) The Convex hull (solid lines) of the Nb-Ge system. Phases (blue circles) that are plotted above the Convex hull are considered metastable at this temperature (500 K) [86]

2.2.10 Nb-Si-Ge

There are no ternary compounds present in ternary Nb-Si-Ge system according to the most recent understanding of this system as well as constituent binary systems. As such the phases present are listed in Table 2.1 and Table 2.8 described in the Nb-Si and Nb-Ge phase diagrams, respectively. There is limited data in the literature regarding the Nb-Si-Ge ternary system. Recently an experimental and thermodynamic assessment of the system was undertaken by Utton *et al* which will be the primary source for this system [86]. Using the CALPHAD method isothermal sections of the system were described. Calculated isothermal sections at 1200°C, 1500°C and 1820°C are included in Figure 2.19, Figure 2.20, and Figure 2.21. In addition, several alloys were made with Nb content equal to 62.5 at.% and variable Ge/Si content in order to study the pseudo binary between βNb_5Si_3 and Nb_5Ge_3. Whilst the alloys made by Utton *et al* matched well with the modelled system, ternary alloys from an external source [96] could not be fully integrated to the model. Pan *et al* constructed isothermal sections of the Nb rich corner of the ternary system [97][98]. The model generally agrees with the experimental data from Pan *et al*, however these are limited by the inaccurate binary systems available at the time.

The high temperature tetragonal W_5Si_3-type βNb_5Si_3 and the similar tetragonal W_5Si_3-type Nb_5Ge_3 are modelled as isomorphs with stability ranges extending completely from the Nb-Si binary to the Nb-Ge binary at temperatures greater than 1648°C. At lower temperatures where in the Nb-Si binary βNb_5Si_3 would not be stable, Ge additions stabilise this phase significantly. Hexagonal $CrSi_2$-type $NbSi_2$ and Hexagonal $CrSi_2$-type $NbGe_2$ are also considered isomorphous and are stable from room temperature to the melting points, which is reduced with increasing Ge content. The 3-1 configurations, the tetragonal Ti_3P-type Nb_3Si and the cubic Cr_3Si-type Nb_3Ge, are not isomorphous and do not share a two or three phase region.

There is complete solid solubility between βNb_5Si_3 and Nb_5Ge_3 above 1934°C for stoichiometric $Nb_5(Ge,Si)_3$ composition, and for non-stoichiometric composition this solid solubility would extend down to 1648°C, where βNb_5Si_3 is no longer stable in the Nb-Si binary. At the lowest temperature considered in [86], 1200°C, single phase $Nb_5(Ge,Si)_3$ could accommodate between approximately 5 at.% and 41 at.% Ge, and 0 at.% to 35 at.% Si. Conversely, the αNb_5Si_3 only has maximum solubility of Ge of approximately 13 at.%. At 1820°C this is reduced according to the phase diagram (Figure 2.21).

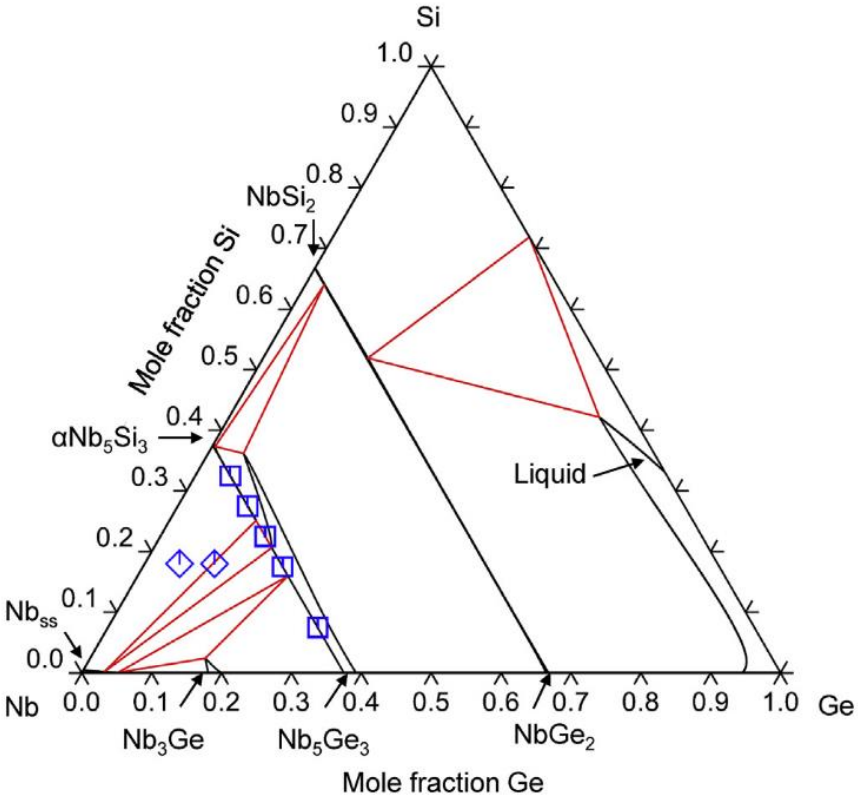

Figure 2.19) Nb-Si-Ge isothermal section at 1200°C [86]. Blue squares denote alloy compositions made by Utton et al. Blue diamonds are made by [96]

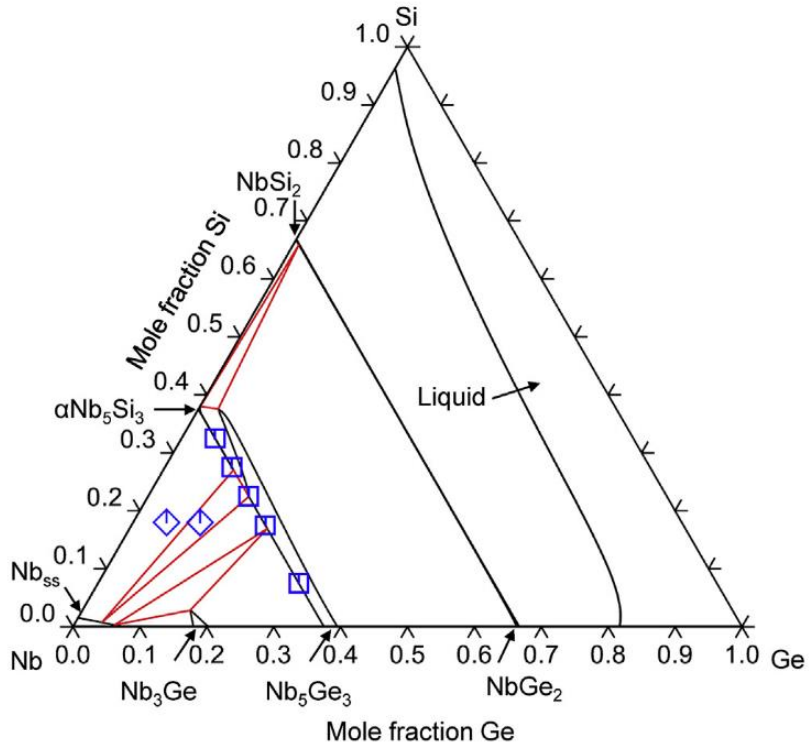

Figure 2.20) Nb-Si-Ge isothermal section at 1500°C [86]. Blue squares denote alloy compositions made by Utton et al. Blue diamonds are made by [96]

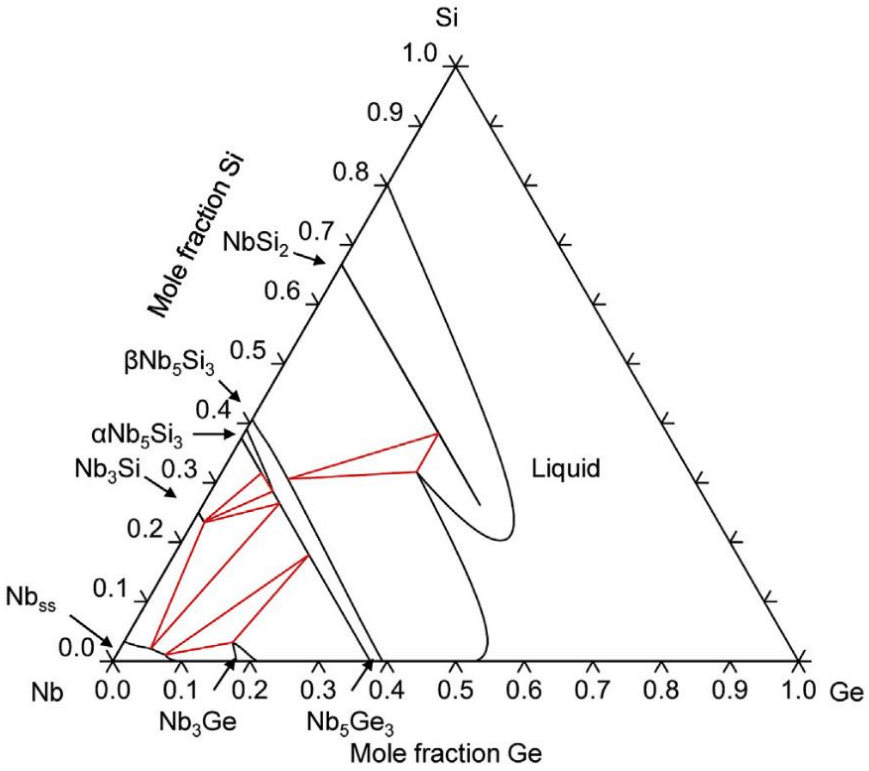

Figure 2.21) Nb-Si-Ge isothermal section at 1820°C [86].

2.3 Mechanical properties

2.3.1 Mechanical properties of Nb-Si alloys

Niobium silicide-based alloys received interest due to their high melting temperature but also mechanical properties where fracture toughness, creep resistance and high temperature strength are of vital importance to the application as turbine blades and disks [5]. The binary Nb-Si system was found to have potential in terms of fracture toughness and strength when the intermetallic phase was strengthened by the (Nb) solid solution phase [99]. These properties could be improved by significant margins by hot extrusion and grain refinement to take room temperature strength and fracture toughness from 334 MPa to 1344 MPa and 11 MPa.m$^{0.5}$ to 27 MPa.m$^{0.5}$, respectively, for a (Nb) + Nb_3Si alloy [100]. Fracture is mainly controlled by the more brittle silicide failure, so refinement of this phase and interspersion with (Nb) is beneficial in (Nb) + Nb_5Si_3/Nb_3Si [101][102][103]. An increase in Si content and subsequent decrease in dendritic (Nb) volume fraction in the binary has been shown to result in fracture toughness degradation from 14.2 MPa.m$^{0.5}$ to as low as 5.8 MPa.m$^{0.5}$ in the (Nb) + Nb_3Si system with Si content 10 at.% and 18 at.%, respectively [28].

In past research the goal of alloy fracture toughness was deemed to be 20 MPa.m$^{0.5}$, considered the minimum value to provide damage tolerance for critical components by Bewlay *et al* [104][5]. Adequate fracture toughness has been achieved in higher order systems containing Ti,Hf,Cr,Al [105]. As the solid solution phase is critical to fracture toughness, its composition should be considered. Research into the Si content of the (Nb) phase in relation to mechanical properties is limited, but one study [106] found fracture toughness is negatively effected by any Si solute present in the solid solution, reducing by over half for Si = 0 at.% to Si = 0.5, 0.8 and 1.0 at.%. This decrease is mitigated partially by grain refinement of (Nb) in the microstructure as a result of Si additions. In earlier work the reduction in Si content in (Nb) is attributed to an improvement in bending properties of a Nb-10Si alloy [102].

The creep resistance goal outlined by Bewlay *et al* [101] and since designed towards [107] was to have a secondary creep rate under 2.2E10-8 s^{-1} at 1200^{o}C and 170 MPa. The single phase Nb_5Si_3 has been demonstrated to have sufficient creep properties [108], and the Nb-16Si binary alloy has been shown to have promising creep rates at 140 MPa and 210 MPa, 1.5E10-8 and 4.9E10-8 s^{-1}, respectively [105]. However, alloying additions often diminish the creep properties, especially titanium when the hP16 Ti_5Si_3 phase is stabilised which is detrimental to creep rate. In a silicide and (Nb) dual phase alloy the αNb_5Si_3 and βNb_5Si_3 phases are the preferred silicide due to superior creep resistance compared to Nb_3Si and especially γNb_5Si_3 [109]. Hence the Ti content of alloys in development at present is usually kept below 24 at.% in order to avoid detrimental phases. On the other hand, an investigation into the relationship between Si content, and consequently silicide volume fraction, and optimised creep performance was conducted by Bewlay [105] *et al*. It was shown that in quaternary Nb-Si-Ti-Hf alloys the optimal Si content was 18 at.%, resulting in a silicide volume fraction of ~70%, for which a creep rate <2.2E10-8 s^{-1} was reported (Figure 2.22).

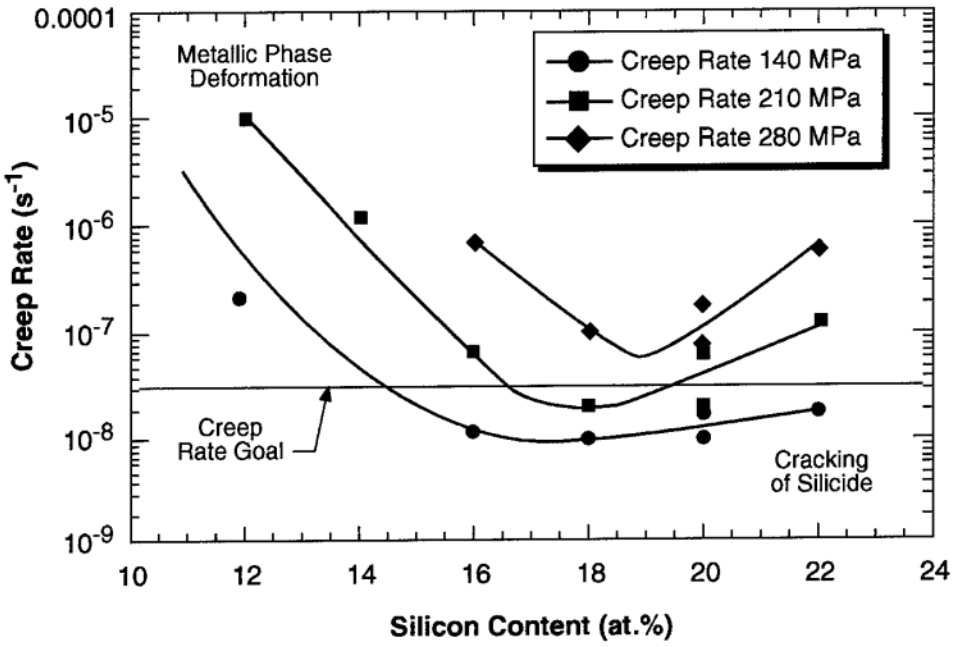

Figure 2.22) The creep rate variation with Si content of Nb-8Hf-25Ti-XSi alloys, and consequently silicide volume fraction, at 140 MPa, 210 MPa, and 280 MPa stress [105].

2.3.2 The effect of alloying additions Ti, Cr, Al, Ge and B on the mechanical properties of Nb-Si alloys

Titanium additions into the binary Nb-Si alloy were found experimentally to improve fracture toughness as Ti containing (Nb) is proposed to have higher intrinsic ductility [110], but for Ti contents between 21 at.% and 33 at.% no systematic improvement was noted as a range of values are reported for varied Ti content. Al potentially leads to increased fracture toughness though a similar mechanism as well [111], however microstructural difference between samples are not taken into account. It is often difficult to separate microstructural phenomena from the effect of altered phase composition. Ti partitioning into the silicide phase (Nb_5Si_3) may also aid fracture toughness of the alloy as a whole [112]. Modelling by Chan [113] based on the surface energy and the Peierls–Nabarro (P–N) barrier energy predicts Ti to increase fracture toughness and Al and Cr to decrease fracture toughness in Nb-Ti-Cr-Al solid solutions, so effectively the (Nb) phase in a niobium silicide-based alloy, but how this relates to a microstructure containing the silicide phase is not modelled. An example of complications arising from alloying additions to the (Nb) is how the laves phase forms as a result of Cr additions. This phase has poor intrinsic fracture toughness of approximately 1 $MPa.m^{0.5}$, and can act as the initiation sites for failure before transferring into the more integral silicide phase for continued propagation [112].

Despite this, the fracture toughness goal has been approached and achieved in alloys containing Al, Cr and Ti additions [9]. An alloy known as MASC (Nb-24.7Ti-8.2Hf-2.0Cr-1.9Al-16Si, compositions presented in this way are in atomic percent unless otherwise stated) has received interest in the past as a promising balance of mechanical properties was achieved whilst containing elements that are beneficial for oxidation resistance, Cr and Al [114]. The Cr and Al additions in this case, as well as Ti and Hf, improve tensile strength as well through solid solution strengthening and increasing the volume fraction and size of eutectic cells [115].

Significant Ti additions reduce creep resistance at high temperature (1200°C) owing to the formation of hP16 Ti_5Si_3, an effect which is exacerbated at stresses > 210 MPa [104]. Some degree of alloying additions can be tolerated [116], but empirical relationships are difficult to formulate based on the current information given the varied microstructures that are produced through as-cast ingots, directional solidification and extrusion [117]. Alloys Nb-8Hf-25Ti-16Si and Nb-8Hf-25Ti-2Al-2Cr-16Si can be compared with creep rates of 6.3E-09 s^{-1} and 9.1E-08 s^{-1} at 1200°C and 70 MPa, respectively, and 2.3E-08 s^{-1} and failure at 1200°C and 140 MPa, respectively, in order to experimentally show the potential negative effect Al and Cr have on creep rates in higher order alloys [105].

Tsakiropoulos [118][107] has systematically assessed a large volume of data on niobium silicide-based alloys and related mechanical properties, such as hardness, creep, coefficient of thermal expansion anisotropy and Young's modulus, to intrinsic composition based properties, such as composition weighted differences in electronegativity (Δ_χ) and an average valence electron concentration (VEC). Here an increased VEC of the silicide phase was linked to a lower creep rate, hypothesised to be due to a higher VEC being related to a greater degree of covalent bonding, and as such reduced freedom of dislocations. Generally, Cr, Ti, Al and B reduce the VEC parameter, and in turn would increase creep rate which is in agreement with what was found in early experimental work. Germanium substitution for silicon on the other hand results in increased VEC, and therefore it could be estimated that Ge is beneficial for creep resistance, although to the authors knowledge this has not been conducted experimentally. For the previously discussed models [113][107], intrinsic fracture toughness as a result of B and Ge additions is as yet to be explored. Experimentally limited data is available, but Ge + Si partitioning into the Laves phase has been shown to promote the transition of C15 (Pearson symbol: cF24, space group: $Fd\bar{3}m$) to C14 (Pearson symbol: hP12, space group: $P6_3/mmc$) with improved intrinsic fracture toughness of 2 to 5 $MPam^{0.5}$ compared to approximately 1 $MPam^{0.5}$ [112] as a result of lower energy barrier slip planes. This benefit could translate to multiphase alloys. And finally, an investigation into the high temperature compressive strength (1250°C) and room temperature fracture toughness of B and Ge additions into a base alloy of composition Nb-22Ti-12Si showed improvement was possible using these elements [119]. For fracture toughness initially additions (3 at.% Ge, 0.1, 0.5, 1.0 at.% B) resulted in marginally worse values, but large amounts (6 at.% Ge, 3 at.% B) saw improvements of 18.5% and 22.3%, respectively. For compressive strength, 6 at.% Ge resulted in a 88.2% increase and 0.1 at.% B resulted in a 45.7% increase, although 3 at.% B actually saw a slight reduction in compressive strength. The improvements seen due to 6 at.% Ge is likely a result of βNb_5Si_3 being stabilised as opposed to the standard Nb_3Si in these hypoeutectic alloys, which has superior mechanical properties to the Nb_3Si phase. In the case of boron, solid solution strengthening was proposed to be taking place, resulting in the higher compressive strength, but again the fracture toughness is attributed to large refined areas of microstructure consisting of fine silicide and solid solution which aid in deflection of cracks for the improved fracture toughness seen. This highlights the difficulty in quantification and trend fitting of mechanical properties, given the wide array of microstructural, compositional and phase changes that occur though alloying additions into multicomponent systems.

2.4 Oxidation

2.4.1 Oxidation of niobium silicide-based alloys

In the case of typical nickel-based superalloys, the passivating oxide layer that forms is primarily of Al_2O_3 or Cr_2O_3 [120]. The silicide refractory system has received interest for the possibility of a passivating SiO_2 oxide layer forming during oxidation, as well as suitable high temperature mechanical properties. SiO_2 and Al_2O_3 have high thermodynamic stability, with Al_2O_3 having superior thermodynamic stability. However, the growth rate of SiO_2 is slower than that of Al_2O_3 above 1000°C, so SiO_2 forming materials offer potentially superior oxidation resistance at high temperature [121].

In niobium silicide-based alloys with a silicide and a solid solution phase, the preferential oxidation of (Nb) and rapid formation of Nb_2O_5 have limited their oxidation resistance. The rapid formation of Nb_2O_5 on niobium silicide-based alloys prevents a continuous SiO_2 layer from forming [122][123]. Nb_2O_5 is not protective and compared to SiO_2 has higher molecular diffusivity of oxygen [124]. Therefore, oxidation resistance remains a limitation of niobium silicide-based alloys. A number of alloying additions have been investigated to improve oxidation resistance [125][126][127][128][129][130][131]. In this current work, Ti, Cr, Al, Ge and B are of particular interest and will be discussed in more detail.

2.4.2 Oxidation kinetics

Rates of oxidation of complex niobium silicide-based alloy systems can be considered in terms of linear and parabolic oxidation kinetics. Equations (1) and (2) describe linear and parabolic rates of oxidation, respectively [132], where *mg* is mass gain due to oxidation, *S* is surface area of the sample, *t* is time, *K* is oxidation rate and *l* and *p* denote linear or parabolic kinetics, respectively. These are applied to thermogravimetric experiments where normalised mass gain is plotted against time, and temperature is kept constant, i.e. isothermal oxidation rather than cyclic oxidation tests.

Over periods of time on the scale of 100 hours, graphs of oxidation can often be best described in separated sections where linear or parabolic behaviour may act over a certain period of time, but not the entire time of the experiment [133]. This may be a period of rapid, linear oxidation initially and then, after an oxide scale has built up sufficiently parabolic behaviour, limited primarily by diffusion though the oxide scale, takes over. Alternatively, parabolic behaviour could be seen for the beginning of the experiment, but later a linear rate of oxidation better models the mass gain over time. This could occur due to the oxide layer becoming non-protective, micro-cracking of said layer exposing new unoxidised materials continuously, or the rate limiting step of solid state oxide reactions becoming more relevant to oxidation kinetics.

The linear and parabolic rates calculated in previous studies are not full descriptions of the oxidation regime of these alloys, but allow for comparison between niobium silicide-based alloys. This is especially useful as alloying compositions can vary drastically. Parabolic oxidation behaviour is preferred to linear, as this implies some degree of passivating oxide layer has formed which over longer periods of time would extend the service life of components. Equation (3) [132] can be used to model the whole oxidation graph and assess the degree to which the oxidation behaviour is parabolic in nature through the *n* exponent [134][121][124][135]. An *n* exponent value of 1 transforms the equation in to the linear rate equation, and an *n* exponent of 0.5 transforms the equation in to the parabolic rate equation.

$$\frac{mg}{S} = k_l t \qquad (1)$$

$$\frac{mg}{S} = (k_p t)^{0.5} \qquad (2)$$

$$\frac{mg}{S} = (kt)^n \qquad (3)$$

2.4.3 Pesting phenomena

Niobium silicide-based alloys can also suffer from a phenomena known as 'pest' oxidation, where intermediate temperatures result in catastrophic oxidation, resulting in samples being reduced to a powder [126][136][128][137]. Refractory silicides, and other intermetallics, have been shown to pest at temperatures <1000°C [138][139]. Although early studies of single phase Nb_5Si_3 noted "pest-like behaviour" up to 1200°C [140].

Pesting of Mo-silicide materials has been more thoroughly investigated than the niobium equivalent [141]. An early proposed model by Westbrook and Wood [138] for the general pesting phenomena highlighted the importance of grain boundary embrittlement due to oxidation. Pesting was deemed to occur due to preferential oxidation of grain boundaries which results in grain boundary hardening and voluminous expansion of oxide products. This causes internal stresses, and the insufficient plasticity of the hard, brittle, intermetallic phases to accommodate such stresses results in fracture and micro-cracks. This process is repeated, exposing new material to oxidise continuously, until a fine powder of oxidised material is produced. At low temperatures, diffusion of oxygen along grain boundaries is limited so oxidation occurs mostly at the surface of the material. At high temperatures, embrittlement of grain boundaries is limited as intragranular diffusion of O can take place, and the stresses developed are somewhat alleviated by the high temperature [138]. Therefore, an intermediate temperature range exists for materials susceptible to pesting.

2.4.4 The addition of Ti

Titanium is a common alloying addition in Nb-Si alloys as not only does it improve mechanical properties as mentioned previously, but also results in improved oxidation resistance. The solid solution phase has wide solubility for Ti [34] (Figure 2.3), and the susceptibility to oxidation is reduced as a result of Ti substitution [142]. This is a result of a reduced oxygen diffusivity through the (Nb) phase. Substitution of metallic elements into pure (Nb) have been shown to reduce oxygen diffusion [143][144], and [107] calculated 25 at.% Ti into the (Nb) phase to reduce oxygen diffusivity by a factor of 20. It is unclear how Si content in the (Nb) phase affects O diffusivity. Solubility is low (Table 2.1), but [145] comments that a small amount of Si may still reduce unit cell volume of (Nb) given its strong covalent bonding. It is feasible that a reduced unit cell could restrict O diffusion through the interstitial octahedral sites of (Nb). A phase with a higher diffusivity of oxygen is likely more susceptible to oxidation, as oxidation rate is partly related to the diffusivity of oxygen into the material [146].

Studies of niobium silicide-based alloy also show improvement to oxidation resistance when Ti is included. In [147][136] a 70% reduction in linear oxidation rate at 800°C was reported on the addition of 24 at.% Ti into an alloy with composition Nb–18Si–5Al–5Cr–5Mo, despite pest oxidation still occurring. In [124] Nb-Si alloys also containing Mo were shown to have total mass gains consistently reduced upon the addition of Ti for experiments performed at 1000°C, 1100°C and 1200°C. In earlier experiments concerning systems with less complexity, [111] reported Ti additions to a binary Nb-Si alloy reduce the metal recession rate during cyclic oxidation experiments by a

factor of ten at 1200°C. This effect is again partly prescribed to a reduction in oxygen penetration depth in the solid solution phase, a 60% reduction, related to the oxygen diffusivity through (Nb). [110][111] [140] are in agreement with this conclusion regarding Ti improvements to oxidation resistance.

The oxidation products of the Nb-Si binary alloys are usually Nb_2O_5 and SiO_2. In Ti containing alloys, monoclinic titanium niobates $Ti_2Nb_{10}O_{29}$ (Pearson symbol mC82, space group A2/m) and $TiNb_2O_7$ (Pearson symbol mC60, space group I2/m) form. Felton [148] reported $TiNb_2O_7$ forming at temperatures above 1000°C according to Equation (4), whereas the lower temperature titanium niobate, $Ti_2Nb_{10}O_{29}$, forms below this. These titanium niobate oxides have not been found to form a protective oxide layer [136].

$$3TiO_2 + Ti_2Nb_{10}O_{29} = 5TiNb_2O_7 \quad (4)$$

$$5Nb_2O_5 + 2TiO_2 = Ti_2Nb_{10}O_{29} \quad (5)$$

2.4.5 The addition of Cr

Cr additions are widely accepted to improve oxidation resistance of niobium silicide-based alloys, primarily due to the formation of Laves type phases which promotes the growth of $CrNbO_4$ upon oxidation. The formation of the Laves phase $NbCr_2$ has been shown to improve oxidation resistance at high temperature (1204°C and 1316°C) [104]. Figure 2.23 shows the material loss due to spallation of the oxide scales, and how a significant volume fraction of $NbCr_2$ reduces this loss. In alloys oxidised at 1250°C containing Ti, Zr and Cr, alloys with higher Cr content (5 vs 10 at.%) resulted in reductions in parabolic oxidation rate constants between 25% and 42% [149]. In an alloys with composition Nb–22Ti–16Si–3Al–2B with and without 4 at.% Hf present, 5 at.% Cr reduced the total mass gain after oxidation at 1250°C for 50 hours from 100.4 to 86.6 mg/cm^2 and 133.7 to 90.5 mg/cm^2, respectively [150]. In alloys containing Nb-Si-Ti-Hf-Al-Cr, an increased Cr (and Al) content results in a shift of mixed parabolic-linear oxidation kinetics to parabolic oxidation kinetics as well as reduced mass gain [151]. In each of these cases the improvement is associated with a combination of the $CrNbO_4$ oxide formation which although non-protective slows the rate of diffusion of oxygen into the bulk of the alloy more so than Nb_2O_5, development of a more continuous, thinner and denser oxide scale (i.e. with fewer visible pores/voids) as a result of $CrNbO_4$, and less internal stresses within the oxide scale as a result of $CrNbO_4$ having less voluminous expansion from the original metallic phases compared to Nb_2O_5. In addition, it is often the case that laves volume fraction comes at the expense of the susceptible to oxidation (Nb) phase, hence a general reduction in mass gain is seen. However, at the lower temperature of 800°C, [128] reports that the oxide scale of Cr containing Nb-Ti-Si alloys are less adherent due to cracking than Cr-free counterparts. Whilst certainly an improvement on the ternary alloy Nb–24Ti–18Si (see Figure 2.24), Cr is perhaps less effective at reducing mass gain and providing an adherent scale than the equivalent amount of Al according to this study [128].

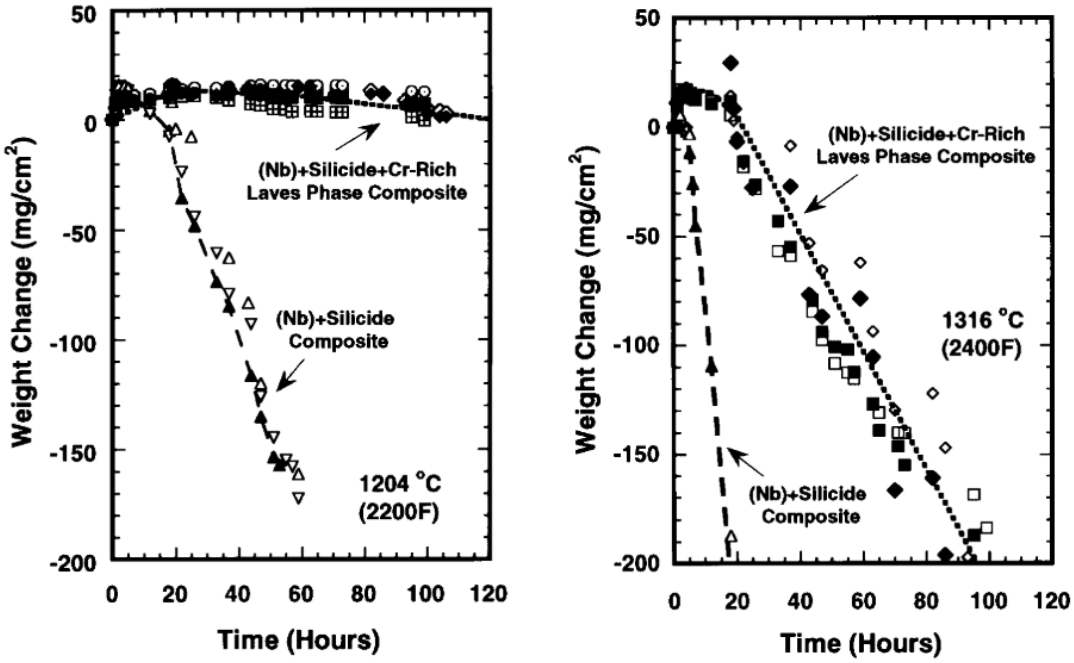

Figure 2.23) Comparison of MASC alloy ((Nb)+Silicide Composite) and alloys with composition Nb-18Ti-7Hf-20Cr-2Al-18Si ((Nb)+Silicide+Cr-rich Laves Phase Composite) at temperatures 1204°C (a) and 1316°C (b). The higher Cr concentration in Nb-18Ti-7Hf-20Cr-2Al-18Si leads to stabilization of a Laves phase, and superior resistance to oxidation. [104]

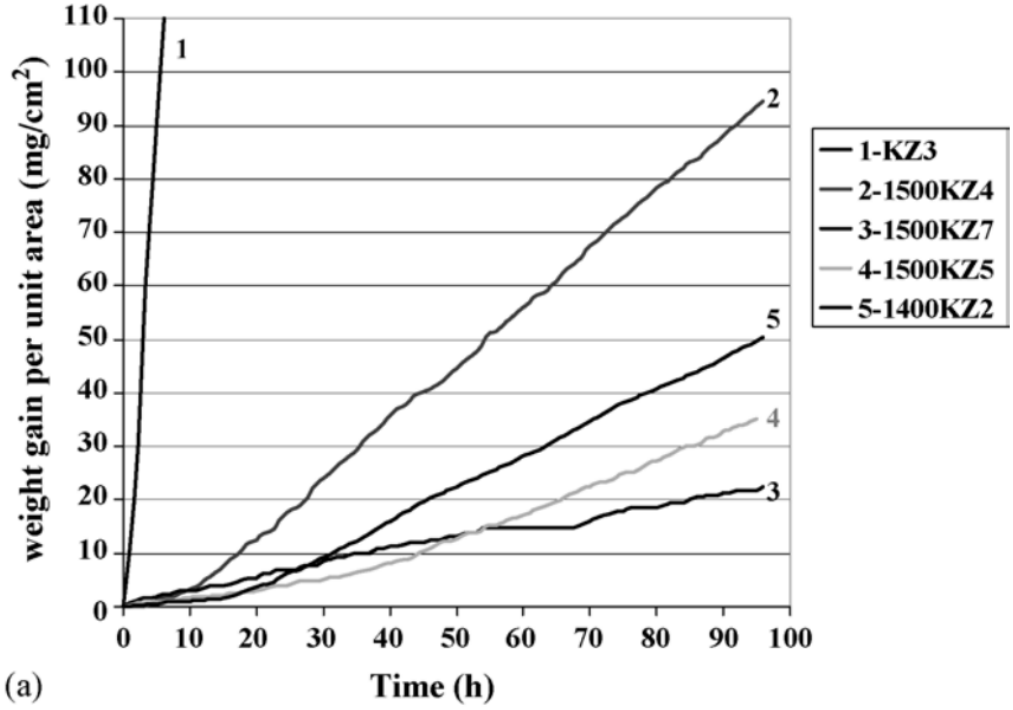

Figure 2.24) TGA results of KZ alloys oxidised at 800°C. KZ3 (Nb–24Ti–18Si), KZ4 (Nb–24Ti–18Si–5Cr), KZ7(Nb–24Ti–18Si–5Al), KZ5(Nb–24Ti–18Si–5Cr–5Al), KZ2 (Nb–24Ti–18Si–8Cr–4Al). The number proceeding the alloy indicates the heat-treatment temperature (or lack of). [128]

2.4.6 The addition of Al

Aluminium, much like Cr and Ti, reduces the diffusivity of O through the (Nb) phase and has been shown to reduce the recession rate of cyclically oxidised samples [111]. Aluminium reduces pesting according to [128] by substituting into Nb_5Si_3 for Si. Since Al has a higher affinity for O than Si, Al_2O_3 forms in small amount at grain boundaries of Nb_5Si_3 during oxidation as opposed to SiO_2, which lessens the intergranular embrittlement associated with the pesting phenomena. At 1200°C, direct comparison of Cr to Al in the form of alloys Nb-24Ti-18Si-5Cr (KZ4) and Nb-24Ti-18Si-5Al (KZ7) shows that Al is more beneficial in these quantities than Cr additions, where weight gains are reported as 139 mg/cm^2 and 101 mg/cm^2 after 65 hours, respectively [152]. This is proposed to be a results of Al based oxides ($AlNbO_4$) having a slower growth rate than the Cr equivalent. In fact, when both Cr and Al are added in equal quantities further improvement in oxidation resistance is seen, with a mass gain of 64 mg/cm^2 for alloy KZ5 (Nb-24Ti-18Si-5Al-5Cr). The alloy KZ5 will form a suitable base alloy for this current work given that its microstructure is well described in the literature [9][118][152][153].

2.4.7 The addition of B

To understand the interest in alloying niobium silicide-based alloys with boron, previous studies concerning the Mo-Si-B system should be considered. MoSi alloys have been investigated alongside NbSi alloys as both show promising creep resistance at high temperatures [154]. The catastrophic pest oxidation at 800°C and high temperature oxidation of MoSi composites are improved by the addition of boron into specifically the Mo_5Si_3 phase. A borosilicate glassy layer ($SiO_2 – B_2O_3$) was observed which was attributed to the enhanced oxidation performance through providing a barrier to further oxidation [6]. The low viscosity of this layer at high temperature allows flow into an adherent oxide scale, providing self-healing capabilities by the filling in of cracks that form during oxidation. Mo-Si-B alloys have been designed with the goal of having molybdenum solid solution and silicides present in the microstructure for desirable room temperature fracture toughness and creep resistance respectively, and for the formation of a borosilicate layer to be able to take place [155][156][157][158][159][160]. It follows that given the similarities of the niobium and molybdenum silicide alloys, boron additions to niobium silicides may yield alloys with improved oxidation resistance if a borosilicate layer is able to form.

The results of boron doping of niobium silicide-based alloys have been mixed. There seems to be a consensus among the literature that boron doping of the Nb_5Si_3 or $NbSi_2$ intermetallic phase improves oxidation resistance of this phase, whether either T2 or $D8_8$ is formed, through encouraging a thinner less porous B_2O_3 containing oxide scale that as a result is less susceptible to spallation [161][162][163][164]. According to [161] the T2 phase has better oxidation resistance than that of the $D8_8$ phase in air at 1000°C, with parabolic rate constants calculated as 20.3 and 115 mg^2/cm^4 per hour respectively. Although it should be noted that these results may be influenced by the difficulty in densification of $D8_8$ as the samples tested were not fully dense, rather than a measure on the intrinsic oxidation resistance of the phases. In addition, this was effectively a study on single silicide phases and not the desired (Nb) and silicide microstructure. The oxidation of a silicon free phase NbB_2 showed inferior oxidation resistance to the Nb_5Si_3 phase with and without boron additions [163].

However, when an intermetallic/solid solution composite is examined, the substantial improvement to oxidation resistance seen in MoSi alloys is not observed likely due to differences in oxide products [162][165][166][167]. MoO_3 is volatile above 600°C and immediately vaporises above 1000°C upon formation [168][169] which allows the slower forming protective SiO_2 layer to form [121]. Nb_2O_5 is

non-volatile and is stable at it least 1200°C, so prevents the borosilicate layer from being as effective.

However, this does not mean that no benefits of boron additions have be observed. Small amounts of boron have been added to compositions Nb-22Ti-16Si-3Al and Nb-24Ti-16Si-6Cr-6Al-2Hf in studies by Song Zhang *et al* [166] and Aiqin Liu *et al* [170] respectively. In the former, 2 at% B resulted in a 36% decrease in mass gain per unit area compared to the base alloy over 50 hours at 1250°C. In the latter, the most successful composition at reducing the mass gain per surface area included 1 at% B, resulting in a 52% decrease in mass gain per surface area compared to the base alloy over 100 hours at 1250°C. The reasons for these improved oxidation properties are proposed as an increased adherence between the oxide scale and substrate as a result of small amounts of B_2O_3 forming alongside Nb_2O_5 and silica, and boron inhibiting oxygen diffusion into the bulk material by residing on interstitial sites in (Nb) and increasing the volume fraction of silicide material.

Borosilicate has been reported to form on niobium silicides [162][164]. However, the composition of these alloys is often high in silicon as they are intended for application as coatings, where room temperature fracture toughness is less of a requirement. In niobium silicide-based alloys intended for structural applications (and indeed some coating materials [171]), formation of a borosilicate layer is more elusive [161][163][165][166]. The formation of a complete, adherent and passivating borosilicate layer would advance niobium silicide-based alloys' progress towards viability.

2.4.8 The addition of Ge

Silicide based coating materials are seen as a promising route to counter the poor oxidation resistance of niobium silicide-based alloys [164][121][172]. These coatings are successful when an amorphous layer of SiO_2 is able to form on the surface and act as a barrier to further oxygen diffusion into the bulk material. Germanium additions to these high silicon content coatings has been investigated. The formation of GeO_2 and subsequent dissolution into SiO_2 gives several benefits to the coating system; namely that GeO_2-SiO_2 has a greater thermal expansion coefficient that more closely matches the NbSi substrate, glassy GeO_2-SiO_2 provides better sealant capabilities, and GeO_2 solute in SiO_2 reduces its viscosity allowing cracks to be 'healed' during cyclic oxidation [173][174][175][176][177][178][179]. B and Ge additions have similar purpose and effect, and their combination will be the focus of this work.

When Ge is added to alloys intended for bulk component application rather than coating materials, improvements to oxidation resistance are also seen. [127] examined alloys Nb-24Ti-18Si-5Ge-5Cr (ZF4), Nb-24Ti-18Si-5Ge-5Al (ZF5), Nb-24Ti-18Si-5Al-5Cr-5Ge (ZF6). After 100 hours at 1200°C in an oxidising atmosphere total normalised mass gains were recorded as 59 mg·cm^{-2}, 55 mg·cm^{-2}, and 39.9 mg·cm^{-2}, respectively. [152] examined alloys Nb-24Ti-18Si-5Cr (KZ4), Nb-24Ti-18Si-5Al (KZ7) and Nb-24Ti-18Si-5Cr-5Al (KZ5). After only 65 hours at 1200°C in an oxidising atmosphere mass gains of KZ4 and KZ7 were recorded as 139 mg·cm^{-2} and 101 mg·cm^{-2}. After 100 hours under the same conditions KZ5 had total normalised mass gain of 64 mg·cm^{-2}. In each case the effective replacement of 5 at.% Nb with 5 at.% Ge resulted in significant reductions in oxidation. This is likely a result of reduced volume fraction of (Nb) as well as small amounts of GeO_2 in the scale possibly reducing oxygen diffusivity compared to titanium niobates. These tests were performed by the same group, so it is assumed that the results are directly comparable.

B and Ge have been added to niobium silicide-based alloys and silicide-based coatings for the same purposes regarding improvements to oxidation resistance through better adherence of the SiO_2 layer, or formation of an amorphous glassy SiO_2 layer that is capable of self-healing any cracks that may form during the oxidation process. There has not been a great deal of investigations regarding

the oxidation of niobium silicide-based alloys that contain both B and Ge. Where this has been investigated experimentally, a reduction in oxidation is reported in terms of mass gain of 118.7 $mg.cm^{-2}$ to 26.7 $mg.cm^{-2}$ after 100 hours at 1200^{o}C in air for the additions of 4 at.% B and 5 at.% Ge to the base alloy (Nb–24Ti–15Si–13Cr–2Al–2Hf) [167]. However, examination of the oxidised alloy was insufficient to confirm a borosilicate layer as boron proved difficult to measure and evidence for an amorphous glassy layer was based on the lack of SiO_2 peaks in XRD patterns. The combined efficacy of B and Ge additions to a multiple component alloy system, KZ5 (Nb-18Si-24Ti-5Cr-5Al), will be investigated in this current study. A SiO_2-GeO_2-B_2O_3 glassy layer is desirable, and would likely be of great benefit to the oxidation resistance of a niobium silicide-based alloy.

Chapter 3

3 Experimental procedure

3.1 Alloy selection and composition

The purpose of this research is to improve the understanding of the role that boron and germanium have on the oxidation properties and microstructure of niobium silicide-based alloys. The self-healing capabilities of Mo-Si-B systems owing to the formation of a glassy borosilicate layer during oxidation is attempted to be reproduced in the Nb-Si-B system intended for bulk alloy components through the inclusion of germanium alongside boron. To achieve this, a composition is selected as a base alloy that is intended for applications of turbine blades and disks rather than a coating material. KZ5 [153] (Nb-18Si-24-Ti-5Cr-5Al) contains elemental additions that are promising for the future of niobium silicide-based alloys; titanium, chromium and aluminium.

Titanium improves the room temperature fracture toughness and improves oxidation resistance as it readily partitions into the (Nb) phase promoting solid solution strengthening and reducing the susceptibility to oxygen diffusion. Titanium content was kept at 24 at.% to avoid Ti_5Si_3 formation as this is detrimental to creep performance. Chromium and aluminium both improve oxidation resistance, partly though $NbCr_2$ formation, and are deemed acceptable in terms of mechanical property degradation when considering the success of MASC alloy [114]. The destabilisation of the Nb_3Si in preference of Nb_5Si_3 as a result of Cr and Al additions is also expected to somewhat mitigate the negatives, as the 5:3 phases are preferable for creep resistance. Additions of 5 at.% of both chromium and aluminium will be sufficient to achieve this according to previous iterations of KZ5 [153].

KZ5 is well characterised in the literature and has a desirable silicide + eutectic ((Nb) + silicide) microstructure. 5 at.% of each element of interest, B and Ge, will be added to KZ5 to make JW1 (Nb-18Si-24-Ti-5Cr-5Al-5Ge-5B). The purpose of JW1 is to create an alloy that has comparable microstructure to KZ5 and other niobium silicide-based alloys, but has superior oxidation resistance. Further B addition to JW1 will create JW2 (Nb-18Si-24-Ti-5Cr-5Al-5Ge-10B) and further Ge addition to JW1 will create JW3 (Nb-18Si-24-Ti-5Cr-5Al-10Ge-5B), which are designed to confirm whether or not a borosilicate glassy layer is possible to generate during oxidation in alloys intended for bulk components in the expanded Nb-Si-B system. Compositions of the alloys investigated are given in Table 3.1. The silicon content is kept at 18 at.% in these alloys to realistically maintain a volume fraction of solid solution phase (Nb), and as this is the optimal Si content for creep resistance [105]. 5 at.% of B and Ge are initially used in JW1 as this is expected to be sufficient to promote phases not seen in KZ5, such as T2 and $D8_8$ phases based on the ternary systems, so clear comparisons of the microstructures and their effects on oxidation resistance can be made. When small amounts (≤ 2 at.%) of B are added the desired borosilicate layer is not observed [166][165]. Where a silica layer was speculated to have formed, 4B-5Ge was used [167], so JW1 will use similar amounts as this previous study to improve oxidation resistance and to promote this borosilicate layer formation. Then an increase to 10 at.% is examined in order to better understand the individual effects of B and Ge elemental additions in JW2 and JW3, respectively. 10 at.% was selected as to be a significant increase when compared to the initial 5 at.% addition to promote more obvious changes to the microstructure and oxidation properties.

3.2 Ingot manufacture

Alloy ingots of mass 30g were made using an Arcast Arc 200 equipped with a water cooled copper crucible and non-consumable tungsten electrode. The arc-melting chamber was flushed using argon gas three times before being filled to ~ 40 KPa of an argon atmosphere. Melting was carried out with a maximum direct current of 300 A and voltage of 12-20 V for 90 second intervals. After each

completed melt, once the ingot button had cooled it was flipped over to increase homogeneity. Each alloy was melted a total of five times. Magnetic stirring was utilised for the last four melts, again to improve homogeneity of elements and microstructure. Elements were weighed out to the nearest milligram and were of the following purities; Nb 99.8%, Si 99.9999%, Ti 99.99%, Cr 99.995%, Al 99.999%, Ge 99.999, B 99.5%. Due to the volatile nature of Al and B during the arc melting process and the material loss observed during preliminary melts, an extra mass of 10 and 20% respectively was added to each initial crucible load to counteract the material that was lost.

The actual compositions were measured using inductively coupled plasma optical emission spectroscopy (ICP-OES). The nominal compositions and actual compositions are displayed in Table 3.1. Actual compositions were within 1.4 at. % of the nominal composition for each element in each alloy. The extra B and Al added to each alloy to compensate for volatility and mass loss has been successful for B where only JW3 AC has less than nominal composition, and only by 0.1 at.%. Actual Al contents are generally still lower than nominal compositions with the exception of KZ5-AC and JW1-HT13; so in future work the value of 10% additional mass should be reconsidered. No alloy had greater than 0.2 at. % oxygen contamination, however carbon and nitrogen contents were not measured so other impurities could be present.

Ingots were approximately 4 cm in diameter and 1 cm thick. Buttons were sectioned into various samples sizes using the Secotom-50. Main motor load was kept below 20% and feed speed was kept at or below 0.035 $mm.s^{-1}$ to prevent serious surface damage. The recommend 2000 rpm was used for directional sectioning. For initial cuts of the thick ingots a Struers diamond cut-off wheel B0D20 with a 0.9mm thickness was used. For finer cuts of smaller samples, such as TGA and Electron backscatter diffraction (EBSD) samples, a Struers diamond cut-off wheel M1D20 was used with a thickness of 0.6mm to reduce material losses and potential damage to the microstructure on the surface of the samples.

Table 3.1) Measured compositions of alloys using ICP-OES and nominal compositions in at.%.

		Nb	Si	Ti	Cr	Al	Ge	B	O
Nominal composition	KZ5	48.0	18.0	24.0	5.0	5.0	-	-	-
	JW1	38.0	18.0	24.0	5.0	5.0	5.0	5.0	-
	JW2	33.0	18.0	24.0	5.0	5.0	5.0	10.0	-
	JW3	33.0	18.0	24.0	5.0	5.0	10.0	5.0	-
KZ5-AC / KZ5-HT15		48.6	17.5	23.2	4.9	5.6	-	-	0.2
JW1-AC / JW1-HT15		38.8	17.1	24.3	4.9	4.5	4.8	5.4	0.2
JW2-AC / JW2-HT15		34.4	17.5	23.7	4.3	3.7	4.9	11.3	0.2
JW3-AC / JW3-HT15		34.3	17.5	23.9	4.8	4.6	9.8	4.9	0.2
JW1-HT13		37.4	17.6	24.6	5.1	5.1	4.6	5.4	0.2
JW2-HT13		32.0	17.7	24.9	5.5	4.6	4.8	10.5	0.1
JW3-HT13		33.4	18.4	24.1	4.7	4.2	9.7	5.3	0.1

3.3 Metallographic preparation

Samples were prepared for scanning electron microscopy (SEM) and EBSD by mounting in conductive Bakelite using a Simplimet Mounting Press. Where an oxide cross section was to be examined under electron microscopy techniques, an epoxy resin and hardener were used to avoid disruption of the oxide scale. Epothin2 resin and hardener system was selected to reduce the degassing problem commonly encountered with epoxy resins under SEM vacuum chambers [180].

Grinding and polishing steps were performed on an AutoMet. Mounted samples were ground using silicon carbide grinding papers in the following regime: P400, P800, P1200, P1200, P2500, P4000.

Three grinding papers were used at each grit level for 100 seconds each, with the following settings: 12N of force, platen speed 241 rpm, head speed 60 rpm. Mounted samples were then polished using a Buehler MicroCloth polishing cloth with 1µm Monocrystalline diamond suspension for 5 minutes with adjusted platen speed to 151 rpm, and then finally with a Buehler ChemoMet polishing cloth with 0.25µm Polycrystalline diamond suspension for 10 minutes with the same settings as the previous step. For samples prepared for EBSD, the last polishing media was replaced with colloidal silica in order to prevent residual stress in the finished sample which can lead to poor readings during EBSD. Carbon coating was generally avoided with samples mounted in conductive Bakelite as this interferes with light element detection and quantification. A combination of copper tape and silver DAG were used to prevent charging during electron microscopy. However, a 20nm layer of carbon was deemed necessary for samples mounted in epoxy.

Samples for testing mechanical properties such as hardness, creep rate and fracture toughness were not prepared in this work. Although useful data, especially with the low volume fraction (Nb) alloys, time constraints and a low production capacity of the arc melting procedure meant that the oxidation properties of these alloys were prioritised.

3.4 Heat treatments

Heat-treatments were performed on the arc melted alloys KZ5, JW1, JW2 and JW3 in an attempt to reach equilibrium phases. Niobium silicide alloys manufactured through arc melting have been known to retain the high temperature βNb_5Si_3 in alloys where the low temperature αNb_5Si_3 is thermodynamically stable due to sluggish transformation kinetics [27]. Preliminary differential scanning calorimetry (DSC) showed no melting up to 1600°C and so a heat-treatment temperature of 1500°C was selected and performed for 100 hours in a TSH18/75 Single Zone Tube furnace. This was the highest feasible temperature available during alloy production, and is well within the (Nb) + αNb_5Si_3 phase region in the Nb-Si system. In past work on KZ5 [153] a heat-treatment of 1500°C for 100 hours was used and was acceptable to avoid melting, however an equilibrium was likely not reached as both versions of Nb_5Si_3 were present. Unfortunately, longer heat-treatments were not possible due to furnace constraints and would need to be significantly longer to produce an equilibrium alloy.

Specimens were cut from ingots and wrapped in tantalum foil and placed inside the furnace tube with a crucible of titanium sponge to act as an oxygen getter during heat-treatment in an argon atmosphere. These samples will be referred to as HT15 hence forth. A scale was noted on the Ta foil that was in contact with the samples, which through transmission XRD using the STOE STADI P with a MoKα source (λ=0.70930 Å) was found to be Ta oxide and/or titanium niobates, so some degree of oxygen impurities were present in the protective Ar gas.

An additional heat-treatment regime at 1300°C for 100 hours in a Shimadzu AG-I universal testing machine equipped with a vacuum furnace was performed on as-cast alloys JW1, JW2 and JW3. Samples heat-treated at 1300°C will be referred to as HT13 hence forth. This temperature was selected as it was the maximum possible in the vacuum environment. Additionally, preliminary DSC indicated a possible minor phase transition event at approximately 1350-1400°C, so this 1300°C heat-treatment could reveal the cause. HT13 samples were sectioned from a second batch of arc-melted samples. ICP analysis showed generally good agreement between the alloys manufactured separately. When compared to the first batch of alloys, those used in as-cast and HT15 samples, there are four cases where element content is greater than 1.0 at.% different. Nb in JW1 (1.4 at.%), and Nb, Ti and Cr in JW2 (2.4 at.%, 1.2 at.% and 1.2 at.% respectively).

3.5 X-ray diffraction (XRD)

3.5.1 Bulk phases

A Panalytical X'Pert^3 Powder with Cu Kα (λ=1.54056 Å) radiation was used for phase identification of bulk as-cast and heat-treated alloys. The acquisition of the X-rays was performed using a step size of 0.013 and a range of 10^o to 90^o 2θ. Phases were verified using PDF (Powder Diffraction File) entries in the PDF-4+ ICDD (International Centre for Diffraction Data). The same phase verification was used for all following XRD techniques described, and PDF codes are displayed in Table 8.1 (appendix).

3.5.2 Oxides

The Panalytical X'Pert^3 Powder was also used in grazing incident mode (also referred to as glancing angle) for surface analysis of oxidised specimens. The acquisition of the X-rays was performed using a step size of 0.020, a collection range of 15^o to 80^o 2θ and an omega angle of 2^o. Various omega angles were used in preliminary studies and 2^o was found to give the greatest signal to noise ratio for oxidised specimens making analysis possible. To compliment this grazing incident XRD, the Panalytical Aeris with Cu Kα (λ=1.54060 Å) was used with a step size of 0.022 and a collection range of 10^o to 100^o 2θ. It was found that, despite the thin oxide layers present in some oxidise samples, the same peak positions obtained in grazing incident XRD of as cast alloys were found using standard Bragg-Brentano Geometry on the Panalytical Aeris. The obtained X-ray patterns had greater intensity and more distinguishable peaks, with little to no sign of underlying bulk phases. This was used for the remainder of TGA oxidised samples, and is the main source of oxide XRD data.

3.6 Electron probe micro-analysis (EPMA)

Electron probe micro-analysis (EPMA) was performed using two JEOL JXA-8530F Electron Microprobes at different sites. For bulk phase analysis of as-cast and heat-treated alloys the JEOL JXA-8530F Electron Microprobe was capable of wavelength dispersive spectroscopy (WDS) and soft X-ray emission spectrometry (SXES) and utilised 'Probe for EPMA' software for quantification. For macrosegregation measurements and oxidised sample analysis the JEOL JXA8530F Electron Microprobe used wavelength dispersive spectroscopy (WDS) incorporating JEOL OEM PC-EPMA software for quantification. WDS was utilised in preference to energy dispersive spectroscopy (EDS), as the former technique has higher spectral resolution which is required for quantification of light elements such as boron.

In the case of bulk analysis, polished high purity elemental standards and boron-tungsten were used. In the case of macrosegregation and oxide analysis, polished high purity elemental standards, alumina, Jadeite (Si) and boron-nitride were used. A matrix correction using the PRZ model with an interference correction for an Nb M_2 satellite peak interfering with B Kα was used in both cases. The boron peak position and shape is sensitive to B bonding environment since characteristic x-rays are produced by outer shell bonding electrons transitioning to less excited states. Thus, it was important to monitor any B peak shift and change of B peak shape during the analysis routines. For bulk phases, B content was measured using an SXES attachment which makes integration of the characteristic peak area possible, reducing sensitivity of the peak shift effect. Other elements were recoded using WDS.

Quantitative maps (150 µm by 150 µm) were taken at the central regions of each as-cast and heat-treated sample, and additional maps at top and bottom location were taken of as-cast samples. A dwell time of 100 ms and step size of 0.5 µm was used, with accelerating voltage of 10 kV. 200 pixels were selected of a phase and averaged to give the mean composition, as well as maximum value, minimum value and standard error. In the cases where phases were present in low volume fraction, 40 pixels were used.

Quantitative maps (170 µm by 125 µm) were taken to show the oxide scale and underneath alloy of each oxidised specimen. A dwell time of 50 ms and step size of 0.5 µm was used, with accelerating voltage 10 kV. Often oxide scales and intergranular areas had a fine distribution of phases in the oxidised sample maps, so a minimum of 10 points were taken of each phase present in these maps and central parts of phases were prioritised. Certain limitations were present with the techniques used in these maps owing to the necessity to carbon coat the epoxy mounted samples and difficulty in oxygen quantification. In general, total weight percentages of the oxidised samples maps were reduced to 90%, were as in other forms of EPMA used weight percentages rarely deviated 0.5 wt.% from 100 wt.%. This is a result of dwell time for oxidised sample maps being reduced to allow for all oxide samples to be recorded and a reduced received signal as a result of the carbon coating layer.

Specifically for oxide phases found in the oxide layer, further difficulties in accurate quantification arise as total weight percentages are reduced to approximately 60 wt.%. If the missing wt.% was added to oxygen content then composition of phases match well with expected oxides, so the majority of the missing wt.% is assumed to be oxygen and the ratios of other elements can be used for phase analysis. The oxide layer and oxygen readings are affected by several factors, which include un-optimised oxide standards of solely alumina, a receiving angle altered by a bevelled edge of the sample arising from different hardnesses of the oxide layer and bulk alloy, hence decreasing x-ray yield, a receiving angle altered by the expected porosity of oxide phases compared to bulk phases, the possibility of epoxy resin penetration into the more porous oxide layer, the tendency of O characteristic peaks to shift in the same manner as other light elements, and the absorption of O kα x-rays by carbon in the carbon coating [181].

In order to quantify boron more accurately macrosegregation was measured using EPMA quantitative maps (200 µm by 150 µm) as opposed to EDS large area analysis as the majority of the alloys contain boron. Due to the time scale required for EPMA WDS maps versus EDS large area analysis, three maps were taken at each top, middle and bottom region of alloy ingots as opposed to the ten EDS area measurements that is common in the literature [182][183][184]. A dwell time of 50 ms and step size of 1 µm was used, with accelerating voltage 10 kV.

3.7 Scanning electron microscopy – Backscattered electrons (SEM-BSE)

BSE images were used to calculate the area fraction of the phases identified through EPMA using the Inspect F50 scanning electron microscope. Ten images at 500x magnification were taken from the centre of each alloy and software ImageJ [185] was used to calculate the percentage of each phase present based of the different contrasts and geometry. Where phases are indistinguishable from each other, or present but too small to resolve, it is noted where the data is presented. Supplementary information from EPMA maps is used to estimate area fractions of indistinguishable phases, such as (Nb) and $NbCr_2$ based on the ratio they appear in these EPMA maps when applicable.

3.8 Electron backscatter diffraction (EBSD)

Electron backscatter diffraction spectroscopy (EBSD) was used for phase identification in each as-cast and heat-treated at 1500^{o}C alloy. The JEOL 7900F was used with as accelerating voltage of 20 kV and specimen tilt of 70^{o}. PDF cards used for phase identification are displayed in Table 8.1 (appendix). Complimentary qualitative EDS maps of elements were also recorded during the use of the EBSD probe. AZtecCrystal EBSD Processing Software was used to construct phase maps at low (400x) and high (1000x) magnification.

3.9 Thermal analysis

3.9.1 Isothermal thermogravimetric analysis (TGA)

Thermogravimetric analysis using the Netzsch STA 449 F1 Jupiter was used to assess the oxidation performance of each alloy under isothermal conditions at 800°C, 1000°C and 1200°C under an atmosphere of air with a flow rate of 20 ml/min. The temperates of 1000°C and 1200°C are selected as a temperature where nickel-based super alloys are capable of operating as a comparison, and a temperature where future engines incorporating niobium silicide-based alloys may be able to operate at with improved efficiency, respectively. In addition, these temperatures are consistent with previous work on the oxidation of niobium silicide-based alloys. 800°C was selected to assess the alloys in the pesting regime.

Samples are placed in an alumina crucible and into the balance at room temperature and heated to temperature at 3°C per minute in a silicon carbide furnace and held at temperature for up to 100 hours. After the isothermal hold the samples were cooled at 3°C per minute to room temperature. The balance is accurate to 0.01 mg and records the mass change as a result of oxygen adsorption and oxide formation at 30 second intervals. Samples are sectioned from the centre of the alloy ingots, so it is assumed that where the central microstructure is displayed that this is representative of the whole oxidised specimen. Samples are sectioned to approximately 5 mm cubes, have surfaces ground to 1200 grit and are cleaned in isopropanol in an ultrasonic bath prior to oxidation testing. Surface areas are measured using a Nikon Eclipse LV150 optical microscope.

Rates of oxidation are calculated according to Equation (1), (2) and (3) for linear, parabolic and mixed oxidation behaviour, respectively. The point of transition from parabolic oxidation behaviour to linear oxidation behaviour is modelled using a Matlab script that plots both simultaneously and assesses the goodness of fit. If the entire time of the experiment is 100 hours and X is the transition time, curves are fitted using nonlinear regression with parabolic behaviour for 0 to X hours and linear behaviour for X to 100 hours. X is given values between 1 and 99 hours and with 1000 second intervals for a total of 350 plots. Through this method the lowest combined value of MSE (mean square error) and highest combined R^2 value are taken to be the point of transition, where both parabolic and linear behaviour are fitted well. Where the n value is calculated from Equation 3, the graph is fitted for the full 100 hours to obtain n, as well as the combined rate of oxidation which has variable units, $g.cm^{-2}s^{n}$.

3.9.2 Differential scanning calorimetry (DSC)

Differential scanning calorimetry (DSC) was performed up to 1600°C to identify if any phase transformations or melting occurred in the samples. DSC was used to determine the temperatures for heat treatment of alloys. Samples up to 200 mg were placed in an alumina crucible and put onto the DSC holder. An empty alumina crucible was used as a reference. Samples were heated and cooled under flowing Argon (20ml/min) at 20°C per minute to 1600°C using a Netzsch STA 449 F1 Jupiter with a Pt/Rh furnace. Endothermic and exothermic events were recorded along with any changes in the mass of the sample with simultaneous thermogravimetric measurements.

Chapter 4

4 The effect of boron and germanium additions on the microstructure of as-cast KZ5 (Nb-18Si-24Ti-5Cr-5Al)

4.1 Introduction

This chapter will present and compare the phases present and microstructures of four as-cast alloys; KZ5 (Nb-18Si-24Ti-5Cr-5Al), JW1 (Nb-18Si-24Ti-5Cr-5Al-5Ge-5B), JW2 (Nb-18Si-24Ti-5Cr-5Al-5Ge-10B), JW3 (Nb-18Si-24Ti-5Cr-5Al-10Ge-5B). The effects of B and Ge additions to the base alloy KZ5 will be discussed, as well as the effects of higher content of B in JW2 and higher content of Ge in JW3. Well characterised microstructures are critical in understanding the role B and Ge play in improvements to oxidation resistance. The changes in oxidation prone phases and oxidation resistant phases will be considered in relation to the overall oxidation resistance of the as-cast alloys. Phases are identified through a combination of X-ray diffraction (XRD), Electron probe micro-analysis (EPMA), and Electron Backscatter Diffraction (EBSD). Microstructures are characterised by backscattered electon (BSE) imaging and additional information is given from the area fraction of each phase and macrosegregation of elements across the arc-melted ingots' profile. The as-cast (AC) alloys are not expected to be in an equilibrium state and as such solidification routes will be considered.

4.2 Results

4.2.1 KZ5-AC (Nb-24Ti-18Si-5Cr-5Al)

4.2.1.1 XRD

The X-ray diffraction pattern of KZ5-AC (Nb-24Ti-18Si-5Cr-5Al) is given in Figure 4.1. In KZ5-AC, two phases are identified; the silicide βNb_5Si_3 and Nb solid solution (Nb). The tendency of (Nb) peaks to be broader than other phase(s) and shift in position with respect to the pure Nb reference can be explained by a high degree of substitution of other metal atoms, i.e. Ti, Cr, Al, which alter the lattice parameters of the BCC structure [147]. Other broadening factors that may play a lesser role include residual stresses in this phase and lattice defects. Peaks at positions corresponding to αNb_5Si_3 are notably absent in the XRD pattern despite being an equilibrium phase stable below ~1930°C in the Nb-Si binary system [32], which is explained by the sluggish transformation kinetics of the 5:3 silicides. The two phase microstructure identified through XRD is consistent with previous work on KZ5 [186].

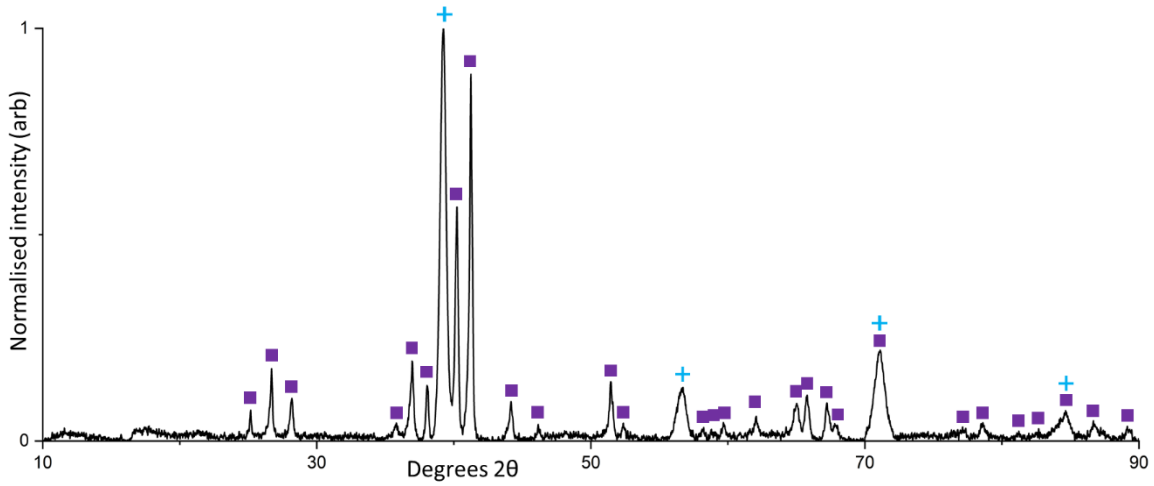

Figure 4.1) XRD pattern of KZ5-AC. ■ = βNb_5Si_3, + = (Nb).

4.2.1.2 EBSD

EBSD maps of KZ5-AC are presented in Figure 4.2 and Figure 4.3 with corresponding EDS maps of the areas examined. Maps were taken was from the middle of the alloy ingot, at two different magnifications to show the general microstructure (Figure 4.2) and more detailed microstructure (Figure 4.3). The βNb_5Si_3 phase expected from XRD results was identified as both the large grains of silicide phase and the intergranular silicide phase that forms as part of the eutectic structure. However, the (Nb) phase could not be matched to any areas in the lower magnification map and only matched to a small number of isolated areas in the higher magnification map. No pattern of Kikuchi lines was generated from the unassigned areas, as if the phase was amorphous, or had insufficient degree of crystallinity. Possible explanations include a poor surface finish, either inadequately polished or a thin layer of oxide preventing diffraction of the underlying (Nb) phase, or a nano-crystalline structure whose unit cells are too small for diffraction to occur. In the later explanation, the bulk XRD of KZ5-AC would still produce diffraction peaks associated with (Nb) as the entire surface area of the sample participates in the data acquisition process of this technique. The areas that were assigned to (Nb) in Figure 4.3 were not noteworthy in their compositions according to EDS mapping.

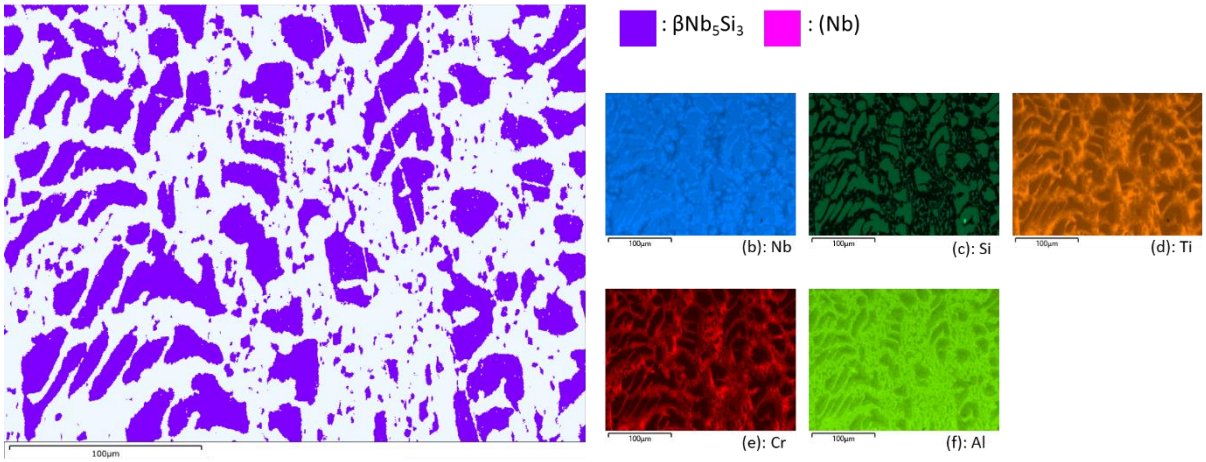

Figure 4.2a-f) EBSD map of KZ5 at lower magnification (a), and corresponding qualitative EDS maps of Nb (b), Si (c), Ti (d), Cr (e) and Al (f)

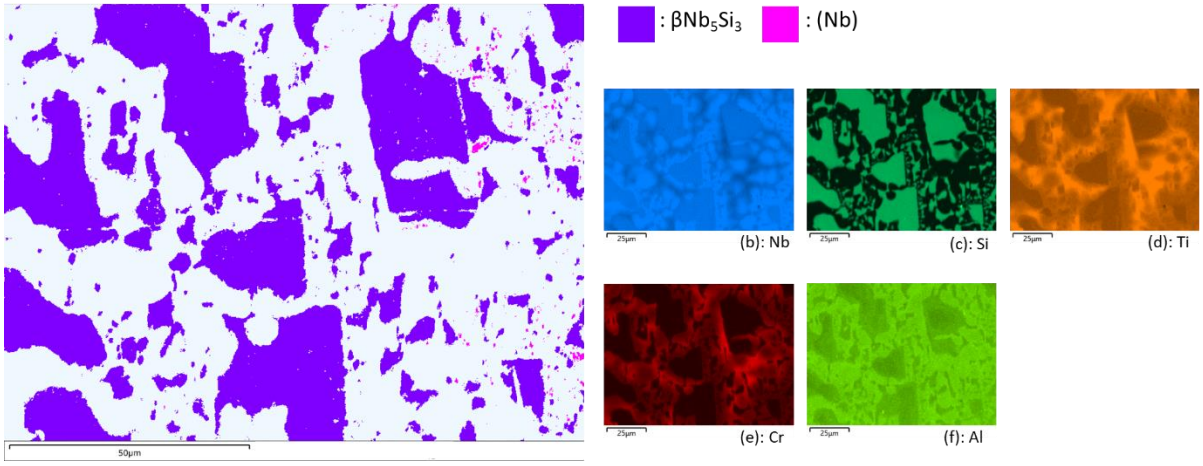

Figure 4.3a-f) EBSD map of KZ5 at higher magnification (a), and corresponding qualitative EDS maps of Nb (b), Si (c), Ti (d), Cr (e) and Al (f)

4.2.1.3 EPMA

EPMA mapping of the central region of KZ5-AC identifies the phases (Nb) and βNb_5Si_3. The compositions of these phases are given in Table 4.1. βNb_5Si_3 is split into two compositions; the composition of primary grains of βNb_5Si_3 and the composition of intergranular βNb_5Si_3. There are significant differences between the two phases due to the phases having formed at different times during solidification from the melt. The (Nb) phase is also split into two compositions; regular (Nb) that makes up the majority of the non-silicide microstructure, and Ti-rich (Nb) that appears as a darker contrast region in BSE images (Figure 4.4a and Figure 4.4b). These are both the BCC $Im\bar{3}m$ structured niobium solid solution. In previous work on this alloy [186], small amounts of the Laves phase $NbCr_2$ were found in certain areas connecting (Nb) dendrites. This phase could not be confirmed though XRD, EBSD or EPMA, and is considered absent in KZ5-AC in this present work.

The phase assigned to (Nb) has a high content of metallic elements, 26.4 at.% Ti, 7.5 at.% Cr, 6.2 at.% Al. This shows preferential partition of Ti, Cr, and Al to the (Nb) phase. The Si content is the lowest in this phase, at 2.0 at.%. Ti-rich (Nb) has greater Ti and Cr content, 34.1 at.% and 12.5 at.%, respectively. This increase of Ti and Cr is mainly at the expense of Nb content, which reduced from 57.9 at% to 44.7 at.%. Slightly more Si is accommodated in the Ti-rich (Nb) at 2.5 at.%, suggesting Si solubility is increased by Ti and Cr substitutions, although this difference is with the error range.

Primary βNb_5Si_3 has a Si content of 31.6 at.%. This is below the stoichiometric Si composition for this phase, 37.5 at.% ((Si_3 / Nb_5)*100). Therefore Nb, Ti and Al are expected to be substituted onto Si sites in this phase. The intergranular βNb_5Si_3 has a slightly lower Si content, at 30.7 at.%. The main difference between primary and intergranular βNb_5Si_3 is the Nb and Ti contents. Primary βNb_5Si_3 was found to have 47.6 at.% Nb and 16.7 at.% Ti whereas intergranular βNb_5Si_3 was found to have 41.7 at.% Nb and 22.4 at.% Ti. This suggests the intergranular βNb_5Si_3 formed from a liquid that was Nb-poor and more Ti-rich than the initial melt that Primary βNb_5Si_3 formed from.

EPMA was also performed on regions from the top and bottom of the alloy ingot. Calculated compositions from these regions are presented in Table 4.2. At the top of the alloy ingot, phases (Nb), Ti-rich (Nb), Primary βNb_5Si_3, and Eutectic βNb_5Si_3 were found. At the bottom of the alloy button the same phases were found. Compositions of these phases at both locations are similar to those at the centre of the alloy ingot, with no large differences in terms of mean composition.

Table 4.1) Compositions of phases found in the central region of KZ5-AC using EPMA mapping in at.%. Mean ± stdev, minimum value - maximum value.

	Nb	Si	Ti	Cr	Al
Primary βNb_5Si_3	47.6 ± 0.6	31.6 ± 0.9	16.7 ± 0.4	0.9 ± 0.1	3.2 ± 0.4
	45.8 - 49.1	29.1 - 34.1	15.8 - 17.6	0.6 - 1.1	2.3 - 4.0
Intergranular βNb_5Si_3	41.7 ± 1.9	30.7 ± 1.1	22.4 ± 1.8	1.7 ± 0.4	3.5 ± 0.2
	35.0 - 46.3	25.1 - 33.1	19.5 - 29.8	1.2 - 4.7	2.9 - 4.0
(Nb)	57.9 ± 2.4	2.0 ± 0.4	26.4 ± 1.4	7.5 ± 1.1	6.2 ± 0.2
	50.5 - 61.9	1.1 - 3.6	23.9 - 30.6	5.6 - 10.4	5.5 - 6.9
Ti-rich (Nb)	44.7 ± 2.8	2.5 ± 1.0	34.1 ± 1.6	12.5 ± 1.3	6.3 ± 0.3
	37.4 - 53.0	1.1 - 6.7	29.2 - 38.3	8.8 - 16.5	5.6 - 7.4

*Table 4.2) Compositions of phases found in the top and bottom regions region of the KZ5-AC ingot using EPMA mapping in at.%. Mean ± stdev, minimum value - maximum value. * marks phases that were in small quantities and only 40 pixels were taken.*

-Top region-	Nb	Si	Ti	Cr	Al
Primary βNb_5Si_3	47.0 ± 0.6	31.4 ± 0.8	17.0 ± 0.2	0.9 ± 0.1	3.6 ± 0.2
	45.4 - 48.5	29.6 - 33.6	16.3 - 17.6	0.7 - 1.2	3.2 - 4.5
Intergranular βNb_5Si_3*	42.5 ± 1.5	28.6 ± 2.1	22.8 ± 1.6	2.1 ± 0.6	4.0 ± 0.3
	39.3 - 46.0	22.6 - 31.9	20.5 - 26.2	1.3 - 3.9	3.7 - 4.8
(Nb)	56.4 ± 1.6	2.5 ± 1.1	26.9 ± 0.8	7.6 ± 0.5	6.6 ± 0.3
	51.5 - 59.5	1.1 - 7.0	24.9 - 29.1	6.4 - 9.1	5.8 - 7.3
Ti-rich (Nb)*	45.8 ± 2.1	2.4 ± 1.1	33.4 ± 1.3	11.5 ± 1.1	6.9 ± 0.3
	40.7 - 48.7	0.9 - 5.6	30.9 - 36.7	9.6 - 13.7	6.2 - 7.5
-Bottom region-	Nb	Si	Ti	Cr	Al
Primary βNb_5Si_3	47.0 ± 1.7	31.1 ± 0.9	17.4 ± 1.5	0.9 ± 0.2	3.5 ± 0.5
	40.7 - 49.7	28.6 - 33.4	15.8 - 22.9	0.6 - 1.7	2.3 - 4.5
Intergranular βNb_5Si_3	42.9 ± 1.6	28.9 ± 2.6	22.4 ± 1.0	1.9 ± 0.5	3.9 ± 0.3
	39.8 - 47.8	20.3 - 32.7	19.9 - 26.4	1.3 - 4.6	3.2 - 4.8
(Nb)	56.5 ± 1.0	2.1 ± 0.4	26.9 ± 0.6	7.8 ± 0.5	6.7 ± 0.2
	53.6 - 58.8	1.1 - 4.5	25.8 - 29.2	6.6 - 8.9	6.1 - 7.4
Ti-rich (Nb)*	48.3 ± 2.1	3.3 ± 2.0	31.2 ± 1.1	10.6 ± 1.1	6.7 ± 0.4
	43.3 - 51.9	1.4 - 8.7	29.5 - 35.0	8.5 - 13.1	5.8 - 7.4

4.2.1.4 BSE - SEM Imaging

Figure 4.4a and Figure 4.4b show the typical microstructure of KZ5-AC, taken from the centre of the alloy ingot using BSE imaging. Figure 4.5a and Figure 4.5b show the microstructure from the top of the alloy, where the alloy is in contact with the argon atmosphere. Figure 4.6a and Figure 4.6b show the microstructure from the bottom of the alloy, where the alloy is closest to the copper cooled crucible and for this reason is assumed to have the highest cooling rate. Top and bottom regions of the alloy ingot are included to gain insight into the solidification profile and non-equilibrium phases as the different cooling rates result in different microstructures.

The centre region of KZ5 (Figure 4.4) shows large βNb_5Si_3 grains, presumably the first phase to form from the melt. These are surrounded by a lighter contrast (Nb) and darker contrast βNb_5Si_3 mixture. The intergranular (Nb) and βNb_5Si_3 mixed areas consists in primarily two forms; a fine eutectic with interphase spacing on the scale of a micron, and coarser dendritic areas which may have formed later during less rapid solidification, where the interphase spacing is on the scale of tens of microns. As was the case with this alloy in a previous study, KZ5-AC can be considered hypereutectic [186]. The Nb_3Si phase is destabilised by the Cr and Al present [117], so the eutectic structure of (Nb) + βNb_5Si_3 is able to form. The (Nb) phase is in a continuous matrix. There also are areas within the (Nb) and βNb_5Si_3 mixture that are darker in contrast than the surrounding phases. According to EPMA data (section 4.2.1.3) these are Ti-rich (Nb).

At the bottom and top regions of the ingot (Figure 4.5 and Figure 4.6), the grains of βNb_5Si_3 are smaller, which is due to faster cooling rates produced by being in contact with the argon atmosphere or water cooled copper crucible, respectively. The top region has a similar two phase mixture of (Nb) and βNb_5Si_3 as seen in the middle region and the same areas of (Nb) that are darker in contrast, suggesting variation in composition of the (Nb) phase. Composition of phases is discussed in the EPMA results (Section 4.2.1.3). This feature is not seen in the bottom region of the ingot. Instead larger primary grains of βNb_5Si_3 are less numerous and the (Nb) and βNb_5Si_3 mixture makes up a higher proportion of the alloy.

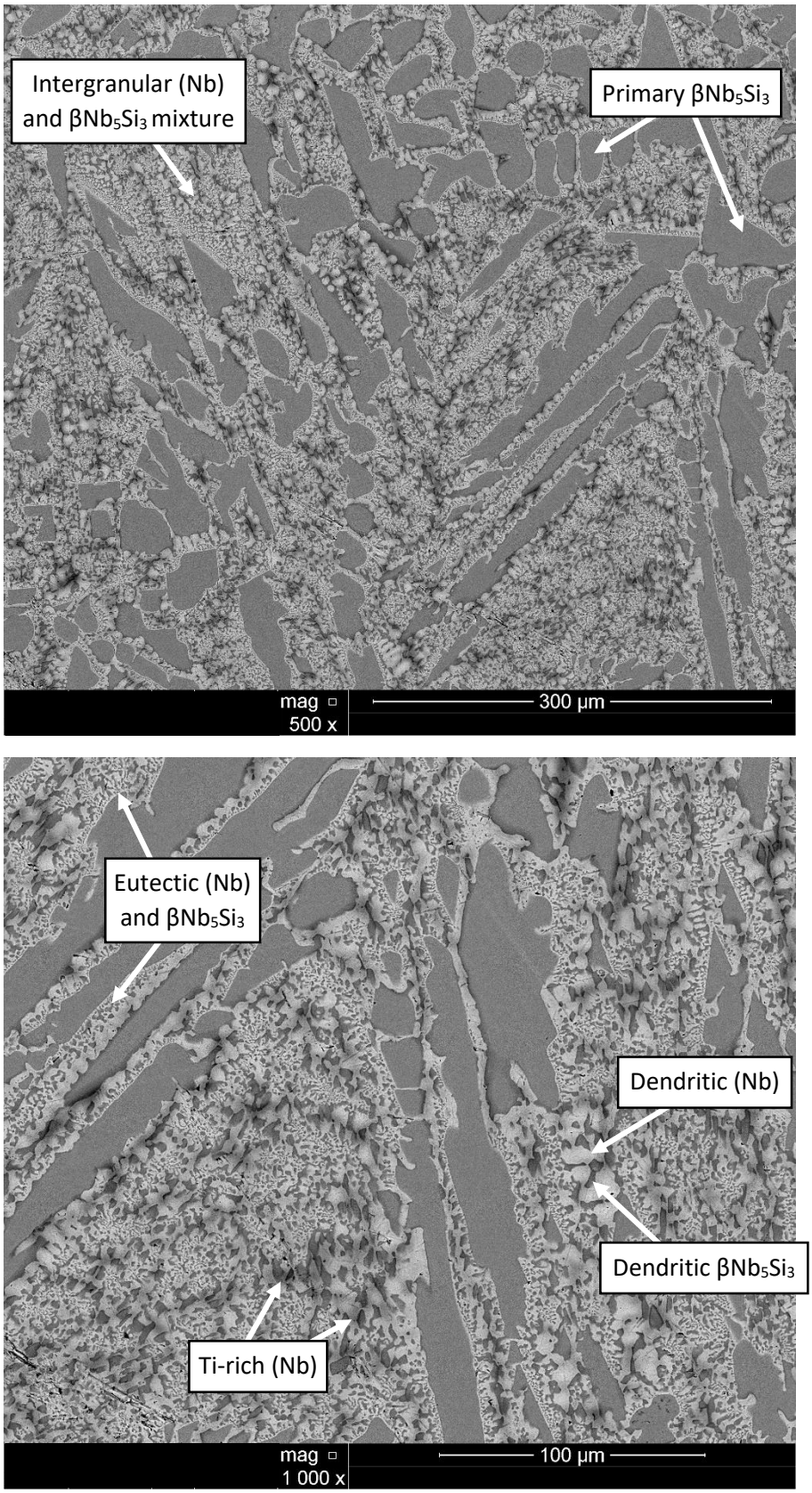

Figure 4.4a-b) BSE images of the central region of KZ5-AC taken at lower magnification (a) and higher magnification (b)

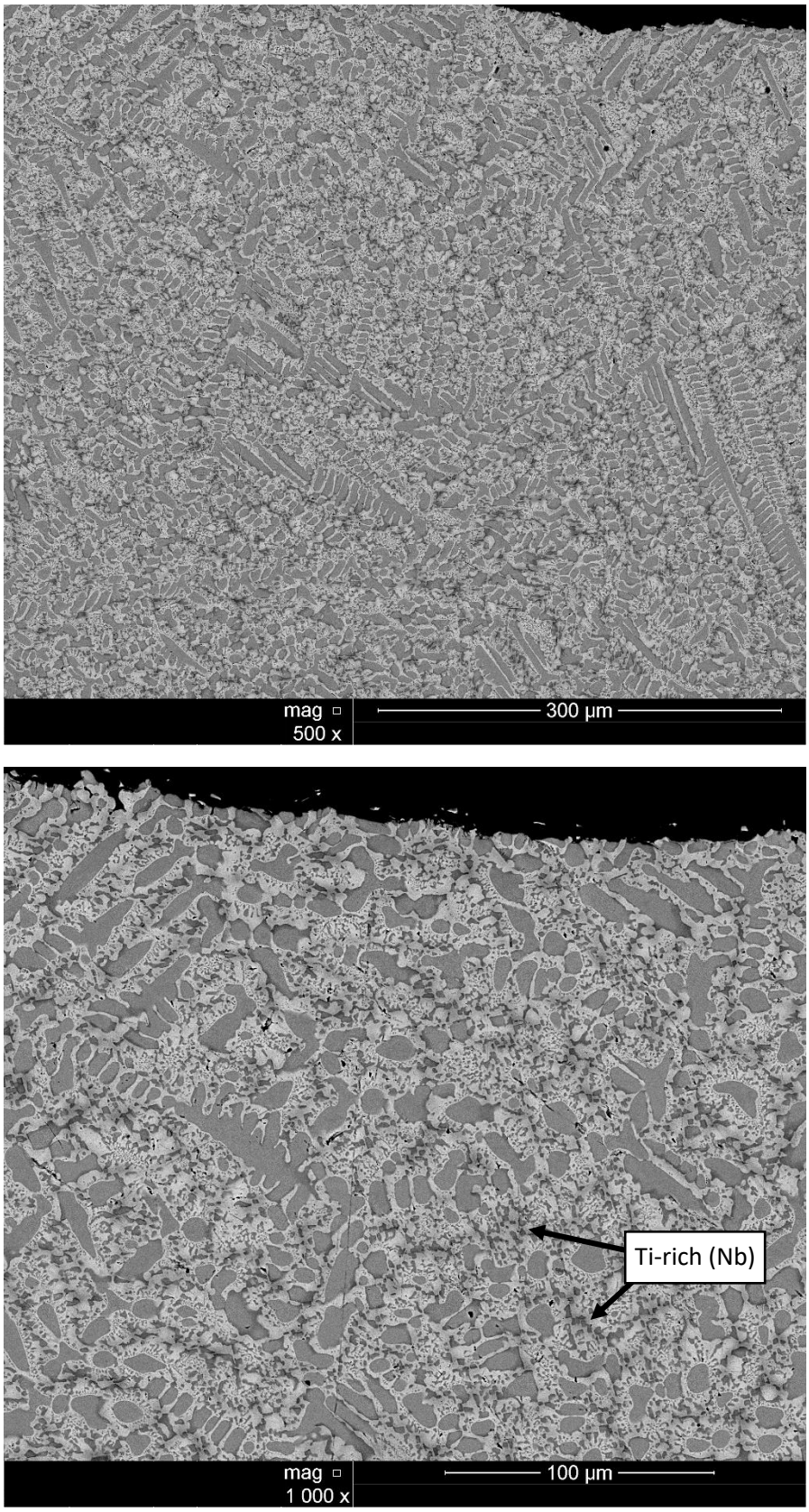

Figure 4.5a-b) BSE images of the top region of KZ5-AC taken at lower magnification (a) and higher magnification (b)

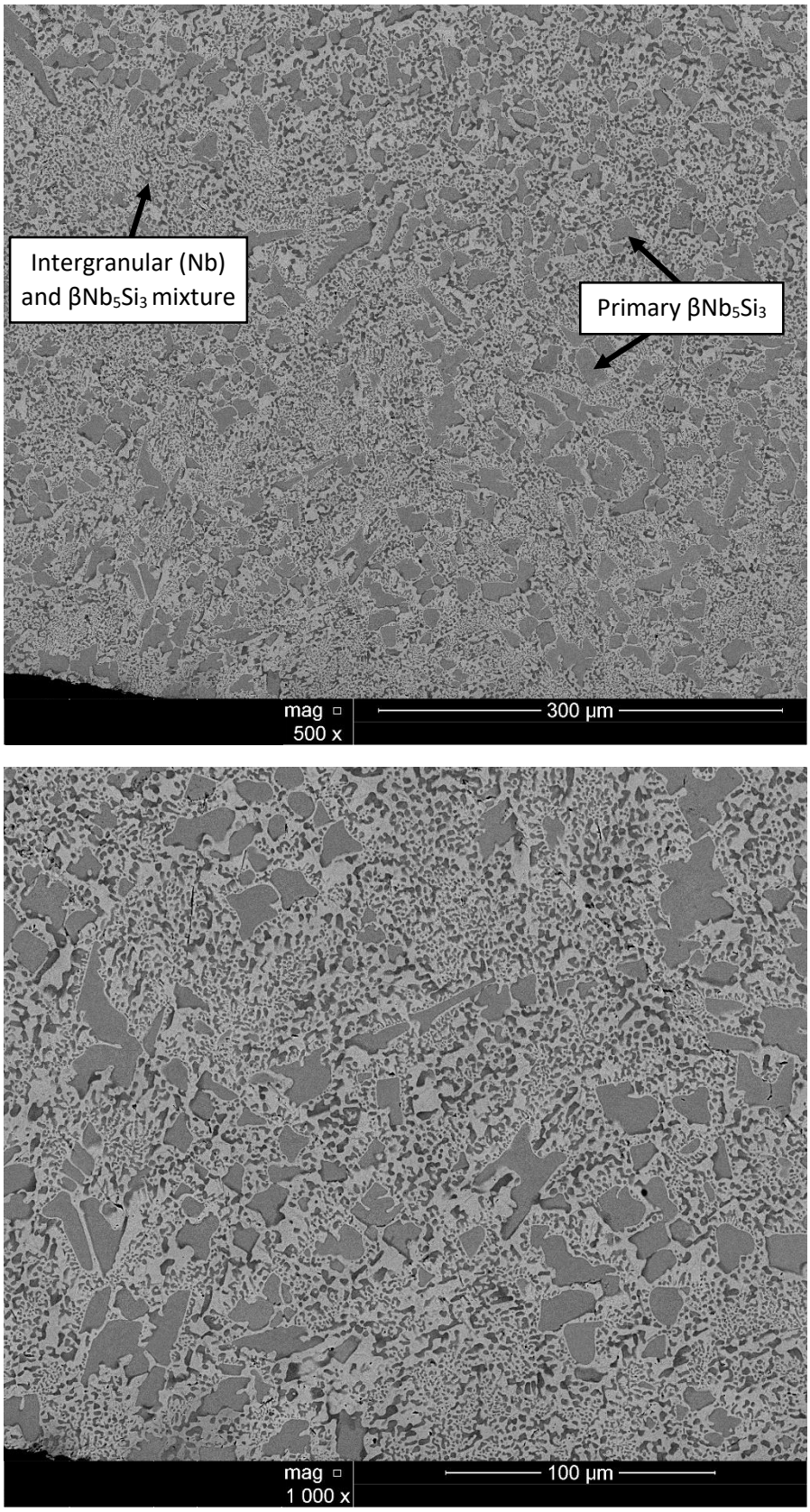

Figure 4.6a-b) BSE images of the bottom region of KZ5-AC taken at lower magnification (a) and higher magnification (b)

4.2.1.5 Area Fraction

The area fractions of phases βNb_5Si_3 and (Nb) at the centre of the ingot were calculated from BSE images according the methodology laid out in Section 3.6 and results are given in Table 4.3. The contrast of these phases was used to differentiate between them. On average the central area of KZ5 was 43.9% ± 4.2% (Nb) and 56.1% βNb_5Si_3 by area. The βNb_5Si_3 phase can be further differentiated as 41.5% ± 4.7% of the total area being the large primary grains and 14.6% ± 3.3% being the intergranular/eutectic βNb_5Si_3. In the work where KZ5 was first produced [152], calculated values of βNb_5Si_3 and (Nb) volume fractions were 45-52% and 48-55%, respectively. Although this was in a heat-treated version of KZ5.

Table 4.3) The area fraction of each phase present in each as cast alloy. Calculated from BSE image contrast taken at the centre of the alloy ingot. EPMA maps were additionally used to estimate the $NbCr_2$ content of JW1-AC as it was not possible to distinguish from Intergranular $D8_8$, and to estimate the $NbCr_2$ and (Nb) content of JW2-AC and JW3-AC as it was not possible to distinguish from each other.

		Intergranular		Intergranular				
Alloy	βNb_5Si_3	βNb_5Si_3	$D8_8$	$D8_8$	T2	NbB	(Nb)	$NbCr_2$
KZ5-AC	41.5 ± 4.7	14.6 ± 3.3	-	-	-	-	43.9 ± 4.2	-
JW1-AC	-	-	68.6 ± 3.4	7.7 ± 1.8	4.3 ± 0.5	-	18.5 ± 2.2	0.9 ± 0.2
JW2-AC	-	-	80.3 ± 3.1	-	0.7 ± 0.2	9.0 ± 1.6	8.1 ± 1.5	2.5 ± 0.5
JW3-AC	-	-	87.8 ± 1.3	-	-	0.6 ± 0.3	6.0 ± 0.7	5.5 ± 0.6

4.2.2 JW1-AC (Nb-24Ti-18Si-5Cr-5Al-5Ge-5B)

4.2.2.1 XRD

The X-ray diffraction pattern of JW1-AC (Nb-24Ti-18Si-5Cr-5Al-5-Ge-5B) is given in Figure 4.7. In JW1, four phases are identified; the silicides $D8_8$ and T2, the Nb solid solution (Nb), and a Laves phase $NbCr_2$. $D8_8$ has a hexagonal Mn_5Si_3-type crystal structure, the same structure as metastable γNb_5Si_3, where boron can substitute onto interstitial sites. T2 has the tetragonal Cr_5B_3-type crystal structure, which is the same as the low temperature stable phase αNb_5Si_3, where boron can substitute on to Si sites (8h Wyckoff positions discussed in Chapter 2 [83]). The Laves $NbCr_2$ phase is the high temperature version, otherwise known as C14 (Pearson symbol: cF24 Space group: $P6_3/mmc$ Prototype structure: $MgZn_2$). These phases are described in more detail in Chapter 2. The relative intensities of the (Nb) peaks are diminished in JW1 compared to KZ5, suggesting a lower volume fraction of (Nb). As XRD results presented in this work are from solid samples and not prepared powders, relative peak intensities and their relationship to phase volume fraction are not quantifiable as preferred crystal orientations and microstructural texture could exist due to the solidification conditions. However, large disparities in peak heights can qualitatively be used to comment on more obvious differences in phase volume fractions.

Both βNb_5Si_3 and αNb_5Si_3 are absent in the XRD pattern of JW1-AC. Whilst a high degree of confidence can be placed in the phases $D8_8$, T2 and (Nb) being present, with multiple unique peaks assigned to phases $D8_8$ and T2 and sufficient broadness of peaks due to substitution associated with (Nb). The same cannot be said for $NbCr_2$. Only one small independent peak is assigned to solely $NbCr_2$, with the rest overlapping with $D8_8$ or (Nb). Further confirmation of this phase is therefore required from EBSD and EPMA.

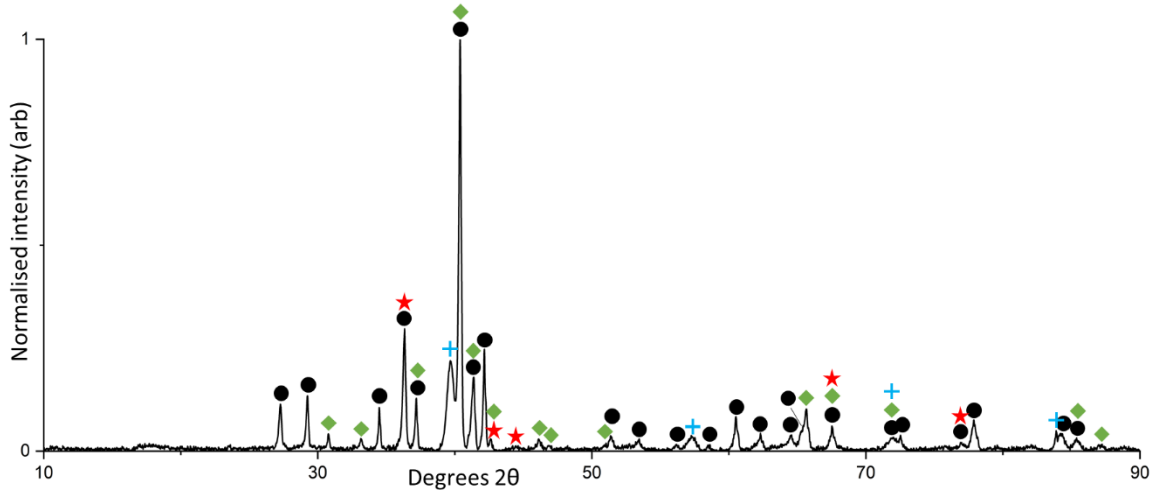

Figure 4.7) XRD pattern of JW1-AC. ● = $D8_8$, ★ = $NbCr_2$, ◆ = T2, + = (Nb).

4.2.2.2 EBSD

EBSD maps of JW1-AC are presented in Figure 4.8 and Figure 4.9 with corresponding EDS maps of the areas examined. These maps are taken from the middle of the alloy ingot, at two different magnifications to show the general microstructure (Figure 4.8) and more detailed microstructure (Figure 4.9). The (Nb), $D8_8$ and T2 phases expected from XRD results were identified comprehensively in both Figure 4.8 and Figure 4.9. The majority of the area is made up of $D8_8$, present as both large grains and intergranular forms. The (Nb) phase is present in the intergranular regions, and the T2 phase is seen as elongated phases generally aligned left to right in this specific area of sample. For confirmation of $NbCr_2$, which is only present in small quantities, the higher

magnification map (Figure 4.9) provides some evidence of this phase. The corresponding Cr EDS map (Figure 4.9e) highlights a small number of places with high Cr content which could potentially be $NbCr_2$, ringed for clarity. When examining these same areas on the higher magnification image, some but not all are assigned to the $NbCr_2$ phase. Two IPF maps are also presented in Figure 4.10 and Figure 4.11 of the same regions and magnifications to highlight the orientation of T2 grains. In Figure 4.10, there are multiple instances where portions of the T2 phase are separated by other phases and yet have the same orientation. This occurs over the entire horizontal length of the map that was taken (300 µm). If these isolated portions of T2 had varied orientations, then it would seem likely that $D8_8$ formed first as the primary phase and then T2 solidification in isolated portions of remaining liquid occurred. Since this is not the case, it is difficult to confirm which silicide phase in this case is the primary phase to solidify. The T2 shown in Figure 4.10 could be connected to each other out of the imaged plane and formed after $D8_8$ in between $D8_8$ grains, or $D8_8$ may have formed around previously connected elongated T2 grains which became segmented during cooling. Alternatively, a local microstructural texture could have occurred due to preferential solidification orientations with respect to the direction of heat flow. However, as T2 exists with alternate crystal orientations in close proximity of each other (Figure 4.11), despite having the same elongated physical orientation, this cannot be confirmed.

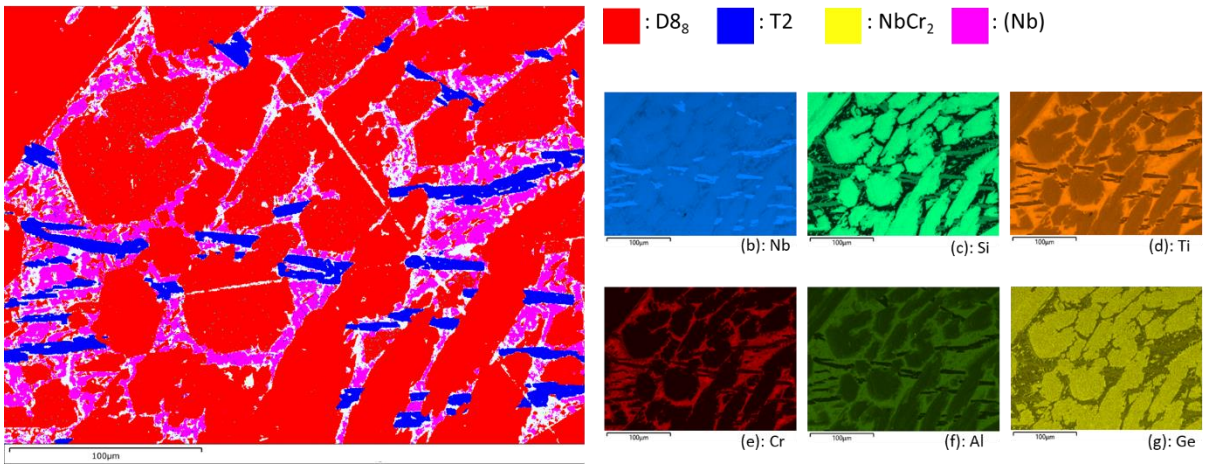

Figure 4.8a-g) EBSD map of JW1-AC at lower magnification (a), and corresponding qualitative EDS maps of Nb (b), Si (c), Ti (d), Cr (e), Al (f) and Ge (g)

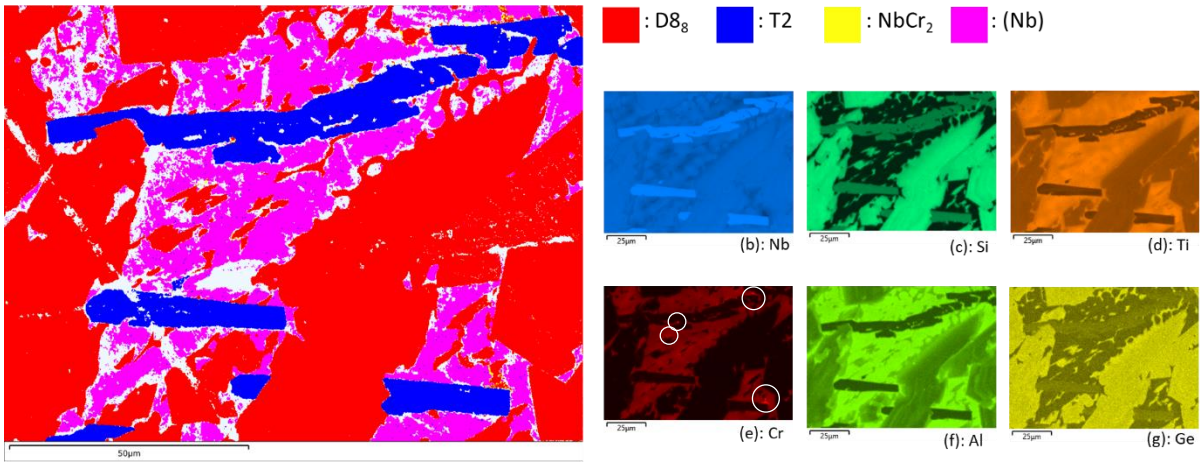

Figure 4.9a-g) EBSD map of JW1-AC at higher magnification (a), and corresponding qualitative EDS maps of Nb (b), Si (c), Ti (d), Cr (e), Al (f) and Ge (g). The Cr EDS map (e) has had areas particularly high in Cr ringed in white; in the EBSD map (a) these are not always found to be $NbCr_2$

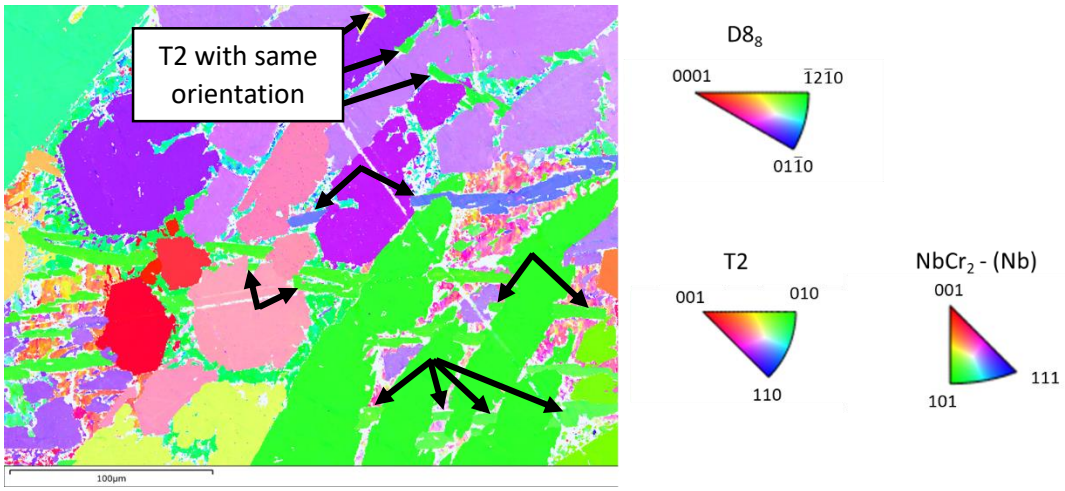

Figure 4.10) Lower magnification IPF maps of JW1-AC with corresponding grain orientation for the hexagonal ($D8_8$), tetragonal (T2) and cubic ((Nb), $NbCr_2$) systems. Black arrows label T2 phase that are believed to be the same original grain separated by $D8_8$ and (Nb).

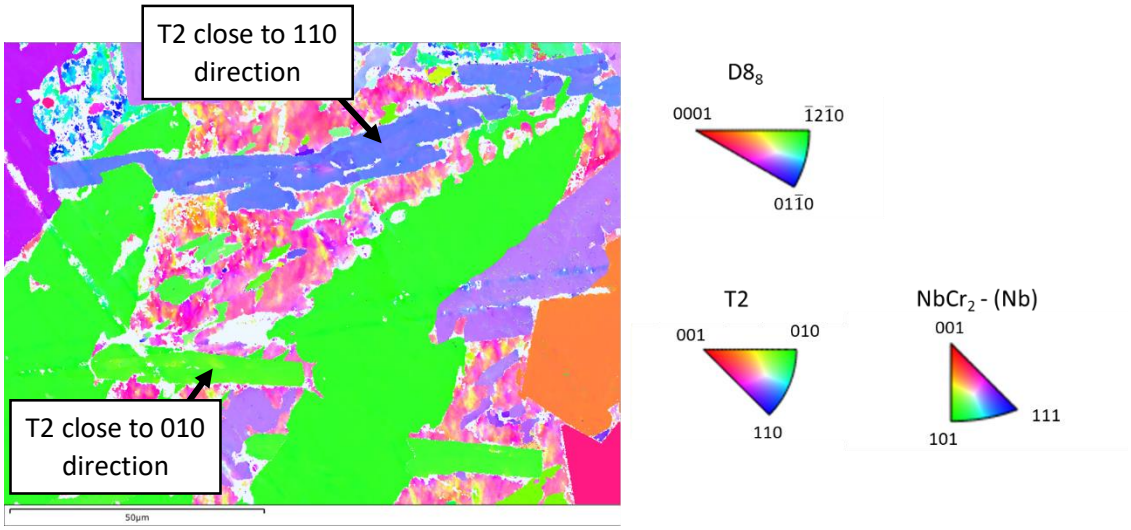

Figure 4.11) Higher magnification IPF maps of JW1-AC with corresponding grain orientation for the hexagonal ($D8_8$), tetragonal (T2) and cubic ((Nb), $NbCr_2$) systems

4.2.2.3 EPMA

EPMA mapping of the central region of JW1-AC identifies phases (Nb), $D8_8$, $NbCr_2$ and T2. The compositions of these phases are given in Table 4.4. $D8_8$ is split into two compositions; the composition of large grains of $D8_8$ and the composition of intergranular $D8_8$, as there are significant differences and these are believed to have formed at different times during solidification from the melt. The phase assigned to (Nb) has a high content of metallic elements, 34.0 at.% Ti, 15.1 at.% Cr, 7.8 at.% Al, as well as 39.9 at.% Nb. Elements Si, Ge and B have contents in (Nb) of 1.3 at.%, 0.8 at.%, and 1.0 at.%, respectively. Areas of (Nb) rich in Ti (Ti-rich (Nb)) are also found and have lower Nb contents and higher Ti and Cr contents compared to the previously reported (Nb).

T2 has the highest B content of the phases in JW1-AC, at 20.4 at.%. This is almost double the Si content of T2, indicating significant substitution of B onto Si sites. The maximum solubility of B in the T2 phase is reported between 24.8 and 25.1 at.% at 1700°C [81][84], so the reported values for this current study are in agreement with the literature. The B content of $D8_8$ grains is higher than the

intergranular $D8_8$, 6.2 at.% compared to 4.6 at.%, respectively. As these two B contents are either side of the nominal composition of B in the alloy, 5 at.%, this reveals that the intergranular formation of $D8_8$ occurred in a boron poor melt, whereas $D8_8$ large grain formation did not (the actual B content measured with ICP-EOS presented in Table 3.1 was also between these two values, 5.4 at.%). Original $D8_8$ grain formation is potentially a contributing factor to the boron poor melt, as it follows boron preferentially segregates into early forming $D8_8$ grains rather than the remaining liquid. Additionally, Ti, Cr and Al contents are higher in the intergranular $D8_8$, whilst Nb and Si contents are lower in the intergranular $D8_8$ when compared to the large $D8_8$ grains. The previous section presents EBSD data to confirm that both large grains and intergranular $D8_8$ are indeed the same hexagonal hP16 Mn_5Si_3-type crystal structure silicide. As expected, the $NbCr_2$ Laves phase is mostly made up of Cr, 50.8 at.%, but this is lower than the nominal composition of the binary phase (66.6 at.%). This is a result Al and Si substitution reducing the Cr content required to form the phase, which is explained in Chapter 2 in more detail.

EPMA was also performed on regions from the top and bottom of the alloy ingot, calculated compositions from these regions are presented in Table 4.5. At the top and bottom of the alloy ingot, the same phases present in the middle of the ingot were found: (Nb), Ti-rich (Nb), large grain $D8_8$, Eutectic $D8_8$, T2, and $NbCr_2$. Compositions of these phases at both locations are relatively similar to those at the centre of the alloy ingot, but differences are found. Most notably B content is generally lower in phases found at the top and bottom of the ingot. In phases (Nb), Ti-rich (Nb) and $NbCr_2$ this could be considered within error, but for high boron phases large grain $D8_8$, Eutectic $D8_8$, and T2, the differences are more obvious. Top and bottom $D8_8$ have B contents of 3.7 at.% and 2.7 at.%, respectively, compared to the middle locations content of 6.2 at.%. Top and bottom T2 have B contents of 17.8 at.% and 13.3 at.%, respectively, compared to the middle locations content of 20.4 at.%. This may indicate boron volatilisation during the arc-melting process, and this is not seen for any other elements across each phase. Slight pull-away of the liquid alloy during solidification from the copper cooled crucible could also result in volatilisation at the bottom on the ingot, and it may be compounded in this location due to macrosegregation effects, discussed in Section 4.2.2.6, where overall B content is lower at the bottom of the ingot. There are minor variations in compositions likely linked to the varied cooling rates at the three locations. These include marginally lower Al and Nb contents and slightly higher Cr content at the top and bottom versions of (Nb), approximately 5 at.% lower Cr content of the $NbCr_2$ phase at the top and bottom locations, and slightly lower Ti content in both $D8_8$ and eutectic $D8_8$ in the top and bottom locations.

*Table 4.4) Compositions of phases found in the central region of JW1-AC using EPMA mapping, values given in at.%. Mean ± stdev, minimum value - maximum value. * marks phases that were in small quantities and only 40 pixels were taken.*

	Nb	Si	Ti	Cr	Al	Ge	B
$D8_8$	40.7 ± 0.9	25.0 ± 1.0	19.6 ± 0.6	0.7 ± 0.2	1.8 ± 0.5	6.0 ± 0.2	6.2 ± 1.0
	38.6 - 42.8	22.0 - 27.2	18.2 - 21.1	0.5 - 2.3	1.0 - 2.8	5.4 - 6.8	4.0 - 8.2
Intergranular $D8_8$	31.6 ± 2.4	19.3 ± 2.0	29.7 ± 2.3	2.4 ± 1.6	4.8 ± 0.5	7.7 ± 0.6	4.6 ± 1.1
	23.7 - 38.5	11.7 - 22.8	22.7 - 37.5	1.0 - 9.8	3.5 - 6.5	4.7 - 8.6	1.5 - 7.0
T2	49.6 ± 0.8	12.1 ± 0.6	13.9 ± 0.4	1.6 ± 0.1	0.2 ± 0.1	2.1 ± 0.1	20.4 ± 0.7
	47.7 - 51.6	9.9 - 13.8	13.0 - 14.8	1.3 - 2.0	0.1 - 0.4	2.0 - 2.3	18.9 - 22.2
(Nb)	39.9 ± 1.8	1.3 ± 0.3	34.0 ± 0.9	15.1 ± 1.0	7.8 ± 0.3	0.8 ± 0.1	1.0 ± 0.7
	35.3 - 43.6	0.5 - 2.6	32.2 - 36.5	13.2 - 17.5	6.8 - 8.6	0.7 - 1.1	0.0 - 2.9
Ti-rich (Nb)*	33.1 ± 1.6	1.3 ± 0.5	37.8 ± 1.4	18.4 ± 1.1	7.5 ± 0.3	0.8 ± 0.1	1.1 ± 0.7
	30.0 - 35.5	0.7 - 3.5	35.4 - 41.1	15.7 - 20.3	6.9 - 8.1	0.7 - 0.9	0.0 - 2.8
$NbCr_2$*	17.7 ± 0.9	6.1 ± 0.8	21.6 ± 1.7	51.1 ± 2.7	2.0 ± 0.7	0.8 ± 0.1	0.8 ± 0.7
	16.7 - 21.2	3.8 - 7.6	20.2 - 31.0	38.0 - 53.8	1.5 - 4.4	0.6 - 1.2	0.0 - 2.3

*Table 4.5) Compositions of phases found in the top and bottom regions region of the JW1-AC ingot using EPMA mapping. Mean ± stdev, minimum value - maximum value. * marks phases that were in small quantities and only 40 points could be taken.*

-Top region-	Nb	Si	Ti	Cr	Al	Ge	B
$D8_8$	40.5 ± 1.2	24.2 ± 1.7	21.0 ± 1.1	0.7 ± 0.1	3.0 ± 1.1	6.9 ± 0.4	3.7 ± 0.7
	37.7 - 43.5	19.4 - 28.1	18.8 - 22.7	0.4 - 0.9	1.0 - 4.9	5.9 - 7.6	2.5 - 5.9
Intergranular $D8_8$	27.6 ± 1.0	21.1 ± 0.8	34.5 ± 0.9	2.0 ± 0.3	4.6 ± 0.2	8.8 ± 0.3	1.5 ± 0.5
	25.8 - 31.2	19.4 - 23.0	32.1 - 36.4	1.7 - 3.1	4.0 - 5.2	7.9 - 9.4	0.6 - 2.7
T2	49.8 ± 1.2	11.2 ± 0.7	16.1 ± 1.0	2.3 ± 0.3	0.3 ± 0.2	2.5 ± 0.1	17.8 ± 0.7
	46.0 - 52.8	9.3 - 13.6	14.0 - 18.8	1.7 - 3.3	0.0 - 1.2	2.2 - 3.1	15.8 - 20.1
(Nb)	41.1 ± 1.7	1.2 ± 0.3	33.8 ± 0.9	13.8 ± 1.1	9.2 ± 0.4	0.9 ± 0.1	0.0 ± 0.1
	36.9 - 45.1	0.4 - 2.0	31.9 - 36.1	11.7 - 17.0	8.1 - 10.2	0.7 - 1.5	0.0 - 0.9
Ti-rich (Nb)	30.1 ± 0.9	1.0 ± 0.3	42.6 ± 1.3	16.8 ± 1.1	8.6 ± 0.4	0.9 ± 0.1	0.0 ± 0.0
	28.5 - 32.3	0.4 - 1.6	40.3 - 45.7	15.0 - 18.9	7.8 - 9.6	0.8 - 1.1	0.0 - 0.3
$NbCr_2$*	20.3 ± 1.7	5.3 ± 0.7	24.4 ± 2.0	45.6 ± 4.3	3.5 ± 1.1	0.9 ± 0.1	0.0 ± 0.1
	18.3 - 24.3	3.6 - 6.5	21.8 - 28.6	36.3 - 51.2	2.4 - 5.6	0.8 - 1.3	0.0 - 0.3
-Bottom region-	Nb	Si	Ti	Cr	Al	Ge	B
$D8_8$	40.1 ± 1.2	23.5 ± 1.5	22.1 ± 1.2	0.8 ± 0.1	3.8 ± 1.0	7.1 ± 0.4	2.7 ± 0.6
	37.4 - 42.9	20.3 - 26.8	19.9 - 24.7	0.6 - 1.1	2.0 - 5.6	6.3 - 7.8	0.2 - 4.6
Intergranular $D8_8$*	30.8 ± 2.2	20.7 ± 0.9	31.5 ± 2.0	2.0 ± 0.7	5.2 ± 0.5	8.1 ± 0.3	1.7 ± 0.7
	24.1 - 33.7	18.8 - 23.8	29.6 - 37.6	1.3 - 5.8	3.8 - 6.0	7.3 - 8.8	0.0 - 2.8
T2	54.3 ± 0.9	13.4 ± 0.7	15.0 ± 0.4	1.5 ± 0.2	0.2 ± 0.1	2.4 ± 0.1	13.3 ± 0.5
	50.4 - 56.1	11.6 - 15.0	13.8 - 16.7	1.2 - 3.1	0.1 - 1.1	2.2 - 2.7	11.8 - 14.7
(Nb)	44.1 ± 2.6	1.4 ± 0.3	32.2 ± 1.4	12.3 ± 1.7	8.9 ± 0.4	0.9 ± 0.1	0.1 ± 0.2
	36.3 - 49.7	0.8 - 3.3	29.2 - 37.4	9.2 - 17.6	8.0 - 10.0	0.8 - 1.1	0.0 - 0.8
Ti-rich (Nb)	33.2 ± 2.9	1.3 ± 0.4	38.6 ± 2.7	18.1 ± 1.2	7.9 ± 0.4	0.8 ± 0.1	0.1 ± 0.2
	26.0 - 39.2	0.5 - 3.8	34.7 - 46.8	15.2 - 22.5	6.9 - 9.2	0.6 - 1.6	0.0 - 1.0
$NbCr_2$*	18.7 ± 2.3	6.2 ± 1.1	25.3 ± 4.6	45.9 ± 7.5	2.5 ± 0.9	1.0 ± 0.4	0.3 ± 0.8
	16.7 - 27.9	3.1 - 8.4	21.6 - 39.1	25.5 - 51.6	1.7 - 5.0	0.7 - 2.5	0.0 - 3.5

4.2.2.4 BSE - SEM Imaging

Figure 4.12a and Figure 4.12b show the typical microstructure of JW1-AC, taken from the centre of the alloy ingot using BSE imaging. Figure 4.13a and Figure 4.13b show the microstructure from the top of the alloy, where the alloy is closest in contact to the argon atmosphere. Figure 4.14a and Figure 4.14b show the microstructure from the bottom of the alloy, where the alloy is closest to the copper cooled crucible and is therefore assumed to have the highest cooling rate.

The centre region of JW1 (Figure 4.12) shows $D8_8$ grains, bright contrast T2 grains, and a mixture of intergranular phases that exist between these silicide phases. The $D8_8$ grains are more angular than the βNb_5Si_3 found in KZ5-AC with well-defined straight edges. $D8_8$ exists as larger discrete grains than in the B and Ge free alloy when comparing both central regions. The T2 phase, which appears as a white contrast phase in the BSE imaging, also has some well-defined straight edges, and can be described as generally more rectangular and elongated than the $D8_8$. There is significant cracking of both these silicide phases, but it is not clear whether this is a result of the surface preparation technique being poorly suited to a sample with high fraction of hard intermetallic phases or if upon cooling stresses were introduced to the system that eventually lead to cracking. From visual inspection of these BSE images it appears that the cracking is almost exclusive to these silicide phases.

The mixture of intergranular phases that exist between T2 and $D8_8$ phases are identified as the solid solution (Nb) and intergranular $D8_8$. The lighter of the two phases is (Nb). Certain areas of this (Nb) are darker in contrast, similarly to KZ5-AC, indicating Ti-rich regions of the niobium solid solution. Intergranular $D8_8$ is the darker contrast intergranular phase. Similarly to the KZ5-AC microstructure, within the intergranular region there are coarser dendritic areas of (Nb) and $D8_8$ which may have formed earlier during more rapid solidification, and there is a fine eutectic like structure of (Nb) and $D8_8$. In the case of JW1-AC this eutectic structure is usually found next to the (Nb) – $D8_8$ grain interface.

$NbCr_2$ cannot be distinguished in SEM-BSE imaging from intergranular $D8_8$. However, taking into account EPMA and EBSD results for JW1-AC, it is predicted to be forming in the central regions of the intergranular space where the contrast appears darkest. The (Nb) phase is still in a continuous matrix, although isolated areas may exist.

At the bottom region of the JW1-AC ingot (Figure 4.14), the microstructure is similar to the central region displayed in Figure 4.12. The bottom region has comparable grain size of T2 and $D8_8$ for the most part, with the exception of some $D8_8$ grains which are found close to the bottom surface on the order of tens of microns. The (Nb) and $D8_8$ intergranular areas are also visually similar in structure to the central part of the ingot. Darker contrast (Nb) phase due to Ti enrichment and the absence of any clear $NbCr_2$ phase are in line with the central region. The top region is notably different than the central region (Figure 4.13). There is a finer distribution of smaller T2 phases and a reduced amount of the (Nb) and $D8_8$ mixture, replaced with large grain $D8_8$. This is in contrast to KZ5-AC where the top region was most similar to the middle region, and the bottom region was distinctively different. Regardless, the same three phases; $D8_8$, T2 and (Nb), were identified across the whole ingot.

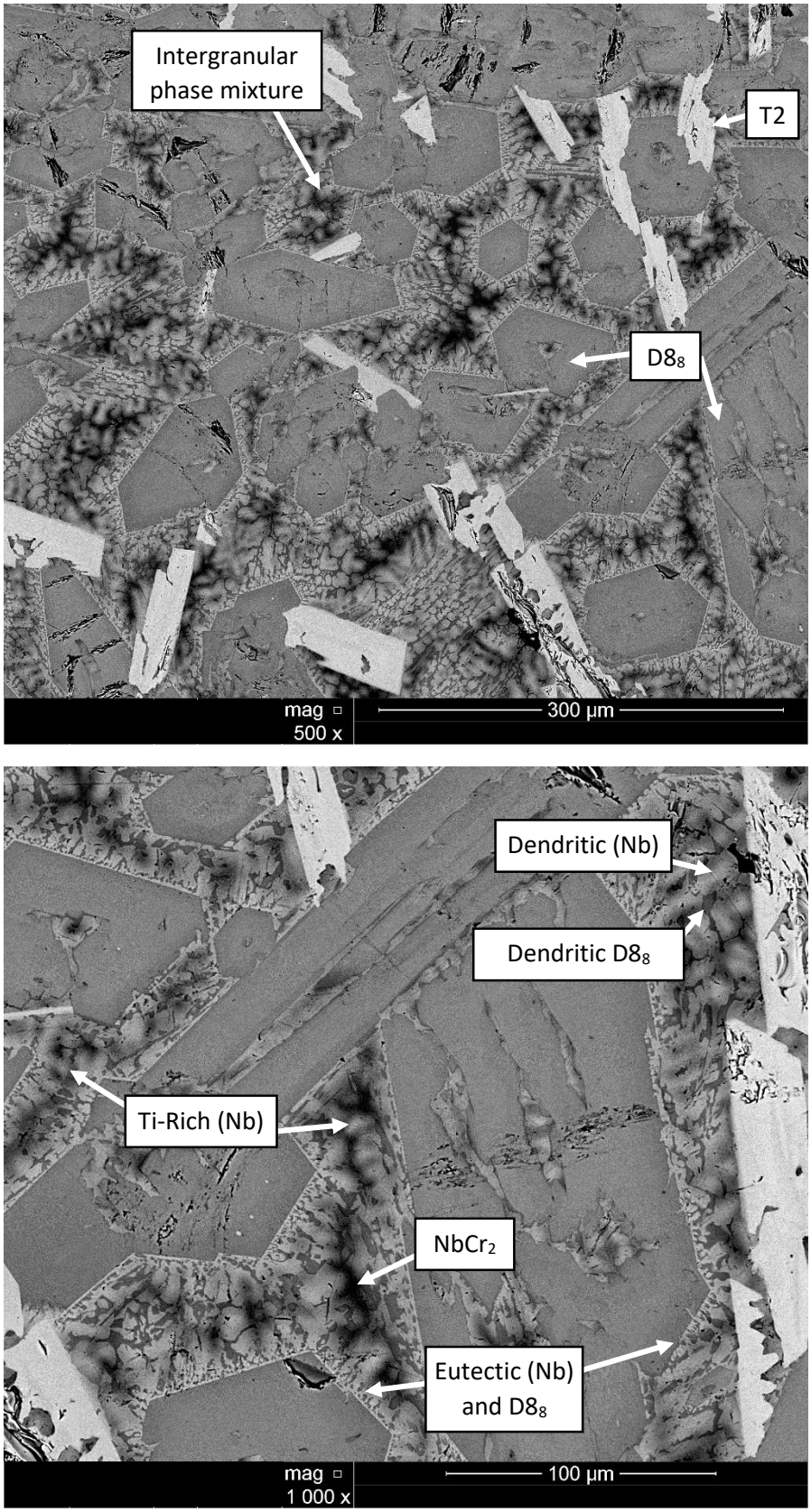

Figure 4.12a-b) BSE images of the central region of JW1-AC taken at lower magnification (a) and higher magnification (b)

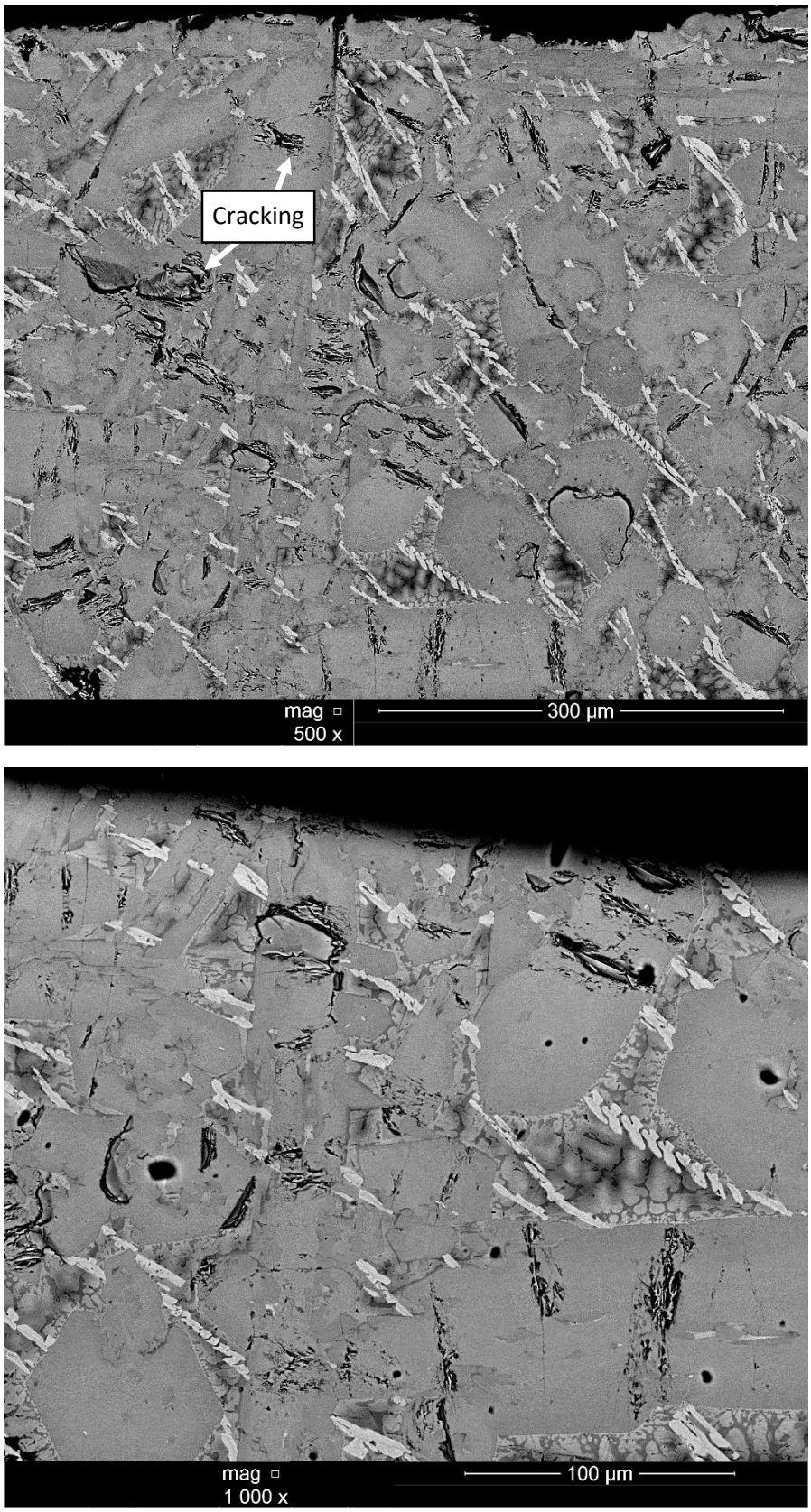

Figure 4.13a-b) BSE images of the top region of JW1-AC taken at lower magnification (a) and higher magnification (b)

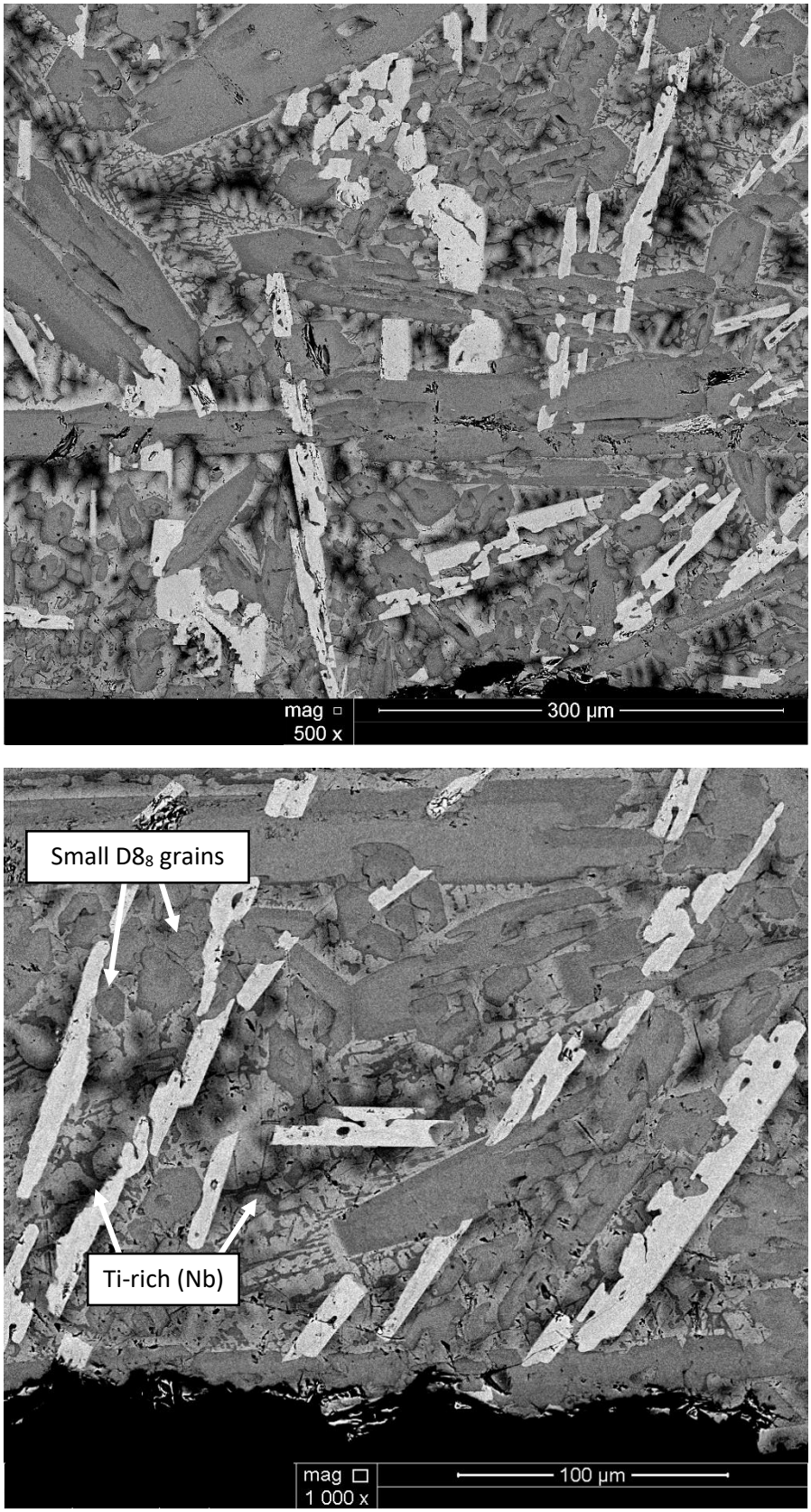

Figure 4.14a-b) BSE images of the bottom region of JW1-AC taken at lower magnification (a) and higher magnification (b)

4.2.2.5 Area Fraction

The area fractions of phases $D8_8$, T2 and (Nb) at the centre of the alloy ingot were calculated from BSE images and are given in Table 4.3. The contrast of these three phases was used to differentiate between them. On average the central area of JW1-AC contained 77.2% $D8_8$, 4.3% T2 and 18.5% (Nb) by area. EPMA analysis reveals that, as expected, B and Ge preferentially segregate to the silicide phases rather than the solid solution. It therefore follows that the amount of (Nb) decreases with the addition of the silicide forming elements. This is the case, as (Nb) area fraction reduces from 43.9% to 18.5% in alloys KZ5-AC and JW1-AC, respectively.

The $D8_8$ phase can be further differentiated with 68.6% of the total area being the large grains. The area percent of intergranular/eutectic $D8_8$ was measured to be 8.6%. The amount of intergranular $D8_8$ is likely an overestimate, because of similarity in contrast of $D8_8$ and $NbCr_2$ which is also present in these regions. Based on EPMA mapping however at the central area of JW1-AC, it is estimated that 0.9% of the total area is $NbCr_2$, and therefore intergranular $D8_8$ area fraction is expected to be reduced (7.7%). It should be noted that this estimation is based on one EPMA map of significantly less total area, and therefore cannot be treated with the same confidence as the remaining phases in Table 4.3.

In regards to the silicide phases, there is a higher proportion of main silicide compared to intergranular silicide in JW1-AC than in KZ5-AC, indicated by the ratio between the phases of 68.6/8.6 = 8.0 and 41.5/14.6 = 2.8 respectively. Regardless of whether T2 or even $NbCr_2$ mistaken as $D8_8$ is included in the main silicide or intergranular silicide side of the ratio, the overall conclusion is the same, as less than 6% area fraction of the alloy is made up of T2 and $NbCr_2$.

4.2.2.6 Macrosegregation

Macrosegregation from the top, middle and bottom regions of the as-cast ingot has occurred within the JW1-AC alloy to various extents depending on the element. *MACX* (C_{max} – C_{min}) values are displayed in Table 4.6. These values are calculated by subtracting the lowest average content of an element (C_{min}) from the highest average content of the same element (C_{max}). The average elemental contents for each element at the top, middle and bottom of the ingot are also calculated and displayed in Table 4.6 in order to identify trends that may emerge.

The highest values of *MACX* in the alloy JW1-AC are for Si, Ti and Cr with values of 8.8, 5.0 and 5.1 at.%, respectively. With the exception of Cr, the elements with the lowest macrosegregation values, Al, B, and Ge, were the elements with the lowest nominal content of 5 at.%, perhaps somewhat explaining their resistance to macrosegregation in the case of this alloy. Macrosegregation of Cr is fairly severe as it exceeds the nominal composition of Cr in alloy JW1 of 5 at.%, and actual commotion of Cr, 4.9 at.% (Table 3.1).

The elements Ti, Cr, Al and B follow a trend of reducing in content across the alloy from the top of the arc-melted ingot to the bottom. For example, average Al content is 5.6 at.% at the top of the ingot, 5.0 at.% in the central region, and 3.9 at.% in the bottom region of the ingot. Conversely, elements Nb, Si and Ge follow the opposite trend of increasing in content across the entire alloy from the top of the arc-melted ingot to the bottom. For example, average Nb content is 37.2 at.% at the top of the ingot, 38.8 at.% in the central region, and 41.2 at.% in the bottom region of the ingot.

Table 4.6) Average content of the top, middle and bottom regions of JW1-AC. Values given in at.%. Mean ± stdev, minimum value - maximum value. And macrosegregation ($C_{max} – C_{min}$ = MACX) values for JW1-AC. MACX values given in at.%.

	Nb	Si	Ti	Cr	Al	Ge	B
Top Region	37.2 ± 0.1	11.7 ± 0.4	30.4 ± 0.3	8.0 ± 0.2	5.6 ± 0.1	2.8 ± 0.1	4.3 ± 0.2
	37.1 - 37.3	11.4 - 12.3	30.1 - 30.7	7.7 - 8.2	5.5 - 5.8	2.7 - 2.9	4.1 - 4.5
Middle Region	38.8 ± 0.7	13.5 ± 1.8	29.5 ± 1.0	6.1 ± 1.2	5.0 ± 0.4	3.3 ± 0.4	3.8 ± 0.6
	37.8 - 39.5	11.6 - 16.0	28.2 - 30.6	4.4 - 7.1	4.5 - 5.3	2.9 - 3.9	3.2 - 4.5
Bottom Region	41.2 ± 0.4	18.9 ± 1.1	26.5 ± 0.6	3.8 ± 0.5	3.9 ± 0.3	3.4 ± 0.1	2.3 ± 0.3
	40.6 - 41.7	17.7 - 20.3	25.8 - 27.2	3.1 - 4.2	3.6 - 4.2	3.3 - 3.6	1.9 - 2.6
MACX	4.6	8.8	5.0	5.1	2.2	1.2	2.6

4.2.3 JW2-AC (Nb-24Ti-18Si-5Cr-5Al-5Ge-10B)

4.2.3.1 XRD

The X-ray diffraction pattern of JW2-AC (Nb-24Ti-18Si-5Cr-5Al-5Ge-10B) is given in Figure 4.15. In JW2, four phases are identified; the silicide $D8_8$, the $NbCr_2$ Laves, a niobium-titanium boride phase NbB and Nb solid solution (Nb). $D8_8$, $NbCr_2$, and (Nb) were all identified in the XRD pattern of as-cast JW1. The peaks associated with (Nb) are significantly reduced compared to the previously discussed alloys KZ5-AC and JW1-AC. However, there is significant enough broadness at the base of the largest $D8_8$ peak at approximately 41°, where the most intense peak of (Nb) would be, that (Nb) can be considered present in this alloy.

Peaks at positions corresponding to the T2 phase are notably absent in the XRD pattern of JW2-AC despite the increase in B content of the alloy when compared to JW1-AC. Most likely related to this observation is the assignment of multiple unique peaks to a niobium boride phase NbB. A large amount of substitution is expected for this phase as the pdf-4+ card for pure NbB (00-032-0709 - Pearson symbol oC8, Space group Cmcm, prototype structure CrB) is slightly shifted from the peaks that appear in the pattern in Figure 4.15, likely due to a large amount of Ti substitution for Nb. (Nb,Ti)B can accommodate approximately 15 at% Ti at 1400°C [77].

A high degree of confidence can be placed in the phases $D8_8$ and (Nb) being present, as well as a form of (Nb,Ti)B which will hence forth be referred to as NbB. This is due to there being either multiple unique peaks assigned to these phases or aforementioned broadness of the peaks at approximately 41°. Peak assignment to the $NbCr_2$ is based on the expectation that this phase can be found through EBSD phase analysis and EPMA compositional analysis, as the peaks associated with $NbCr_2$ are indistinct and relatively small.

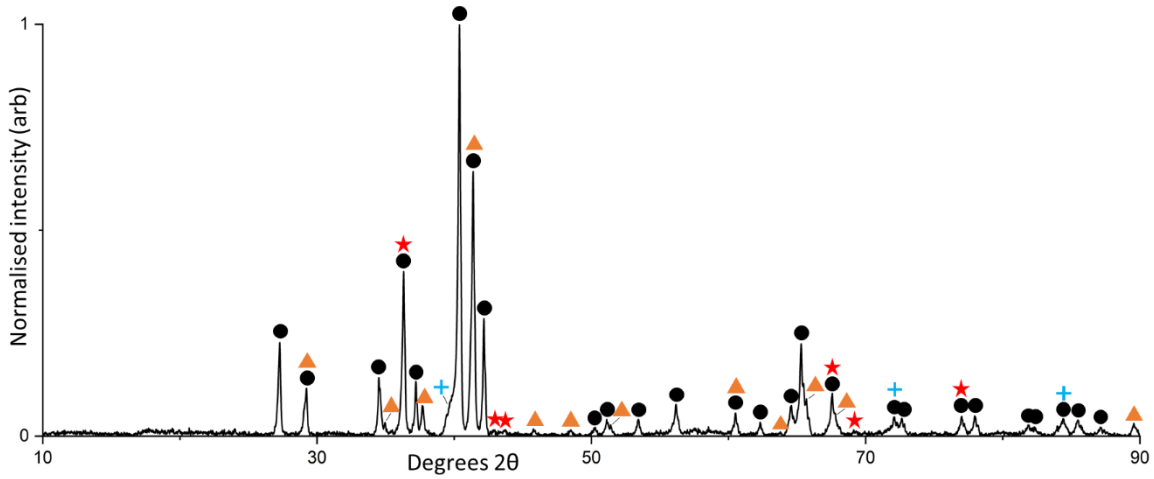

Figure 4.15) XRD pattern of JW2-AC. ● = $D8_8$, ★ = $NbCr_2$, ▲ = NbB, + = (Nb).

4.2.3.2 EBSD

EBSD maps of JW2-AC are presented in Figure 4.16 and Figure 4.17 with corresponding EDS maps of the areas examined. These maps are taken from the middle of the alloy ingot, at two different magnifications to show the general microstructure (Figure 4.16) and more detailed microstructure (Figure 4.17). The NbB, (Nb), $D8_8$ phases expected from XRD results were identified comprehensively in both Figure 4.16 and Figure 4.17 with the majority of the area being made up of $D8_8$ present as large grains, the intergranular (Nb) phase, and the NbB phase seen as irregularly shaped phases.

For confirmation of $NbCr_2$, which is only present in small quantities, the higher magnification map (Figure 4.17) provides evidence of this phase. The corresponding Cr EDS map corroborates this phase being $NbCr_2$, labelled for clarity. In addition, T2 is assigned to regions in both maps, but most easily seen in Figure 4.17.

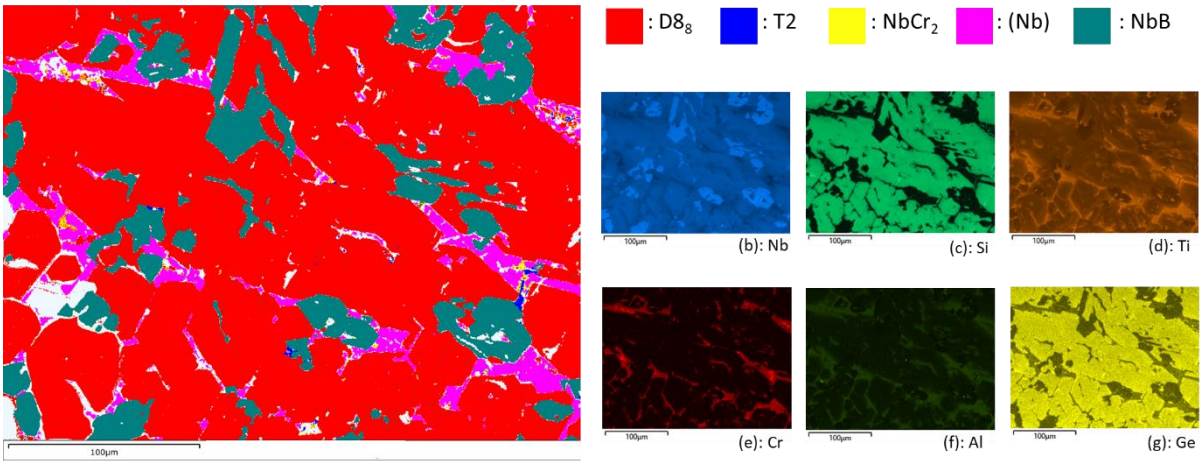

Figure 4.16a-g) EBSD map of JW2-AC at lower magnification (a), and corresponding qualitative EDS maps of Nb (b), Si (c), Ti (d), Cr (e), Al (f) and Ge (g).

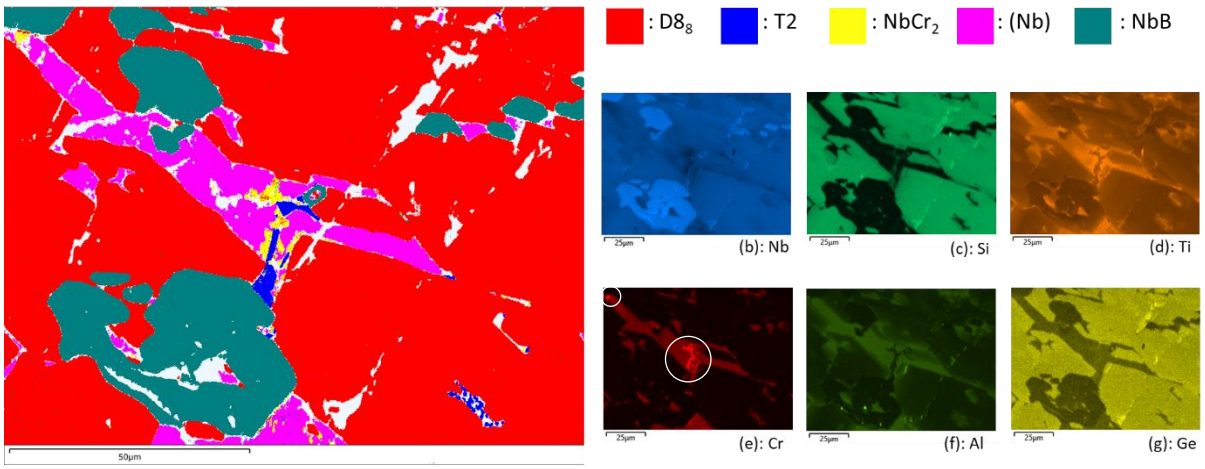

Figure 4.17a-g) EBSD map of JW2-AC at higher magnification (a), and corresponding qualitative EDS maps of Nb (b), Si (c), Ti (d), Cr (e), Al (f) and Ge (g). The Cr EDS map (e) has had areas particularly high in Cr ringed in white; in the EBSD map (a) these are found to be $NbCr_2$.

4.2.3.3 EPMA

EPMA mapping of the central region of JW2-AC showed the phases (Nb), $D8_8$, $NbCr_2$ and NbB. The compositions of these phases are given in Table 4.7. Unfortunately, no T2 phase was captured during the experiment owing to its scarcity in the microstructure. The $D8_8$ phase is not present as an intergranular/eutectic in this alloy and as such is reported as a single phase, $D8_8$.

The phase assigned to (Nb) has a high content of metallic elements, 37.0 at.% Ti, 18.8 at.% Cr, 8.4 at.% Al, as well as 32.9 at.% Nb. Elements Si, Ge and B have similar concentration in (Nb), but are much lower than metallic elements; 1.1 at.%, 0.7 at.%, and 1.2 at.%, respectively. These values are comparable to the (Nb) phase found in JW1-AC, with the main differences being lower Nb content and slightly higher content of each metallic element. As expected, the $NbCr_2$ Laves phase is mostly

made up of Cr, 42.6 at.%, which is lower than the nominal binary composition of 66.6 at.% due to Al and Si substitution. Since there is no eutectic or $D8_8$ in the intergranular region, it could be assumed that the final liquid to solidify into intergranular phases (Nb) and $NbCr_2$ would be higher in Si content than in JW1-AC, where eutectic and intergranular $D8_8$ was found. However, this is not reflected in the Si content of phases (Nb) and $NbCr_2$ in JW2-AC, equal to 1.1 at.% and 4.7 at.%, respectively. In fact, these are slightly lower values of Si in (Nb) and $NbCr_2$ compared to those same phases in JW1-AC. It therefore follows that the final melt is relatively Si poor compared to the nominal composition of the alloy, perhaps due to a large amount of $D8_8$ forming.

The niobium boride phase NbB identified in XRD and EBSD was found through EPMA spectroscopy. Measured B content is slightly below nominal 50 at.%, with a value of 45.7 at.%. This phase has the highest concentration of B in this alloy. There is also a significant substitution of Ti onto Nb sites, with respective concentrations of 14.1 at.% and 39.6 at.%. Other than the three major elements present in this NbB phase, Nb, Ti and B, the content of other elements is remarkably low. Minor elements Si, Cr, Al and Ge have average contents of 0.2 at.%, 0.3 at.%, 0.1 at.%, and 0.0 at.% in this phase, respectively. Evidently solubility of elements other than Ti is close to zero in the NbB phase. Throughout this work the niobium boride phase (with Pearson symbol oC8, Space group Cmcm, prototype CrB) will be referred to as NbB to differentiate from TiB (Pearson symbol oP8, Space group Pnma, prototype FeB) [33]. Unless otherwise stated this includes a significant Ti substitution for Nb on Nb 4c Wyckoff sites.

EPMA was also performed on regions from the top and bottom of the alloy ingot, calculated compositions from these regions are presented in Table 4.8. At the top and bottom of the alloy ingot, the same phases present in the middle of the ingot were found: (Nb), $D8_8$, and $NbCr_2$. T2 was also found at the bottom of the ingot, and NbB was found at the top. As was the case with JW1-AC, B content is generally lower in phases found at the top and bottom of the ingot. T2 at the bottom of the ingot had a boron composition measured as 14.6 at.%. In the case of top NbB, the boron content was only 41.5 at.%. This is an oddity, as unlike in the T2 phase there is little solubility range of B in NbB. Considering other Nb, B and Ti phases, this could instead be Nb_3B_2, but the maximum Ti solubility is approximately 10 at.% at 1400°C [77]. In addition, in the quaternary Nb-Ti-Si-B system with Si content of 18 at.%, the reported Nb_2B_3 phase had Si solubility between 14.0 at.% and 17.8 at.% in each alloy it was reported in [187], whereas is this instance Si content was 0.2 at.%. Therefore, the label NbB is used, but there exists some uncertainty regarding this phase, which further EBSD analysis would be required in future work to solve. Another general trend common to multiple phases is the Al content of phases present at the bottom of the ingot. In (Nb), $D8_8$ and $NbCr_2$ aluminium content is significantly greater in the bottom version of these phases, perhaps indicating local segregation of this element.

*Table 4.7) Compositions of phases found in the central region of JW2-AC using EPMA mapping, values given in at.%. Mean ± stdev, minimum value - maximum value. * marks phases that were in small quantities and only 40 points could be taken.*

	Nb	Si	Ti	Cr	Al	Ge	B
$D8_8$	39.1 ± 1.3	24.3 ± 0.9	21.7 ± 1.3	0.8 ± 0.1	1.1 ± 0.3	6.4 ± 0.3	6.6 ± 1.0
	35.4 - 41.5	21.2 - 26.3	19.6 - 24.8	0.5 - 1.2	0.7 - 2.1	5.7 - 7.2	4.1 - 9.3
NbB	39.6 ± 1.4	0.2 ± 0.1	14.1 ± 1.2	0.3 ± 0.1	0.1 ± 0.0	0.0 ± 0.0	45.7 ± 0.4
	35.6 - 42.1	0.0 - 0.5	12.3 - 17.2	0.1 - 0.5	0.0 - 0.2	0.0 - 0.1	44.8 - 47.2
(Nb)	32.9 ± 2.4	1.1 ± 0.4	37.0 ± 1.7	18.8 ± 1.2	8.4 ± 0.4	0.7 ± 0.0	1.2 ± 0.7
	27.6 - 37.4	0.4 - 3.9	34.1 - 42.2	16.2 - 21.1	7.4 - 9.5	0.5 - 0.8	0.0 - 2.8
$NbCr_2$*	20.1 ± 1.4	4.7 ± 1.3	26.7 ± 1.5	42.6 ± 2.6	3.6 ± 0.8	1.1 ± 0.6	1.2 ± 0.9
	17.7 - 22.2	2.8 - 7.7	23.9 - 29.7	39.5 - 47.6	2.1 - 5.4	0.7 - 3.6	0.0 - 3.6

*Table 4.8) Compositions of phases found in the top and bottom regions region of the JW2-AC ingot using EPMA mapping, values given in at.%. Mean ± stdev, minimum value - maximum value. * marks phases that were in small quantities and only 40 points could be taken.*

-Top region-	Nb	Si	Ti	Cr	Al	Ge	B
$D8_8$	37.4 ± 1.6	25.7 ± 1.0	23.9 ± 1.6	0.8 ± 0.2	1.4 ± 0.6	6.8 ± 0.3	4.0 ± 0.8
	34.2 - 40.7	22.6 - 28.4	20.9 - 27.2	0.4 - 1.1	0.5 - 2.8	6.0 - 7.4	1.8 - 6.0
NbB	41.5 ± 0.8	0.2 ± 0.1	16.6 ± 0.8	0.2 ± 0.1	0.0 ± 0.0	0.0 ± 0.0	41.5 ± 0.5
	39.4 - 43.2	0.0 - 0.5	15.2 - 18.9	0.0 - 0.3	0.0 - 0.1	0.0 - 0.0	39.9 - 42.7
(Nb)	32.5 ± 1.6	1.1 ± 0.3	38.1 ± 1.2	18.4 ± 1.0	9.2 ± 0.4	0.7 ± 0.1	0.0 ± 0.1
	26.8 - 35.3	0.3 - 2.5	36.5 - 43.9	16.6 - 21.4	8.0 - 10.2	0.5 - 1.6	0.0 - 0.7
$NbCr_2$*	18.2 ± 1.0	5.5 ± 1.0	25.9 ± 3.0	45.9 ± 4.9	2.6 ± 0.6	1.4 ± 1.1	0.4 ± 0.5
	16.4 - 19.6	4.2 - 8.2	21.9 - 33.6	37.2 - 52.8	2.0 - 3.9	0.6 - 4.7	0.0 - 1.4
-Bottom region-	Nb	Si	Ti	Cr	Al	Ge	B
$D8_8$	34.1 ± 0.6	18.1 ± 1.0	26.4 ± 0.6	2.2 ± 0.3	9.8 ± 0.8	6.7 ± 0.3	2.7 ± 0.6
	32.5 - 35.5	15.7 - 20.9	25.3 - 28.0	1.9 - 4.9	7.5 - 11.5	6.0 - 7.3	0.9 - 4.2
T2	46.3 ± 2.0	11.2 ± 1.2	18.3 ± 1.1	6.8 ± 1.1	0.8 ± 1.5	2.0 ± 0.1	14.6 ± 0.5
	34.2 - 49.8	5.5 - 13.5	16.1 - 28.5	4.6 - 11.6	0.1 - 9.9	1.5 - 2.3	12.9 - 15.8
(Nb)	22.9 ± 1.6	0.6 ± 0.2	38.1 ± 2.0	19.1 ± 1.1	18.6 ± 0.5	0.6 ± 0.1	0.2 ± 0.7
	18.5 - 29.0	0.2 - 1.6	26.6 - 43.4	16.0 - 21.4	17.3 - 20.2	0.4 - 1.1	0.0 - 7.0
$NbCr_2$	19.7 ± 0.7	4.9 ± 0.9	19.1 ± 1.8	46.6 ± 3.3	8.7 ± 1.9	0.8 ± 0.1	0.1 ± 0.4
	17.1 - 23.1	1.6 - 7.0	17.7 - 28.5	29.5 - 49.6	7.2 - 20.1	0.7 - 2.2	0.0 - 3.8

4.2.3.4 BSE - SEM Imaging

Figure 4.18a and Figure 4.18b show the typical microstructure of JW2-AC, taken from the centre of the alloy ingot using BSE imaging. Figure 4.19a and Figure 4.19b show the microstructure from the top of the alloy, where the alloy is closest in contact to the argon atmosphere. Figure 4.20a and Figure 4.20b show the microstructure from the bottom of the alloy, where the alloy is closest to the copper cooled crucible and is assumed to have the highest cooling rate.

The centre region of JW2-AC (Figure 4.18) shows large $D8_8$ grains, the NbB phase, small amounts of bright contrast T2 grains, and a mixture of intergranular phases that exist between these silicide and boride phases. The $D8_8$ and NbB phases are difficult to distinguish from each other visually as the have similar contrasts, although NbB is slightly lighter grey contrast. The shape of NbB grains are less angular in nature than $D8_8$ grains and the diameter of NbB grains is fairly consistently less than 80 µm, whereas $D8_8$ grains can be greater than 300 µm. The bright contrast T2 phase has some well-defined straight edges and can be described as generally more rectangular and elongated. This is similar to the T2 phase in JW1-AC BSE imaging (Figure 4.12), although in significantly lower quantities in JW2-AC. Also similarly to JW1-AC, there is significant cracking and surface defects in Figure 4.18. From visual inspection of these BSE images it appears that the cracking is almost exclusively in the silicide phases and niobium-titanium boride phase NbB, and not the intergranular regions in between these phases.

The mixture of intergranular phases that exist between the silicide phases and NbB are identified as the solid solution (Nb) and $NbCr_2$. They cannot be distinguished visually from BSE imaging from each other. This is partly because they have similar contrast to each other, which is then exacerbated by the varied contrast of the (Nb) phase owing to variation in Ti content throughout the phase. The (Nb) phase is no longer a continuous matrix as it was in the central regions of KZ5-AC and JW1-AC.

The top region of JW2-AC (Figure 4.19) has distinct columnar grains of $D8_8$ making up the majority of the microstructure. NbB is more difficult to identify through BSE imaging but NbB is found in significant quantities as well. The T2 phase is absent from the top region of the alloy. The same mixture of (Nb) and $NbCr_2$ is also found in between the columnar $D8_8$ similarly to the middle region. The angular nature of the major phase, $D8_8$, is likely linked to the solidification process and cooling rate of this part of the ingot.

The bottom region of the alloy shown in Figure 4.20a can be described in two parts; the very-bottom region extending from the surface of the alloys to approximately 200 µm inwards and the transitional region shown in the top half of Figure 4.20a which extends approximately 650 µm into the alloy until the microstructure resembles that of Figure 4.18, the middle region. The very-bottom region contains significantly more (Nb) and $NbCr_2$ mixture than the middle region. Here the (Nb) and $NbCr_2$ phases can be distinguished as they exist in coarser arrangements, with (Nb) having a darker contrast than the $NbCr_2$ phase. Smaller $D8_8$ grains are spread throughout the very-bottom region, with less common bright T2 identified too. The transitional region is a fine mixture of T2 and $D8_8$ with very little if any formation of $NbCr_2$, NbB or (Nb). This two region structure suggests severe local segregation of primarily Si, as the very-bottom region contains mostly phases where Si content is low, and the transitional region contains only silicides.

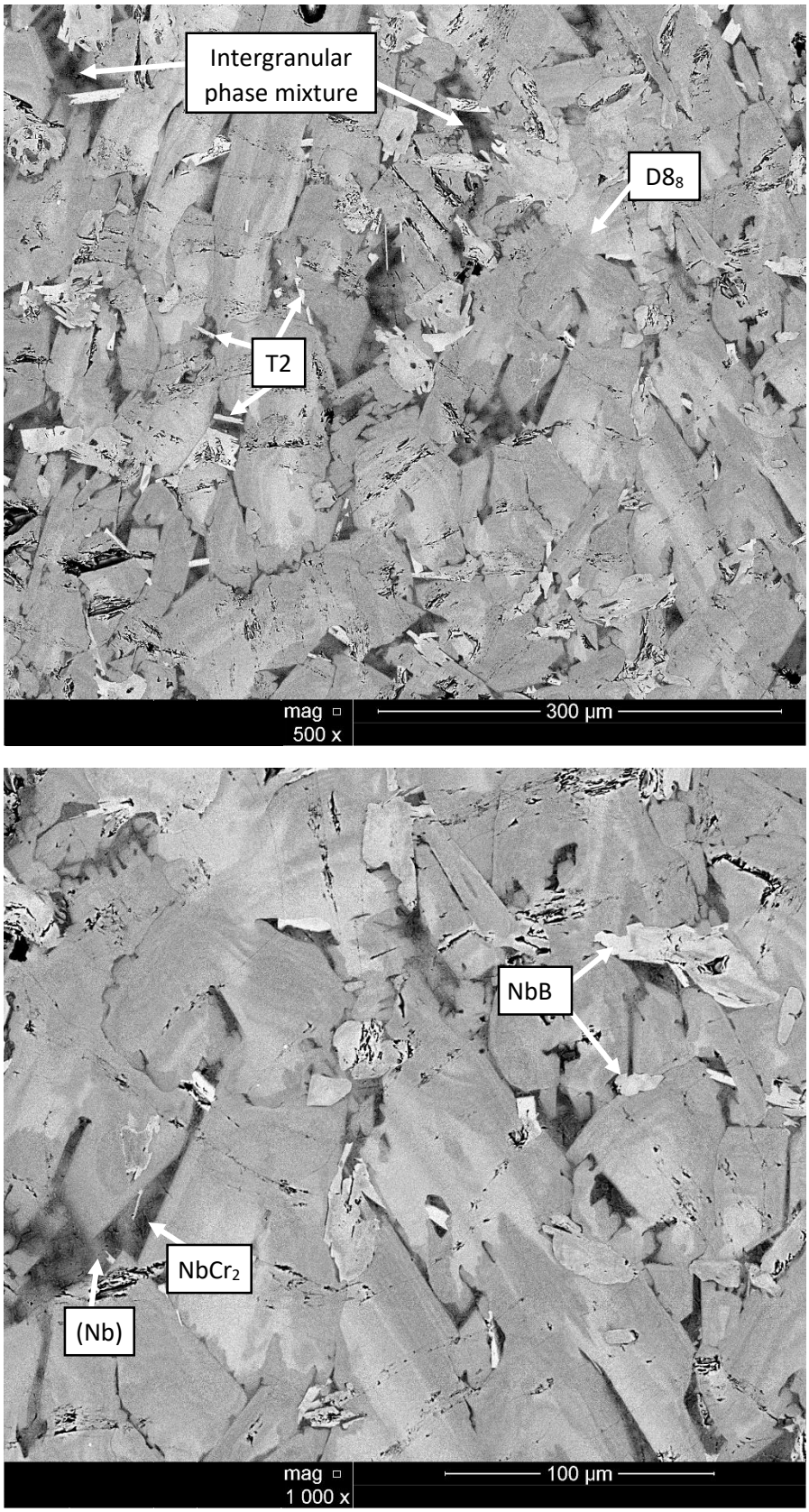

Figure 4.18a-b) BSE images of the central region of JW2-AC taken at lower magnification (a) and higher magnification (b)

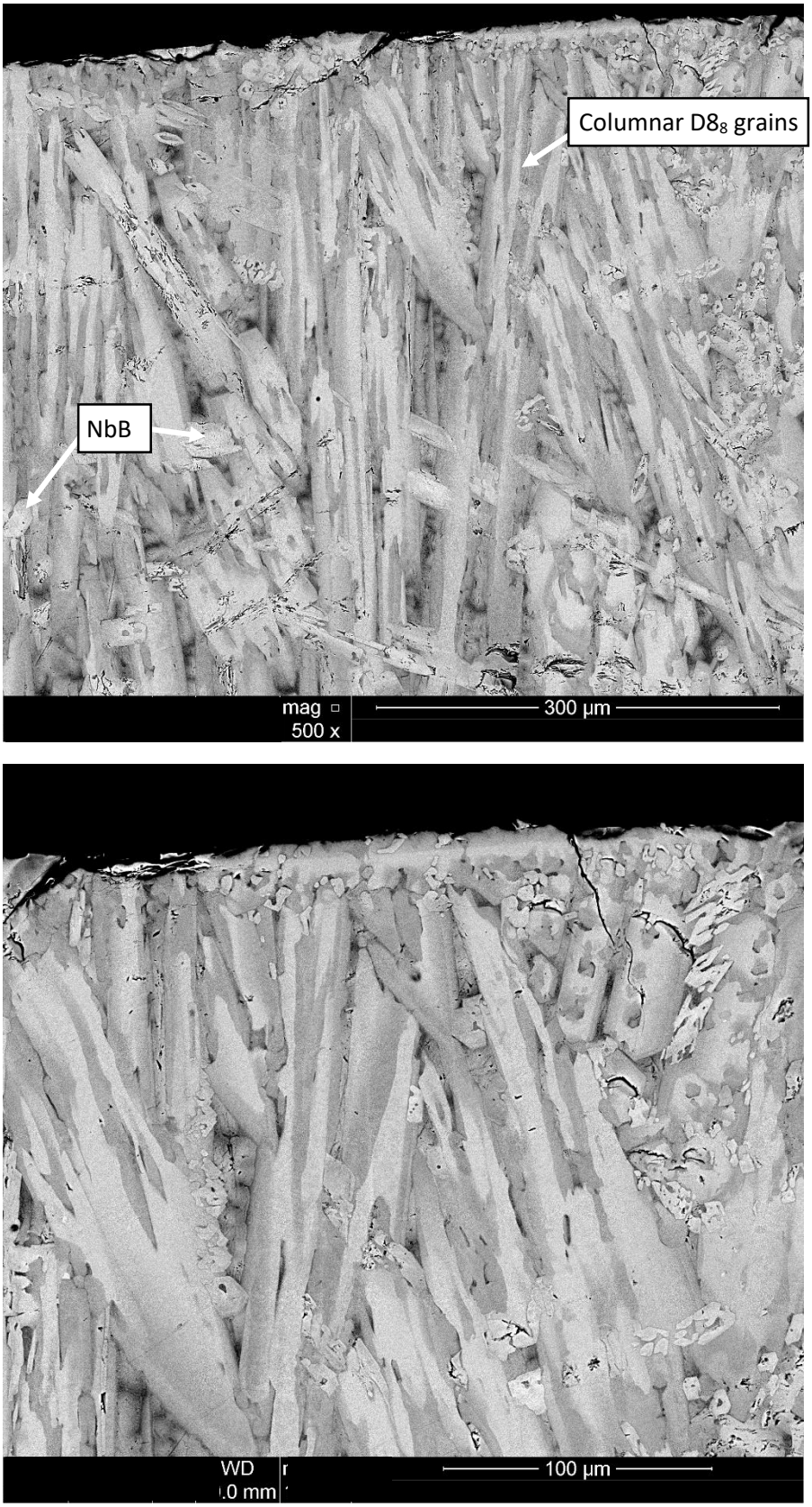

Figure 4.19a-b) BSE images of the top region of JW2-AC taken at lower magnification (a) and higher magnification (b)

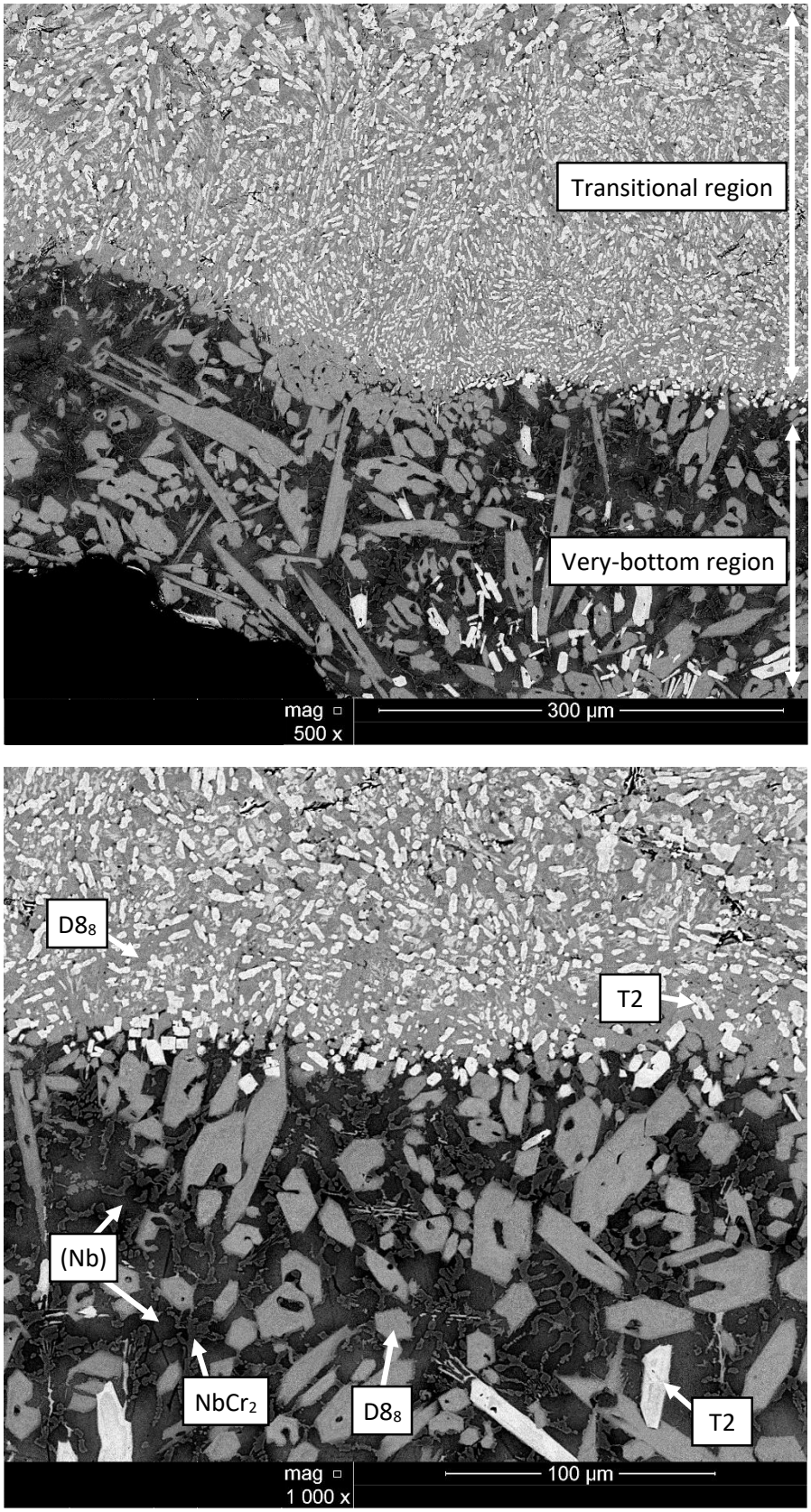

Figure 4.20a-b) BSE images of the bottom region of JW2-AC taken at lower magnification (a) and higher magnification (b)

4.2.3.5 Area Fraction

The area fractions of phases $D8_8$, T2, NbB, $NbCr_2$ and (Nb) at the centre of the alloy ingot were calculated from BSE imaging and are given in Table 4.3. The contrast of these phases was used to differentiate between them, with the exception of $NbCr_2$ and (Nb). In this case the contrast was too similar to distinguish these phases apart. Instead the ratio of $NbCr_2$ and (Nb) that appears in EPMA mapping at the central area of JW2-AC was used to estimate the area fractions of $NbCr_2$ and (Nb). On average 10.66% of JW2-AC was composed of $NbCr_2$ and (Nb), which can then be assigned to each phase based on the ratio of 1 : 3.19 ($NbCr_2$: (Nb)) to give 2.5% and 8.1%, respectively. Similarly, to the case $D8_8$ and $NbCr_2$ indistinguishability in JW1-AC, it should be noted that this estimation is based on only one EPMA map of significantly less total area. More confidence can be placed in the other phases. On average the central area of JW2-AC was 80.3% $D8_8$, 0.7% T2 and 9.0% NbB by area.

Initial B and Ge additions to the alloy KZ5 (Nb-24Ti-18Si-5Cr-5Al) resulted in less (Nb) forming, as B and Ge preferentially segregate to silicide phases. In JW2-AC, with an additional 5 at.% B content compared to JW1-AC, (Nb) area fraction has been further reduced as would be expected. This remains the case despite large amounts of boron being contained in the NbB phase, as approximately equal amounts of combined Nb and Ti are also taken up by this phase. The area fraction of NbB in JW2-AC is larger than the area fraction of T2 in JW1-AC, with values of 9.0% and 4.3%, respectively.

4.2.3.6 Macrosegregation

Macrosegregation from the top, middle and bottom regions of the as-cast ingot has occurred within the JW2-AC alloy to various extents depending on the element. *MACX* ($C_{max} - C_{min}$) values are displayed in Table 4.9. The average elemental contents for each element at the top, middle and bottom of the ingot are also calculated and displayed in Table 4.9 in order to identify trends that may emerge.

The highest values of *MACX* in the alloy JW2-AC are Si, Ti and B with values of 4.9, 3.9 and 8.1 at.%, respectively. With the exception of Nb, the elements with the lowest macrosegregation values, Cr, Al, and Ge, were the elements with the lowest nominal content of 5 at.%, perhaps somewhat explaining their resistance to macrosegregation in the case of this alloy. Macrosegregation of Nb is remarkably low considering it is the main element in JW2-AC, with a value of 1.6 at.%.

B is found to be more concentrated in the middle region of the alloy where NbB can be found regularly, and less so at the top and bottom regions where EPMA results revealed individual phases tend to have less boron content than their central region counterparts. The high *MACX* value of B is linked to the volume fraction of the high boron phase that forms. In the middle region one such area had abnormally low B and therefore less NbB formation, resulting in the greatest difference of measured values solely in this region, 3.6 at.% compared to 11.8 at.% B.

The elements Cr and Al follow a trend of increasing in content across the entire alloy from the top of the arc-melted ingot to the bottom. For example, average Al content is 2.2 at.% at the top of the ingot, 2.7 at.% in the central region, and 3.7 at.% in the bottom region of the ingot. Ti also has a higher average content at the bottom region, 29.9 at.%, than at the top region, 28.9 at.%, but the middle region is the lowest and closest to nominal composition at 27.8 at.%. Conversely, Nb follows the opposite trend of decreasing in content across the entire alloy from the top of the arc-melted ingot to the bottom. Average Nb content is 38.7 at.% at the top of the ingot, 38.5 at.% in the central region, and 38.3 at.% in the bottom region of the ingot.

Table 4.9) Average content of the top, middle and bottom regions of JW2-AC, values given in at.%. Mean ± stdev, minimum value - maximum value. And macrosegregation ($C_{max} – C_{min}$ = MACX) values for JW1-AC. MACX values given in at.%.

	Nb	Si	Ti	Cr	Al	Ge	B
Top Region	38.7 ± 0.1	17.0 ± 1.0	28.9 ± 0.1	2.9 ± 0.4	2.2 ± 0.1	4.5 ± 0.2	5.6 ± 0.7
	38.6 - 38.8	16.0 - 18.5	28.8 - 29.1	2.3 - 3.2	2.1 - 2.4	4.3 - 4.8	4.9 - 6.5
Middle Region	38.5 ± 0.7	15.0 ± 1.7	27.8 ± 1.4	3.6 ± 0.4	2.7 ± 0.2	4.0 ± 0.5	8.4 ± 3.4
	37.8 - 39.4	13.6 - 17.4	26.3 - 29.7	3.0 - 3.9	2.4 - 2.9	3.6 - 4.7	3.6 - 11.8
Bottom Region	38.3 ± 0.1	15.2 ± 0.2	29.9 ± 0.2	4.4 ± 0.1	3.7 ± 0.2	4.0 ± 0.0	4.4 ± 0.1
	38.2 - 38.5	15.0 - 15.5	29.8 - 30.2	4.2 - 4.6	3.4 - 4.0	4.0 - 4.1	4.3 - 4.5
MACX	1.6	4.9	3.9	2.2	2.0	1.2	8.1

4.2.4 JW3-AC (Nb-24Ti-18Si-5Cr-5Al-10Ge-5B)

4.2.4.1 XRD

The X-ray diffraction pattern of JW3-AC (Nb-24Ti-18Si-5Cr-5Al-10Ge-5B) is given in Figure 4.21. In JW3, three phases are identified; the silicide $D8_8$, the $NbCr_2$ Laves, and Nb solid solution (Nb) which were all identified in the XRD pattern of JW1-AC and JW2-AC. Similarly to JW2-AC, the peaks for (Nb) were reduced, however broadening of $D8_8$ peak at 41° 2θ indicated the presence of (Nb).

Peaks at positions corresponding to the NbB phase are notably absent in the XRD pattern of JW3-AC, likely due to the nominal B content of 5 at.%. Peaks associated with T2 are also absent from this pattern, indicating increasing Ge content from 5 to 10 at.% at the expense of Nb has not stabilised this phase. A high degree of confidence can be placed in the phase $D8_8$ being present, as this phase matches almost all of the peaks in Figure 4.21. Peak assignment to the $NbCr_2$ is based on the expectation that this phase can be found through EBSD phase analysis and EPMA compositional analysis, as the peaks associated with $NbCr_2$ with the exception of a single peak at approximately 43° are indistinct and relatively small.

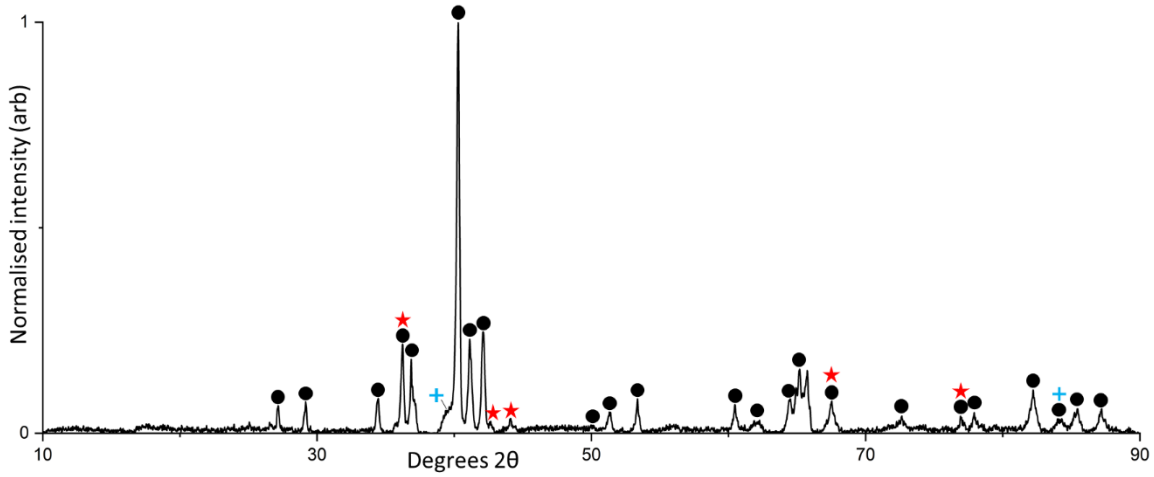

Figure 4.21) XRD pattern of JW3-AC. ● = $D8_8$, ★ = $NbCr_2$, + = (Nb).

4.2.4.2 EBSD

EBSD maps of JW3-AC are presented in Figure 4.22 and Figure 4.23 with corresponding EDS maps of the areas examined. These maps are taken from the middle of the alloy ingot, at two different magnifications to show the general microstructure (Figure 4.22) and more detailed microstructure (Figure 4.23). The (Nb), $D8_8$ and $NbCr_2$ phases expected from XRD results were identified comprehensively in both Figure 4.22 and Figure 4.23. With the majority of the area being made up of $D8_8$ present as large grains, and intergranular (Nb) and $NbCr_2$ phases.

The NbB phase could not be found through EBSD mapping, which is an indication of rarity of this phase in the JW3-AC alloy. Areas in Figure 4.22 and Figure 4.23 that appear white could not be assigned to a phase. This is a result of poor surface preparation and residual stresses, but mainly in this case surface cracks result in no possible Kikuchi line pattern being generated.

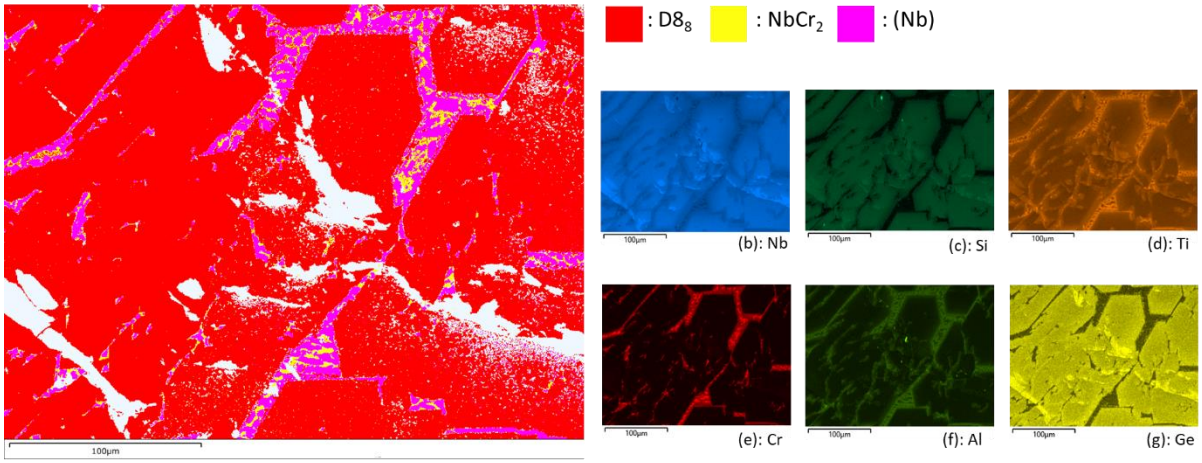

Figure 4.22a-g) EBSD map of JW3-AC at lower magnification (a), and corresponding qualitative EDS maps of Nb (b), Si (c), Ti (d), Cr (e), Al (f) and Ge (g).

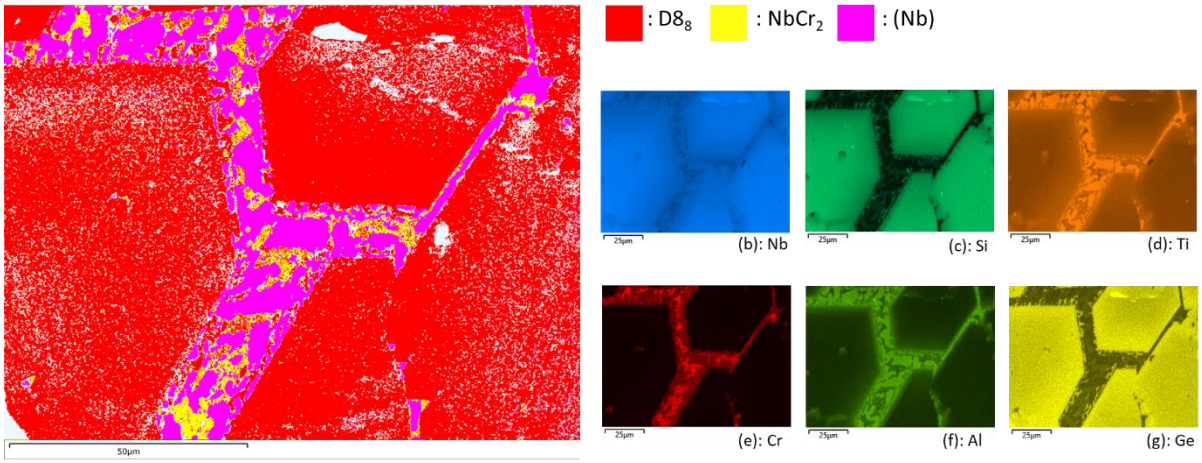

Figure 4.23a-g) EBSD map of JW3-AC at higher magnification (a), and corresponding qualitative EDS maps of Nb (b), Si (c), Ti (d), Cr (e), Al (f) and Ge (g).

4.2.4.3 EPMA

EPMA mapping of the central region of JW3-AC identifies phases (Nb), $D8_8$, $NbCr_2$ and NbB. The compositions of these phases are given in Table 4.10. The $D8_8$ phase is not present as an intergranular/eutectic in this alloy and as such is reported as a single phase, $D8_8$. The $D8_8$ phase has a high Ge content of 12.2 at.% as a result of having a higher overall content of Ge within the alloy.

The phase assigned to (Nb) has a high content of metallic elements, 42.9 at.% Ti, 18.0 at.% Cr, 14.9 at.% Al, as well as 21.9 at.% Nb. Ti content is almost double that of Nb content in this phase, and Al content is also significantly greater when compared to (Nb) in JW1-AC and JW2-AC. Elements Ge and B have similar concentrations in (Nb), but are much lower than metallic elements; 0.9 at.% and 1.1 at.%, respectively. These values of Ge and B contents are comparable to the (Nb) phase found in JW1-AC and JW2-AC. However, Si content is notably lower in JW3-AC with a value of 0.4 at.%.

The $NbCr_2$ Laves phase is mostly made up of Cr, 50.3 at.%, with Si and Al contents of 3.8 and 6.1 at.%, respectively. Minor amounts of Ge and B are found within this phase also. Despite not being detected by XRD or EBSD, NbB was found in small quantities in JW3-AC. The boron content was 45.9 at.%, almost identical to that of NbB in JW2-AC, 45.7 at.%. The Ti and Nb contents varied by up to 5.4

at.% between these alloys showing a solubility range exists for Ti and Nb in this phase. NbB was the highest B containing phase in JW3-AC.

EPMA was also performed on regions from the top and bottom of the alloy ingot, calculated compositions from these regions are presented in Table 4.11. At the top and bottom of the alloy ingot, phases (Nb), $D8_8$, and $NbCr_2$ were found. NbB was not found in either top or bottom regions. As was the case with JW2-AC, Al content was generally higher in the bottom location for all three phase, reaching 21.4 at.% in the (Nb) which is comparable to the Nb content (20.5 at.%). In $D8_8$ the boron content at the bottom of the ingot was notably lower than the middle region $D8_8$, however the top versions of $D8_8$ had higher boron content so the potential volatilisation that was proposed to occur in other alloys has not occurred in the case of JW3-AC, it least in the top region. B content is oddly high in the $NbCr_2$ phase in the top region as well, which is unusual as B solubility in this phase is not typically seen, and Cr content is low at 31.3 at.%. In general, the phases presented in JW3-AC are less similar across the alloy ingot than in the case of other alloys, and 'gradients' exists when comparing top to middle to bottom regions. In the example of $D8_8$, Nb, Si, B reduce from top to bottom and Ti, Cr, Al and Ge increase from top to bottom.

Table 4.10) Compositions of phases found in the central region of JW3-AC using EPMA mapping, values given in at.%. Mean ± stdev, minimum value - maximum value

	Nb	Si	Ti	Cr	Al	Ge	B
$D8_8$	33.9 ± 0.9	18.0 ± 0.9	25.4 ± 0.7	1.5 ± 0.3	2.6 ± 0.4	12.2 ± 0.3	6.4 ± 1.1
	32.1 - 36.5	15.6 - 20.7	23.5 - 27.0	1.1 - 4.7	1.7 - 4.2	11.3 - 12.9	1.9 - 8.7
NbB	34.2 ± 2.3	0.1 ± 0.3	18.8 ± 2.0	0.8 ± 0.5	0.1 ± 0.2	0.1 ± 0.2	45.9 ± 0.8
	27.7 - 39.5	0.0 - 1.7	14.0 - 23.4	0.2 - 3.3	0.0 - 1.2	0.0 - 1.4	41.4 - 47.7
(Nb)	21.9 ± 1.4	0.4 ± 0.2	42.9 ± 1.7	18.0 ± 1.2	14.9 ± 0.6	0.9 ± 0.1	1.1 ± 0.8
	18.9 - 24.8	0.1 - 1.0	39.0 - 46.8	15.0 - 21.3	13.8 - 16.9	0.7 - 1.0	0.0 - 3.4
$NbCr_2$	19.1 ± 0.6	3.8 ± 0.5	18.5 ± 1.3	50.3 ± 2.2	6.1 ± 1.0	1.2 ± 0.3	1.0 ± 0.9
	17.3 - 21.3	1.6 - 5.2	17.2 - 28.8	36.5 - 52.8	4.8 - 12.0	1.0 - 4.8	0.0 - 4.4

Table 4.11) Compositions of phases found in the top and bottom regions region of the JW3-AC ingot using EPMA mapping, values given in at.%. Mean ± stdev, minimum value - maximum value.

	Nb	Si	Ti	Cr	Al	Ge	B
-Top region-							
$D8_8$	35.7 ± 1.4	21.2 ± 1.4	21.3 ± 1.3	0.9 ± 0.2	1.4 ± 0.6	10.8 ± 0.6	8.7 ± 1.8
	30.9 - 39.1	16.7 - 24.7	19.4 - 26.0	0.6 - 1.5	0.8 - 4.0	9.6 - 12.9	1.8 - 12.7
(Nb)	28.0 ± 1.2	0.6 ± 0.3	39.8 ± 2.2	17.6 ± 2.0	12.7 ± 0.7	1.0 ± 0.1	0.2 ± 0.6
	24.8 - 31.9	0.1 - 2.1	24.5 - 43.7	15.1 - 35.3	9.0 - 14.5	0.8 - 1.8	0.0 - 4.2
$NbCr_2$	22.4 ± 0.9	3.6 ± 0.6	26.3 ± 2.8	31.3 ± 4.1	6.2 ± 1.3	1.8 ± 0.2	8.5 ± 2.9
	20.0 - 24.8	1.9 - 5.1	19.8 - 34.0	21.5 - 40.6	3.2 - 10.5	1.3 - 2.4	1.1 - 14.9
-Bottom region-							
$D8_8$	31.9 ± 1.0	16.1 ± 1.4	28.3 ± 0.9	2.1 ± 0.2	5.7 ± 1.4	13.3 ± 0.6	2.5 ± 0.7
	30.0 - 34.2	13.1 - 19.9	26.2 - 30.6	1.6 - 2.6	3.5 - 8.9	11.7 - 15.5	0.0 - 4.3
(Nb)	20.5 ± 1.2	0.9 ± 0.9	39.5 ± 3.5	16.0 ± 2.9	21.4 ± 1.7	1.6 ± 1.3	0.2 ± 0.4
	17.7 - 24.6	0.1 - 4.8	22.6 - 45.6	10.0 - 34.8	16.2 - 25.6	0.5 - 5.9	0.0 - 3.1
$NbCr_2$	19.7 ± 1.0	3.5 ± 0.7	19.6 ± 3.6	45.3 ± 3.9	10.3 ± 1.5	1.3 ± 0.5	0.2 ± 0.4
	16.5 - 21.8	1.2 - 5.4	16.6 - 37.9	24.8 - 49.4	8.0 - 18.5	0.6 - 4.8	0.0 - 2.8

4.2.4.4 BSE - SEM Imaging

Figure 4.24a and Figure 4.24b show the typical microstructure of JW3-AC, taken from the centre of the alloy ingot using BSE imaging. Figure 4.25a and Figure 4.25b show the microstructure from the top of the alloy, where the alloy is closest in contact to the argon atmosphere. Figure 4.26a and Figure 4.26b show the microstructure from the bottom of the alloy, where the alloy is closest to the copper cooled crucible and is assumed to have the highest cooling rate.

The centre region of JW3-AC (Figure 4.24) shows $D8_8$ grains, small amounts of a slightly brighter phase that is presumably NbB, and a mixture of intergranular phases between these silicide and boride phases. The slightly brighter phase labelled as NbB has morphology more similar to the T2 phase identified in JW1-AC and JW2-AC. However, EPMA results in section 4.2.4.3 provide more conclusive evidence that the NbB phase is present in the central region of JW3-AC, and that T2 is not found. EBSD cannot confirm either phase is present in the central region of JW3-AC.

The mixture of intergranular phases between the silicide phases and NbB are identified as the solid solution (Nb) and $NbCr_2$. They cannot be easily distinguished visually from BSE imaging, due to similar contrast and compositional variation. As was the case with JW2-AC, the (Nb) phase is not a continuous matrix. Similarly, to the previous B and Ge containing alloys, there is significant cracking and surface defects. From visual inspection of these BSE images, it appears that the cracking is again almost exclusively in the silicide phase, and not the intergranular regions in between these phases

The top region of JW3-AC (Figure 4.25) has distinct columnar grains of $D8_8$ at the left and right-most edges of Figure 4.25a. These columnar grains exist to a lesser extent than was seen in JW2-AC and a microstructure similar to the central region of JW3-AC makes up the majority on the top region as it does in Figure 4.24a. The NbB phase is absent from the top region of the alloy. The same mixture of (Nb) and $NbCr_2$ is also found in between the $D8_8$ phase as it was in the middle region.

The bottom region of the alloy shown in Figure 4.26 can be described in two parts; the very-bottom region extending from the surface of the alloys to around 500 µm and the 'normal' region shown in the top half of Figure 4.26 which resembles that of Figure 4.24, the central region. The very-bottom region contains significantly more (Nb) and $NbCr_2$ mixture than the middle region. Here the (Nb) and $NbCr_2$ phases can be distinguished as they exist in coarser arrangements, with (Nb) having a darker contrast than the $NbCr_2$ phase. Smaller $D8_8$ grains are spread throughout the very-bottom region. The normal region is the same as the middle region with a $NbCr_2$ and (Nb) mixture existing between $D8_8$ grains, but with the exception that no NbB can be found. There is no NbB present in the very-bottom region either. The very-bottom region is similar to what was seen in the bottom region of the JW2-AC alloy, but the T2/$D8_8$ transitional region is not seen in JW3-AC. This still suggests severe local segregation of primarily Si as it did in the JW2-AC bottom region, but perhaps to a lesser extend as the solely silicide transitional region is absent in the JW3-AC bottom region.

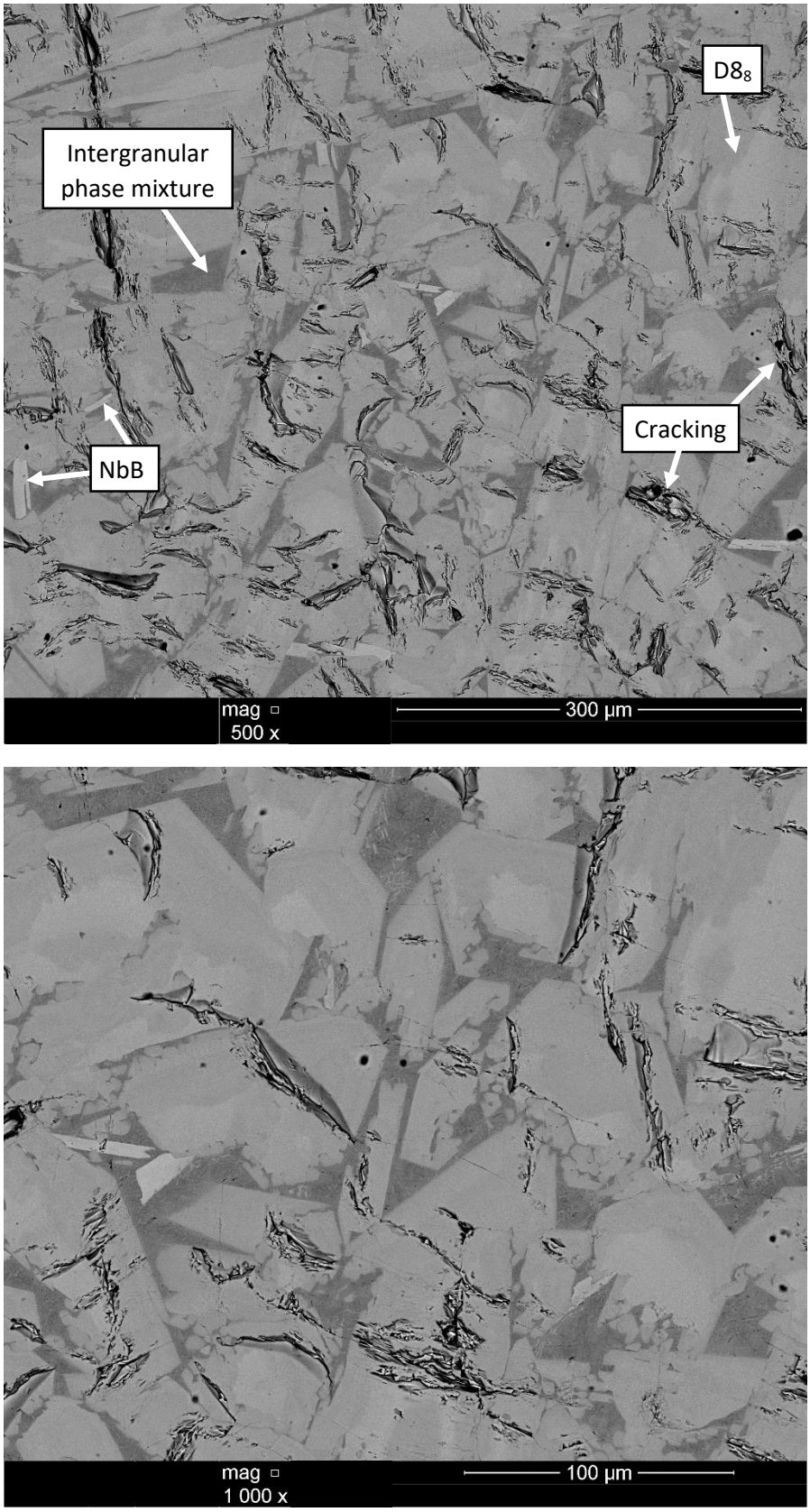

Figure 4.24a-b) BSE images of the central region of JW3-AC taken at lower magnification (a) and higher magnification (b)

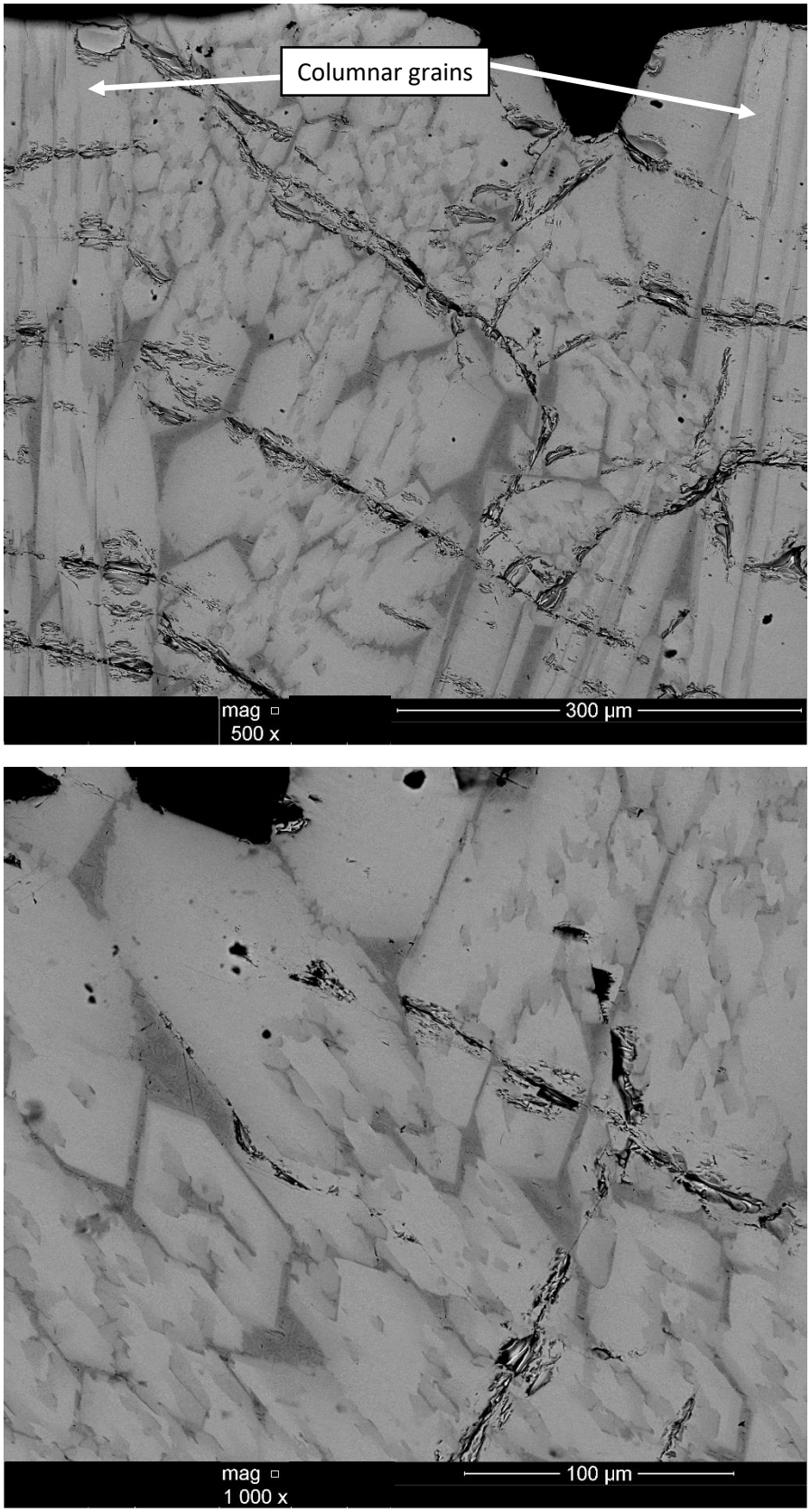

Figure 4.25a-b) BSE images of the top region of JW3-AC taken at lower magnification (a) and higher magnification (b)

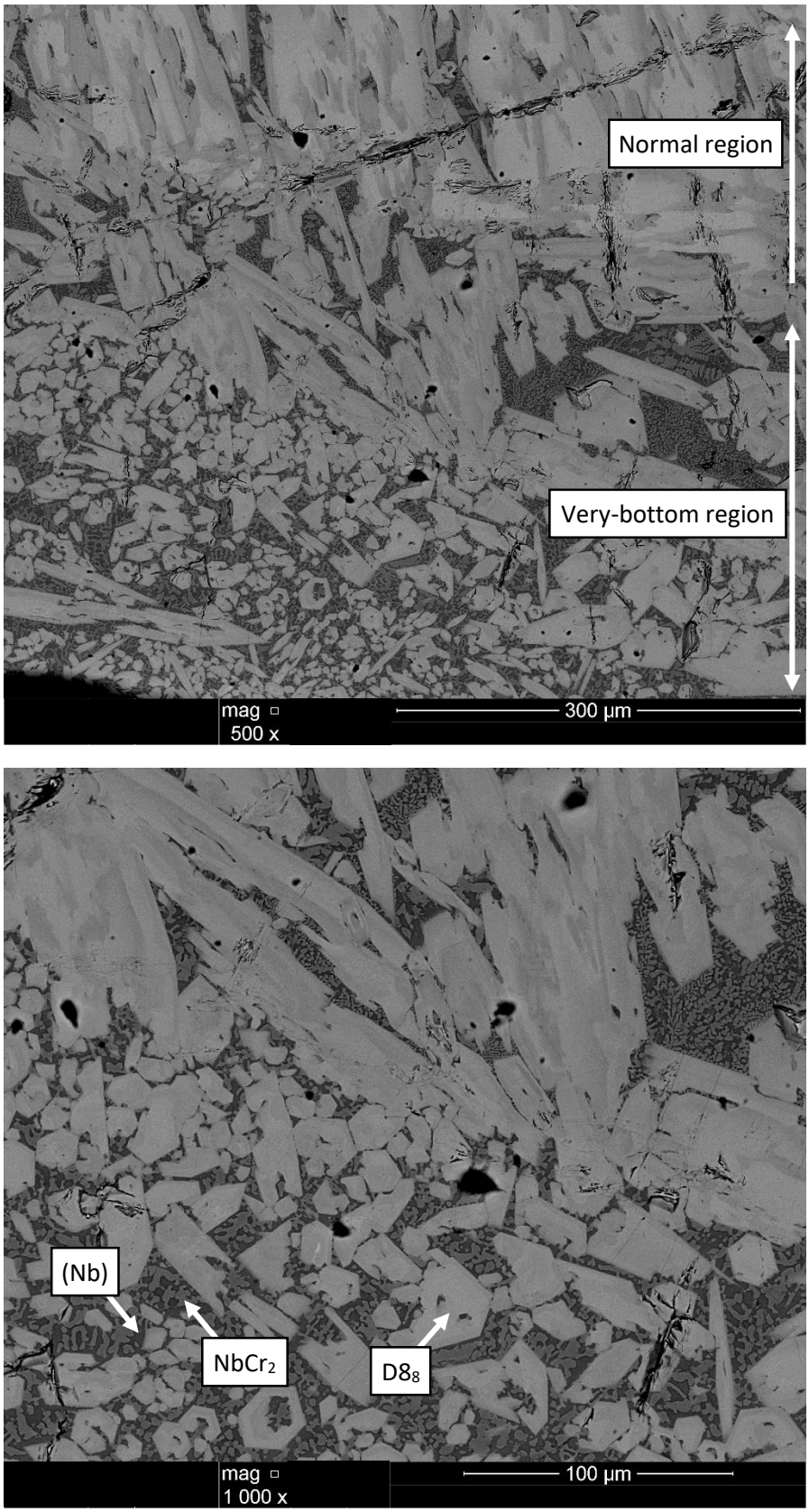

Figure 4.26a-b) BSE images of the bottom region of JW3-AC taken at lower magnification (a) and higher magnification (b)

4.2.4.5 Area Fraction

The area fractions of phases $D8_8$, NbB, $NbCr_2$ and (Nb) at the centre of the alloy ingot were calculated from BSE imaging and are given in Table 4.3. The contrast of these phases was used to differentiate between them, with the exception of $NbCr_2$ and (Nb). In this case the contrast was too similar to distinguish these phases apart. Instead the ratio of $NbCr_2$ and (Nb) that appears in EPMA mapping at the central area of JW3-AC was used to estimate the area fractions of $NbCr_2$ and (Nb).

On average 11.5% of JW3-AC was composed of $NbCr_2$ and (Nb), which can then be assigned to each phase based on the ratio of 1 : 1.09 ($NbCr_2$: (Nb)) to give 5.5% and 6.0%, respectively. Similarly to the $NbCr_2$ and (Nb) overlap of contrasts in JW2-AC, it should be noted that this estimation is based on only one EPMA map of significantly less total area. More confidence can be placed in the other phases. On average the central area of JW3-AC was 87.8% $D8_8$ and 0.6% NbB by area.

Initial B and Ge additions to the alloy KZ5 (Nb-24Ti-18Si-5Cr-5Al) resulted in less (Nb) forming, as B and Ge preferentially segregate to silicide phases. In JW3-AC, with an additional 5 at.% Ge content compared to JW1-AC, (Nb) area fraction has been further reduced as would be expected. The area fractions of (Nb) in JW2-AC and JW3-AC are 8.1% and 6.0%, respectively. If the estimates for (Nb) area fraction is accurate, in the as-cast state Ge has had a greater effect at reducing (Nb) area fraction than the equivalent atomic percent of B.

4.2.4.6 Macrosegregation

Macrosegregation from the top, middle and bottom regions of the as-cast ingot has occurred within the JW3-AC alloy to various extents depending on the element. *MACX* ($C_{max} - C_{min}$) values are displayed in Table 4.12. The average elemental contents for each element at the top, middle and bottom of the ingot are also calculated and displayed Table 4.12 in order to identify trends that may emerge.

The highest values of *MACX* in the alloy JW3-AC are Nb, Si, Cr and Al with values of 11.7, 9.7, 10.1, and 9.3 at.%, respectively. These macro segregation values are the largest calculated across all the alloys considered; JW1-AC, JW2-AC, JW3-AC. The higher degree of macrosegregation is primarily a results of the bottom region of the alloy having significantly different elemental contents to the other maps taken in the middle and top regions. Nb and Si in the bottom region are on average 8.2 at.% and 5.6 at.% lower than the most similar region, respectively, and Cr and Al in the bottom region are on average 7.1 at.% and 6.3 at.% higher than the most similar region, respectively. The very bottom region of JW3-AC that contains significant amounts of (Nb) and $NbCr_2$ was on average approximately twice as thick (500 µm) as the very bottom region of JW2-AC. As a result, more of this region was recorded in JW3 EPMA large area maps used to calculate macrosegregation values, and more of the transitional region was recorded in the case of JW2-AC. JW2-AC has consistently lower or the same values of macrosegregation for all elements when compared to JW3-AC. The only exception of this phenomena is B macrosegregation. JW2-AC had a value of 8.1 at.% and JW3-AC had a value of 2.8 at.%.

The elements Ti, Cr, Al and B follow a trend of increasing in content across the entire alloy from the top of the arc-melted ingot to the bottom. For example, average Ti content is 27.1 at.% at the top of the ingot, 28.4 at.% in the central region, and 30.5 at.% in the bottom region of the ingot. Conversely, Nb, Si and Ge follow the opposite trend of decreasing in content across the entire alloy from the top of the arc-melted ingot to the bottom. For example, average Ge content is 9.9 at.% at the top of the ingot, 9.8 at.% in the central region, and 7.9 at.% in the bottom region of the ingot.

Table 4.12) Average content of the top, middle and bottom regions of JW3-AC. Values given in at.%. Mean ± stdev, minimum value - maximum value. And macrosegregation ($C_{max} – C_{min}$ = MACX) values for JW1-AC. MACX values given in at.%.

	Nb	Si	Ti	Cr	Al	Ge	B
Top Region	37.2 ± 0.2	16.7 ± 0.3	27.1 ± 0.2	3.7 ± 0.2	2.8 ± 0.1	9.9 ± 0.2	2.6 ± 0.3
	37.0 - 37.6	16.4 - 17.1	26.9 - 27.4	3.4 - 4.0	2.7 - 3.0	9.6 - 10.0	2.4 - 3.0
Middle Region	34.9 ± 2.4	14.6 ± 0.9	28.4 ± 1.7	5.2 ± 0.8	4.0 ± 0.6	9.8 ± 0.2	3.1 ± 0.2
	31.6 - 37.1	13.4 - 15.6	26.9 - 30.8	4.2 - 6.1	3.4 - 4.8	9.5 - 9.9	3.0 - 3.4
Bottom Region	26.7 ± 0.9	8.7 ± 1.3	30.5 ± 0.1	11.3 ± 2.2	10.3 ± 1.6	7.9 ± 1.1	4.6 ± 0.6
	25.8 - 27.6	7.4 - 10.0	30.5 - 30.6	9.1 - 13.5	8.8 - 11.9	6.8 - 9.0	4.0 - 5.2
MACX	11.7	9.7	3.9	10.1	9.3	3.2	2.8

4.2.5 Differential scanning calorimetry

Differential scanning calorimetry results of each as-cast alloy are presented in Figure 4.27, alongside the recorded mass gain as a percentage of the initial mass during each experiment measured using thermogravimetry. During cooling, an exothermic peak is identified which is proposed to be a result of solidification of a liquid, as it is only visible on the cooling curve. On heating, there is a corresponding melting endothermic peak which is broad and barely visible below the base line, but is evident in the JW alloy series especially. These peaks suggest partial melting of the alloy around 1350-1400°C. The approximate locations of the endothermic and exothermic events coincide with a sharp uptake in mass and reduction in the rate of mass gain, respectively. This is thought to be a result of a small amount of liquid phase forming which reacts readily with available oxygen in the gas flow. Although inert gas was used, metallic liquids at high temperatures will readily react with low amounts of oxygen. Full melting of the sample did not appear to occur as peaks were small and the samples retained their initial shape after testing, although even thin oxide layers could contain the liquid in the case of these very small samples.

For the JW series the solidification peak is at approximately 1380°C in each case, whereas KZ5-AC has a solidification peak at approximately 1400°C. Since this peak is seen in all alloys, the responsible phase should be present in each alloy. Melting at this temperature is proposed to be due to either melting of an especially inhomogeneous part of the solid solution where substitution of Nb with solute elements (Ti, Cr, Al, etc.) can reduce melting temperatures, or melting of the $NbCr_2$ phase identified in JW1, JW2, and JW3 but not KZ5-AC. It is possible that $NbCr_2$ was present in KZ5-AC, as [186] found in past studies, but this could not be confirmed in this current work. The latter explanation would require substitution of Al and Ti but low Si substitution into $NbCr_2$ to reduce the melting temperature [44][48][58], as it is typically ~1700 °C [43].

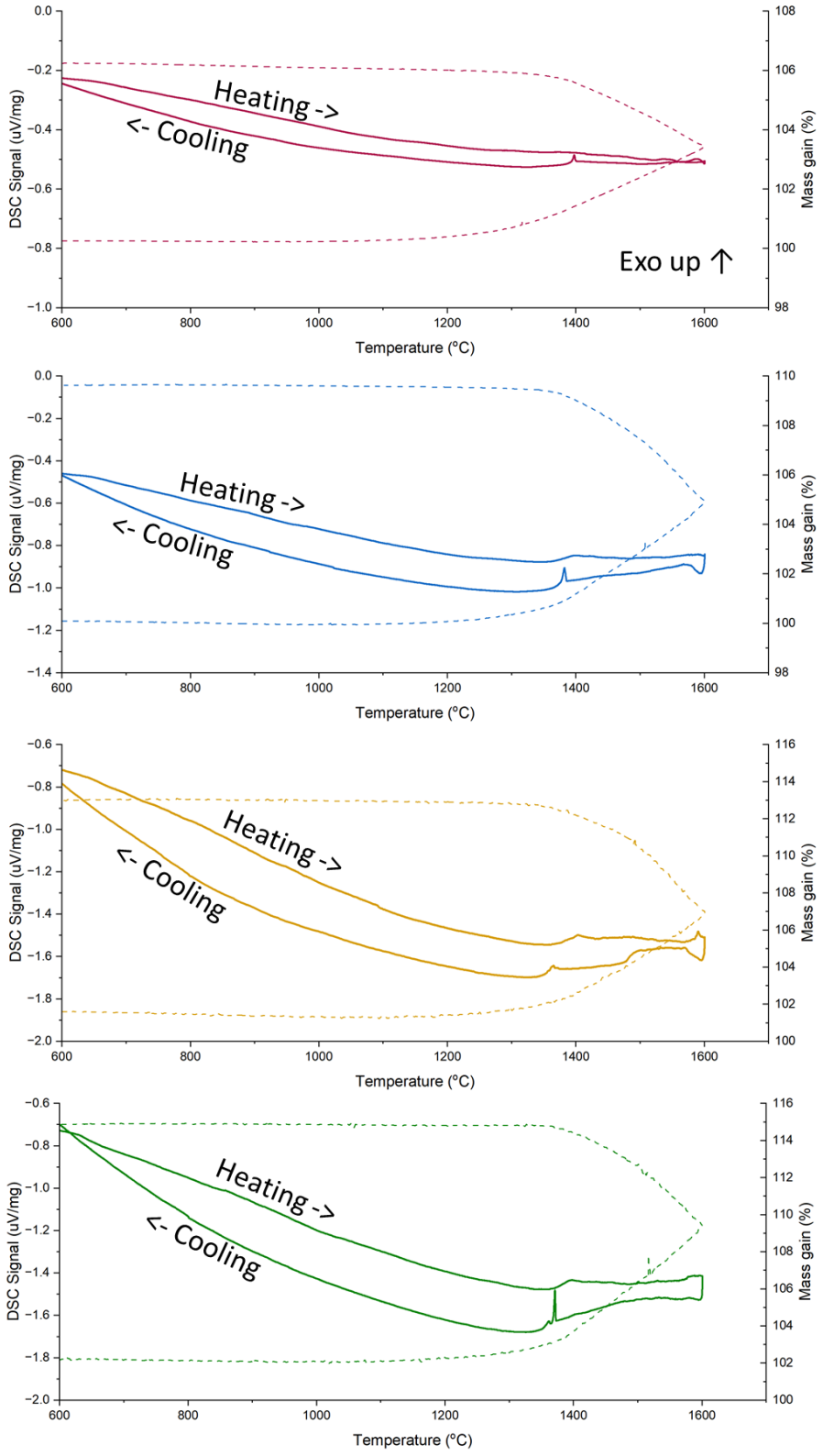

Figure 4.27) Differential scanning calorimetry (DSC) of as-cast samples of KZ5 (red), JW1 (blue), JW2 (yellow), and JW3 (green). Samples were heated to and cooled from 1600°C. Corresponding mass gain of each sample is plotted on the right-hand axis (dotted lines).

4.3 Discussion

4.3.1 The effect of 5 at.% B and 5 at.% Ge on the microstructure and phases of KZ5 (Nb-24Ti-18Si-5Cr-5Al)

The addition of 5 at.% B and 5 at.% Ge to KZ5 (Nb-24Ti-18Si-5Cr-5Al), accommodated by a corresponding reduction in Nb content, has significantly changed the microstructure and phases that have formed in the alloy JW1 (Nb-24Ti-18Si-5Cr-5Al-5Ge-5B). The purpose of such additions is to primarily improve oxidation performance, however the effects to microstructure and phases are important to consider when designing an alloy intended for functional components such as jet engine turbine blades and discs.

The high temperature tetragonal form of Nb_5Si_3, βNb_5Si_3, that is stable in the binary Nb-Si system as well as the KZ5-AC alloy produced in this study is not formed in JW1-AC, or indeed any B and Ge containing alloy in this study. Instead, additions of B and Ge have resulted in the formation of phases known as T2 and $D8_8$ in the as-cast microstructure. There is evidence in the literature that both of these phases have superior oxidation resistance compared to the boron-free Nb_5Si_3 structures [162][163]. JW1-AC contained small quantities of the $NbCr_2$ Laves phase, where KZ5-AC did not. This phase is reported to improve oxidation resistance when present in similar (Nb) + silicide alloys [104].

The (Nb) phase is usually the most susceptible to oxidation in niobium-silicide based alloys and therefore its quantity and composition are important. The amount (area fraction) of solid solution is reduced from 43.9% in KZ5-AC to 18.5% in JW1-AC. An improvement in oxidation resistance would be expected based on these values alone. Despite this reduction in phase volume, it appears a continuous matrix of (Nb) is still formed in the as-cast state of JW1 which is desirable for fracture toughness. Compositionally, Nb content of (Nb) is reduced from 57.9 at.% in KZ5-AC to 39.9 at.% in JW1-AC. Niobium is replaced by mainly Ti, but also Al and Cr. This likely reduces creep resistance [105], but Ti is often included in niobium silicide-based alloys to improve fracture toughness by increasing ductility [110] and Al potentially has the same effect [111], so JW1-AC would be expected to have enhanced fracture toughness if this compositional change outweighs the development of the $NbCr_2$ phase which reduces fracture toughness [112]. The silicide phase is crucial to creep resistance and fails in a brittle mode, so when the solid solution phase can be alloyed to fail in a ductile mode an acceptable balance of mechanical properties can be achieved effectively though ductile phase toughening [188]. In KZ5-AC, Si content of (Nb) is 2.0 at.%. In JW1-AC, Si content of (Nb) is 1.3 at.%. However, 0.8 at.% of Ge and 1.0 at.% of B are also present in the (Nb) of JW1-AC. A total Si+Ge+B content of 3.1 at.% would make the (Nb) more brittle than the Ge and B free counterpart in KZ5-AC if Ge and B have the same reported effect as Si where Si solute in (Nb) results in lattice distortion and dislocation impediment [106], but this is also likely to reduce the oxygen diffusivity through this vulnerable phase.

Despite the differences to phases formed, KZ5-AC and JW1-AC share similarities that suggest the solidification routes they undergo may not be so different. Firstly, large silicide grains are present in the central region of the alloy. In the case of KZ5-AC this is the primary phase, for JW1-AC the primary phase is uncertain but this could be the case. It is suggested that these form in the early stages of solidification and grow relatively unimpeded for a period of time. Both alloys also have a eutectic silicide that is poorer in Nb and richer in Ti than the main silicide variant in the corresponding alloy. This is found alongside a (Nb) phase. In both as-cast alloys the (Nb) phase has Ti-rich parts too, indicating the final melt which forms the (Nb) and $D8_8/\beta Nb_5Si_3$ is rich in Ti compared to the nominal compositions of the alloy and does not reach homogeneity through diffusion during rapid cooling. When considering the respective top and bottom regions of the alloy ingots there is relatively little difference between the microstructures in the middle regions of KZ5-

AC and JW1-AC aside from size differences of grains. The same phases in the same arrangements of main silicide and eutectic mixture is found, in contrast to the drastically different bottom regions of JW2-AC and JW3-AC.

The main difference between the two alloys microstructures' when excluding the difference between βNb_5Si_3 and $D8_8$ is the formation of a secondary silicide phase in JW1-AC, T2. It is not clear from BSE-imaging of the microstructure when the formation of T2 occurs, and therefore the primary phase of JW1-AC is unknown. The Nb-Si-B ternary system liquidus projection (Figure 2.16) indicates that it is possible for both $D8_8$ or T2 to form first from the liquid, depending on composition. EBSD performed on JW1-AC can provide insight into the question of which silicide phase forms first, but ultimately there still exists uncertainty. In IPF maps Figure 4.10 and Figure 4.11, T2 grains that are separated by large $D8_8$ grains and the (Nb)/$D8_8$ mixture have similar IPF colouring and therefore crystal orientation. It seems unlikely that the crystal orientation of two T2 grains that formed independently of each other would share the same orientation when different orientations are clearly possible, i.e in Figure 4.10 where a T2 grain with orientation closer to the 110 orientation and a T2 grain with orientation closer to the 010 orientation are labelled. Therefore, the T2 imaged through EBSD is either connected out of plane of the image, or was separated after formation by main $D8_8$ grain growth. In either case, T2 did not form in isolated portions of the final melt alongside the intergranular mixture of phase((Nb), $NbCr_2$, and Eutectic $D8_8$) as it must have formed beforehand in order to have the same crystallographic orientation. Therefore, T2 or $D8_8$ may be the primary phase in the case of JW1-AC.

Whilst $NbCr_2$ is another phase that is present in JW1-AC and not KZ5-AC, this is more easily understood as the final melt of JW1-AC having Cr content sufficiently high enough to form $NbCr_2$ instead of the Cr being accommodated into the solid solution. The reason for Cr being higher in the final stages of JW1-AC solidification is related to the amount of silicide forming and apparent low solubility of Cr in said silicides [60][62]. In JW1-AC main silicide ($D8_8$) made up 68.6% of the alloy. In KZ5-AC it was only 41.5%. The primary βNb_5Si_3 in KZ5-AC and the main $D8_8$ in JW1-AC had Cr contents of 0.9 ± 0.1 at.% and 0.7 ± 0.2at.%, respectively. The slightly lower preference for segregation of Cr into main $D8_8$ and larger amount of $D8_8$ forming results in a Cr rich melt in the final stages of solidification which allows $NbCr_2$ to form. The volume fractions of phases are likely a larger factor given the error ranges of Cr contents in the βNb_5Si_3 and $D8_8$ phases overlap.

To more fully comprehend phase stability as a result of B and Ge additions, heat treatments have been performed and are discussed in the following chapter.

4.3.2 The effect of 10 at.% B and 10 at.% Ge on the microstructure and phases of JW1 (Nb-24Ti-18Si-5Cr-5Al-5Ge-5B)

Further modification to the JW1 alloy composition (Nb-24Ti-18Si-5Cr-5Al-5Ge-5B) was performed by increasing nominal B content to 10 at.% in the case of JW2 (Nb-24Ti-18Si-5Cr-5Al-5Ge-10B) and by increasing Ge content to 10 at.% in the case of JW3 (Nb-24Ti-18Si-5Cr-5Al-10Ge-5B). The purpose of this alloy pair is to assess if either element, B or Ge, provides enhanced oxidation resistance when making up a larger proportion of the composition. The microstructure and phases that form must be considered if this potential enhanced oxidation resistance is to be fully understood.

For the most part, alloys JW2-AC and JW3-AC have similar phases compared to the lower B and Ge alloy JW1-AC. The similarities include 1) the microstructure is majority $D8_8$, 2) less (Nb) is identified in between large $D8_8$ grains, and 3) $NbCr_2$ is observed in small quantities.

A significant microstructural difference between JW1-AC and the higher B+Ge content alloys, JW2-AC and JW3-AC, is the lack of intergranular $D8_8$. This is proposed to be a result of the final liquid being especially poor in silicide forming elements, Ge and Si, in JW2-AC and JW3-AC when compared to JW1-AC. It would therefore be expected that the intergranular phases that have formed in JW2-AC and JW3-AC, (Nb) and $NbCr_2$, would have lower total Ge + Si content than the equivalent phases in JW1-AC. For the (Nb) phase, Ge + Si content is 2.1 at.%, 1.8 at.% and 1.3 at.% for alloys JW1-AC, JW2-AC and JW3-AC, respectively for the central regions of the alloys. For the $NbCr_2$ phase Ge + Si content is 6.9 at.%, 5.8 at.% and 5.0 at.% for alloys JW1-AC, JW2-AC and JW3-AC, respectively for the central regions of the alloys. For intergranular $D8_8$ in JW1-AC, Ge + Si content is 27.0 at.%. Using the estimated area fractions of intergranular phases ((Nb), $NbCr_2$, intergranular $D8_8$) with these phase specific values of Ge + Si content, the average Ge + Si content of the final melt can be estimated. In JW1-AC Ge + Si content of the intergranular regions, i.e. the predicted final melt, is 9.3 at.%, in JW2-AC it is 2.7 at.%, and in JW3-AC it is 3.1 at.%. Much of the Ge + Si required to form intergranular $D8_8$ preferentially segregates to primarily the large grain $D8_8$ in JW2-AC and JW3-AC, resulting in its absence. Increasing B or Ge content stabilises initial $D8_8$ formation.

The (Nb) phase volume is further reduced from the amount in JW1-AC, 18.5%, to 8.1% in JW2-AC and 6.0% in JW3-AC. The conclusion that Ge additions reduce (Nb) volume fraction forming in the as-cast state to a greater extent than the same quantity of B additions could be drawn. However it should be noted that in the case of JW2-AC and JW3-AC, (Nb) and $NbCr_2$ could not be separated based on the contrast of BSE images for area fraction analysis so EPMA mapping was used to estimate the ratio of (Nb):$NbCr_2$. A low degree of confidence can be placed in this method given the EPMA phase analysis maps were performed over a small area and the lack of repeat maps. Instead it can be concluded that Ge at the very least encouraged $D8_8$ formation in the as-cast state to a greater extent than B, as main $D8_8$ area fractions in JW2-AC and JW3-AC are 80.3 and 87.8, respectively. Both JW2-AC and JW3-AC are likely more brittle as a results [99], and BSE images (Figure 4.18 and Figure 4.24) show significant cracking of the $D8_8$ phase to reflect this. Additionally, $D8_8$ is likely not the preferred silicide, as at high stresses and temperature the hP16 structure has been shown to have inferior creep properties [109].

A high boron phase referred to as NbB has formed in JW2-AC and JW3-AC. NbB is found in the ternary systems Nb-Si-B (Figure 2.14 [77]) and Nb-Ti-B (Figure 2.11 [84]) with low and high solubility ranges, respectively, and is stable up to ~2900^{o}C. In the case of JW2-AC, this phase exists in a greater amount than T2 in JW1-AC and is a significant part of the microstructure making up 9.0% volume of the alloy. In the same way there was uncertainty in the case of JW1-AC regarding the primary phase to solidify, there also is in the case of JW2-AC. The NbB phase is present in the intergranular areas

but also in places entirely surrounded by $D8_8$, so it cannot be said to form alongside the (Nb) and $NbCr_2$ phase, which are presumably the last to solidify. In JW3-AC NbB is a more minor phase, only making up 0.6% of the alloy and it was not possible to detect the NbB phase though XRD or EBSD analysis techniques. Literature regarding the NbB phase is lacking, but if NbB_2 is used an analogous material, in terms of oxidation resistance it has been show to have inferior oxidation resistance to βNb_5Si_3, T2, and $NbSi_2$ in single phase isothermal studies [163].

In the as-cast state the three B and Ge containing alloys; JW1-AC, JW2-AC, and JW3-AC, have the possibility of providing insight into the effect certain secondary boron-containing phases have on the oxide scale behaviour. JW1-AC contains T2 in significant quantities and not NbB, JW2-AC contains NbB in significant quantities and not T2, and JW3 contains neither T2 nor NbB in significant quantities. Oxide scales of these as-cast alloys will be examined though EPMA to assess if the presence or absence of these secondary boron-containing phases, T2 and NbB, is positive or negative for the overall oxidation resistance of the alloys.

In terms of non-central microstructures, both JW2-AC and JW3-AC were found to have distinct layers of different microstructures at the bottom of the alloy in a way that was not present in either JW1-AC or KZ5-AC. In JW2-AC there are two layers of microstructure different to that of the middle region which are referred to as the very-bottom region and the transitional region. In JW3-AC there is one layer of microstructure different to that of the middle region which gradually changes to resemble the middle region, also referred to as the very-bottom region. Both very-bottom regions in JW2-AC and JW3-AC are comprised of higher amounts of $NbCr_2$ and (Nb), and lower amounts of smaller $D8_8$ grains. The very-bottom region of JW2-AC additionally contains T2 grains. The fact that both of these regions that are in direct contact with the cooled copper crucible are similar implies a similar process of formation. The rapid cooling rate results in less time for $D8_8$ grain growth, hence smaller $D8_8$ grains, and solidification of (Nb) and $NbCr_2$ from the melt before preferential segregation of elements occurs, hence the higher volume of these phases as well as triple the Si + Ge content in (Nb). The transitional region is exclusive to JW2-AC, and is primarily a fine distribution of T2 and $D8_8$. It can be concluded that this region is related to higher boron content as it is not seen in KZ5 (B = 0 at.%), JW1-AC (B = 5 at.%), or JW3-AC (B = 5 at.%). The fast cooling rate has significantly limited grain growth, resulting in this fine microstructure. It is not clear why this layer has formed in the way it has. The assumption is made that during the arc melting process the entire ingot is made liquid during the re-melting process, however this layering structure of both JW2-AC and JW3-AC could be an indication that this is not the case.

Macrosegregation has occurred within all three B and Ge containing as-cast alloys to various extents dependant of element and composition. Table 4.13 presents *MACX* values for an alloy known as TT4 from the literature with nominal composition Nb-24Ti-18Si-5Cr-5Al-8B [131]. This is an alloy that has the same nominal composition of Ti, Si, Cr and Al, contains B, but does not contain Ge. The actual composition has a B content of 6.9 at.%, making this alloy comparable with JW1, which has an actually B content of 5.4 at.%. TT4 consistently has lower *MACX* values for each element present when compared to JW1-AC (Table 4.5), with the exception of B, where the value reduces from 2.9 at.% to 2.6 at.% upon the addition of 5 at.% Ge to the nominal composition. This suggests Ge has an increasing effect on macrosegregation, but may reduce $C_{max}^{B} - C_{min}^{B}$ values.

In alloy JW3-AC, the effects that increasing Ge content has on macrosegregation can be seen. Compared to JW1-AC, each element has a larger degree of macrosegregation with the exception of Ti. Further additions of Ge have again resulted in increasing macrosegregation values of the other elements present. Although $C_{max}^{B} - C_{min}^{B}$ is slightly greater in JW3-AC than in JW1-AC, 2.8 at.% compared to 2.6 at.% respectively, this is still marginally lower than the B macrosegregation

reported in TT4, at 2.9 at.%. This would support the proposed effect that Ge reduces macrosegregation of B. In alloy JW2-AC, the effects that increasing B content has on macrosegregation can be seen. Compared to JW1-AC, each element has a smaller degree of macrosegregation with the exceptions of Ge which is the same (1.2 at.%) and B itself which has a large $C_{max}^{B} - C_{min}^{B}$ value of 8.1 at.%. This suggests B has the reverse effect that Ge has on macrosegregation, and actually leads to a more homogeneous distribution of elements across the alloy at the expense of itself being concentrated in the middle region. The low boron content of individual phases in JW1 and JW2 top and bottom regions compared to the respective central regions was noted in EPMA results, and could indicate loss of boron to the atmosphere during the arc-melting process and boron's volatility. The actual bulk B content according to ICP-OES data of JW2-AC was 11.4 at.% (Table 3.1). The 4.5 at.% increase in B content from TT4 to JW2-AC has partially alleviated the increased macrosegregation that arises from Ge being present in JW series alloys, as JW2-AC *MACX* values are all within 0.9 at.% of TT4 *MACX* values with the exception of $C_{max}^{B} - C_{min}^{B}$. Given that macrosegregation is significant in it least one element in each JW series alloy, samples for thermogravimetric analysis must be taken from the same region, i.e. the middle region, to reduce variance not related to nominal composition during oxidation experiments.

Macrosegregation is inhomogeneity in composition at a macroscopic scale of a manufactured alloy. Usually this is a phenomenon that effects castings and is in effect on the scale of the whole casting. It exists in many forms and is the result of multiple factors [189]. This includes microsegregation on the local scale occurring to varying degrees dependant on solute concentration and diffusion during solidification, early to solidify grains can break off and move through the liquid (during the manufacturing process this is believed to have been witnessed), and convention currents in the liquid can generate flow, as well as buoyancy induced flows from density variation of the liquid that is high and low in solute atoms. In these alloys this would support lighter elements moving to the surface, but this is complicated by the multiple melt stages with flipped ingots as well as magnetic stirring. In the case of ingots produced by arc melting in a copper cooled crucible, the relevant effects include the thermal gradient created by a strongly concentrated energy source, which results in a fast moving and possibly unstable solid-liquid interface, and the partitioning of different solutes between intermetallic and metallic phases. This can be simplified to the relative movement of one phase to another, including the liquid phase, hence why the solid-liquid interface is important. In the case of niobium silicide-based alloys, Tsakiropoulos [184] reviewed 69 alloy compositions and their macrosegregation in order to correlate certain material parameters with macrosegregation. The alloy melting temperature, T_m, was considered a key material parameter, where $T_m\ (K) = \Sigma x_i T_{mi}$ and x_i is the at.% content x of element i in the alloy, and T_{mi} is the melting temperature of element i. A higher T_m is correlated with lower *MACX*, due to the potential for steeper temperature gradients, which in turn reduce the ease with which supercooled regions of the melt are created, and therefore the solid-liquid interface progresses more stably during solidification. Other key parameters identified that resulted in lower *MACX* values were a lower H_m/T_m , a lower T_m^{sp} , and a higher T_m^{sd}/T_m^{sp} where $H_m\ (kJ/mol) = \Sigma x_i H_{mi}$ and H_{mi} is the enthalpy of fusion of element i, and $T_m^{sp}\ (K) = \Sigma x_i T_{mi}^{sp}$ and $T_m^{sd} = \Sigma x_i T_{mi}^{sd}$ where T_{mi}^{sp} is the melting temperature of sp orbital elements i (Si, Ge, B, Al) and T_{mi}^{sd} is the melting temperature of sd orbital elements i (Nb, Ti, Cr).

The macrosegregation considered in [184] is exclusive to *MACSi* values so the *MACSi* of JW1, JW2 and JW3 can be considered, 8.8 at.%, 4.9 at.% and 9.7 at.%, respectively. The difference between JW1 and JW3 is in agreement with these trends, with T_m, H_m/T_m, T_m^{sp} and T_m^{sd}/T_m^{sp} values of 2162 K, 13.65 kJ/molK, 518K and 3.18 for JW1 and 2085 K, 14.40 kJ/molK, 573K and 2.64 for JW3, respectively [190] (values calculated from actual compositions in Table 3.1). However, comparing

JW1 to JW2, one would not expect the reduction in macrosegregation of Si based on the values of T_m, H_m/T_m, T_m^{sp} and T_m^{sd}/T_m^{sp} calculated for JW2, 2156 K, 14.47 KJ/molK, 658 K, and 2.28, respectively. The issue most likely lies with experimental procedure, introducing variability, and the fact that only a small number of samples have been assessed. It is possible that more repetitions would lead to higher macrosegregation results for JW2, however in the TT alloy series [131] another boron containing alloy (TT8 – Nb-17Si-24Ti-5Cr-3.5Al-2Mo-6B) did not match the above trends, whereas the other TT alloys did. This perhaps indicates a unique effect of boron in some cases, which potentially warrants further investigation if the alloying addition of boron is to be further considered for niobium silicide-alloy development.

Elements in JW1, JW2, JW3 and TT4 tend to show similar trends in terms of where the highest and lowest average contents are found regionally. In the alloys previously stated, elements Nb, Si, and Ge generally have higher contents at the top of the alloy ingot and lower contents at the bottom, with the obvious exception of Ge in TT4 where it was not present. In the alloys previously stated, elements Ti, Cr and Al generally have higher contents at the bottom of the alloy ingot and lower at the top, with the exception of Al in TT4 where the was only 0.1 at.% difference between regional averages. In the case of B, generally the bottom region had higher content in the alloys discussed, with the exception of JW2-AC where the highest content was found in the middle of the ingot and beyond this the top region had higher content than the bottom region. These trends agree well with the results for the $D8_8$ phase in JW3-AC, where it was noted that the composition of this phase also varied significantly when measured at top, middle and bottom regions of the alloy ingot (Table 4.11). Elements Nb and Si have higher contents in the top version of $D8_8$ and lower contents at the bottom, whereas Ti, Cr and Al follow the reverse trend. This is an indication that macrosegregation is linked to $D8_8$ solidification and segregation of elements into and out of this phase, at the very least in the case of JW3-AC.

Table 4.13) Average content of the top, middle and bottom regions of TT4. Values given in at.%. Mean ± stdev, minimum value - maximum value. And macrosegregation ($C_{max} – C_{min}$ = MACX) values for JW1-AC. MACX values given in at.%. [124]

	Nb	Si	Ti	Cr	Al	B
Top Region	42.8 ± 1.3	16.4 ± 1.3	24.1 ± 1.6	5.0 ± 0.1	5.1 ± 0.2	6.7 ± 0.4
	41.7 - 44.1	14.3 - 17.9	22.7 - 25.8	4.8 - 5.2	4.8 - 5.4	5.7 - 7.2
Middle Region	42.5 ± 1.0	15.5 ± 0.6	24.6 ± 0.8	5.5 ± 0.3	5.0 ± 0.1	6.9 ± 1.2
	41.7 - 43.5	15.0 - 16.2	23.2 - 25.6	5.2 - 5.9	4.3 - 5.2	5.3 - 8.2
Bottom Region	42.3 ± 0.3	15.2 ± 1.6	25.0 ± 0.6	5.6 ± 0.4	5.0 ± 0.3	7.0 ± 0.6
	42.0 - 42.7	13.2 - 17.2	24.3 - 26.0	5.0 - 6.2	4.6 - 5.4	5.5 - 8.0
MACX	2.4	4.7	3.3	1.4	1.1	2.9

4.4 Conclusions

- βNb_5Si_3 is destabilised by B and Ge additions to such an extent that it is not found in any as-cast B and Ge containing alloy in this study. Instead, $D8_8$ is formed when B and Ge are added to the base alloy KZ5 (Nb-18Si-24Ti-5Cr-5Al), with higher Ge content resulting in larger amounts of $D8_8$ compared with the higher B content alloy.
- (Nb) volume fraction is reduced significantly upon the addition of B and Ge. Ge is more effective at reducing (Nb) volume fraction than B. Cracking of the silicide phases can be observed in JW2-AC and JW3-AC especially.
- The composition of JW1 maintains a eutectic formation of $D8_8$ and (Nb), with the later in a continuous matrix in the central region of the alloy. This is a promising microstructure that may retain mechanical properties associated with Niobium silicide in-situ composites.
- The higher B containing alloy, JW2-AC with 10 at.% B content, has not resulted in more T2 formation. Instead a secondary high B phase has formed, NbB.
- Ge additions have been found to increase the degree that macrosegregation occurs. B additions have been found to reduce the degree that macrosegregation occurs, at the expense of a high value of macrosegregation for B itself.

Chapter 5

5 The effect of heat-treatments on KZ5 (Nb-18Si-24Ti-5Cr-5Al), JW1 (Nb-18Si-24Ti-5Cr-5Al-5Ge-5B), JW2 (Nb-18Si-24Ti-5Cr-5Al-5Ge-10B), JW3 (Nb-18Si-24Ti-5Cr-5Al-10Ge-5B).

5.1 Introduction

This chapter will assess the effects of heat-treatments on the four alloys presented in chapter 4; KZ5 (Nb-18Si-24Ti-5Cr-5Al), JW1 (Nb-18Si-24Ti-5Cr-5Al-5Ge-5B), JW2 (Nb-18Si-24Ti-5Cr-5Al-5Ge-10B), JW3 (Nb-18Si-24Ti-5Cr-5Al-10Ge-5B). As high temperature operating conditions are to be encountered should these materials find use in turbine blade and disk components, the equilibrium state is of vital importance when considering alloy design. In a complex alloy system such as those described in chapter 4, there is uncertainty as to which phases are stabilised by the numerous alloying additions to the Nb-Si binary system. Two heat-treatment regimens are performed on as-cast JW1, JW2, and JW3. One regime is a hold at 1300°C for 100 hours to produce the HT13 alloy series, and the other is a hold at 1500°C for 100 hours to produce the HT15 alloy series. The time scale of 100 hours was selected because the transformation kinetics of this system are sluggish so a long time is required to reach equilibrium. It is likely that longer treatments would be required to reach equilibrium, but this was feasibly the longest safe treatment that could be performed without risking tube rupture, at which point the alloys would be severely contaminated. The base alloy, KZ5, has the latter performed on it as well. This is summarised in Table 5.1. These heat-treatment regimens allow multiple microstructures of the alloys to be characterised, as well as an indication of the process of certain phase transitions. Through experimental techniques of X-ray diffraction (XRD), Electron probe micro-analysis (EPMA), and Electron Backscatter Diffraction (EBSD), the phases found after heat-treatments are characterised in this chapter. The microstructures of these alloys, crucial for mechanical properties and oxidation resistance, will be described though backscattered electron (BSE) imaging and area fraction analysis.

Table 5.1) A matrix of alloys studied and heat-treatments performed on these alloys. In each case the temperature was held for 100 hours. In the case of 1300°C this was performed in a vacuum furnace. In the case of 1500°C this was perfored in a tube furnace under Ar gas flow

Heat treatment temperature	Alloy			
	KZ5	JW1	JW2	JW3
As-cast	X	X	X	X
1300°C		X	X	X
1500°C	X	X	X	X

5.2 Results

5.2.1 KZ5 (Nb-24Ti-18Si-5Cr-5Al)

5.2.1.1 XRD

XRD results of each heat-treated alloy are presented in this chapter for angles of 2θ 10° to 90° and normalised intensities. The X-ray diffraction pattern of KZ5-HT15 (Nb-24Ti-18Si-5Cr-5Al) is given in Figure 5.1. In KZ5-HT15, three phases are identified; the silicides αNb_5Si_3 and βNb_5Si_3, and the Nb BCC solid solution (Nb). A high degree of confidence can be placed in each phase being present as there are multiple unique high intensity peaks assigned to each of these phases. The transition from αNb_5Si_3 to βNb_5Si_3 has not fully completed according to this XRD pattern even after 100 hours, highlighting again the sluggish transformation kinetics of the Nb-Si system. In the binary Nb-Si system the αNb_5Si_3 phase is stable below ~1930°C [32]. When KZ5 has been heat-treated in other studies, the XRD pattern was similar to that presenting in Figure 5.1 [153].

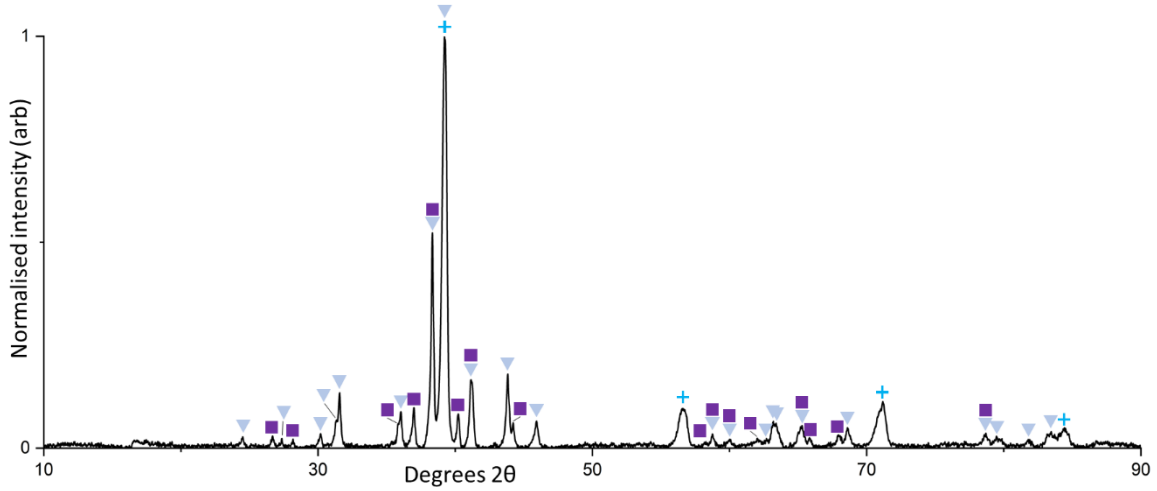

Figure 5.1) XRD pattern of KZ5-AC. ■ = βNb₅Si₃, ▼ =αNb₅Si₃ + = (Nb).

5.2.1.2 EBSD

EBSD maps of KZ5-HT15 are presented in Figure 5.2 and Figure 5.3 with corresponding EDS maps of the areas examined. These maps are taken from the middle of the alloy ingot, at two different magnifications to show the general microstructure (Figure 5.2) and more detailed microstructure (Figure 5.3). The αNb_5Si_3, βNb_5Si_3 and (Nb) phases expected from XRD results were identified comprehensively in both figures.

Generally, the βNb_5Si_3 is found surrounded by the newly formed αNb_5Si_3. It appears as though the transition from βNb_5Si_3 to αNb_5Si_3 proceeds from the outside of βNb_5Si_3 grains towards the centre and this transition is incomplete. Although large grains of αNb_5Si_3 can also be seen. The (Nb) no longer exists as a eutectic structure that was identified in KZ5-AC, and is even present within some of the αNb_5Si_3 grains in a speckled formation. This may be linked to the βNb_5Si_3 to αNb_5Si_3 transition. In the higher magnification image (Figure 5.3) certain areas are unidentified that according to correspond EDS maps are high in Ti. Further confirmation using EPMA results is required to adequately report this phase.

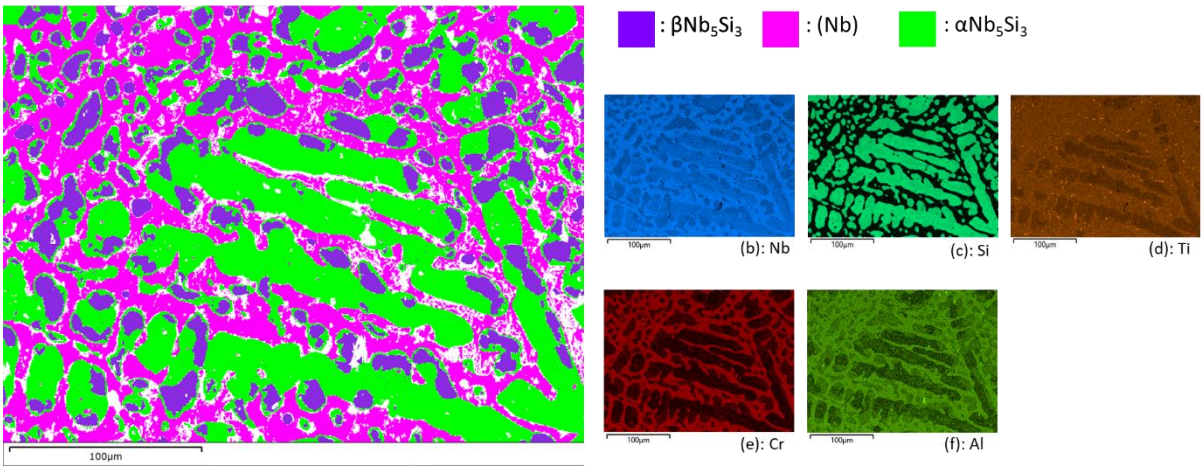

Figure 5.2a-f) EBSD map of KZ5-HT15 at lower magnification (a), and corresponding qualitative EDS maps of Nb (b), Si (c), Ti (d), Cr (e) and Al (f).

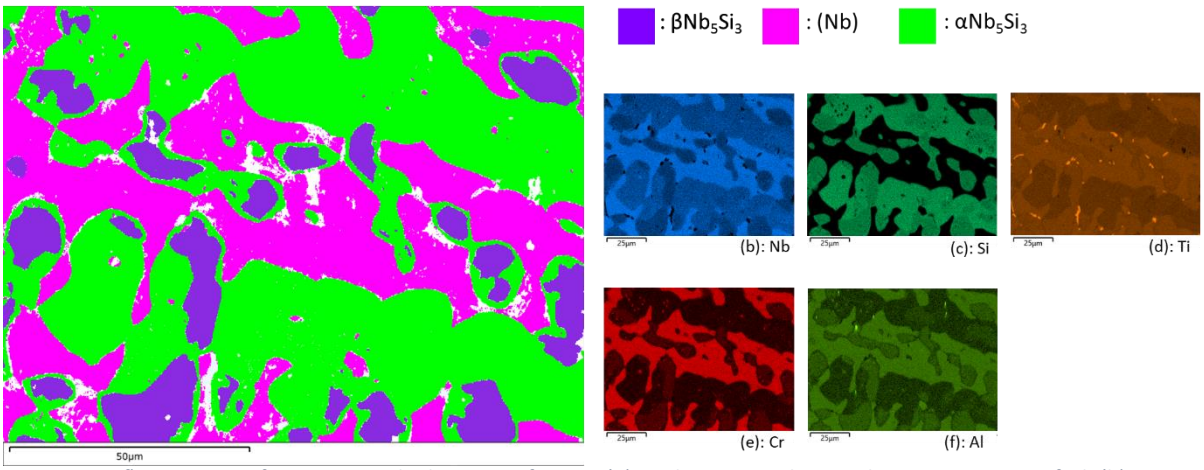

Figure 5.3a-f) EBSD map of KZ5-HT15 at higher magnification (a), and corresponding qualitative EDS maps of Nb (b), Si (c), Ti (d), Cr (e) and Al (f).

5.2.1.3 EPMA

EPMA mapping of the central region of KZ5-HT15 identifies phases αNb_5Si_3, βNb_5Si_3, (Nb) and a high-Ti phase. The compositions of these phases are given in Table 5.2. Phases αNb_5Si_3, βNb_5Si_3, (Nb) are in agreement with XRD results presented previously. The high-Ti phase has main elements Ti and Nb. However it is considered a distinct phase from the (Nb), and not merely a Ti-rich (Nb), as it has considerably higher Ti content than Nb content, 68.9 at.% compared to 26.7 at.%, respectively.

This phase remains undefined as there is uncertainty as to if it is a TiN compound, TiO_2 or development of a titanium HCP solid solution (Ti). In addition, there no longer seems to be areas of the (Nb) that are higher in Ti, as was the case with the as-cast version, as the (Nb) phase has been homogenised by the heat-treatment. The range of composition of Ti in (Nb) is 25.6-27.1 at.% in KZ5-HT15, compared to 23.9-30.6 at.% in KZ5-AC.

The two Nb_5Si_3 silicides can be distinguished based on composition and labelled accordingly based on EBSD mapping. It was found that βNb_5Si_3 in this alloy after heat-treatment had notably higher Ti content and lower Nb and Si content than αNb_5Si_3. In addition, Al solubility in αNb_5Si_3 appears to be somewhat limited, with a compositional range of 1.3–1.7 at.% compared to βNb_5Si_3 Al content of 3.2-3.8 at.%. Also detected through EPMA was a third type of silicide that could be distinguished based on Al content with an average value of 2.2 at.% and a range that lies in the middle of the αNb_5Si_3 and βNb_5Si_3 ranges, 1.8-2.9 at.%. This third silicide phase was found to have small speckles of another phase higher in niobium that is identified as internal (Nb). In EBSD mapping the speckles

of (Nb) are seen to be located within the αNb_5Si_3 phase, and the composition of this third silicide is most similar to αNb_5Si_3 rather than βNb_5Si_3, so it is concluded that this phase is indeed αNb_5Si_3 but perhaps at different stage of transition, labelled as $\alpha Nb_5Si_3^T$ in Table 5.2.

*Table 5.2) Compositions of phases found in the central region of KZ5-HT15 using EPMA mapping, values given in at.%. Mean ± stdev, minimum value - maximum value. * marks phases that were in small quantities and only 40 points could be taken*

	Nb	Si	Ti	Cr	Al
Primary βNb_5Si_3	42.3 ± 0.5	30.4 ± 0.5	21.8 ± 0.3	1.9 ± 0.1	3.6 ± 0.1
	40.5 - 42.8	28.8 - 31.5	20.7 - 22.2	1.6 - 2.0	3.2 - 3.8
αNb_5Si_3	46.2 ± 0.6	33.7 ± 0.6	18.2 ± 0.2	0.4 ± 0.0	1.5 ± 0.1
	44.0 - 47.0	31.3 - 34.6	17.3 - 18.4	0.2 - 0.5	1.3 - 1.7
$\alpha Nb_5Si_3^T$	47.7 ± 0.7	32.6 ± 0.9	17.0 ± 0.4	0.5 ± 0.2	2.2 ± 0.2
	44.5 - 48.9	27.4 - 34.4	15.8 - 18.8	0.3 - 1.7	1.8 - 2.9
(Nb)	56.7 ± 0.5	0.8 ± 0.5	26.7 ± 0.3	8.9 ± 0.2	6.9 ± 0.2
	54.5 - 57.2	0.2 - 2.9	25.6 - 27.1	8.2 - 9.1	6.4 - 7.2
Internal (Nb)	51.9 ± 3.7	2.9 ± 2.0	27.6 ± 2.3	9.3 ± 0.9	8.3 ± 1.3
(Speckles)*	45.3 - 57.2	0.3 - 6.9	21.9 - 31.2	7.2 - 10.2	5.8 - 10.9
High Ti phase*	26.1 ± 6.5	0.6 ± 0.7	68.9 ± 7.3	2.3 ± 1.1	2.2 ± 0.7
	15.6 - 38.2	0.0 - 2.6	46.4 - 76.7	0.9 - 5.3	1.0 - 3.4

5.2.1.4 BSE – SEM imaging

Figure 5.4a and Figure 5.4b show the typical microstructure of KZ5-HT15, taken from the centre of the alloy ingot using BSE imaging. Two images were taken to show the general microstructure (Figure 5.4a) as well as at a higher magnification for clarity (Figure 5.4b).

The centre region of KZ5-HT15 consists of two silicides αNb_5Si_3 and βNb_5Si_3, the solid solutions (Nb), and a high-Ti phase. αNb_5Si_3 and βNb_5Si_3 can be difficult to distinguish visually but their existence has been confirmed through EBSD mapping and EPMA results. αNb_5Si_3 is the lighter contrast of the two, whereas βNb_5Si_3 is slightly darker in contrast. This contrast disparity is presumably due to higher Nb content and lower Ti content in αNb_5Si_3. 'Speckles' of (Nb) can be seen in the αNb_5Si_3 phase as reported in EBSD and EPMA result sections. This suggests that the decomposition of βNb_5Si_3 to αNb_5Si_3 involves the development of small amounts of (Nb); βNb_5Si_3 -> αNb_5Si_3 + (Nb). In the Nb-Si binary system no such phase transition exists, but since the Nb_3Si phase is destabilised by Cr and Al additions [153][117] there apparently exists a $\beta Nb_5Si_3/\alpha Nb_5Si_3$ boundary. The areas of αNb_5Si_3 that are absent in (Nb) speckles are proposed to be further along the decomposition where excess Nb content that results in (Nb) formation has had time to diffuse out of αNb_5Si_3 grains. The silicide large grain and intergranular silicide structure present in the as-cast version of KZ5 is somewhat preserved in this heat-treated version, but the intergranular silicide has coarsened significantly. Generally, the intergranular silicide has remained βNb_5Si_3, whereas the large grains of silicide are more prone to transition to αNb_5Si_3. This is likely due to the original compositions of intergranular βNb_5Si_3 and primary βNb_5Si_3 grains in the as-cast alloy being closer to the compositions of βNb_5Si_3 and αNb_5Si_3 in the heat-treated sample, respectively.

The bright contrast (Nb) is a continuous matrix throughout the centre of the heat-treated alloy, as it was in the as-cast version. In the higher magnification image (Figure 5.4b), the black contrast high-Ti phase can be seen and generally forms on the (Nb) silicide boundaries. Although it should be noted that some of the black contrast areas, especially in the lower magnification image, are in fact porosity or surface cracks due to sample preparation techniques.

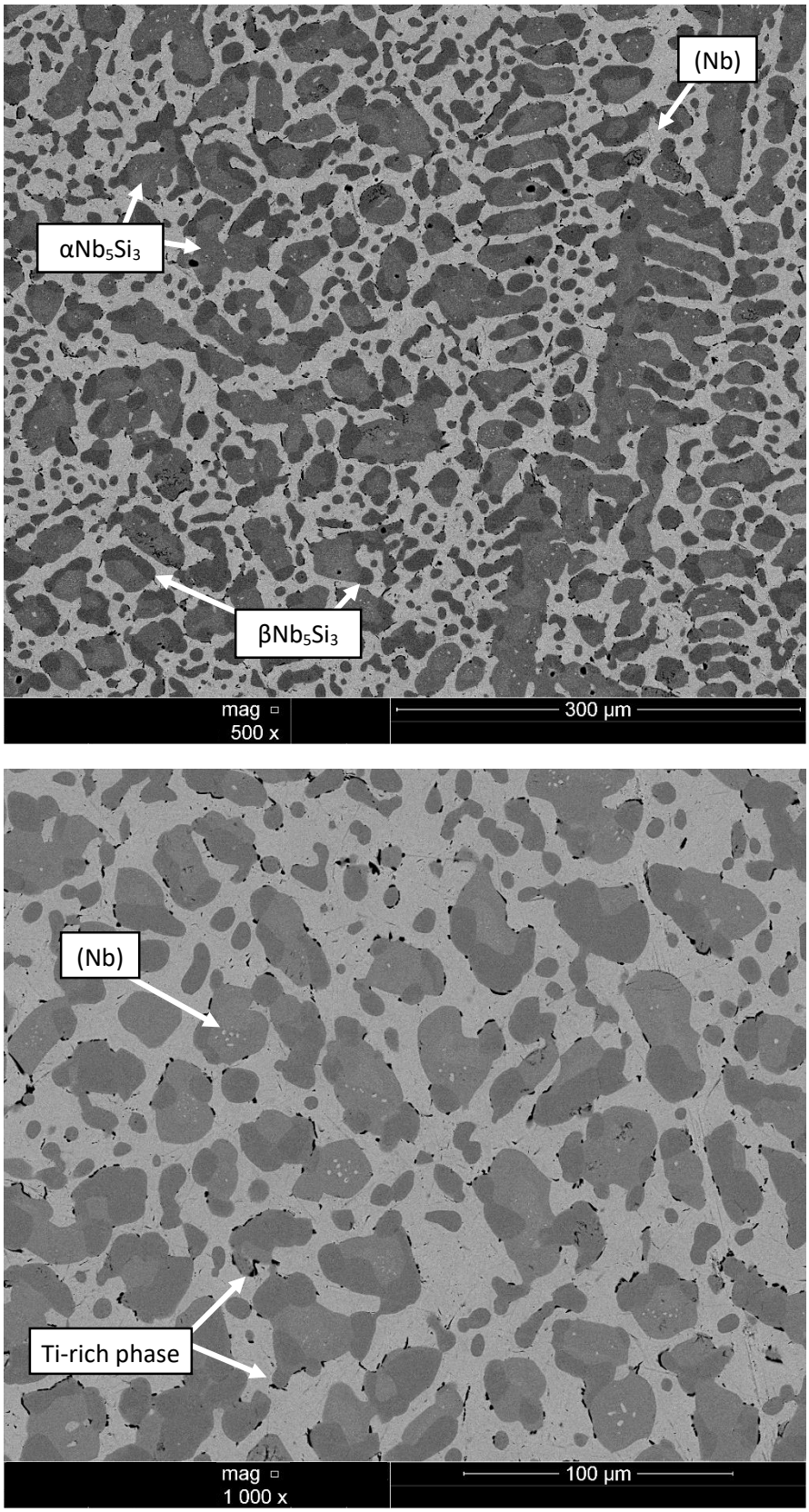

Figure 5.4a-b) BSE images of the central region of KZ5-HT15 taken at lower magnification (a) and higher magnification (b)

5.2.1.5 Area fraction

The area fractions of phases αNb_5Si_3, βNb_5Si_3 and (Nb) within KZ5-HT15 at the centre of the alloy ingot were calculated from BSE images and are given in Table 5.4. The contrast of these three phases was used to differentiate between them according to the methodology laid out in chapter 3. On average KZ5-HT15 contained 25.7% αNb_5Si_3, 31.3% βNb_5Si_3, and 43.0% (Nb) by area, which is assumed to be equal to volume fraction. The silicide phases include intergranular areas and primary large grains made up of the respective phases. This is different to the as-cast version where βNb_5Si_3 was split based on if it was in intergranular areas or primary large grains. Regardless, total silicide volume and total (Nb) of KZ5-AC and KZ5-HT15 are practically identical with values that are within error of each other. Total silicide volume in KZ5-AC is 56.1%, total silicide volume in KZ5-HT15 is 57.0%. The high-Ti phase was not included in the area fraction analysis as the phase could not be distinguished from cracks.

*Table 5.3) The area fraction (%) of each phase present. Calculated from BSE image contrast taken at the centre of the alloy ingot. EPMA maps were additionally used to estimate the $NbCr_2$/(Nb) content as it was not possible to distinguish between these phases in the case of JW2-HT15. *The T2 and NbB phases could not be distinguished in the case of JW2-HT13. $^+$T2 likely existed in JW3-TH13 but could not be distinguish from $D8_8$. The as-cast values are presented below for comparison.*

			Intergranular					
Alloy	βNb_5Si_3	αNb_5Si_3	$D8_8$	$D8_8$	T2	NbB	(Nb)	$NbCr_2$
KZ5-HT15	31.3 ± 2.6	25.7 ± 1.3	-	-	-	-	43.0 ± 1.6	-
JW1-HT13	-	-	61.9 ± 7.3	11.7 ± 2.6	5.7 ± 1.2	-	18.6 ± 3.9	2.1 ± 0.4
JW1-HT15	-	-	81.5 ± 3.1	-	6.4 ± 1.2	-	11.3 ± 3.4	1.5 ± 0.4
JW2-HT13	-	-	77.5 ± 3.0	-	9.7 ± 1.1*		5.4 ± 1.3	6.7 ± 1.6
JW2-HT15	-	-	70.3 ± 1.6	-	27.9 ± 1.7	-	0.5 ± 0.2	1.4 ± 0.5
JW3-HT13	-	-	94.4 ± 4.2$^+$	-	-	-	0.7 ± 0.6	5.0 ± 1.7
JW3-HT15	-	-	89.9 ± 2.4	-	9.0 ± 2.2	-	-	1.1 ± 0.4
KZ5-AC	41.5 ± 4.7	14.6 ± 3.3	-	-	-	-	43.9 ± 4.2	-
JW1-AC	-	-	68.6 ± 3.4	7.7 ± 1.8	4.3 ± 0.5	-	18.5 ± 2.2	0.9 ± 0.2
JW2-AC	-	-	80.3 ± 3.1	-	0.7 ± 0.2	9.0 ± 1.6	8.1 ± 1.5	2.5 ± 0.5
JW3-AC	-	-	87.8 ± 1.3	-	-	0.6 ± 0.3	6.0 ± 0.7	5.5 ± 0.6

5.2.2 JW1 (Nb-24Ti-18Si-5Cr-5Al-5Ge-5B)

5.2.2.1 XRD

The X-ray diffraction pattern of JW1-HT13 (Nb-24Ti-18Si-5Cr-5Al-5Ge-5B) is given in Figure 5.5. The X-ray diffraction pattern of JW1-HT15 is given in Figure 5.6. In JW1-HT13 and JW1-HT15, four phases are identified; the silicides $D8_8$ and T2, the Nb solid solution (Nb), and a Laves phase $NbCr_2$. A high degree of confidence can be placed in the phases $D8_8$, T2 and (Nb) being present, as there are multiple unique high intensity peaks assigned to each of these phases. In the case of $NbCr_2$ only relatively low intensity peaks are assigned to solely $NbCr_2$, with the rest overlapping with other phases. Further confirmation of this phase is therefore required from EBSD and EPMA.

Whilst relative intensities of phases in XRD pattern of JW1-HT13 and JW1-HT15 are slightly different, peak positions and phases are relatively unchanged. The same is true when comparing the heat-treated alloys to the as-cast version of JW1. The position of the main (Nb) peak has notably shifted to a lower 2θ angle after heat-treatments.

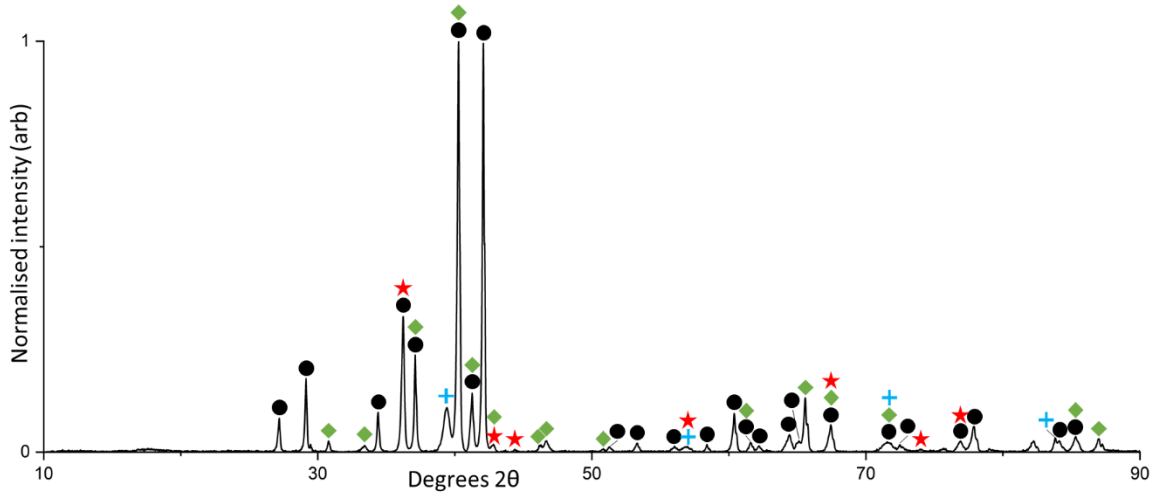

Figure 5.5) XRD pattern of JW1-HT13. ● = $D8_8$, ★ = $NbCr_2$, ◆ = T2, + = (Nb).

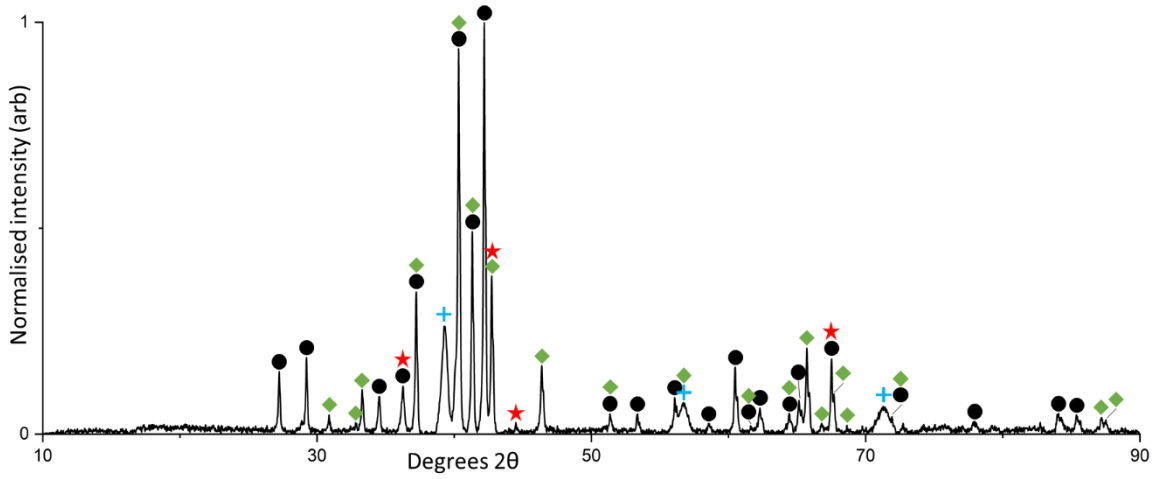

Figure 5.6) XRD pattern of JW1-HT15. ● = $D8_8$, ★ = $NbCr_2$, ◆ = T2, + = (Nb).

5.2.2.2 EBSD

EBSD maps of JW1-HT15 are presented in Figure 5.8 and Figure 5.7 with corresponding EDS maps of the areas examined. These maps are taken from the middle of the alloy ingot, at two different magnifications to show the general microstructure (Figure 5.8) and more detailed microstructure (Figure 5.7). The (Nb), T2, $D8_8$, and $NbCr_2$ phases expected from XRD results were identified comprehensively in both figures.

The majority of the area is made up of $D8_8$, present as large grains. Intergranular (Nb) phase is present between the $D8_8$. No intergranular $D8_8$ is present as the (Nb) phase is in coarse arrangements. The (Nb) is surrounded by small amounts of the $NbCr_2$ phase in a shell like structure, with $NbCr_2$ being present on the (Nb) and $D8_8$ boundary. T2 exists adjacent to the (Nb)/$NbCr_2$ areas as well as completely within grains of $D8_8$.

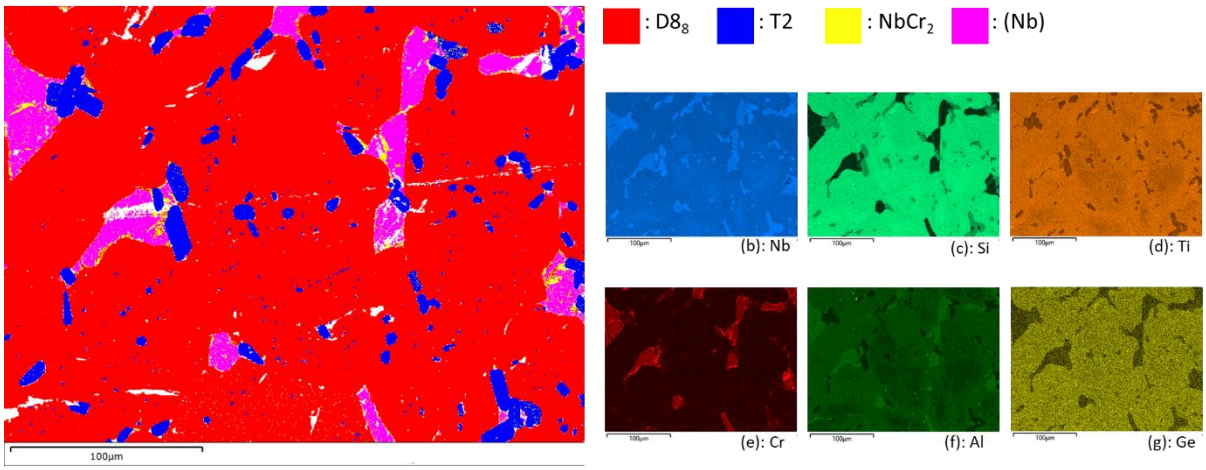

Figure 5.8a-h) EBSD map of JW1-HT15 at lower magnification (a), and corresponding qualitative EDS maps of Nb (b), Si (c), Ti (d), Cr (e), Al (f), and Ge (g).

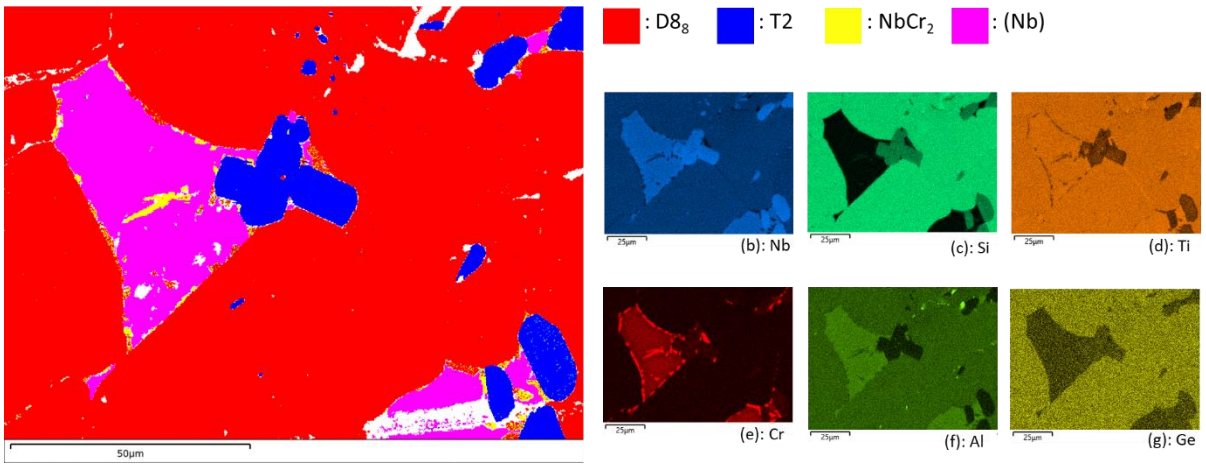

Figure 5.7a-h) EBSD map of JW1-HT15 at higher magnification (a), and corresponding qualitative EDS maps of Nb (b), Si (c), Ti (d), Cr (e), Al (f), and Ge (g).

5.2.2.3 EPMA

EPMA mapping of the central region of JW1-HT13 identifies phases (Nb), $D8_8$, $NbCr_2$ and T2. The compositions of these phases are given in Table 5.5. These phases are in agreement with XRD results presented previously. As was the case in the as-cast version of JW1, $D8_8$ is split into two compositions; the composition of grains of $D8_8$ and the composition of intergranular $D8_8$ as there are significant compositional differences. The B content of $D8_8$ grains is higher than the intergranular $D8_8$, 5.9 at.% compared to 4.6 at.%, respectively. Additionally, Nb and Si contents are lower and Ti, Al and Ge content are higher in intergranular $D8_8$. The highest B content is found in T2, with 21.4 at.%. The phase assigned to (Nb) has a high content of metallic elements, 36.5 at.% Ti, 13.4 at.% Cr, 10.8 at.% Al, as well as 37.3 at.% Nb. Elements Si, Ge and B have similar contents in (Nb), 0.5 at.%, 0.4 at.%, and 1.0 at.%, respectively. And finally the $NbCr_2$ is expectedly rich in Nb and Cr with contents of 22.9 at.% and 53.5 at.%, respectively.

EPMA mapping of the central region of JW1-HT15 identifies the same phases; (Nb), $D8_8$, $NbCr_2$ and T2. The compositions of these phases are given in Table 5.6. These phases are in agreement with XRD results presented previously. There now only exists one form of $D8_8$ as the intergranular form has been removed through heat-treatment. The $D8_8$ grains of JW1-HT15 has composition similar to the $D8_8$ grains in JW1-HT13. However, in the case of all elements the values for each element in $D8_8$ grains in JW1-HT15 are in between those of $D8_8$ grains and intergranular $D8_8$ in JW1-HT13, so some homogenisation has taken place in regard to this phase. T2 is still present with a high B content, 21.6 at.%, as is $NbCr_2$ with similar composition to that of JW1-HT13. The solid solution (Nb) is notably higher in Nb, 49.0 at.% and 37.3 at.%, and lower in Ti, 27.7 at.% and 36.5 at.%, when comparing JW1-HT15 to JW1-HT13, respectively.

Table 5.5) Compositions of phases found in the central region of JW1-HT13 using EPMA mapping, values given in at.%. Mean ± stdev, minimum value - maximum value..

	Nb	Si	Ti	Cr	Al	Ge	B
$D8_8$	39.4 ± 0.7	23.0 ± 0.9	21.2 ± 0.4	1.0 ± 0.1	3.4 ± 0.4	6.2 ± 0.2	5.9 ± 1.0
	37.9 - 41.8	20.4 - 25.1	20.3 - 22.2	0.8 - 1.2	2.7 - 4.3	5.7 - 6.6	2.3 - 8.5
Intergranular $D8_8$	30.1 ± 1.5	19.0 ± 1.1	30.9 ± 1.6	1.6 ± 0.5	6.0 ± 0.4	7.8 ± 0.5	4.6 ± 1.1
	26.3 - 33.2	14.7 - 22.0	27.6 - 35.4	0.9 - 4.0	3.4 - 7.5	6.7 - 9.4	2.2 - 7.7
T2	47.3 ± 1.8	10.8 ± 0.7	14.1 ± 0.6	4.7 ± 1.4	0.1 ± 0.1	1.7 ± 0.2	21.4 ± 0.9
	44.3 - 51.7	9.3 - 12.8	12.5 - 17.0	2.0 - 6.6	0.0 - 0.8	1.4 - 2.1	19.1 - 23.5
(Nb)	37.3 ± 0.4	0.5 ± 0.2	36.5 ± 0.3	13.4 ± 0.2	10.8 ± 0.3	0.4 ± 0.0	1.0 ± 0.7
	36.1 - 38.3	0.1 - 1.0	35.7 - 37.4	12.9 - 14.3	10.1 - 11.7	0.3 - 0.5	0.0 - 3.4
$NbCr_2$	22.9 ± 0.7	5.0 ± 0.6	14.1 ± 0.6	53.5 ± 1.8	3.3 ± 0.5	0.5 ± 0.1	0.8 ± 0.7
	21.7 - 30.0	2.9 - 9.9	13.5 - 20.3	37.4 - 55.6	2.8 - 9.1	0.4 - 1.7	0.0 - 3.4

*Table 5.6) Compositions of phases found in the central region of JW1-HT15 using EPMA mapping, values given in at.%. Mean ± stdev, minimum value - maximum value. * marks phases that were in small quantities and only 40 points could be taken.*

	Nb	Si	Ti	Cr	Al	Ge	B
$D8_8$	37.2 ± 2.2	21.5 ± 1.2	23.7 ± 2.1	1.4 ± 0.2	4.1 ± 0.8	7.0 ± 0.4	5.0 ± 1.1
	33.8 - 41.3	19.1 - 24.3	20.0 - 26.8	0.9 - 1.9	2.6 - 5.2	6.1 - 7.8	1.6 - 7.8
T2	50.6 ± 1.0	11.0 ± 0.5	11.9 ± 0.7	3.2 ± 0.1	0.2 ± 0.0	1.6 ± 0.1	21.6 ± 0.6
	47.9 - 53.7	9.6 - 12.0	10.4 - 13.3	2.8 - 3.6	0.1 - 0.3	1.5 - 1.8	19.4 - 23.2
(Nb)	49.0 ± 0.9	0.5 ± 0.2	27.7 ± 1.0	12.5 ± 0.5	8.5 ± 0.3	0.6 ± 0.1	1.3 ± 0.7
	46.5 - 50.6	0.1 - 1.5	26.4 - 30.6	11.3 - 14.1	7.8 - 9.3	0.4 - 0.7	0.0 - 3.0
$NbCr_2$*	26.4 ± 2.3	4.5 ± 0.8	13.0 ± 1.7	51.0 ± 3.1	3.0 ± 0.5	1.1 ± 0.6	1.0 ± 1.0
	23.0 - 30.7	3.4 - 7.2	9.9 - 17.4	44.4 - 55.7	2.4 - 4.3	0.5 - 3.1	0.0 - 3.7

5.2.2.4 BSE – SEM imaging

Figure 5.9a and Figure 5.9b show the typical microstructure of JW1-HT13, taken from the centre of the alloy ingot using BSE imaging. Figure 5.10a and Figure 5.10b show the typical microstructure of JW1-HT15, taken from the centre of the alloy ingot using BSE imaging.

The centre region of JW1-HT13 consists of grains of $D8_8$, bright contrast T2, and an intergranular mixture of $NbCr_2$, $D8_8$, and (Nb) that exists between these silicide phases. $D8_8$ is the main phase and exists as discrete grains with straight edges separated by a continues matrix of solid solution (Nb), both of which have similar contrasts in the BSE images. T2 is identified as the bright phase and the elongated formation that was noted in the case of JW1-AC persists in the heat-treated structure. Between and around T2 and $D8_8$ phases exists a mixture of phases containing $NbCr_2$, which is the darkest contrast phase in this region, intergranular $D8_8$, which is similar in contrast to $NbCr_2$ but slightly lighter, and (Nb), which is the majority phase in this region. (Nb) usually borders the larger $D8_8$ grains whereas the $NbCr_2$ and intergranular $D8_8$ phase are generally surrounded by (Nb). A certain degree of cracking is observed in this alloy and is mainly found in the $D8_8$ grains. Aside from coarsening of the intergranular region and perhaps more rounded edges of T2 and $D8_8$ grains, the microstructure of JW1-HT13 is similar to that of the as-cast version.

The centre region of JW1-HT15 consists of grains of $D8_8$, bright contrast T2, and an intergranular area of bright contrast (Nb) and $NbCr_2$ that exists between these silicide phases. T2 and (Nb) have more similar contrast in these BSE images, but can be resolved by the fact that the (Nb) phase is interspersed by thin Laves phase $NbCr_2$, whereas T2 is more homogenous in contrast and therefore appearance. The $NbCr_2$ phase is found within (Nb) regions as well as on the border of (Nb) and $D8_8$ as was noted in EBSD imaging, i.e. the ‘shell’ structure. No intergranular $D8_8$ exists as this has apparently been removed by heat-treatment at the higher temperature, 1500^{o}C. The cracking observed in this alloy is more obviously favoured to be in the $D8_8$ phase, with relatively crack free (Nb) areas. Whilst the phases of JW1-HT15 are the same as in JW1-HT13 and JW1-AC, the microstructure is significantly different with more connected $D8_8$, no intergranular $D8_8$, and finer $NbCr_2$.

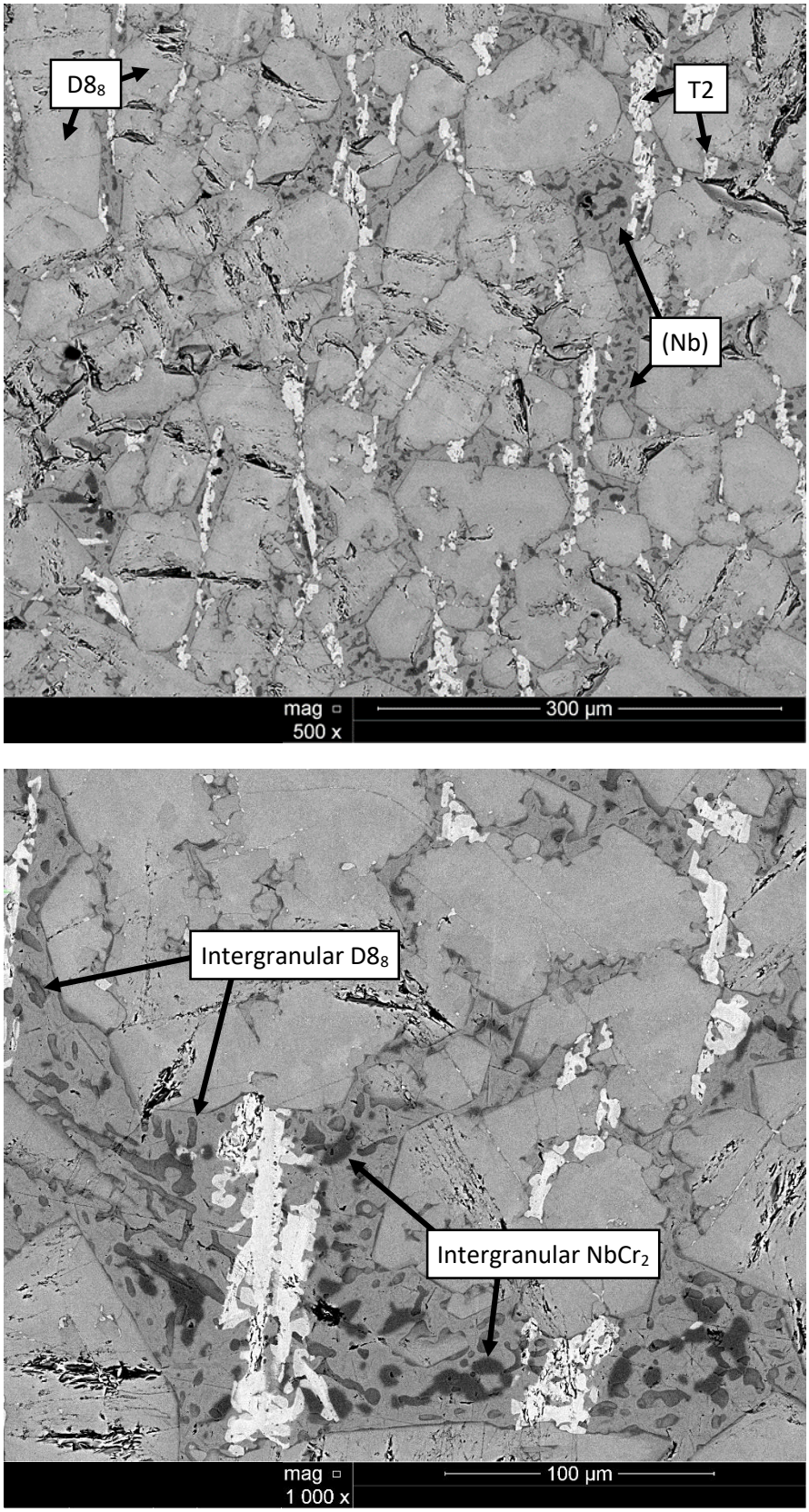

Figure 5.9a-b) BSE images of the central region of JW1-HT13 taken at lower magnification (a) and higher magnification (b)

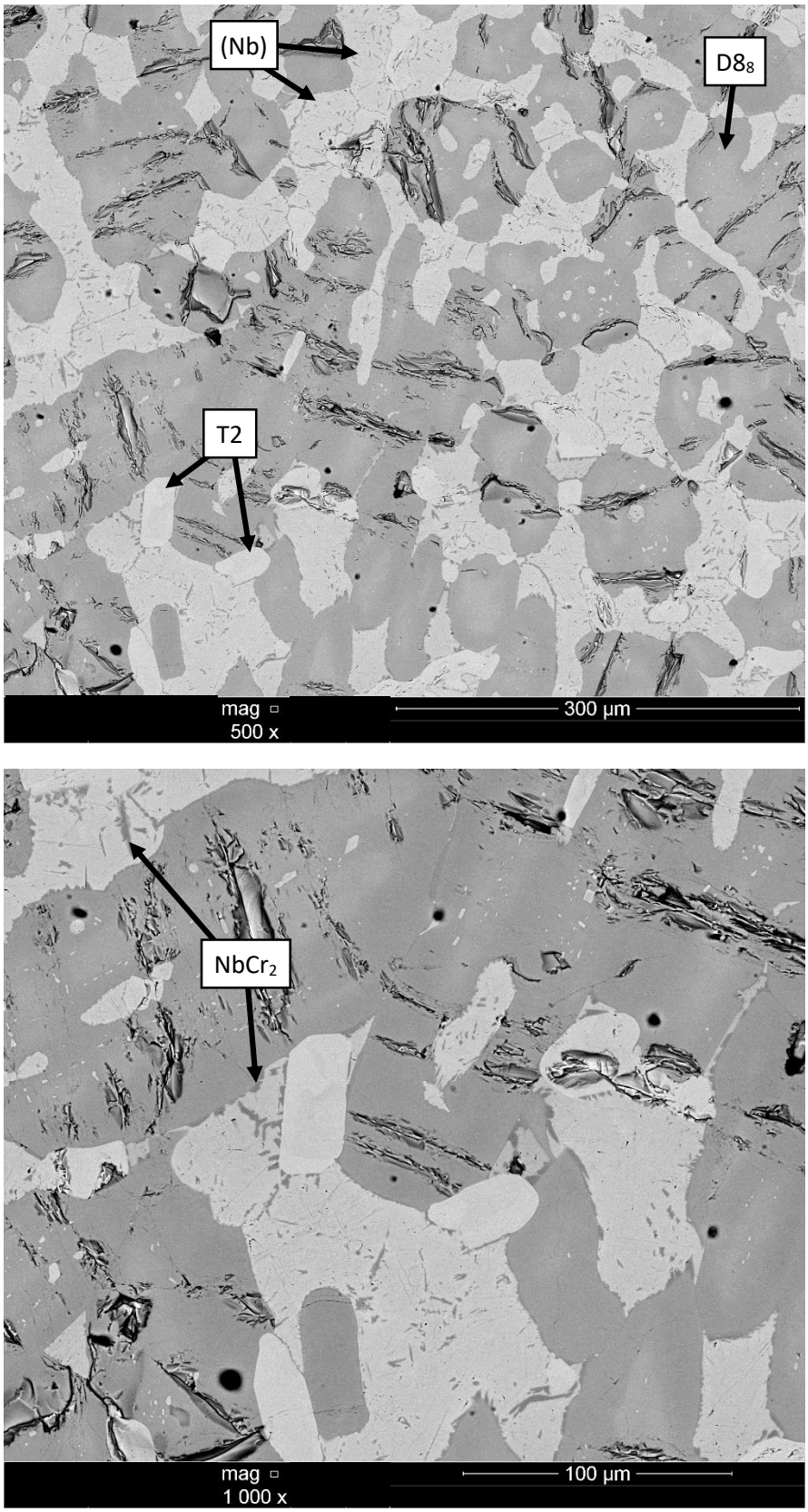

Figure 5.10a-b) BSE images of the central region of JW1-HT15 taken at lower magnification (a) and higher magnification (b)

5.2.2.5 Area fraction

The area fractions of phases $D8_8$, T2, (Nb) and $NbCr_2$ within JW1-HT13 and JW1-HT15 at the centre of the alloy ingot were calculated from BSE images and are given in Table 5.4. The contrast of these three phases was used to differentiate between them. On average JW1-HT13 contained 73.6% $D8_8$, 5.7% T2, 18.6% (Nb) and 2.1% $NbCr_2$ by area. The $D8_8$ phase can be further differentiated with 61.9% of the total area being the larger grains. The area percent of intergranular $D8_8$ was measured to be 11.7%. On average JW1-HT15 contained 81.5% $D8_8$, 6.4% T2, 11.3% (Nb) and 1.5% $NbCr_2$ by area.

Compared to the as-cast version of JW1, JW1-HT13 has a similar (Nb) area fraction whereas JW1-HT15 has a significant reduction in (Nb) volume. T2 area fraction is increased from JW1-AC to JW1-HT13 to JW1-HT15 by a small amount, with areas of 4.3%, 5.7% and 6.4%, respectively, although error ranges overlap. $D8_8$ area fraction is more complicated as after the 1300°C heat treatment there is less main grain $D8_8$, 61.9% compared to 68.6% in JW1-AC, but a larger proportion of intergranular $D8_8$, 11.7% compared to 7.7% in JW1-AC. However, the total $D8_8$ present of JW1-AC and JW1-HT13 are within error of each other, 76.3% and 73.6%, respectively. $D8_8$ was not present as an intergranular phase in JW1-HT15, and only had a slightly larger area fraction than in the other two processing states of JW1. The area fraction of $NbCr_2$ is increased by heat treatment either at 1300°C or 1500°C when compared to the as-cast alloy, however the 1300°C treatment seems to have had slightly greater stabilising effect on $NbCr_2$.

5.2.3 JW2 (Nb-24Ti-18Si-5Cr-5Al-5-Ge-10B)

5.2.3.1 XRD

The X-ray diffraction pattern of JW2-HT13 (Nb-24Ti-18Si-5Cr-5Al-5-Ge-10B) is given in Figure 5.11. In JW2-HT13, five phases are identified; the silicides $D8_8$ and T2, the Nb solid solution (Nb), a niobium titanium boride NbB, and a Laves phase $NbCr_2$. A high degree of confidence can be placed in the silicide phase $D8_8$, as there are multiple unique high intensity peaks assigned to this phase. As can a high degree of confidence be placed in T2, NbB, (Nb) and $NbCr_2$ phases being present, as there are multiple unique peaks assigned to each of these phases.

The X-ray diffraction pattern of JW2-HT15 is given in Figure 5.12. In JW2-HT15, three phases are identified; the silicides $D8_8$ and T2, and a Laves phase $NbCr_2$. A high degree of confidence can be placed in the phases $D8_8$ and T2 being present, as there are multiple unique high intensity peaks assigned to each of these phases. In the case of $NbCr_2$ relatively low intensity peaks are assigned to $NbCr_2$, but these are unique and consistent with the phase when it is identified in JW2-HT13.

The (Nb) phase is absent from the pattern of JW2-HT15, and T2 peaks have higher relative intensity relative to $D8_8$ peaks when compared to other patterns of JW2 and pattern of JW1. NbB is found in JW2-HT13 but is not seen in JW2-HT15. Compared to the as-cast XRD pattern of JW2, T2 has been developed through heat-treatment in both JW2-HT13 and JW2-HT15. However as previously mentioned in regards to microstructural texture due to the solidification conditions, this must be coupled with volume fraction results (Table 5.4) to make an accurate assessment.

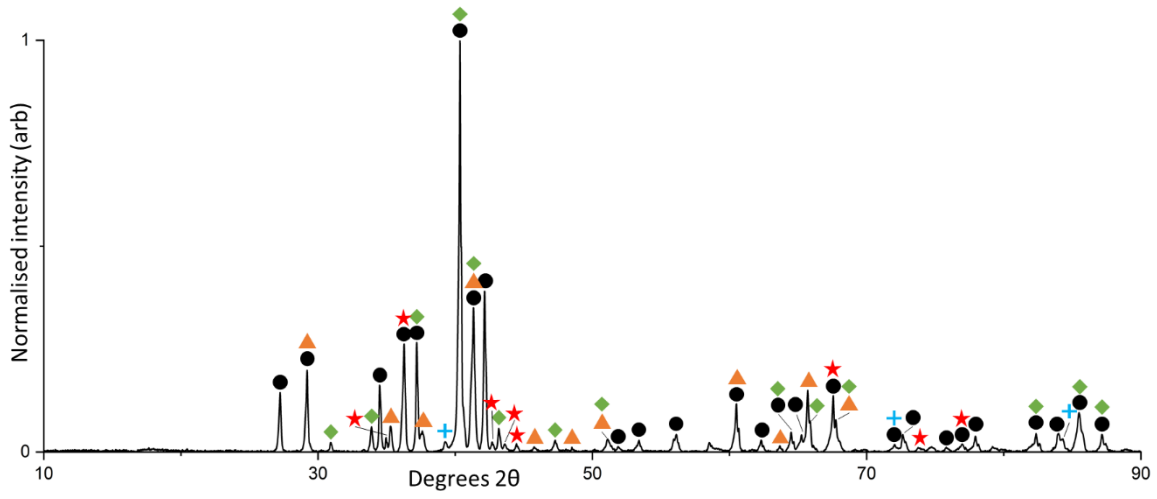

Figure 5.11) XRD pattern of JW2-HT13. ● = $D8_8$, ★ = $NbCr_2$, ◆ = T2, ▲ = NbB, + = (Nb)

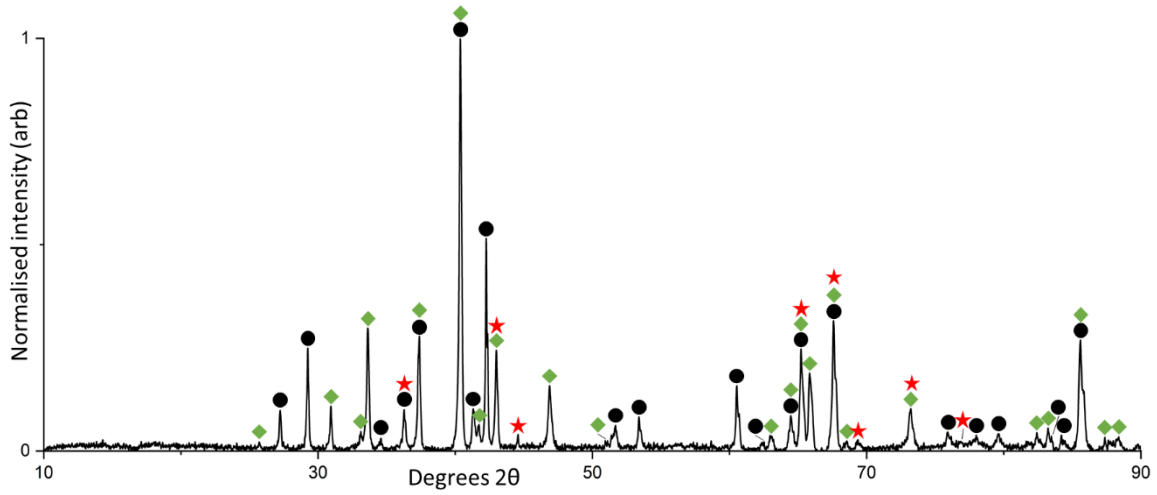

Figure 5.12) XRD pattern of JW2-HT15. ● = $D8_8$, ★ = $NbCr_2$, ◆ = T2.

5.2.3.2 EBSD

EBSD maps of JW2-HT15 are presented in Figure 5.13 and Figure 5.14 with corresponding EDS maps of the areas examined. These maps are taken from the middle of the alloy ingot, at two different magnifications to show the general microstructure (Figure 5.13) and more detailed microstructure (Figure 5.14). The T2 and $D8_8$ phases expected from XRD results were identified comprehensively in both figures. The $NbCr_2$ phase identified in XRD was found in high Cr areas identified in corresponding EDS maps. Small amounts of the (Nb) are seen more clearly in the higher magnification EBSD figures adjacent to the T2 phase. For such small amounts of this phase it follows that it would not be detected in XRD pattern presented in Figure 5.12. The majority of the sample is made up of large $D8_8$ and coarse T2 grains, with some T2 phase existing within $D8_8$ grains in a 'speckled' formation.

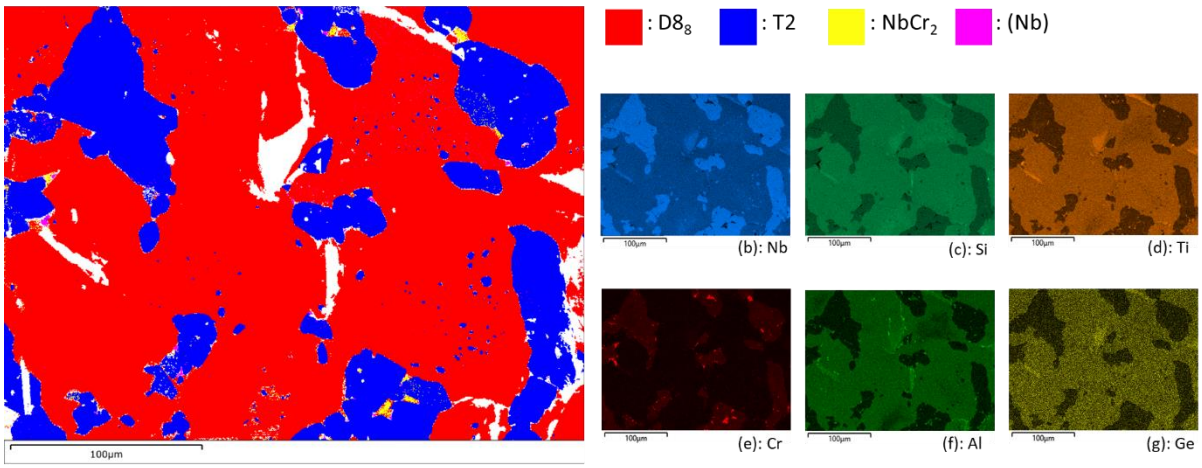

Figure 5.13a-h) EBSD map of JW2-HT15 at lower magnification (a), and corresponding qualitative EDS maps of Nb (b), Si (c), Ti (d), Cr (e), Al (f), and Ge (g).

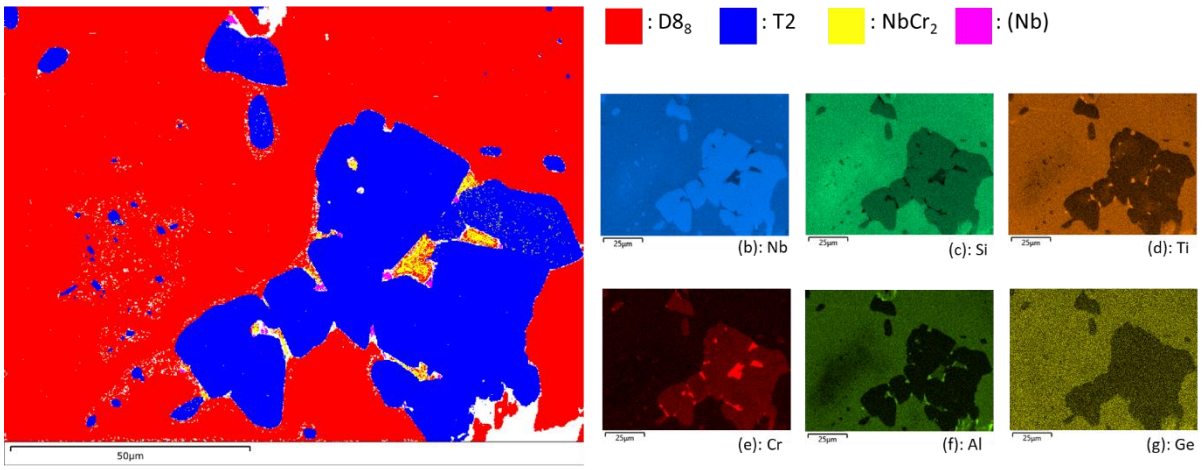

Figure 5.14a-h) EBSD map of JW2-HT15 at higher magnification (a), and corresponding qualitative EDS maps of Nb (b), Si (c), Ti (d), Cr (e), Al (f), and Ge (g).

5.2.3.3 EPMA

EPMA mapping of the central region of JW2-HT13 identifies phases (Nb), $D8_8$, NbB, $NbCr_2$ and T2. The compositions of these phases are given in Table 5.8. These phases are in agreement with XRD results presented previously. The (Nb) in this alloy is rare, and has almost double the amount of Ti content as Nb content. However, this phase is still identified as the same BCC niobium solid solution seen in the other alloys in this study, and not an HCP titanium solid solution because of the EBSD findings that show a (Nb) phase in the AC and HT15 versions of the alloy. An assumption is made that if (Nb) is the high Nb and Ti content phase in the AC version and HT15 version of JW2 then this will be the case for the HT13 version as well. The $D8_8$ silicide makes up the majority of the alloy and has a boron content, 5.9 at.%, that is similar with $D8_8$ found in JW1 alloys despite the JW2 alloy having 10 at.% B content nominally. In JW2-HT13, both T2 and NbB are found. In the location that the EPMA data was collected from, T2 is consistently found alongside NbB which strongly suggests the heat-treatment at 1300°C results in a decomposition of NbB into T2.

EPMA mapping of the central region of JW2-HT15 identifies phases (Nb), $D8_8$, $NbCr_2$ and T2. The compositions of these phases are given in Table 5.7. These phases are in agreement with XRD results presented previously, with the exception of (Nb) which was not found with XRD but was identified in EBSD mapping. $NbCr_2$, which could not be found in EBSD mapping but had a low degree of confidence based on XRD pattern, was confirmed in this EPMA analysis based on composition of the high Cr content phase. The NbB to T2 transition noted in JW2-HT13 EPMA analysis appears to have fully taken place as no NbB is found in the microstructure. Most of the sample is made up of $D8_8$, which has a similar composition to the $D8_8$ found in the JW2-HT13 sample but with lower Nb content replaced by Ti, and lower Si content replaced by Al. B content of JW2-HT15 $D8_8$ is slightly lower than JW2-HT13 $D8_8$, 5.3 at.% and 5.9 at.%, respectively.

*Table 5.8) Compositions of phases found in the central region of JW2-HT13 using EPMA mapping, values given in at.%. Mean ± stdev, minimum value - maximum value. * marks phases that were in small quantities and only 40 points could be taken*

	Nb	Si	Ti	Cr	Al	Ge	B
$D8_8$	37.9 ± 1.9	25.7 ± 1.2	22.0 ± 1.7	1.3 ± 0.3	1.4 ± 0.6	5.8 ± 0.3	5.9 ± 1.0
	32.4 - 40.1	21.7 - 28.3	20.1 - 26.9	0.8 - 2.1	0.9 - 3.4	5.4 - 7.0	2.5 - 8.4
T2	35.2 ± 1.4	10.4 ± 0.6	20.2 ± 1.4	9.6 ± 0.4	0.1 ± 0.1	1.5 ± 0.2	23.1 ± 1.6
	30.1 - 37.4	8.9 - 12.3	16.7 - 24.2	8.0 - 10.8	0.0 - 0.4	0.6 - 1.8	20.7 - 29.7
NbB	40.1 ± 1.0	0.3 ± 0.2	14.1 ± 0.6	0.4 ± 0.2	0.1 ± 0.1	0.0 ± 0.0	45.1 ± 0.8
	36.7 - 42.7	0.0 - 1.4	11.9 - 15.7	0.2 - 1.5	0.0 - 0.5	0.0 - 0.1	41.1 - 47.6
(Nb)*	21.1 ± 0.4	0.5 ± 0.3	42.1 ± 0.9	14.1 ± 1.1	20.6 ± 0.7	0.4 ± 0.1	1.2 ± 0.9
	20.4 - 22.2	0.1 - 1.5	40.1 - 44.5	11.6 - 15.6	18.8 - 22.2	0.3 - 1.0	0.0 - 3.6
$NbCr_2$*	20.3 ± 0.4	5.2 ± 0.5	15.6 ± 0.5	50.2 ± 0.9	7.6 ± 0.5	0.5 ± 0.1	0.6 ± 0.7
	19.4 - 21.5	3.8 - 6.9	14.6 - 16.8	46.7 - 52.5	6.6 - 9.1	0.4 - 0.9	0.0 - 2.6

Table 5.7) Compositions of phases found in the central region of JW2-HT15 using EPMA mapping, values given in at.%. Mean ± stdev, minimum value - maximum value.

	Nb	Si	Ti	Cr	Al	Ge	B
$D8_8$	32.9 ± 0.6	19.4 ± 0.7	26.8 ± 0.5	2.4 ± 0.1	6.5 ± 0.4	6.7 ± 0.2	5.3 ± 1.1
	31.6 - 34.7	17.3 - 21.3	25.5 - 28.2	2.1 - 2.8	5.6 - 7.3	6.3 - 7.3	2.0 - 8.0
T2	44.9 ± 0.9	10.4 ± 0.5	14.2 ± 0.7	6.8 ± 0.3	0.2 ± 0.0	1.5 ± 0.1	22.1 ± 0.6
	42.2 - 46.8	8.9 - 11.4	13.4 - 16.7	5.7 - 7.5	0.0 - 0.3	1.4 - 1.8	20.7 - 24.0
(Nb)	24.6 ± 0.8	0.4 ± 0.3	45.9 ± 1.3	9.8 ± 1.3	17.3 ± 0.6	0.5 ± 0.2	1.5 ± 1.1
	23.1 - 31.0	0.0 - 1.8	35.4 - 49.3	5.9 - 11.5	15.7 - 19.3	0.4 - 1.7	0.0 - 6.2
$NbCr_2$	20.6 ± 0.7	4.9 ± 0.5	15.9 ± 0.8	51.9 ± 0.8	5.2 ± 0.2	0.6 ± 0.0	0.8 ± 0.8
	18.8 - 21.7	3.6 - 6.2	15.0 - 21.6	46.8 - 54.5	4.6 - 6.2	0.5 - 0.7	0.0 - 4.4

5.2.3.4 BSE – SEM imaging

Figure 5.15a and Figure 5.15b show the typical microstructure of JW2-HT13, taken from the centre of the alloy ingot using BSE imaging. Figure 5.16a and Figure 5.16b show the typical microstructure of JW2-HT15, taken from the centre of the alloy ingot using BSE imaging.

The centre region of JW2-HT13 consists of grains of $D8_8$, T2, and NbB rounded globules, and an intergranular mixture of $NbCr_2$ and (Nb) which both have darker contrasts. $D8_8$ is the main phase and exists as large, discrete grains with straight edges similar to what was seen in the AC version of JW2. However individual grains of $D8_8$ are more clear since edges of some of these grains are a darker contrast as they have higher Ti and Al content, and less Nb. T2 and NbB are indistinguishable from each other in this alloy under these conditions as contrast is similar where usually T2 is the brightness contrast phase and shape is similar where usually T2 is more angular than NbB. Both phases are also found in similar places as it is believed that T2 is forming from NbB due to the heat treatment of the JW2 alloy, and after 100 hours at 1300°C this phase transition is only part way completed. Darker areas exist between $D8_8$ grains made up of (Nb), the darkest contrast phase present, and coarse $NbCr_2$, the slightly lighter contrast phase that is present alongside (Nb). (Nb) is likely the darkest contrast phase now, where it was not in JW1 or KZ5 alloys, due to the high content of Ti now present. This (Nb) is evidently not a continuous matrix.

The centre region of JW2-HT15 consists of grains of $D8_8$, bright contrast T2, and small amounts of (Nb) and $NbCr_2$ that exists primarily in and around T2 formations. (Nb) and $NbCr_2$ are indistinguishable as both take the same shape and contrast, as well as being positioned adjacent to areas of T2. The $D8_8$ phase has less defined edges and grains are difficult to isolate, as evidently

some homogenisation of this phase has occurred compared to the $D8_8$ seen in JW2-HT13. This microstructure shows the largest amounts of T2 seen in any alloy investigated in this study, and it exists in large groupings as well as speckled within $D8_8$. No NbB is recorded in this alloy through any technique and it is not seen visually in these BSE images either. Therefore, in the other versions of JW2, NbB can be said to be metastable.

The microstructures and phases of JW2-AC and JW2-HT13 are relatively similar with areas of (Nb) and $NbCr_2$ mixture within a predominantly $D8_8$ grain network, with NbB and T2 being present throughout the alloys. However, JW2-HT15 is significantly different to these two other forms of JW2, with much reduced amounts of (Nb) and $NbCr_2$, and large formation of T2 as oppose to NbB.

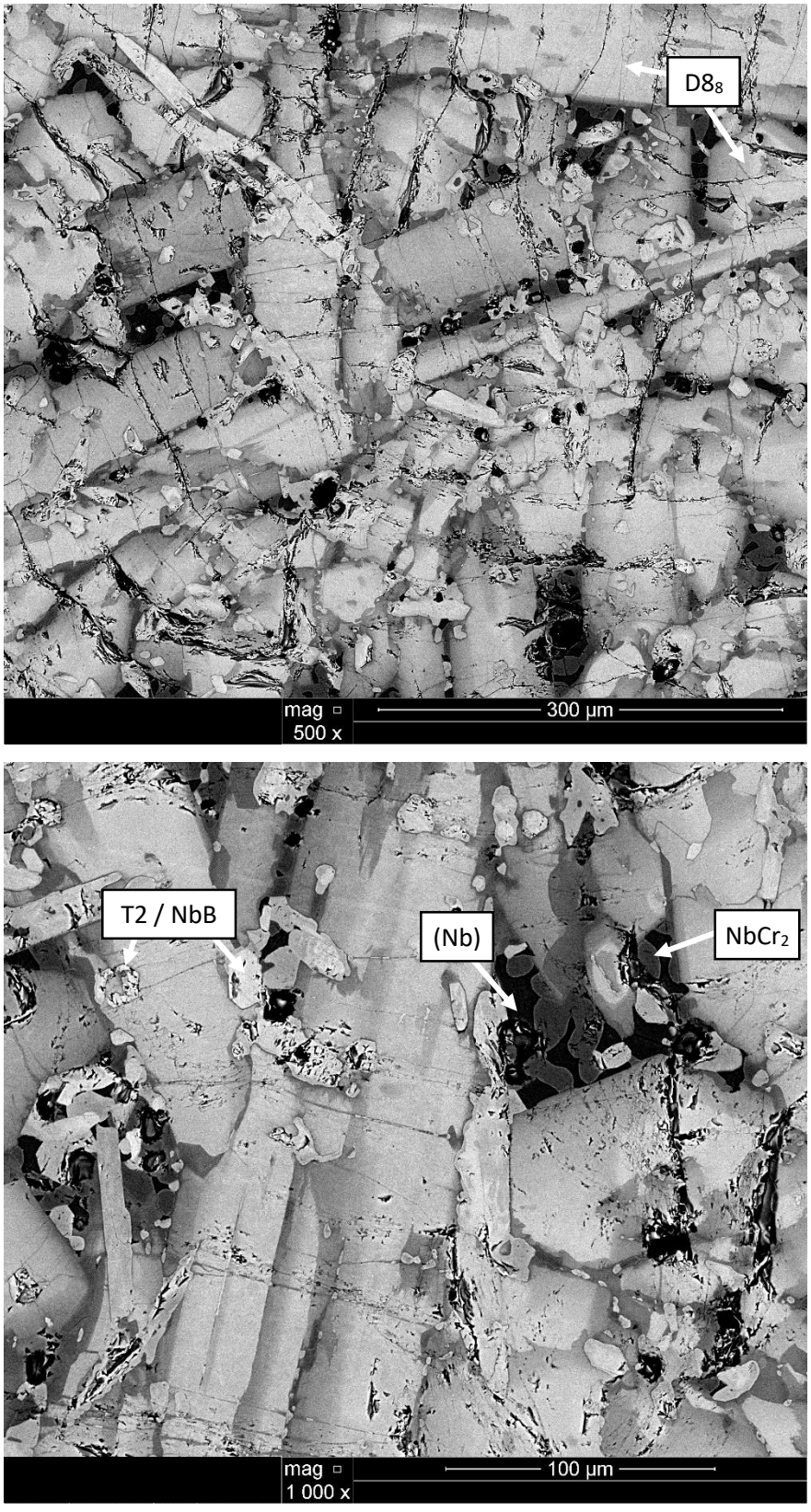

Figure 5.15a-b) BSE images of the central region of JW2-HT13 taken at lower magnification (a) and higher magnification (b)

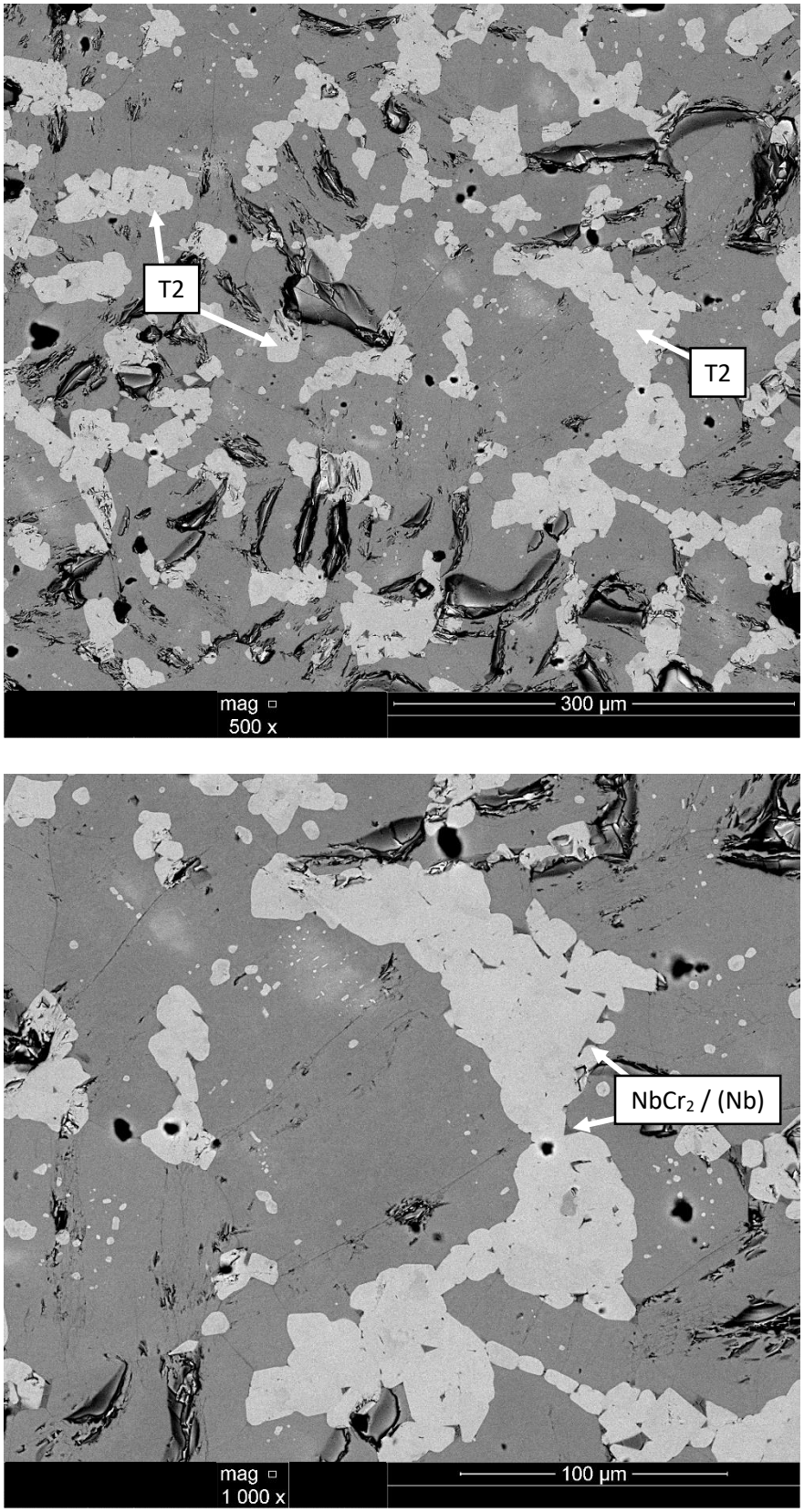

Figure 5.16a-b) BSE images of the central region of JW2-HT15 taken at lower magnification (a) and higher magnification (b)

5.2.3.5 Area fraction

The area fractions of phases $D8_8$, T2, NbB, (Nb) and $NbCr_2$ within JW2-HT13 at the centre of the alloy ingot were calculated from BSE images and are given in Table 5.4. The area fractions of phases $D8_8$, T2, (Nb) and $NbCr_2$ within JW2-HT15 are also given in Table 5.4. The contrast of these five phases was used to differentiate between them. In the case of NbB and T2 in JW2-HT13 these contrasts were too similar to resolve into separate phases so the value reflects a combination of these two phases. On average JW2-HT13 contained 77.5% $D8_8$, 9.7% T2 and NbB, 5.4% (Nb) and 6.7% $NbCr_2$ by area. On average JW2-HT15 contained 70.3% $D8_8$, 27.9% T2, 0.5% (Nb) and 1.4% $NbCr_2$ by area.

General trends can be seen when comparing the area fractions of each phase of each alloy at different processing states. (Nb) gradually reduces from JW2-AC to JW2-HT13 to JW2-HT15, as does $D8_8$ and NbB. Whereas T2 increases from a negligible 0.7% in JW2-AC, to a value in-between 0% and 9.7% in JW2-HT13, to a large 27.9% volume fraction in JW2-HT15. The only phase not to follow a trend is $NbCr_2$ which has its highest content, 6.7%, in JW2-HT13 which suggests this phase is more stable at 1300°C than it is at 1500°C or in the slow argon cooled as-cast state.

5.2.4 JW3 (Nb-24Ti-18Si-5Cr-5Al-10Ge-5B)

5.2.4.1 XRD

The X-ray diffraction pattern of JW3-HT13 (Nb-24Ti-18Si-5Cr-5Al-10Ge-5B) is given in Figure 5.17. In JW3-HT13, four phases are identified; the silicides $D8_8$ and T2, the Nb solid solution (Nb), and a Laves phase $NbCr_2$. A high degree of confidence can be placed in the phases $D8_8$ and (Nb) being present, as there are multiple unique peaks assigned to each of these phases, with $D8_8$ having peaks of a high intensity too. In the case of $NbCr_2$ and T2, only relatively low intensity peaks are assigned to solely these phases, with the rest overlapping with other phases. Further confirmation of these phases is therefore required from EBSD and EPMA.

The X-ray diffraction pattern of JW3-HT15 (Nb-24Ti-18Si-5Cr-5Al-10Ge-5B) is given in Figure 5.18. In JW3-HT15, three phases are identified; the silicides $D8_8$ and T2, and a Laves phase $NbCr_2$. A high degree of confidence can be placed in the phases $D8_8$ and T2 being present, as there are multiple unique high intensity peaks assigned to each of these phases. In the case of $NbCr_2$ only relatively low intensity peaks are assigned to solely $NbCr_2$, with the rest overlapping with other phases. Further confirmation of this phase is therefore required. EBSD of JW3-HT15 was not acquired, but EPMA results can be used to confirm compositions of these phases.

The (Nb) phase is absent from the pattern of JW3-HT15, as was the case with the other high Ge+B alloy heat-treated at 1500°C, JW2-HT15. Compared to the as-cast alloy JW3-AC, both heat-treated XRD pattern show the development of the T2 phase through heat-treatment.

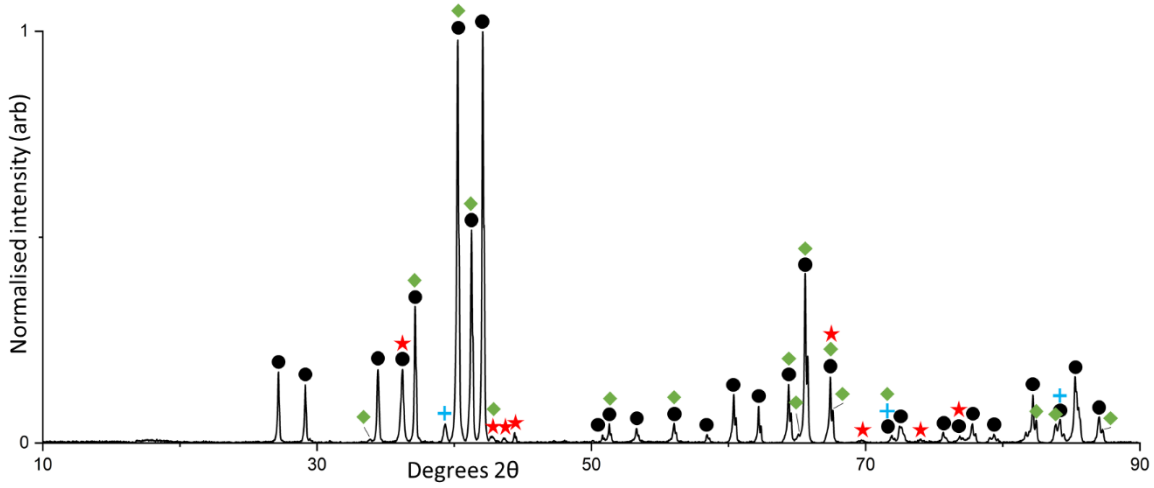

Figure 5.17) XRD pattern of JW3-HT13. ● = $D8_8$, ★ = $NbCr_2$, ◆ = T2, + = (Nb).

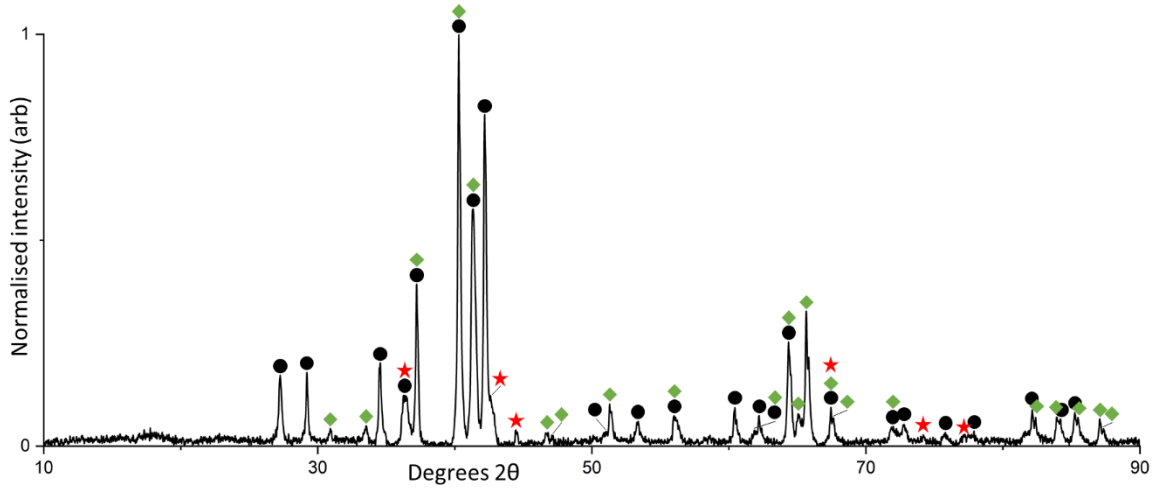

Figure 5.18) XRD pattern of JW3-HT15. ● = $D8_8$, ★ = $NbCr_2$, ◆ = T2.

5.2.4.2 EPMA

EPMA mapping of the central region of JW3-HT13 identifies phases (Nb), $D8_8$, $NbCr_2$ and T2. The compositions of these phases are given in Table 5.10. These phases are in agreement with XRD results presented previously. As was the case with JW2 alloys, Ti content of (Nb) is approximately double that of Nb content in this phase, 43.8 at.% compared to 19.8 at.%. In fact, (Nb) has the lowest Nb content of any phase found in JW3-HT13. The $D8_8$ silicide makes up the majority of the alloy and has a boron content of 5.8 at.%, which is consistent with $D8_8$ found in JW1 and JW2 alloys. The Ge content of $D8_8$ in JW3-HT13 is 10.3 at.%. The increased Ge content in JW3 has resulted in a higher Ge content of the $D8_8$ phase compared to alloys with only 5 at.% Ge nominal composition. T2 is found in JW3-HT13 where as NbB is not. NbB has been removed from the bulk of the microstructure by the heat treatment at 1300°C.

EPMA mapping of the central region of JW3-HT15 identifies phases $D8_8$, $NbCr_2$ and T2. The compositions of these phases are given in Table 5.9. These phases are in agreement with XRD results presented previously. Most of the sample remains $D8_8$, which has a similar composition to the $D8_8$ found in the JW3-HT13 sample but with a slightly lower boron content of 5.1 at.%. T2 remains in the microstructure after the heat treatment at 1500°C, with the main differences in composition being variations in metallic elements Nb, Ti, and Cr which increase from 36.3 at.% to 42.8 at.%, reduce from 19.6 at.% to 15.4 at.%, and reduce from 9.3 at.% to 7.6 at.%, respectively for JW3-HT13 to JW3-HT15. The increase in Nb content after heat treatments is likely a contributing factor to the lack of (Nb) in the JW3-HT15 microstructure as even less Nb is available for its formation.

*Table 5.10) Compositions of phases found in the central region of JW3-HT13 using EPMA mapping, values given in at.%. Mean ± stdev, minimum value - maximum value. * marks phases that were in small quantities and only 40 points could be taken*

	Nb	Si	Ti	Cr	Al	Ge	B
$D8_8$	36.8 ± 2.7	20.7 ± 2.0	22.9 ± 2.5	1.5 ± 0.4	2.0 ± 1.1	10.3 ± 0.9	5.8 ± 1.2
	32.8 - 42.2	17.0 - 25.2	18.8 - 27.0	0.6 - 2.3	0.5 - 4.2	8.9 - 12.7	1.5 - 9.3
T2*	36.3 ± 1.6	9.8 ± 0.6	19.6 ± 1.0	9.3 ± 0.6	0.4 ± 0.4	2.5 ± 0.4	22.1 ± 1.3
	30.7 - 39.3	8.5 - 11.2	17.7 - 21.5	6.9 - 10.4	0.0 - 2.1	2.1 - 4.5	19.8 - 24.9
(Nb)	19.6 ± 0.3	0.2 ± 0.3	43.2 ± 1.2	12.5 ± 1.1	24.0 ± 0.6	0.5 ± 0.1	0.1 ± 0.3
	19.1 - 20.6	0.0 - 1.6	40.1 - 45.7	11.2 - 14.9	23.1 - 25.4	0.3 - 0.8	0.0 - 1.2
$NbCr_2$	21.1 ± 0.4	4.0 ± 0.6	14.7 ± 0.5	50.0 ± 0.8	8.6 ± 0.6	0.7 ± 0.1	0.8 ± 0.8
	20.1 - 22.4	2.8 - 8.1	13.8 - 17.3	47.5 - 52.0	6.8 - 10.2	0.4 - 1.8	0.0 - 3.4

Table 5.9) Compositions of phases found in the central region of JW3-HT15 using EPMA mapping, values given in at.%. Mean ± stdev, minimum value - maximum value.

	Nb	Si	Ti	Cr	Al	Ge	B
$D8_8$	33.3 ± 1.5	18.7 ± 1.5	26.4 ± 1.4	1.7 ± 0.2	3.3 ± 0.9	11.5 ± 0.6	5.1 ± 1.3
	30.3 - 37.3	15.0 - 22.1	22.7 - 29.1	1.2 - 2.3	1.5 - 4.9	8.1 - 12.7	1.0 - 9.8
T2	42.8 ± 1.0	9.5 ± 0.6	15.4 ± 0.5	7.6 ± 0.3	0.1 ± 0.1	2.8 ± 0.3	21.7 ± 1.0
	40.5 - 45.7	8.1 - 10.8	14.3 - 17.3	6.8 - 8.3	0.0 - 0.5	2.4 - 3.6	17.3 - 23.7
$NbCr_2$	23.5 ± 0.4	6.1 ± 0.5	12.1 ± 0.3	52.8 ± 1.0	3.7 ± 0.2	1.0 ± 0.2	0.7 ± 0.7
	22.6 - 25.2	4.6 - 8.4	11.5 - 15.0	44.4 - 55.0	3.1 - 4.2	0.8 - 3.6	0.0 - 3.0

5.2.4.3 BSE – SEM imaging

Figure 5.19a and Figure 5.19b show the typical microstructure of JW3-HT13, taken from the centre of the alloy ingot using BSE imaging. Figure 5.20a and Figure 5.20b show the typical microstructure of JW3-HT15, taken from the centre of the alloy ingot using BSE imaging.

The centre region of JW3-HT13 consists of grains of $D8_8$, T2 and dark contrast intergranular areas of (Nb) and $NbCr_2$. $D8_8$ is the main phase and exists as large, discrete grains with some straight edges similar to what was seen in the as-cast version of JW3. Darker areas exist between $D8_8$ grains made up of (Nb), the darkest contrast phase present, and coarse $NbCr_2$, the slightly lighter contrast phase that is present alongside (Nb). Intergranular T2 also exists in this alloy and is found alongside $NbCr_2$ but not usually with (Nb). i.e. there are two intergranular formations; (Nb) and $NbCr_2$, and T2 and $NbCr_2$. The contrast of these BSE images is increased in order to be able to identify the T2 phase, hence the increased brightness of all other phases and almost black appearance of (Nb).

The centre region of JW3-HT15 consists of grains of $D8_8$, bright contrast T2, and dark contrast $NbCr_2$. The $D8_8$ phase has less defined edges and grains are difficult to isolate, as evidently some homogenisation of this phase has occurred compared to the $D8_8$ seen in JW3-HT13, in the same way the was observed in JW2 at the different heat-treatment temperatures. T2 now exists in coarse areas within the majority $D8_8$ microstructure in larger quantities than was observed in the JW3-HT13 microstructure. It is unclear where the required boron for this formation of T2 has come from since there was no NbB present in JW3-HT13, which would otherwise be one potential explanation. The $NbCr_2$ is most often found adjacent to T2 in this microstructure, as whilst T2 typically has a higher solubility of Cr atoms than $D8_8$ does, this is not enough to accommodate the Cr that is rejected from the $D8_8$ formation, and therefore $NbCr_2$ is stabilised in these high Cr areas of the microstructure.

The microstructure is altered from JW3-AC to JW3-HT13 by the coarsening of the intergranular region where in the as-cast version (Nb) and $NbCr_2$ were too fine to distinguish in BSE imaging, and

the removal of small amounts of NbB replaced by small amounts of T2. The grain structure of $D8_8$ was relatively unchanged; JW3-HT13 $D8_8$ seems more elongated but this is assumed to be a quirk of the specific area selected. JW3-HT15 is more visually different to both other processing states of JW3, with no clearly defined grains of $D8_8$ and more rounded formations of $NbCr_2$. The T2 phase has replaced the NbB found in the as-cast state, as was the case with the heat treatment at 1300°C. All three states of JW3 showed significant cracking, likely due to the limited amount of (Nb) in the microstructures and brittle nature of the intermetallic phases.

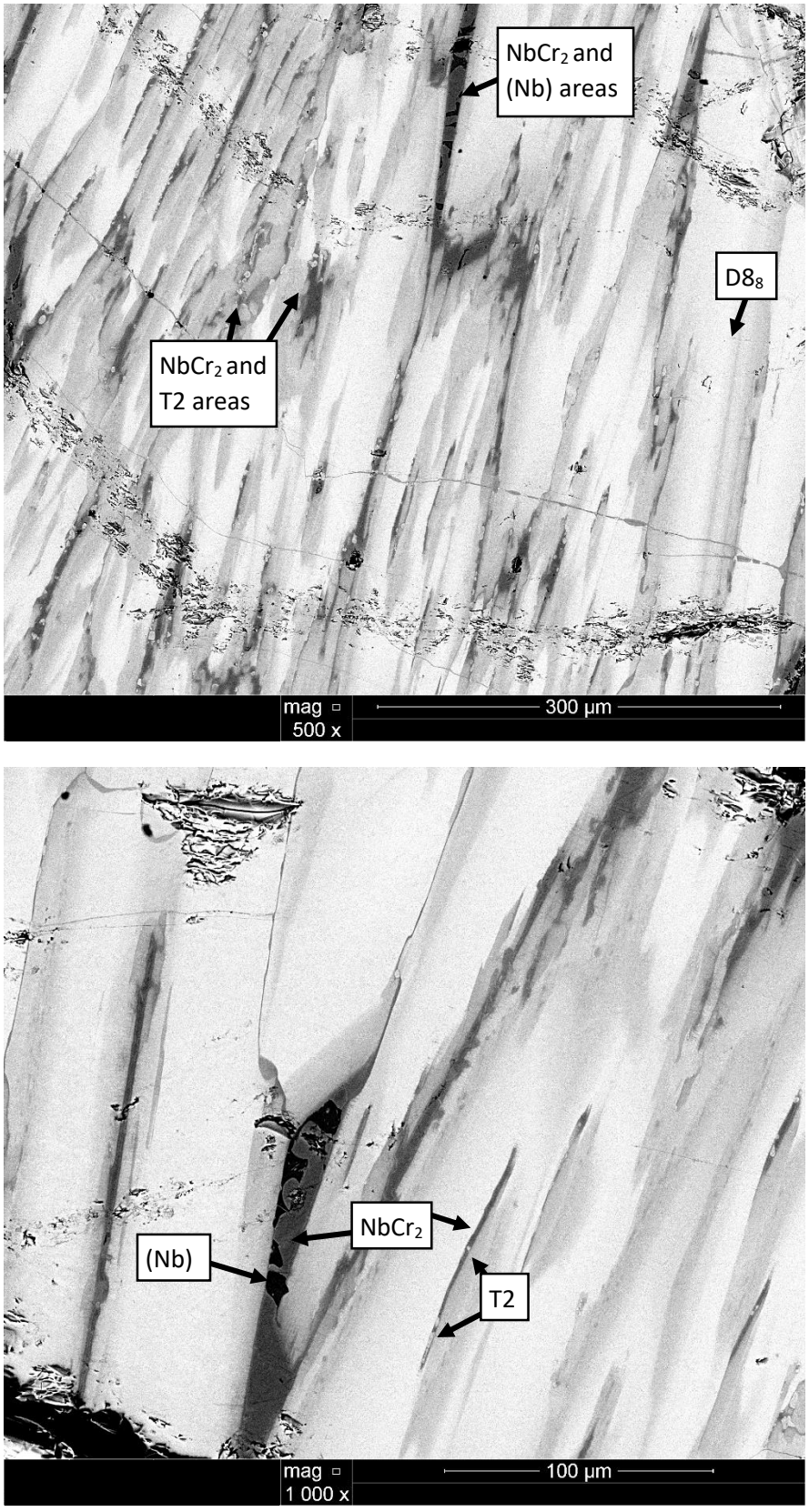

Figure 5.19a-b) BSE images of the central region of JW3-HT13 taken at lower magnification (a) and higher magnification (b)

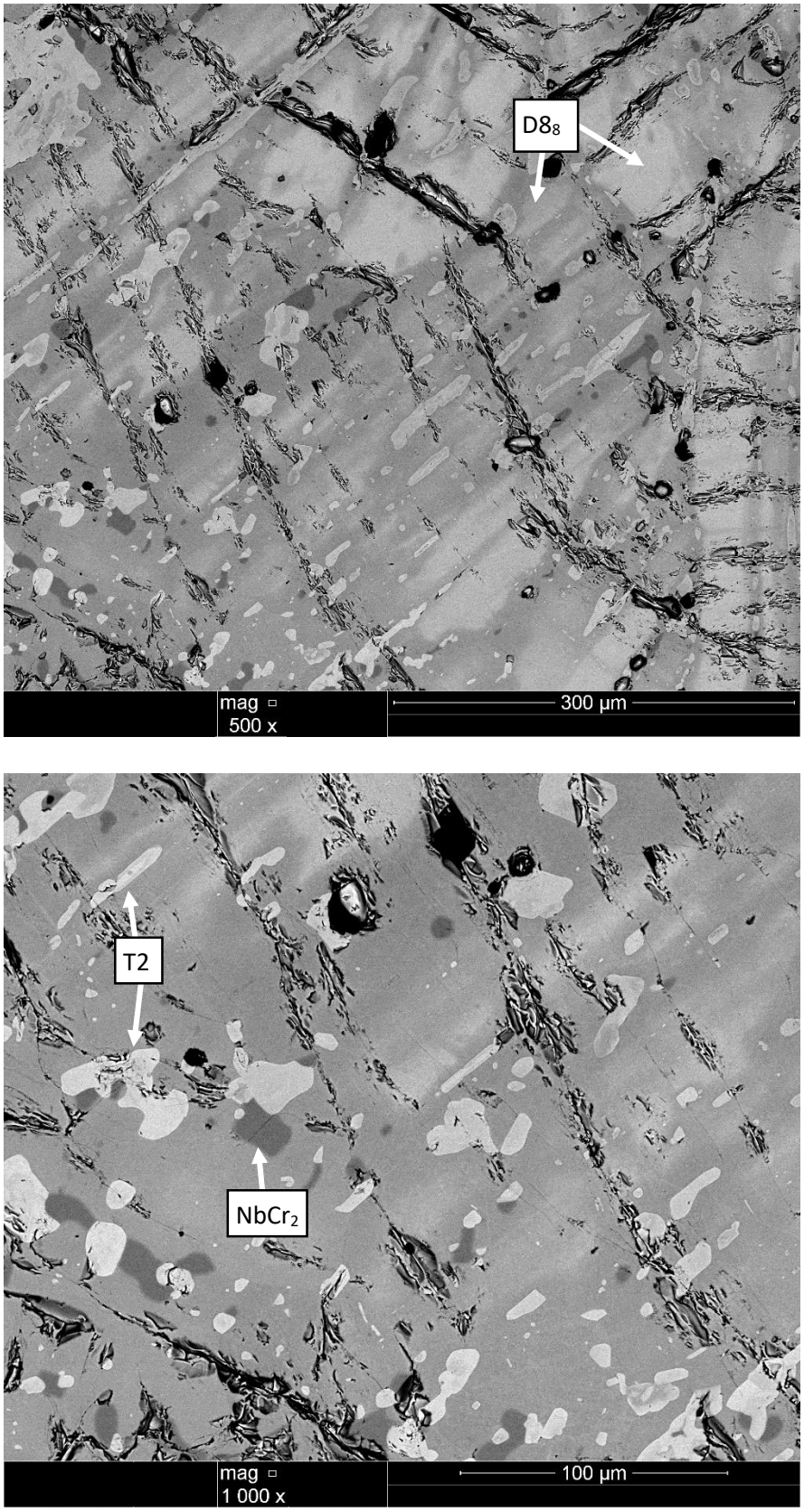

Figure 5.20a-b) BSE images of the central region of JW3-HT15 taken at lower magnification (a) and higher magnification (b)

5.2.4.4 Area fraction

The area fractions of phases $D8_8$, (Nb) and $NbCr_2$ within JW3-HT13 at the centre of the alloy ingot were calculated from BSE images and are given in Table 5.4. The area fractions of phases $D8_8$, T2 and $NbCr_2$ within JW3-HT15 are also given in Table 5.4. The contrast of these four phases was used to differentiate between them. On average JW3-HT13 contained 94.4% $D8_8$, 0.7% (Nb) and 5.0% $NbCr_2$ by area. On average JW3-HT15 contained 89.9% $D8_8$, 9.0% T2, and 1.1% $NbCr_2$ by area.

(Nb) and $NbCr_2$ are reduced from JW3-AC to JW3-HT13 to JW3-HT15, with (Nb) being non-existent in JW3-HT15 and $NbCr_2$ being 1.1%. From JW3-AC to JW3-HT13 small amounts of NbB, less than 1%, are replaced by small amounts of T2 that could not be distinguished from $D8_8$. In JW3-HT15 T2 becomes a significant part of the microstructure, 9.0% T2, in a similar way to how T2 area fraction was large in JW2-HT15. In all of the B and Ge containing alloys T2 is stabilised by the heat-treatment at 1500°C.

5.3 Discussion

5.3.1 The effect of heat-treatment on a boron and germanium free alloy (KZ5: Nb-24Ti-18Si-5Cr-5Al)

In chapter 4, it was shown that the high temperature phase βNb_5Si_3 forms in the as-cast sample. This is due to βNb_5Si_3 being stabilised by Al additions, as well as Cr additions retarding the βNb_5Si_3 to αNb_5Si_3 transition [153]. The effect of Al additions, as well as the sluggish transformation kinetics of the Nb-Si system, is evident in the heat-treated version of KZ5 where a large area fraction of βNb_5Si_3 is retained. The transition to αNb_5Si_3 is less than half way complete as βNb_5Si_3 area fraction is in fact still larger than that of αNb_5Si_3. No Nb_3Si phase is seen in KZ5-AC or KZ5-HT15. Ti has a stabilising effect on Nb_3Si [191][192], however Cr and Al both destabilise Nb_3Si [153][117]. In this current study, additions of Cr + Al = 10 at.% have a greater effect on Nb_3Si stability than Ti = 24 at.%.

The heat-treated version of KZ5 has been examined in the literature [153]. The same dual silicide microstructure was found through XRD, but which portions of Nb_5Si_3 composition material were αNb_5Si_3 and which were βNb_5Si_3 was unclear. It was proposed that the silicide areas higher in Ti, Cr and Al corresponded to the βNb_5Si_3, and conversely the areas lower in Ti, Cr and Al corresponded to the αNb_5Si_3 phase. This can be confirmed as correct based on the EBSD results present in Section 5.2.1.2 combined with the EPMA results presented in Section 5.2.1.3. The mechanism for the βNb_5Si_3 to αNb_5Si_3 solid state phase transition presented in [153] is a precipitation reaction; βNb_5Si_3 -> αNb_5Si_3 + (Nb), where Al is ejected from the βNb_5Si_3 structure. This precipitation reaction is observed in the current work where small particles of (Nb) are observed exclusively in silicide grains identified as αNb_5Si_3. More evidence for this mechanism is provided by the observation that intergranular βNb_5Si_3 has resisted the phase transition to αNb_5Si_3 more so than the primary βNb_5Si_3 grains. Intergranular βNb_5Si_3 is higher in Ti, Al and Cr content when compared to primary βNb_5Si_3, so more ejection of elements would have to take place for the precipitation reaction to proceed.

The homogenising effect that the 1500°C heat-treatment has on the (Nb) phase is also noted in [153]. Although, the effect of the heat-treatment at 1500°C for 100 hours has appears to be minimal, and only in the 200-hour heat-treatment are the ranges of elements reduced in the (Nb) phase. The heat-treatments in this current work were performed for 100 hours also, but a homogenising effect has still taken place. Every element with the exception of Si has a smaller range of compositions in the (Nb) phase. Si was also not homogenised in [153], and had a higher range in the heat-treated versions of KZ5. This suggests that despite overall Si content in the (Nb) phase reducing upon heat-treatment, diffusion of this element in this phase is sluggish as areas still high in Si remain. The silicon content of (Nb) in KZ5-AC is 2.0 at.%, in KZ5-HT15 it is 0.8 at.%. In [153], as-cast KZ5 (Nb) Si content was 2.0–2.1 at.%, after 100 hours at 1500°C it was 0.5–1.2 at.%, after 200 hours at 1500°C it was 0.0–0.6 at.%.

In KZ5-AC and KZ5-HT15, the phases to be considered in terms of mechanical properties are βNb_5Si_3 and (Nb), and βNb_5Si_3, αNb_5Si_3, and (Nb), respectively. A higher volume of silicide phase compared to (Nb) volume fraction reduces fracture toughness in (Nb)-Nb_5Si_3 alloys [188]. Volume fraction of (Nb) in this alloy is maintained after heat-treatment, so fracture toughness is likely preserved. Large silicide particles are expected to reduce tensile strength [101]. There has been a coarsening of βNb_5Si_3 eutectic-like phase in KZ5-HT15 so a reduction in tensile strength is expected, although the size of primary βNb_5Si_3 has not been altered to a great degree. If implemented as a blade or disk alloy, the gradual phase transition from βNb_5Si_3 to αNb_5Si_3 would occur in service during the life time of components if an extensive heat treatment is not performed first. This could result in unpredictable mechanical properties, especially if the core and shell microstructure of βNb_5Si_3 and αNb_5Si_3 observed introduces crack initiation sites. As the (Nb) volume fraction would likely be

retained during service, as operating temperatures are lower than the 1500°C heat-treatment, fracture toughness would be expected not to deteriorate during operation, it least not as a result of (Nb) factors. Since coarsening of primary βNb_5Si_3 was observed not to occur to a large degree, mechanical properties may be preserved, although the eutectic structure would likely be removed through operation over significant time scales as demonstrated in the heat-treated alloy.

Creep rate experiments of single phase silicide samples performed by Bewlay *et al* [109] show that Nb_3Si has inherently worse creep performance compared to Nb_5Si_3, so the destabilisation of the Nb_3Si phase through Cr and Al additions is a benefit to creep performance. Single phase alloys consisting of αNb_5Si_3 or βNb_5Si_3 have not been directly compared in terms of creep rates. Multiphase alloys with αNb_5Si_3 and βNb_5Si_3 as main phases have not been compared in the literature either. KZ5 would make a suitable candidate alloy for these experiments to be performed on given that the silicide phase volume fraction can be adjusted through heat treatment from 100% βNb_5Si_3 to part βNb_5Si_3 and part αNb_5Si_3. If further heat treatments for much longer time periods produced an alloy with silicide phase that is 100% αNb_5Si_3 then the optimal heat-treatment time and $\alpha Nb_5Si_3/\beta Nb_5Si_3$ ratio for creep resistance could be found. It is also not clear how the particles of (Nb) that form inside αNb_5Si_3 during the βNb_5Si_3 to αNb_5Si_3 phase transition would affect creep resistance and other mechanical properties. This speckling effect was seen in other studies ([193][194][195]) as well, and as a ductile phase within a brittle phase, it is possible that the intragranular formation of (Nb) would enhance fracture toughness of the alloy as a whole. This speckling effect appears to be a result of the βNb_5Si_3 -> αNb_5Si_3 + (Nb) transition caused by the heat-treatment. The precipitation of (Nb) within αNb_5Si_3 was found to be directly related to the partitioning of solutes in previous studies [196]. In this study the metallic solute elements Ti, Cr, and Al are found in higher concentrations in βNb_5Si_3 than αNb_5Si_3, so these are ejected upon the transition reaction as it appears αNb_5Si_3 has lower solubility of these elements. It also follows that there is greater Ti, Cr, and Al contents of internal (Nb) compared to (Nb) found in KZ5-HT15.

In terms of oxidation resistance, again the lack of Nb_3Si is beneficial for oxidation resistance, especially in the pesting regime [128]. The fine eutectic-like structure of (Nb) + βNb_5Si_3 is lost during heat-treatment. In a comparable refractory silicide (Mo-16.5Si-7.5B), a fine microstructure was beneficial to oxidation resistance [197]. This is proposed to be because diffusion paths to all constituent phases are shorter in a finer microstructure, so elements that lead to protective oxide layers are activated sooner, and in a coarser microstructure grain boundaries are larger, which allows more rapid oxygen diffusion into the bulk of the microstructure in the initial stages of oxidation. In the case of KZ5, the relevant elements would be Si and Cr contained in $\beta Nb_5Si_3/\alpha Nb_5Si_3$ and $NbCr_2$ (that may have gone undetected), respectively. And the larger grain boundaries would be between (Nb) and $\beta Nb_5Si_3/\alpha Nb_5Si_3$ in the heat-treated state. A comparison of inherent oxidation resistance of αNb_5Si_3 and βNb_5Si_3 is not found in the literature, given that formation and retention of αNb_5Si_3 and βNb_5Si_3 are often dependant on composition. Therefore, this will be considered in the oxidation results of KZ5-AC and KZ5-HT15.

$NbCr_2$ is reported to form in as-cast KZ5 [153], but only in small amounts, with results partly originating from surface regions of the ingot. In the heat-treated state, $NbCr_2$ is also reported to have formed on the interface between Nb_5Si_3 and (Nb), but no EPMA data is provided to support this. $NbCr_2$ is stabilised by Cr additions that are greater than 5 at.% in the Nb-Ti-Cr-Si quaternary system [104], and Al additions promote $NbCr_2$ formation where Cr is present in Nb-Si based alloys [191]. As there is a combination of Al and Cr in KZ5 it would be conceivable for $NbCr_2$ to form. In this current study $NbCr_2$ was not found in the as-cast microstructure of KZ5, but there were parts of the (Nb) that were especially high in Cr (labelled Ti-rich (Nb) in Table 4.1) so it is feasible very small

amounts of $NbCr_2$ could have formed in unseen locations where Cr content is highest. However, after heat-treatment there were no such Cr-rich areas of (Nb) due to the aforementioned homogenisation, and the Nb_5Si_3 / (Nb) boundary phase is either not present on retained βNb_5Si_3 or in the cases where a boundary phase is present it is identified as an αNb_5Si_3 shell around retained βNb_5Si_3 according to EBSD mapping and EPMA results. Therefore, it is concluded that $NbCr_2$ is not an equilibrium phase in KZ5.

The Ti-rich phase identified in EDS and EPMA mapping is suspected to be either a titanium nitride, which would be in agreement with [153], or a titanium solid solution with different structure to the niobium solid solution. No nitrogen mapping was performed, so this phase remains unidentified. However, in [153] the composition of the high-Ti black contrast phase was given as 60 at.% Ti, 33 at.% N and 2at.% Nb. This was not heat-treated KZ5, but a different alloy of similar composition and only taken from one point of WDS analysis. The average Nb content of the Ti-rich phase in the present study is 26.1 at.%, with a minimum value reported as 15.6 at.%. Therefore, there is reason to doubt the Ti-rich phase is TiN, and not a titanium HCP solid solution, (Ti). Thermodynamic modelling of the Nb-Ti system was performed to provide explanation to this dual solid solution microstructure and it was found small additions of oxygen, presumably penetrating the sample during heat-treatment, result in a split of the (Nb) phase to a (Nb) phase and a (Ti) phase. (See appendix section Figure 8.1 and Figure 8.2 for thermocalc modelling). In this case it is predicted that the (Ti) is the $P6_3/mmc$ lower temperature stable phase, as seen in the Nb-Ti binary system (Figure 2.3 [34]).

5.3.2 The effect of heat treatment on boron and germanium containing alloys

It has been established in chapter 4 that the replacement of 10 at.% Nb with 5 at.% B and 5 at.% Ge completely changes the silicide structure that forms from the melt in the as-cast alloys. Neither αNb_5Si_3 nor βNb_5Si_3 forms, instead the main silicide phase is $D8_8$. $D8_8$ shares the same structure as the meta-stable γNb_5Si_3 phase that forms in the Nb-Si binary when impurity interstitials are present.

$D8_8$ has better oxidation resistance as a single phase than the tetragonal Nb_5Si_3 equivalent phases [163][162]. However, mechanical properties are thought to be diminished when γNb_5Si_3 is present. It follows the hexagonal structured $D8_8$ would also not be an ideal silicide to maintain creep resistance, especially at high stresses [109]. T2 on the other hand has both the same structure as αNb_5Si_3, which is promising for mechanical properties of a silicide – solid solution alloy, and has better oxidation resistance as a single phase than $D8_8$ or the tetragonal Nb_5Si_3 equivalents [162][161]. However, a predominantly T2 and (Nb) microstructure was not achieved in any as-cast B and Ge containing alloy in this present study. Heat-treatments have resulted in an increase in T2 area fraction in JW1, JW2 and JW3, and in each case to a greater extent in the higher temperature heat-treatments. This shows either a larger T2 phase field at 1500°C, or the enhanced transition kinetics at higher temperature and that T2 is an equilibrium phase in these alloy compositions.

In contrast to T2, (Nb) shows the opposite trends across the B and Ge containing alloys of reducing in area fraction after heat-treatments. In each alloy, heat-treatment at 1500°C reduces the (Nb) volume fraction to greater extent than the heat-treatment at 1300°C. As (Nb) volume fraction is near zero in JW2 and JW3 after 100 hours at 1500°C, this phase can be concluded to not be an equilibrium phase in these alloys. The enhanced transformation kinetics at 1500°C are responsible for its elimination, whilst heat-treatment at 1300°C only partly dissolves this phase. This has negative implications for the mechanical properties of JW2 and JW3, and therefore usefulness of the heat-treated alloys, as the silicide phases in Nb-Si alloys are notoriously brittle. A large amount of cracking can be seen in BSE images of the heat-treated alloys as the (Nb) is known to provide a degree of fracture toughness to the alloys [99]. It is assumed that phase stability of (Nb) at 1300°C is not greater than it is at 1500°C, or in the case of JW2 and JW3 that (Nb) is stable at 1300°C and not stable at 1500°C, and instead the enhanced transformation kinetics at higher temperature are responsible for these changes in area fraction. This is because in the Nb-Si binary phase diagram, the point of highest solubility of elements in (Nb), or where the solvus meets the solidus on the niobium rich side, is at 1916°C [32]. For the case to be that the (Nb) phase field is larger at 1300°C than at 1500°C, the solvus-solidus intersection would have to have been reduced by >600°C by the alloying additions. An assumption is made that this is not the case.

However, some amount of promise can be seen in the JW1 alloy series with regards to mechanical properties and phase stability. Whilst the 1500°C heat-treatment has reduced the area fraction of (Nb) from 18.5 % to 11.3 %, it has not been removed showing that it is likely an equilibrium phase in this alloy system. In addition, at 1300°C the area fraction is not reduced at all. The implications of this are that at 1200°C in an oxidising atmosphere during operation, the (Nb) volume fraction of JW1 would be retained and potentially the mechanical properties this phase provides. In fact, area fraction analysis was performed on oxidised specimens of JW1-HT13 at 1000°C and 1200°C and it was found (Nb) volume fraction was retained at approximately 20% in each case in the centre of these samples.

According to Bewlay [109], the minimum creep rate seen in Nb-25Ti-8Hf-XSi composites had X equal to between 18 and 20 at.%. This is reported as being equivalent to 62.0% and 70.0% silicide by volume fraction. In JW1-HT13, silicide area fraction of the larger $D8_8$ grains, intergranular $D8_8$ and T2

combined is 79.3%. Minor adjustments to the composition of this alloy for future work could easily bring the (Nb)/silicide ratio into the desired range for creep resistance.

The effect Ge has on Nb-Si microstructure, often where Ti, Cr, or Al are present, has been extensively studied by Li and Tsakiropoulos [96][193][198] [199][200]. Ge preferentially partitions into the Nb_5Si_3 silicide rather than the (Nb), and, in alloys with only Nb, Si and Ge, destabilises the Nb_3Si phase. In such ternary alloys, (Nb) and βNb_5Si_3 form from the melt, and αNb_5Si_3 is developed in addition after heat treatment [96]. When Ti is introduced to the system, (Nb), Nb_3Si, βNb_5Si_3 and hexagonal Mn_5Si_3-type Ti_5Si_3 (effectively $D8_8$) form from the melt and after heat-treatment (Nb), Nb_3Si and βNb_5Si_3 remain [198]. Cr additions to the Nb-Si-Ti-Ge alloy results in the formation of (Nb), βNb_5Si_3, and $NbCr_2$ from the melt, and again αNb_5Si_3 is developed after heat-treatment [193]. Al additions to the Nb-Si-Ti-Ge alloy result in a (Nb) - βNb_5Si_3 two phase microstructure, with αNb_5Si_3 developed after heat-treatment [199]. Finally, in an alloy similar to JW1 minus the B content known as ZF6 (Nb-24Ti-18Si-5Cr-5Al-5Ge), (Nb), βNb_5Si_3, and $NbCr_2$ form from the melt, and the phases present after heat-treatment are (Nb), βNb_5Si_3, and αNb_5Si_3 [200]. From these comprehensive studies on how Ge effected microstructures several key points are inferred; as long as other Nb_3Si destabilisers are present such as Cr and Al, the Ti content of 24 at.% in these alloys is not sufficient to produce Nb_3Si, αNb_5Si_3 is an equilibrium phase in all but the Nb-Si-Ge-Ti alloy (ZF3 (Nb-24Ti-18Si-5Ge)) and is not destabilised by Ge, Cr or Al additions, and Ge additions do not result in the stabilisation of the metastable hexagonal Mn_5Si_3-type $\gamma Nb_5Si_3/Ti_5Si_3$ phase unless Ti is also present. Volume fraction of (Nb) is significantly affected by Ge additions however, decreasing from 35-36% in alloy KZ3 (Nb-24Ti-18Si) [152] to 6.0-10.9% in ZF3 (Nb-24Ti-18Si-5Ge). The volume fraction of (Nb) is then increased upon Cr and Al additions in ZF6 (Nb-24Ti-18Si-5Cr-5Al-5Ge) to approximately 17%. Evidently Ge additions somewhat destabilise the (Nb) phase or stabilise the Nb_5Si_3 intermetallic as additional Si would.

Boron additions to KZ3 (Nb-24Ti-18Si) resulted in the formation of (Nb), Nb_3Si and T2 in the as-cast and heat-treated states in an alloy labelled as TT1 (Nb-24Ti-18Si-8B) [201]. A volume fraction of (Nb) of ~37% was recorded, very similar to that of KZ3. This shows B additions do not have a large effect of (Nb) volume fraction and stability. T2 is confirmed in TT1 through XRD spectroscopy, utilising a study by Rodrigues *et al* [83] which gives several XRD patterns of αNb_5Si_3, T2 with a low amount of B, and T2 with a high amount of boron. The T2 identified in this current study in alloys JW1 and JW2 matches well with the high boron pattern of T2, whereas the T2 identified in TT1 matches well with the low boron alloy. This is in agreement with EPMA results for JW alloys and TT1, where average boron contents of T2 are greater than 20.0 at.% and less than 14.0 at.%, respectively. Although it should be noted that the stabilising effect of B on T2 on its own is sensitive to alloy composition. Where Si and B contents are slightly lower in the quaternary Nb-Si-Ti-B system, 12.0 at.% and 1-4 at.% respectively, T2 has been reported not to be stabilised and βNb_5Si_3 is found instead [119].

Another alloy in the TT series, TT2 (Nb-24Ti-18Si-5Cr-8B), shows the effect Cr has when B is also present on the Nb-Si-Ti ternary system [131]. After Heat-treatment, the microstructure consists of (Nb) and T2. Nb_3Si does form in the as-cast alloy, as was the case in TT1, but evidently Cr additions destabilise this phase as it is removed upon heat-treatment. Volume fraction of (Nb) is measured at 37-38%, similar to TT1 and KZ3, so Cr and B in synergy do not reduce (Nb) volume fraction.

In the alloy TT3 (Nb-24Ti-18Si-5Al-8B), the role of Al can be assessed [131]. Phases (Nb) and T2 are found in the as-cast and heat-treated states. Al addition has destabilised the Nb_3Si phase to a greater degree than the Cr additions of TT2. Volume fraction of (Nb) is measured at 38-42%, even slightly higher than in Al free alloys. No $D8_8$ was found in either of these TT alloys.

Finally, an alloy with close composition to JW1 is presented by Thandorn [131], known as TT4 (Nb-24Ti-18Si-5Cr-5Al-8B). The phases found in this alloy are (Nb), T2, and $D8_8$. In the present author's opinion, compared to the current study, there appears to be some confusion in regards to the labelling of T2 and $D8_8$ in this alloy in [131]. In BSE imaging of TT4 performed by [131] the bright contrast silicide phase is assigned $D8_8$ and the grey contrast silicide phase is assigned T2. In TT4-HT 'T2' is measured as having 5.5 at.% B content and '$D8_8$' is measured as having 29.2 at.% B. This seems unlikely given the given the more recent ternary Nb-Si-B phase diagrams presented in chapter 2, which show B maximum solubility as larger in T2 rather than $D8_8$ [81][84]. In the current work, the gain of the bright contrast phase through heat-treatment labelled T2 in JW2 and JW3 coincides with T2 peaks appearing and increasing in intensity in XRD patterns of JW2 and JW3. Most convincingly, in the case of JW1 the bright contrast phase with approximately 21 at.% B is identified clearly as T2 and not the 5 at.% B $D8_8$ through EBSD results (Figure 4.8 and Figure 5.8). In this current work Al content is also an indicator of silicide phase type, as Al solubility in the central region T2 is consistently between 0.1 – 0.4 at.%, whereas $D8_8$ has Al content between 2.0 at.% and 6.5 at.% in the heat-treated alloys. Al content in TT4-HT 'T2' was 3.3 at.% and 0 in '$D8_8$'. This proposed mislabelling is likely due to changing contrasts of phases, as different compositions can alter this, as well as settings used when capturing specific images, and the uncertainty generated from XRD patterns; in some cases peaks are misassigned to T2, which if instead were assigned to $D8_8$ would indicate proportionally larger amounts of $D8_8$ in the TT4 alloy. The change in peak positions in XRD patterns of T2 are responsible for this in the present author's opinion, as lattice parameters are influenced by the degree of B substitution onto Si sites. A higher amount of boron can alter the XRD pattern of T2 quite significantly [83]. In any case, T2 and $D8_8$ are both still present in heat-treated TT4 (Nb-24Ti-18Si-5Cr-5Al-8B). This indicates a combination of Al and Cr in the presence of B stabilises $D8_8$ in Nb-Si-Ti alloys, as no such phase was found in TT2 or TT3. In addition, the combination of Cr and Al in the presence of B has little effect on the volume fraction of (Nb) present in the heat-treated and therefore closer to equilibrium state TT4 alloy where it is 39%. Although in the as-cast state it was 30%.

Due to the compositional similarities and differences, comparison of the phase composition of the JW series of alloys with TT4 illustrates the effect of Ge, while the effect of B can be revealed by comparison with ZF6. In KZ5 (Nb–24Ti–18Si–5Cr–5Al), γNb_5Si_3 was not an equilibrium phase. An addition of 5 at.% Ge (ZF6 Nb–24Ti–18Si–5Cr–5Al-5Ge) resulted in the same equilibrium phases (Nb), αNb_5Si_3 and possibly βNb_5Si_3. A further addition of 5 at.% B (JW1 Nb–24Ti–18Si–5Cr–5Al-5Ge-5B) results in γNb_5Si_3, in this case referred to as $D8_8$, being stabilised. This was an equilibrium phase, and the majority phase, in each JW alloy. βNb_5Si_3 is completely destabilised by the addition of 5 at.% B. αNb_5Si_3, in this case referred to as T2, is seen as an equilibrium phase as its volume fraction increases from the AC, to HT13, to HT15 states of JW1.

Further B additions, investigated by the manufacture of JW2 (Nb–24Ti–18Si–5Cr–5Al-5Ge-10B), result in a larger volume fraction of T2, 27.9%. The mechanism of T2 increase during heat-treatment appears to be related to the reduction in NbB volume fraction. NbB is clearly a metastable phase in this alloy as it is not found in JW2-HT15. In EPMA mapping of JW2-HT13 it was noticed that T2 is found adjacent to NbB. It is proposed that in JW2-HT13 the decomposition of NbB was part way to completion, and T2 formation is possible once the boron content in NbB is released. In JW1-AC no NbB was found, so the formation of new T2 was slower as B supply was less readily available, hence the only slight increase in T2 volume fraction in the HT15 state. In the JW2 alloy, some degree of Si diffusion must have taken place to the NbB phase for T2 to form. In JW3 (Nb–24Ti–18Si–5Cr–5Al-10Ge-5B) the same decomposition of NbB into T2 has also occurred but to a lesser degree. In the as-cast alloy NbB volume fraction was only 0.6%. This has resulted in 9.0% T2 formation in JW3-HT15.

The intermediate state in this case, JW3-HT13, was not seen partway through completion of NbB decomposition. Instead there was no NbB found in the JW3-HT13 sample and small amounts of T2 were present. Considering the composition JW1 as a starting point, additional boron content in the presence of 5 at.% Ge results in a larger volume fraction of T2, as seen in the case of JW2-HT15. Whereas additional germanium content in the presence of 5 at.% B results in a larger volume fraction of $D8_8$, as seen in the case of JW3-HT15, despite the original 5 at.% B added into ZF6 Nb–24Ti–18Si–5Cr–5Al-5Ge stabilising the $D8_8$ phase.

The volume fraction of (Nb) in heat-treated TT4 was reported as 39%. In JW1-HT15 the volume fraction of (Nb) is 11.3%. This means the change in nominal composition of 3 at.% less B, 2 at.% less Nb, and 5 at.% more Ge has had a dramatic effect on the (Nb) phase. This also suggests that Ge and B in combination reduce the (Nb) volume fraction to a greater degree than either B or Ge alone. KZ5 to TT4 (+8 at.% B) results in 4% less (Nb), but ZF6 to JW1 (+5 at.% B) results in 6% less (Nb) when Ge is present. KZ5 to ZF6 (+5 at.% Ge) results in 25.7% less (Nb), but TT4 to JW1 (-3at.% B, +5 at.% Ge) results in 27.7% less (Nb) when B is present.

In alloy TT4 (Nb–24Ti–18Si–5Cr–5Al-8B), T2, $D8_8$ and (Nb) were equilibrium phases. Upon the addition of 5 at.% Ge additions, as well as a slight decrease in B content, the same three phases are present in the heat-treated JW series alloys. Additionally, the C14 Laves phase $NbCr_2$ was found in each B and Ge containing alloy. This phase formed from the melt and was preserved even after heat-treatments so is likely an equilibrium phase. This was not the case in TT4, absent of Ge, or in heat-treated ZF6, absent of B, although the as-cast version of ZF6 did contain the Laves phase. Ge does not substitute into the $NbCr_2$ phase to a particularly high degree. In as-cast ZF6 Ge content was 1.2 at.%, and in the JW alloy series the highest Ge content was 1.3 at.%. Therefore, the stabilisation of this phase is likely more linked to the reduction in (Nb) volume fraction, i.e. where Cr content is highest and Cr substitution is greatest outside of $NbCr_2$, rather than the added Ge further stabilising this phase. A reduction in (Nb) volume fraction effectively increases the Cr content available, as Cr solubility in other phases is less than 10 at.% in these alloys. Although it should be noted Ge and Si do stabilise the hexagonal C14 phase over the cubic C15 phase [112]. The $NbCr_2$ phase has been shown to be beneficial to oxidation resistance [104], possibly related to densification of the oxide scale and reducing the tendency of scale spallation [122][202], but could present an issue for the mechanical properties, namely the fracture toughness where it can act as initiation site for cracks [112]. The C14 $NbCr_2$ is preferred compared to the C15 $NbCr_2$ as fracture toughness is slightly higher (2 to 5 $MPam^{0.5}$ compared to approximately 1 $MPam^{0.5}$) [112].

In the (Nb) phase, heat-treatments have resulted in the diffusion of elements to varying degrees. In JW1, the heat-treatment at 1500°C resulted in a larger content of Nb and a correspondingly lower Ti content. The opposite was seen in alloys JW2 and JW3, where heat-treated versions had lower Nb contents and higher Ti contents than their as-cast counterparts. In KZ5, the Si decrease through heat-treatment was noted. In addition, the Cr content has increased slightly, and the Nb and Al contents have reduced by a minor degree. This is the opposite in the B and Ge containing alloys. In all cases, the Cr content is reduced by heat-treatments, and to a greater extent in the HT15 alloy series. In all cases, the Al content is increased by heat-treatments, but in JW1 and JW2 the largest Al content in (Nb) is found in the HT13 samples. Although error margins are large, Si content in the heat-treated samples tends to be lower than in the as-cast state. In the case of JW3, the Si is already low at 0.4 at.%, but Ge and B content are reduced upon heat-treatment at 1300°C. Generally, in JW1 and JW2, B and Ge contents are unaffected by heat-treatments as although there are changes to Ge content, these are too minor to draw conclusions from.

In terms of compositional ranges of the (Nb) phase, in each B and Ge containing alloy Nb content was homogenised after heat-treatments. In the JW1 alloy series every element except boron, which maintained a range of approximately 3 at.%, had smaller compositional ranges of central region phases in the heat-treated states. This was not the case for JW2 or JW3 alloy series. This is possibly an effect of having much smaller (Nb) volume fractions, resulting in EPMA data points being taken from smaller areas where the surrounding phases and underlying phases may contribute to the measurement to a greater degree.

In the case of the T2 phase, the same trend that was seen in alloy JW1, and then JW2 and JW3 with regards to (Nb) compositional changes was seen in Nb and Ti contents. In the JW1 series, Nb gradually increased and Ti content gradually decreased as a result of higher temperature heat-treatment. The opposite is seen in JW2 and JW3, where the phase became richer in Nb and poorer in Ti through heat-treatment. The B content is relatively stable in terms of composition across these heat-treated alloys and no clear trends as a result of heat-treatments emerge, with average composition between 19.7 at.% and 23.1 at.% in the central regions.

In the case of $D8_8$, although margins are small, B content reduces from the as-cast to HT13, to HT15 samples in each alloy. The reverse trend, also only with small margins, is seen in Cr in this phase for each alloy. In JW1 and JW2, Nb content is reduced and Ti content is increased after heat-treatment, with the 1500^{o}C having the largest effect.

In the $NbCr_2$ Laves phase, each alloy series shows an increase in Nb content and decrease in Ti content. For JW2 this is practically non-existent for Nb content, and the effect of the 1300^{o}C heat treatment on Ti content is the same as that of the 1500^{o}C heat-treatment. However, these trends in JW1 and JW3 are outside the margin for error given for the Nb and Ti contents. In JW1 Si content follows the same trend as the Ti content and decreases upon heat-treatments, in JW3 Si content follows the same trend as Nb content and increases upon heat-treatments.

Considering these trends, it can be concluded that during heat-treatments of the JW1 alloy, Nb atoms diffuse from the T2 and $D8_8$ silicides into the (Nb) and $NbCr_2$ phases. Ti atoms do the opposite and diffuse from the (Nb) and $NbCr_2$ phases to the silicides. A higher temperature of heat-treatment encourages this exchange of elements. Whether this is due to increased diffusion kinetics at higher temperature or changes to phase stabilities at different temperatures is unclear.

Heat-treatments of alloy JW2 result in the diffusion of Nb atoms from the (Nb) and $D8_8$ phases to the T2 phase. The reverse is true for Ti atoms, as (Nb) and $D8_8$ become richer in Ti, and T2, as well as $NbCr_2$, becomes poorer in Ti. Heat-treatments of alloy JW3 result in the diffusion of Nb atoms from the (Nb) phase to the T2 and $NbCr_2$ phases. The reverse is true for Ti atoms, as (Nb) becomes richer in Ti, and T2 and $NbCr_2$ become poorer in Ti. The compositions of $D8_8$ in JW3-AC, JW3-HT13 and JW3-HT15 do not follow the trends listed above. This may be a result of the $D8_8$ dominating the microstructure of JW3 in terms of volume fraction, so any loss/gain of elements would have a much less noticeable effect than seen in the smaller volume fraction phases; (Nb), T2, $NbCr_2$ and NbB.

In the high B and Ge alloys, JW2 and JW3, there is less Nb overall due to the replacement for 5 at.% of either B or Ge, respectively. Also, there is more $D8_8$ in these alloys compared to JW1 as this phase is stabilised by B and Ge. The $D8_8$ phase takes in Nb which also reduces the total amount of Nb available for the (Nb) phase. Therefore, the high Ge and B alloys have solid solutions with considerably less Nb and more Ti. This is highlighted by the heat treatments where Nb content reduces and Ti content increases towards what would be the equilibrium composition of the (Nb) phase. Ti content in the solid solution has been demonstrated to improve fracture toughness [110]

and improve the oxidation resistance of the solid solution phase [142]. Regardless of the Ge and B contents of the JW series alloys, the Cr content of the solid solution is decreased on heat-treatment, and the Al content is increased. This is expected to have a mixed effected on fracture toughness [113], and Cr and Al additions into (Nb) + silicide alloys reduces creep resistance [113] but the specific effect on the (Nb) phase is not studied in the literature. Al content in the (Nb) phase has been shown to be particularly effective at reducing oxygen penetration into Nb-Si alloys, and to therefore improve oxidation resistance [111]. The increase in Al content likely comes from the $D8_8$ during heat-treatments, but a respective decrease in Al content is not seen in $D8_8$ after heat-treatments. This is related to the previously mentioned effect of $D8_8$ being the majority phase, where small changes to composition are not detected but may have a large effect on the more minor volume fraction phases.

NbB is only detected in multiple processing states of a single alloy in one alloy, JW2. Here the as-cast composition and composition after 100 hours at 1300^{o}C of NbB are very similar and all element compositions of the as-cast alloy are within error of the heat-treated counterparts. This shows little diffusion of elements into or out of this phase takes place during heat-treatment at 1300^{o}C. Whether this is the case for oxidation experiments at 1000^{o}C or 1200^{o}C remains to be seen.

5.4 Conclusions

- Heat-treatments revealed what are likely the equilibrium phases of each alloy; KZ5 (Nb-24Ti-18Si-5Cr-5Al) – (Nb), αNb_5Si_3. JW1 (Nb-24Ti-18Si-5Cr-5Al-5Ge-5B) – (Nb), $D8_8$, T2, $NbCr_2$. JW2 (Nb-24Ti-18Si-5Cr-5Al-5Ge-10B) – $D8_8$, T2, $NbCr_2$. JW3 (Nb-24Ti-18Si-5Cr-5Al-10Ge-5B) - $D8_8$, T2, $NbCr_2$.
- The (Nb) phase is reduced in volume fraction in the high B and Ge alloys, JW2 and JW3, to practically zero. B and Ge have a synergistic effect of reducing (Nb) volume fraction.
- The NbB phase is revealed to be metastable in JW2-AC and JW3-AC, as it was completely removed during heat-treatments. Additionally, a mechanism for NbB conversion to T2 is predicted given the structure of T2 and NbB phases seen in the 1300°C treatment, part way through the conversion. Given the consistent composition of NbB in JW2 in the as-cast and heat-treated states, it appears diffusion of elements into and out of this phase is minimal
- The area fractions of phases in alloys JW2 and JW3 show that B additions in the presence of Ge stabilise the T2 phase, whereas Ge additions in the presence of B stabilises the $D8_8$ phase. In the heat-treated alloy JW2-HT15, a large part of the microstructure was made up of the T2 phase (27.9%).
- The solid solution phase becomes richer in Nb through heat-treatments when B and Ge contents are 5 at.% and 5 at.%. Upon the addition of an extra 5 at.% B or Ge, heat-treatments reduce the amount of Nb in the (Nb) phase and increase Ti content.
- EBSD and EPMA have confirmed the composition of T2 and $D8_8$ phases, with T2 having significantly higher B solubility than $D8_8$. B content in T2 is relatively unchanged by heat-treatments, whereas B content in $D8_8$ reduces slightly upon heat-treatment.

Chapter 6

6 The isothermal oxidation behaviour of boron and germanium containing alloys at 1000°C and 1200°C

6.1 Introduction

Isothermal Oxidation experiments were performed at 1000°C and 1200°C in order to assess the high temperature oxidation behaviour of each alloy; KZ5 (Nb-18Si-24Ti-5Cr-5Al), JW1 (Nb-18Si-24Ti-5Cr-5Al-5Ge-5B), JW2 (Nb-18Si-24Ti-5Cr-5Al-5Ge-10B), JW3 (Nb-18Si-24Ti-5Cr-5Al-10Ge-5B). The performance of the as-cast, heat-treated at 1300°C and heat-treated at 1500°C versions of each alloy are assessed at these two temperatures to determine the effects of alloy composition with regards to B and Ge additions, and the effect a heat-treated microstructure has on oxidation behaviour.

Thermogravimetric analysis (TGA) was performed over a 100-hour period at constant temperature. The total mass gain of each experiment over the 100-hour period is presented, as well as several oxidation parameters; Parabolic rate K_p, Linear rate K_l, Parabolic time, Combined rate, and the *n* exponent. K_l, K_p, and parabolic time are obtained from Equation (1), Equation (2), and the method described in Chapter 3, where the graph of oxidation is split into two sections; initially parabolic and then the remainder linear, to better fit the observed oxidation kinetics. The combined rate and *n* exponent are calculated using Equation (3) described in Chapter 2 where the whole oxidation curve is modelled in order to obtain an *n* exponent value; a measure of the degree to which oxidation behaviour is more parabolic or more linear in nature.

X-ray diffraction (XRD) spectroscopy has been performed on the oxidised samples to identify oxide phases that have formed. Conventional Bragg-Brentano Geometry XRD was found to be sufficient for oxide identification and was used to categorise as-cast, heat-treated at 1300°C and heat-treated at 1500°C versions of each oxidised alloy. Additionally, grazing angle XRD which is more surface sensitive was performed on each as-cast oxidised alloy at 1000°C and 1200°C to confirm that it was the surface oxide phases that were identified.

6.2 Oxidation at 1000°C

6.2.1 Oxidation behaviour

6.2.1.1 KZ5

The TGA curves of oxidised alloy KZ5 are displayed in Figure 6.1. This alloy was prepared in only as-cast and heat-treated at 1500°C states. The edges of both 1000°C KZ5 sample cubes had experience spallation and the oxide scale at the edges had broken off during the oxidation experiment, or possibly during the cooling process. Small parts of two of the faces of KZ5-HT15 experience this spallation as well.

Oxidation parameters are displayed in Table 6.1. When the whole oxidation graph is modelled according to Equation (3), the *n* exponents of KZ5-AC and KZ5-HT15 are calculated as 0.63 and 0.56, respectively. The oxidation behaviour of KZ5-HT15 is therefore more parabolic than KZ5-AC, with the linear mechanism of oxidation being less of a contributing factor. However, in both cases parabolic and linear mechanisms of oxidation are both in effect as n values are greater than 0.5.

Therefore, to facilitate comparison between the TGA oxidation curves, both samples oxidation behaviour can be modelled as initially parabolic followed by linear mass gain. In the case of the as-cast alloy, the parabolic rate constant is 9.99E-11 $g^2.cm^{-4}.s^{-1}$ and the linear rate constant is 1.62E-08 $g.cm^{-2}.s^{-1}$. Parabolic behaviour is dominant for the initial 15.9 hours. For the 1500°C heat-treated alloy, the parabolic rate constant is 1.42E-10 $g^2.cm^{-4}.s^{-1}$ and the linear rate constant is slightly smaller at 1.54E-08 $g.cm^{-2}.s^{-1}$. The parabolic behaviour of KZ5-HT15 is dominant for approximately 3 times as long (49.8 hours). As a result of the greater initial parabolic rate of KZ5-HT15 but then similar linear rates for the remainder of the experiments, KZ5 has similar total mass gains for the as-cast and heat-treated at 1500°C states, at 7.29 $mg.cm^{-2}$ and 7.92 $mg.cm^{-2}$, respectively. These total mass gains are the largest when compared to all alloys in this work tested at this temperature.

Table 6.1) Oxidation parameters for alloys KZ5, JW1, JW2 and JW3 oxidised at 1000°C for 100 hours. 'P' signifies a TGA curve modelled as completely parabolic, whereas the corresponding '' represents a linear rate taken from 40-100 hours to facilitate comparison.*

Alloy	Parabolic rate K_p ($g^2.cm^{-4}.s^{-1}$)	Linear rate K_l ($g.cm^{-2}.s^{-1}$)	Parabolic time (hours)	Combined rate K^n ($g.cm^{-2}.s^{-n}$)	n exponent	Total mass gain ($mg.cm^{-2}$)
KZ5-AC	9.99E-11	1.62E-08	15.9	2.16E-06	0.63	7.29
KZ5-HT15	1.42E-10	1.54E-08	49.8	6.04E-06	0.56	7.92
JW1-AC	1.48E-11^P	4.41E-09*	-	5.27E-06	0.47	2.37
JW1-HT13	1.61E-11	5.16E-09	45.9	2.11E-06	0.56	2.64
JW1-HT15	1.81E-11	6.39E-09	32.6	1.20E-06	0.61	3.07
JW2-AC	1.68E-11	1.14E-08	13.4	5.15E-07	0.72	4.89
JW2-HT13	1.36E-11^P	3.91E-09*	-	3.40E-06	0.51	2.23
JW2-HT15	7.06E-12^P	3.12E-09*	-	4.84E-06	0.45	1.66
JW3-AC	8.86E-12	5.13E-09	39.5	4.77E-07	0.66	2.27
JW3-HT13	1.27E-11	4.32E-09	43.7	2.05E-06	0.55	2.28
JW3-HT15	1.04E-10	1.48E-08	33.1	3.02E-06	0.61	7.22

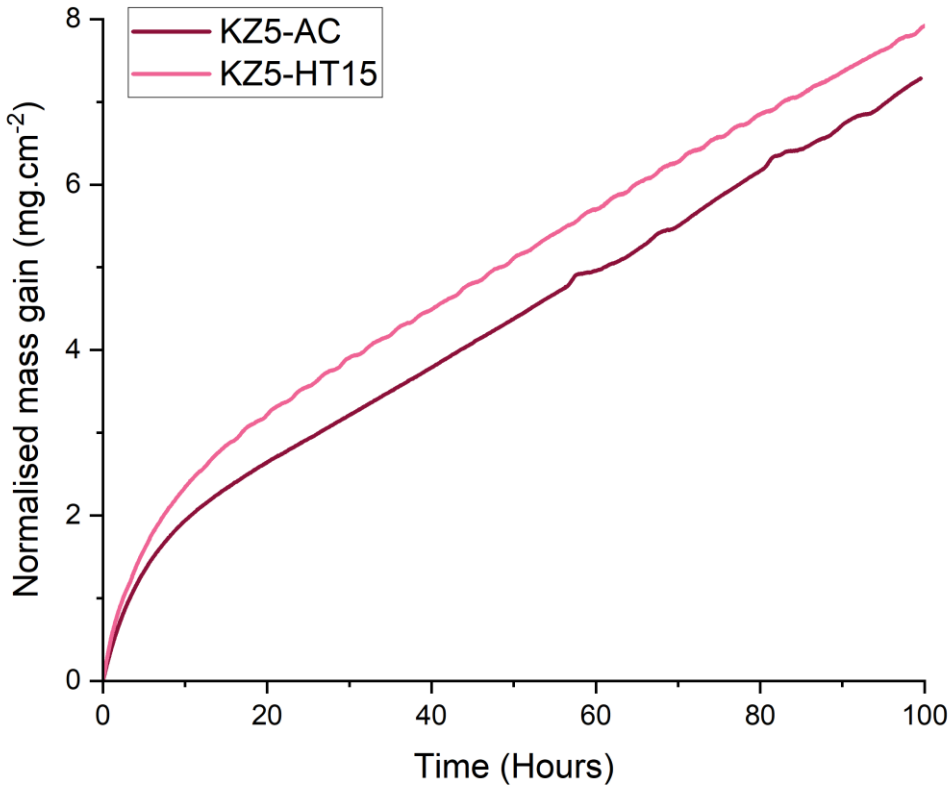

Figure 6.1) Normalised mass gain of KZ5 in the as-cast and heat-treated-1500°C states over a 100 hour period at 1000°C

6.2.1.2 JW1

In order to determine the effect B and Ge have on the oxidation resistance of base alloy KZ5, alloy JW1 of composition Nb-18Si-24Ti-5Cr-5Al-5Ge-5B was examined experimentally through thermogravimetric analysis (TGA). Spallation had not occurred in any of the 1000°C JW1 samples during oxidation experiments, nor in the other B and Ge containing alloys JW2 and JW3. During handling of JW3-AC small fragments of the scale did break off from one of the edges of the oxidised sample.

The TGA curves of oxidised alloy JW1 are displayed in Figure 6.2. This alloy was prepared in as-cast, heat-treated at 1300°C and heat-treated at 1500°C states. Oxidation parameters are displayed in Table 6.1. The *n* exponents of JW1-AC, JW1-HT13 and JW1-HT15 are calculated as 0.47, 0.56 and 0.61, respectively. Therefore, the oxidation behaviour of JW1 samples can generally be said to be more parabolic than linear with values closer to 0.5 than 1. The linear mechanism of oxidation is more of a contributing factor to JW1-HT15 when compared to the JW1-AC and JW1-HT13. The oxidation behaviour of JW1-AC is sufficiently parabolic to be modelled as parabolic for the entirety of the experiment, whereas JW1-HT13 and JW1-HT15 are modelled as being initially parabolic and then linear for the remainder of the experiment.

The heat-treated at 1300°C alloy has a parabolic rate constant of 1.61E-11 $g^2.cm^{-4}.s^{-1}$ and linear rate constant of 5.16E-09 $g.cm^{-2}.s^{-1}$. JW1-HT15 has parabolic and linear rate constants of the same order of magnitude, 1.81E-11 $g^2.cm^{-4}.s^{-1}$ and 6.39E-09 $g.cm^{-2}.s^{-1}$, respectively. The parabolic oxidation rate

constant of JW1-AC is 1.48E-11 $g^2.cm^{-4}.s^{-1}$. Initial oxidation of JW1-AC can be seen to be comparable to JW1-HT13 and JW1-HT15 (Figure 6.2), but over the course of the experiment due to the parabolic oxidation kinetics of JW1-AC, oxidation proceeded at a reduced rate and resulted in JW1-AC having the lowest mass gain at 2.37 $mg.cm^{-2}$. Although the total mass gains for all JW1 samples were similar (within 0.7 $mg.cm^{-2}$), there is a trend of increasing from JW1-AC, to JW1-HT13, to JW1-HT15, with values of 2.37, 2.64, 3.07 $mg.cm^{-2}$, respectively. There is a correlation between more parabolic behaviour and lower total mass gain in this alloy, suggesting formation of passivating oxides and diffusion of oxygen through the scale as the rate limiting step.

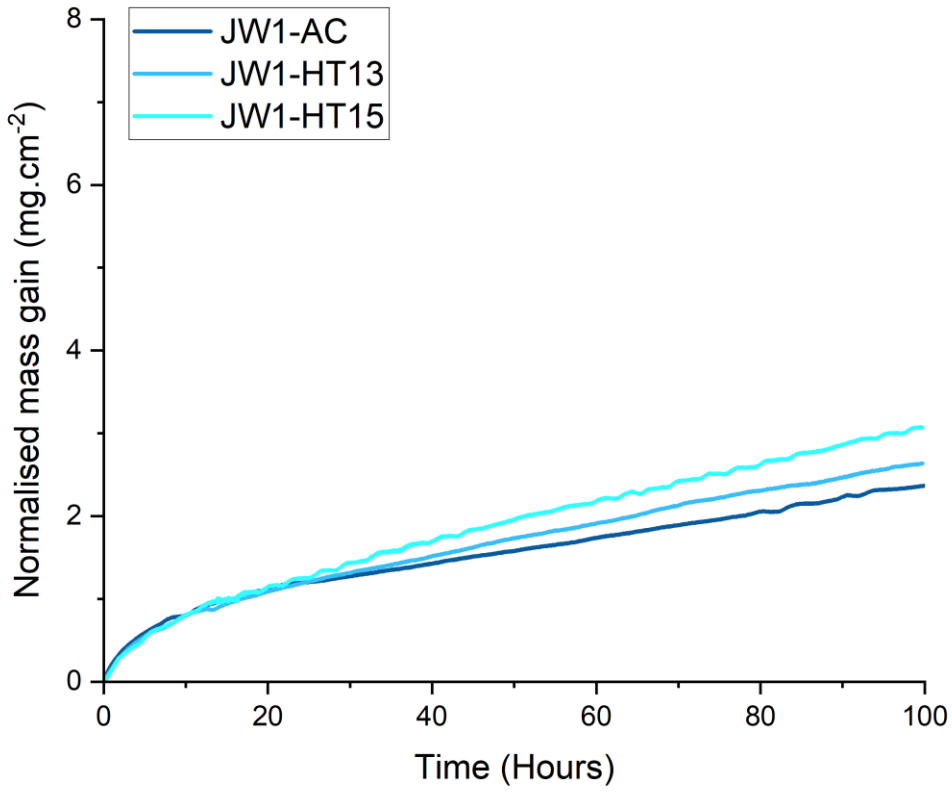

Figure 6.2) Normalised mass gain of JW1 in the as-cast, heat-treated-1300°C and heat-treated-1500°C states over a 100 hour period at 1000°C

6.2.1.3 JW2

In order to better understand the role B and Ge play during oxidation, their contents are varied in alloys JW2 (Nb-18Si-24Ti-5Cr-5Al-5Ge-10B) and JW3 (Nb-18Si-24Ti-5Cr-5Al-10Ge-5B). In this section boron's effect on oxidation parameters will be considered. JW2 has 10 at.% B where as JW1 has 5 at.%. The TGA curves of oxidised alloy JW2 are displayed in Figure 6.3. This alloy was prepared in as-cast, heat-treated at 1300°C and heat-treated at 1500°C states. Oxidation parameters are displayed in Table 6.1.

The *n* exponents of JW2-AC, JW2-HT13 and JW2-HT15 are calculated as 0.72, 0.51 and 0.45, respectively. The oxidation behaviour of JW2-HT13 and JW2-HT15 is sufficiently parabolic to be modelled as parabolic for the entirety of the experiments, with values close or less than to 0.5. This implies that the linear mechanism of oxidation has a negligible effect on rate of oxidation for JW2-

HT13 and JW2-HT15. The as-cast JW2 alloy has an *n* exponent value that suggests linear and parabolic oxidation kinetics are both equally relevant.

The as-cast alloy showed parabolic behaviour up to 13.4 hours with rate constant of 1.68E-11 $g^2.cm^{-4}.s^{-1}$ and subsequent linear rate constant of 1.14E-08 $g.cm^{-2}.s^{-1}$. The heat-treated alloys have parabolic oxidation rate constants of 1.36E-11 $g^2.cm^{-4}.s^{-1}$ and of 7.06E-11 $g^2.cm^{-4}.s^{-1}$ for JW2-HT13 and JW2-HT15, respectively. In addition, the linear rates of oxidation for JW2-HT13 and JW2-H15, calculated by taking the 40 to 100-hour portion of the TGA graph and treating it as operating under linear oxidation behaviour, are both an order of magnitude lower than the equivalent linear oxidation rate constant for JW2-AC. The higher rate constants of JW2-AC result in a mass gain of 4.89 $mg.cm^{-2}$, over double that of JW2-HT13, 2.23 $mg.cm^{-2}$, and almost triple that of JW2-HT15, 1.66 $mg.cm^{-2}$. Evidently the Heat treatments have had a positive effect on oxidation resistance at 1000°C.

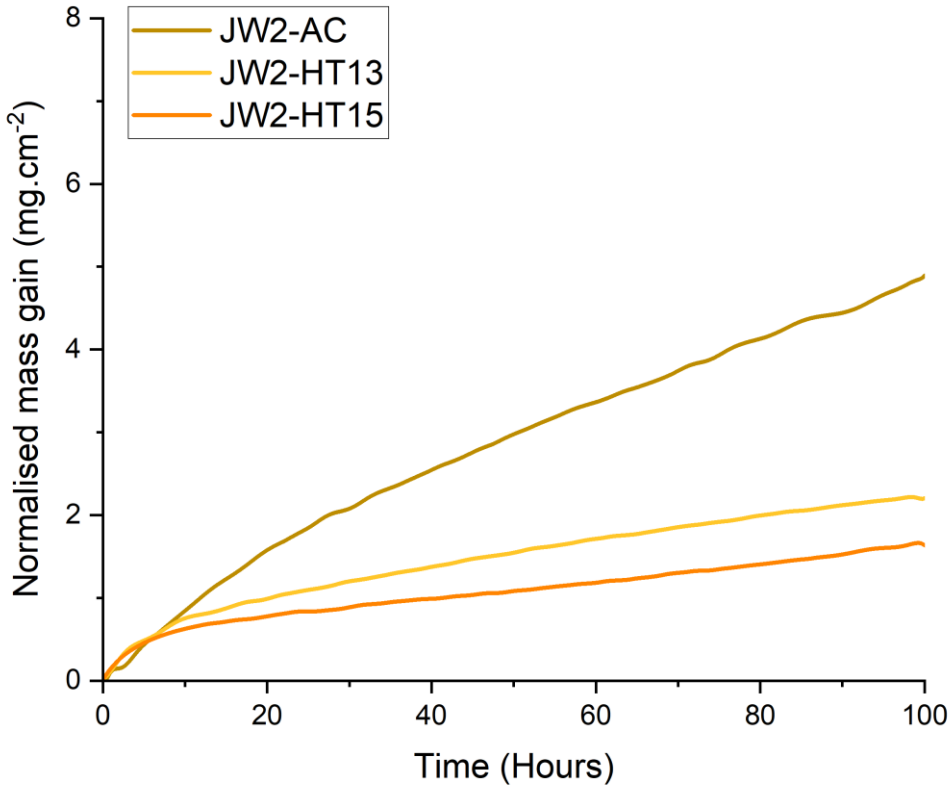

Figure 6.3) Normalised mass gain of JW2 in the as-cast, heat-treated-1300°C and heat-treated-1500°C states over a 100 hour period at 1000°C

6.2.1.4 JW3

In this section germanium's effect on oxidation parameters will be considered. JW3 has 10 at.% Ge where as JW1 has 5 at.%. The TGA curves of oxidised alloy JW3 are displayed in Figure 6.4. This alloy was prepared in as-cast, heat-treated at 1300°C and heat-treated at 1500°C states. Oxidation parameters are displayed in Table 6.1.

The *n* exponents of JW3-AC, JW3-HT13 and JW3-HT15 are calculated as 0.66, 0.55 and 0.61, respectively. Therefore, the oxidation behaviour of JW3 samples can generally be said to be more

parabolic in nature than linear with values closer to 0.5 than 1. The linear mechanism of oxidation is more of a contributing factor to JW3-AC when compared to the other states of JW3.

As with previous samples, oxidation was initially parabolic followed by linear mass gain. The as-cast alloy has a parabolic rate constant of 8.86E-12 $g^2.cm^{-4}.s^{-1}$ and linear rate constant of 5.13E-09 $g.cm^{-2}.s^{-1}$. For the heat-treated at 1300°C version of JW3 both parabolic and linear rates were similar. JW3-HT13 has an initial parabolic rare of 1.27E-11 $g^2.cm^{-4}.s^{-1}$, slightly greater than that of JW3-AC, and linear rate of 4.32E-09 $g.cm^{-2}.s^{-1}$, slightly lower than that of JW3-AC. Regardless, JW3-AC and JW3-HT13 have near identical total mass gains of 2.27 $mg.cm^{-2}$, and 2.28 $mg.cm^{-2}$, respectively. However, JW3-HT15 has significantly higher initial parabolic rate constant, 1.04E-10 $g^2.cm^{-4}.s^{-1}$, and linear rate constant, 1.48E-08 $g.cm^{-2}.s^{-1}$, and therefore total mass gain, 7.22 $mg.cm^{-2}$. Evidently the high temperature heat treatment has had a negative effect on oxidation resistance at 1000°C. The JW3-HT15 sample was the worst performing B and Ge containing alloy and had comparable mass gain to those of KZ5-AC and KZ5-HT15.

The TGA oxidation curves of all the 1000°C experiments conducted in this study are presented in Figure 6.6. In addition, further graphs are included to highlight each processing state in order to assess the potential effects these processing conditions on each alloys oxidation resistance. These are presented in Figure 6.5 (as-cast), Figure 6.8 (heat-treated at 1300°C) and Figure 6.7 (heat-treated at 1500°C).

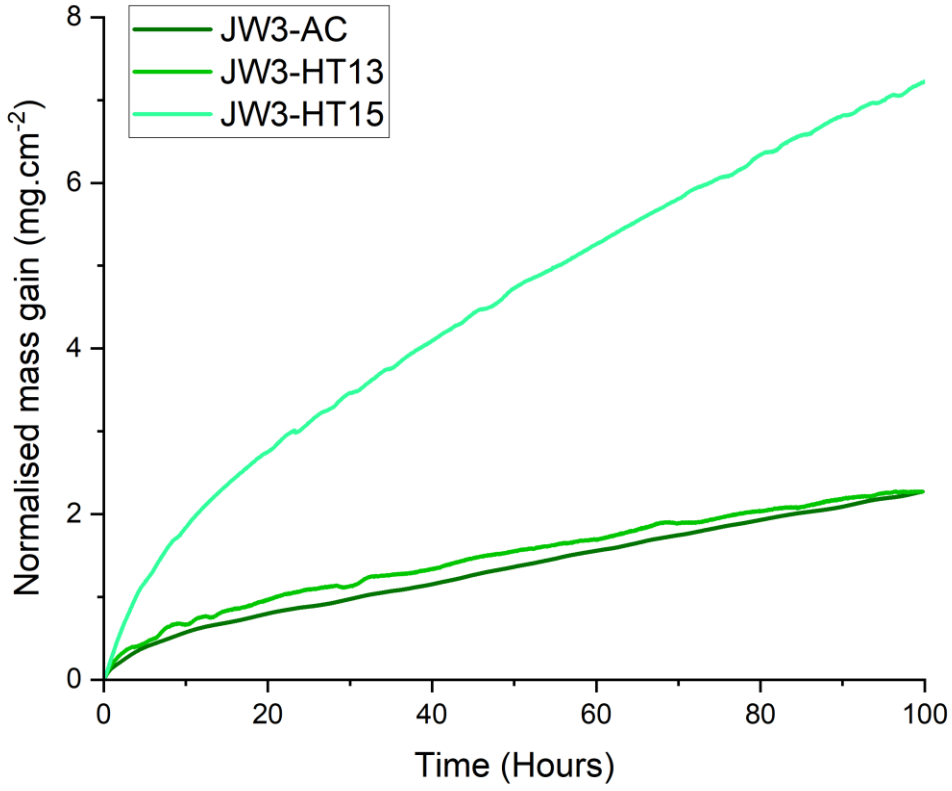

Figure 6.4) Normalised mass gain of JW3 in the as-cast, heat-treated-1300°C and heat-treated-1500°C states over a 100 hour period at 1000°C

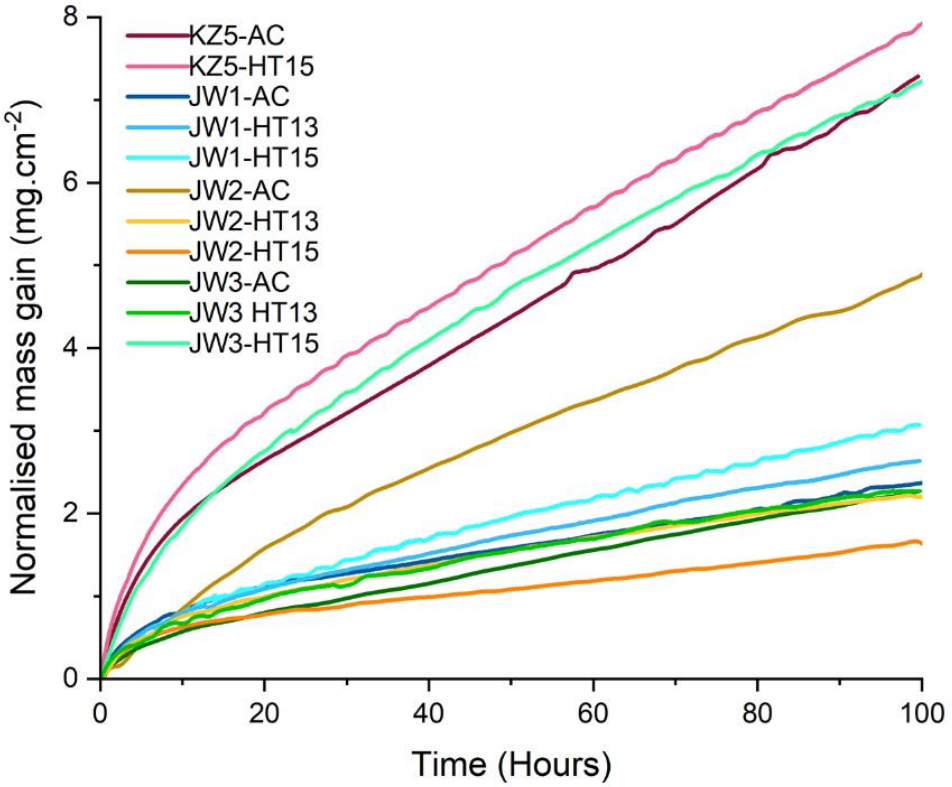

Figure 6.6) Normalised mass gain of all samples oxidised at 1000°C over a 100 hour period.

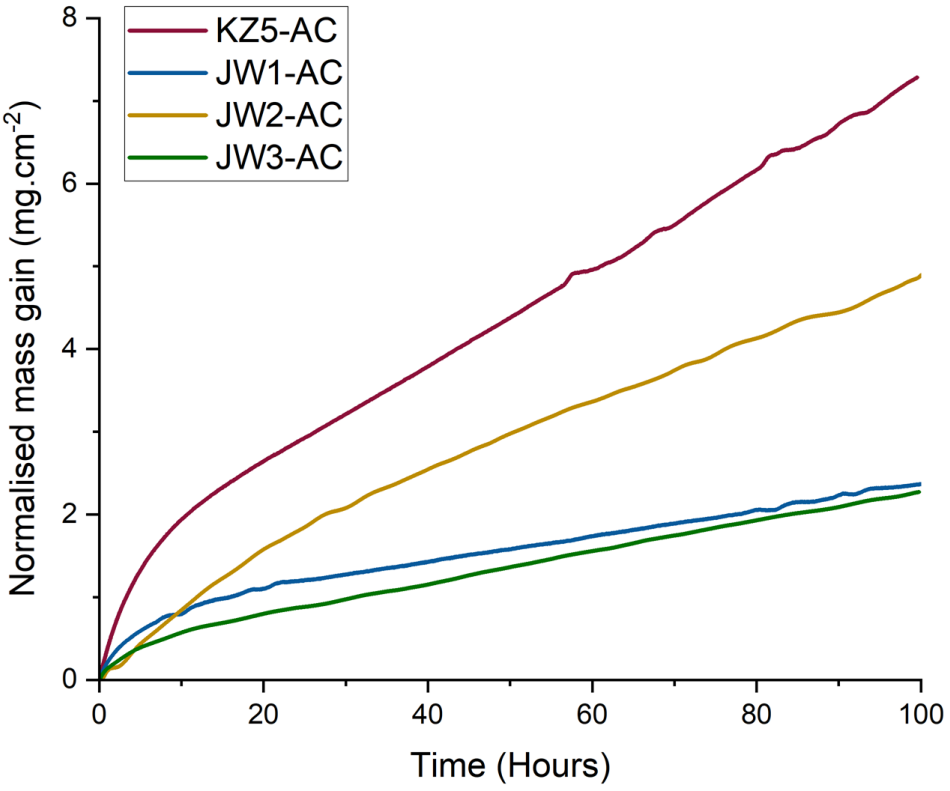

Figure 6.5) Normalised mass gain of KZ5, JW1, JW2, and JW3 in the as-cast state over a 100 hour period at 1000°C

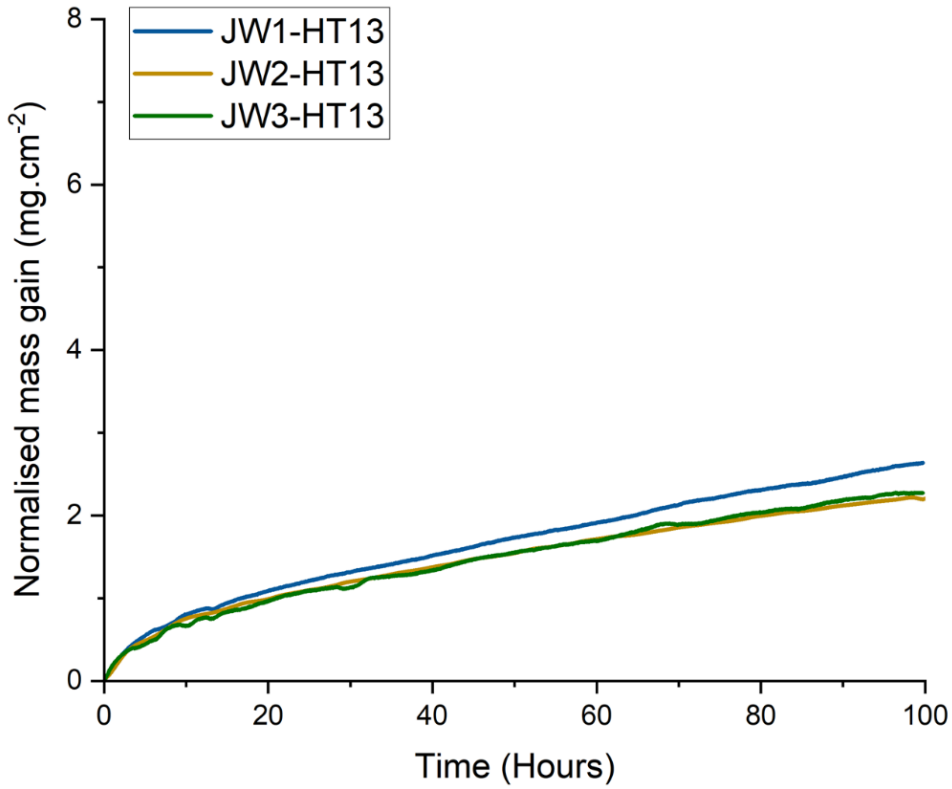

Figure 6.8) Normalised mass gain of JW1, JW2, and JW3 in the Heat-treated at 1300°C state over a 100 hour period at 1000°C

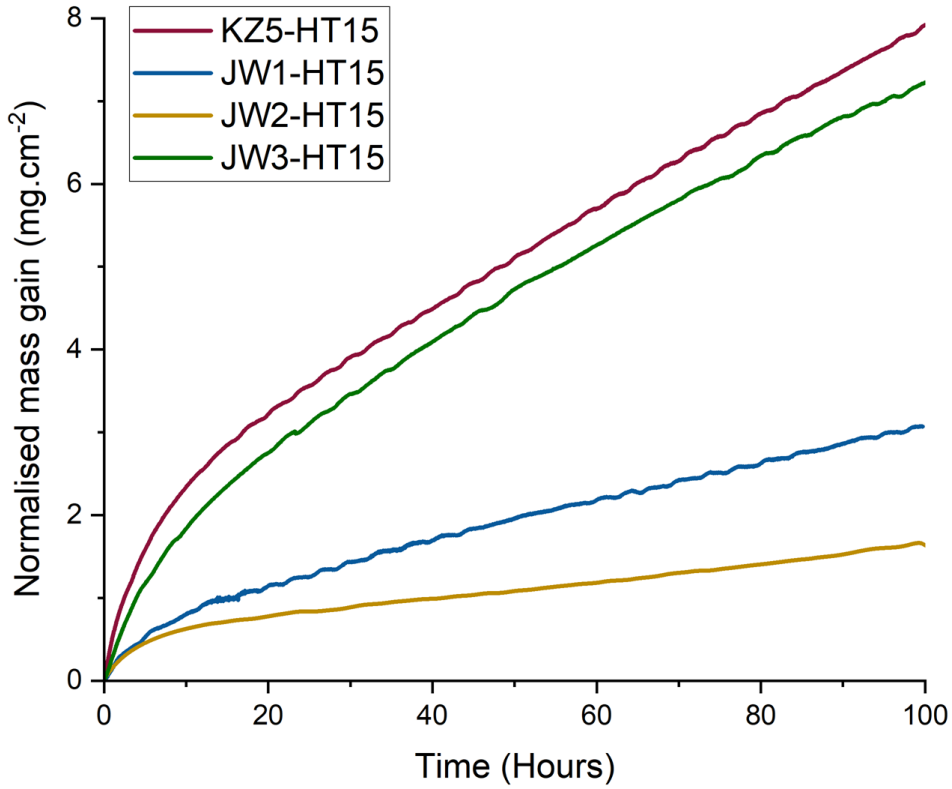

Figure 6.7) Normalised mass gain of KZ5, JW1, JW2, and JW3 in the Heat-treated at 1500°C state over a 100 hour period at 1000°C

6.2.2 Oxide scale

6.2.2.1 KZ5

6.2.2.1.1 XRD

The XRD pattern of KZ5-AC is shown in Figure 6.9. The phases that are identified are a rutile structured TiO_2 (Pearson symbol tP6, space group $P4_2/mnm$) and monoclinic titanium-niobate $Ti_2Nb_{10}O_{29}$ (Pearson symbol mC82, space group A2/m). It should be noted that wherever the TiO_2 phase is reported in XRD patterns in this section, TiO_2 is used as a simplification of mixed element rutile structured tetragonal oxides. These include $Ti_{0.8}Nb_{0.1}Cr_{0.1}O_2$, $Ti_{0.6}Nb_{0.2}Cr_{0.2}O_2$, $Ti_{0.34}Nb_{0.33}Cr_{0.33}O_2$ as well as TiO_2, which all have similar lattice parameters and reflections Table 8.1. The slight difference in peak positions assigned to TiO_2 peaks between oxidised samples is suspected to be a result of different ratios of Nb, Cr and Ti substituting into the rutile structure. Generally, the higher degree of substitution of Nb and Cr onto Ti sites, the lower the 2θ angle for the three most intense peaks. The XRD pattern of KZ5-HT15 is shown in Figure 6.10. The phases that are identified are TiO_2 and $Ti_2Nb_{10}O_{29}$.

The XRD pattern of the as-cast and heat-treated KZ5 samples are very similar, with the minor exception indicated in Figure 6.9 with a star symbol. In the as-cast pattern a peak at 31.0° exist and is absent from the heat-treated version. The 31.0° peak could possibly be a sign of $TiNb_2O_7$, a higher temperature stable titanium-niobate phase (Pearson symbol mC60, space group I2/m) [148], but other major peaks of this phase are absent so this peak remains unassigned.

For the as-cast specimens, grazing incident XRD (GIXRD) was performed as well in order to better examine the oxide phases on the surface. An omega angle of 2° is used for all presented GIXRD results as it gave the best signal to noise ratio. From this omega angle the penetration depth into the oxide layer is estimated to be between 0.7 µm and 4.3 µm for fully dense TiO_2 and SiO_2, respectively. Other omega angles were tested, however they resulted in undefinable peaks as the signal to noise ratio became too great and the peak intensity too low to distinguish between the background and actual peaks. This is likely due to the small size of the samples and minor unalignment of the parabolic Göbel mirror in the Panalytical X'pert^3.

The GIXRD pattern of KZ5-AC is displayed in Figure 6.11. The phases identified through GIXRD are TiO_2 and $Ti_2Nb_{10}O_{29}$. This is in agreement with the XRD pattern presented in Figure 6.9. This shows that standard XRD is more than sufficient to identify oxides that have formed in comparison to grazing incident techniques, and as such standard XRD results are reported for remaining samples. For GIXRD patterns of 1000°C JW series alloys see appendix section Figure 8.4, Figure 8.6, Figure 8.8.

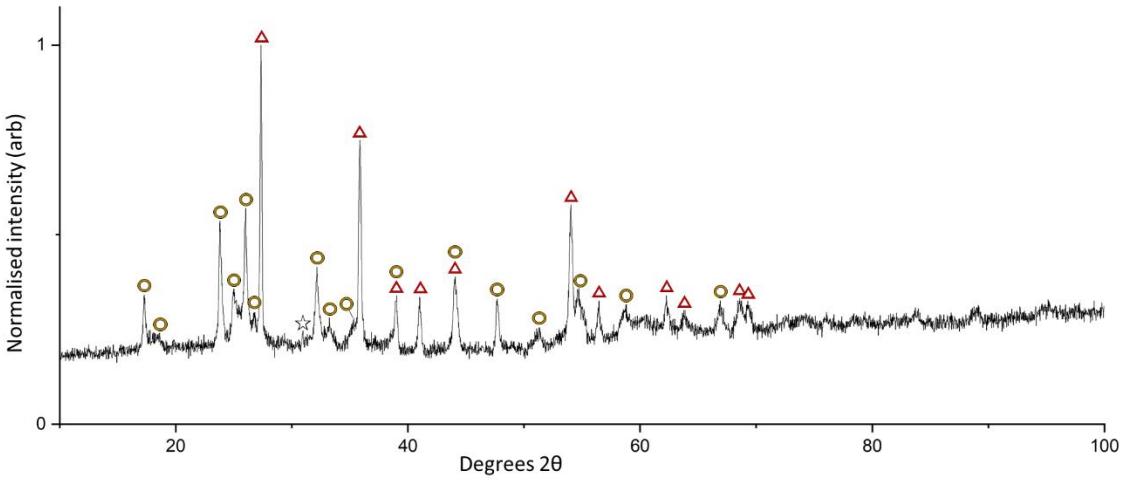

Figure 6.9) XRD pattern of oxidised at 1000°C KZ5-AC. △= TiO_2, ○= $Ti_2Nb_{10}O_{29}$, ☆= Unknown

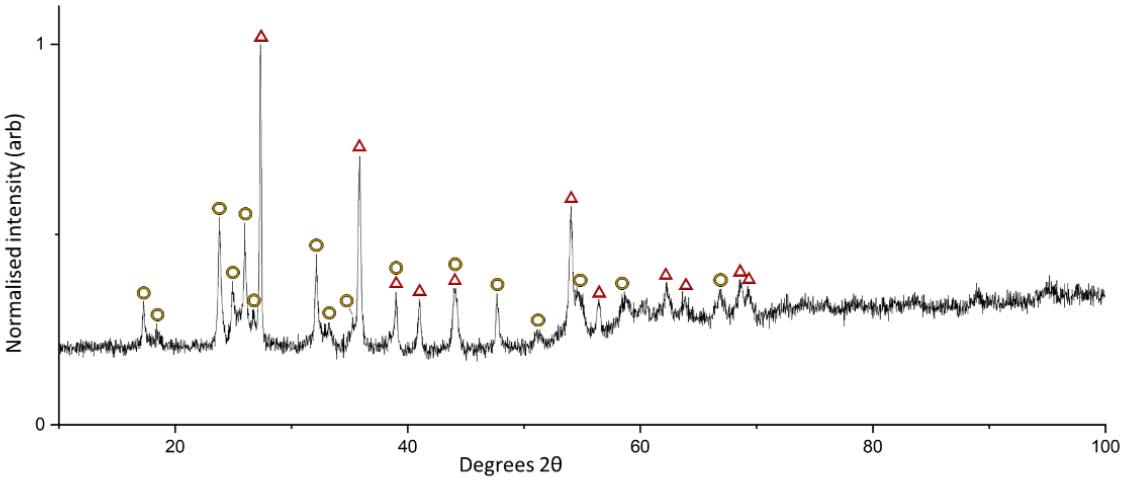

Figure 6.10) XRD pattern of oxidised at 1000°C KZ5-HT15. △= TiO_2, ○= $Ti_2Nb_{10}O_{29}$

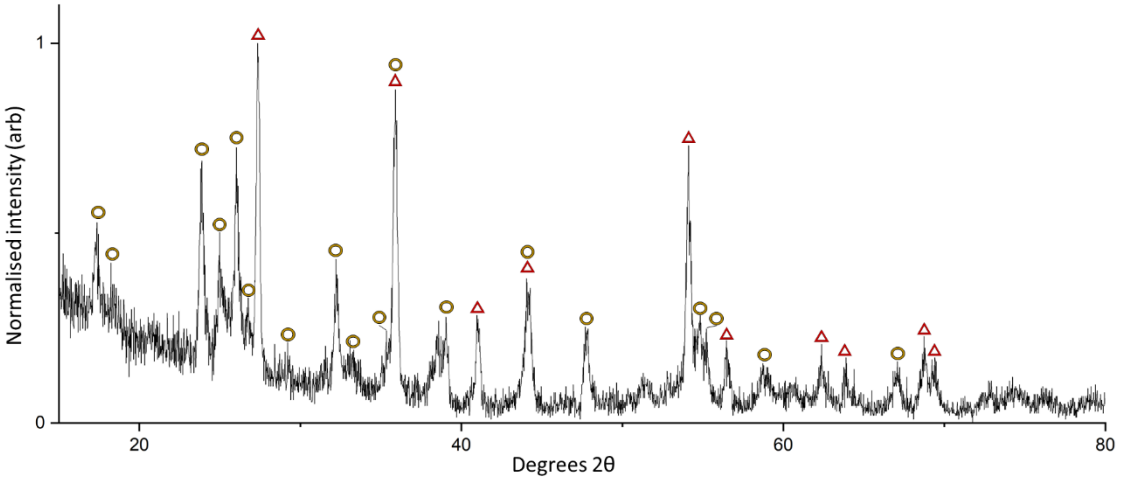

Figure 6.11) Grazing incident XRD pattern of oxidised at 1000°C KZ5-AC. An omega angle of 2° was used. △= TiO_2, ○= $Ti_2Nb_{10}O_{29}$

6.2.2.1.2 EPMA

EPMA mapping of oxidised KZ5 samples at 1000°C including elements Nb, Si, Ti, Cr, Al, and O is presented in Figure 6.12 and Figure 6.13 for the as-cast state and heat-treated at 1500°C state, respectively. Individual pixels can be taken from these quantitative maps as point analysis provided that the phase exists in large enough quantities for at least 10 measurements to be taken, and the phase is coarse enough to take central points that will not be affected by a boundary effect of other neighbouring phases. To gain a perspective on how oxygen is transported from the surface of the sample into the bulk material, the composition of phases close to and far from the oxide scale is calculated where possible, as well as the average composition from the portion of the sample mapped. Typically, in the case of KZ5, this results in compositions given from 0µm to 20µm from the oxide scale compared to composition from 90µm to 120µm from the oxide scale, for 'close to' and 'far from' labels, respectively. The results from this bulk phase analysis are presented in Table 6.2 and Table 6.3. Area analysis was performed using this EPMA data in order to report average compositions of specific areas of the oxide scale, shown in Table 6.4. These areas include the total oxide scale, and in the case of B and Ge containing alloys the germanium-rich layer. In addition, point analysis similar to that performed for phases in the bulk of the sample can be performed within the oxide scale, shown in Table 6.5.

In the bulk of each oxidised sample, three phases were identified; (Nb), βNb_5Si_3 and a titanium solid solution (Ti). Also identified were a Cr-rich phase thought to be $NbCr_2$ Laves phase in the KZ5-AC sample. In the case of KZ5-HT15, the Cr-rich phase was too finely distributed to measure accurately. In the case of KZ5-AC and KZ5-HT15, (Nb) and βNb_5Si_3 are consistent with the unoxidised microstructure, and $NbCr_2$ and (Ti) are a result of oxidation. The compositions each of these phases in the oxidised samples are listed in Table 6.2.

In the majority of both the oxidised samples, the (Nb), $NbCr_2$ and (Ti) phases exist in intergranular regions between βNb_5Si_3 grains. In the case of KZ5-HT15, the (Ti) phase also exists in larger single phase areas. As was the case with the $NbCr_2$ phase in KZ5-HT15, the (Ti) in KZ5-HT15 was too fine to reliably measure, so the larger areas were used to report composition. The phase assigned to (Ti) in KZ5-AC and KZ5-HT15 is proposed to be a titanium solid solution (Ti) given the large Ti contents with only 18.3 at.% and 3.9 at.% Nb content., respectably. The $NbCr_2$ is assigned as such given the high Cr content of 43.4 at.%. This is less than the nominal 66.7 at.% in $NbCr_2$ but several factors likely contribute to this lower than expected value; substitution of Si, underlying phases are likely picked up in this fine distribution of non-silicide phases, and this phase has been partly oxidised, with an O content of 7.7 at.%. The high Cr areas in KZ5-HT15 are assumed to be $NbCr_2$ also, given the similarities of the microstructures in each processing state of KZ5. Interestingly, alloy KZ5-HT15 did not develop any Laves phase upon heat treatment (section 5.2.1). So like the (Ti) phase found in KZ5-AC, the $NbCr_2$ is being stabilised in oxidised KZ5 by factors relating to the presence of oxygen diffusing into the bulk. A Ti-rich phase is actually found in small amounts in the heat-treated version of KZ5 presented in chapter 5, and therefore it can be concluded that during this heat treatment some oxidation occurred due to an impure argon protective atmosphere if these are the same phases.

In the case of KZ5-AC, the silicide phase is considered to be βNb_5Si_3 as there are no signs of transition into αNb_5Si_3 (i.e. there is only one type of silicide present with fairly consistent composition) and even after 100 hours at a temperature of 1000°C is not expected to overcome the sluggish transformation conditions of the Nb-Si system. The same consistent composition of the silicide phase is seen in KZ5-HT15. This is unexpected given the partial transition of βNb_5Si_3 to αNb_5Si_3 after heat treatment, and yet there is one silicide phase present in the oxidised sample. This silicide phase

is considered to be βNb_5Si_3 as otherwise a complete transition from βNb_5Si_3 to αNb_5Si_3 would need to have occurred due to an additional pseudo-heat treatment at 1000°C, which from the KZ5-HT15 oxidised at 1200°C sample considered later in this chapter it is known that this would not be the case. An SEM-BSE image accompanies the oxide maps taken form a separate location that shows evidence of αNb_5Si_3 and βNb_5Si_3 coexisting (Figure 6.14). Both alloys lack eutectic βNb_5Si_3. This is expected in the heat-treated version of KZ5, but surprising in the as-cast state according to chapter 4. This particular area of oxidised as-cast sample happens to be taken from a location where the eutectic βNb_5Si_3 is not present so may not be fully representative of the oxidised sample microstructure. An SEM-BSE image accompanies the oxide maps taken form a separate location that shows the eutectic/intergranular structure more clearly (Figure 6.15).

Oxygen contents are lowest in the bulk phases for the silicide phase βNb_5Si_3 at 1.4 at.% and 1.8 at.% for KZ5-AC and KZ5-HT15, respectively, and highest for the (Ti) phase at 9.5 at.% and 9.9 at.%, respectively. Limitations exist with the accuracy of reporting oxygen contents of phases, hence why in the case of oxide phases discussed later, ratios of non-oxygen elements are used to identify these phases. For the bulk phases, content of oxygen is assumed to be more reliable given the less porous structure and inability of resin penetration, but it should be noted that the same issues of adsorption of characteristic X-rays of oxygen by the carbon coating layer still persist. As such, small differences between O contents of bulk phases may not hold much significance, but trends such as those described above for βNb_5Si_3 and (Ti) O contents contribute to the understanding of the oxidation mechanism of these alloys.

For phases (Nb), (Ti) and βNb_5Si_3 it was possible to obtain average compositions close to and far from the oxide scale, with the exception of (Ti) in KZ5-HT15 (Table 6.3). βNb_5Si_3 has a relatively consistent composition across the area where the map was taken from, with no element in either alloy have larger than a 1.0 at.% difference. O content at close to the scale (<10μm) is 2.0 at.% and 1.2 at.% far from the scale (100-120μm) in KZ5-AC, and in KZ5-HT15 O content close to the scale (<10μm) is 2.0 at.% and 1.8 at.% far from the scale (90-100μm). (Nb) and (Ti) have more significant decreases in oxygen content when comparing close to the oxide scale and far from it. (Nb) reduces from 16.2 at.% to 4.2 at.% in KZ5-AC. (Ti) decreases from 26.5 at.% to 9.0 at.% in KZ5-AC. This is as expected, as (Ti) and (Nb) are more susceptible to oxidation than βNb_5Si_3 [122]. An assumption is made that O content of a bulk phase is related to its solubility of oxygen, which is further assumed to correlate with the diffusivity of oxygen through that phase. A phase with a higher diffusivity of oxygen, or oxygen diffusion coefficient, is regarded as being more susceptible to oxidation as rate of oxidation is partly related to diffusivity of oxygen into the metal [146].

Area analysis was performed using this EPMA data in order to report average compositions of specific areas of the oxide scale, shown in Table 6.4. These areas include the total oxide scale, and in the case of B and Ge containing alloys the germanium-rich layers. The layer of oxidised material of KZ5-AC had an average composition of 25.2 at.% Nb, 9.5 at.% Si, 16.1 at.% Ti, 2.5 at.% Cr, 1.1 at.% Al and 45.2 at.% O. The layer of oxidised material of KZ5-HT15 had an average composition of 37.5 at.% Nb, 11.5 at.% Si, 10.6 at.% Ti, 4.2 at.% Cr, 1.2 at.% Al, and 35.1 at.% O. Within the oxide layer areas exists which were clearly prior silicide grains, and areas lacking Si, implying prior solid solution regions.

Point analysis similar to that performed for phases in the bulk of the sample can be performed within the oxide scale, shown in Table 6.5. Phases within the oxide scales of alloys oxidised at 1000°C are quite finely distributed however, and there exists a likelihood that the interaction volume of the electron beam is not restricted to a single phase. As with analysis of phases in the bulk, coarser areas of the relevant phases are selected preferentially for point analysis to minimise this effect. It should

be noted that the total weight percentage of elements received from EPMA in the oxide scale and oxide phases does not sum to be 100% and is considerably lower than the sum in the bulk phases of oxidise specimens, which were approximately 90%. This is explained in more detail in Section 3.1 but essentially several contributing factors, such as carbon adsorption of oxygen characteristic x-rays, un-optimised oxide standards, a bevelling effect due to differences in hardness of bulk material and oxide scale, porosity of the oxide scale compared to the bulk material, and possibility of resin penetration into the less dense oxide layer, lead to total weight percentage of the oxide phases around 60 wt.%. Most of the missing wt% is likely oxygen if titanium-niobate phases have formed as surface XRD has suggested. Oxygen content of pure $Ti_2Nb_{10}O_{29}$ and $TiNb_2O_7$ would be 70.7 at.% and 70.0 at% respectively. If results presented in Table 6.4 and Table 6.5 were adjusted to have the missing wt.% reduced to bulk phase totals by adding in suspected missing oxygen, atomic percent of oxygen would be within a 5 at.% range of 70 at%. However, as the Oxygen content is perhaps unreliable, the unadjusted values will be presented and oxygen content will not be used to reason which oxides are present, but can be used especially within bulk phases to assess the susceptibility of certain phases to oxidation. In the oxide scale the ratio of key elements Nb, Ti and Si can be used to identify phases. For example, $Ti_2Nb_{10}O_{29}$ and $TiNb_2O_7$ would have ratios of Nb to Ti of 5 and 2, respectively.

Compositions of phases and regions within the oxide layer of each alloy are presented in Table 6.5. In each of the oxide scales three oxide phases are reported on and are designated based on their most notable element; Nb-rich oxide, Ti-rich oxide, and Si-rich oxide. In addition, each alloy had areas of Nb-rich oxide and Ti-rich oxide that were particularly rich in Cr, but not to a great enough degree to be considered a separate phase, with maximum Cr not exceeding 20 at.%. In alloys KZ5-AC and KZ5-HT15, quite coarse areas of Ti-rich oxide, Nb-rich oxide and Si-rich oxide are present which allows phase analysis with less risk of reporting non-single phase areas.

In KZ5-AC the Ti-rich oxide phase has titanium content of 34.6 at.% whilst Nb and Cr contents were 12.3 at.% and 4.3 at.%, respectively. As a result of having higher Ti content whilst containing significant amounts of Nb and Cr, this phase is considered to be rutile TiO_2 with substitution of mainly Nb and Cr onto Ti sites, i.e. $(Ti,Cr,Nb)O_2$. The Nb-rich phase had Nb content of 43.2 at.% and Ti content of 7.2 at.%, with the Nb/Ti ratio equal to 6.0. This ratio is closer to the expected value of $Ti_2Nb_{10}O_{29}$ rather than $TiNb_2O_7$, so this phase is considered to be the $Ti_2Nb_{10}O_{29}$ oxide also identified through XRD. The fact that the ratio of Nb/Ti is greater than expected for $Ti_2Nb_{10}O_{29}$, i.e. larger than 5, could possibly indicate small amounts of Nb_2O_5 yet to combine with TiO_2 to transition into $Ti_2Nb_{10}O_{29}$ or remaining (Nb) in the scale.

The Si-rich oxide phase in the oxide layer appears to still be in its previous silicide grain structure. The composition recorded for the Si-rich oxide phase is given in Table 6.5 for each alloy. Si content in each Si-rich phase are 16.8 at.% and 21.2 at.% for alloys KZ5-AC and KZ5-HT15, respectively, whilst average Nb contents are 23.3 at.% and 32.4 at.%, respectively, and average Ti content are 12.9 at.% and 10.4 at.%, respectively. Although no SiO_2 phase or other Si containing oxide was detected through XRD spectroscopy, it is proposed that this is a fine mixture of oxides including SiO_2, where the significant Si content comes from, and TiO_2 , $Ti_2Nb_{10}O_{29}$ and $TiNb_2O_7$ where the Ti and Nb come from. The reason for this is that O content of these Si-rich areas is comparable to other oxide phases located within the layer, and the total wt% of these measurements is in line with what is expected from oxide phases.

In KZ5-HT5 the Ti-rich phase has titanium content of 25.0 at.% whilst Nb and Cr contents were 27.4 at.% and 4.9 at.%, respectively. This phase is considered to be rutile TiO_2 with substitution of mainly Nb and Cr onto Ti sites. The substitution of Nb is large in this case. The Nb-rich phase had Nb content

of 54.3 at.% and Ti content of 5.1 at.%, with the Nb/Ti ratio equal to 10.6. This ratio is closer to the expected value of $Ti_2Nb_{10}O_{29}$ rather than $TiNb_2O_7$, so this phase could be considered to be the $Ti_2Nb_{10}O_{29}$ oxide also identified through XRD. However, the ratio of Nb/Ti is double that of what was expected and indicates either Nb_2O_5 yet to combine with TiO_2 to transition into $Ti_2Nb_{10}O_{29}$ or remaining niobium solid solution in the scale. It should also be noted that if Cr is considered to substitute onto solely Ti sites in this oxide then the ratio of Nb/(Ti+Cr) becomes 6.3, which is consistent with the ratio reported for KZ5-AC. Nb_2O_5 was not identified through XRD, however the thickness of the scale could have prevented this phase from being reached by X-rays.

In fact, every oxide phase in the oxide scale as well as the average for the whole scale of KZ5-HT15 had reduced Ti content compared to the as-cast version. This is true for O content as well, despite comparable total weight percent of the phases measured. The oxygen content of all of the phases in KZ5-HT15 presented in Table 6.5 is similar and in the range of 35.0 at.% to 36.3 at.% versus 45.0 at.% to 47.3 at.% in the case of KZ5-AC. This reflects generally less complete oxidation of the phases in the oxide layer, but note that O content in bulk phases shows the reverse when considering the phases (Nb), (Ti) and βNb_5Si_3. The O content of (Nb) was 4.8 at.% and 8.6 at.%, the O content of (Ti) was 9.5 at.% and 9.9 at.% and the O content of βNb_5Si_3 was 1.4 at.% and 1.8 at.%, for KZ5-AC and KZ5-HT15, respectively. Given the unreliability of these values and small margins between them no conclusion can be confirmed, although the increased diffusion of O into the bulk of the sample would be in agreement with the TGA results, where the difference of oxidation performance between KZ5-AC and KZ5-HT15 is minimal at 1000^{o}C but favours KZ5-AC.

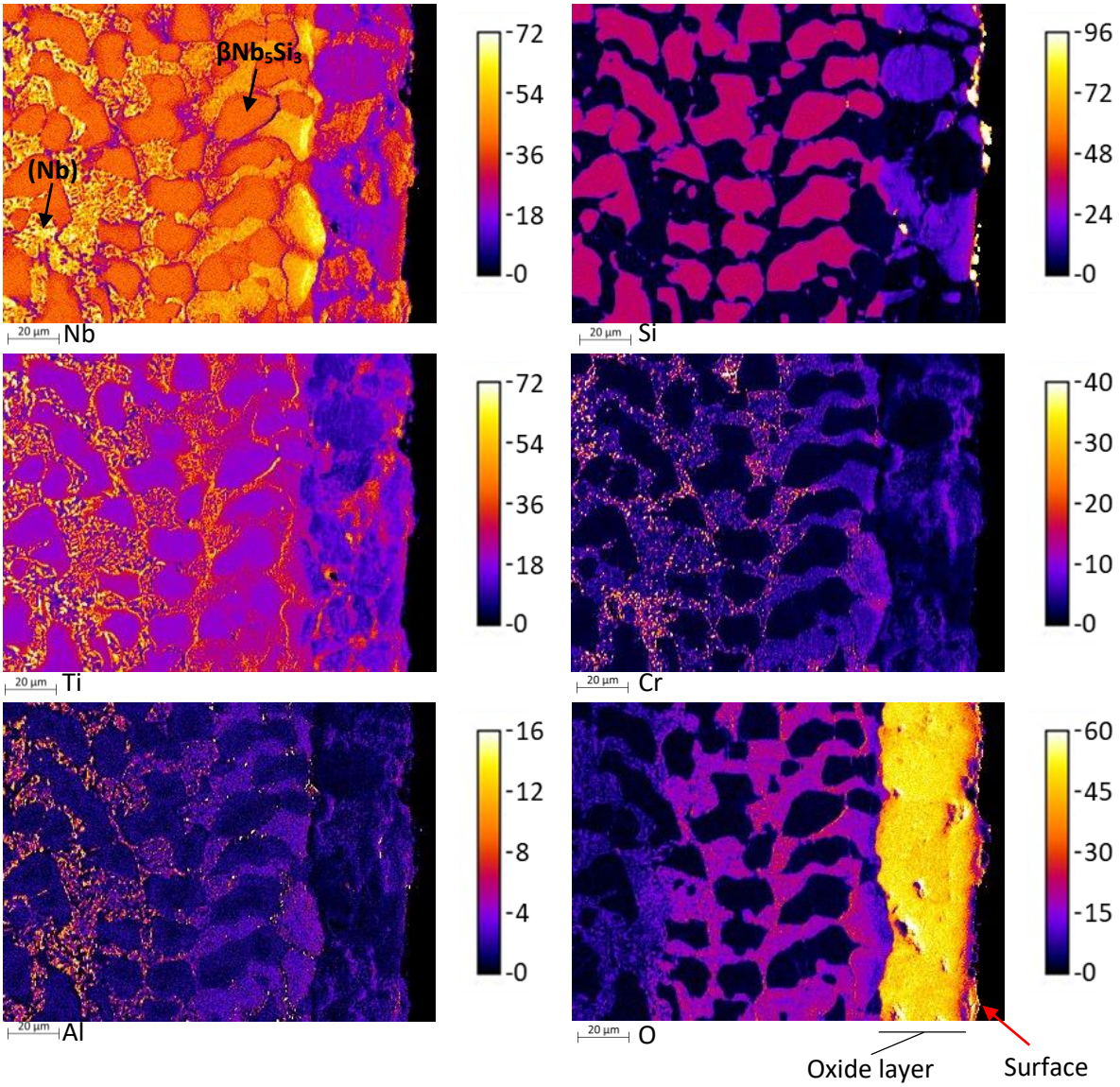

Figure 6.12a-f) EPMA maps of the oxide layer of KZ5-AC in at.% of elements a) Nb, b) Si, c) Ti, d) Cr, e) Al, f) O.

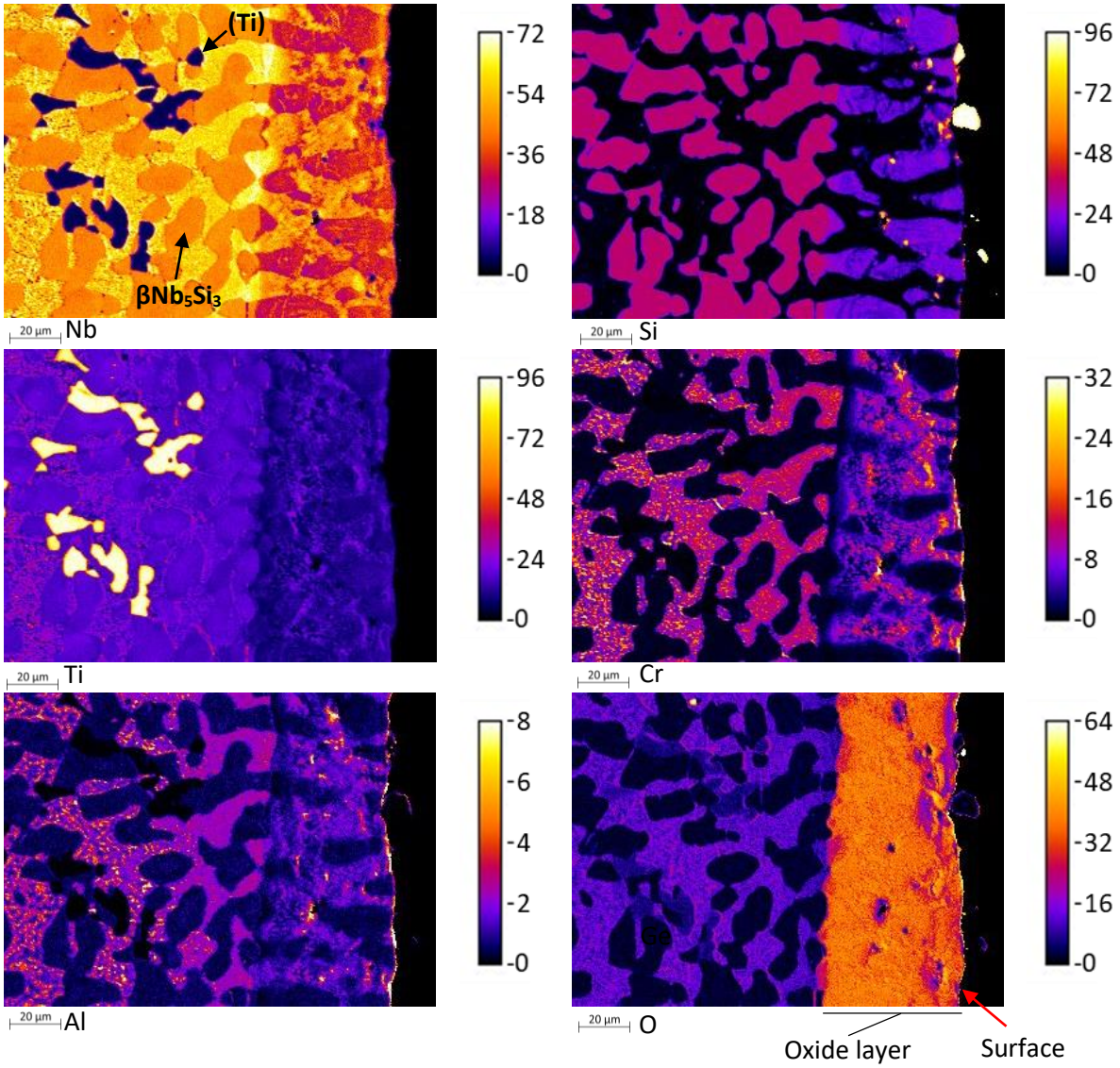

Figure 6.13a-f) EPMA maps of the oxide layer of KZ5-HT in at.% of elements a) Nb, b) Si, c) Ti, d) Cr, e) Al, f) O.

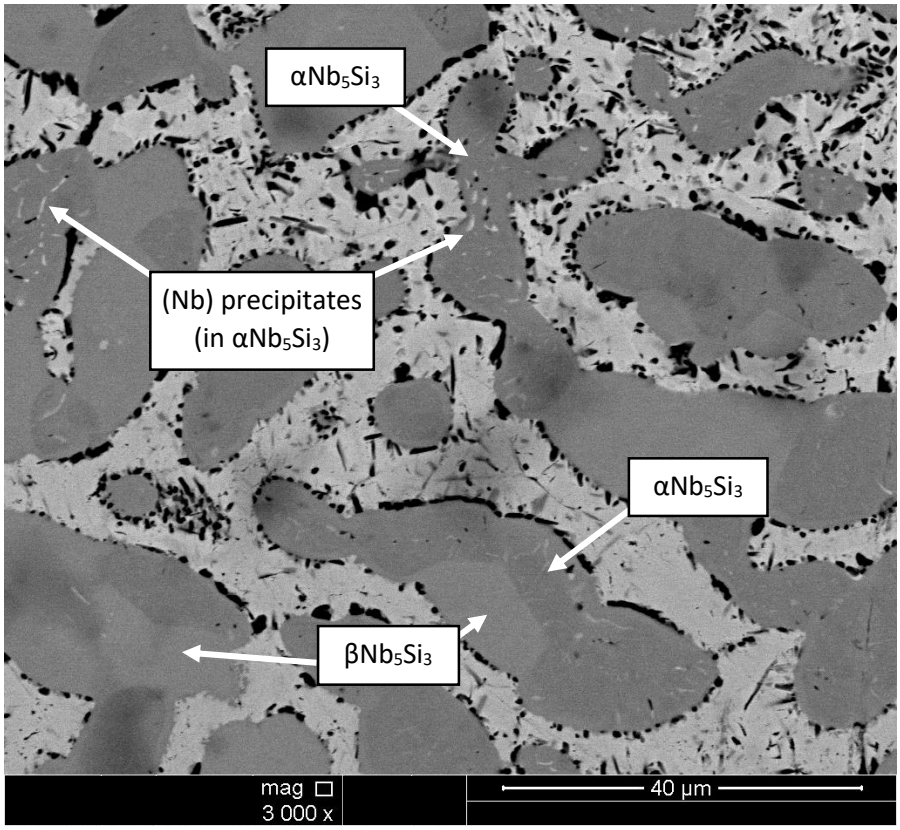

Figure 6.14) BSE image of oxidised KZ5-HT15 to show the existence of both αNb_5Si_3 and βNb_5Si_3, indicated by the presence of (Nb) particles within silicide grains, which were previously found to be a result of βNb_5Si_3 to αNb_5Si_3 transition

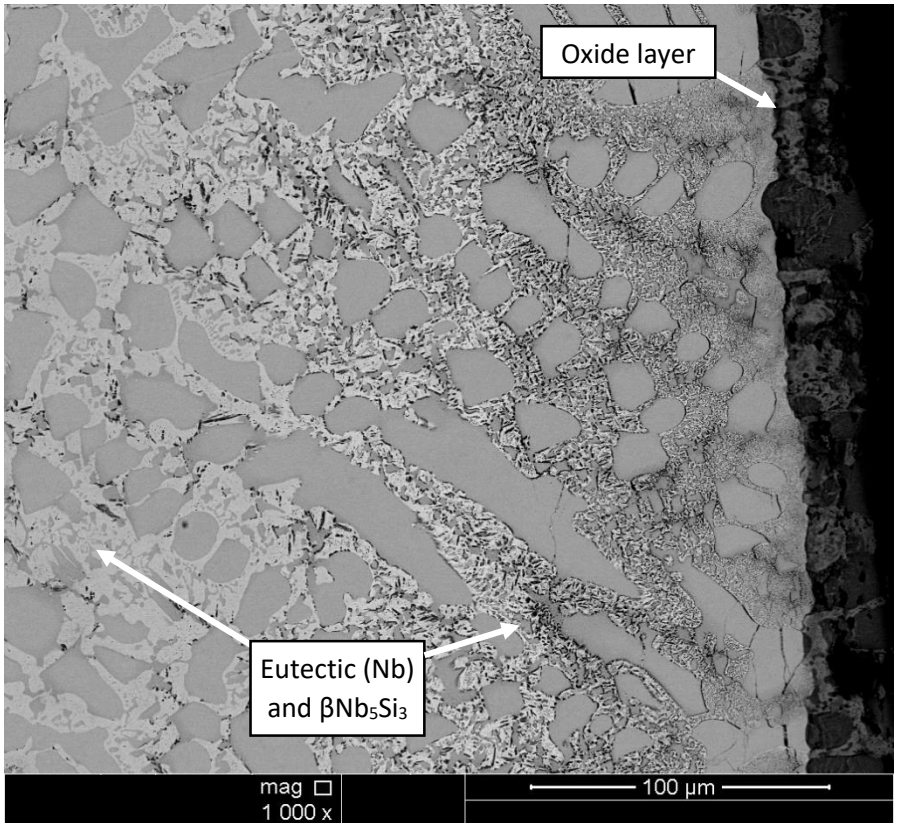

Figure 6.15) BSE image of oxidised KZ5-AC to show the existence intergranular and eutectic βNb_5Si_3 which was absent from the oxidised sample EPMA mapped location

Table 6.2) Phase analysis of bulk phases present in each KZ5 oxidised sample EPMA map, values given in at.%.

		Nb	Si	Ti	Cr	Al	O
βNb_5Si_3	KZ5-AC	40.9 ± 2.6	36.4 ± 2.2	19.3 ± 1.5	1.0 ± 0.5	1.1 ± 0.8	1.4 ± 1.1
	KZ5-HT15	43.7 ± 2.8	36.9 ± 2.3	16.5 ± 1.7	0.5 ± 0.4	0.5 ± 0.3	1.8 ± 1.2
(Nb)	KZ5-AC	67.1 ± 4.3	1.7 ± 1.5	16.4 ± 9.5	5.6 ± 4.8	4.4 ± 3.2	4.8 ± 3.1
	KZ5-HT15	63.9 ± 2.9	0.8 ± 0.5	13.7 ± 4.2	11.3 ± 4.9	1.8 ± 0.7	8.6 ± 3.7
(Ti)	KZ5-AC	18.3 ± 7.8	2.0 ± 4.9	69.2 ± 3.8	0.8 ± 1.2	0.2 ± 0.5	9.5 ± 2.2
	KZ5-HT15	3.9 ± 1.2	0.1 ± 0.2	85.9 ± 3.5	0.2 ± 0.2	0.1 ± 0.1	9.9 ± 2.0
$NbCr_2$	KZ5-AC	26.4 ± 7.2	4.8 ± 2.4	17.2 ± 8.1	43.4 ± 3.2	0.5 ± 0.5	7.7 ± 3.6

Table 6.3) Phase analysis of bulk phases present in each KZ5 oxidised sample from locations close to the oxide layer (top lines) and from locations far from the oxide layer (bottom lines). Values given in at.%. The distances from the oxide scale vary dependent on what was possible to measure. Alloy:phase-close to:far from; KZ5-AC:(Nb) - <20µm : 115-120µm, KZ5-HT15:(Nb) - <20µm : 90-100µm, KZ5-AC:(Ti) - <15µm : 105-120µm, KZ5-AC:βNb_5Si_3 - <10µm : 100-120µm, KZ5-HT15:βNb_5Si_3 - <10µm : 90-100µm.

		Nb	Si	Ti	Cr	Al	O
βNb_5Si_3	KZ5-AC	40.1 ± 3.1	36.4 ± 2.3	19.4 ± 2.0	1.1 ± 0.5	1.1 ± 0.7	2.0 ± 1.4
		41.1 ± 2.6	36.4 ± 2.2	19.3 ± 1.4	0.9 ± 0.4	1.1 ± 0.7	1.2 ± 1.1
	KZ5-HT15	43.7 ± 2.8	37.0 ± 2.3	16.3 ± 1.6	0.5 ± 0.3	0.5 ± 0.3	2.0 ± 1.2
		43.4 ± 2.7	37.0 ± 2.4	16.8 ± 1.8	0.5 ± 0.4	0.5 ± 0.3	1.8 ± 1.2
(Nb)	KZ5-AC	50.5 ± 2.9	2.5 ± 0.8	22.6 ± 3.2	5.5 ± 2.1	2.8 ± 1.3	16.2 ± 3.8
		68.2 ± 4.6	1.3 ± 1.0	13.4 ± 2.2	9.4 ± 7.6	3.6 ± 3.8	4.2 ± 2.2
	KZ5-HT15	62.7 ± 4.1	0.5 ± 0.4	13.5 ± 2.4	10.8 ± 2.0	2.8 ± 0.4	9.7 ± 2.6
		67.4 ± 3.1	0.6 ± 0.8	14.6 ± 4.8	6.6 ± 3.1	2.2 ± 1.0	8.7 ± 3.4
(Ti)	KZ5-AC	9.3 ± 6.9	7.1 ± 7.0	56.1 ± 2.1	0.5 ± 0.3	0.5 ± 0.6	26.5 ± 3.7
		19.1 ± 9.5	1.4 ± 1.8	68.4 ± 6.6	1.8 ± 1.9	0.2 ± 0.4	9.0 ± 1.9

Table 6.4) Area analysis of the entire oxide layers shown in EPMA maps for KZ5 oxidised samples, values given in at.%.

		Nb	Si	Ti	Cr	Al	O
Total oxide layer:	KZ5-AC	25.5 ± 6.7	9.5 ± 9.4	16.1 ± 7.1	2.5 ± 2.1	1.1 ± 1.1	45.2 ± 14.0
	KZ5-HT15	37.5 ± 9.7	11.5 ± 12.8	10.6 ± 3.5	4.2 ± 3.4	1.2 ± 0.9	35.1 ± 11.0

Table 6.5) Phase analysis of oxide phases in each KZ5 oxidised sample from locations in the oxide scale, values given in at.%.

		Nb	Si	Ti	Cr	Al	O
Ti-rich oxide	KZ5-AC	12.3 ± 2.8	2.2 ± 2.5	34.6 ± 3.1	4.3 ± 1.4	1.6 ± 0.9	45.0 ± 8.3
	KZ5-HT15	27.4 ± 4.1	5.3 ± 5.3	25.0 ± 3.7	4.9 ± 2.2	1.2 ± 0.6	36.3 ± 6.0
Nb-rich oxide	KZ5-AC	43.2 ± 2.8	1.1 ± 0.9	7.2 ± 1.3	0.5 ± 0.4	0.7 ± 0.9	47.3 ± 5.7
	KZ5-HT15	54.3 ± 4.3	0.2 ± 0.4	5.1 ± 1.9	3.5 ± 3.3	1.5 ± 1.9	35.3 ± 5.0
Si-rich oxide	KZ5-AC	23.3 ± 2.6	16.8 ± 2.1	12.9 ± 2.3	1.1 ± 0.7	0.7 ± 0.6	45.2 ± 8.4
	KZ5-HT15	32.4 ± 3.2	21.2 ± 3.1	10.4 ± 1.5	0.5 ± 0.4	0.5 ± 0.2	35.0 ± 6.5

6.2.2.2 JW1

6.2.2.2.1 XRD

The XRD pattern of JW1-AC is shown in Figure 6.16. The phases that are identified are TiO_2, $Ti_2Nb_{10}O_{29}$, $TiNb_2O_7$ and a cristobalite form of SiO_2 (Pearson symbol tP12, space group $P4_12_12$). The XRD pattern of JW1-HT13 is shown in Figure 6.17. The phases that are identified are TiO_2, $Ti_2Nb_{10}O_{29}$, $TiNb_2O_7$ and SiO_2.The XRD pattern of JW1-HT15 is shown in Figure 6.18. The phases that are identified are TiO_2, $Ti_2Nb_{10}O_{29}$, $TiNb_2O_7$ and SiO_2.

Whilst there is significant overlap between the two niobium-titanium oxides, there are two main pieces of evidence used to identify if $TiNb_2O_7$ is present; splitting of the low angle peaks between 17° and 19°, and whether lower intensity unique peaks are present in the 23° to 27° range. $Ti_2Nb_{10}O_{29}$ is more easily confirmed as being present in the oxide layer as there exists a peak at approximately 25° that is distinct enough from the nearby $TiNb_2O_7$ and TiO_2 peaks to be attributed to solely $Ti_2Nb_{10}O_{29}$.

In each processing state of JW1, a high degree of confidence can be placed in phases TiO_2 and $Ti_2Nb_{10}O_{29}$ as there are high intensity unique peaks with positions that agree well with the database. The SiO_2 phase is less apparent as only one unique peak, with a slight shift in position compared to the reference pattern (00-039-1425), is identified in these samples. SiO_2 is included as no other phase with this low angle peak position that is seen at approximately 21.5° 2θ in each XRD pattern of JW1 was considered. Cristobalite was reported in high silicon content Nb-Si-B alloys at temperatures above 800°C [164]. A high degree of confidence can be placed in $TiNb_2O_7$ in JW1-AC. However, in JW1-HT13 and JW1-HT15 peaks associated solely with $TiNb_2O_7$ are diminished and less distinguishable when compared to JW1-AC, indicating that this phase is possibly not present or at the very least not as developed in the heat-treated at 1300°C and 1500°C version of the alloy. The three XRD pattern of JW1 in different processing states are none the less very similar.

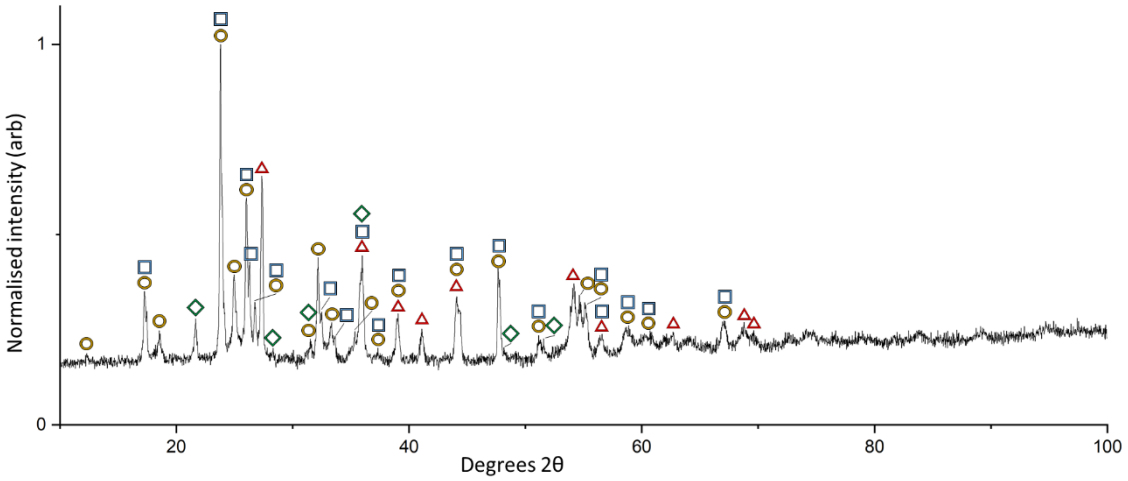

Figure 6.16) XRD pattern of oxidised at 1000°C JW1-AC. △ = TiO_2, ○ = $Ti_2Nb_{10}O_{29}$, □ = $TiNb_2O_7$, ◇ =SiO_2

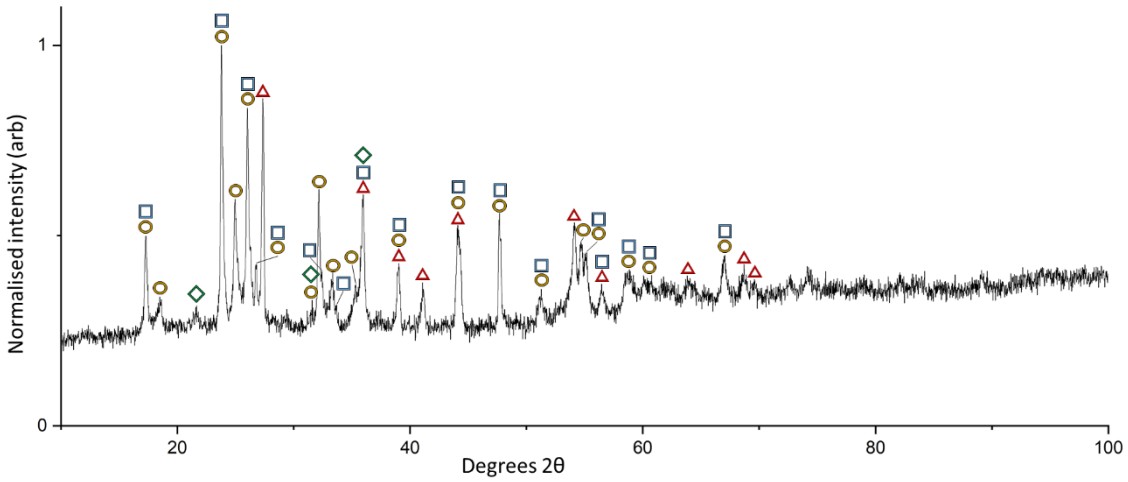

Figure 6.17) XRD pattern of oxidised at 1000°C JW1-HT13. △ = TiO_2, ○ = $Ti_2Nb_{10}O_{29}$, □ = $TiNb_2O_7$, ◇ = SiO_2

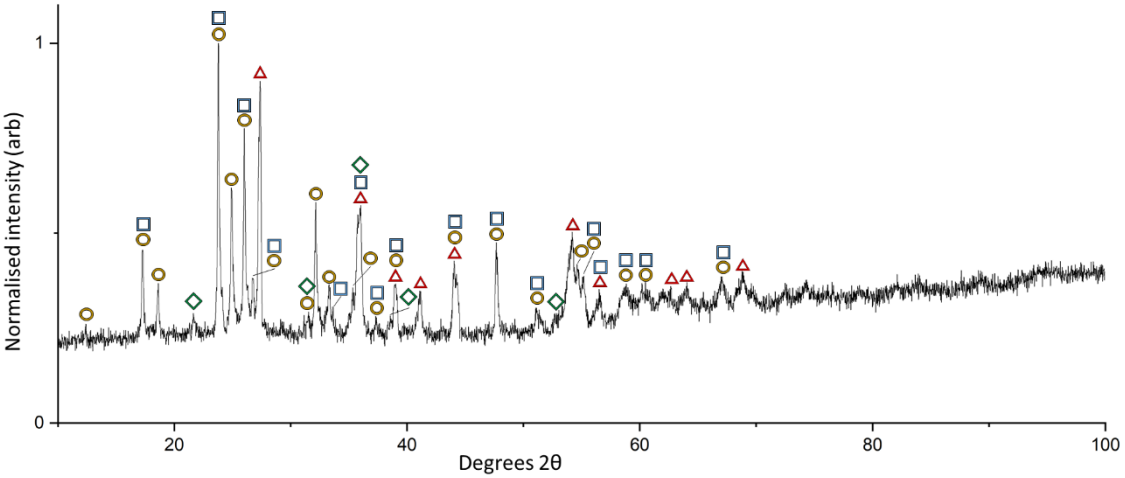

Figure 6.18) XRD pattern of oxidised at 1000°C JW1-HT15. △ = TiO_2, ○ = $Ti_2Nb_{10}O_{29}$, □ = $TiNb_2O_7$, ◇ = SiO_2

6.2.2.2 EPMA

EPMA mapping of oxidised JW1 samples at 1000°C including elements Nb, Si, Ti, Cr, Al, Ge, B and O is presented in Figure 6.19, Figure 6.20, and Figure 6.21 for the as-cast state, heat-treated at 1300°C state and heat-treated at 1500°C state, respectively. In the bulk of each oxidised sample, five phases were identified; (Nb), (Ti), $NbCr_2$, $D8_8$ and T2. Phases (Nb), $NbCr_2$, $D8_8$ and T2 are in agreement with the un-oxidised microstructures of JW1-AC identified in Chapter 4, and JW1-HT13 and JW1-HT15 identified in Chapter 5. (Ti) is not found in un-oxidised microstructures and is therefore a result of oxidation. (Ti) is considered a distinct phase from (Nb) and not merely a Ti-rich from of (Nb) as its composition is significantly different, with at least over 70 at.% Ti content and the highest Nb content only 12.0 at.% found in JW1-HT15. The compositions of each of these phases in the oxidised samples are listed in Table 6.6.

The (Nb), (Ti), and $NbCr_2$ phases appear alongside each other in the intergranular areas between $D8_8$ and T2 grains. The average O contents of (Nb) in JW1-AC, JW1-HT13, and JW1-HT15 are 3.0 at.%, 2.2 at.% and 5.9 at.%, respectively. The average O contents of (Ti) in JW1-AC, JW1-HT13, and JW1-HT15 are 8.1 at.%, 7.3 at.% and 9.7 at.%, respectively. The average O contents of $NbCr_2$ in JW1-AC, JW1-HT13, and JW1-HT15 are 1.8 at.%, 1.7 at.% and 3.3 at.%, respectively. This shows that generally the (Ti) phase has a higher affinity for O and is more susceptible to diffusion of oxygen. On the other hand the Laves phase $NbCr_2$, with a Cr content between 53.0 at.% and 56.6 at.% across JW1 samples,

is less susceptible to oxidation with the lowest O contents of non-silicide phases when compared within each respective JW1 alloy processing state.

Further away from the scale of JW1-AC, on the left hand side of the EPMA maps in Figure 6.19, the mixture of phases (Nb), (Ti) and $NbCr_2$ begins to no longer fill up the intergranular areas between $D8_8$ and T2 grains. Instead a Ti-rich (Nb) phase is identified. The three main elements in this phase are Nb, Ti and Cr, with elemental contents of 37.7 at.%, 41.1 at.% and 10.7 at.%, respectively. Its position in the bulk suggests that as oxygen content becomes larger in the intergranular regions during oxidation, this Ti-rich (Nb) segregates into the phases found closer to the scale in intergranular regions; (Nb), (Ti) and $NbCr_2$. A Ti-rich (Nb) phase is also found in JW1-HT13 in the upper region of the EPMA maps Figure 6.20 with similar composition of main elements Nb, Ti and Cr; 34.5 at.%, 44.0 at.% and 9.9 at.%, respectively. Although in the case of JW1-HT13, lesser amounts of (Nb) and coarser $NbCr_2$ are found alongside the Ti-rich (Nb). No Ti-rich (Nb) is found in JW1-HT15 in the area EPMA mapping was performed on, so a BSE image is included to provide evidence that Ti-rich (Nb) exists in JW1-HT15 further into the sample (Figure 6.22). Unique to JW1-HT15, the $NbCr_2$ phase forms in a coarser, non-continues layer on $D8_8$ boundaries with the intergranular mixture of (Nb), (Ti), and $NbCr_2$. This is the same structure of $NbCr_2$ observed in the un-oxidised microstructure of JW1-HT15 in Chapter 5. In this alloy there is no silicide present in the intergranular regions as this was removed during heat-treatment.

Where possible the average compositions of bulk phases close to and far from the oxide scales were calculated. Typically, in the case of JW1, this results in compositions given from 0µm to 40µm from the oxide scale compare to composition from 50µm to 130µm from the oxide scale, for 'close to' and 'far from' labels, respectively. Phases $D8_8$ and T2 generally had the lowest oxygen contents of the bulk phases, as is to be expected. In the case of (Nb) in JW1-HT15, there was notably greater oxygen content closer to the oxide scale (<15µm) than far from it (100-130µm); 10.7 at.% close to the scale to 4.5 at.% far from the scale. This is not the case with (Nb) in JW1-AC and JW1-HT13 which have more consistent O composition being measured close to and far from the scale. This is likely a result of no feasible (Nb) being located close enough to the scale in JW1-AC and JW1-HT13 maps to measure the different (Nb) composition there. Despite this a clear trend is seen in (Nb) across the three JW1 oxidised samples in terms of composition close to and far from the scale. Close to the oxide scale Nb content is higher and Ti content is lower when compared to (Nb) further from the scale. In the case of (Ti), there is generally higher O contents close to the scale than further from it, with O content close to the scale of 9.1 at.%, 7.9 at.% and 11.8 at.%, and far from the scale of 7.4 at.%, 6.9 at.%, and 8.3 at.% for alloys JW1-AC, JW1-HT13, and JW1-HT15, respectively. In this phase there is a gradient of diffused oxygen. In JW1-HT13, Cr content is also significantly greater in (Ti) further from the scale at 15.5 at.%. This is such a large content compared to any other close to/far from/average value that it is likely that underlying $NbCr_2$ was included in the measurements used to calculate the far from composition of (Ti) in JW1-HT13 and so cannot be relied upon fully.

Area analysis was performed using this EPMA data in order to report average compositions of specific areas of the oxide scale, shown Table 6.8. This is considered area analysis and not phase analysis as the pixels of the EPMA map used to calculate average composition certainly contain multiple phases due to being over such large, indiscriminate areas. The layer of oxidised material of JW1-AC had an average composition of 23.2 at.% Nb, 13.6 at.% Si, 17.0 at.% Ti, 1.8 at.% Cr, 0.9 at.% Al, 0.7 at.% Ge, 2.0 at.% B, and 40.8 at.% O. The layer of oxidised material of JW1-HT13 had an average composition of 18.5 at.% Nb, 12.2 at.% Si, 14.3 at.% Ti, 2.3 at.% Cr, 0.5 at.% Al, 1.1 at.% Ge, 0.9 at.% B, and 50.1 at.% O. The layer of oxidised material of JW1-HT15 had an average composition

of 18.1 at.% Nb, 12.2 at.% Si, 16.6 at.% Ti, 1.9 at.% Cr, 0.8 at.% Al, 0.7 at.% Ge, 1.7 at.% B, and 47.9 at.% O. Compositions of these oxide layers are fairly similar considering the potential for variation.

A layer that is rich in germanium can be seen between the oxide layer and the bulk alloy in each sample of JW1. The average area compositions of these layers are given in Table 6.8. Ge-rich is defined as greater than 10 at.% Ge in this case. It is unclear whether this layer is made up of a new phase or an existing phase has been enriched in Ge during the oxidation process. Considering the Ge content of these layers was at least 16.8 at.% in JW1-HT15, which is greater than any $D8_8$ Ge composition found in the un-oxidised states of any JW series alloy despite this layer also containing a significant amount of O, it is suspected this is a distinct phase. The likely candidates to consider are Nb-Ge phases since these are the major elements in this phase, with the exception of O. It is not considered to be an oxide, or at the very least not a single phase oxide, since total wt% for these layers was more in line with what was found for bulk alloy phases, and not the lower wt% found for oxide phases. In the case of JW1-AC, the ratio of Nb + Ti to Ge + Si is 1.09, so it is uncertain from this compositional information what phase has formed, i.e Nb_5Ge_3, Nb_3Ge, $NbGe_2$, or if multiple phases are present in too fine a distribution to resolve. In the case of JW1-HT13, the ratio of Nb + Ti to Ge + Si is 1.53. This suggest Nb_5Ge_3 is the most likely Ge phase to have formed as this would have a Nb to Ge ratio of 1.67. The hexagonal Mn_5Si_3-type Nb_5Ge_3 can have a higher Ge content than stoichiometry would suggest due to Ge residing on interstitial sites, hence why the phase is sometimes referred to as Nb_3Ge_2 or $Nb_{10}Ge_7$. This usually metastable version of the Nb_5Ge_3 would have slightly lower than 1.67 Nb to Ge ratio. In the case of JW1-HT15, the ratio of Nb + Ti to Ge + Si is 1.27. This alone is not a good indication of which phase is present in this layer as it does not match well to any Nb-Ge phase composition ratio.

There are clear areas where Ge content is greater than the rest of the Ge-rich layer in EPMA maps for JW1-AC, JW1-HT13 and JW1-HT15. Points were taken from these high-Ge areas to calculate the composition given in Table 6.9 for a Nb-Ge phase. Average Nb and Ge contents of this phase in JW1-AC were 24.6 at.% and 52.6 at.%. The ratio of Nb + Ti to Ge + Si is calculated as 0.49. Average Nb and Ge contents of this phase in JW1-HT13 were 19.0 at.% and 37.7 at.%. The ratio of Nb + Ti to Ge + Si is calculated as 0.49. This indicates that $NbGe_2$ has formed in certain places along the Ge-rich layer in JW1-AC and JW1-HT13, as the expected ratio of Nb to Ge in pure $NbGe_2$ would be 0.5. In the case of JW1-HT13, O content of the entire Ge layer is 6.4 at.% greater and O content of the Nb-Ge phase is 14.5 at.% greater when compared to the JW1-AC oxidised specimen. For JW1-HT15 average Nb and Ge contents of this phase were 33.9 at.% and 28.9 at.%. The ratio of Nb + Ti to Ge + Si is calculated as 1.16. This ratio is not indicative of either Nb_5Ge_3 or $NbGe_2$ as a single phase.

Compositions of phases and regions within the oxide layer of each alloy are presented in Table 6.9. Whilst limitation exists with oxygen quantification, which would usually be extremely useful for identification and confirmation of oxide phases, the ratio of key non-oxygen elements can still be relied upon to identify oxides that have formed when used in combination with XRD. For example, the oxide $Ti_2Nb_{10}O_{29}$ would have five times the amount of Nb as Ti present and the oxide $TiNb_2O_7$ only two times, regardless of O content. In each of the oxide scales four oxides are reported on and are designated based on their primary element; Nb-rich oxide, Ti-rich oxide, Cr-rich oxide, and Si-rich oxide. In alloy JW1-AC, quite coarse areas of Ti-rich oxide and Nb-rich oxide are present which allows phase analysis with less risk of reporting non-single phase areas. In JW1-HT13, this is the case for Ti-rich oxide and Cr-rich oxide. In JW1-HT15 there are no coarse areas of oxides so there exists a higher possibility that measurements associated with these phases are not from a single phase. Despite this, compositions of Nb-rich, Ti-rich, Cr-rich and Si-rich oxides are reported in order to facilitate comparison between each oxidised alloy.

For JW1-AC, the Nb-rich phase has Nb and Ti contents of 44.3 at.% and 9.3 at.%, respectively. With a Nb to Ti ratio of 4.79, this phase can be identified as $Ti_2Nb_{10}O_{29}$ which would have a Nb to Ti ratio of 5. Whilst other metallic elements are less than 1 at.%, B content is 5.8 at.%. For JW1-HT13, the Nb-rich phase has Nb and Ti contents of 36.4 at.% and 8.6 at.%, respectively. With a Nb to Ti ratio of 4.21, this phase can be identified as $Ti_2Nb_{10}O_{29}$. This is in agreement with XRD analysis of the oxide surfaces of JW1-AC and JW1-HT13. For JW1-HT15, the Nb-rich phase has Nb and Ti contents of 27.3 at.% and 13.7 at.%, respectively. With a Nb to Ti ratio of 2.00, this phase can be identified as $TiNb_2O_7$ which would have a Nb to Ti ratio of 2. This is in marginal conflict with XRD results, which although found peaks associated with $TiNb_2O_7$, $Ti_2Nb_{10}O_{29}$ was more prominent in all JW1 XRD pattern and $TiNb_2O_7$ was less easily identified in JW1-HT15 compared to JW1-AC and JW1-HT13. This may be explained by the uncertainty that a single phase is being measured, and with a Si content of 8.5 at.% this Nb-rich 'phase' may indeed be made up of multiple oxides that happen to result in a 2:1 ratio of Nb to Ti. This is a limitation to this form of analysis, however certain phenomena such as the Ge layer would have been overlooked had mapping at this magnification not been performed.

For JW1-AC, the Ti-rich phase had average Nb, Ti and Cr contents of 5.0 at.%, 58.8 at.% and 5.2 at.%, respectively. For JW1-HT13, the Ti-rich phase had average Nb, Ti and Cr contents of 8.8 at.%, 40.4 at.% and 3.8 at.%, respectively. For JW1-HT15, the Ti-rich phase had average Nb, Ti and Cr contents of 13.7 at.%, 29.1 at.% and 2.2 at.%, respectively. These phases are identified as rutile TiO_2 with substitution of Nb and Cr onto Ti sites. This is in agreement with XRD of the oxide surface, however the compositions of Nb, Ti and Cr in these Ti rich phases implies a higher degree of substitution of Ti which was not predicted from XRD results as TiO_2 peaks were in near identical locations. In the case of JW1-HT15 since Si content is recorded as 6.6 at.%, where in JW1-AC and JW1-HT13 it was less than 2 at.%, it is more likely this TiO_2 composition is simply not a pure phase and nearby SiO_2 is being included in the measurement.

There exists a partial Cr-rich layer within each of the oxide scales. Points from the thickest parts of these layer were analysed in order to give a phase composition, however there exists the possibility that this measurement is not from a single phase. None the less, EPMA analysis shows Cr is the highest content element excluding O in each instance of the Cr-rich oxide with contents of 32.4 at.%, 31.4 at.% and 21.5 at.% for alloys JW1-AC, JW1-HT13 and JW1-HT15, respectively. In the clearest instance of this Cr-rich phase that is located in JW1-HT13, content of the next two highest elements are 3.0 at.% Nb and 5.8 at.% Ti. This suggests a Cr-O oxide as other elements are relatively minor, therefore this phase is suspected to be Cr_2O_3, although oxide surface XRD evidence and an exact composition match is lacking. There are also small amounts of what appears to be Al-rich partial layers in the oxide scale, but these are too fine to report a reliable composition for any JW1 alloy.

In the Si and Ti maps of each JW1 alloy, a banding structure can be seen of alternating areas richer in Si and Ti in the oxidised $D8_8$ grains. The distribution of these layers is too fine to accurately evaluate phase composition, but the Si-rich parts have been analysed to provide explanation to the peaks assigned to an SiO_2 phase in oxide surface XRD. The compositions recorded for the Si-rich bands in the $D8_8$ structure are given in Table 6.9 for each alloy. Si content in each Si-rich phase are 28.1 at.%, 35.4 at.% and 22.6 at.% for alloys JW1-AC, JW1-HT13 and JW1-HT15, respectively, whilst average Nb content ranges from 10.3 at.% to 18.4 at.% and average Ti content ranges from 9.0 at.% to 11.7 at.%. It is proposed that this is a fine mixture of oxides including SiO_2, where the significant Si content comes from, and TiO_2, $Ti_2Nb_{10}O_{29}$ and $TiNb_2O_7$ where the Ti and Nb come from. The oxides other than SiO_2 that are present in these phases are likely in different quantities in different JW1 alloys, with more $Ti_2Nb_{10}O_{29}$ and $TiNb_2O_7$ in the JW1-AC and JW1-HT15 versions to explain the higher Nb content and more TiO_2 in the JW1-HT13 version to explain the higher proportion of Ti present.

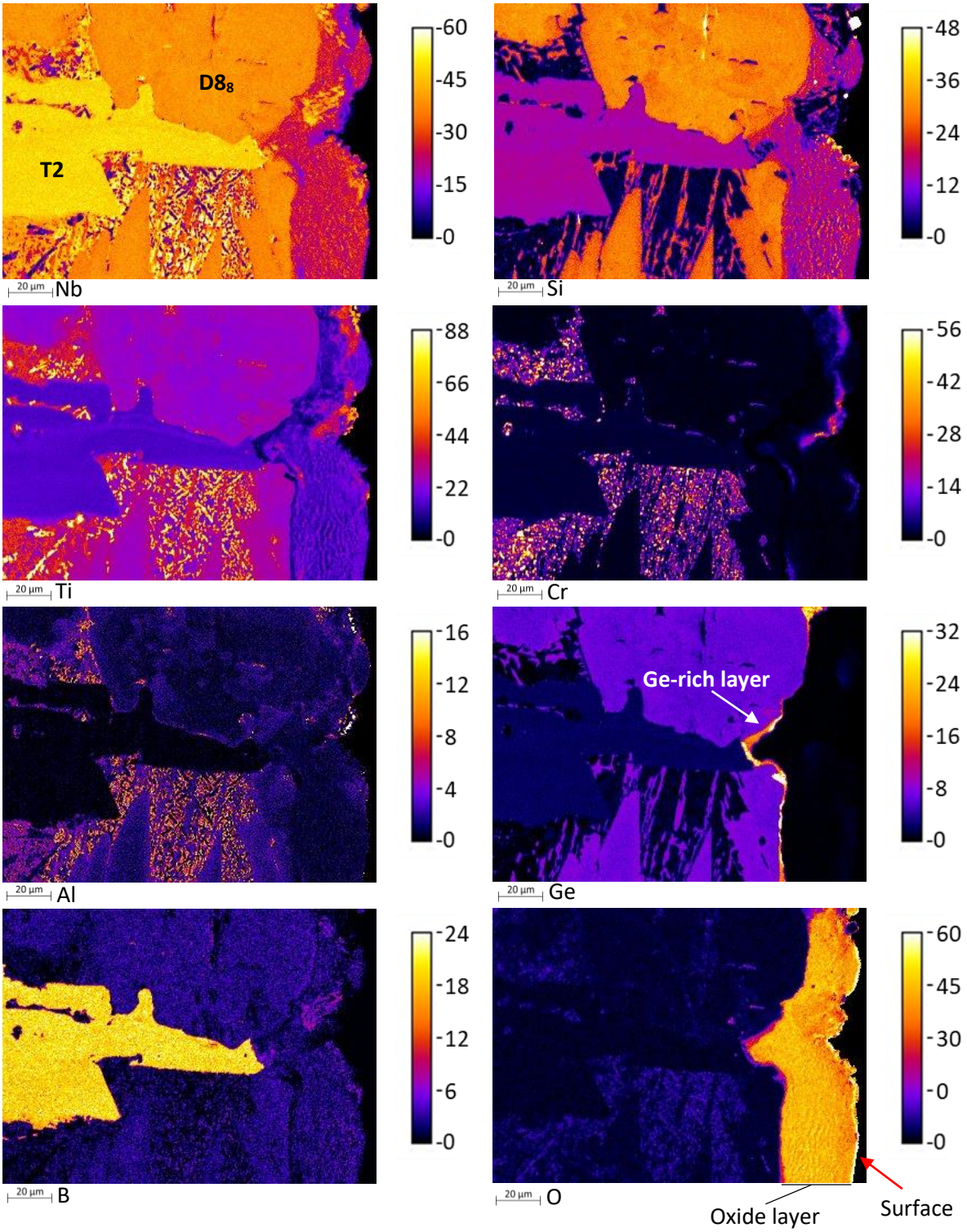

Figure 6.19a - h) EPMA maps of the oxide layer of JW1-AC in at.% of elements a) Nb, b) Si, c) Ti, d) Cr, e) Al, f) Ge, g) B h) O.

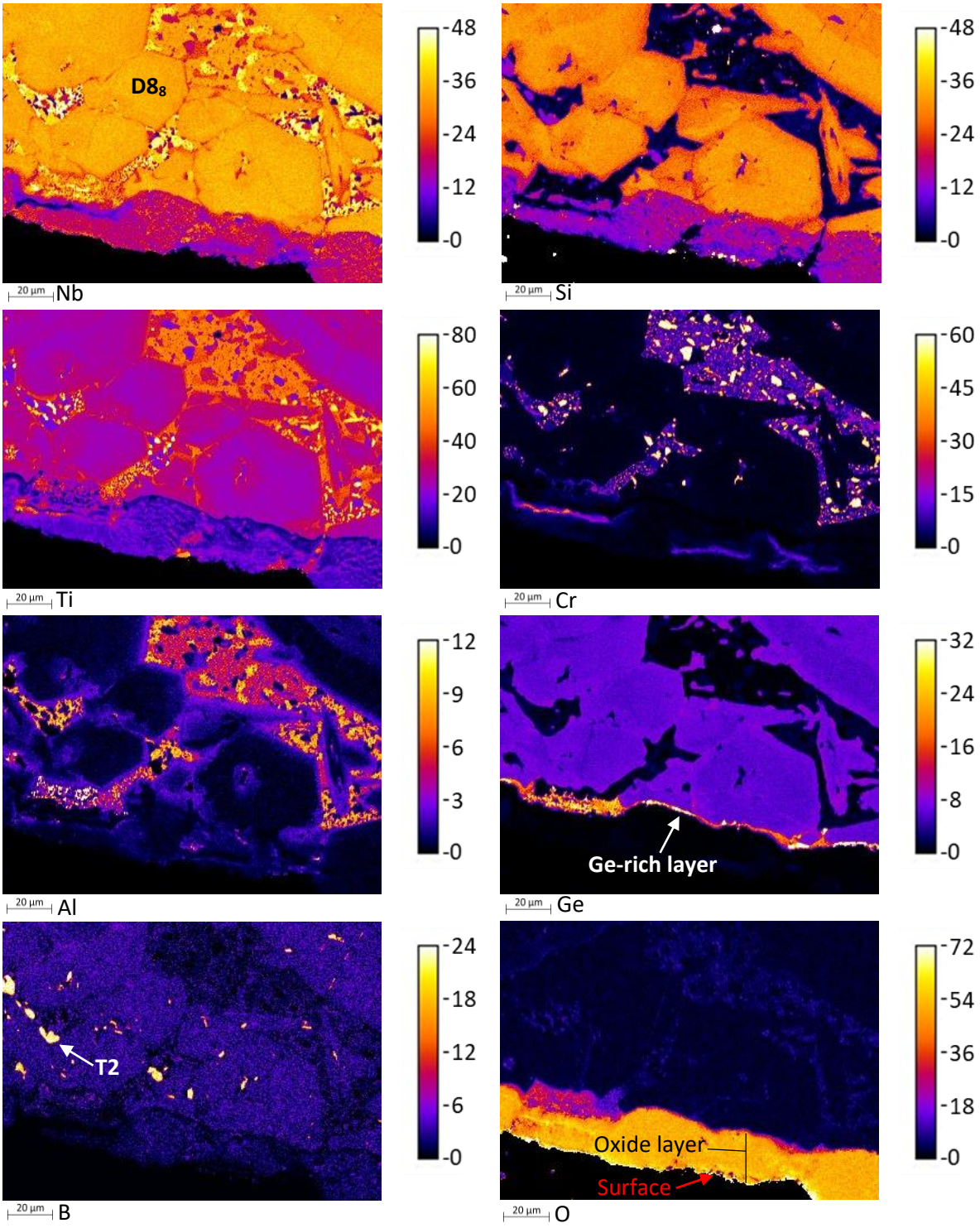

Figure 6.20a-h) EPMA maps of the oxide layer of JW1-HT13 in at.% of elements a) Nb, b) Si, c) Ti, d) Cr, e) Al, f) Ge, g) B h) O.

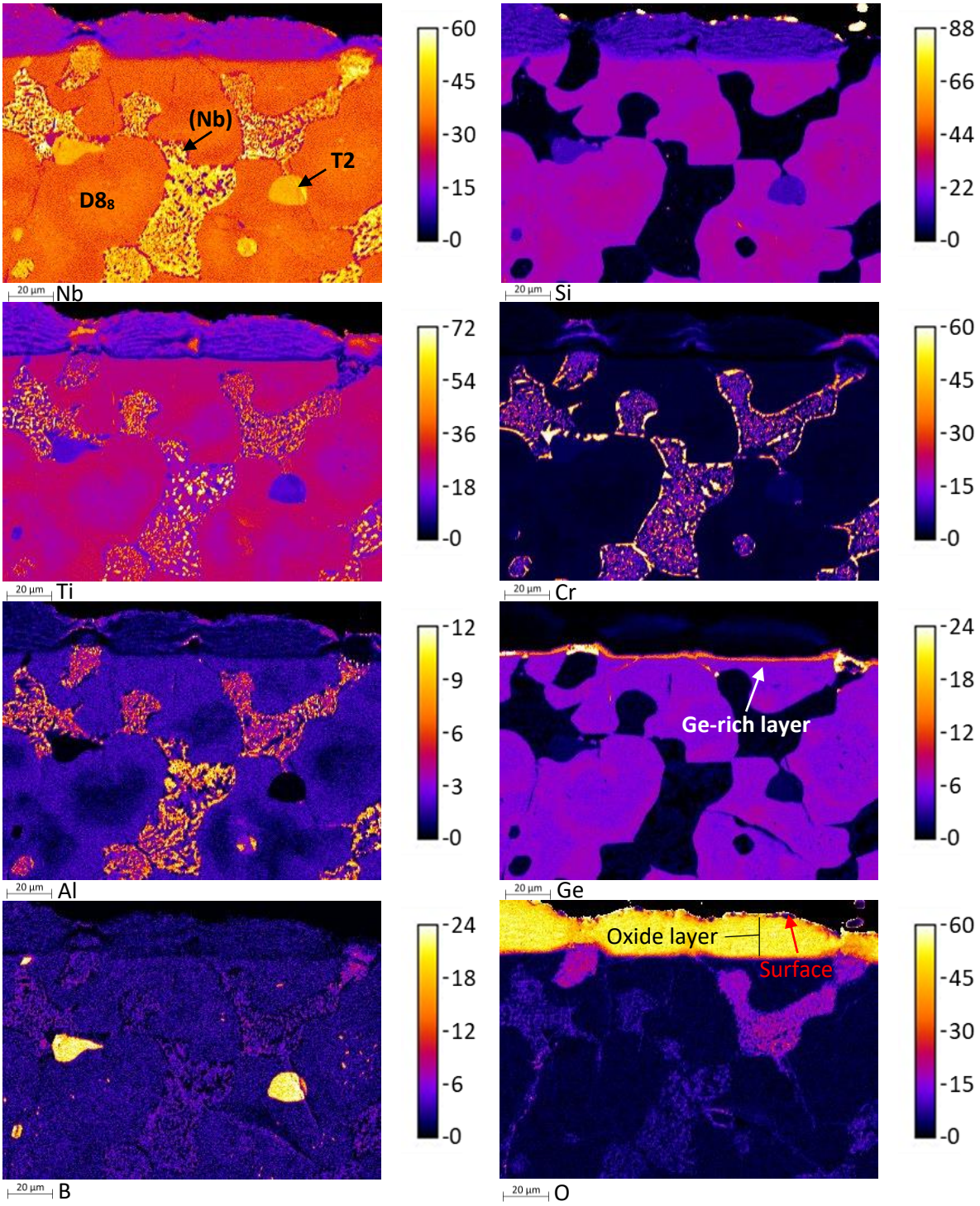

Figure 6.21a-h) EPMA maps of the oxide layer of JW1-HT15 in at.% of elements a) Nb, b) Si, c) Ti, d) Cr, e) Al, f) Ge, g) B h) O.

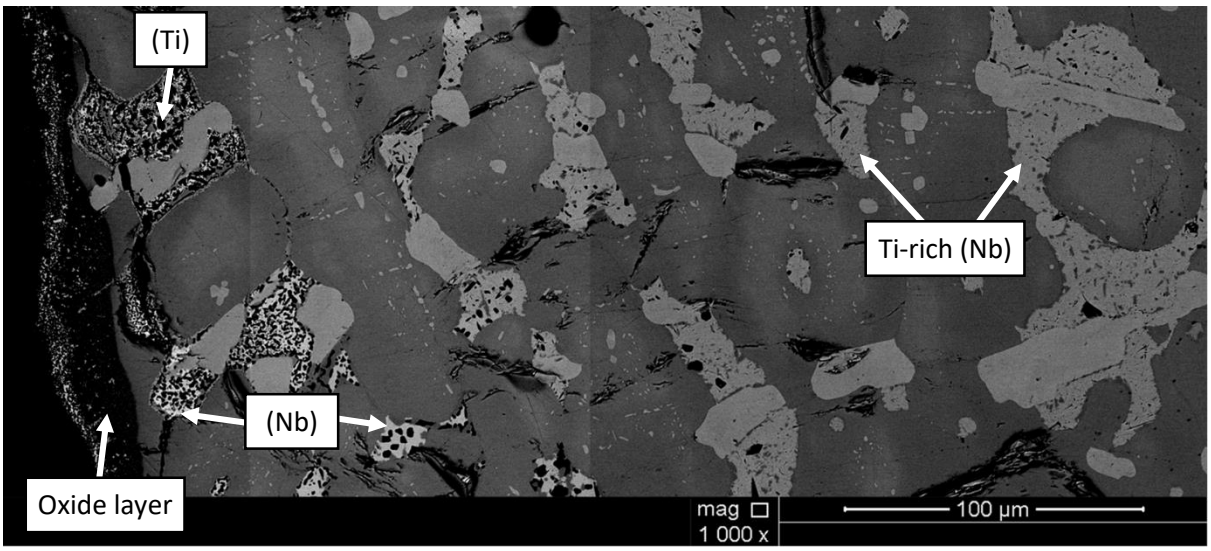

Figure 6.22) SEM-BSE images of JW1-HT15 oxidised at 1000°C overlaid to show the slight difference in contrast between (Nb) and Ti-rich (Nb), as well as lack of (Ti) forming alongside Ti-rich (Nb)

Table 6.6) Phase analysis of bulk phases present in each JW1 oxidised sample EPMA map, values given in at.%.

		Nb	Si	Ti	Cr	Al	Ge	B	O
$D8_8$	JW1-AC	36.0 ± 2.6	28.3 ± 2.5	23.9 ± 1.7	0.7 ± 0.4	0.8 ± 0.8	5.9 ± 0.7	2.5 ± 1.6	1.8 ± 1.2
	JW1-HT13	36.2 ± 2.7	29.6 ± 2.6	22.9 ± 2.0	0.8 ± 0.4	0.5 ± 0.4	5.5 ± 0.8	2.5 ± 1.7	2.0 ± 1.4
	JW1-HT15	33.5 ± 2.6	27.1 ± 2.4	26.3 ± 2.2	1.4 ± 0.4	1.2 ± 0.5	6.1 ± 0.8	2.4 ± 1.9	2.1 ± 1.3
T2	JW1-AC	45.2 ± 2.7	14.5 ± 1.4	14.9 ± 1.1	1.5 ± 0.5	0.1 ± 0.3	1.7 ± 0.4	20.7 ± 2.5	1.4 ± 1.0
	JW1-HT13	40.8 ± 2.5	12.8 ± 1.2	17.0 ± 1.2	5.6 ± 0.8	0.1 ± 0.1	1.4 ± 0.4	21.0 ± 2.3	1.4 ± 1.0
	JW1-HT15	43.3 ± 3.6	13.5 ± 1.4	13.4 ± 1.2	3.1 ± 0.5	0.1 ± 0.2	1.3 ± 0.4	23.7 ± 3.0	1.6 ± 1.5
(Nb)	JW1-AC	51.5 ± 4.8	2.2 ± 1.6	23.5 ± 7.3	8.6 ± 5.0	6.7 ± 2.9	1.3 ± 0.5	3.3 ± 3.2	3.0 ± 1.9
	JW1-HT13	47.5 ± 4.0	2.9 ± 3.3	28.2 ± 4.5	6.1 ± 4.7	8.2 ± 2.7	1.1 ± 0.4	3.8 ± 5.9	2.2 ± 1.6
	JW1-HT15	55.1 ± 4.4	0.8 ± 0.5	20.9 ± 14.0	6.1 ± 3.6	5.1 ± 3.2	0.6 ± 0.6	5.6 ± 2.8	5.9 ± 4.9
Ti-rich (Nb)	JW1-AC	37.7 ± 2.9	1.7 ± 2.0	41.1 ± 2.3	10.7 ± 4.3	3.4 ± 2.3	0.9 ± 1.6	1.2 ± 1.5	3.2 ± 1.4
	JW1-HT13	34.5 ± 2.5	0.7 ± 1.0	44.0 ± 3.0	9.9 ± 5.3	4.9 ± 0.9	0.1 ± 0.2	1.1 ± 1.2	4.7 ± 2.2
(Ti)	JW1-AC	5.3 ± 3.6	0.6 ± 1.8	83.2 ± 14.0	2.4 ± 5.0	0.3 ± 0.4	0.1 ± 0.2	0.1 ± 0.6	8.1 ± 3.0
	JW1-HT13	4.8 ± 4.1	1.6 ± 1.6	76.3 ± 9.7	8.3 ± 7.7	1.0 ± 0.5	0.3 ± 0.4	0.2 ± 0.5	7.3 ± 1.9
	JW1-HT15	12.0 ± 8.0	1.1 ± 3.0	73.1 ± 11.6	2.7 ± 2.9	0.7 ± 0.6	0.3 ± 0.7	0.3 ± 1.1	9.7 ± 3.4
$NbCr_2$	JW1-AC	22.0 ± 3.8	3.8 ± 1.6	18.3 ± 4.5	53.0 ± 3.9	0.4 ± 0.6	0.5 ± 0.5	0.2 ± 0.5	1.8 ± 1.2
	JW1-HT13	19.8 ± 1.8	4.2 ± 1.0	16.6 ± 1.8	56.6 ± 3.0	0.7 ± 0.4	0.2 ± 0.2	0.2 ± 0.5	1.7 ± 1.4
	JW1-HT15	22.5 ± 2.4	4.3 ± 1.6	13.1 ± 3.0	55.3 ± 5.4	0.8 ± 0.7	0.3 ± 0.3	0.4 ± 0.8	3.3 ± 3.0

Table 6.7) Phase analysis of bulk phases present in each JW1 oxidised sample from locations close to the oxide layer (top lines) and from locations far from the oxide layer (bottom lines). Values given in at.%. The distances from the oxide scale vary dependent on what was possible to measure. Alloy:phase-close to:far from; JW1-AC:(Nb) – 20-30µm : 100-130µm, JW1-HT13:(Nb) – 10-15µm : 100-130µm, JW1-HT15:(Nb) - <15µm : 100-130µm, JW1-AC:(Ti) – 15-40µm : 90-125µm, JW1-HT13:(Ti) – 10-35µm : 50-65µm, JW1-HT15:(Ti) - <30µm : 80-100µm, JW1-AC:($D8_8$) - <15µm : 80-125µm, JW1-HT13:($D8_8$) - <15µm : 70-105µm, JW1-HT15:($D8_8$) - <15µm : 90-100µm, JW1-AC:(T2) - <20µm : 110-120µm, JW1-HT13:(T2) – 10-20µm : 65-95µm.

		Nb	Si	Ti	Cr	Al	Ge	B	O
$D8_8$	JW1-AC	35.7 ± 2.6	27.9 ± 2.5	24.3 ± 1.6	0.7 ± 0.3	0.9 ± 0.9	5.9 ± 0.8	2.8 ± 1.6	1.8 ± 1.2
		36.0 ± 2.9	28.4 ± 2.6	23.7 ± 2.2	0.8 ± 0.4	0.8 ± 0.8	5.9 ± 0.8	2.3 ± 1.6	2.2 ± 1.4
	JW1-HT13	35.8 ± 2.7	28.4 ± 2.7	24.0 ± 2.0	0.9 ± 0.5	0.7 ± 0.6	5.9 ± 0.8	2.1 ± 1.5	2.3 ± 1.4
		35.7 ± 2.7	28.5 ± 2.7	23.9 ± 2.3	0.8 ± 0.4	0.6 ± 0.5	5.7 ± 0.8	2.5 ± 1.7	2.2 ± 1.5
	JW1-HT15	33.0 ± 2.6	26.8 ± 2.2	26.5 ± 1.5	1.5 ± 0.4	1.5 ± 0.5	6.0 ± 0.9	2.5 ± 1.8	2.2 ± 1.4
		32.9 ± 2.5	26.5 ± 2.2	27.3 ± 1.9	1.5 ± 0.4	1.3 ± 0.5	6.2 ± 0.8	2.3 ± 1.8	1.9 ± 1.3
T2	JW1-AC	44.5 ± 2.8	14.7 ± 1.3	15.0 ± 1.1	1.4 ± 0.4	0.1 ± 0.3	1.7 ± 0.4	21.0 ± 2.5	1.5 ± 1.0
		45.0 ± 2.7	14.6 ± 1.4	15.2 ± 1.0	1.5 ± 0.4	0.2 ± 0.3	1.8 ± 0.4	20.4 ± 2.6	1.4 ± 1.0
	JW1-HT13	41.4 ± 2.8	12.7 ± 1.1	17.1 ± 1.1	5.7 ± 0.7	0.1 ± 0.1	1.5 ± 0.4	20.1 ± 2.1	1.5 ± 1.1
		40.1 ± 2.3	12.6 ± 1.1	16.9 ± 1.8	5.3 ± 1.2	0.1 ± 0.1	1.6 ± 0.4	22.5 ± 2.0	0.9 ± 0.8
(Nb)	JW1-AC	52.6 ± 2.9	1.8 ± 0.7	20.5 ± 6.8	10.7 ± 6.0	6.8 ± 3.9	1.0 ± 0.4	3.7 ± 2.5	2.8 ± 1.7
		46.5 ± 3.3	1.8 ± 0.7	29.0 ± 4.8	8.6 ± 4.6	7.2 ± 1.9	1.3 ± 0.4	2.6 ± 1.3	3.0 ± 2.1
	JW1-HT13	49.7 ± 5.4	1.9 ± 0.9	26.6 ± 4.7	7.8 ± 7.0	8.8 ± 1.7	1.0 ± 0.5	2.4 ± 1.9	1.8 ± 1.6
		46.7 ± 2.6	2.1 ± 0.7	30.4 ± 1.9	6.1 ± 5.2	9.1 ± 1.6	1.1 ± 0.3	1.8 ± 1.8	2.6 ± 1.7
	JW1-HT15	57.2 ± 3.2	0.8 ± 0.3	12.6 ± 5.1	5.2 ± 3.7	6.2 ± 2.0	0.8 ± 0.7	6.5 ± 3.2	10.7 ± 6.2
		49.9 ± 3.1	0.8 ± 0.6	29.1 ± 18.3	7.2 ± 3.0	3.4 ± 2.5	0.3 ± 0.4	4.8 ± 2.0	4.5 ± 3.3
(Ti)	JW1-AC	7.3 ± 4.6	1.0 ± 3.0	80.0 ± 18.5	2.2 ± 2.2	0.1 ± 0.3	0.1 ± 0.1	0.2 ± 1.0	9.1 ± 4.4
		3.6 ± 1.5	0.1 ± 0.2	87.2 ± 2.2	1.2 ± 1.6	0.3 ± 0.5	0.1 ± 0.1	0.0 ± 0.0	7.4 ± 1.7
	JW1-HT13	6.5 ± 5.2	0.4 ± 0.3	82.6 ± 6.6	1.9 ± 3.2	0.8 ± 0.4	0.1 ± 0.1	0.0 ± 0.0	7.9 ± 2.6
		4.5 ± 4.0	3.2 ± 1.0	67.2 ± 4.9	15.5 ± 4.8	1.5 ± 0.4	0.7 ± 0.3	0.5 ± 0.7	6.9 ± 1.3
	JW1-HT15	13.4 ± 8.1	0.6 ± 0.4	68.5 ± 14.0	3.9 ± 3.3	1.2 ± 0.8	0.2 ± 0.2	0.3 ± 1.1	11.8 ± 5.3
		15.8 ± 8.6	2.5 ± 5.0	68.9 ± 6.8	2.7 ± 2.0	0.5 ± 0.4	0.6 ± 1.1	0.7 ± 1.6	8.3 ± 1.8

Table 6.8) Area analysis of the entire oxide layers and Ge-rich layers shown in EPMA maps for JW1 oxidised samples

		Nb	Si	Ti	Cr	Al	Ge	B	O
Total oxide layer:	JW1-AC	23.2 ± 6.1	13.6 ± 6.8	17.0 ± 7.8	1.8 ± 3.5	0.9 ± 4.0	0.7 ± 3.1	2.0 ± 2.0	40.8 ± 8.9
	JW1-HT13	18.5 ± 4.3	12.2 ± 5.1	14.3 ± 5.6	2.3 ± 4.3	0.5 ± 0.6	1.1 ± 3.6	0.9 ± 1.1	50.1 ± 9.6
	JW1-HT15	18.1 ± 3.8	12.2 ± 5.1	16.6 ± 6.1	1.9 ± 2.8	0.8 ± 0.6	0.7 ± 2.0	1.7 ± 1.4	47.9 ± 7.9
Ge-rich layer:	JW1-AC	31.2 ± 6.9	13.2 ± 7.8	9.3 ± 5.7	0.7 ± 1.3	1.4 ± 2.9	24.1 ± 9.7	1.5 ± 2.6	18.5 ± 7.8
	JW1-HT13	28.3 ± 5.7	9.2 ± 9.2	14.8 ± 8.8	1.1 ± 1.2	2.1 ± 3.0	18.9 ± 6.8	0.7 ± 1.0	24.9 ± 10.6
	JW1-HT15	29.8 ± 5.5	14.6 ± 9.2	10.0 ± 4.6	1.1 ± 1.8	1.8 ± 2.0	16.8 ± 4.4	1.4 ± 1.4	24.6 ± 10.0

Table 6.9) Phase analysis of oxide phases in each JW1 oxidised sample from locations in the oxide scale, values given in at.%.

		Nb	Si	Ti	Cr	Al	Ge	B	O
Ge-rich phase	JW1-AC	24.6 ± 3.0	4.7 ± 5.9	3.8 ± 3.8	0.2 ± 0.2	1.6 ± 2.1	52.6 ± 7.3	0.0 ± 0.0	12.6 ± 4.7
	JW1-HT13	19.0 ± 2.6	10.6 ± 3.3	4.6 ± 2.0	0.2 ± 0.2	0.4 ± 0.3	37.7 ± 3.6	0.4 ± 1.2	27.2 ± 8.8
	JW1-HT15	33.9 ± 10.9	6.3 ± 8.2	7.0 ± 5.5	2.0 ± 1.7	2.0 ± 2.5	28.9 ± 4.7	1.5 ± 1.6	18.4 ± 8.5
Ti-rich oxide	JW1-AC	5.0 ± 3.9	0.7 ± 1.0	58.8 ± 5.6	5.2 ± 2.0	0.2 ± 0.3	0.0 ± 0.1	0.0 ± 0.0	30.1 ± 7.8
	JW1-HT13	8.8 ± 3.5	1.8 ± 2.4	40.4 ± 7.5	3.8 ± 3.3	0.3 ± 0.4	0.1 ± 0.1	0.2 ± 0.4	44.6 ± 6.1
	JW1-HT15	13.7 ± 2.8	6.6 ± 2.9	29.1 ± 2.2	2.2 ± 0.7	2.1 ± 0.8	0.4 ± 0.3	1.0 ± 1.1	44.9 ± 8.3
Nb-rich oxide	JW1-AC	44.3 ± 2.2	1.6 ± 0.6	9.3 ± 5.1	0.5 ± 0.9	0.6 ± 0.7	0.1 ± 0.1	5.8 ± 2.7	37.8 ± 2.7
	JW1-HT13	36.4 ± 2.2	1.5 ± 2.4	8.6 ± 2.3	0.3 ± 0.4	0.5 ± 0.8	0.0 ± 0.1	3.9 ± 0.9	48.6 ± 4.7
	JW1-HT15	27.3 ± 2.1	8.5 ± 4.7	13.7 ± 4.1	0.8 ± 0.5	0.9 ± 0.5	0.3 ± 0.3	4.0 ± 2.5	44.5 ± 7.0
Si-rich oxide	JW1-AC	18.4 ± 2.9	28.1 ± 4.1	9.0 ± 2.4	0.2 ± 0.3	0.5 ± 0.5	0.2 ± 0.2	1.3 ± 1.4	42.4 ± 5.4
	JW1-HT13	10.3 ± 7.8	35.4 ± 5.6	10.4 ± 6.3	1.2 ± 1.3	0.3 ± 0.3	0.2 ± 0.4	0.2 ± 0.5	42.0 ± 28.8
	JW1-HT15	15.6 ± 2.6	22.6 ± 4.6	11.7 ± 3.3	0.7 ± 0.4	0.6 ± 0.4	0.4 ± 0.3	0.7 ± 0.6	47.8 ± 8.1
Cr-rich oxide	JW1-AC	5.4 ± 2.6	2.3 ± 2.3	10.9 ± 2.9	32.4 ± 8.4	3.9 ± 3.5	0.0 ± 0.1	0.0 ± 0.0	45.1 ± 13.7
	JW1-HT13	3.0 ± 3.5	1.1 ± 1.9	5.8 ± 2.6	31.4 ± 9.7	0.8 ± 0.4	0.0 ± 0.1	0.0 ± 0.0	58.0 ± 9.0
	JW1-HT15	9.7 ± 4.9	7.4 ± 6.8	12.1 ± 3.6	21.5 ± 7.8	1.3 ± 1.4	0.0 ± 0.1	0.4 ± 0.6	47.6 ± 10.8

6.2.2.3 JW2

6.2.2.3.1 XRD

The XRD pattern of JW2-AC is shown in Figure 6.23. The phases that are identified are TiO_2, $Ti_2Nb_{10}O_{29}$ and $TiNb_2O_7$. The XRD pattern of JW2-HT13 is shown in Figure 6.24. The phases that are identified are TiO_2, $Ti_2Nb_{10}O_{29}$ and $TiNb_2O_7$. The XRD pattern of JW2-HT15 is shown in Figure 6.25. The phases that are identified are TiO_2, $Ti_2Nb_{10}O_{29}$, $TiNb_2O_7$, SiO_2, Nb_5Ge_3.

In the case of the JW2-HT13 XRD pattern, $TiNb_2O_7$ cannot be confirmed to the same degree of confidence as other phases present throughout JW2 patterns since $Ti_2Nb_{10}O_{29}$ and $TiNb_2O_7$ peaks are interfering to a greater degree. Also in the JW2-HT13 pattern is an unexplained peak at approximately 19° that does not match to any phase considered. In the case of JW2-HT15, phases $Ti_2Nb_{10}O_{29}$ and $TiNb_2O_7$ are significantly diminished compared to the as-cast pattern but both can both still be identified. Whilst minor differences in relative intensities of peaks could be associated to relative orientation of TiO_2, $Ti_2Nb_{10}O_{29}$ and $TiNb_2O_7$ phases within the samples, this large disparity would suggest proportionally more TiO_2 is present relative to other Ti and Nb oxides in JW2-HT15 and JW2-HT13 than in JW2-AC. The existence of the SiO_2 phase in JW2-HT15 is more speculative than in JW1, as the unique low angle peak is less apparent and has intensity barely above background readings. Also in the JW2-HT15 oxidised specimen it is proposed that some hexagonal Nb_5X_3 phase with the Mn_5Si_3-prototype structure is identified through XRD beneath the oxide scale. Whilst this could be underlying $D8_8$, the metastable germanium phase Nb_5Ge_3 is a better match to these peaks, would not be as deep below the scale as $D8_8$, and can be confirmed through EPMA results as a Ge-rich layer with approximate elements ratios of Nb_5Ge_3 in the following section (6.2.2.3.2). Hence why Nb_5Ge_3 is included in the phases in Figure 6.25 to explain peaks either side of 40°. A thinner oxide scale compared to other specimens may have allowed this.

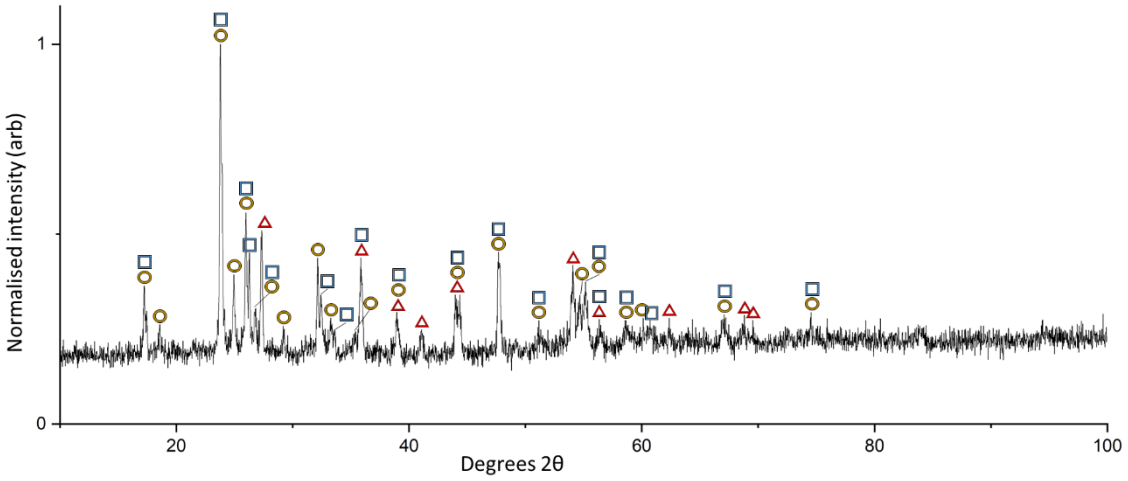

Figure 6.23) XRD pattern of oxidised at 1000°C JW2-AC. △ = TiO_2, ○ = $Ti_2Nb_{10}O_{29}$, □ = $TiNb_2O_7$

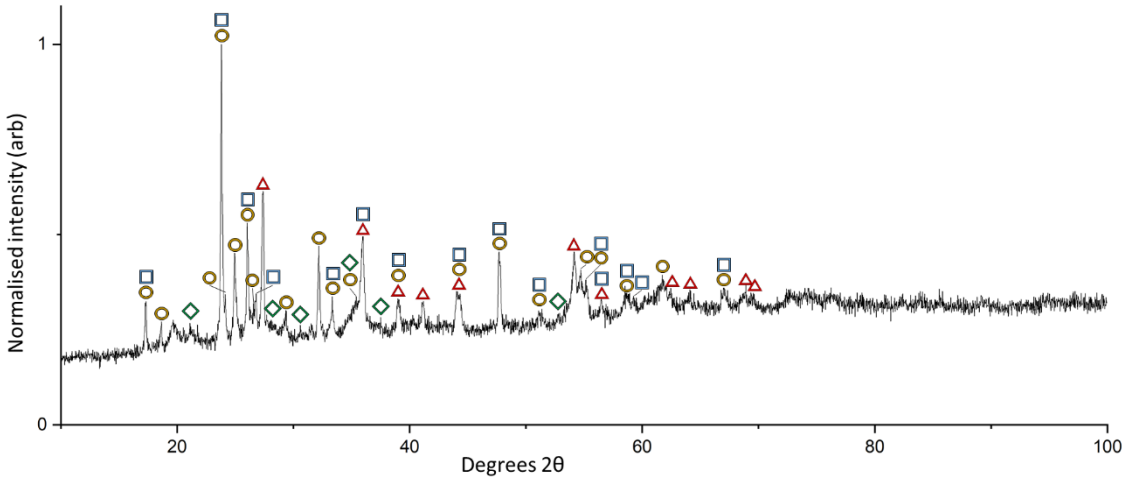

Figure 6.24) XRD pattern of oxidised at 1000°C JW2-HT13. △ = TiO_2, ○ = $Ti_2Nb_{10}O_{29}$, □ = $TiNb_2O_7$

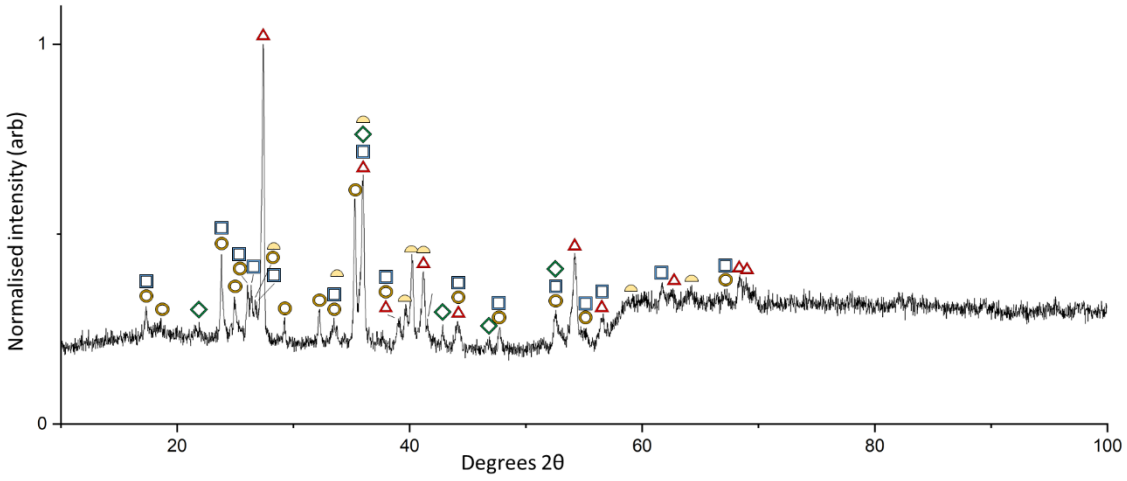

Figure 6.25) XRD pattern of oxidised at 1000°C JW2-HT15. △ = TiO_2, ○ = $Ti_2Nb_{10}O_{29}$, □ = $TiNb_2O_7$, ◇ = SiO_2, ◠ = Nb_5Ge_3

6.2.2.3.2 EPMA

EPMA mapping of oxidised JW2 samples at 1000°C including elements Nb, Si, Ti, Cr, Al, Ge, B and O is presented in Figure 6.26, Figure 6.27 and Figure 6.28 for the as-cast state, heat-treated at 1300°C state and heat-treated at 1500°C state, respectively.

In the bulk of each oxidised sample, four phases were identified; (Ti), $NbCr_2$, $D8_8$ and T2. Phases (Nb) and NbB were identified in JW2-AC and JW2-HT13, as well as a Ti-rich (Nb) phase in JW2-AC. These compositions are listed in Table 6.10. Phases $NbCr_2$, $D8_8$ and T2 are in agreement with the un-oxidised microstructures, and NbB is expected in JW2-AC and JW2-HT13. (Nb) being found in JW2-AC and JW2-HT13 is consistent with un-oxidised microstructures as well, but would also be expected in small quantities in JW2-HT15 but this is not the case. The (Ti) phase is again unique to the oxidised microstructures with considerably more Ti than Nb content in each instance of this phase.

Similar to the microstructure of JW1 specimens, (Nb), (Ti), and $NbCr_2$ exists in a mixture located between $D8_8$ and NbB grains in JW2-AC and JW2-HT13. The (Nb) phase found in JW2-HT13 is particularly high in Al, 26.4 ± 12.0 at.%, compared to other occurrences of this phase in oxidised

JW2-AC and all oxidised JW1 specimens discussed previously. However, this is within error of the Al content found in un-oxidised (Nb) in JW2-HT13, 20.6 at.%, so this is in line with the un-oxidised microstructure. In the case of JW2-HT15, there is considerably less of these phases and no (Nb) present in this mapped location, although (Ti) and $NbCr_2$ are usually found together still. A notable difference between the as-cast sample and the heat-treated samples with regards to these non-silicide/non-boride phases is how $NbCr_2$ is not only found in a fine mixture with (Nb) and (Ti), but also in coarse arrangements that are orders of magnitude larger in the case of the heat-treated alloys. In terms of oxygen content of these phases, (Nb) had 3.7 at.% and 3.7 at.% O in JW2-AC and JW2-HT13 respectively, (Ti) had 4.4 at.%, 8.3 at.%, and 12.6 at.% O in JW2-AC, JW2-HT13, and JW2-HT15 respectively, and $NbCr_2$ had 1.6 at.%, 3.3 at.%, and 1.9 at.% in JW2-AC, JW2-HT13, and JW2-HT15 respectively. In the JW1 counterparts of these phases, (Ti) was deemed the most susceptible to oxidation and $NbCr_2$ the least. Although this trend is less obvious across all JW2 samples than was the case with JW1 samples due to varied O contents, this trend holds true for each individual JW2 alloy when comparing the phases internally. The same limitations apply regarding O content as described in previous sections.

Further away from the scale of JW2-AC, on the right hand side of the EPMA maps in Figure 6.26, the Ti-rich (Nb) appears to replace the (Nb) in the same manner observed in JW1 samples. The same mechanism of Ti-rich (Nb) -> (Ti) + (Nb) is proposed to also be taking place in this sample. This is not observed in JW2-HT13 or JW2-HT15, likely in this case related to the disconnected and lesser amounts of oxygen susceptible phases.

Where possible the average composition of bulk phases close to and far from the oxide scales were calculated (Table 6.11). Typically, in the case of JW2, this results in compositions given from 0µm to 65µm from the oxide scale compare to composition from 40µm to 125µm from the oxide scale, for 'close to' and 'far from' labels, respectively. For phase $D8_8$, T2, NbB and (Ti) there was less than 1 at.% variance in O content from close to and far from the oxide scale so no significant gradient in O content exists. In the case of (Nb) in JW2-AC and $NbCr_2$ in JW2-HT13, O content reduced from 5.9 at.% to 2.4 at.% and 11.7 at.% to 2.4 at.%, respectively.

Area analysis was performed using EPMA data in order to report average compositions of specific areas of the oxide scale, shown in Table 6.13. The layer of oxidised material of JW2-AC had an average composition of 19.9 at.% Nb, 15.7 at.% Si, 18.1 at.% Ti, 2.2 at.% Cr, 0.3 at.% Al, 1.1 at.% Ge, 1.4 at.% B, and 41.3 at.% O. The layer of oxidised material of JW2-HT13 had an average composition of 15.3 at.% Nb, 11.7 at.% Si, 18.7 at.% Ti, 3.1 at.% Cr, 3.1 at.% Al, 1.4 at.% Ge, 1.2 at.% B, and 45.6 at.% O. The layer of oxidised material of JW1-HT15 had an average composition of 21.0 at.% Nb, 13.0 at.% Si, 19.3 at.% Ti, 2.1 at.% Cr, 1.2 at.% Al, 2.9 at.% Ge, 2.0 at.% B, and 38.5 at.% O.

A layer that is rich in Ge can be seen between the oxide layer and the bulk alloy in each sample of JW2 in a similar way to the JW1 samples. As was also the case with JW1 Ge-rich phases, the ratios of certain elements are considered to identify this phase. The Ge-rich layer of JW2-AC has a ratio of Nb + Ti to Ge + Si of to 0.97, so it is uncertain from this compositional information what phase has formed, i.e Nb_5Ge_3, Nb_3Ge, $NbGe_2$, or if multiple phases are present in too fine a distribution to resolve. In the case of JW2-HT13, the ratio of Nb + Ti to Ge + Si is 1.07. So again it is uncertain from this compositional information what phase has formed. In the case of JW2-HT15, the ratio of Nb + Ti to Ge + Si is 1.49. This is closer to the ratio expected for Nb_5Ge_3 (1.67), therefore there is a strong possibility that this is the phase to have formed.

There are clear areas where Ge content is greater than the rest of the Ge-rich layer in EPMA maps for JW2-AC and JW2-HT13. Points were taken from these high-Ge areas to calculate the composition

given in Table 6.14 for a Nb-Ge phase. Average Nb and Ge contents of this phase in JW2-AC were 22.6 at.% and 45.6 at.%. The ratio of Nb + Ti to Ge + Si is calculated as 0.58. Average Nb and Ge contents of this phase in JW2-HT13 were 19.3 at.% and 38.7 at.%. The ratio of Nb + Ti to Ge + Si is calculated as 0.57. This indicates that $NbGe_2$ has formed in certain places along the Ge-rich layer in JW2-AC and JW2-HT13, as the expected ratio of Nb to Ge in pure $NbGe_2$ would be 0.5. The ratio of Nb + Ti to Ge + Si in the highest Ge locations in the Ge-rich layer in JW2-HT15 is 1.40, indicating that if a niobium germanium phase has formed it is most likely Nb_5Ge_3, as was the case with the entire Ge layer of JW2-HT15.

Compositions of phases and regions within the oxide layer of each alloy are presented in Table 6.14. The same limitation with oxygen quantification discussed previously exists in the following JW2 results, so the ratio of key non-oxygen elements can be relied upon to identify oxides that have formed when used in combination with XRD. In each of the oxide scales four oxides are reported on and are designated based on their primary element: Nb-rich oxide, Ti-rich oxide, Cr-rich oxide, and Si-rich oxide. In alloy JW2-AC, quite coarse areas of Ti-rich oxide and Cr-rich oxide are present which allows phase analysis with less risk of reporting non-single phase areas. In addition, with JW2-AC there is a portion of Ti-rich oxide that is reported on separately as it is considered to have a low degree of substitution compared to the usual Ti-rich oxide $(Ti,Cr,Nb)O_2$. This is labelled low-sub TiO_2 in Table 6.14. In JW2-HT13, this is also the case regarding low substitution TiO_2, and for the coarse Ti-rich oxide and Cr-rich oxide. There is also an Al-rich layer that is large enough to obtain reliable results for in JW2-HT13. In JW2-HT15 the Ti-rich oxide phase is the only oxide phase that exists in a coarse enough arrangement to have confidence placed that this a single phase. Despite a greater risk of reporting on non-single phases, compositions of Nb-rich, Ti-rich, Cr-rich and Si-rich oxides are reported on in order to facilitate comparison between each oxidised alloy.

For JW2-AC, the Nb-rich phase has Nb and Ti contents of 29.2 at.% and 15.9 at.%, respectively. With a Nb to Ti ratio of 1.84, this phase can be identified as $TiNb_2O_7$ which would have a Nb to Ti ratio of 2. For JW2-HT13, the Nb-rich phase has Nb and Ti contents of 29.1 at.% and 10.8 at.%, respectively. With a Nb to Ti ratio of 2.69, this phase can be identified as $TiNb_2O_7$. For JW2-HT15, the Nb-rich phase has Nb and Ti contents of 36.5 at.% and 10.2 at.%, respectively. With a Nb to Ti ratio of 3.58, this phase cannot be identified as either $TiNb_2O_7$ or $Ti_2Nb_{10}O_{29}$. In all cases of the Nb-rich oxide phase in JW2 there exists the possibility of non-single phase measurements being recorded due to the fine nature of this phase. The Si contents of this Nb-rich oxide phase are a good indication that this is the case, ranging from 6.6 at.% to 11.2 at.%, as where this was recorded as a single phase in JW1-AC the Si content was expectedly low in $Ti_2Nb_{10}O_{29}$, at 1.6 at.%. Especially for JW2-HT15 it is likely that the Nb-rich oxide phase is made up of both $TiNb_2O_7$ and $Ti_2Nb_{10}O_{29}$ given the corresponding Nb/Ti ratio. Both $TiNb_2O_7$ and $Ti_2Nb_{10}O_{29}$ are predicated from XRD in all three JW2 alloys, so these results are in agreement, although more evidence of $Ti_2Nb_{10}O_{29}$ would be expected.

For JW2-AC, the Ti-rich phase had average Nb, Ti and Cr contents of 11.3 at.%, 42.4 at.% and 2.5 at.%, respectively. For JW2-HT13, the Ti-rich phase had average Nb, Ti and Cr contents of 12.1 at.%, 32.1 at.% and 2.6 at.%, respectively. For JW2-HT15, the Ti-rich phase had average Nb, Ti and Cr contents of 10.2 at.%, 49.2 at.% and 5.2 at.%, respectively. These phases are identified as rutile TiO_2 with substitution of Nb and Cr onto Ti sites. These phases were measured from the banding structure seen in the Ti and Si maps in the oxidised layer.

In Ti maps of JW2-AC and JW2-HT13, higher concentrations of Ti in coarser arrangements can be seen in areas of the oxide scale that formed on locations that were absent of $D8_8$. In these cases, the phase is almost solely made up of Ti and O. No splitting of the peaks assigned to TiO_2 in XRD Figure 6.23 or Figure 6.24 was noted, so this 'low substitution' TiO_2 exists in small enough quantities to not

be detected through XRD or is superseded by the mixed rutile peaks of (Ti,Cr,Nb)O_2. In JW2-AC and JW2-HT13 Ti contents of this low substitution TiO_2 phase were 61.8 at.% and 56.7 at.% respectively. The only other element in both versions of this phase that existed in greater amounts than 1.0 at.% was Cr at 1.8 at.% and 1.5 at.% for JW2-AC and JW2-HT13, respectively. There is evidence for this phenomena occurring in JW2-HT15 in the area of the oxide scale at the top of the image that formed on T2 and not $D8_8$, but could not reliably be measured.

There exists a partial Cr-rich layer within each of the oxide scales. This is most prominent where the oxide scale has formed on an area absent of $D8_8$ in alloys JW2-AC and JW2-HT13 as was the case with the pure TiO_2 phase. Cr is the dominant element excluding O in each of these layers, but both JW2-AC and JW2-HT15 have more of Nb, Si and Ti than the JW2-HT13 version as the JW2-AC and JW2-HT15 Cr layers are likely not single phase. In JW2-HT13 the Cr and O contents are 34.7 at.% and 55.8 at.%, respectively. With a Cr/O ratio of 0.62, a high degree of confidence that this phase is Cr_2O_3, as this would have a Cr/O ratio of 0.67. It is plausible that other instances where Cr is the highest non-oxygen element could be Cr_2O_3 as well, except with more substitution or contamination from other underlying phases. There was no Cr oxide phase identified in XRD of JW2 samples, likely due to forming in too small amounts to be detected. Also in JW2-HT13 adjacent to the Cr-rich oxide phase is a portion of the oxide scale that is especially rich in Al. It was possible to reliably measure the composition of this area due to its thickness, and a total wt.% of 90.8 was achieved which is more in line with the bulk phases measured. This Al-rich phase was mainly Al and O, 69.7 at.% and 28.1 at.%, respectively. An Al solid solution has very low solubility of oxygen [203] and the only oxide of Al stable at room temperature is Al_2O_3, so this phase is proposed to be a mixture of (Al) and Al_2O_3, although why Al has segregated is currently unclear.

In the Si and Ti maps of each JW2 alloy, a banding structure can be seen of alternating areas richer in Si and Ti. These bands are found in the scale paralleled to where $D8_8$ was exposed to the surface, and is presumably mainly oxidised $D8_8$. The Ti-rich bands are previously discussed as the TiO_2 phase with Nb and Cr substitutions. The Si-rich bands are in too a fine distribution to accurately evaluate phase composition. However, the Si-rich parts have been analysed to provide explanation to the peaks assigned to an SiO_2 phase in oxide surface XRD. The composition recorded for the Si-rich bands in the $D8_8$ structure is given in Table 6.14 for each alloy. Si content in each Si-rich phase is 25.9 at.%, 25.6 at.% and 29.4 at.% for alloys JW2-AC, JW2-HT13 and JW2-HT15, respectively, whilst average Nb content ranges from 11.8 at.% to 14.0 at.% and average Ti content ranges from 8.1 at.% to 17.3 at.%. It is proposed that this is a fine mixture of oxides including SiO_2, where the significant Si content comes from, and TiO_2 , $Ti_2Nb_{10}O_{29}$ and $TiNb_2O_7$ where the Ti and Nb come from. The oxides other than SiO_2 that are present in these phases are likely in different quantities in different JW2 alloys, with more $Ti_2Nb_{10}O_{29}$ and $TiNb_2O_7$ in the JW2-AC and JW2-HT13 versions to explain the higher Nb content and more TiO_2 in the JW2-HT15 version to explain the higher proportion of Ti present. This is consistent with XRD results for this alloy where in Figure 6.25 the XRD pattern of JW2-HT15 is dominated by TiO_2 peaks.

There exists small amount of a high niobium and high boron phase just below the oxide layer to the right side of the EPMA of JW2-HT13. The composition of this phase is recorded in Table 6.10 as niobium-boron phase as it is not clear what this phase is based on composition alone. The B content of this phase is only 23.0 at.% and the Ti content is only 4.1 at.%. These are both significantly lower than what would be expected in NbB. There is potential that this is the result of the beginning of NbB oxidation where elements with a higher affinity to O, such as Ti, and elements that may be more volatile, such as B, leave the structure of NbB and what is recorded is what remains, i.e high Nb content and reduced B content. Where the NbB phase was encountered in the bulk material it was

the least oxidised phase within the respective alloy. However, this may have led to little boron interaction with the oxide scale as there is no significant difference between JW1 and JW2 alloys in terms of B contents of oxides, despite the 10 at.% of B in JW2. In the alloy where NbB was removed through heat treatment at 1500^{o}C, the best oxidation performance was seen in JW2-HT15 at 1000^{o}C. B is shown to mainly be found in the Nb-rich oxide phases, whether that be $Ti_2Nb_{10}O_{29}$ or $TiNb_2O_7$, and not particularly in the Si-rich phase associated with SiO_2.

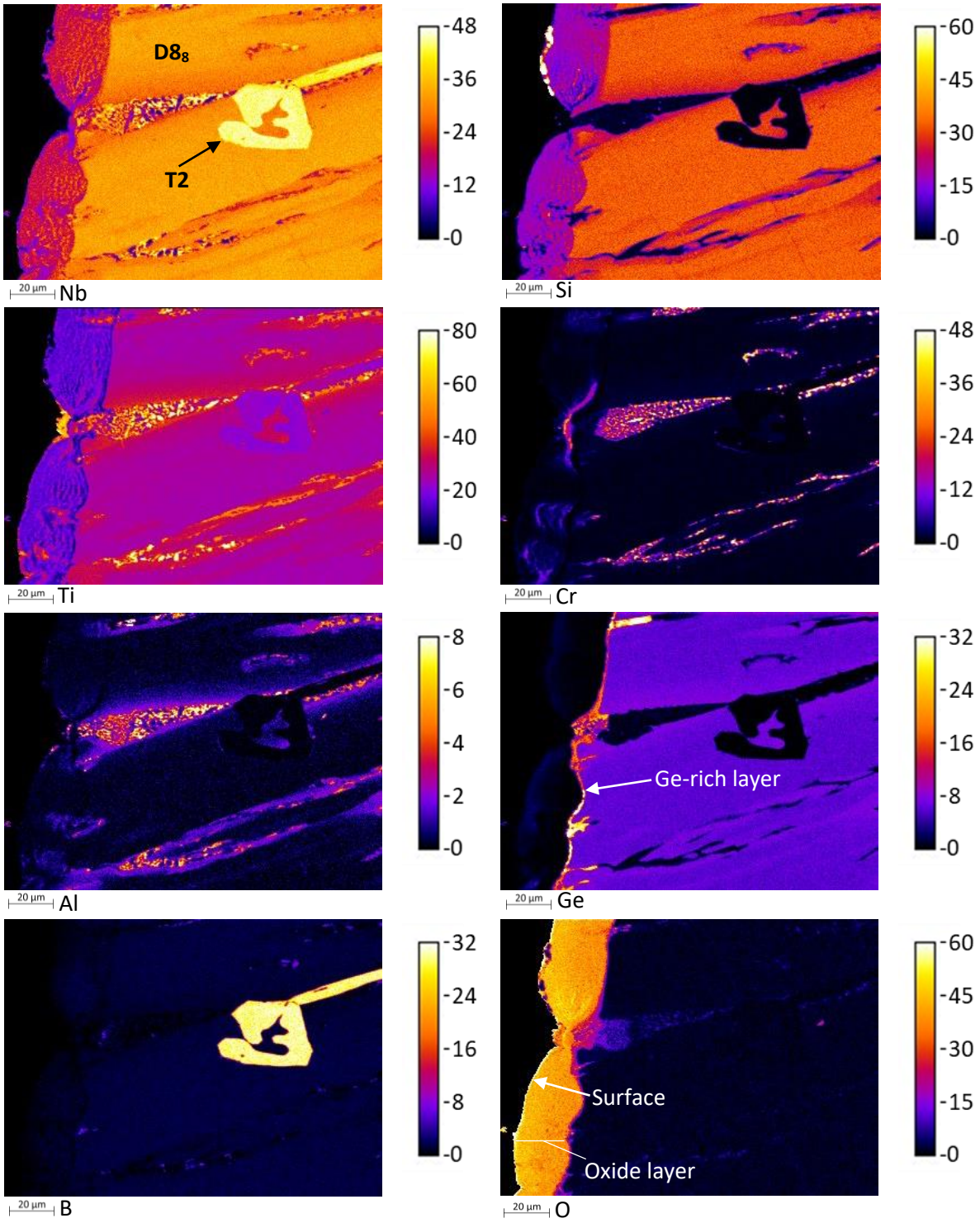

Figure 6.26a-h) EPMA maps of the oxide layer of JW2-AC in at.% of elements a) Nb, b) Si, c) Ti, d) Cr, e) Al, f) Ge, g) B h) O.

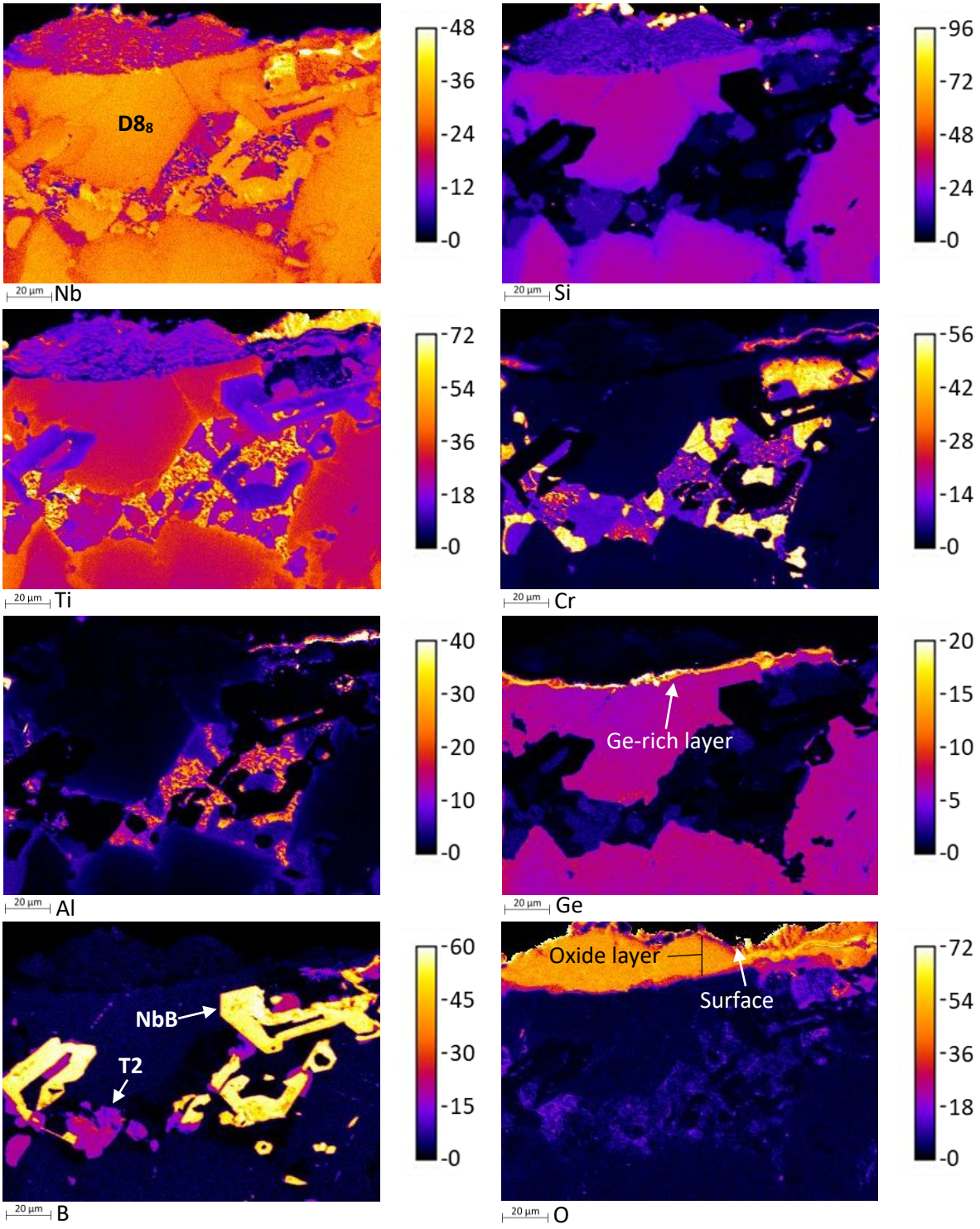

Figure 6.27a-h) EPMA maps of the oxide layer of JW2-HT13 in at.% of elements a) Nb, b) Si, c) Ti, d) Cr, e) Al, f) Ge, g) B h) O.

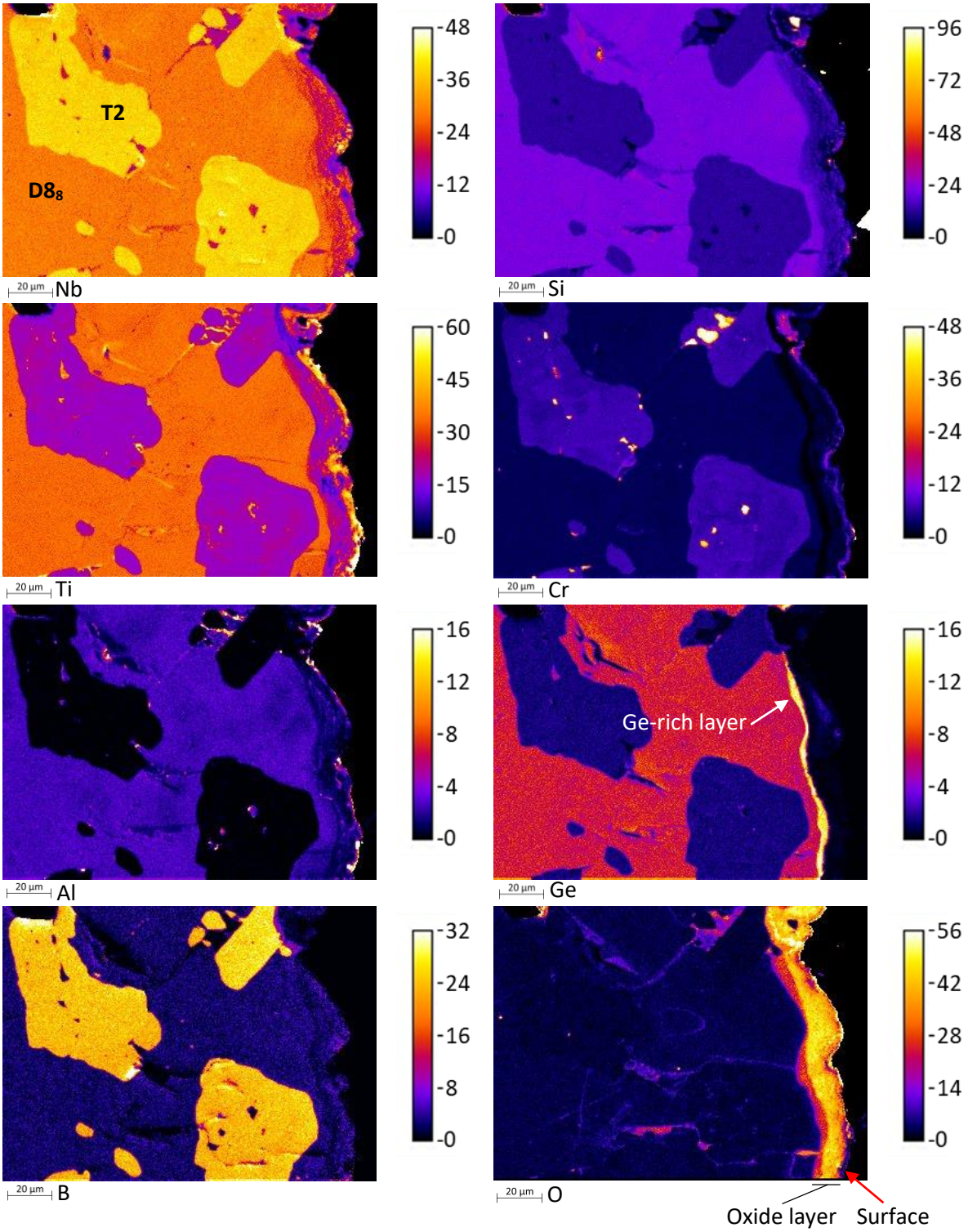

Figure 6.28a-h) EPMA maps of the oxide layer of JW2-HT15 in at.% of elements a) Nb, b) Si, c) Ti, d) Cr, e) Al, f) Ge, g) B h) O.

Table 6.10) Phase analysis of bulk phases present in each JW2 oxidised sample EPMA map, values given in at.%.

		Nb	Si	Ti	Cr	Al	Ge	B	O
$D8_8$	JW2-AC	33.0 ± 2.4	31.0 ± 2.2	24.8 ± 1.8	0.7 ± 0.3	0.2 ± 0.2	6.0 ± 0.7	3.0 ± 1.3	1.2 ± 0.9
	JW2-HT13	31.5 ± 2.6	28.3 ± 2.4	26.8 ± 2.4	1.5 ± 0.4	0.8 ± 0.7	6.5 ± 0.8	2.2 ± 1.4	2.4 ± 1.3
	JW2-HT15	29.3 ± 2.3	21.6 ± 1.8	32.6 ± 1.5	2.5 ± 0.5	2.2 ± 0.5	7.0 ± 0.8	2.1 ± 1.4	2.7 ± 1.5
T2	JW2-AC	31.6 ± 5.3	8.5 ± 4.8	23.4 ± 4.6	9.6 ± 8.3	0.8 ± 0.9	6.2 ± 7.4	17.5 ± 2.1	2.5 ± 1.7
	JW2-HT13	31.4 ± 5.3	10.2 ± 3.8	20.3 ± 7.3	10.7 ± 2.9	0.6 ± 2.2	1.3 ± 0.5	21.4 ± 5.8	4.1 ± 5.4
	JW2-HT15	38.7 ± 2.5	11.5 ± 1.3	16.3 ± 1.0	6.5 ± 0.8	0.1 ± 0.1	1.4 ± 0.4	23.6 ± 2.9	1.9 ± 1.2
NbB	JW2-AC	30.7 ± 1.9	0.2 ± 0.2	14.5 ± 1.2	0.2 ± 0.2	0.0 ± 0.1	0.0 ± 0.1	53.6 ± 2.5	0.7 ± 0.6
	JW2-HT13	29.8 ± 2.1	0.2 ± 0.2	12.8 ± 1.9	0.4 ± 0.3	0.0 ± 0.1	0.0 ± 0.1	55.1 ± 3.8	1.6 ± 1.1
(Nb)	JW2-AC	42.4 ± 5.0	2.4 ± 2.8	29.9 ± 11.5	12.0 ± 9.8	4.6 ± 2.0	1.4 ± 1.9	3.6 ± 4.4	3.7 ± 3.1
	JW2-HT13	33.5 ± 1.4	0.6 ± 0.3	27.5 ± 3.4	7.6 ± 3.6	26.4 ± 12.0	0.4 ± 0.2	0.3 ± 0.5	3.7 ± 1.9
Ti-rich (Nb)	JW2-AC	31.4 ± 3.8	3.4 ± 4.9	47.8 ± 6.4	8.7 ± 3.8	3.5 ± 1.7	1.2 ± 1.6	1.8 ± 2.3	2.1 ± 1.3
(Ti)	JW2-AC	7.5 ± 4.7	1.7 ± 2.5	80.8 ± 8.8	4.2 ± 3.8	0.7 ± 0.3	0.4 ± 0.6	0.2 ± 0.5	4.4 ± 1.7
	JW2-HT13	4.8 ± 2.5	0.9 ± 0.5	65.6 ± 4.6	8.2 ± 4.8	11.1 ± 10.5	0.3 ± 0.2	0.8 ± 1.2	8.3 ± 3.1
	JW2-HT15	11.6 ± 4.9	2.1 ± 2.4	58.1 ± 5.5	8.8 ± 6.0	5.7 ± 3.9	0.7 ± 0.9	0.3 ± 0.6	12.6 ± 6.1
$NbCr_2$	JW2-AC	20.7 ± 3.9	4.3 ± 2.9	21.1 ± 5.2	49.4 ± 6.5	1.1 ± 0.6	0.7 ± 0.9	1.2 ± 1.6	1.6 ± 1.3
	JW2-HT13	19.3 ± 2.2	3.7 ± 0.7	17.7 ± 2.6	51.0 ± 2.4	4.5 ± 1.4	0.3 ± 0.3	0.1 ± 0.3	3.3 ± 1.7
	JW2-HT15	19.2 ± 2.8	4.7 ± 0.8	16.7 ± 2.9	53.1 ± 3.6	2.7 ± 1.7	0.8 ± 0.5	0.8 ± 2.3	1.9 ± 1.4
Nb-B phase	JW2-HT13	59.2 ± 4.2	2.5 ± 2.6	4.1 ± 4.4	4.3 ± 4.2	0.3 ± 0.4	1.1 ± 1.1	23.0 ± 2.4	5.6 ± 3.8

Table 6.11) Phase analysis of bulk phases present in each JW2 oxidised sample from locations close to the oxide layer (top lines) and from locations far from the oxide layer (bottom lines). Values given in at.%. The distances from the oxide scale vary dependent on what was possible to measure. Alloy:phase-close to:far from; JW2-AC:(Nb) –<15µm : 40-55µm, JW2-AC:(Ti) –<25µm : 50-65µm, JW2-AC:($D8_8$) - <10µm : 115-125µm, JW2-HT13:($D8_8$) - <5µm : 70-105µm, JW2-HT15:($D8_8$) - <5µm : 70-105µm, JW2-HT13:(T2) - <10µm : 65-75µm, JW2-HT15:(T2) – <30µm : 110-120µm, JW2-AC:(NbB) - 55-65µm : 115-125µm, JW2-HT13:(NbB) – <10µm : 75-90µm, JW2-AC:($NbCr_2$) – 5-20µm : 100-120µm, JW2-HT13:($NbCr_2$) – <10µm : 75-95µm.

		Nb	Si	Ti	Cr	Al	Ge	B	O
$D8_8$	JW2-AC	33.0 ± 2.4	30.9 ± 2.2	25.0 ± 1.8	0.7 ± 0.3	0.2 ± 0.2	6.1 ± 0.7	2.7 ± 1.2	1.3 ± 1.0
		32.1 ± 2.7	30.3 ± 2.7	26.2 ± 2.8	0.9 ± 0.4	0.4 ± 0.4	6.2 ± 0.8	2.8 ± 1.3	1.3 ± 1.0
	JW2-HT13	32.0 ± 2.8	28.8 ± 2.2	25.8 ± 2.1	1.4 ± 0.4	0.6 ± 0.4	6.3 ± 0.7	2.6 ± 1.5	2.7 ± 1.5
		30.5 ± 3.2	27.6 ± 3.1	28.2 ± 4.0	1.4 ± 0.4	1.2 ± 1.3	6.5 ± 0.7	2.1 ± 1.4	2.4 ± 1.5
	JW2-HT15	28.7 ± 2.1	21.7 ± 2.0	32.6 ± 1.6	2.4 ± 0.5	2.2 ± 0.6	6.6 ± 0.7	2.6 ± 1.6	3.2 ± 1.6
		29.6 ± 2.2	21.7 ± 1.7	32.3 ± 1.4	2.6 ± 1.2	2.3 ± 0.4	7.0 ± 0.8	2.0 ± 1.3	2.6 ± 1.3
T2	JW2-HT13	35.9 ± 5.2	8.8 ± 4.1	13.8 ± 10.2	11.9 ± 4.1	0.1 ± 0.1	1.3 ± 0.6	23.7 ± 3.6	4.6 ± 2.5
		28.2 ± 6.3	10.0 ± 4.5	23.4 ± 3.6	11.1 ± 2.9	1.4 ± 3.5	1.3 ± 0.5	19.5 ± 8.4	5.2 ± 8.4
	JW2-HT15	37.0 ± 2.2	11.0 ± 1.4	16.7 ± 1.1	5.6 ± 0.9	0.1 ± 0.2	1.5 ± 0.5	26.0 ± 4.2	2.0 ± 1.4
		39.4 ± 1.9	12.1 ± 1.0	16.5 ± 0.8	5.9 ± 0.6	0.0 ± 0.1	1.4 ± 0.4	22.5 ± 3.3	2.1 ± 1.2
NbB	JW2-AC	31.2 ± 1.8	0.2 ± 0.2	14.6 ± 1.1	0.2 ± 0.2	0.0 ± 0.1	0.0 ± 0.1	53.1 ± 2.4	0.6 ± 0.6
		30.5 ± 1.6	0.2 ± 0.2	14.6 ± 0.8	0.2 ± 0.2	0.1 ± 0.1	0.0 ± 0.1	53.7 ± 3.2	0.7 ± 0.5
	JW2-HT13	28.5 ± 2.1	0.2 ± 0.1	14.1 ± 2.2	0.4 ± 0.2	0.0 ± 0.1	0.0 ± 0.0	55.1 ± 2.8	1.6 ± 0.8
		29.3 ± 1.6	0.3 ± 0.2	13.7 ± 1.6	0.4 ± 0.4	0.0 ± 0.1	0.0 ± 0.1	54.6 ± 5.3	1.7 ± 1.1
(Nb)	JW2-AC	39.5 ± 6.2	2.7 ± 3.6	26.6 ± 12.6	16.0 ± 12.3	3.7 ± 2.0	1.9 ± 3.4	3.6 ± 2.9	5.9 ± 4.2
		44.2 ± 1.8	2.2 ± 2.8	32.0 ± 7.8	8.4 ± 4.8	5.4 ± 2.0	1.4 ± 0.4	4.0 ± 5.6	2.4 ± 1.5
(Ti)	JW2-AC	5.6 ± 3.3	1.1 ± 2.0	82.8 ± 5.6	5.2 ± 4.5	0.5 ± 0.2	0.4 ± 0.5	0.0 ± 0.0	4.5 ± 2.3
		9.4 ± 5.7	1.9 ± 3.0	78.5 ± 9.1	4.9 ± 4.3	0.9 ± 0.4	0.4 ± 0.6	0.2 ± 0.3	3.9 ± 1.0
$NbCr_2$	JW2-AC	22.1 ± 3.4	3.7 ± 2.0	22.9 ± 8.5	46.2 ± 6.1	1.5 ± 0.7	0.6 ± 0.7	1.0 ± 1.3	2.0 ± 1.7
		19.4 ± 3.9	4.4 ± 3.2	20.1 ± 3.3	51.9 ± 3.9	0.7 ± 0.3	0.8 ± 1.0	1.5 ± 1.8	1.3 ± 0.9
	JW2-HT13	22.2 ± 2.3	6.5 ± 2.2	8.3 ± 2.7	47.3 ± 3.6	0.7 ± 0.8	1.6 ± 2.1	1.8 ± 4.3	11.7 ± 4.7
		18.8 ± 2.2	4.5 ± 0.9	20.2 ± 2.5	49.8 ± 3.2	3.8 ± 0.7	0.4 ± 0.3	0.1 ± 0.3	2.4 ± 2.0

Table 6.13) Area analysis of the entire oxide layers and Ge-rich layers shown in EPMA maps for JW2 oxidised samples, values given in at.%.

		Nb	Si	Ti	Cr	Al	Ge	B	O
Total oxide layer:	JW2-AC	19.9 ± 4.3	15.7 ± 5.5	18.1 ± 7.7	2.2 ± 3.6	0.3 ± 0.5	1.1 ± 3.2	1.4 ± 1.2	41.3 ± 7.4
	JW2-HT13	15.3 ± 7.8	11.7 ± 7.0	18.7 ± 12.9	3.1 ± 6.3	3.1 ± 13.2	1.4 ± 3.5	1.2 ± 1.3	45.6 ± 12.3
	JW2-HT15	21.0 ± 5.9	13.0 ± 12.1	19.3 ± 7.8	2.1 ± 3.8	1.2 ± 1.3	2.9 ± 4.8	2.0 ± 1.8	38.5 ± 11.9
Ge-rich layer:	JW2-AC	24.8 ± 3.7	18.2 ± 7.4	13.3 ± 6.1	0.7 ± 1.1	0.5 ± 0.5	21.4 ± 8.5	1.7 ± 3.1	19.4 ± 7.3
	JW2-HT13	23.0 ± 4.9	17.0 ± 4.2	11.8 ± 6.9	0.7 ± 1.0	1.9 ± 5.2	15.7 ± 5.5	1.0 ± 1.2	29.0 ± 8.2
	JW2-HT15	25.2 ± 2.8	14.0 ± 2.0	17.5 ± 3.7	0.4 ± 0.5	1.8 ± 0.6	14.6 ± 1.9	1.4 ± 1.3	25.1 ± 4.8

Table 6.14) Phase analysis of oxide phases in each JW2 oxidised sample from locations in the oxide scale , values given in at.%.

		Nb	Si	Ti	Cr	Al	Ge	B	O
Ge-rich phase	JW2-AC	22.6 ± 2.6	9.2 ± 7.0	9.0 ± 3.5	0.2 ± 0.3	0.2 ± 0.3	45.6 ± 6.2	0.5 ± 0.8	12.7 ± 5.5
	JW2-HT13	19.3 ± 3.1	7.8 ± 4.4	7.3 ± 3.4	0.2 ± 0.3	0.1 ± 0.1	38.7 ± 5.2	0.3 ± 0.6	26.2 ± 7.0
	JW2-HT15	25.0 ± 2.0	13.5 ± 1.4	17.8 ± 2.7	0.3 ± 0.3	1.8 ± 0.7	17.0 ± 0.7	0.9 ± 1.1	23.7 ± 2.8
Ti-rich oxide	JW2-AC	11.3 ± 3.4	5.6 ± 4.0	42.4 ± 3.8	2.5 ± 1.2	0.9 ± 0.3	0.0 ± 0.1	0.3 ± 0.2	37.0 ± 6.5
	JW2-HT13	12.1 ± 2.8	8.7 ± 3.3	32.1 ± 5.2	2.6 ± 2.4	0.8 ± 0.6	1.1 ± 2.8	0.7 ± 1.1	42.0 ± 7.3
	JW2-HT15	10.2 ± 2.3	2.9 ± 1.6	49.2 ± 5.1	5.2 ± 1.4	0.9 ± 0.7	0.1 ± 0.1	0.3 ± 0.7	31.2 ± 12.4
Nb-rich oxide	JW2-AC	29.2 ± 4.4	11.2 ± 5.7	15.9 ± 5.1	0.8 ± 0.6	0.3 ± 0.5	3.7 ± 8.1	2.7 ± 1.9	36.2 ± 11.9
	JW2-HT13	29.1 ± 4.6	8.2 ± 2.8	10.8 ± 5.5	0.4 ± 0.3	0.1 ± 0.1	0.1 ± 0.1	3.7 ± 1.9	47.5 ± 5.1
	JW2-HT15	36.5 ± 5.8	6.6 ± 4.8	10.2 ± 2.2	1.0 ± 0.5	0.8 ± 0.6	0.1 ± 0.2	5.2 ± 3.3	39.5 ± 10.8
Si-rich oxide	JW2-AC	13.1 ± 4.8	25.9 ± 6.0	13.2 ± 3.7	2.5 ± 1.3	0.2 ± 0.2	0.3 ± 0.3	1.2 ± 0.9	43.6 ± 7.7
	JW2-HT13	11.8 ± 2.6	25.6 ± 4.2	8.1 ± 3.3	0.5 ± 0.3	0.3 ± 0.3	0.3 ± 0.5	0.6 ± 0.6	52.8 ± 5.9
	JW2-HT15	14.0 ± 6.3	29.4 ± 8.4	17.3 ± 4.4	2.0 ± 0.8	1.1 ± 0.7	0.6 ± 1.0	2.0 ± 2.2	33.7 ± 22.6
Cr-rich oxide	JW2-AC	8.4 ± 6.2	4.3 ± 4.3	15.5 ± 9.4	27.0 ± 9.3	1.6 ± 1.7	0.4 ± 0.7	0.5 ± 0.5	42.3 ± 5.3
	JW2-HT13	0.7 ± 1.5	0.6 ± 0.7	3.7 ± 1.4	34.7 ± 3.2	4.4 ± 3.1	0.1 ± 0.1	0.0 ± 0.0	55.8 ± 9.6
	JW2-HT15	7.0 ± 3.7	7.2 ± 4.5	17.8 ± 9.2	21.1 ± 10.8	1.4 ± 1.5	0.1 ± 0.1	0.2 ± 0.4	45.1 ± 20.2
Al-rich phase	JW2-HT13	0.2 ± 0.4	0.2 ± 0.2	1.3 ± 0.6	0.4 ± 0.4	69.7 ± 5.6	0.0 ± 0.0	0.0 ± 0.0	28.1 ± 6.2
low-sub TiO_2	JW2-AC	0.5 ± 0.3	0.4 ± 0.4	61.8 ± 1.4	1.8 ± 0.3	0.1 ± 0.1	0.1 ± 0.1	0.0 ± 0.0	35.3 ± 5.6
	JW2-HT13	0.1 ± 0.1	0.2 ± 0.2	56.7 ± 2.1	1.5 ± 0.4	0.1 ± 0.1	0.0 ± 0.1	0.0 ± 0.1	41.4 ± 6.8

6.2.2.4 JW3

6.2.2.4.1 XRD

The XRD pattern of JW3-AC is shown in Figure 6.29. The phases that are identified are TiO_2, $Ti_2Nb_{10}O_{29}$, $TiNb_2O_7$ and a suspected niobium germanium phase Nb_5Ge_3 that was identified in JW2-HT15 (Pearson symbol hP16, space group $P6_3/mcm$) explained by the formation of a germanium rich layer just below the oxide scale. The XRD pattern of JW3-HT13 is shown in Figure 6.30. The phases that are identified are TiO_2, $Ti_2Nb_{10}O_{29}$ and $TiNb_2O_7$. The XRD pattern of JW3-HT15 is shown in Figure 6.31. The phases that are identified are TiO_2, $Ti_2Nb_{10}O_{29}$, SiO_2 and Nb_5Ge_3.

The Nb_5Ge_3 identified in JW3-AC and JW3-HT15 is not a precise match to the reference PDF-4+ entry (01-072-9322) so a low degree of confidence can be placed in this phases existence. However, some allowance is made for the fact that this phase, if formed during the oxidation period between the substrate and oxide scale through diffusion, will have a high degree of substitution of other elements and may be under some form of residual stress.

Additionally, evidence for this Nb_5Ge_3 in JW3-AC is the large peak found in the 'unreliable region' past 2θ angle ~60 where the angle of incidence becomes too great to consistently measure surface oxide layers. The Nb_5Ge_3 peak at ~ 82° in Figure 6.29 can be explained by the Nb_5Ge_3 layer being deeper than the other measured oxides, and hence being able to cause a diffraction peak. In JW3-HT15 there is less evidence for this phase as the peaks associate with it are diminished, so it is considered a low confidence phase. The main differences between JW3-AC and JW3-HT15 specimens are less conclusive evidence of Nb_5Ge_3 but also the absence of identifiable $TiNb_2O_7$ in the heat-treated at 1500°C version of JW3. The SiO_2 phase in JW3-HT15 is less apparent than other reported phases as only one unique peak exists, similar to other alloys in this study where SiO_2 is reported, so a lower degree of confidence can be placed in this phase. In JW3-HT13 no $(Nb,Ti)_5(Si,Ge)_3$ phase was detected in the expected 2θ range and $TiNb_2O_7$ is less easily distinguished from $Ti_2Nb_{10}O_{29}$ peaks.

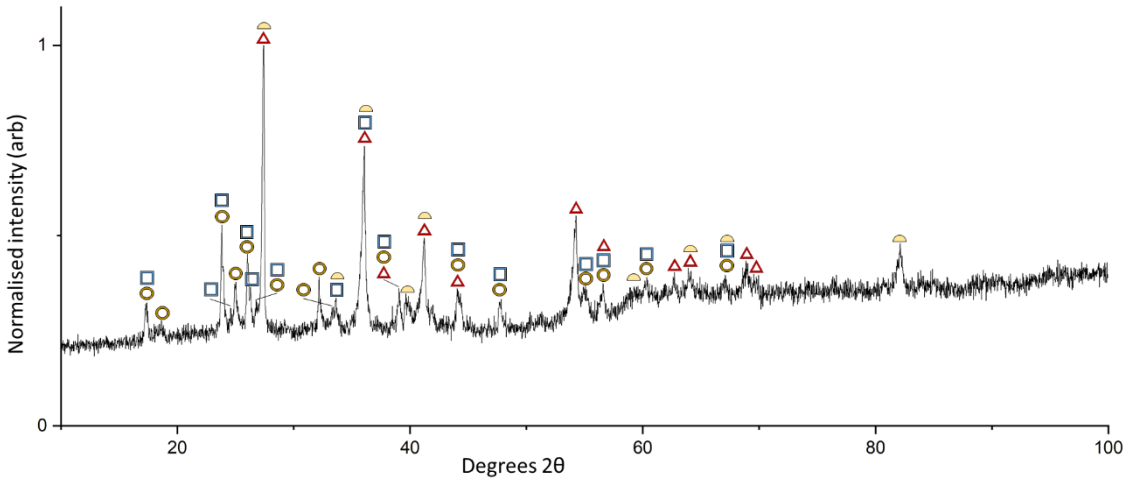

Figure 6.29) XRD pattern of oxidised at 1000°C JW3-AC. △ = TiO_2, ○ = $Ti_2Nb_{10}O_{29}$, □ = $TiNb_2O_7$ ◡ = Nb_5Ge_3

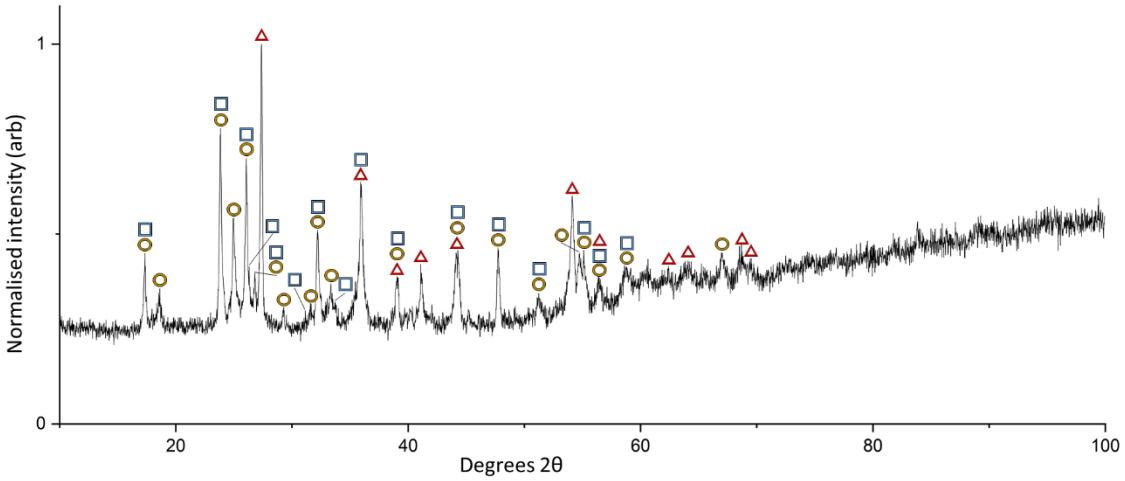

Figure 6.30) XRD pattern of oxidised at 1000°C JW3-HT13. △ = TiO_2, ○ = $Ti_2Nb_{10}O_{29}$, □ = $TiNb_2O_7$

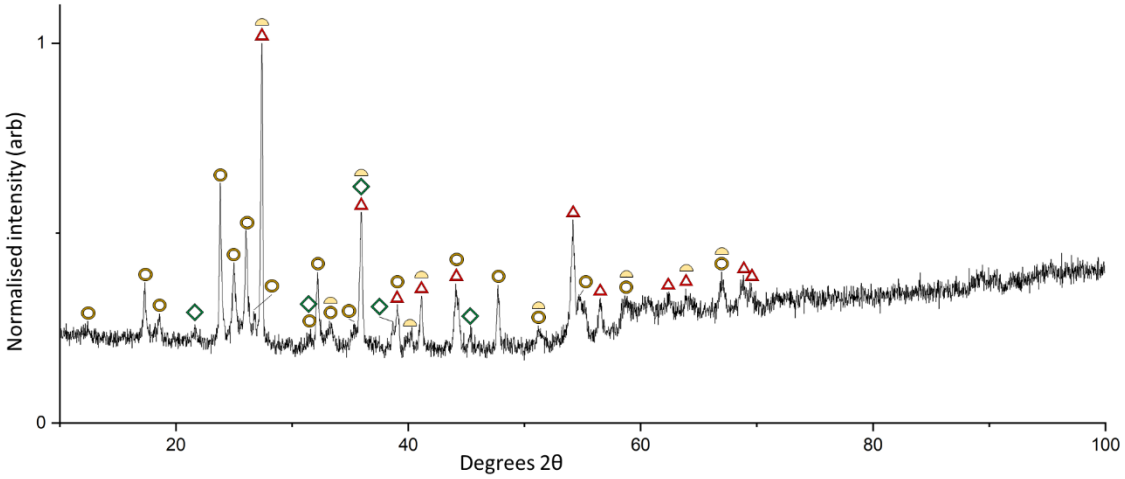

Figure 6.31) XRD pattern of oxidised at 1000°C JW3-HT15. △ = TiO_2, ○ = $Ti_2Nb_{10}O_{29}$, ◇ = SiO_2, ◡ = Nb_5Ge_3

6.2.2.4.2 EPMA

EPMA mapping of oxidised JW3 samples at 1000°C including elements Nb, Si, Ti, Cr, Al, Ge, B and O is presented in Figure 6.32, Figure 6.33 and Figure 6.34 for the as-cast state, heat-treated at 1300°C state and heat-treated at 1500°C state, respectively. In the bulk of each oxidised sample, two phases were identified: (Ti) and $D8_8$. Phases (Nb), NbB and $NbCr_2$ were identified in JW3-AC and JW3-HT13. Small amounts of T2 were found in JW3-HT13 and JW3-HT15, and a segregated Al phase was found in JW3-HT15, as well as a Ti-poor $D8_8$ phase. The compositions of each of the phases in the oxidised samples are listed in Table 6.15.

The $D8_8$ phase is in agreement with the un-oxidised microstructures, as are the NbB, $NbCr_2$ and (Nb) phases found in oxidised JW3-AC and $NbCr_2$, T2 and (Nb) phases found in oxidised JW3-HT13. However, more T2 would be expected to be seen in JW3-HT13 and not NbB. The T2 phase found in JW3-HT15 is in agreement with the unoxidised microstructure, however $NbCr_2$ is expected and not found. In addition, a phase with 85.9 at.% Al is found in the bulk of the sample, labelled as segregated Al as it is proposed that this is an aluminium solid solution, and a phase that has composition similar to $D8_8$, labelled Ti-poor $D8_8$ as Ti is practically absent, both of which are unexpected based on the unoxidised microstructure. The (Ti) phase is again unique to the oxidised

microstructures with considerably more Ti than Nb content in each instance of this phase in each alloy.

In the microstructures of oxidised JW3-AC and JW3-HT13, (Nb), (Ti) and $NbCr_2$ exist in between $D8_8$ grains. Both instances of (Nb) are high in Al, with values of 21.8 at.% and 32.7 at.% for JW3-AC and JW3-HT13, respectively, and the (Nb) in JW3-AC is rich in Ti with a content of 47 at.%. In the unoxidised JW3 alloys where (Nb) is found, Ti content is found to exceed Nb content, so this not unusual. The (Ti) found in JW3-AC and JW3-HT13 has similar compositions, as does the $NbCr_2$ phase to a lesser extent. However, in the heat-treated at 1300°C alloy the $NbCr_2$ exists in coarse regions as well as finely distributed with the (Ti) and (Nb). The final difference regarding the intergranular regions is how NbB is only found in this region in the case of JW3-HT13 but in JW3-AC portions of NbB can be seen detached from the (Nb), (Ti) and $NbCr_2$ phases and is often solely in the $D8_8$ grains. This may be merely due to the regions that have been considered however.

The microstructure of JW3-HT15 is dramatically different from the other processing states of the alloy. No (Nb) is found, which is in agreement with the unoxidised structure, no $NbCr_2$ is found, which is in contradiction with the unoxidised structure, and two phases with some degree of uncertainty make up the intergranular region alongside (Ti); Ti-poor $D8_8$ and (Al). In addition, 'pockets' of oxide material are found in close proximity to the actual oxide scale along its length, one such pocket is seen in the top left of Figure 6.34. These areas will be discussed with the oxides later in this section. The cause of these pockets, as well as the odd intergranular region are unknown, but it may be the case that porosity was introduced during the 1500°C heat treatment and not the 1300°C heat treatment that led to susceptible areas of oxidation despite no (Nb) being present. JW3-HT15 has significantly worse oxidation resistance at 1000°C than the other processing states of JW3 so it seems likely that these factors are related.

In terms of oxygen content of these phases, (Nb) had 3.2 at.% and 2.5 at.% O in JW3-AC and JW3-HT13 respectively, (Ti) had 4.7 at.%, 4.7 at.%, and 4.2 at.% O in JW3-AC, JW3-HT13, and JW3-HT15 respectively, and $NbCr_2$ had 1.9 at.% and 2.5 at.% in JW3-AC and JW3-HT13, respectively. The same trend of (Ti) being the most susceptible to oxidation and $NbCr_2$ the least observed in JW1 and JW2 alloys is again seen in JW3 alloys, however the differences between phases is marginal in this case as O content only varies from minimum 2.5 at.% to maximum 4.7 at.% in these phases across each processing state.

Where possible the average composition of bulk phases close to and far from the oxide scales were calculated. Typically, in the case of JW2, this results in compositions given from 0µm to 25µm from the oxide scale compare to composition from 50µm to 140µm from the oxide scale, for 'close to' and 'far from' labels, respectively. Phases $D8_8$, NbB, (Nb) and $NbCr_2$ have higher O contents in close to the scale measurements that far from measurements, however these cannot be said to be significant due to the small values and overlapping standard errors. In $D8_8$ and NbB the greatest variations for any element was a 3.6 at.% difference in Ti content and a 2.9 at.% difference in B content, respectively. In (Nb) and $NbCr_2$ the greatest variation for any element in any alloy processing state was a 5.2 at.% difference in Cr content and a 5.5 at.% difference in Cr content, respectively. On the other hand, for the (Ti) phase in JW3-HT13, there was a significant oxygen gradient, with a value of 6.9 at.% close to the oxide scale and 3.1 at.% far from the oxide scale, with distances approximately 10-20µm and 50-80µm, respectively. In addition, this phase showed large change in composition compared to other phases as Al content changed from 9.2 at.% to 30.5 at.% and Cr content changed from 15.8 at.% to 1.7 at.% for close to and far from the scale, respectfully.

Area analysis was performed using EPMA data in order to report average compositions of specific areas of the oxide scale, shown in Table 6.17. The layer of oxidised material of JW3-AC had an average composition of 15.4 at.% Nb, 10.7 at.% Si, 14.5 at.% Ti, 2.4 at.% Cr, 0.7 at.% Al, 2.5 at.% Ge, 0.5 at.% B, and 53.8 at.% O. The layer of oxidised material of JW3-HT13 had an average composition of 16.9 at.% Nb, 12.1 at.% Si, 13.9 at.% Ti, 3.5 at.% Cr, 0.3 at.% Al, 2.5 at.% Ge, 1.6 at.% B, and 49.2 at.% O. The layer of oxidised material of JW3-HT15 had an average composition of 19.1 at.% Nb, 11.7 at.% Si, 18.0 at.% Ti, 2.1 at.% Cr, 2.2 at.% Al, 0.3 at.% Ge, 1.4 at.% B, and 45.2 at.% O.

A layer that is rich in Ge can be seen between the oxide layer and the bulk alloy in JW3-AC and JW3-HT13. The average area compositions of these layers are given in Table 6.17. In the case of JW3-HT15 the term 'layer' does not apply as, whilst there are areas of high Ge content on the oxide layer and the bulk interface, they are disconnected in discrete 'clumps'. The ratios of certain elements are considered to identify the phase of this layer for alloys JW3-AC and JW3-HT13. The Ge-rich layer of JW3-AC has a ratio of Nb + Ti to Ge + Si of to 0.77, which is approaching the ratio of 0.5 which would indicate $NbGe_2$ more so than Nb_5Ge_3 or Nb_3Ge. In the case of JW3-HT13, the ratio of Nb + Ti to Ge + Si is 0.74, so again it is predicted that $NbGe_2$ is forming.

Areas where Ge content is greater than the rest of the Ge-rich layer in EPMA maps for JW3-AC, JW3-HT13 and JW3-HT15 were examined. Points were taken from these high-Ge areas to calculate the composition given in Table 6.18. Average Nb and Ge contents of this phase in JW3-AC were 16.8 at.% and 41.4 at.%. The ratio of Nb + Ti to Ge + Si is calculated as 0.63. Average Nb and Ge contents of this phase in JW3-HT13 were 21.9 at.% and 51.1 at.%. The ratio of Nb + Ti to Ge + Si is calculated as 0.50. Average Nb and Ge contents of this phase in JW3-HT15 were 25.9 at.% and 59.4 at.%. The ratio of Nb + Ti to Ge + Si is calculated as 0.48. This indicates that $NbGe_2$ has formed in certain places along the Ge-rich layer in JW3-AC, JW3-HT13 and JW3-HT15, as the expected ratio of Nb to Ge in pure $NbGe_2$ would be 0.5. The oxygen content of these high germanium locations was 27.6 at.%, 15.8 at.% and 4.8 at.% in JW3-AC, JW3-HT13 and JW3-HT15, respectively. The measurements used to calculate these compositions had average weight percentage over 95%, so the O contents can have a higher degree of confidence placed in them than oxide phases reported later. As such, the fact that the Ge-rich areas are discontinuous and that O content of this phase is significantly lower in JW3-HT15 than in any other Ge-rich phase reported on in JW1, JW2 and JW3, coupled with the poor oxidation resistance of JW3-HT15 but not JW3-AC or JW3-HT13, suggests that the formation of this Ge-rich layer and subsequent oxidation is crucial to improved oxidation resistance at 1000°C for niobium silicide-based alloys.

Compositions of phases and regions within the oxide layer of each alloy are presented in Table 6.18. In each of the oxide scales four oxides are reported on and are designated based on their primary element: Nb-rich oxide, Ti-rich oxide, Cr-rich oxide, and Si-rich oxide. In all three of the JW3 alloys quite coarse areas of Nb-rich oxide and Ti-rich oxide phases exist. In JW3-AC and JW3-HT13 coarse areas of a Cr-rich oxide exist. In addition, another Ti majority oxide phase is reported in JW3-AC and JW3-HT13 that is especially low in Nb and Cr substitutions compared to the Ti-rich oxide $(Ti,Cr,Nb)O_2$. This is reported as low-sub TiO_2 in Table 6.18, as was the case with JW2-AC and JW2-HT13. The region in JW3-HT15 referred to as a pocket allows measurements of an Al-rich oxide phase, as well as the other oxide phases that exist there, although these are not as clearly separated from one another. The Si-rich oxide phase is reported on in each alloy in order to facilitate comparison between each oxidised alloy, although it should be noted that this is likely a mixed oxide and not a single phase similar to what was the case in previously discussed alloys.

For JW3-AC, the Nb-rich phase has Nb and Ti contents of 28.1 at.% and 11.6 at.%, respectively. With a Nb to Ti ratio of 2.43, this phase can be identified as $TiNb_2O_7$ which would have a Nb to Ti ratio of

2. For JW3-HT13, the Nb-rich phase has Nb and Ti contents of 35.7 at.% and 8.7 at.%, respectively. With a Nb to Ti ratio of 4.12, this phase has a closer Nb/Ti ratio to that of $Ti_2Nb_{10}O_{29}$. For JW2-HT15, the Nb-rich phase has Nb and Ti contents of 37.5 at.% and 8.8 at.%, respectively. With a Nb to Ti ratio of 4.27, this phase has a closer Nb/Ti ratio to that of $Ti_2Nb_{10}O_{29}$. $TiNb_2O_7$ is most clearly seen in the XRD pattern of the as-cast version of JW3 and only to a lesser degree in JW3-HT13, so these compositional results are in agreement with the XRD experiments. Boron content of this phase is the highest of any oxides in JW3, ranging from 3.1 at.% to 4.2 at.%.

For JW3-AC, the Ti-rich oxide had average Nb, Ti and Cr contents of 10.7 at.%, 29.1 at.% and 5.1 at.%, respectively. For JW3-HT13, the Ti-rich phase had average Nb, Ti and Cr contents of 12.9 at.%, 32.0 at.% and 1.0 at.%, respectively. For JW3-HT15, the Ti-rich phase had average Nb, Ti and Cr contents of 8.7 at.%, 36.8 at.% and 4.8 at.%, respectively. These phases are identified as rutile TiO_2 with substitution of Nb and Cr onto Ti sites. In the case of JW3-HT13 measurements, this was taken from the banding structure seen in the Ti and Si maps that was evidently previously a silicide grain, hence a higher Si content in this TiO_2 phase, 7.0 at.%. There exists a partial Cr-rich layer within the oxide scales of JW3-AC and JW3-HT13. This is most prominent where the oxide scale has formed on an area absent of $D8_8$ in alloys, especially so in the JW3-HT13 oxide scale. Cr is the dominant element excluding O in each of these layers, with the next highest being Ti with the highest value being only 3.4 at.%. The ratios of Cr to O in these phases are 0.52 and 0.63 for JW3-AC and JW3-HT13, respectively. Considering O content is under reported throughout this EPMA analysis, it seems likely that the Cr rich layers in these alloys are made up of the Cr_2O_3 phase, which would have a Cr/O ratio of 0.67. There was no Cr oxide phase identified in XRD of JW3 samples, likely due to forming in too small amounts to be detected.

In JW3-HT15 which had more severe oxidation, a phase that was mostly made of Al and O formed in the 'pocket' area identified in Figure 6.34. Al content is 60.2 at.%, with the next highest non-oxygen phase being Ti at 2.8 at.%. A similar Al-O phase was found in JW2-HT13 which was deemed to be not a single phase but a mixture of (Al), which is also believed to be found in JW3-HT15, and an Al_2O_3 oxide. It seems plausible that this is the same phase, or phases, in JW3-HT15 given the similarly high weight percentage recorded, and the same reasoning that the (Al) has a low solubility of O.

Two other distinct areas are measured in the pocket of JW3-HT15; a Ti-rich oxide phase and a Si-rich oxide phase. The Ti-rich oxide phase has comparable composition to the previously discussed Ti-rich oxide phase of the oxide scale, so is likely a $(Ti,Cr,Nb)O_2$ rutile phase . The Si-rich oxide phase of the pocket has low Si content compared to the other instances of Si-rich oxide phase from the oxide scales discussed below, and is likely not a single phase and is made of SiO_2, $TiNb_2O_7$ and $Ti_2Nb_{10}O_{29}$.

The Si-rich oxide phases of each JW3 alloy are also recorded in Table 6.18. Given that the Si-rich oxide areas are in too fine a distribution with the Ti-rich oxide phases to accurately evaluate phase composition, the value reported in Table 6.18 are likely not of a single phase. However, compositional analysed has been done to provide explanation to the peaks assigned to an SiO_2 phase in oxide surface XRD. Si content in each Si-rich phase are 20.4 at.%, 29.4 at.% and 27.1 at.% for alloys JW3-AC, JW3-HT13 and JW3-HT15, respectively, whilst average Nb content ranges from 6.0 at.% to 15.7 at.% and average Ti content ranges from 6.1 at.% to 12.7 at.%. It is proposed that this is a fine mixture of oxides including SiO_2, where the significant Si content comes from, and TiO_2, $Ti_2Nb_{10}O_{29}$ and $TiNb_2O_7$ where the Ti and Nb come from.

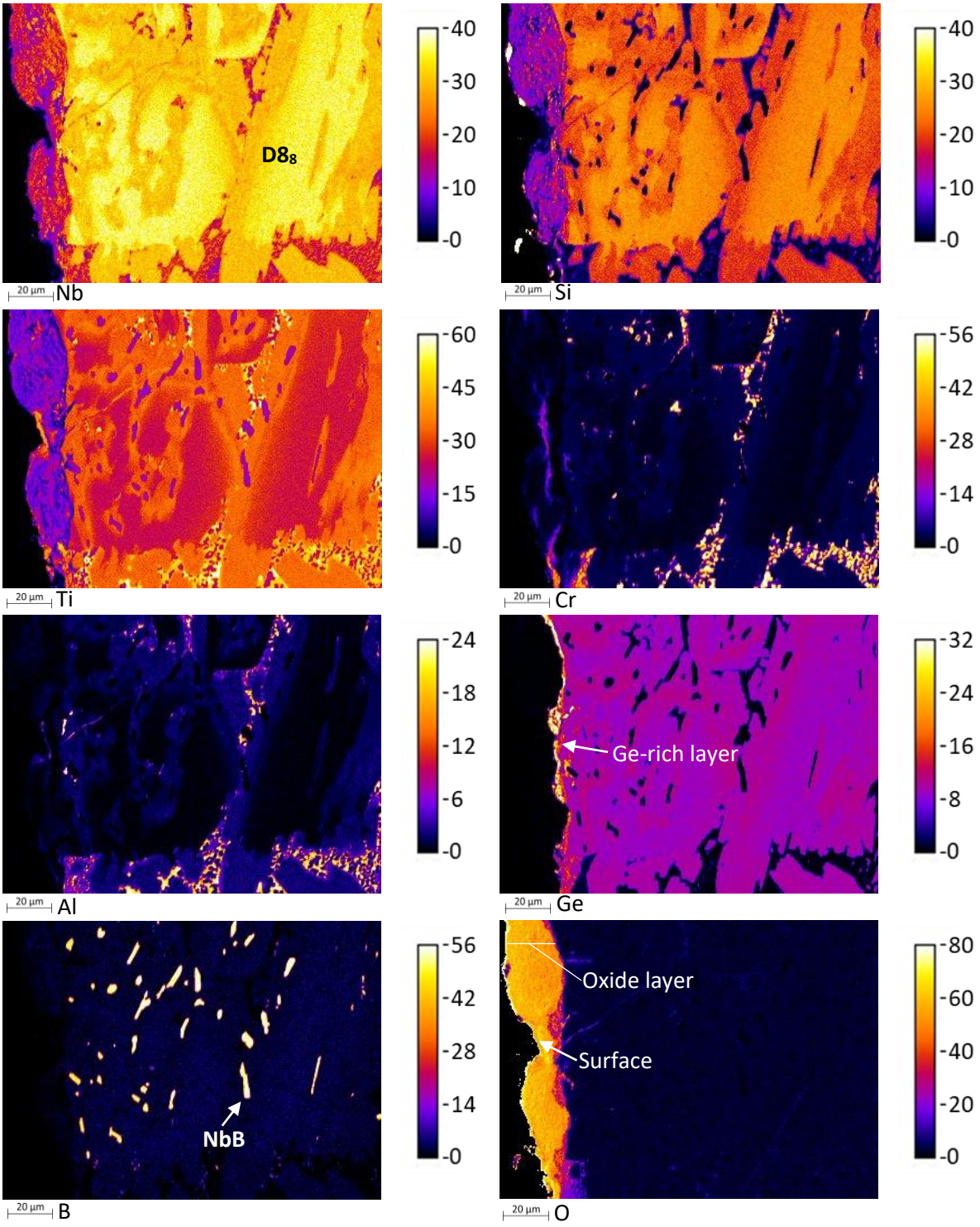

Figure 6.32a-h) EPMA maps of the oxide layer of JW3-AC in at.% of elements a) Nb, b) Si, c) Ti, d) Cr, e) Al, f) Ge, g) B h) O.

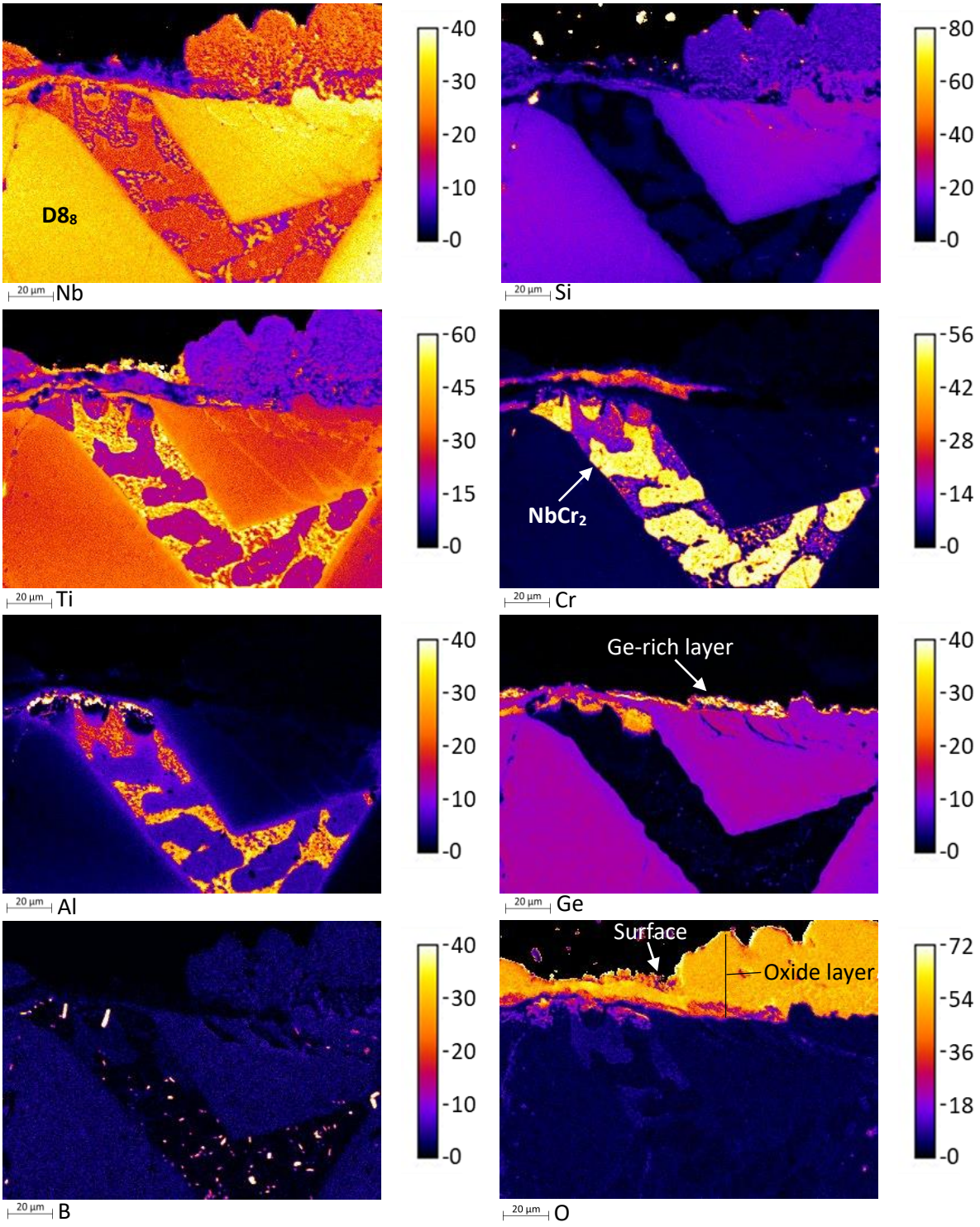

Figure 6.33a-h) EPMA maps of the oxide layer of JW3-HT13 in at.% of elements a) Nb, b) Si, c) Ti, d) Cr, e) Al, f) Ge, g) B h) O.

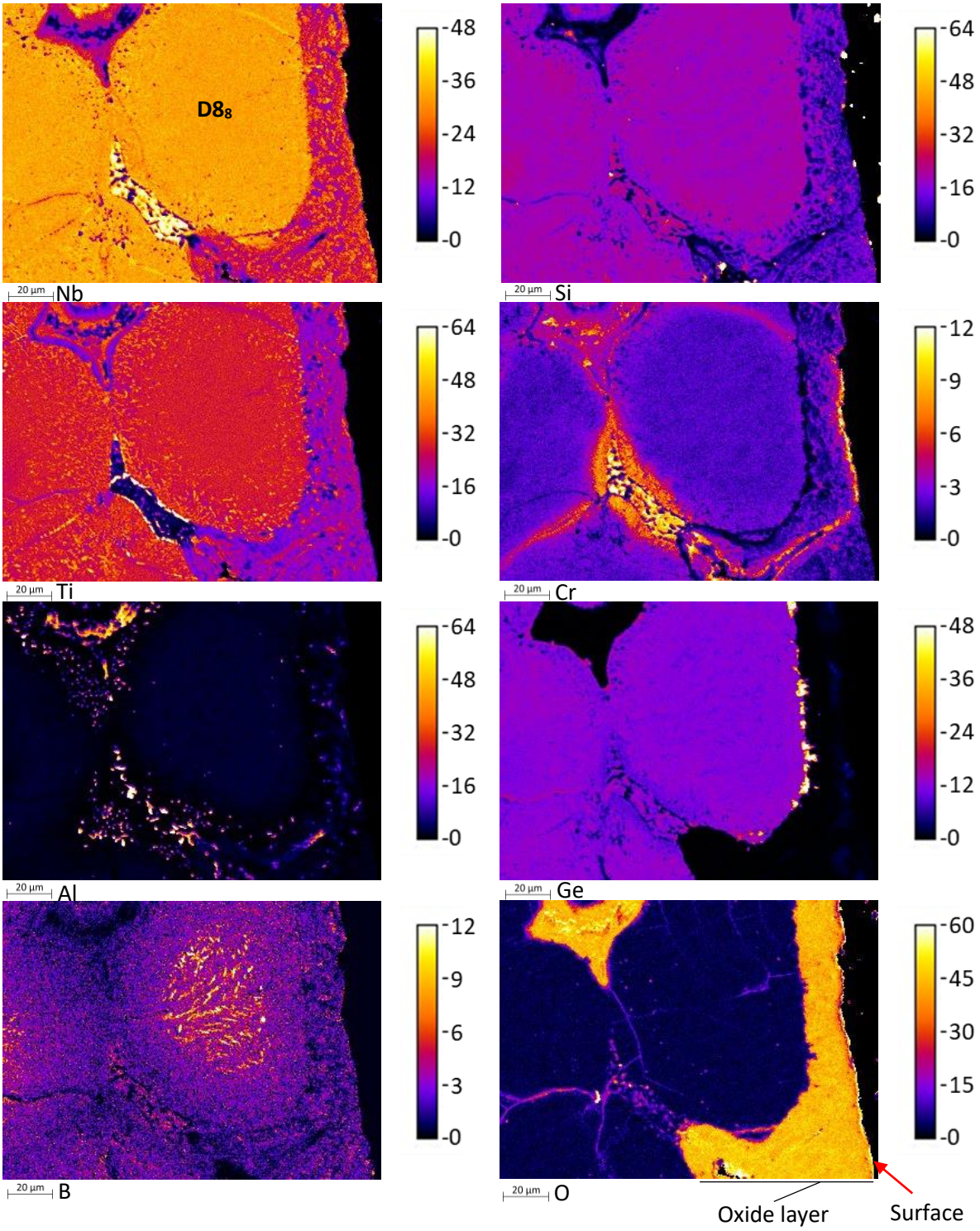

Figure 6.34a-h) EPMA maps of the oxide layer of JW3-HT15 in at.% of elements a) Nb, b) Si, c) Ti, d) Cr, e) Al, f) Ge, g) B h) O.

Table 6.15) Phase analysis of bulk phases present in each JW3 oxidised sample EPMA map, values given in at.%.

		Nb	Si	Ti	Cr	Al	Ge	B	O
$D8_8$	JW3-AC	33.4 ± 2.7	24.6 ± 2.2	25.8 ± 2.4	1.0 ± 0.5	0.3 ± 0.4	10.4 ± 1.0	2.2 ± 1.5	2.3 ± 1.5
	JW3-HT13	29.2 ± 2.7	19.5 ± 2.4	30.1 ± 2.4	1.9 ± 0.6	1.2 ± 0.6	12.8 ± 1.6	2.3 ± 1.5	3.0 ± 1.6
	JW3-HT15	31.2 ± 2.5	19.7 ± 2.0	28.1 ± 2.3	1.8 ± 0.5	1.4 ± 1.3	11.8 ± 1.2	3.0 ± 2.2	2.9 ± 1.7
Ti-poor $D8_8$	JW3-HT15	47.1 ± 2.3	22.7 ± 2.6	2.8 ± 0.7	8.8 ± 1.2	0.2 ± 0.2	12.8 ± 1.9	2.7 ± 1.3	2.9 ± 1.4
T2	JW3-HT13	34.3 ± 2.1	12.2 ± 1.7	21.5 ± 2.5	8.7 ± 1.1	0.3 ± 0.3	2.9 ± 1.2	18.4 ± 1.9	1.7 ± 0.8
	JW3-HT15	31.2 ± 2.5	14.1 ± 1.6	25.3 ± 1.3	1.6 ± 0.4	1.1 ± 0.3	8.4 ± 1.2	15.5 ± 3.1	2.8 ± 1.9
NbB	JW3-AC	28.2 ± 2.0	0.1 ± 0.1	16.9 ± 1.0	0.4 ± 0.3	0.1 ± 0.1	0.1 ± 0.1	53.2 ± 5.1	1.1 ± 0.6
	JW3-HT13	23.2 ± 2.0	0.2 ± 0.3	24.2 ± 3.3	2.1 ± 3.0	0.3 ± 0.4	0.1 ± 0.2	47.7 ± 5.7	2.2 ± 1.1
(Nb)	JW3-AC	17.1 ± 2.1	0.5 ± 0.6	47.7 ± 2.2	9.2 ± 4.0	21.8 ± 4.3	0.2 ± 0.2	0.2 ± 0.4	3.2 ± 2.2
	JW3-HT13	28.6 ± 1.9	0.5 ± 0.3	27.1 ± 3.9	7.6 ± 4.6	32.7 ± 4.7	0.4 ± 0.2	0.7 ± 0.8	2.5 ± 1.4
(Ti)	JW3-AC	9.8 ± 1.9	0.9 ± 0.9	60.2 ± 1.8	4.5 ± 5.6	19.1 ± 8.4	0.5 ± 0.6	0.3 ± 0.8	4.7 ± 1.6
	JW3-HT13	7.3 ± 2.2	0.5 ± 0.5	56.6 ± 3.4	7.2 ± 6.1	22.8 ± 11.5	0.4 ± 0.2	0.5 ± 0.9	4.7 ± 2.1
	JW3-HT15	5.8 ± 1.9	1.8 ± 1.2	86.4 ± 4.8	0.6 ± 0.3	0.1 ± 0.2	1.0 ± 0.8	0.0 ± 0.1	4.2 ± 2.7
$NbCr_2$	JW3-AC	18.0 ± 1.9	3.2 ± 0.9	19.7 ± 3.6	54.6 ± 2.2	2.1 ± 0.7	0.5 ± 0.5	0.0 ± 0.3	1.9 ± 1.2
	JW3-HT13	17.6 ± 1.7	3.5 ± 0.8	20.4 ± 1.8	49.6 ± 2.8	5.4 ± 1.5	0.9 ± 0.6	0.2 ± 0.4	2.5 ± 1.5
Segregated Al	JW3-HT15	3.6 ± 1.9	2.2 ± 1.2	2.9 ± 2.0	0.7 ± 0.4	85.9 ± 5.4	1.7 ± 1.0	0.0 ± 0.1	3.0 ± 1.7

Table 6.16) Phase analysis of bulk phases present in each JW3 oxidised sample from locations close to the oxide layer (top lines) and from locations far from the oxide layer (bottom lines). Values given in at.%. The distances from the oxide scale vary dependent on what was possible to measure. Alloy:phase-close to:far from; JW3-HT13:(Nb) – 15-25µm : 55-80µm, JW3-HT13:(Ti) – 10-20µm : 50-80µm, JW3-AC:($D8_8$) - <5µm : 115-125µm, JW3-HT13:($D8_8$) - <10µm : 115-125µm, JW3-HT15:($D8_8$) - <10µm : 130-135µm, JW3-AC:(NbB) - <10µm : 115-135µm, JW3-HT13:(NbB) – <10µm : 60-75µm, JW3-AC:($NbCr_2$) – <5µm : 130-140µm, JW3-HT13:($NbCr_2$) – <10µm : 75-80µm.

		Nb	Si	Ti	Cr	Al	Ge	B	O
$D8_8$	JW3-AC	30.1 ± 3.1	21.6 ± 2.6	30.2 ± 3.3	2.1 ± 1.6	1.2 ± 0.7	11.1 ± 1.1	1.4 ± 1.2	2.4 ± 1.4
		27.8 ± 2.4	19.6 ± 1.9	33.7 ± 2.0	2.4 ± 1.0	1.9 ± 0.6	10.7 ± 1.0	1.6 ± 1.5	2.2 ± 1.2
	JW3-HT13	30.2 ± 3.7	20.5 ± 3.3	29.2 ± 3.3	1.6 ± 0.8	1.0 ± 0.9	12.1 ± 2.3	2.4 ± 2.4	3.1 ± 1.7
		28.7 ± 3.0	17.8 ± 3.1	31.4 ± 3.1	2.2 ± 0.6	2.0 ± 1.1	12.8 ± 1.3	2.2 ± 1.4	2.8 ± 1.5
	JW3-HT15	31.2 ± 2.8	20.1 ± 1.9	27.8 ± 3.2	2.2 ± 0.7	1.3 ± 1.3	12.1 ± 1.1	2.3 ± 1.5	3.0 ± 2.0
		31.3 ± 2.4	19.9 ± 2.0	28.1 ± 2.5	1.7 ± 0.4	1.3 ± 0.5	12.0 ± 1.2	2.7 ± 1.7	2.9 ± 1.4
NbB	JW3-AC	30.2 ± 2.0	0.1 ± 0.1	17.5 ± 1.4	0.5 ± 0.2	0.1 ± 0.1	0.1 ± 0.3	50.3 ± 2.4	1.2 ± 0.9
		27.5 ± 2.0	0.4 ± 0.6	17.5 ± 2.3	0.3 ± 0.2	0.0 ± 0.0	0.2 ± 0.3	53.2 ± 2.0	0.8 ± 0.8
	JW3-HT13	23.4 ± 1.6	0.2 ± 0.2	23.2 ± 2.2	1.7 ± 1.1	0.5 ± 0.6	0.3 ± 0.5	48.2 ± 4.2	2.5 ± 1.4
		24.0 ± 2.3	0.2 ± 0.2	24.2 ± 1.5	1.7 ± 1.4	0.2 ± 0.2	0.1 ± 0.1	47.9 ± 2.3	1.7 ± 0.8
(Nb)	JW3-HT13	27.5 ± 3.4	0.5 ± 0.2	26.2 ± 6.0	12.3 ± 6.5	28.5 ± 3.9	0.3 ± 0.2	1.0 ± 1.0	3.8 ± 1.5
		28.9 ± 2.4	0.6 ± 0.4	28.1 ± 1.8	7.0 ± 4.4	31.5 ± 6.0	0.4 ± 0.3	1.3 ± 1.3	2.2 ± 1.0
(Ti)	JW3-HT13	5.6 ± 1.8	1.2 ± 0.5	59.3 ± 3.8	15.8 ± 2.6	9.2 ± 2.6	0.6 ± 0.3	1.4 ± 0.7	6.9 ± 1.8
		8.1 ± 0.9	0.2 ± 0.2	56.2 ± 1.6	1.7 ± 0.5	30.5 ± 3.0	0.2 ± 0.2	0.0 ± 0.0	3.1 ± 1.5
$NbCr_2$	JW3-AC	19.6 ± 2.1	4.1 ± 2.2	20.8 ± 7.3	49.9 ± 2.9	2.4 ± 1.4	0.9 ± 1.1	0.2 ± 0.6	2.0 ± 2.0
		16.2 ± 1.6	2.9 ± 0.6	21.5 ± 2.5	55.3 ± 1.4	2.2 ± 0.5	0.3 ± 0.3	0.0 ± 0.0	1.6 ± 1.0
	JW3-HT13	17.7 ± 1.9	3.9 ± 0.7	21.1 ± 2.7	47.4 ± 1.7	4.9 ± 2.2	1.5 ± 0.5	0.2 ± 0.5	3.2 ± 1.7
		17.4 ± 2.0	3.3 ± 0.8	20.3 ± 1.3	51.4 ± 2.4	5.0 ± 0.8	0.6 ± 0.4	0.1 ± 0.2	1.9 ± 1.3

Table 6.17) Area analysis of the entire oxide layers and Ge-rich layers shown in EPMA maps for JW3 oxidised samples, values given in at.%.

		Nb	Si	Ti	Cr	Al	Ge	B	O
Total oxide layer:	JW3-AC	15.4 ± 5.1	10.2 ± 5.1	14.5 ± 6.3	2.4 ± 4.3	0.7 ± 3.9	2.5 ± 6.7	0.5 ± 0.8	53.8 ± 13.9
	JW3-HT13	16.9 ± 5.2	12.1 ± 5.4	13.9 ± 5.6	3.5 ± 8.8	0.3 ± 0.5	2.5 ± 7.3	1.6 ± 1.4	49.2 ± 11.2
	JW3-HT15	19.1 ± 4.1	11.7 ± 5.7	18.0 ± 5.1	2.1 ± 1.5	2.2 ± 7.2	0.3 ± 0.6	1.4 ± 1.3	45.2 ± 6.6
Inner oxide:	JW3-HT15	11.6 ± 4.9	6.1 ± 5.9	18.7 ± 6.6	3.6 ± 1.7	15.0 ± 27.1	0.1 ± 0.3	0.6 ± 0.7	44.3 ± 11.2
Ge-rich layer:	JW3-AC	16.2 ± 4.8	9.8 ± 4.4	13.4 ± 9.3	0.2 ± 0.4	0.6 ± 0.5	28.4 ± 9.7	0.2 ± 0.5	31.2 ± 12.9
	JW3-HT13	15.6 ± 4.8	9.2 ± 5.3	14.7 ± 8.6	0.3 ± 0.6	0.5 ± 0.5	32.0 ± 9.1	0.4 ± 0.8	27.4 ± 12.1

Table 6.18) Phase analysis of oxide phases in each JW3 oxidised sample from locations in the oxide scale, values given in at.%.

		Nb	Si	Ti	Cr	Al	Ge	B	O
Ge-rich phase	JW3-AC	16.8 ± 1.9	2.6 ± 2.3	10.9 ± 5.2	0.1 ± 0.2	0.5 ± 0.3	41.4 ± 1.8	0.1 ± 0.4	27.6 ± 6.0
	JW3-HT13	21.9 ± 2.4	4.2 ± 3.5	5.8 ± 4.1	0.2 ± 0.3	0.4 ± 0.4	51.1 ± 4.2	0.6 ± 1.3	15.8 ± 8.4
	JW3-HT15	25.9 ± 2.2	4.8 ± 1.0	4.7 ± 2.1	0.2 ± 0.2	0.2 ± 0.3	59.3 ± 2.8	0.1 ± 0.3	4.8 ± 2.0
Ti-rich oxide	JW3-AC	10.7 ± 4.9	2.0 ± 0.9	29.1 ± 3.6	5.1 ± 2.1	0.1 ± 0.1	0.1 ± 0.1	0.1 ± 0.3	52.9 ± 6.6
	JW3-HT13	12.9 ± 2.9	7.0 ± 4.1	32.0 ± 5.2	1.0 ± 0.6	0.5 ± 0.4	0.3 ± 0.4	0.7 ± 0.6	45.6 ± 5.7
	JW3-HT15	8.7 ± 5.8	1.7 ± 0.8	36.8 ± 6.4	4.8 ± 1.7	1.7 ± 2.7	0.1 ± 0.1	0.2 ± 0.4	46.0 ± 8.5
Nb-rich oxide	JW3-AC	28.1 ± 2.2	2.7 ± 2.2	11.6 ± 6.9	0.3 ± 0.3	0.4 ± 0.3	0.0 ± 0.1	3.1 ± 1.3	53.7 ± 6.2
	JW3-HT13	35.7 ± 2.2	3.0 ± 1.4	8.7 ± 2.5	0.2 ± 0.1	0.2 ± 0.2	0.1 ± 0.1	4.0 ± 2.4	48.2 ± 5.0
	JW3-HT15	37.5 ± 1.3	6.8 ± 2.7	8.8 ± 3.5	0.6 ± 0.5	0.3 ± 0.3	0.2 ± 0.2	4.2 ± 1.5	41.7 ± 6.2
Si-rich oxide	JW3-AC	8.5 ± 1.7	20.4 ± 1.8	10.1 ± 4.5	0.7 ± 0.5	0.2 ± 0.3	0.1 ± 0.2	0.8 ± 0.7	59.2 ± 8.3
	JW3-HT13	6.0 ± 3.8	29.4 ± 5.2	6.1 ± 3.7	0.2 ± 0.2	0.1 ± 0.1	0.1 ± 0.2	1.2 ± 0.9	56.7 ± 14.1
	JW3-HT15	15.7 ± 4.8	27.1 ± 6.7	12.7 ± 5.8	1.4 ± 0.7	0.6 ± 0.5	0.3 ± 0.3	1.1 ± 1.2	41.2 ± 8.7
Cr-rich oxide	JW3-AC	2.6 ± 2.2	1.4 ± 1.1	3.4 ± 2.4	31.4 ± 4.5	0.5 ± 0.4	0.0 ± 0.1	0.0 ± 0.0	60.7 ± 5.9
	JW3-HT13	0.5 ± 0.4	0.1 ± 0.1	2.9 ± 1.4	37.1 ± 2.0	0.4 ± 0.2	0.0 ± 0.1	0.0 ± 0.0	58.9 ± 4.4
Low-sub TiO_2	JW3-AC	0.1 ± 0.2	0.5 ± 0.6	41.6 ± 3.5	2.6 ± 0.6	0.1 ± 0.1	0.0 ± 0.0	0.0 ± 0.0	55.0 ± 5.5
	JW3-HT13	2.3 ± 1.8	1.5 ± 1.6	49.4 ± 4.4	2.7 ± 1.1	0.1 ± 0.1	0.0 ± 0.1	0.0 ± 0.0	43.9 ± 13.0
JW3-HT15 pocket oxides phases	Al-rich	1.0 ± 0.4	0.4 ± 0.3	2.8 ± 1.0	2.6 ± 1.0	60.2 ± 1.9	0.0 ± 0.0	0.0 ± 0.1	33.0 ± 6.1
	Ti-rich	16.2 ± 1.5	1.8 ± 1.4	32.3 ± 2.4	3.6 ± 0.7	0.7 ± 1.4	0.1 ± 0.1	1.2 ± 1.1	44.2 ± 5.4
	Si-rich	19.2 ± 2.1	17.2 ± 2.4	15.1 ± 1.4	2.6 ± 0.6	0.2 ± 0.2	0.1 ± 0.1	0.8 ± 0.7	44.8 ± 7.3

6.2.3 Discussion

6.2.3.1 The effect of alloy composition on oxidation resistance

For oxidation at 1000°C, B and Ge additions have generally improved the oxidation resistance of the base alloy, KZ5. However, there are certain B and Ge containing alloys that performed poorly in terms of oxidation resistance at certain processing states when compared to the generally improvement seen. These alloys are JW2-AC and JW3-HT15. The heat-treatments have had a significant effect on the higher boron and higher germanium alloys, JW2 and JW3. Despite this, mass gain and linear rates of oxidation were lower in the case of B and Ge containing alloys when compared to KZ5-AC and KZ5-HT in all cases. In Figure 6.6, the large spread of TGA curves can be seen. The impact of boron and germanium additions can be more easily considered at each individual processing state.

In the as-cast state, the best performing alloy in terms of total mass gain at 1000°C was JW3-AC. If the experiments were allowed to continue however, JW1-AC would likely have the smallest mass gain given that JW1-AC has parabolic oxidation kinetics. The addition of 5 at.% Ge added to JW3-AC has improved the oxidation resistance only marginally in the as-cast state, where as an additional 5 at.% B, i.e. JW2-AC, has had a detrimental effect on oxidation resistance with both linear oxidation rate and total mass gain. The B and Ge free alloy, KZ5, is still the worst preforming alloy, so evidently the B and Ge additions are beneficial still.

In the heat-treated at 1300°C state, the three alloys JW1, JW2 and JW3 had relatively similar mass gain to time curves, where total mass gains, parabolic and linear oxidation rates, and *n* exponent values were similar to each other. JW2-HT13 and JW3-HT13 had near identical oxidation curves, but JW2-HT13 was modelled as having completely parabolic oxidation behaviour due to slight difference in *n* value. These oxidation parameters of JW2-HT13 and JW3-HT13 cannot be used to state that JW2-HT13 had superior oxidation resistance to JW3-HT13, or that B additions are more effective then Ge additions after heat treatment at 1300°C, since the difference between them is so small. Repeat measurements would be likely to show the reverse in some cases. The JW1-HT13 measurement does however suggest slightly worse oxidation performance given the initial parabolic rate, linear rate, and total mass gain are all larger than the JW2-HT13 and JW3-HT13 counterparts.

In the heat-treated at 1500°C state, the best performing alloy was JW2-HT15 by a significant margin with a mass gain of only 1.66 $mg.cm^{-2}$ after 100 hours. The nature of the oxidation in this alloy is modelled as entirely parabolic according to the *n* exponent, with a value of 0.45. JW1-HT15 performed the next best, although JW1 in the heat-treated at 1500°C state performed the worst out of the JW1 alloys. In this case the extra 5 at.% B added to JW2 has improved oxidation significantly compared to JW1-HT15. JW3-HT15 performed almost as poorly as the B and Ge free alloy KZ5, indicating the additional Ge content in JW3-HT15 has been detrimental to oxidation resistance.

The reasons for the effects of different B and Ge contents will now be considered. In all cases where B and Ge are added to the KZ5 base alloy, total mass gain and linear rate of oxidation are lower than the KZ5 alloy. This is likely a result of a reduction in (Nb) content, as this is the most susceptible phase to oxidation. However, this is not the only factor, as there are examples of B and Ge containing alloys with low amounts of (Nb) that perform worse than other alloys with higher amounts of (Nb), such as JW3-HT15 (0% (Nb)) compared to JW1-AC (18.5% (Nb)). $D8_8$ forms in B and Ge containing alloys and βNb_5Si_3 is destabilised. $D8_8$ is reported to have greater resistance to oxidation than βNb_5Si_3 in single phase experiments [162][163], so in these multiphase alloys it follows that this silicide is beneficial for oxidation resistance. The $NbCr_2$ Laves phase forms in each B

and Ge containing alloy. This phase has been showed to improve oxidation resistance in niobium silicide-based alloys [104].

The most significant differences between JW2-AC and the B and Ge containing alloys that performed well at 1000°C in the as-cast state, JW1-AC and JW3-AC, is the formation on the NbB phase in JW2-AC. This phase is metastable according to the heat-treated microstructure of JW2, and is a result of increased boron in the alloys composition. This is possibly evidence of either NbB itself has poor oxidation resistance, or that B is beneficial to oxidation resistance when in other phases, as boron can be considered 'locked away' in NbB in the as-cast alloy. JW3-AC is less prone to oxidation in the experiments performed in this study compared to JW1-AC, however if the experimental was allowed to proceed for longer, the higher linear rate of oxidation and less parabolic in nature oxidation curve of JW3-AC would have resulted in a total mass gain of JW3-AC that would have exceeded that of JW1-AC. This could be explained by the intergranular microstructures of JW1-AC and JW3-AC. JW1-AC has a eutectic like structure of the susceptible (Nb) and $D8_8$, whereas JW3-AC has no intergranular $D8_8$. Diffusion of oxygen into the sample, and therefore internal oxidation, may face more resistance in the alloy where diffusion pathways ways are blocked by $D8_8$ over a longer time scale.

After a heat-treatment at 1300°C for 100 hours, each B and Ge containing alloy performed relatively similar. JW2 is no longer severely oxidised and has a very similar oxidation curve to that of JW3-HT13. A significant part of the NbB phase has been converted into T2 according to area fraction analysis, which is likely a factor in reducing oxidation of this alloy after heat-treatment. JW1-HT13 and JW3-HT13 have similar oxidation curves as well, as they did in the as-cast state, but in this case JW3 is not likely to exceed the mass gain of JW1 if the experiment was allowed to continue as JW3 no longer has a higher linear rate of oxidation than JW1 in the heat-treated at 1300°C state. This follows the reasoning that was used to explain why this was the case in the AC state of each alloy, in that JW1-HT13 no longer has a fine eutectic like structure of (Nb) and $D8_8$, and instead is more similar to the intergranular region of JW3-HT13.

After a heat-treatment at 1500°C for 100 hours, the NbB phase is almost completely removed from JW2-HT15 in place of T2 which makes up over 25% of the alloy by volume. This results in an alloy that has very little (Nb) and two boron containing silicides, T2 and $D8_8$, in coarse arrangements. This in turn result in the best oxidation resistance observed at 1000°C in this study. Conversely JW3-HT15 has a microstructure that is made up of T2 and $D8_8$ in coarse arrangements but no detectable (Nb), which results in the worse oxidation performance seen in any B and Ge containing alloy at 1000°C in this study. It is proposed that the lack of a solid solution phase results in a very brittle structure where cracks are able to form during oxidation and therefore a much larger surface area is actually exposed to the oxidising atmosphere. Internal oxidation areas, referred to as 'pockets' are evidence of this phenomenon, which has similarities to 'pest' oxidation. The pest phenomenon is generally considered to occur below 1000°C, however, and no spallation of the scale or conversion of the sample into powder is observed. Pesting that results in disintegration of an alloy did not occur in any experiment within this study. Spallation of the oxide scale was eliminated by the addition of B and Ge and was not seen in any B and Ge containing sample, whereas KZ5 did experience mild spallation at the sample cube edges.

The addition of 5 or 10 at.% germanium has resulted in a germanium-rich layer and possible phases $NbGe_2$ and Nb_5Ge_3. In some cases, areas within the oxide scale appear to be prior $D8_8$ grains or prior intergranular areas. $D8_8$ in unoxidised alloys has Ge content of at least 5.8 at.%. However, Ge is largely absent from the high Si areas of the oxide scale. Therefore, it is proposed that the formation of the Ge-rich layer in the JW series of alloys is a result of inwards diffusion of Ge from the oxidising

outer surface. As Ge containing $D8_8$ is oxidised, elements with a higher affinity to oxygen form oxides such as TiO_2, Nb_2O_5 and SiO_2. GeO_2 does not form, instead Ge diffuses into the sample along with O, as more reactive elements Nb and Ti diffuse out to continue oxide formation within the oxide layer and at the oxide-bulk interface. At the oxide-bulk interface, Ge content increases as the oxidation process continues, where niobium germanium phases become stabilised due to the changing composition such as Nb_5Ge_3 and $NbGe_2$. This is supported by thermocalc modelling of the Nb-Si-Ge system combined with an oxide data base, where $NbGe_2$ is stable at increasing O content before GeO_2 or other Ge containing oxides (appendix section Figure 8.3). These Nb-Ge phases, forming in seemingly complete layers, are proposed to improve the oxidation resistance of Ge containing alloys by limiting further diffusion of oxygen into the bulk of the material. The diffusion of Ge away from these regions may also be a limiting factor in the formation of oxides, slowing the oxide formation. Boron on the other hand generally favours titanium niobates in the oxide scale. Therefore, no borosilicate glassy layer is found in any B containing alloy in this study.

6.2.3.2 The effects of processing on oxidation resistance

The effect of heat treatment on these alloys has had mixed results. For alloys KZ5, JW1 and JW3, heat-treated samples at 1500°C have higher total mass gains than heat-treated samples at 1300°C, which in turn have higher total mass gains than samples in the as-cast state. The opposite is true for JW2 samples.

In the case of KZ5 the linear rate is actually lower in the HT15 version, and the oxidation behaviour is more parabolic in nature with an *n* exponent of 0.56 compared to 0.63 in the AC version. The increased mass gain is a result of the higher initial parabolic rate which acts for over three times as long in the HT15 version compared to the AC version. In the case of JW1, the increasing total mass gains from AC to HT13 to HT15 versions of the samples follow the same trend as the increasing linear rate, increasing parabolic rate, and increasing *n* exponent as linear behaviour becomes more of a factor. In the case of JW3, whilst the total mass gains do follow the stated trend, it would be misleading to claim this was representative of oxidation resistance as a whole with regards to the AC and HT13 version of the alloys. Whilst JW3-HT13 has 0.01 $mg.cm^{-2}$ more total mass gain than JW3-AC, the linear rate and *n* exponent, and therefore influence of linear oxidation kinetics, are lower in the HT13 version of the alloy. Much like in KZ5 the initial parabolic period of JW3-HT13 is large compared to the AC version, which in this case despite having superior oxidation parameters, total mass gain values at the end of experiment are near identical. For the HT15 version of the alloy, oxidation has clearly been more severe due to high parabolic and linear rates. There is nuance to the effect of heat treatments on KZ5, JW1 and JW3 oxidation resistance, but generally heat treatments have resulted in poorer oxidation resistance or at the very least no significant benefit.

For the JW2 alloy, the heat-treated sample at 1500°C has lower total mass gains than the heat-treated sample at 1300°C, which in turn has lower total mass gains than samples in the as-cast state. Heat treatment of JW2 had positive effects on the oxidation resistance, and results in the lowest mass gain observed at 1000°C, 1.66 $mg.cm^{-2}$. The initial parabolic rate, the linear rate and the *n* exponent all follow the same trend as the total mass gain in JW2 and decrease from AC to HT13 to HT15 samples. JW2-HT13 and JW2-HT15 were modelled as having entirely parabolic oxidation behaviour. In general, parabolic behaviour is preferred as in the case where mass gains are similar at the 100-hour point, i.e. what is tested in these experiments, parabolic oxidation kinetics would result in less oxidation compared to linear oxidation kinetics when the alloy is actually in service and much longer exposure times are encountered. For parabolic oxidation behaviour to be observed, some degree of passivation occurs as the rate limiting step of oxidation is the diffusion of oxygen through the oxide layer. In service, these alloys would experience a range of temperatures during the start-up and cool down of the engines which may adversely affect the effectiveness of a passivating layer. For example, if it were to experience spallation from differences in thermal expansion. Cyclical oxidation experiments should be performed in future stages of alloy development to assess this closer approximation to service life.

The reasons for the effects of heat-treatments on oxidation resistance will now be considered. Compositions of the (Nb) phase in each oxidised specimen showed higher Ti content in the AC version of KZ5 compared to KZ5-HT15, 16.0 at.% compared to 13.5 at.%. Si content and Al content are also lower in the heat-treated alloy. These elements can alter the diffusivity of O through the susceptible (Nb) phase [142][143], and so could be related to the marginally better oxidation performance of KZ5-AC, it least in terms of total mass gain. However, the margins of error for these compositions overlap, and in the pre-oxidised compositions of the (Nb) phase reported in Chapters 4 and 5, only the reduction in Si content upon heat-treatment is observed. Another potential factor, although not seen in the specific area of KZ5-AC mapped, is the fine eutectic that exists throughout

KZ5-AC and not KZ5-HT15. Alloys of similar composition but with coarser microstructures, whether due to heat-treatment [136][124] or different manufacture techniques [197], have been shown to have reduced oxidation resistance in part attributed to the coarsening of (Nb). The eutectic structure is lost through heat-treatment, effectively coarsening the KZ5-HT15 microstructure. This would affect the oxidation of the intergranular region, as there is less impediment for diffusing oxygen.

In every oxide phase measured in the oxide scale of KZ5-HT15 as well as the entire oxide scale, the O content was lower when compared to KZ5-AC. Conversely, the bulk phases (Nb), (Ti) and βNb_5Si_3 had slightly higher O contents in the HT15 version of KZ5. The portion of the EPMA map () labelled as the oxide layer of KZ5-HT15 is therefore oxidised to a lesser degree and may retain more unoxidised material than the KZ5-AC oxide layer, whilst the bulk phases are more affected by oxygen. This could be an indication that diffusion of oxygen into the KZ5-HT15 sample is more prevalent than in the case of the KZ5-AC sample, proposed to be a result of microstructural differences. In KZ5-AC more complete oxidation of the oxide layer region, i.e. larger O contents of oxide phases, takes place, as diffusion of oxygen into the bulk of the sample is marginally more difficult. As the oxidation behaviour is more linear in nature this suggests this oxidation reaction that occurs in the oxide layer is a linear rate limiting step. The oxidation reaction is likely more than one single reaction, given the multiple oxide phases found within the layer.

The purpose of adding B and Ge in combination to the base composition of KZ5 (Nb-24Ti-18Si-5Cr-5Al) was to assess the viability of a B-Ge-Si oxide layer forming in an alloy intended for bulk components and not a coating material. In JW1, with 5 at.% B and 5 at.% Ge, no such layer was seen in the oxide scales formed at 1000°C. Boron was found in the highest quantities in titanium niobate oxides $TiNb_2O_7$ and $Ti_2Nb_{10}O_{29}$.

There was however a Ge-rich layer located on the interface between the bulk material and oxide scale. When averaging the composition of this layer, the ratio of Nb+Ti to Ge+Si is in between that of $NbGe_2$ and Nb_5Ge_3. The highest Ge parts of the Ge-rich layer had ratios more in line with $NbGe_2$ for JW1-AC and JW1-HT13 but not for JW1-HT15. This is possibly an indication that a more complete Ge layer, with higher Ge content allowing the formation $NbGe_2$, is beneficial for oxidation resistance as JW1-HT15 performed the worst out of JW1 alloys at 1000°C during oxidation experiments. Generally, the highest areas of Ge in the Ge-rich layer are adjacent to places where the bulk microstructure was not $D8_8$. This provides further insight into the mechanism of Ge-rich layer formation, as it follows that diffusion of reactive species such as Ti and Nb out of the bulk material towards the oxide layer would be more prevalent in locations with (Nb) present. At these locations a higher quantity of Nb and Ti ions diffusing out of the material would require a higher volume of O and evidently Ge ions diffusing in. Hence Ge in the Ge-rich layer is more concentrated at these non-$D8_8$ locations.

In terms of oxides detected, XRD spectroscopy found TiO_2, $Ti_2Nb_{10}O_{29}$, $TiNb_2O_7$, and SiO_2 in each alloy. A difference between the alloys is that $TiNb_2O_7$ was more easily identified and a higher degree of confidence can be placed in its existence in the pattern of JW1-AC, which performed the best in oxidation experiments. The SiO_2 peak is also clearest in the JW1-AC pattern.

The eutectic silicide $D8_8$ is also eliminated in the HT15 version of JW1 and reduced in the HT13 version. Therefore, the same effect of more diffusion of O into the bulk material would be expected in heat-treated samples, as was the case with KZ5. This is generally the case for JW1-AC compared to JW1-HT15, oxygen content in the bulk phases is increased by small amounts. However, JW1-HT13 does not fit this trend of more oxygen in the bulk phases of heat-treated alloys after oxidation, so other factors must be considered.

A Ti-rich (Nb) was found in JW1-AC and JW1-HT13 furthest away from the oxide scale, and replaced moving towards the oxide scale by the (Nb), (Ti), $NbCr_2$ intergranular mixture. The composition of the Ti-rich (Nb) phase is actually closer to the composition of the (Nb) phase reported in unoxidised specimens of JW1-AC and JW1-HT13 than it is to the (Nb) found in the oxidised specimens. Therefore, the Ti-rich (Nb) is an original part of the microstructure and (Nb) is also a result of oxidation as (Ti) is in this alloy. From this assumption, a mechanism of oxidation is proposed; Ti-rich (Nb), or the original (Nb) in un-oxidised specimens, is subjected to oxidation and O begins to diffuse through this phase. Eventually maximum solubility is reached, approximately below 5 at.% according to EPMA results, and this results in a transition of Ti-rich (Nb) -> (Nb) + (Ti) to accommodate the increasing O content as (Ti) has an apparent higher solubility, at least up to 9.7 at.%. It is unclear how $NbCr_2$ fits into this process but it too could be a product of Ti-rich (Nb) segregation. Ti-rich (Nb) is not found in JW1-HT15 from the EPMA map taken. It is therefore proposed that the Ti-rich (Nb) segregation is more complete in this alloy due to a greater degree of oxidation and transportation of O further into the alloy, and that Ti-rich (Nb) is found at a greater depth into the bulk material. Figure 6.22 is included to provide evidence of this based on the different contrasts of (Nb) and Ti-rich (Nb). This is in accordance with the slightly worse oxidation performance of JW1-HT15. The reasons for this increased O solubility and diffusion are not fully explained, but are expected to include the previously discussed less extensive Ge layer which presumably limits oxygen diffusion, and loss of the eutectic structure on a macroscopic scale.

The Ge-rich layer observed in JW1 was also observed in JW3, which is the alloy with the highest Ge content with composition Nb-24Ti-18Si-5Cr-5Al-10Ge-5B. In JW3-AC and JW3-HT13, the whole Ge-rich layer had elemental ratios closer to $NbGe_2$ than other phases considered, and the highest Ge points along this layer were closer still to the 0.5 ratio of Nb+Ti to Ge+Si that would be expected in $NbGe_2$. On the other hand, the alloy that performed the worst of the JW3 alloys, JW3-HT15, did not form a complete Ge-rich layer. Instead discrete particles of Ge-rich phase, which were identified as $NbGe_2$, formed on the outer oxide layer and bulk material interface. Curiously no Ge-rich phase or layer formed in the internal oxide pockets either. Another point of interest is how in JW3-AC and JW3-HT13, the O content of the Ge-rich phase is 27.6 at.% and 15.8 at.%, respectively, indicating a partially oxidised phase. Where as in JW3-HT15, the Ge-rich phase only had O content of 4.8 at.%. This suggests the Ge-rich phase in JW3-HT15, which did not form into a Ge-rich layer, did not provide nearly as much resistance to oxidation as was the case in the better performing alloys JW3-AC and JW3-HT13. In this case it is proposed that incoming oxygen bypasses the Ge-rich phase in the case of JW3-HT15 and preferentially oxidises the more susceptible phases, especially (Nb), hence why alloys where the Ge-rich layer is more complete have higher oxygen content of this layer.

The composition of the (Nb) phase in JW3 alloys is less important to overall oxidation resistance since it makes up significantly less of the alloy when compared to KZ5 and JW1. However, a major difference between the versions of JW3 that performed well and JW3-HT15 is how (Nb) exists in JW3-AC and JW3-HT13 where as in JW3-HT15 it is completely removed by the heat treatment. This is likely a contributing factor to the segregation of Al in JW3-HT15 as the phase where it usual is accommodated is not present and its solubility in the most common phase, $D8_8$, is evidently low. In the unoxidised $D8_8$ present in JW3-HT15, Al content was 3.3 at.%. In oxidised $D8_8$ in JW3-HT13, the content of Al less than half of this.

A combination of XRD and EPMA analysis of the Nb-rich phases in each alloy show that $TiNb_2O_7$ formed in JW3-AC more so than the other two alloys, as EPMA and XRD detected it, where as XRD was the only technique to detect $TiNb_2O_7$ in JW3-HT13, and only $Ti_2Nb_{10}O_{29}$ was detected in JW3-HT15 through XRD or EPMA. It therefore seems more complete oxidation occurred in the oxide scale

of the as-cast specimen, as $TiNb_2O_7$ forms after $Ti_2Nb_{10}O_{29}$ which forms after TiO_2 and Nb_2O_5. TiO_2 was found in all oxide layers. SiO_2 was only detected by the characteristic peak around 21° in JW3-HT15, and this was a relatively minor intensity peak compared to what was seen in the JW1 alloy series. Boron was again found in the Nb-rich oxide phases $TiNb_2O_7$ and $Ti_2Nb_{10}O_{29}$ in the oxide scale more than any other oxide phase, but no boron layer was detected through EPMA.

There is evidence for underlying phases being detected in XRD in JW3-AC and JW3-HT15, but is not clear if this is $D8_8$, Nb_5Ge_3 or some other similarly structured phase which would have similar peaks in the region in question, ~40° 2θ. It is unclear why this has been observed in JW3 and not JW1. There is also evidence of Cr-rich layers in each of the oxide scales, but only in JW3-AC and JW3-HT13 were they large enough to be measured, and these had compositions suggesting Cr_2O_3. These Cr-rich layers being thicker and more prevalent in the two alloys that did well in oxidation experiments is another factor to consider when assessing why these alloys had superior oxidation resistance.

The oxidation parameters for JW2 alloys show linear oxidation behaviour is more of a factor in the worst performing alloy, JW2-AC, where the *n* exponent is 0.72. Whereas the better performing alloys were much more parabolic in nature with values close to 0.5. This difference is highlighted by considering the first 5 hours of the experiment where JW2-AC actually had less mass gain compared to the heat-treated versions, but due to more linear kinetics this became no longer the case shortly after the experiment had started.

The differences between oxidation graphs of JW2 alloys at different processing states are larger than the differences observed in JW1 at different processing states, to an extent that clear improvement is made between JW2 alloys. Since this is the opposite trend as seen in the other alloys, one would expect other factors to be influencing the oxidation resistance other than those already presented for KZ5, JW1 and JW3. XRD results show TiO_2, $Ti_2Nb_{10}O_{29}$ and $TiNb_2O_7$ are present in all the JW2 samples. Whilst JW2-AC and JW2-HT13 have fairly similar pattern, JW2-HT15 has significantly higher intensity TiO_2 peaks, a minor SiO_2 peak, and the possibility of underlying phases. The underlying Nb_5Ge_3 phases could be an indication of a thinner oxide scale due to less oxidation, but from XRD results for JW3 alloys this is not a guaranteed correlation.

The increased boron content of this alloy compared to JW1 has not resulted in the formation of any B-rich oxide layers, and B content is still only seen in significant quantities in the Nb-rich phase in the oxide layer. The Ge-rich layer found in JW1 and JW3 is also found in JW2 alloys. In the AC and HT13 versions the composition of this layer did not correlated well with either $NbGe_2$ or Nb_5Ge_3, but the HT15 version was close to Nb_5Ge_3 composition. The highest Ge parts of the Ge-rich layer suggest $NbGe_2$ was present in JW2-AC and JW2-HT13, but Nb_5Ge_3 was still the most likely phase in JW2-HT15. In the case of JW1 it was proposed that $NbGe_2$ formation indicated a more fully formed Ge-rich layer that had higher Ge content and was therefore improving oxidation resistance. However generally the same Ge-rich phases are seen in the AC, HT13 and HT15 versions of JW2 and the opposite trend of oxidation performance is seen. It could still be the case that this more developed Ge-rich layer is beneficial to oxidation resistance, but more factors are influencing the oxidation resistance of JW2 alloys compared to the relatively minor differences in JW1 oxidation results.

Whilst there is no silicide eutectic as was the case with JW1 and KZ5 AC samples, there is a mixture of intergranular phases with lower O content, $NbCr_2$, alongside the susceptible (Nb) phase in JW2-AC. In JW2-HT13 this intergranular mixture is in a coarser arrangement. This would mean in JW2-HT13 the oxygen would have less resistance to diffusion of oxygen compared to JW2-AC according to what was concluded for alloys KZ5 and JW1, resulting in inferior oxidation resistance. Whilst O

content of (Ti), $NbCr_2$, $D8_8$, T2, NbB, and Ti-rich (Nb), was greater in JW2-HT13, it still had superior oxidation resistance compared to JW2-AC.

It can therefore be concluded that the increase in oxidation resistance is due to another factor not relevant for KZ5, JW1, or JW3. In the unoxidised bulk phases, as well as the oxidised sample presented in this chapter, heat treatment results in the reduction of NbB phase volume fraction and increase in T2 phase volume fraction. On the macroscopic scale this appears to improve oxidation resistance of the alloys at 1000^{o}C based on the oxidation results as there is no other change in microstructure of this scale. Where T2 can be seen in contact with the oxide scale in Figure 6.28, no Ge layer is forming, indicating that the mechanism of Ge transport during oxidations is not occurring here as it is not being oxidised to the same degree as the adjacent $D8_8$. This effect can also be seen to the top right of Figure 6.27. T2 is proposed to have inherently superior oxidation resistance than $D8_8$, it least when the compositions of T2 and $D8_8$ are those that are reported in this study. This would be in agreement with the limited studies on single phase alloys [161]. This current work highlights the importance of processing on the oxidation properties of niobium silicide-based alloys. Oxidation studies reported in the literature may only include the as-cast state, where as this work shows that for particular alloys there may be significant differences between the oxidation properties of as-cast and heat-treated alloys, which should be considered for future alloy design.

6.2.4 Conclusions

- All B and Ge containing alloys perform better in oxidation experiments compared to the base alloy KZ5 (Nb-24Ti-18Si-5Cr-5Al). Spallation of the oxide scale was eliminated in JW1, JW2 and JW3. Processing conditions also played a large role on oxidation parameter in the case of high B and high Ge alloys, JW2 and JW3, respectively.
- The best oxidation performance was that of JW2-HT15. This is attributed to low (Nb) volume fraction, but also large amounts of the high boron silicide known as T2, developed through heat-treatment.
- A low volume fraction of (Nb) generally resulted in improvements to oxidation parameters, however a complete lack of this phase was seen as detrimental to oxidation resistance in the case of JW3-HT15.
- JW1 (5B-5Ge) has consistent oxidation across the three processing states examined; as-cast, heat-treated at 1300^{o}C and heat-treated at 1500^{o}C. This is a result of little phase change during heat-treatment, although a coarsening effect on the microstructure resulted in slightly worse oxidation after each degree of heat-treatment
- A borosilicate glassy layer did not form in any alloy, and boron was found in primarily titanium niobate oxides in the oxide scale.
- Germanium-rich layers were seen in most B and Ge containing alloys, and more developed, complete layers were beneficial to oxidation resistance. When it did not form, oxidation resistance was inferior to Ge-layer containing samples, i.e. KZ5-AC, KZ5-HT15, JW3-HT15. The mechanism for the formation of these layers is proposed to be Ge not forming oxides when surface $D8_8$ is oxidised, and diffusing inwards to form Nb_5Ge_3 and $NbGe_2$ on the oxide scale-bulk material boundary.
- The mechanism of (Nb) segregation due to oxygen is also described. Original (Nb) from the pre-oxidised microstructure absorbs oxygen, and separated into (Nb) that is more rich in Nb and a titanium solid solution that has higher solubility of oxygen. The chromium released from original (Nb) also is likely responsible for additional $NbCr_2$ formation.

6.3 Oxidation at 1200°C

6.3.1 Oxidation behaviour

6.3.1.1 KZ5

The TGA curves of oxidised alloy KZ5 are displayed in Figure 6.35. This alloy was prepared in only as-cast and heat-treated at 1500°C states. The edges of both 1200°C KZ5 sample cubes had experience spallation and the oxide scale at the edges had broken off during the oxidation experiment, or possibly during the cooling process. At a later time upon handling, some of the faces of each cube broke off as well.

Oxidation parameters are displayed in Table 6.19. When the whole oxidation graph is modelled according to Equation (3), the *n* exponents of KZ5-AC and KZ5-HT15 are calculated as 0.75 and 0.60, respectively. The oxidation behaviour of KZ5-HT15 is therefore more parabolic than KZ5-AC, with the linear mechanism of oxidation being less of a contributing factor. However, in both cases parabolic and linear mechanisms of oxidation are both in effect as *n* values are greater than 0.5.

Therefore, to facilitate comparison between the TGA oxidation curves, both samples oxidation behaviour can be modelled as initially parabolic followed by linear mass gain. In the case of the as-cast alloy, the parabolic rate constant is 2.95E-10 $g^2.cm^{-4}.s^{-1}$ and the linear rate constant is 3.96E-08 $g.cm^{-2}.s^{-1}$. Parabolic behaviour is dominant for the initial 8.7 hours. For the 1500°C heat-treated alloy, the parabolic rate constant is 4.80E-10 $g^2.cm^{-4}.s^{-1}$ and the linear rate constant is slightly smaller at 3.21E-08 $g.cm^{-2}.s^{-1}$. The parabolic behaviour of KZ5-HT15 is dominant for 3 times as long (33.7 hours), similarly to the 1000°C oxidation experiments performed on KZ5. In fact, further similarities between the 1000°C and 1200°C oxidation experiments performed on KZ5 are observed; An initially higher parabolic rate constant of the heat-treated at 1500°C alloy, a lower linear rate constant for the heat-treated at 1500°C alloy, and a more parabolic in nature oxidation graph of the heat-treated at 1500°C alloy. In the case of 1200°C experiments these features occur to a larger degree and so, although the rates of oxidation are of the same order of magnitude, total mass gain of the 1500°C heat-treated alloy is lower than that of the as-cast alloy, at 15.37 $mg.cm^{-2}$ and 16.18 $mg.cm^{-2}$, respectively. These total mass gains are the largest when compared to all alloys in this work tested at this temperature.

Table 6.19) Oxidation parameters for alloys KZ5, JW1, JW2 and JW3 oxidised at 1200°C for 100 hours. 'P' signifies a TGA curve modelled as completely parabolic, whereas the corresponding '' represents a linear rate taken from 40-100 hours to facilitate comparison.*

Alloy	Parabolic rate K_p ($g^2.cm^{-4}.s^{-1}$)	Linear rate K_l ($g.cm^{-2}.s^{-1}$)	Parabolic time (hours)	Combined rate K^n ($g.cm^{-2}.s^{-n}$)	n exponent	Total mass gain ($mg.cm^{-2}$)
KZ5-AC	2.95E-10	3.96E-08	8.7	1.12E-06	0.75	16.18
KZ5-HT15	4.80E-10	3.21E-08	33.7	7.30E-06	0.60	15.37
JW1-AC	2.63E-10	2.19E-08	23.9	7.88E-06	0.56	10.77
JW1-HT13	1.95E-10	2.30E-08	20.1	3.04E-06	0.63	10.39
JW1-HT15	2.52E-10[P]	2.01E-08*	-	1.01E-05	0.54	10.06
JW2-AC	2.26E-10[P]	1.65E-08*	-	1.50E-05	0.50	9.20
JW2-HT13	1.22E-10	1.88E-08	25.1	2.12E-06	0.65	8.56
JW2-HT15	1.21E-10	1.79E-08	25.6	2.59E-06	0.63	8.38
JW3-AC	1.73E-10[P]	1.46E-08*	-	1.07E-05	0.52	8.08
JW3-HT13	1.82E-10	1.74E-08	40.1	5.88E-06	0.57	9.03
JW3-HT15	2.04E-10	1.87E-08	21.7	7.77E-06	0.55	9.10

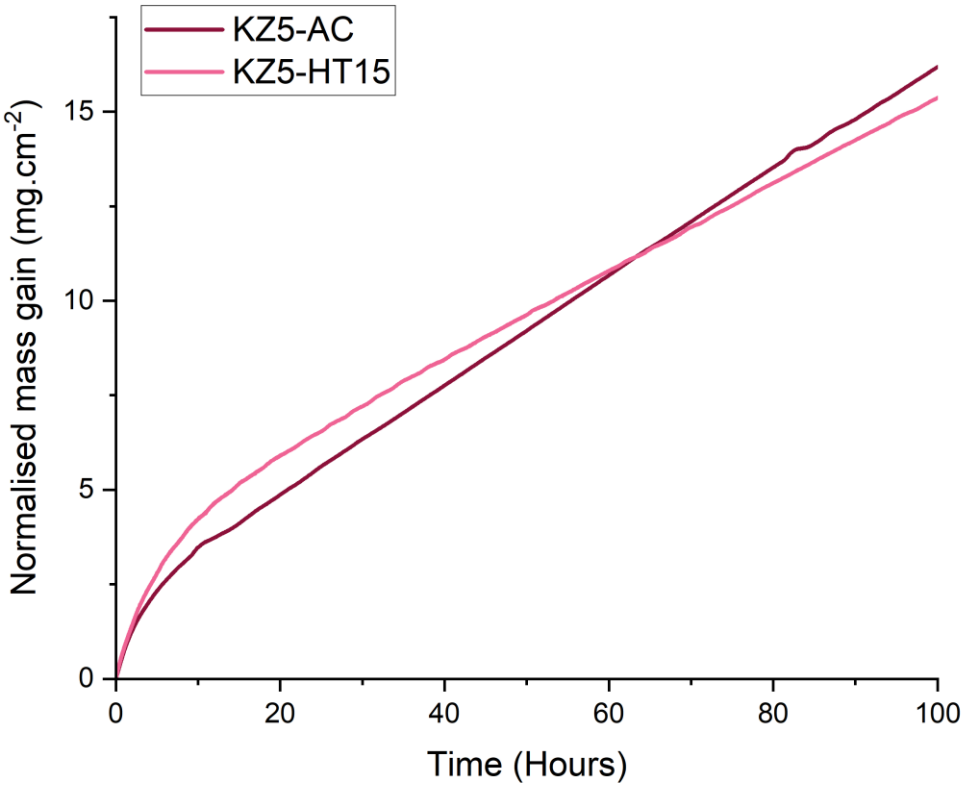

Figure 6.35) Normalised mass gain of KZ5 in the as-cast and heat-treated-1500°C states over a 100 hour period at 1200°C

6.3.1.2 JW1

The TGA curves of oxidised alloy JW1 are displayed in Figure 6.36. This alloy was prepared in as-cast, heat-treated at 1300°C and heat-treated at 1500°C states. Spallation had not occurred in any of the 1200°C JW1 samples during oxidation experiments, nor in the other B and Ge containing alloys JW2 and JW3. Oxidation parameters are displayed in Table 6.19. The *n* exponents of JW1-AC, JW1-HT13 and JW1-HT15 are calculated as 0.56, 0.63 and 0.54, respectively. Therefore, the oxidation behaviour of JW1 samples can generally be said to be more parabolic in nature than linear with values closer to 0.5 than 1. The oxidation behaviour of JW1-HT15 is sufficiently parabolic to be modelled as parabolic for the entirety of the experiment. n exponents less than 0.55, i.e. values that round to 0.5, will be considered suitable to be modelled as parabolic for the entirety of the experiment. Whereas JW1-AC and JW1-HT13 are modelled as being initially parabolic and then linear for the remainder of the experiment. The linear mechanism of oxidation is more of a contributing factor to JW1-HT13 when compared to the other states of JW1.

The as-cast alloy has a parabolic rate constant of 2.63E-10 $g^2.cm^{-4}.s^{-1}$ and linear rate constant of 2.19E-08 $g.cm^{-2}.s^{-1}$. JW1-HT13 has a parabolic rate constant of 1.95E-10 $g^2.cm^{-4}.s^{-1}$ and linear rate constant of 2.30E-08 $g.cm^{-2}.s^{-1}$. These relatively similar rates result in oxidation curves that do not deviated from each other by a great degree (Figure 6.36) and as a result JW1 samples have total mass gains within 0.71 $mg.cm^{-2}$ of each other. Although differences between samples is low, total mass gain still can be said to follow a trend of decreasing with the degree of post-processing; with JW1-AC having a total mass gain value of 10.77 $mg.cm^{-2}$, JW1-HT13 having 10.39 $mg.cm^{-2}$ and JW1-HT15 having 10.06 $mg.cm^{-2}$. The parabolic oxidation rate constant of JW1-HT15 is 2.52E-10 $g^2.cm^{-4}.s^{-1}$. Initial oxidation of JW1-HT15 can be seen to be comparable to JW1-AC, but over the course of the

experiment due to the parabolic oxidation kinetics of JW1-HT15, oxidation proceeded at a reduced rate.

All linear rate constants, parabolic rate constants, and total mass gains are lower for JW1 alloys than KZ5 alloys, indicating a positive effect of adding B and Ge on oxidation resistance at 1200°C. This is most easily seen in Figure 6.40 and Figure 6.42 regarding an as-cast and heat-treated at 1500°C comparison, respectively.

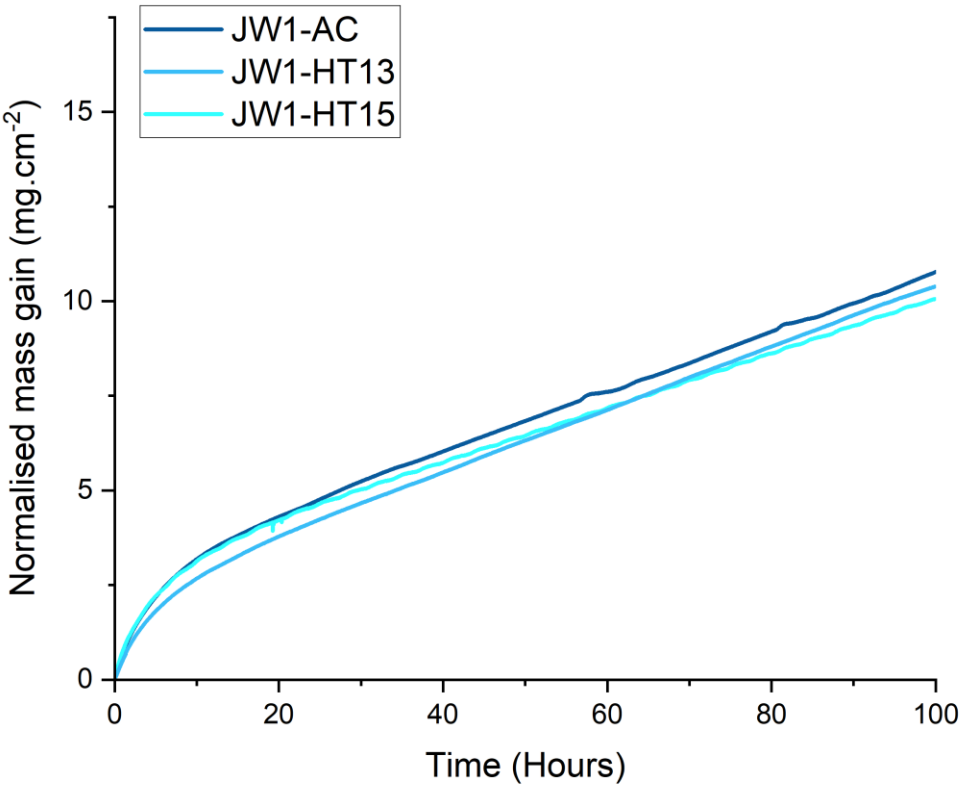

Figure 6.36) Normalised mass gain of JW1 in the as-cast, heat-treated-1300°C and heat-treated-1500°C states over a 100 hour period at 1200°C

6.3.1.3 JW2

The TGA curves of oxidised alloy JW2 at 1200°C are displayed in Figure 6.37. This alloy was prepared in as-cast, heat-treated at 1300°C and heat-treated at 1500°C states. Oxidation parameters are displayed in Table 6.19. The *n* exponents of JW2-AC, JW2-HT13 and JW2-HT15 are calculated as 0.50, 0.65 and 0.63, respectively. Therefore, the oxidation behaviour of JW2 samples is more parabolic than linear with values closer to 0.5 than 1. The oxidation behaviour of JW2-AC can be said to be entirely parabolic in nature with a value of 0.50. This implies that the linear mechanism of oxidation has a negligible effect on the rate of oxidation, and as a result the TGA graph of this alloy is modelled as parabolic for the entirety of the experiment.

The heat-treated at 1300°C alloy has a parabolic rate constant of 1.22E-10 $g^2.cm^{-4}.s^{-1}$ and linear rate constant of 1.88E-08 $g.cm^{-2}.s^{-1}$. JW2-HT15 has a parabolic rate constant of 1.21E-10 $g^2.cm^{-4}.s^{-1}$ and linear rate constant of 1.79E-08 $g.cm^{-2}.s^{-1}$. The oxidation rate constants of these alloys are very similar, highlighted by the TGA curves presented in Figure 6.37 which are almost identical. As was the case with JW1 samples oxidised at 1200°C, the total mass gains of JW2 samples are similar to

each other, and do not deviate from each other by more than 0.82 mg.cm^{-2}. As was also the case with JW1 samples, total mass gain follows a trend of decreasing with the degree of post-processing; with JW2-AC having a total mass gain value of 9.20 mg.cm^{-2}, JW2-HT13 having 8.56 mg.cm^{-2} and JW2-HT15 having 8.38 mg.cm^{-2}.

The parabolic oxidation rate constant of JW2-AC is 2.26E-10 g^{2}.cm^{-4}.s^{-1}. Despite having parabolic behaviour, indicating some degree of passivating oxide layer, the diffusion of oxygen through which being the rate limiting step of oxidation, the as-cast sample has higher mass gain for the duration of the experiment. If the experiment was allowed to continue, and the parabolic behaviour of JW2-AC and linear rates of JW2-HT13 and JW2-HT15 are assumed to continue too, then JW2-AC would be expected to outperform in terms of total mass gain the heat-treated alloys JW2-HT13 and JW2-HT15 at 143 hours and 158 hours, respectively.

All linear rate constants, parabolic rate constants, and total mass gains are lower for JW2 alloys than JW1 and KZ5 alloys, indicating a positive effect of additional B content on oxidation resistance at 1200°C. This is seen in Figure 6.40, Figure 6.41, and Figure 6.42 regarding an as-cast, heat-treated at 1300°C and heat-treated at 1500°C comparison, respectively. Where these three alloys can be compared, i.e. in the as-cast state and the heat-treated at 1500°C state, the initial addition of B and Ge has a greater effect on reducing the oxidation of KZ5 than the additional addition of B content in JW2.

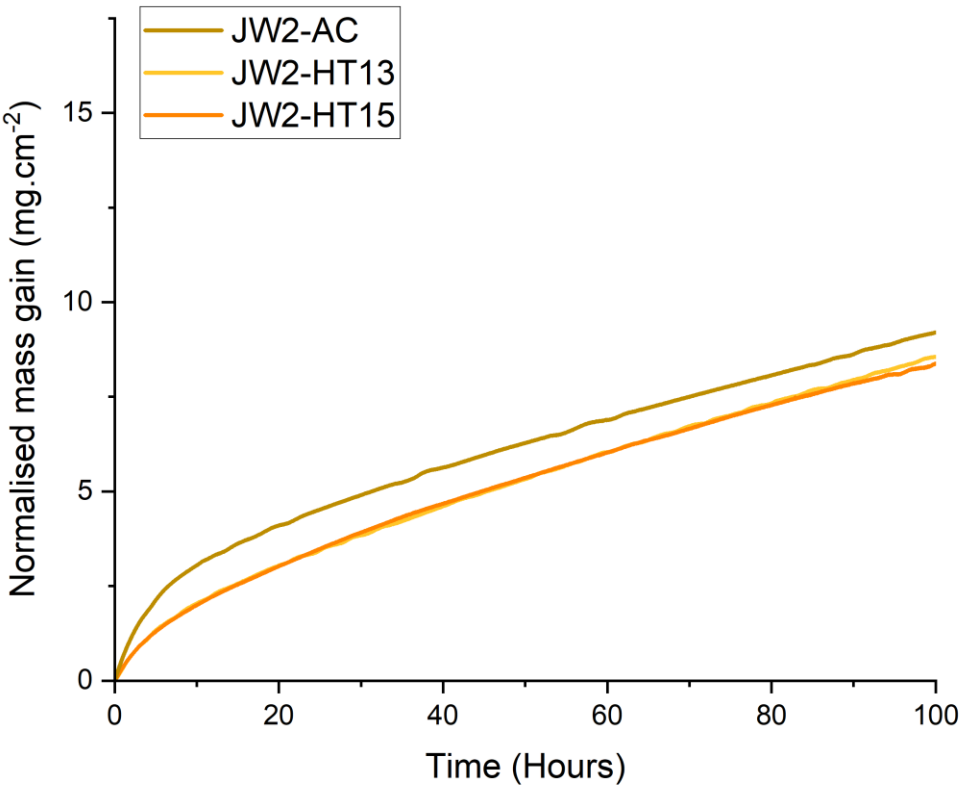

Figure 6.37) Normalised mass gain of JW2 in the as-cast, heat-treated-1300°C and heat-treated-1500°C states over a 100 hour period at 1200°C

6.3.1.4 JW3

The TGA curves of oxidised alloy JW3 are displayed in Figure 6.38. This alloy was prepared in as-cast, heat-treated at 1300°C and heat-treated at 1500°C states. Oxidation parameters are displayed in Table 6.19. The *n* exponents of JW3-AC, JW3-HT13 and JW3-HT15 are similar and are calculated as 0.52, 0.57 and 0.55, respectively. Therefore, the oxidation behaviour of JW3 samples is more parabolic than linear with values closer to 0.5 than 1. The oxidation behaviour of JW3-AC is sufficiently parabolic to be modelled as parabolic for the entirety of the experiment, whereas JW3-HT13 and JW3-HT15 are modelled as being initially parabolic and then linear for the remainder of the experiment.

The heat-treated at 1300°C alloy has a parabolic rate constant of 1.82E-10 $g^2.cm^{-4}.s^{-1}$ and linear rate constant of 1.74E-08 $g.cm^{-2}.s^{-1}$. JW3-HT15 has a parabolic rate constant of 2.04E-10 $g^2.cm^{-4}.s^{-1}$ and linear rate constant of 1.87E-08 $g.cm^{-2}.s^{-1}$. The total mass gain of JW3-AC, JW3-HT13 and JW3-HT15 are calculated as 8.08 $mg.cm^{-2}$, 9.03 $mg.cm^{-2}$ and 9.10 $mg.cm^{-2}$, respectively. Total mass gain follows a trend of decreasing with the degree of post-processing, the opposite of what was seen in KZ5, JW1, and JW2. The heat-treatments have had a negative effect on oxidation resistance in this high Ge alloy only. The largest discrepancies in mass gains within a single alloy oxidised at 1200°C was seen in JW3, with a range of 1.02 $mg.cm^{-2}$, but this is still relatively small considering the difference between alloy compositions, which have a range of 8.10 $mg.cm^{-2}$. The parabolic oxidation rate constant of JW3-AC is 1.73E-10 $g^2.cm^{-4}.s^{-1}$. The initial part of the TGA graphs of JW3 alloys are similar to each other but diverge at approximately 25 hours. In the case of JW3 the parabolic oxidation behaviour of the as-cast sample is beneficial to lowering the total mass gain after 100 hours, which was not the case with JW2-AC.

The linear oxidation rate constants and total mass gains of JW3 alloys are lower than those of the JW1 alloy, and certainly the B and Ge free alloy KZ5. This shows that the 5 at.% extra G added in JW3 has been beneficial for oxidation resistance, although this total 10 at.% Ge generally has had a lesser effect when compared to the original 5 at.% B and 5 at.% Ge that was added to KZ5 to create JW1. The ranges of oxidation rate constants and total mass gains of JW2 and JW3 overlap and so the additional B or additional Ge content has had a similar effect on reducing oxidation resistance. When considering solely the total mass gain as a measure of oxidation resistance, JW3 has performed better in the as-cast state and JW2 has performed better in the heat-treated at 1300°C and heat-treated at 1500°C states (Table 6.19).

The TGA oxidation curves of all the 1200°C experiments conducted in this study are presented in Figure 6.39. In addition, further graphs are included to highlight each processing state in order to assess the potential effects these processing conditions on each alloys oxidation resistance. These are presented in Figure 6.40 (as-cast), Figure 6.41 (heat-treated at 1300°C) and Figure 6.42 (heat-treated at 1500°C

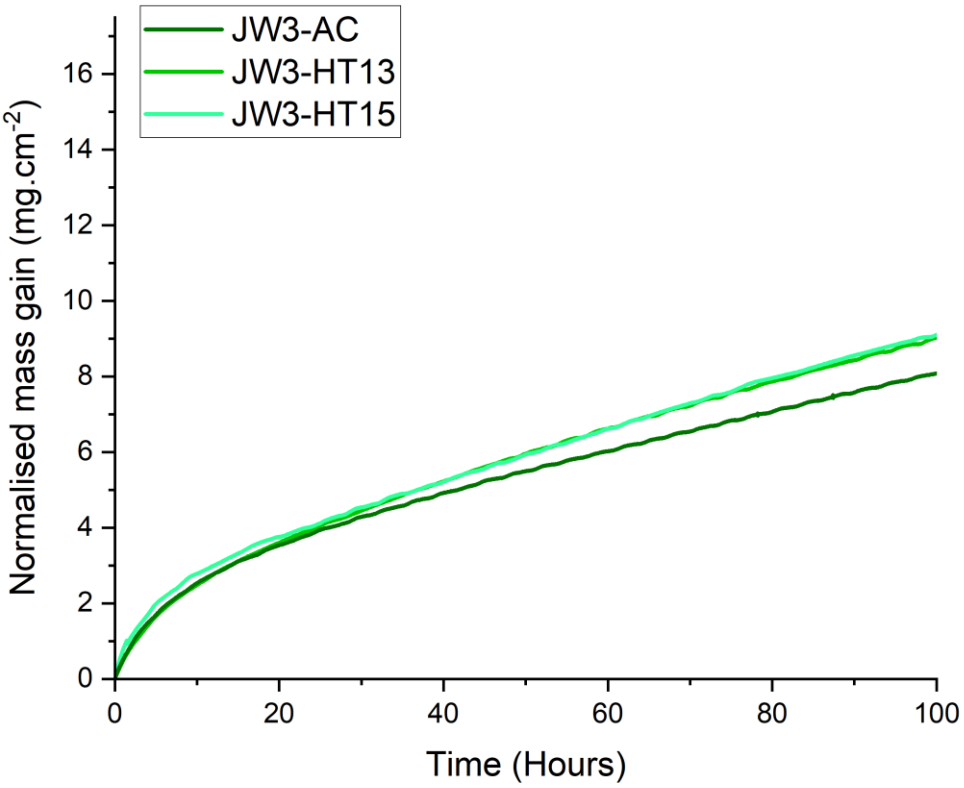

Figure 6.38) Normalised mass gain of JW3 in the as-cast, heat-treated-1300°C and heat-treated-1500°C states over a 100 hour period at 1200°C

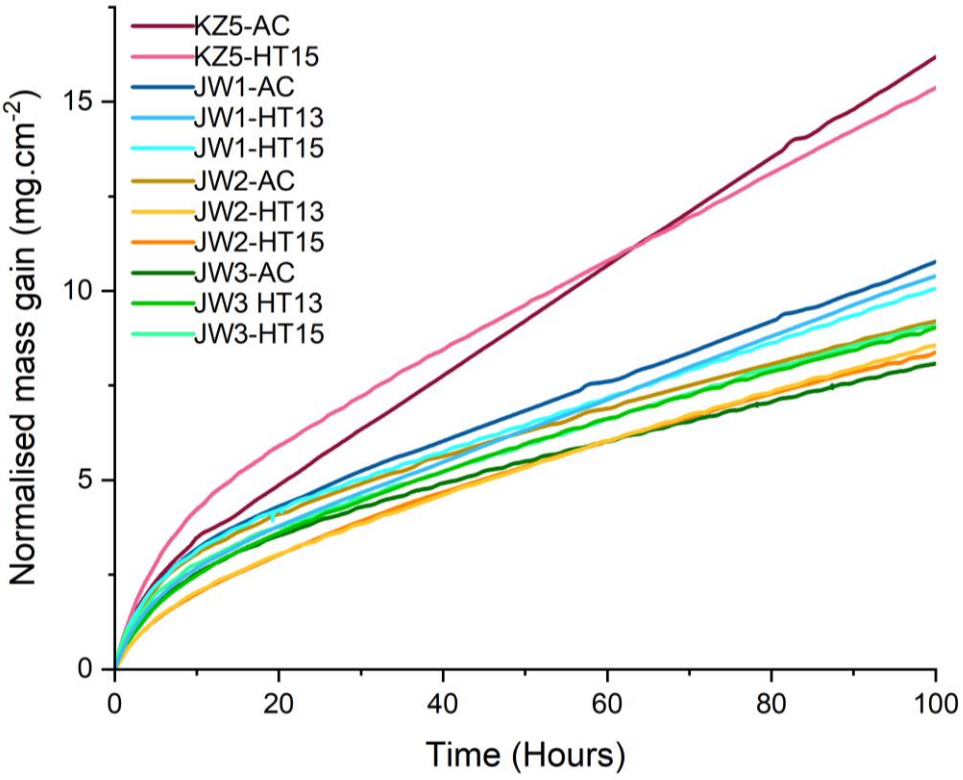

Figure 6.39) Normalised mass gain of all samples oxidised at 1200°C over a 100 hour period.

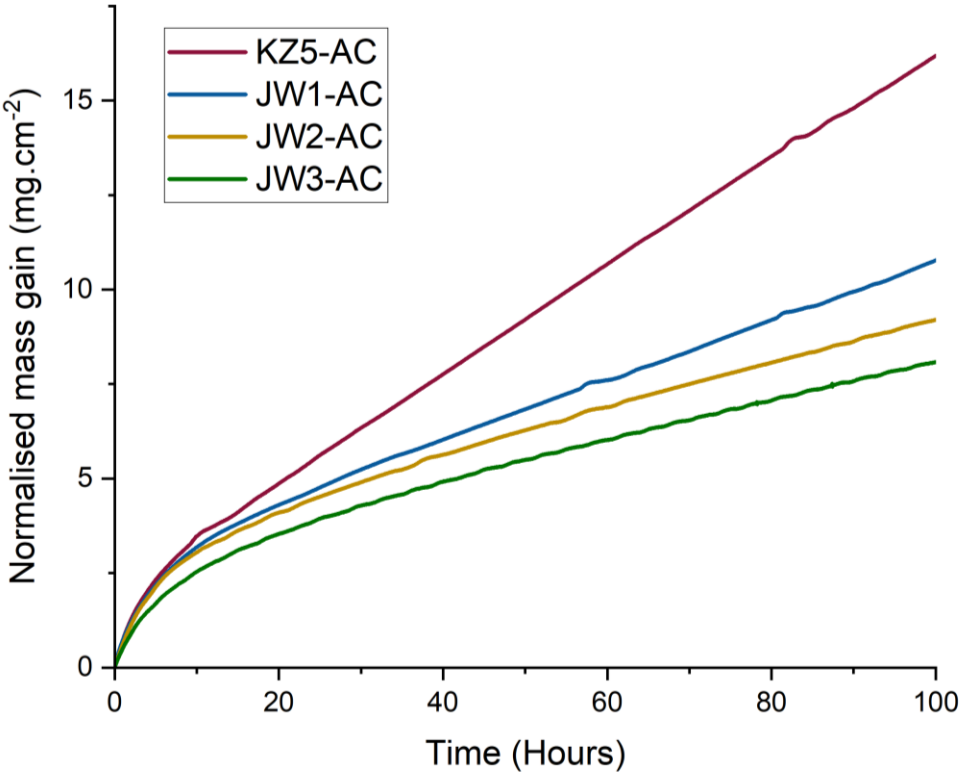

Figure 6.40) Normalised mass gain of as-cast alloys KZ5, JW1, JW2 and JW3 over a 100 hour period at 1200°C

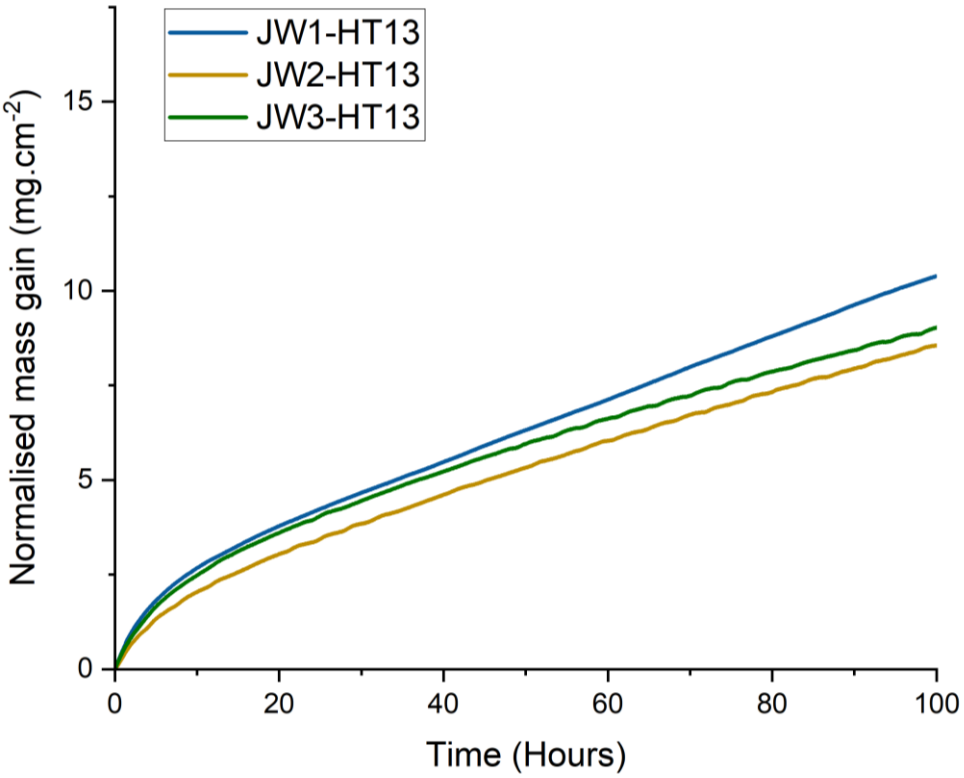

Figure 6.41) Normalised mass gain of Heat-treated at 1300°C alloys JW1, JW2 and JW3 over a 100 hour period at 1200°C

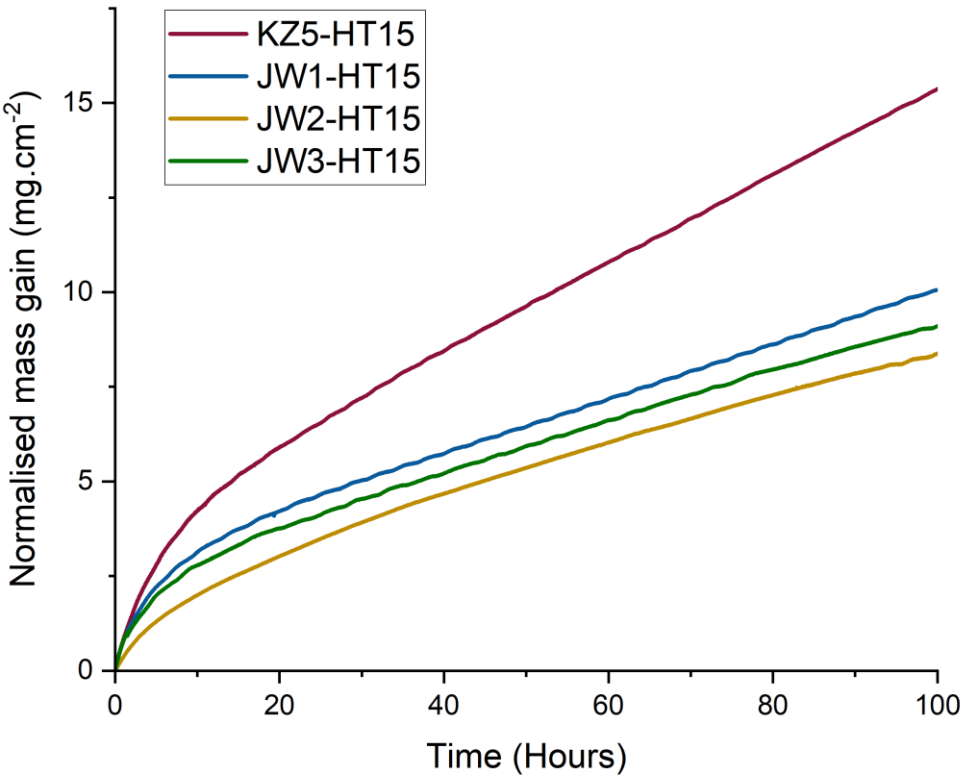

Figure 6.42) Normalised mass gain of Heat-treated at 1500°C alloys KZ5, JW1, JW2 and JW3 over a 100 hour period at 1200°C

6.3.2 Oxide scale

6.3.2.1 KZ5

6.3.2.1.1 XRD

The XRD pattern of KZ5-AC is shown in Figure 6.43. The phases that are identified are a rutile structured TiO_2 (Pearson symbol tP6, space group $P4_2/mnm$), a cristobalite form of SiO_2 (Pearson symbol tP12, space group $P4_12_12$), monoclinic titanium-niobates $Ti_2Nb_{10}O_{29}$ (Pearson symbol mC82, space group A2/m) and $TiNb_2O_7$ (Pearson symbol mC60, space group I2/m). It should be noted that wherever the TiO_2 phase is reported in XRD patterns in this section, TiO_2 is used as a simplification of mixed element rutile structured tetragonal oxides. The XRD pattern of KZ5-HT15 is shown in Figure 6.44. The phases that are identified are a TiO_2, SiO_2, $Ti_2Nb_{10}O_{29}$ and $TiNb_2O_7$. The XRD patterns of the as-cast and heat-treated versions of KZ5 are similar.

The GIXRD pattern of KZ5-AC is displayed in Figure 6.45. The phases identified through GIXRD are TiO_2 and $Ti_2Nb_{10}O_{29}$ and $TiNb_2O_7$. This is in agreement with the XRD pattern presented in Figure 6.43, with the exception that SiO_2 was not found in GIXRD. This shows that regular XRD is more than sufficient to identify oxides that have formed in comparison to grazing incident techniques, as was the case with the 1000°C samples. For GIXRD patterns of 1200°C JW series alloys see appendix section Figure 8.5, Figure 8.7, Figure 8.9.

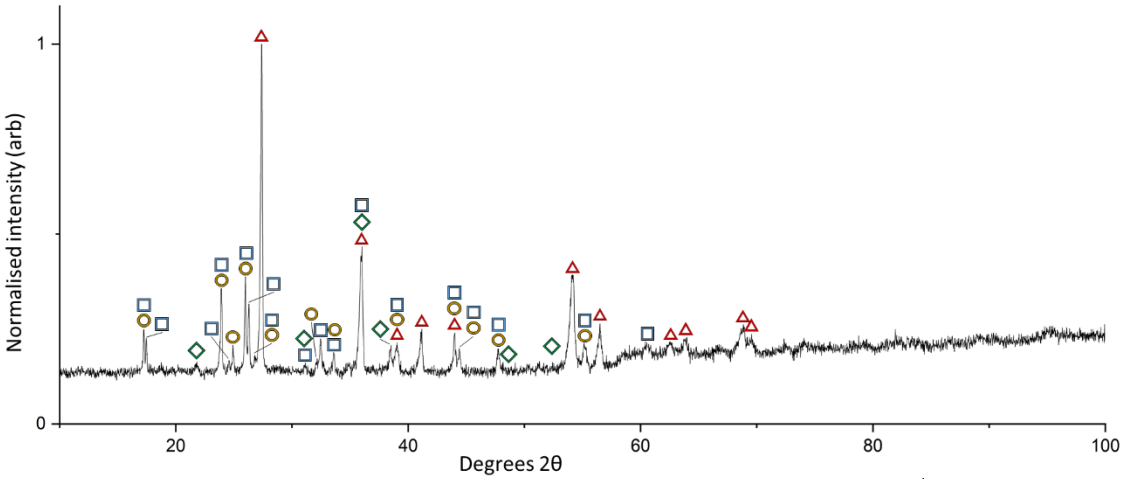

Figure 6.43) XRD pattern of oxidised at 1200°C KZ5-AC. △ = TiO_2, ○ = $Ti_2Nb_{10}O_{29}$ □ =$TiNb_2O_7$, ◇ = SiO_2

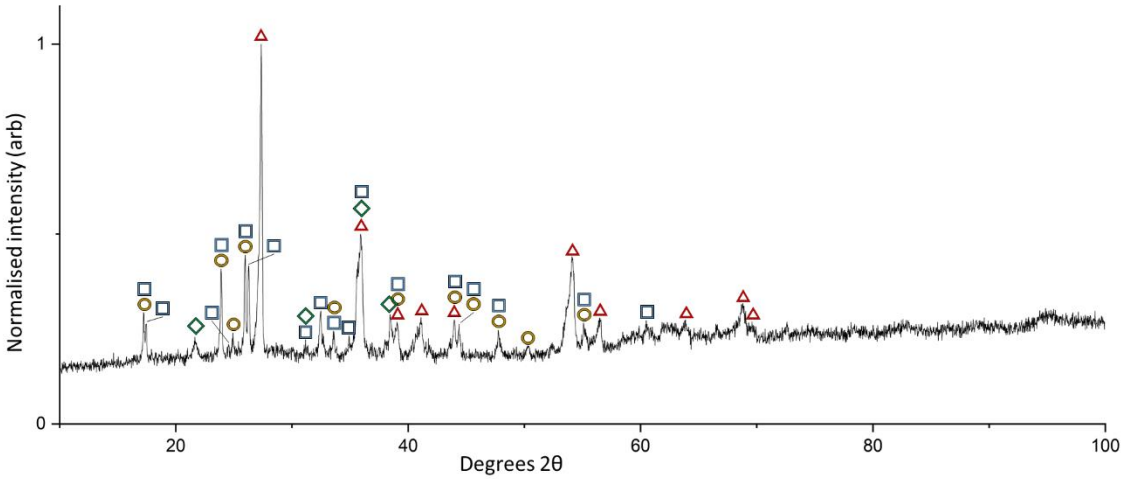

Figure 6.44) XRD pattern of oxidised at 1200°C KZ5-HT15. △ = TiO_2, ○ = $Ti_2Nb_{10}O_{29}$ □ =$TiNb_2O_7$, ◇ = SiO_2

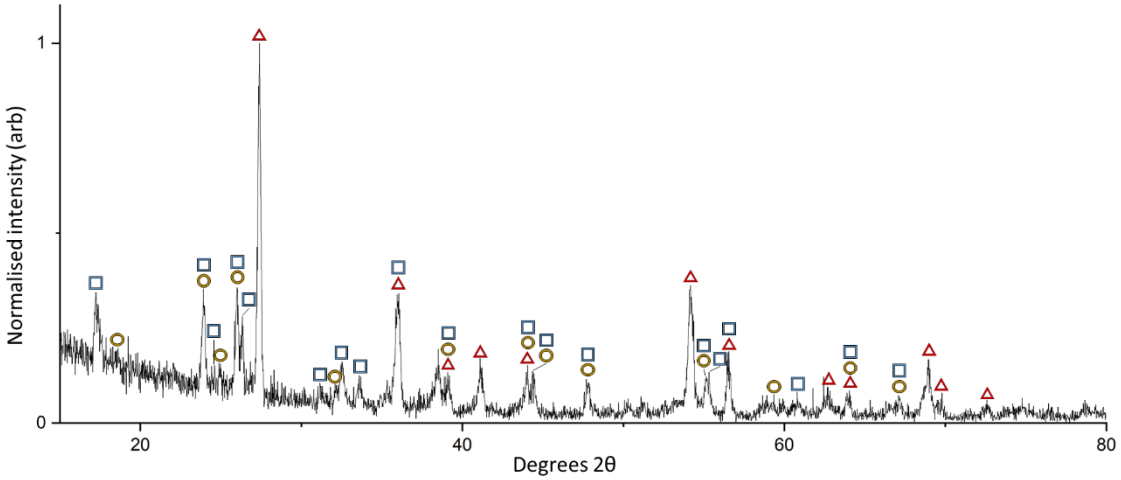

Figure 6.45) GIXRD pattern of KZ5-AC. △ = TiO_2, ○ = $Ti_2Nb_{10}O_{29}$, □ =$TiNb_2O_7$

6.3.2.1.2 EPMA

EPMA mapping of oxidised KZ5 samples at 1200°C including elements Nb, Si, Ti, Cr, Al, and O is presented in Figure 6.46 and Figure 6.47 for the as-cast state and heat-treated at 1500°C state, respectively. In the bulk of each oxidised sample, four phases were identified; (Nb), βNb_5Si_3, $NbCr_2$ and a Ti-rich phase. In the heat-treated version αNb_5Si_3 and an Al-rich phase were also found. An Al-rich phase may have been present in the as-cast alloy but was not coarse enough or in large enough quantities to reliably measure. In the case of KZ5-AC, (Nb) and βNb_5Si_3 are consistent with the unoxidised microstructure and $NbCr_2$ and the Ti-rich phase are a result of oxidation. In the case of KZ5-HT15, (Nb), βNb_5Si_3 and αNb_5Si_3 are consistent with the unoxidised microstructure and $NbCr_2$, the Ti-rich phase and the Al-rich phase are a result of oxidation. The compositions each of these phases in the oxidised samples are listed in Table 6.20.

In the as-cast sample the intergranular areas between primary βNb_5Si_3 grains consists of a mixture of the (Nb), βNb_5Si_3, the Ti-rich phase and $NbCr_2$. In the map presented it appears as though closer to the oxide scale this mixture is finer. This is the case for both KZ5-AC and KZ5-HT15, and in the case of KZ5-HT15 there is also an Al-rich phase within the mixture but no intergranular βNb_5Si_3.

As would be expected from the unoxidised microstructure, both αNb_5Si_3 and βNb_5Si_3 would be present in the KZ5-HT15 version of the alloy. It is proposed that the αNb_5Si_3 phase can be identified by 'speckling' microstructural feature noted in Chapter 5 Section 5.2.1. In the unoxidised microstructure this speckling was thought to be (Nb), forming as a result of the αNb_5Si_3 to βNb_5Si_3 transition. In the oxidised sample this speckling is too fine to measure, but from the EPMA maps in Table 6.20 it appears these small precipitates are low in Nb and high in Ti, and so are likely TiO_2 which is also found on the outer shells of many of these silicide grains as well. O content is greater in αNb_5Si_3, suggesting this silicide is more susceptible to oxidation, at least in this case where the αNb_5Si_3 to βNb_5Si_3 transition has resulted in intergranular (Nb). However, this cannot be confirmed given the large margins of error associated with each O content value.

In 1000°C oxidised samples of each composition where a Ti-rich phase was found in the bulk of the alloy, the weight percentages were in line with those found for other bulk phases in these EPMA maps, i.e. greater than 85 wt.%. Oxygen contents of these Ti-rich phases, which were labelled as a Ti solid solution (Ti), were between 4.2 at.% and 12.6 at.%. In the case of KZ5-AC and KZ5-HT15

oxidised at 1200°C, as well as other alloys oxidised at this temperature that are reported on later in this chapter, total weight percentages are more in line with oxide phases at approximately <70 wt.% and O contents are between 20.1 at.% and 33.3 at.%. Lower weight percentages of oxide phases is expected and attributed to several factors; a receiving angle altered by varied hardness between bulk and oxide phases, a receiving angle altered by the expected porosity of oxide phases compared to bulk phases reducing X-ray yield, the tendency of O characteristic peaks to shift in the same manner as other light elements, and the absorption of O kα x-rays by carbon in the carbon coating. Additionally, content of other elements excluding Ti and O is not recorded as above 3.0 at.%, whereas in 1000°C (Ti) contents of Nb and Cr were frequently larger than this. Therefore, in the 1200°C samples the Ti-rich phase is assigned to TiO_2 and will be referred to as internal TiO_2. The solubility of O in (Ti) is approximately 33 at.% [204], so there is some uncertainty with labelling this phase as TiO_2 as hexagonal αTi solid solution could be considered based on atomic percentages recorded through EPMA. However, given the previous points concerning total weight percentage and content of elements other than Ti and O, the assumption is made that this is TiO_2 rather than heavily substituted (Ti) with O. The oxidation of internal phases has extended beyond the oxide layer/bulk material interface significantly.

Compared to the unoxidised version of KZ5-AC, the (Nb) found in oxidised KZ5-AC is much higher in Nb content and Ti content is reduced to 1.8 at.% from 26.4 at.%. A similar effect is seen for KZ5-HT15. The process of (Nb) -> (Ti) + Nb-rich (Nb) is more developed at the higher temperature of 1200°C, as Ti segregates from (Nb) to form (Ti) which then oxidises to form TiO_2.

The Al-rich phase identified in some 1000°C alloys (e.g. JW2-HT13) was understood to be a mixture of (Al) and Al_2O_3 since total wt% was generally > 90 wt.%, O content was considerably lower than what would be expected in pure Al_2O_3, and O solubility in (Al) is much lower than the O contents found in the Al-rich phase [203]. The same logic is applied to the Al-rich phases found in 1200°C samples that mostly consist of Al and O, as the same factors listed are still relevant.

When considering the O contents of bulk phases in the microstructures of KZ5-AC and KZ5-HT15, the phases in KZ5-HT15 have lower O contents than their KZ5-AC counterparts. This could be related to the better oxidation performance of the KZ5-HT15 alloy at 1200°C according to Figure 6.35. The silicide phases in each alloy are the least susceptible to oxidation. Not including the internal TiO_2 present in the bulk or the Al-rich phase, the (Nb) has the highest O content in both KZ5 alloys which is likely linked to the diffusivity of O in this phase, and therefore the susceptible to oxidation. In the case of maps of 1200°C oxidised samples, the oxide scale takes up a greater proportion of the image than was the case with 1000°C oxidised samples (especially the JW alloy series), and therefore the compositional differences of alloy phases close to and far from the scale are not reported.

Area analysis was performed using this EPMA data in order to report average compositions of specific areas of the oxide scale, shown in Table 6.21. These areas include the total oxide scale, and in the case of B and Ge containing alloys the germanium-rich layer. The layer of oxidised material of KZ5-AC had an average composition of 22.5 at.% Nb, 11.3 at.% Si, 15.8 at.% Ti, 2.4 at.% Cr, 0.8 at.% Al, and 47.1 at.% O. The layer of oxidised material of KZ5-HT15 had an average composition of 25.5 at.% Nb, 10.6 at.% Si, 24.1 at.% Ti, 4.1 at.% Cr, 1.1 at.% Al and 34.6 at.% O.

Compositions of phases and regions within the oxide layer of each alloy are presented in Table 6.22. In each of the oxide scales five oxide phases are reported on and are designated based on their most notable element; Ti-rich oxide, Nb-rich oxide, an alternate Nb-rich oxide, Cr-rich oxide and Si-rich oxide. In the case of 1200°C oxidised samples' oxide phases that will be presented in this section and the for the rest of 1200°C samples, the oxide phases are coarser than was the case with 1000°C

sample oxide phases. Therefore, more confidence can be placed that the presented results are that of a single phase and this also leads to ratios of Ti and Nb that are more clearly associated with either $TiNb_2O_7$ or $Ti_2Nb_{10}O_{29}$ titanium-niobate oxides.

In KZ5-AC the Ti-rich oxide phase has titanium content of 34.4 at.% whilst Nb and Cr contents were 13.2 at.% and 5.5 at.%, respectively. As a result of higher Ti content whilst containing significant amounts of Nb and Cr, this phase is considered to be rutile TiO_2 with substation of mainly Nb and Cr onto Ti sites. The Nb-rich phase had Nb content of 41.3 at.% and Ti content of 16.6 at.%, with the Nb/Ti ratio equal to 2.49. This ratio is closer to the expected value of $TiNb_2O_7$ rather than $Ti_2Nb_{10}O_{29}$, so this phase is considered to be the $TiNb_2O_7$ oxide also identified through XRD. The alternate Nb-rich phase on the other hand has a Nb content of 42.4 at.% and a Ti content of 7.8 at.%, and therefore a Nb/Ti ratio of 5.43. This ratio is close to 5, and so can be considered $Ti_2Nb_{10}O_{29}$.

In KZ5-HT15 the Ti-rich oxide phase has titanium content of 40.5 at.% whilst Nb and Cr contents were 17.4 at.% and 6.9 at.%, respectively. As a result of having higher Ti content whilst containing significant amounts of Nb and Cr, this phase is considered to be rutile TiO_2 with substation of mainly Nb and Cr onto Ti sites. The Nb-rich phase had Nb content of 47.3 at.% and Ti content of 18.8 at.%, with the Nb/Ti ratio equal to 2.52. This ratio is closer to the expected value of $TiNb_2O_7$ rather than $Ti_2Nb_{10}O_{29}$, so this phase is considered to be the $TiNb_2O_7$ oxide also identified through XRD. The alternate Nb-rich phase on the other hand has a Nb content of 54.8 at.% and a Ti content of 9.6 at.%, and therefore a Nb/Ti ratio of 5.70. This ratio is close to 5, and so can be considered $Ti_2Nb_{10}O_{29}$.

Si content in each Si-rich phase are 45.1 at.% and 33.9 at.% for alloys KZ5-AC and KZ5-HT15, respectively, whilst average Nb contents are 6.7 at.% and 16.4 at.%, respectively, and average Ti content are 6.3 at.% and 9.7 at.%, respectively. Since SiO_2 was identified through XRD analysis and this is the highest silicon content phase, it is reasonable to assume this is the SiO_2 phase. The Ti and Nb present in this structure are likely a result underlying titanium-niobate oxide phases and contaminants within the SiO_2 phase.

There are areas in each samples oxide layer that are the TiO_2 phase but are especially rich in Cr, labelled Cr-rich phase in Table 6.22. This is TiO_2 with higher amounts of Cr substitution, which shows composition is especially variable in this phase, unlike in the Ti-rich phase found within the bulk in the case of these KZ5 alloys which has consistently low composition of elements other than Ti and O.

The structure of the oxide layer of the as-cast sample consists of an outer layer of $TiNb_2O_7$ with TiO_2 just beneath. Between this outer layer and the bulk material is either a fine mixture of SiO_2, $TiNb_2O_7$, TiO_2, and $Ti_2Nb_{10}O_{29}$ where silicide grains previously existed in the unoxidised microstructure, or a coarser arrangement of $TiNb_2O_7$, TiO_2, and $Ti_2Nb_{10}O_{29}$ where presumably silicide grains were absent.

The heat-treated alloy's oxide structure in the mapped location is slightly different, with TiO_2 being the outer most layer for the majority of the surface captured in this particular location. Underneath this TiO_2 layer are coarse areas of $TiNb_2O_7$ and $Ti_2Nb_{10}O_{29}$, as well as some areas of broken up silicide grains, oxidised to form SiO_2, TiO_2 and titanium-niobate mixtures similar to the as-cast sample.

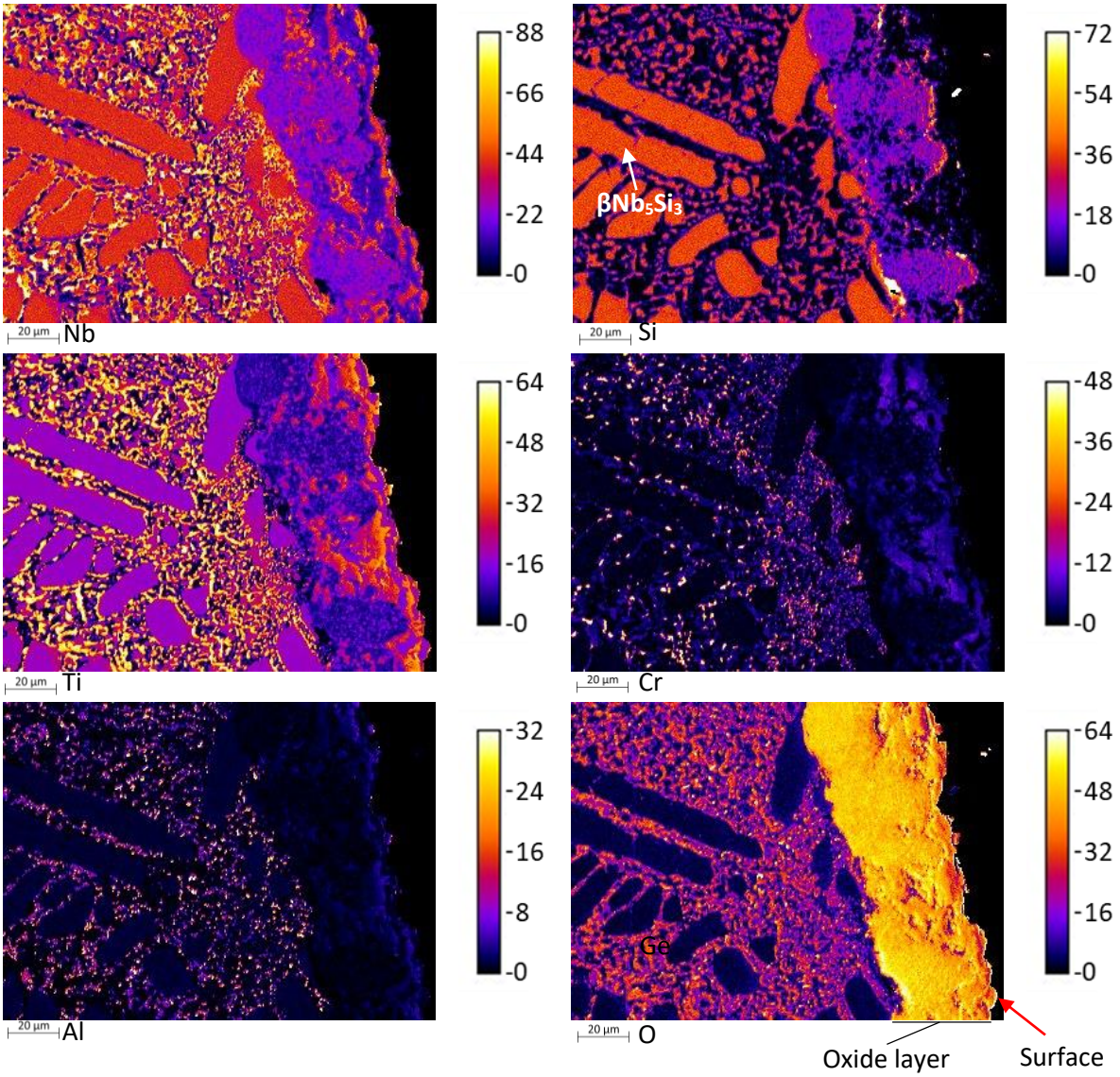

Figure 6.46a-f) EPMA maps of the oxide layer of KZ5-AC in at.% of elements a) Nb, b) Si, c) Ti, d) Cr, e) Al, f) O.

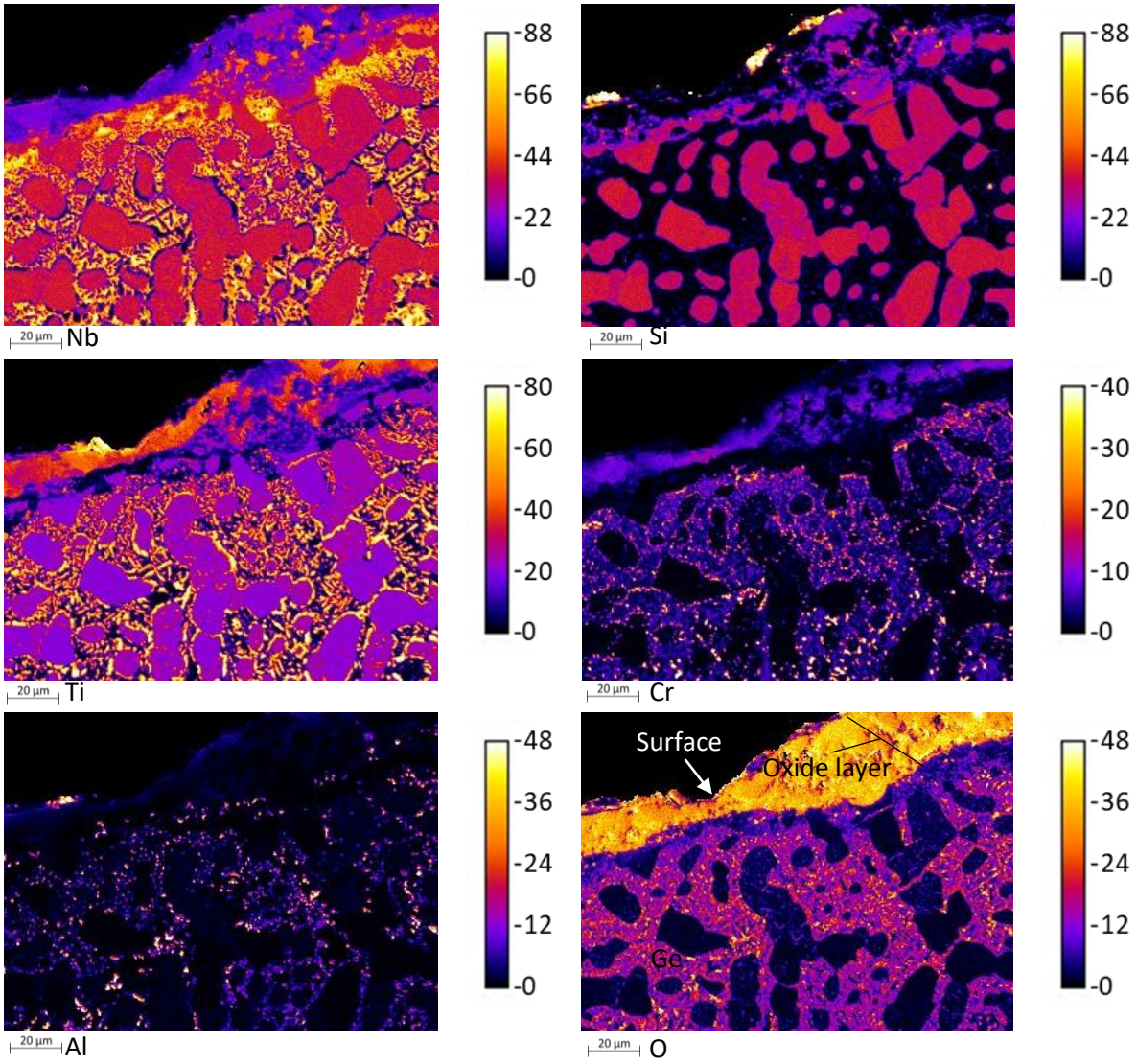

Figure 6.47a-f) EPMA maps of the oxide layer of KZ5-HT15 in at.% of elements a) Nb, b) Si, c) Ti, d) Cr, e) Al, f) O.

Table 6.20) Phase analysis of bulk phases present in each KZ5 oxidised sample EPMA map, values given in at.%.

		Nb	Si	Ti	Cr	Al	O
(Nb)	KZ5-AC	72.7 ± 6.5	2.1 ± 2.0	1.8 ± 1.4	5.1 ± 1.1	8.0 ± 12.2	10.4 ± 9.1
	KZ5-HT15	79.5 ± 7.7	1.3 ± 2.0	2.9 ± 3.1	6.3 ± 1.9	3.0 ± 4.7	7.1 ± 6.3
βNb_5Si_3	KZ5-AC	40.9 ± 2.6	36.1 ± 2.2	18.4 ± 1.2	0.9 ± 0.7	1.0 ± 0.5	2.8 ± 1.6
	KZ5-HT15	39.3 ± 2.5	38.5 ± 2.3	20.3 ± 1.2	0.4 ± 0.3	0.3 ± 0.2	1.3 ± 1.0
Ti-rich phase (TiO_2)	KZ5-AC	2.0 ± 2.5	0.1 ± 0.2	63.9 ± 3.0	0.4 ± 1.0	0.3 ± 0.5	33.3 ± 3.7
	KZ5-HT15	1.7 ± 2.1	0.3 ± 0.4	76.9 ± 3.9	0.4 ± 0.9	0.5 ± 0.4	20.1 ± 4.1
$NbCr_2$	KZ5-AC	29.4 ± 2.6	10.1 ± 1.1	3.9 ± 2.5	50.7 ± 2.7	0.3 ± 0.4	5.6 ± 10.4
	KZ5-HT15	31.0 ± 3.0	9.3 ± 2.7	7.0 ± 5.1	47.8 ± 4.7	0.4 ± 0.7	4.4 ± 2.7
αNb_5Si_3	KZ5-HT15	37.0 ± 3.5	34.7 ± 3.3	23.3 ± 3.9	1.3 ± 2.1	0.9 ± 0.7	2.8 ± 2.2
Al-rich phase	KZ5-HT15	6.8 ± 5.4	0.5 ± 0.6	1.5 ± 1.7	1.3 ± 1.3	63.7 ± 8.4	26.1 ± 5.2

Table 6.21) Area analysis of the entire oxide layers in EPMA maps for KZ5 oxidised samples, values given in at.%.

		Nb	Si	Ti	Cr	Al	O
Total oxide layer:	KZ5-AC	22.5 ± 8.0	11.3 ± 10.4	15.8 ± 9.7	2.4 ± 2.5	0.8 ± 1.0	47.1 ± 15.4
	KZ5-HT15	25.5 ± 11.0	10.6 ± 12.2	24.1 ± 15.3	4.1 ± 3.7	1.1 ± 3.5	34.6 ± 12.5

Table 6.22) Phase analysis of oxide phases in each KZ5 oxidised sample from locations in the oxide scale, values given in at.%.

		Nb	Si	Ti	Cr	Al	O
Ti-rich oxide	KZ5-AC	13.2 ± 1.7	0.5 ± 1.5	34.4 ± 2.6	5.5 ± 1.6	2.8 ± 0.8	43.7 ± 8.4
	KZ5-HT15	17.4 ± 2.3	0.3 ± 0.6	40.5 ± 5.1	6.9 ± 1.8	1.2 ± 0.7	33.8 ± 5.4
Nb-rich oxide	KZ5-AC	41.3 ± 3.0	0.5 ± 2.3	16.6 ± 1.3	0.4 ± 0.3	0.5 ± 0.4	40.7 ± 13.4
	KZ5-HT15	47.3 ± 4.2	0.1 ± 0.1	18.8 ± 1.9	0.7 ± 0.9	0.5 ± 0.4	32.7 ± 4.6
Alternate Nb-rich oxide	KZ5-AC	42.4 ± 2.1	0.4 ± 0.2	7.8 ± 0.8	0.2 ± 0.2	0.1 ± 0.2	49.0 ± 8.5
	KZ5-HT15	54.8 ± 3.5	0.7 ± 1.5	9.6 ± 1.2	0.4 ± 0.3	0.2 ± 0.2	34.3 ± 5.5
Cr-rich oxide	KZ5-AC	13.8 ± 1.5	0.5 ± 0.9	25.9 ± 1.1	10.2 ± 1.1	1.0 ± 0.6	48.5 ± 13.9
	KZ5-HT15	17.9 ± 2.6	0.7 ± 2.1	35.3 ± 3.3	11.1 ± 1.9	0.5 ± 0.4	34.5 ± 7.5
Si-rich oxide	KZ5-AC	6.7 ± 3.0	45.1 ± 13.6	6.3 ± 2.4	1.1 ± 1.0	0.2 ± 0.2	40.6 ± 14.0
	KZ5-HT15	16.4 ± 4.0	33.9 ± 4.7	9.7 ± 2.4	0.9 ± 0.6	0.2 ± 0.2	38.8 ± 7.0

6.3.2.2 JW1

6.3.2.2.1 XRD

The XRD pattern of JW1-AC is shown in Figure 6.48. The phases that are identified are TiO_2, $TiNb_2O_7$ and SiO_2. The XRD pattern of JW1-HT13 is shown in Figure 6.49. The phases that are identified are TiO_2, $TiNb_2O_7$ and SiO_2.The XRD pattern of JW1-HT15 is shown in Figure 6.50. The phases that are identified are TiO_2, $Ti_2Nb_{10}O_{29}$, $TiNb_2O_7$ and SiO_2.

Compared to the 1000°C samples of JW1, the main differences are that $Ti_2Nb_{10}O_{29}$ is absent from the XRD pattern of JW1-AC and JW1-HT13, and the characteristic peak of cristobalite SiO_2 at approximately 22° 2θ has a higher intensity relative to other phases and is more defined in the XRD pattern of JW1-HT13 and JW1-HT15. Even in JW1-HT15 where $Ti_2Nb_{10}O_{29}$ is present, the relative intensity of this phase is clearly diminished and in all 1200°C JW1 samples $TiNb_2O_7$ is more clearly identified than was the case in 1000°C JW1 samples.

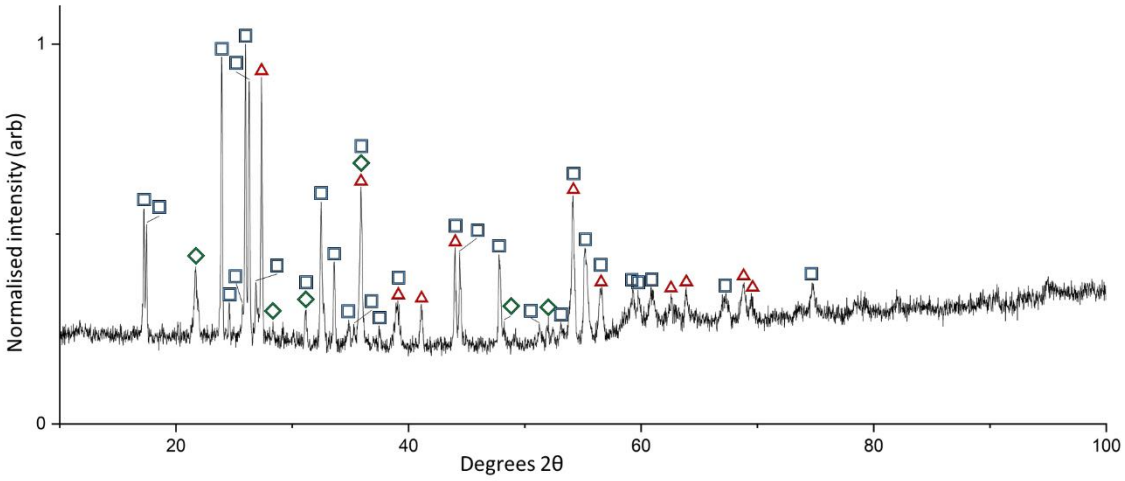

Figure 6.48) XRD pattern of oxidised at 1200°C JW1-AC. △ = TiO_2, □ = $TiNb_2O_7$, ◇ = SiO_2

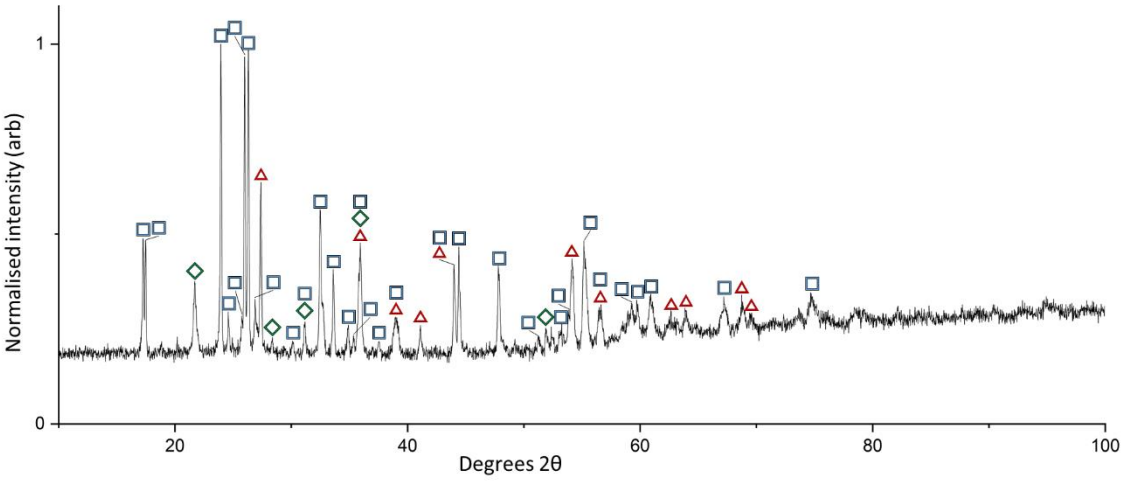

Figure 6.49) XRD pattern of oxidised at 1200°C JW1-HT13. △ = TiO_2, □ =$TiNb_2O_7$, ◇ =SiO_2

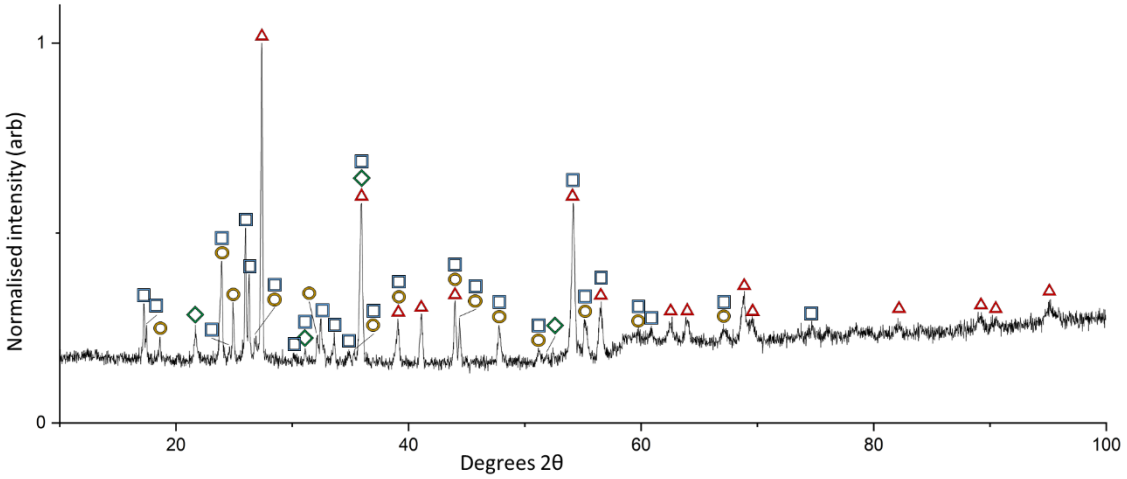

Figure 6.50) XRD pattern of oxidised at 1200°C JW1-HT15. △ = TiO_2, ○ = $Ti_2Nb_{10}O_{29}$ □ =$TiNb_2O_7$, ◇ = SiO_2

6.3.2.2.2 EPMA

EPMA mapping of oxidised JW1 samples at 1200°C including elements Nb, Si, Ti, Cr, Al, Ge, B and O is presented in Figure 6.51, Figure 6.52 and Figure 6.53 for the as-cast state, heat-treated at 1300°C state, and heat-treated at 1500°C state, respectively. In the bulk of each oxidised sample, six phases were identified; (Nb), internal TiO_2, $NbCr_2$, $D8_8$, T2, and an Al-rich phase. The phases (Nb), $NbCr_2$, $D8_8$, and T2, are consistent with the unoxidised microstructures of each alloy; JW1-AC, JW1-HT13, JW1-HT15. The internal TiO_2 and Al-rich phase are a result of oxidation in each case. The compositions each of these phases in the oxidised samples are listed in Table 6.24.

In each alloy the (Nb), internal TiO_2, $NbCr_2$, and Al-rich phase exist in a mixture in the intergranular regions between larger $D8_8$ grains. Areas of T2 are generally larger than the other phases with the exception of $D8_8$. In the case of the internal TiO_2 and Al-rich phase found in the bulk of the oxidised specimens, the same logic that was used to identify these phases in KZ5 is applied to JW1. And therefore the Ti-rich phase is assigned to internal TiO_2 after a precursor (Ti) has been fully oxidised, and Al-rich phase is assigned as a mixture of (Al) and Al_2O_3. Substitution of elements other than Al, Ti and O into these phases is low.

When considering the O contents of bulk phases in the microstructures of JW1 alloys, the silicide phases in each alloy and the $NbCr_2$ phase have similar O contents to each other and are within error of each other given that values of O content are reported as between 1.3 at.% and 3.2 at.% and standard errors are between 1.0 at.% and 1.9 at.%. Not including the internal TiO_2 present in the bulk or the Al-rich phase, the (Nb) has the largest O content, with values of 10.3 at.%, 9.9 at.% and 6.0 at.% for JW1-AC, JW1-HT13 and JW1-HT15, respectively. This (Nb) has seen a large increase in B content upon oxidation at 1200°C as well, an effect which was perhaps seen to a lesser degree after 1000°C oxidation experiments. B content in (Nb) is measured at 10.4, 9.8 and 10.6 for JW1-AC, JW1-HT13 and JW1-HT15, respectively. These B contents are much larger than the solubility of B in the (Nb) phase in the binary system [66], so it may be the case that small amount of Niobium boride phases have precipitated here, but are much too fine to resolve.

Area analysis was performed using this EPMA data in order to report average compositions of specific areas of the oxide scale, shown in Table 6.23. The layer of oxidised material of JW1-AC had an average composition of 19.5 at.% Nb, 12.8 at.% Si, 22.1 at.% Ti, 3.0 at.% Cr, 1.1 at.% Al, 2.1 at.% Ge, 2.4 at.% B, and 36.9 at.% O. The layer of oxidised material of JW1-HT13 had an average composition of 19.0 at.% Nb, 16.8 at.% Si, 12.4 at.% Ti, 1.1 at.% Cr, 0.4 at.% Al, 0.7 at.% Ge, 2.3 at.%

B, and 47.3 at.% O. The layer of oxidised material of JW1-HT15 had an average composition of 17.6 at.% Nb, 10.7 at.% Si, 16.6 at.% Ti, 2.0 at.% Cr, 0.7 at.% Al, 0.6 at.% Ge, 1.6 at.% B, and 50.2 at.% O.

A layer that is rich in Ge can be seen between the oxide layer and the bulk alloy in each sample of JW1. It is unclear whether this layer is made up of a new phase or an existing phase has been enriched in Ge during the oxidation process. Area analysis of this layer was performed and considering the Ge content of these layers was at least 15.7 at.% in JW1-HT15, which is greater than any $D8_8$ Ge composition found in the un-oxidised states of any JW series alloy despite this layer also containing a significant amount of O, it is suspected this is a distinct phase.

In the case of JW1-AC, the ratio of Nb + Ti to Ge + Si is 0.94, so it is uncertain from this compositional information what phase has formed, i.e Nb_5Ge_3, Nb_3Ge, $NbGe_2$, or if multiple phases are present in too fine a distribution to resolve. The same is true for JW1-HT13, where the ratio of Nb + Ti to Ge + Si is 1.26 and in the case of JW1-HT15, where the ratio of Nb + Ti to Ge + Si is 0.97. These ratios alone are not a good indication of which phase is present in these layer as it does not match well to any Nb-Ge phase composition ratio.

Areas where Ge content is greater than the rest of the Ge-rich layer in EPMA maps for JW1-AC, JW1-HT13 and JW1-HT15 were examined. Points were taken from these high-Ge areas to calculate the composition given in Table 6.25 for a Nb-Ge phase. Average Nb and Ge contents of this phase in JW1-AC were 42.9 at.% and 39.8 at.%. The ratio of Nb + Ti to Ge + Si is calculated as 1.03. Therefore, it is still unclear what this phase is, or if even this is a single phase. Average Nb and Ge contents of this phase in JW1-HT13 were 44.9 at.% and 29.3 at.%. The ratio of Nb + Ti to Ge + Si is calculated as 1.48. Average Nb and Ge contents of this phase in JW1-HT15 were 47.8 at.% and 33.1 at.%. The ratio of Nb + Ti to Ge + Si is calculated as 1.37. The ratios of JW1-HT13 and JW1-HT15 at these high Ge points is closer to the expected ratio of Nb_5Ge_3 when compared to the whole Ge-layer measurements. This could be an indication that Nb_5Ge_3 has formed in certain places along the Ge-rich layer in JW1-HT13 and JW1-HT15, with substitutions of Si for Ge and Nb for Ti.

Compositions of phases and regions within the oxide layer of each alloy are presented in Table 6.25. In each of the oxide scales five oxide phases are reported on and are designated based on their most notable element; Ti-rich oxide, Nb-rich oxide, an alternate Nb-rich oxide, Cr-rich oxide and Si-rich oxide. The internal TiO_2 identified in the bulk of the samples that is exceptionally low in elements other than Ti and O is also found in small amounts embedded in each of the scales.

In JW1-AC the Ti-rich oxide phase has titanium content of 55.7 at.% whilst Nb and Cr contents were 8.0 at.% and 5.9 at.%, respectively. As a result of having higher Ti content whilst containing significant amounts of Nb and Cr, this phase is considered to be rutile TiO_2 with substation of mainly Nb and Cr onto Ti sites, $(Ti,Nb,Cr)O_2$. For alloys JW1-HT13 and JW1-HT15 the titanium contents of the Ti-rich phase were lower at 39.7 at.% and 36.4 at.%, but amounts of Nb and Cr still indicate a TiO_2 phase with Ti partially substituted for Cr and Nb.

The Nb-rich phase in JW1-AC had Nb content of 36.7 at.% and Ti content of 18.2 at.%, with the Nb/Ti ratio equal to 2.02. This ratio is expected value of $TiNb_2O_7$ rather than $Ti_2Nb_{10}O_{29}$, so this phase is considered to be the $TiNb_2O_7$ oxide also identified through XRD. The alternate Nb-rich phase on the other hand has a Nb content of 41.4 at.% and a Ti content of 8.8 at.%, and therefore a Nb/Ti ratio of 4.72. This ratio is close to 5, and so can be considered $Ti_2Nb_{10}O_{29}$.

In JW1-HT13 the Nb-rich phase had Nb content of 37.3 at.% and Ti content of 16.5 at.%, with the Nb/Ti ratio equal to 2.27. This ratio is closer to the expected value of $TiNb_2O_7$ rather than $Ti_2Nb_{10}O_{29}$, so this phase is considered to be the $TiNb_2O_7$ oxide also identified through XRD. The alternate Nb-

rich phase on the other hand has a Nb content of 37.4 at.% and a Ti content of 8.6 at.%, and therefore a Nb/Ti ratio of 4.36. This ratio is close to 5, and so can be considered $Ti_2Nb_{10}O_{29}$.

In JW1-HT15 the Nb-rich phase had Nb content of 31.1 at.% and Ti content of 14.2 at.%, with the Nb/Ti ratio equal to 2.18. This ratio is closer to the expected value of $TiNb_2O_7$ rather than $Ti_2Nb_{10}O_{29}$, so this phase is considered to be the $TiNb_2O_7$ oxide also identified through XRD. The alternate Nb-rich phase on the other hand has a Nb content of 35.3 at.% and a Ti content of 7.6 at.%, and therefore a Nb/Ti ratio of 4.67. This ratio is close to 5, and so can be considered $Ti_2Nb_{10}O_{29}$.

Si content in each Si-rich phase is 42.6 at.%, 40.3 at.% and 34.2 at.% for alloys JW1-AC, JW1-HT13 and JW1-HT15, respectively, whilst average Nb contents are only 0.7 at.%, 0.8 at.% and 2.1 at.%, respectively, and average Ti contents are only 3.4 at.%, 1.0 at.% and 1.3 at.%, respectively. This phase is identified as SiO_2, and according to XRD a cristobalite structure. The Si-rich phase is coarser in 1200^{o}C samples compared to the 1000^{o}C oxidised versions of JW1. As a result, the Nb and Ti contents, which are possibly a result of titanium-niobate oxide impurities or underlying phases, are lower in both the as-cast and heat-treated samples of JW1 oxidised at 1200^{o}C. B and Ge contents in this SiO_2 phase are both very low, less than 1.0 at.% in all cases. A glassy layer containing Si, Ge and B is therefore not found in any case of JW1 and Ge and B substitution into this form of SiO_2 phase is extremely limited. Instead within the oxide layer, B is primarily found in titanium-niobate oxides and Ge is primarily found in the Ge-rich layer/Nb_5Ge_3.

Whilst there is a gradient in Cr content in the Ti-rich oxide phase is the oxide layers of each JW1 samples, alloys JW1-AC and JW1-HT15 have a phase that is located adjacent to Cr-rich TiO_2 with considerable Cr content. This Cr-rich phase has Cr content of 33.1 at.% and 25.5 at.% for JW1-AC and JW1-HT15, respectively. Since Ti and Nb content in these phases is lower than 10 at.%, the majority elements O and Cr suggest a Cr oxide. No Cr oxide phase was found in XRD, likely due to the small amounts of this phase in each oxide layer, but Cr_2O_3 is a possibility based on EPMA analysis of elemental contents.

The outer most part of the oxide layers in each sample consists of either coarse $(Ti,Nb,Cr)O_2$ in some cases with SiO_2 forming in small quantities throughout, or a mixture of SiO_2, $TiNb_2O_7$, $(Ti,Nb,Cr)O_2$, and $Ti_2Nb_{10}O_{29}$. Generally, the $Ti_2Nb_{10}O_{29}$ is less common and is found deeper within the scale. At the oxide-bulk interface the Ge-rich layer is found in each sample. In the case of the as-cast sample, where there is a gap in this Ge-rich layer, there appears to be more oxidised material behind it, extending into the bulk material. In the case of JW1-HT13 where the intergranular mixture was in contact with the surface of the sample, more Ge-rich phase appears to be present, and the oxide layer is thinner here compared to adjacent areas which were $D8_8$ before oxidation. This is potentially observed in JW1-HT15 also, but it is less clear given the positioning of the map location. Also observed in the JW1-HT15 oxide microstructure is a T2 grain in contact with the oxide material. In this case the Ge-rich layer is thinner and appears denser. Some degree of B enrichment is seen for this partially oxidised T2 grain, and elements Nb, Ti and Cr have been reduced in the oxidised region where as Si is less effected in this oxidised T2.

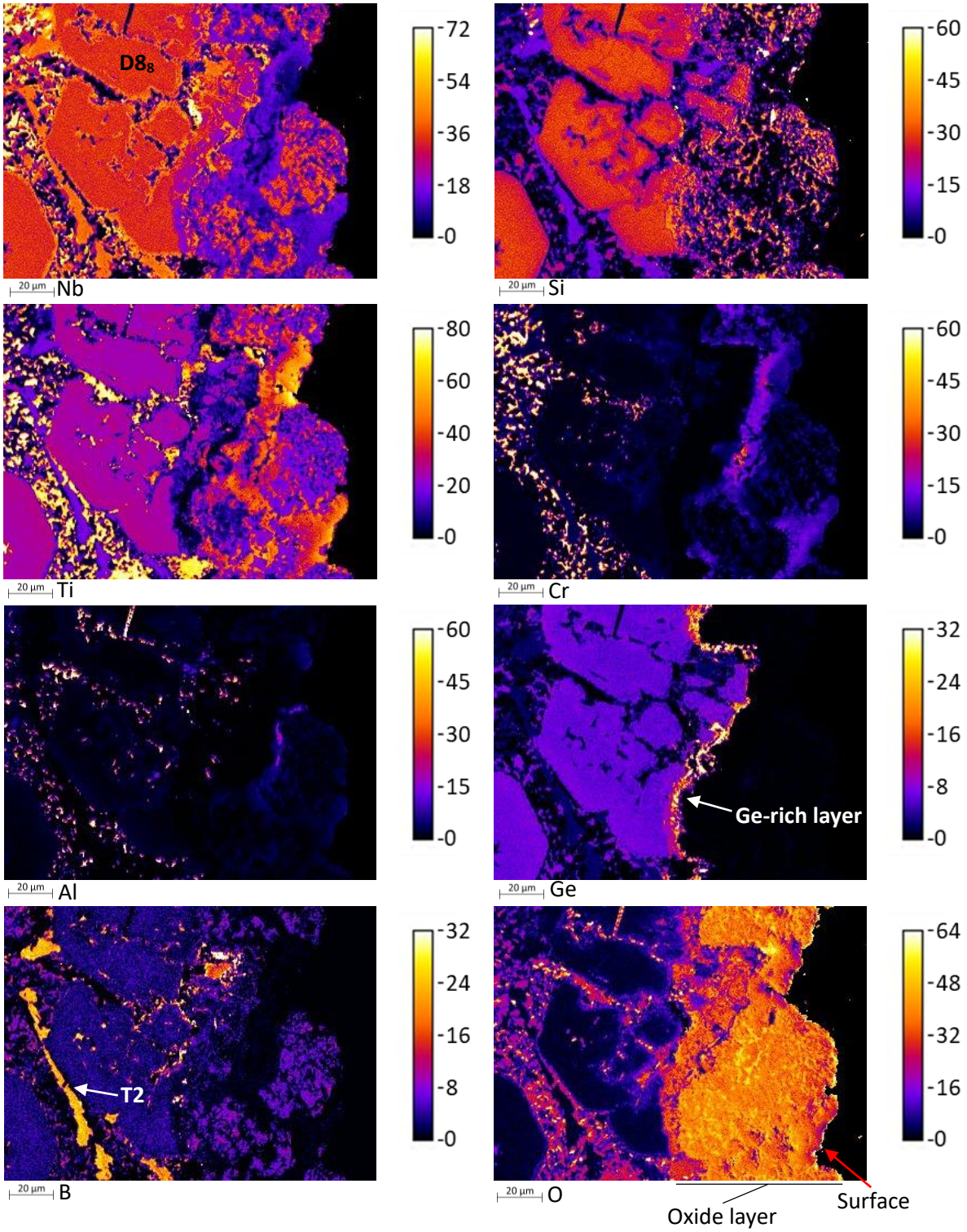

Figure 6.51a-h) EPMA maps of the oxide layer of JW1-AC in at.% of elements a) Nb, b) Si, c) Ti, d) Cr, e) Al, f) Ge, g) B h) O.

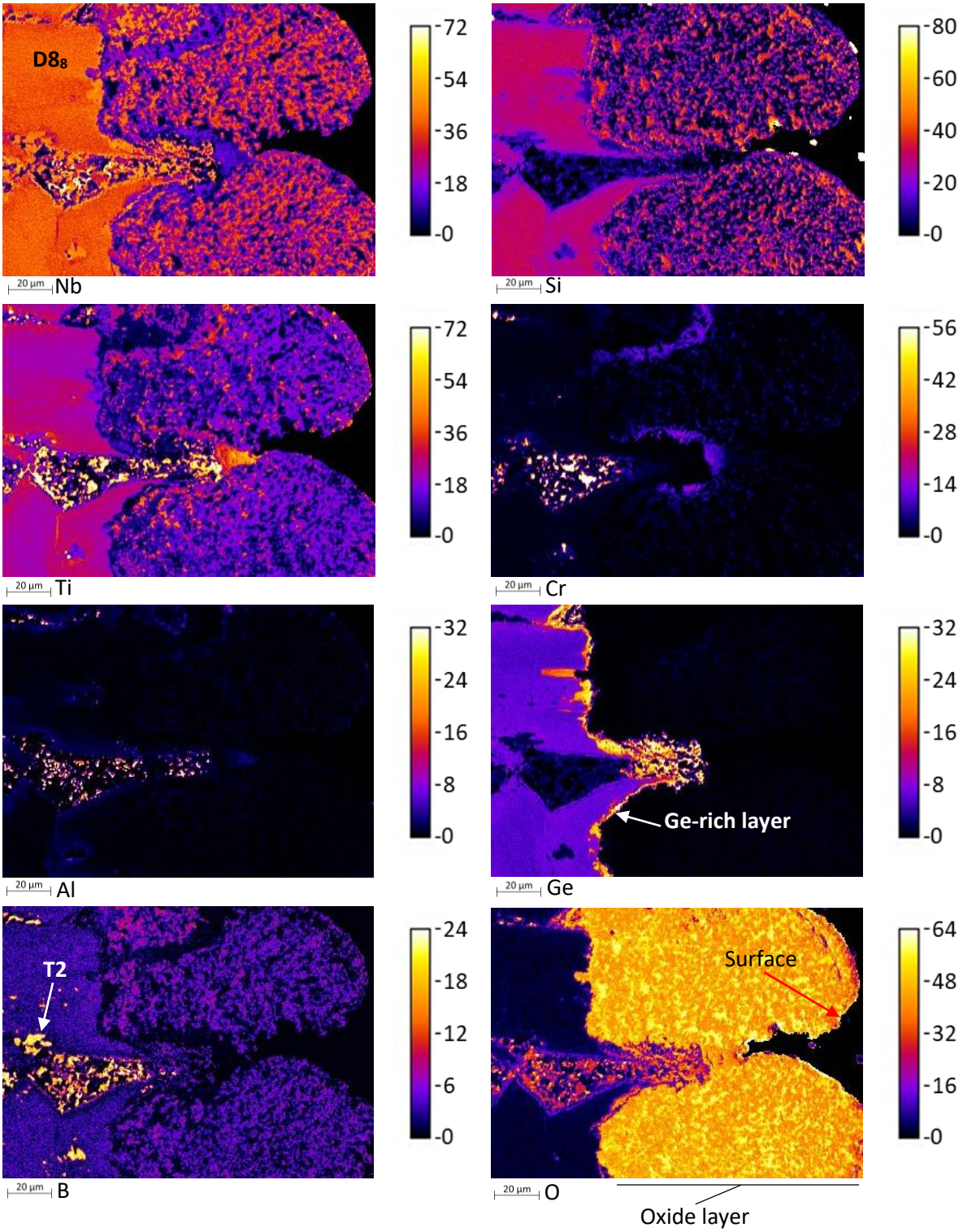

Figure 6.52a-h) EPMA maps of the oxide layer of JW1-HT13 in at.% of elements a) Nb, b) Si, c) Ti, d) Cr, e) Al, f) Ge, g) B h) O.

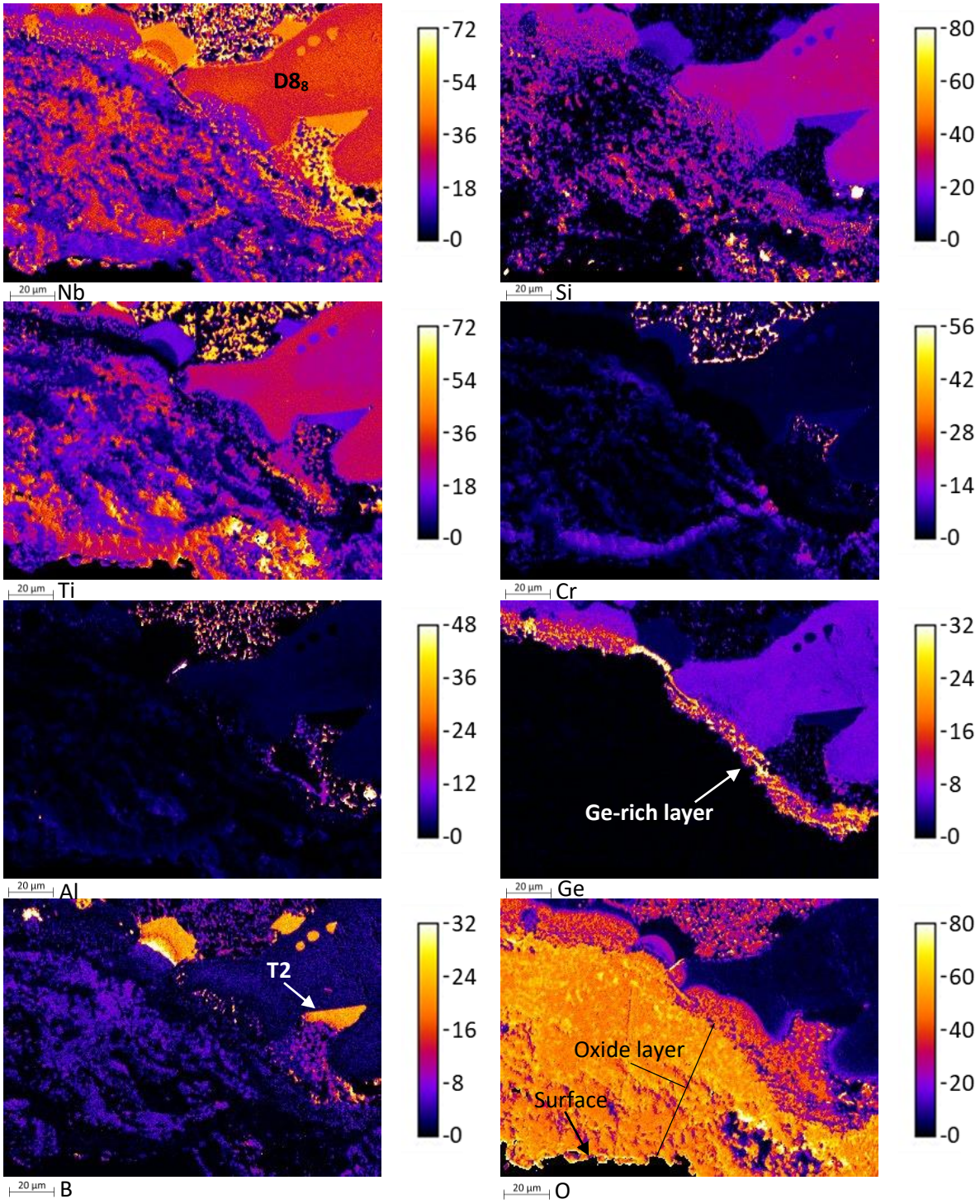

Figure 6.53a-h) EPMA maps of the oxide layer of JW1-HT15 in at.% of elements a) Nb, b) Si, c) Ti, d) Cr, e) Al, f) Ge, g) B h) O

Table 6.24) Phase analysis of bulk phases present in each JW1 oxidised sample EPMA map, values given in at.%.

		Nb	Si	Ti	Cr	Al	Ge	B	O
$D8_8$	JW1-AC	33.7 ± 2.3	29.7 ± 2.3	23.9 ± 1.4	0.7 ± 0.4	0.5 ± 0.3	6.3 ± 0.8	3.1 ± 1.8	2.0 ± 1.3
	JW1-HT13	36.6 ± 2.6	30.8 ± 2.3	21.5 ± 1.7	0.7 ± 0.4	0.3 ± 0.3	5.0 ± 0.7	3.0 ± 1.7	2.0 ± 1.2
	JW1-HT15	33.0 ± 2.7	25.9 ± 2.3	26.9 ± 2.4	1.3 ± 0.6	1.3 ± 0.5	6.2 ± 0.9	2.2 ± 1.7	3.2 ± 1.9
T2	JW1-AC	40.9 ± 2.3	12.9 ± 1.3	17.0 ± 1.3	2.3 ± 0.5	0.1 ± 0.1	2.1 ± 0.5	23.4 ± 2.8	1.3 ± 1.0
	JW1-HT13	42.1 ± 3.3	12.6 ± 1.6	15.0 ± 2.9	4.3 ± 0.9	0.1 ± 0.2	1.5 ± 0.4	22.7 ± 2.6	1.8 ± 1.6
	JW1-HT15	43.6 ± 2.7	13.2 ± 1.3	15.3 ± 1.0	3.3 ± 0.5	0.1 ± 0.2	1.5 ± 0.4	21.4 ± 2.7	1.7 ± 1.2
(Nb)	JW1-AC	67.1 ± 4.7	0.6 ± 0.6	2.0 ± 1.4	7.1 ± 3.5	2.1 ± 3.0	0.3 ± 0.3	10.4 ± 3.2	10.3 ± 5.8
	JW1-HT13	64.2 ± 3.8	2.4 ± 3.4	6.0 ± 6.9	5.0 ± 1.1	1.7 ± 1.7	0.8 ± 1.2	9.8 ± 3.0	9.9 ± 2.3
	JW1-HT15	70.7 ± 4.2	2.5 ± 2.9	3.0 ± 5.1	5.5 ± 1.7	0.5 ± 0.6	1.2 ± 1.4	10.6 ± 3.0	6.0 ± 2.6
Internal TiO_2	JW1-AC	0.4 ± 1.2	0.1 ± 0.2	72.5 ± 3.8	0.2 ± 0.2	0.6 ± 0.5	0.0 ± 0.1	0.0 ± 0.0	26.1 ± 4.0
	JW1-HT13	1.6 ± 1.3	0.1 ± 0.1	66.9 ± 3.0	1.3 ± 0.5	0.1 ± 0.1	0.0 ± 0.1	0.0 ± 0.0	30.0 ± 4.8
	JW1-HT15	0.6 ± 1.4	0.1 ± 0.1	65.8 ± 1.9	0.1 ± 0.1	0.2 ± 0.3	0.1 ± 0.1	0.0 ± 0.1	33.1 ± 4.2
$NbCr_2$	JW1-AC	28.3 ± 2.5	7.6 ± 1.2	2.2 ± 0.9	57.8 ± 1.9	0.2 ± 0.2	1.4 ± 0.6	0.5 ± 1.0	2.0 ± 1.6
	JW1-HT13	30.1 ± 2.6	7.4 ± 1.1	1.0 ± 0.6	57.7 ± 2.3	0.1 ± 0.2	1.5 ± 0.6	0.7 ± 1.1	1.5 ± 1.2
	JW1-HT15	31.3 ± 2.6	6.0 ± 1.4	1.5 ± 1.2	56.2 ± 2.4	0.2 ± 0.3	1.5 ± 0.5	1.2 ± 1.3	2.1 ± 1.7
Al-rich phase	JW1-AC	1.0 ± 1.1	0.5 ± 0.8	1.1 ± 0.9	0.5 ± 1.3	70.4 ± 3.8	0.2 ± 0.3	0.0 ± 0.2	26.3 ± 4.9
	JW1-HT13	2.0 ± 1.4	0.3 ± 0.6	5.3 ± 3.8	0.7 ± 1.0	60.5 ± 7.2	0.1 ± 0.2	0.0 ± 0.0	31.3 ± 4.2
	JW1-HT15	2.6 ± 3.5	0.3 ± 0.4	0.3 ± 0.2	0.7 ± 1.7	58.8 ± 8.0	0.1 ± 0.1	0.4 ± 0.8	36.7 ± 7.9

Table 6.23) Area analysis of the entire oxide layers and Ge-rich layers shown in EPMA maps for JW1 oxidised samples, values given in at.%.

		Nb	Si	Ti	Cr	Al	Ge	B	O
Total oxide layer:	JW1-AC	19.5 ± 9.9	12.8 ± 14.4	22.1 ± 15.2	3.0 ± 4.3	1.1 ± 3.7	2.1 ± 4.8	2.4 ± 4.7	36.9 ± 13.6
	JW1-HT13	19.0 ± 9.0	16.8 ± 16.5	12.4 ± 8.7	1.1 ± 2.1	0.4 ± 2.0	0.7 ± 2.7	2.3 ± 2.2	47.3 ± 15.5
	JW1-HT15	17.6 ± 9.8	10.7 ± 13.1	16.6 ± 11.1	2.0 ± 2.8	0.7 ± 1.0	0.6 ± 2.8	1.6 ± 2.1	50.2 ± 20.7
Ge-rich layer	JW1-AC	29.5 ± 9.1	19.7 ± 14.0	5.7 ± 9.0	0.4 ± 1.1	0.4 ± 1.1	17.8 ± 7.0	2.5 ± 3.5	24.0 ± 15.9
	JW1-HT13	35.0 ± 7.6	16.3 ± 10.7	8.6 ± 6.5	0.4 ± 0.6	0.9 ± 1.7	19.0 ± 4.4	2.9 ± 2.3	16.8 ± 16.8
	JW1-HT15	27.0 ± 9.1	17.1 ± 11.8	4.7 ± 7.8	0.3 ± 0.9	0.9 ± 2.1	15.7 ± 5.9	1.8 ± 2.1	32.6 ± 21.1

Table 6.25) Phase analysis of oxide phases in each JW1 oxidised sample from locations in the oxide scale, values given in at.%.

		Nb	Si	Ti	Cr	Al	Ge	B	O
Ge-rich phase	JW1-AC	42.9 ± 10.0	3.3 ± 1.8	1.6 ± 1.7	0.3 ± 0.4	0.4 ± 1.2	39.8 ± 7.3	3.4 ± 3.1	8.3 ± 5.3
	JW1-HT13	44.9 ± 2.7	5.5 ± 3.1	6.5 ± 6.4	0.4 ± 0.5	0.4 ± 0.6	29.3 ± 2.5	5.5 ± 2.5	7.4 ± 3.9
	JW1-HT15	47.8 ± 3.4	2.3 ± 2.3	0.7 ± 0.5	0.5 ± 0.5	0.1 ± 0.2	33.1 ± 1.6	3.9 ± 1.9	11.6 ± 15.0
Ti-rich oxide	JW1-AC	8.0 ± 3.5	0.1 ± 0.1	55.7 ± 10.6	5.9 ± 2.1	0.9 ± 0.8	0.0 ± 0.1	0.1 ± 0.4	29.3 ± 8.6
	JW1-HT13	10.2 ± 2.1	0.8 ± 1.1	39.7 ± 4.4	5.1 ± 3.9	1.3 ± 1.0	0.0 ± 0.1	0.1 ± 0.3	42.6 ± 5.1
	JW1-HT15	8.9 ± 1.1	0.4 ± 1.1	36.4 ± 2.5	2.9 ± 1.6	1.8 ± 0.8	0.0 ± 0.1	0.1 ± 0.2	49.5 ± 12.2
Nb-rich oxide	JW1-AC	36.7 ± 3.6	1.1 ± 3.3	18.2 ± 1.3	0.4 ± 0.4	0.5 ± 0.4	0.1 ± 0.2	5.5 ± 2.7	37.5 ± 5.4
	JW1-HT13	37.3 ± 3.2	0.6 ± 1.1	16.5 ± 1.0	0.2 ± 0.2	0.2 ± 0.2	0.1 ± 0.1	5.4 ± 2.6	39.6 ± 3.8
	JW1-HT15	31.1 ± 2.2	1.4 ± 2.0	14.2 ± 1.3	0.2 ± 0.2	0.4 ± 0.3	0.1 ± 0.1	4.0 ± 1.7	48.7 ± 5.2
Alternative Nb-rich oxide	JW1-AC	41.4 ± 3.0	0.9 ± 0.8	8.8 ± 0.7	0.2 ± 0.2	0.3 ± 0.2	0.0 ± 0.1	7.3 ± 3.8	41.2 ± 6.0
	JW1-HT13	37.4 ± 2.2	2.0 ± 1.7	8.6 ± 0.7	0.1 ± 0.2	0.1 ± 0.2	0.1 ± 0.1	7.2 ± 1.6	44.4 ± 5.5
	JW1-HT15	35.3 ± 2.6	1.1 ± 0.7	7.6 ± 1.6	0.1 ± 0.2	0.2 ± 0.2	0.1 ± 0.1	5.5 ± 1.7	50.2 ± 5.4
Si-rich oxide	JW1-AC	0.7 ± 0.5	42.6 ± 3.7	3.4 ± 2.1	0.8 ± 0.6	0.1 ± 0.2	0.3 ± 0.4	0.1 ± 0.3	51.8 ± 5.2
	JW1-HT13	0.8 ± 0.7	40.3 ± 2.2	1.0 ± 0.4	0.0 ± 0.1	0.0 ± 0.1	0.4 ± 0.2	0.2 ± 0.3	57.3 ± 8.4
	JW1-HT15	2.1 ± 1.8	34.2 ± 4.1	1.3 ± 0.6	0.1 ± 0.2	0.1 ± 0.1	0.3 ± 0.2	0.7 ± 0.7	61.4 ± 20.1
Cr-rich oxide	JW1-AC	5.1 ± 2.4	4.8 ± 3.6	6.6 ± 2.4	33.1 ± 5.1	0.2 ± 0.2	0.1 ± 0.1	0.0 ± 0.1	50.1 ± 6.0
	JW1-HT15	6.0 ± 2.5	4.7 ± 3.5	4.4 ± 1.9	25.5 ± 3.6	0.1 ± 0.1	0.3 ± 0.5	0.2 ± 0.3	59.0 ± 7.3

6.3.2.3 JW2

6.3.2.3.1 XRD

The XRD pattern of JW2-AC is shown in Figure 6.54. The phases that are identified are TiO_2, SiO_2 and $TiNb_2O_7$. The XRD pattern of JW2-HT13 is shown in Figure 6.55. The phases that are identified are TiO_2, SiO_2 and $TiNb_2O_7$. The XRD pattern of JW2-HT15 is shown in Figure 6.56. The phases that are identified are TiO_2, $Ti_2Nb_{10}O_{29}$, $TiNb_2O_7$ and SiO_2.

Compared to the 1000°C samples of JW2, the main differences are that $Ti_2Nb_{10}O_{29}$ is absent from the XRD pattern of JW2-AC and JW2-HT13, and SiO_2 is found in JW2-AC and JW2-HT13 1200°C samples. The underlying phases seen in the 1000°C JW2-HT15 sample, $D8_8$ and T2, were not found in the 1200°C samples. In the case of JW2-AC and JW2-HT15 the TiO_2 peaks dominate the XRD pattern.

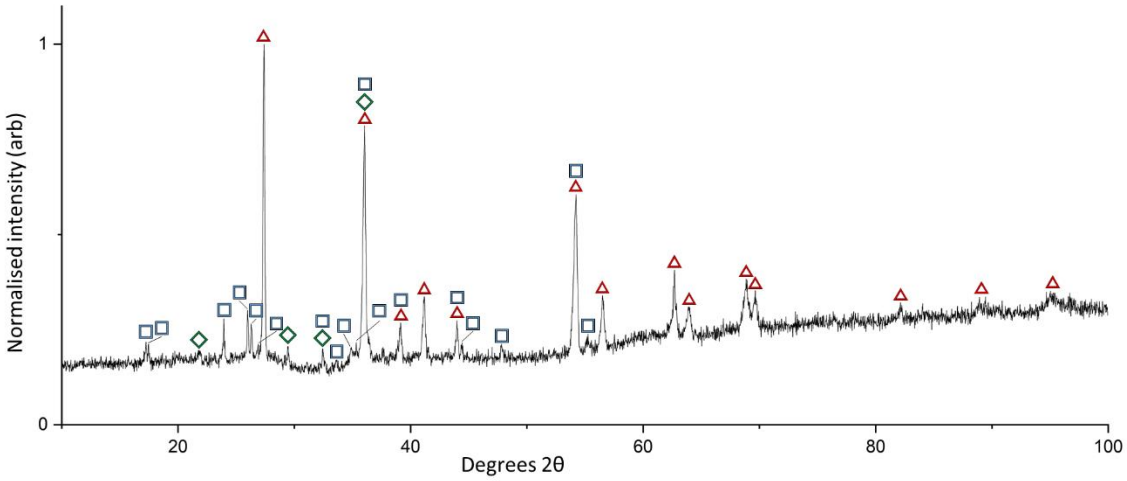

Figure 6.54) XRD pattern of oxidised at 1200°C JW2-AC. △ = TiO_2, □ =$TiNb_2O_7$, ◇ = SiO_2

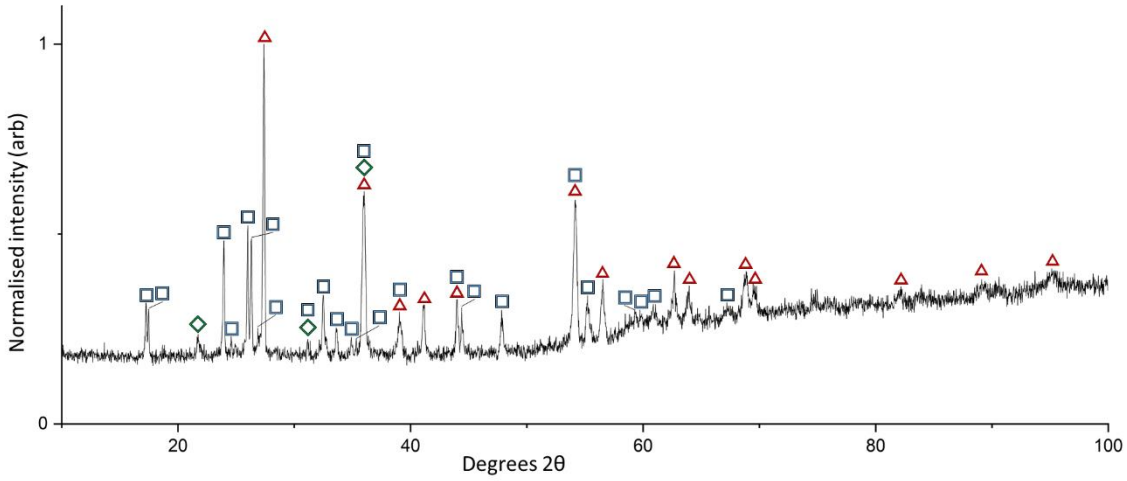

Figure 6.55) XRD pattern of oxidised at 1200°C JW2-HT13. △ = TiO_2, □ =$TiNb_2O_7$ ◇ = SiO_2

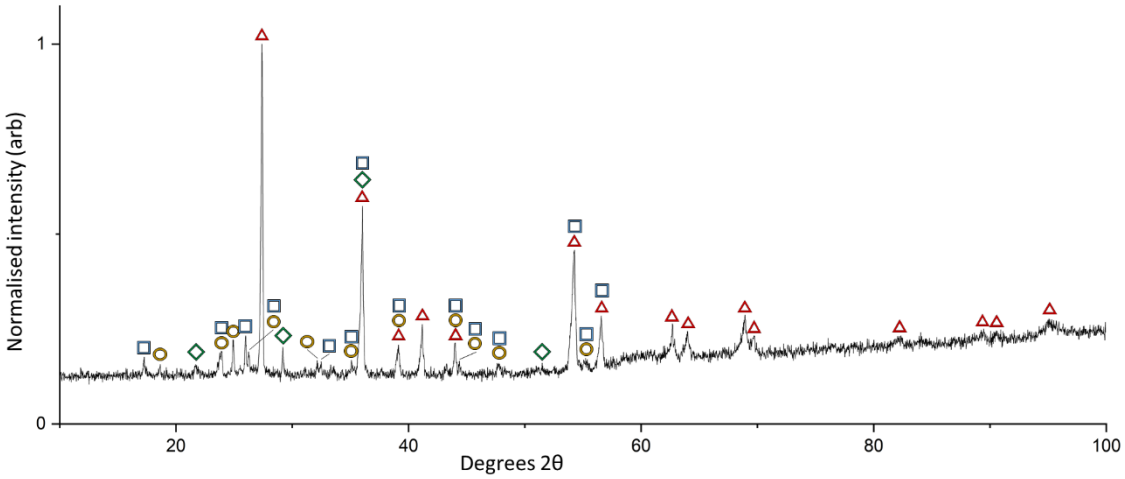

Figure 6.56) XRD pattern of oxidised at 1200°C JW2-HT15. △ = TiO_2, □ =$TiNb_2O_7$ ○ = $Ti_2Nb_{10}O_{29}$ ◇ = SiO_2

6.3.2.3.2 EPMA

EPMA mapping of oxidised JW2 samples at 1200°C including elements Nb, Si, Ti, Cr, Al, Ge, B and O is presented in Figure 6.57, Figure 6.58 and Figure 6.59 for the as-cast state, heat-treated at 1300°C state, and heat-treated at 1500°C state, respectively. In the bulk of each oxidised sample, 5 phases were identified: internal TiO_2, $NbCr_2$, $D8_8$, T2, and an Al-rich phase. The phases $NbCr_2$ and $D8_8$ are consistent with the unoxidised microstructures of each alloy; JW2-AC, JW2-HT13, JW2-HT15. No (Nb) phase could be found in any of the location measured in these samples. Original amounts of (Nb) in the unoxidised alloys were between 8.1% and 0.5% by volume fraction, which have been further reduced to near zero by oxidation. The T2 phase found in JW2-AC implies 1200°C treatment is enough to start transformation, as in the unoxidised specimen this was largely absent. T2 was also found in JW2-HT13 and JW2-HT15, which is as expected.

An NbB phase is found in JW2-HT13 in agreement with the unoxidised microstructure and is clearly identifiable as grains approximately 5-40 µm across. In the particular area of JW2-AC measured no NbB could be found despite this being found in the unoxidised sample. The NbB that is found in JW2-HT15 is unexpected, as the heat-treatment at 1500°C was thought to fully convert NbB to T2. However, in JW2-HT15 this NbB phase is found within the oxide layer adjacent to a T2 grain and also in fine particles distributed in partially oxidised $D8_8$. In fact, this NbB fine particle distribution in the oxide layer is seen in all three JW2 samples to varying extents. This will be presented alongside the oxide layer results in Table 6.28. The internal TiO_2, NbB fine particles and Al-rich phase are a result of oxidation in each case. The compositions of each of these phases in the oxidised samples are listed in Table 6.26.

In each alloy the microstructure consists mainly of large $D8_8$ grains, but in JW2-HT13 NbB and T2 exist in coarse grains too, and in JW2-HT15 T2 exists in large grains as well. In JW2-AC and JW2-HT13 a mixture of T2, $NbCr_2$, the Ti-rich phase and the Al-rich phase exists in the intergranular region. In the case of JW2-HT15 only a small area that is not T2 and $D8_8$ grains is measured, which consists of $NbCr_2$, the Ti-rich phase and the Al-rich phase. In the case of the internal TiO_2 and Al-rich phase found in the bulk of the oxidised specimens, the same logic that was used to identify these phases in KZ5 and JW1 is applied to JW2. And therefore the Ti-rich phase is assigned to TiO_2 after a precursor (Ti) has been fully oxidised, and Al-rich phase is assigned as a mixture of (Al) and Al_2O_3.

Area analysis was performed using this EPMA data in order to report average compositions of specific areas of the oxide scale, shown in Table 6.27. The layer of oxidised material of JW2-AC had

an average composition of 14.5 at.% Nb, 7.1 at.% Si, 25.6 at.% Ti, 5.5 at.% Cr, 1.3 at.% Al, 0.2 at.% Ge, 0.9 at.% B, and 44.9 at.% O. The layer of oxidised material of JW2-HT13 had an average composition of 17.4 at.% Nb, 16.2 at.% Si, 15.7 at.% Ti, 2.0 at.% Cr, 1.0 at.% Al, 0.2 at.% Ge, 1.7 at.% B, and 43.2 at.% O. The layer of oxidised material of JW2-HT15 had an average composition of 20.2 at.% Nb, 14.4 at.% Si, 22.6 at.% Ti, 2.2 at.% Cr, 0.8 at.% Al, 3.8 at.% Ge, 1.6 at.% B, and 34.2 at.% O.

A layer that is rich in Ge can be seen between the oxide layer and the bulk alloy in each sample of JW2. It is unclear whether this layer is made up of a new phase or an existing phase has been enriched in Ge during the oxidation process. Area analysis of this layer was performed and considering the Ge content of these layers was at least 11.9 at.% in JW2-HT13, which is greater than any $D8_8$ Ge composition found in the un-oxidised states of any JW series alloy, with the exception of the high Ge content alloy JW3-AC, despite this layer also containing a significant amount of O, it is suspected this is a distinct phase.

In the case of JW2-AC, the ratio of Nb + Ti to Ge + Si is 1.13, so it is uncertain from this compositional information what phase has formed, i.e Nb_5Ge_3, Nb_3Ge, $NbGe_2$, or if multiple phases are present in too fine a distribution to resolve. The same is true for JW2-HT13, where the ratio of Nb + Ti to Ge + Si is 0.90. In the case of JW2-HT15, the ratio of Nb + Ti to Ge + Si is 1.37 which is a better indication of $Nb_5(Si,Ge)_3$ than calculated in the other two JW2 alloys.

Areas where Ge content is greater than the rest of the Ge-rich layer in EPMA maps for JW2-AC, JW2-HT13 and JW2-HT15 were examined. Points were taken from these high-Ge areas to calculate the composition given in Table 6.28 for a Nb-Ge phase. Average Nb and Ge contents of this phase in JW2-AC were 50.0 at.% and 32.3 at.%. Average Nb and Ge contents of this phase in JW2-HT13 were 45.4 at.% and 30.6 at.%. Average Nb and Ge contents of this phase in JW2-HT15 were 50.8 at.% and 33.3 at.%. The ratios of Nb + Ti to Ge + Si for these alloys are near identical, at 1.48, 1.47 and 1.46 for JW2-AC, JW2-HT13 and JW2-HT15, respectively. These ratios are closer to the expected ratio of elements in Nb_5Ge_3 and with low Si content when compared to the whole Ge-layer measurements, indicating that Nb_5Ge_3 has formed in certain places along the Ge-rich layer.

Compositions of phases and regions within the oxide layer of each alloy are presented in Table 6.28. In each of the oxide scales four oxide phases are reported on and are designated based on their most notable element; Ti-rich oxide, Nb-rich oxide, an alternate Nb-rich oxide, and Si-rich oxide. A Cr-rich phase can also be found in the as-cast sample.

In JW2-AC the Ti-rich oxide phase has titanium content of 42.0 at.% whilst Nb and Cr contents were 9.7 at.% and 3.1 at.%, respectively. As a result of having higher Ti content whilst containing significant amounts of Nb and Cr, this phase is considered to be rutile TiO_2 with substation of mainly Nb and Cr onto Ti sites, $(Ti,Nb,Cr)O_2$. For alloys JW2-HT13 and JW2-HT15 the titanium contents of the Ti-rich phase was 39.7 at.% and 43.9 at.%, and amounts of Nb and Cr still indicate a TiO_2 phase with Ti partially substituted for Cr and Nb. In the outer most part of the scale in JW2-AC and JW2-HT13, Ti content of the Ti-rich oxide phase increases and substitution of Nb and Cr is reduced to the point where the composition resembles the internal TiO_2 phase from the bulk of the JW2 alloys.

The Nb-rich phase in JW2-AC had Nb content of 35.8 at.% and Ti content of 16.2 at.%, with the Nb/Ti ratio equal to 2.21. This ratio is close to the expected value of $TiNb_2O_7$ rather than $Ti_2Nb_{10}O_{29}$, so this phase is considered to be the $TiNb_2O_7$ oxide also identified through XRD. The alternate Nb-rich phase on the other hand has a Nb content of 38.4 at.% and a Ti content of 8.7 at.%, and therefore a Nb/Ti ratio of 4.39. This ratio is close to 5, and so can be considered $Ti_2Nb_{10}O_{29}$.

In JW2-HT13 the Nb-rich phase had Nb content of 34.1 at.% and Ti content of 17.1 at.%, with the Nb/Ti ratio equal to 2.00. This ratio is the expected value of $TiNb_2O_7$, so this phase is considered to be the $TiNb_2O_7$ oxide also identified through XRD. The alternate Nb-rich phase on the other hand has a Nb content of 40.7 at.% and a Ti content of 8.6 at.%, and therefore a Nb/Ti ratio of 4.73. This ratio is close to 5, and so can be considered $Ti_2Nb_{10}O_{29}$.

In JW2-HT15 the Nb-rich phase had Nb content of 41.9 at.% and Ti content of 18.2 at.%, with the Nb/Ti ratio equal to 2.31. This ratio is closer to the expected value of $TiNb_2O_7$ rather than $Ti_2Nb_{10}O_{29}$, so this phase is considered to be the $TiNb_2O_7$ oxide also identified through XRD. The alternate Nb-rich phase on the other hand has a Nb content of 49.2 at.% and a Ti content of 10.6 at.%, and therefore a Nb/Ti ratio of 4.65. This ratio is close to 5, and so can be considered $Ti_2Nb_{10}O_{29}$.

Si content in each Si-rich phase is 38.2 at.%, 40.6 at.% and 40.7 at.% for alloys JW2-AC, JW2-HT13 and JW2-HT15, respectively, whilst average Nb contents are only 2.3 at.%, 0.9 at.% and 1.3 at.%, respectively, and average Ti contents are only 4.1 at.%, 1.5 at.% and 2.7 at.%, respectively. This phase is identified as SiO_2, and according to XRD a cristobalite structure. The Si-rich phase is coarser in 1200°C samples compared to the 1000°C oxidised versions of JW2. As a result, the Nb and Ti contents, which are possibly a result of titanium-niobate oxide impurities or underlying phases, are lower in both the as-cast and heat-treated samples of JW2 oxidised at 1200°C. B and Ge contents in this SiO_2 phase are both very low, less than 1.0 at.% in all cases. A glassy layer containing Si, Ge and B is therefore not found in any case of JW2 and Ge and B substitution into this form of SiO_2 phase is extremely limited. However, in each JW2 alloy there are small particles with high Boron content distributed in partially oxidised $D8_8$ below the Ge-rich layer. In the case of JW2-AC, this high Boron content phase interrupts the Ge-rich layer and forms a partial layer of high boron content phase.

This high boron content phase is likely a result of oxidation, as it is present in JW2-HT15 where none is recorded to exists in the unoxidised structure. However, oxygen content is low so an oxide can be ruled out. The most likely phase for this high Boron content phase is NbB, as it is known this is it least metastable in the alloys in question, where as other high B and high Nb phases are not seen in unoxidised samples.

Generally, in each of the samples, TiO_2 with Cr and Nb substitutions, $(Ti,Nb,Cr)O_2$, exists at the outer part of the oxide scale in coarse arrangements. At the furthest extent the TiO_2 it is more 'pure' with less substitution of Ti for Nb and Cr. In the case of JW2-AC and JW2-HT15, the $(Ti,Nb,Cr)O_2$ is practically a complete outer layer. In JW2-HT13 this phase exists above what would have been the intergranular region containing (Nb), $NbCr_2$ and T2, but above what would have been $D8_8$ a fine mixture of $(Ti,Nb,Cr)O_2$, SiO_2, $TiNb_2O_7$, and $Ti_2Nb_{10}O_{29}$ is seen. This pattern is seen in JW2-AC below the $(Ti,Nb,Cr)O_2$ outer layer too, where areas above $D8_8$ are generally a finer mixture of oxides.

Below these two regions exists the Ge-rich layer that is present in each alloy. However, oxidised or partially oxidised material exists underneath this layer. This is to a greater extent in areas previously described as intergranular (i.e. containing (Nb)) when compared to $D8_8$ regions, but $D8_8$ is still susceptible underneath the Ge-rich layer. In alloy JW2-HT15, the particular region captured though EPMA mapping shows T2 in contact with the material surface adjacent to $D8_8$. As can be seen in Figure 6.59, the T2 is less susceptible to oxidation than the $D8_8$ phase, possibly due to the high boron phase and denser Ge-rich layer that has formed on this area of T2 phase. This high-boron phase, expected to be NbB, has formed in small particles within the partially oxidised $D8_8$ phase below the Ge-rich layer in each JW2 alloy after oxidation. In the AC sample this NbB phase has even replaced some of the Ge-rich layer that forms parallel to the oxide sample surface.

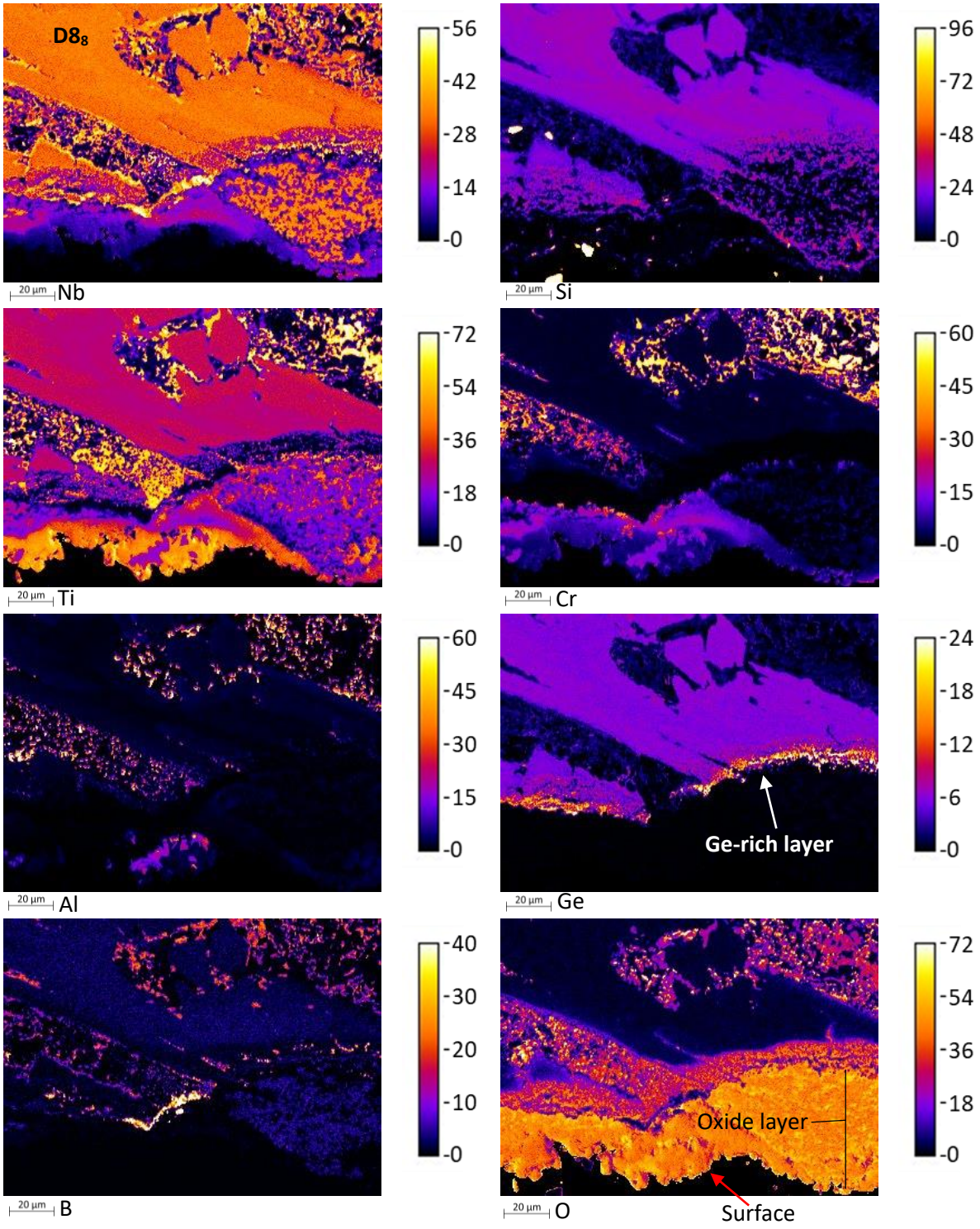

Figure 6.57a- h) EPMA maps of the oxide layer of JW2-AC in at.% of elements a) Nb, b) Si, c) Ti, d) Cr, e) Al, f) Ge, g) B h) O.

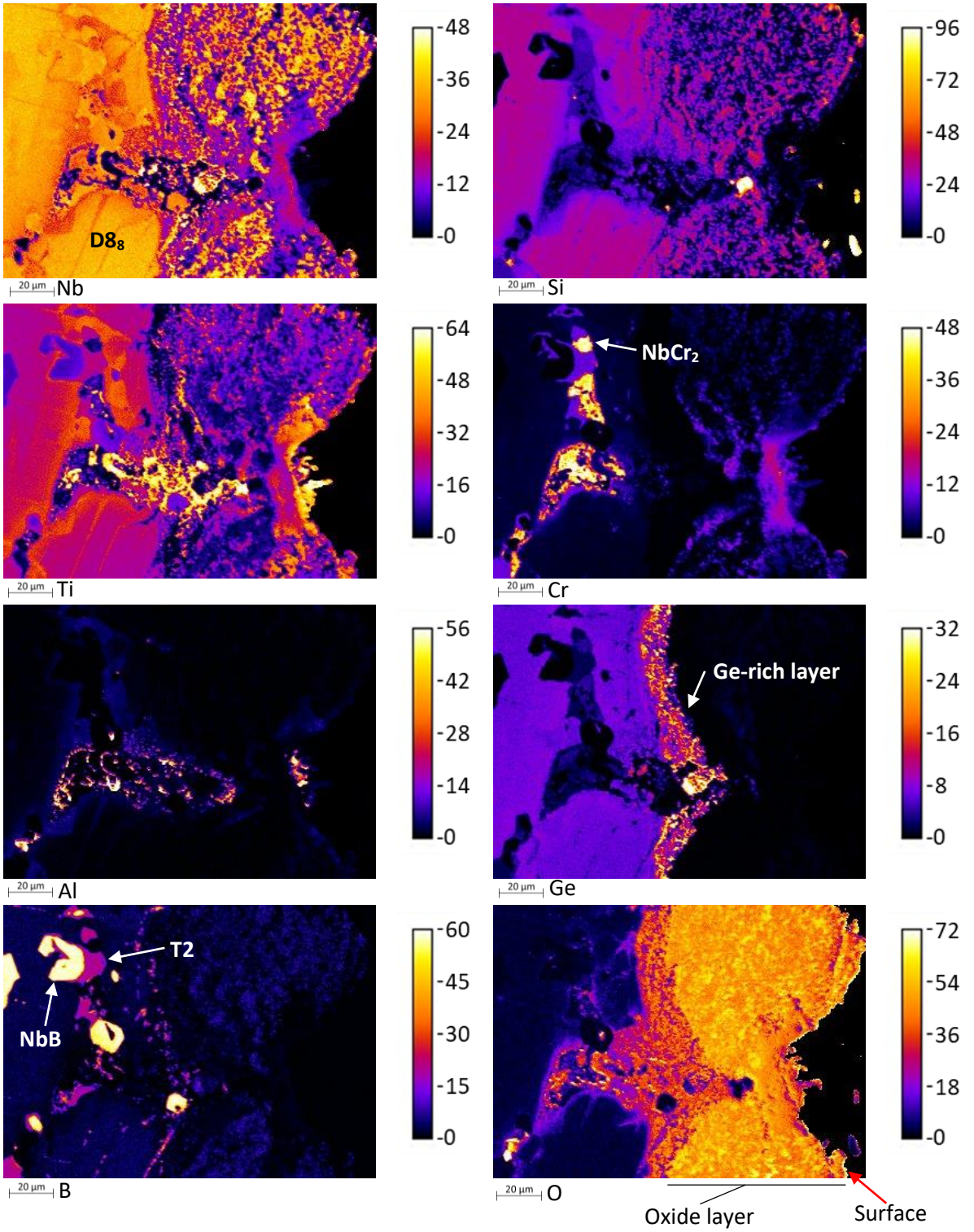

Figure 6.58a-h) EPMA maps of the oxide layer of JW2-HT13 in at.% of elements a) Nb, b) Si, c) Ti, d) Cr, e) Al, f) Ge, g) B h) O.

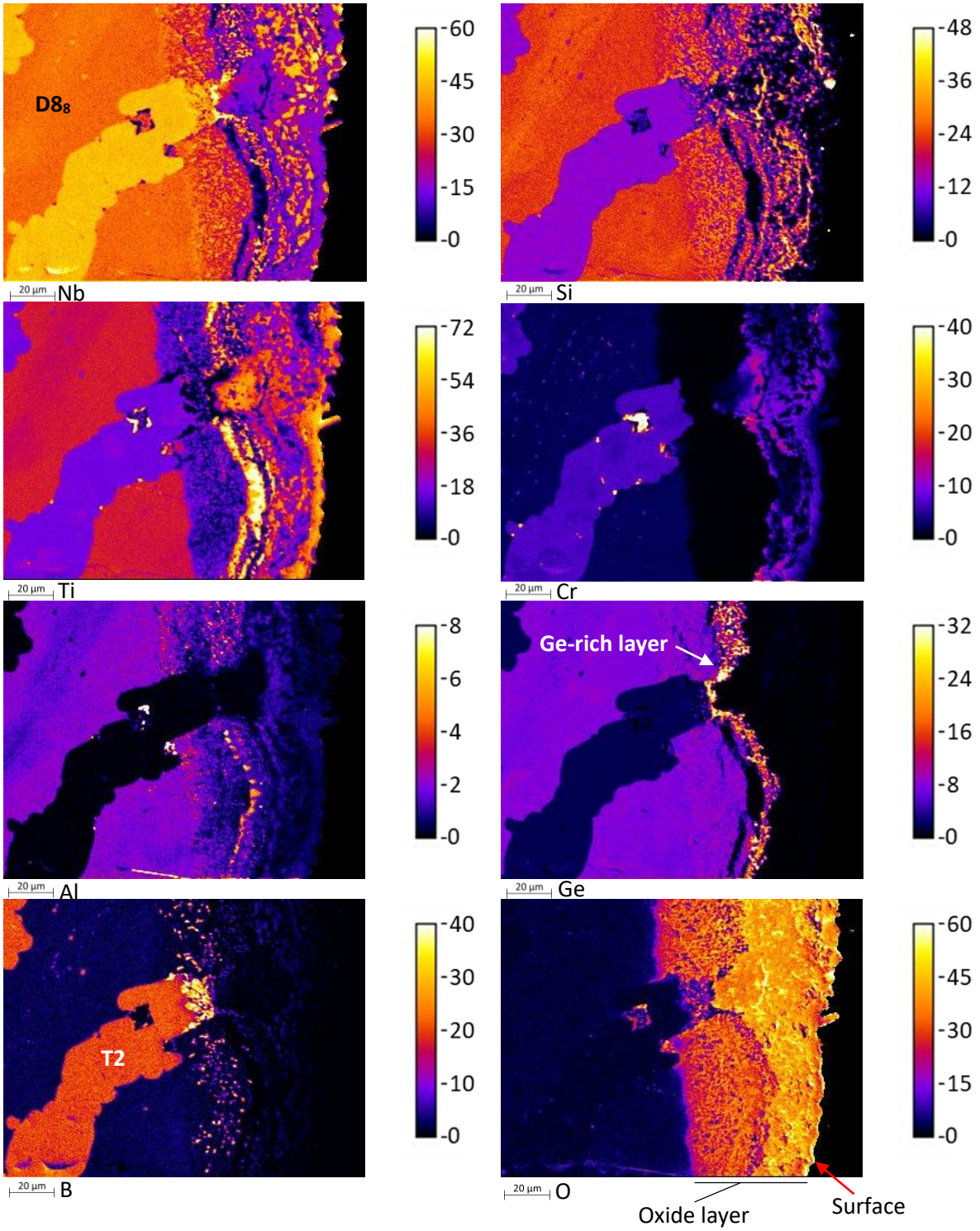

Figure 6.59a-h) EPMA maps of the oxide layer of JW2-HT15 in at.% of elements a) Nb, b) Si, c) Ti, d) Cr, e) Al, f) Ge, g) B h) O.

Table 6.26) Phase analysis of bulk phases present in each JW2 oxidised sample EPMA map, values given in at.%.

		Nb	Si	Ti	Cr	Al	Ge	B	O
$D8_8$	JW2-AC	32.2 ± 2.4	26.8 ± 2.3	28.1 ± 1.6	1.3 ± 0.4	0.9 ± 0.4	6.4 ± 0.7	2.2 ± 1.5	2.1 ± 1.4
	JW2-HT13	33.4 ± 2.5	29.8 ± 2.1	24.3 ± 2.1	1.2 ± 0.4	0.4 ± 0.3	6.0 ± 0.8	2.7 ± 1.5	2.3 ± 1.3
	JW2-HT15	31.2 ± 2.4	23.6 ± 2.0	30.0 ± 1.6	2.2 ± 0.7	1.7 ± 0.4	6.8 ± 0.8	2.2 ± 1.4	2.3 ± 1.3
T2	JW2-AC	43.2 ± 4.4	11.1 ± 1.2	13.4 ± 4.0	6.4 ± 1.5	0.3 ± 0.7	1.9 ± 0.5	22.0 ± 2.1	1.7 ± 1.2
	JW2-HT13	32.3 ± 2.3	12.5 ± 1.9	23.0 ± 2.4	9.4 ± 1.3	0.1 ± 0.1	1.6 ± 1.3	18.4 ± 2.8	2.6 ± 4.8
	JW2-HT15	41.7 ± 2.6	12.4 ± 1.2	15.8 ± 1.4	6.0 ± 0.7	0.1 ± 0.1	1.4 ± 0.4	20.9 ± 2.6	1.7 ± 1.1
NbB	JW2-HT13	30.6 ± 2.3	0.2 ± 0.2	13.3 ± 2.5	0.3 ± 0.2	0.0 ± 0.1	0.0 ± 0.1	54.4 ± 3.4	1.2 ± 0.7
Internal TiO_2	JW2-AC	1.7 ± 2.7	0.4 ± 0.7	67.0 ± 4.6	2.2 ± 3.7	0.5 ± 0.4	0.1 ± 0.1	0.1 ± 0.4	28.0 ± 4.7
	JW2-HT13	1.5 ± 1.5	0.1 ± 0.2	63.5 ± 2.6	3.0 ± 0.7	0.1 ± 0.1	0.0 ± 0.1	0.0 ± 0.1	31.7 ± 3.6
	JW2-HT15	1.1 ± 1.0	0.2 ± 0.2	71.9 ± 2.0	1.1 ± 1.2	0.4 ± 0.4	0.0 ± 0.0	0.0 ± 0.0	25.3 ± 4.0
$NbCr_2$	JW2-AC	29.5 ± 2.4	4.6 ± 1.9	2.3 ± 1.5	60.8 ± 2.3	0.2 ± 0.2	0.9 ± 0.5	0.6 ± 0.9	1.2 ± 1.1
	JW2-HT13	25.0 ± 2.4	12.4 ± 3.4	7.9 ± 3.3	44.4 ± 2.8	0.2 ± 0.3	3.2 ± 0.7	0.2 ± 0.5	6.8 ± 2.2
	JW2-HT15	26.8 ± 2.5	6.6 ± 1.4	9.5 ± 7.0	49.8 ± 2.4	0.1 ± 0.2	1.6 ± 0.5	0.5 ± 1.0	5.0 ± 4.3
Al-rich phase	JW2-AC	2.1 ± 3.3	0.3 ± 0.4	2.4 ± 4.8	1.6 ± 3.1	58.3 ± 13.8	0.1 ± 0.2	0.1 ± 0.3	35.1 ± 8.1
	JW2-HT13	0.9 ± 1.0	0.5 ± 0.6	0.8 ± 1.0	0.9 ± 1.1	60.9 ± 3.6	0.1 ± 0.2	0.0 ± 0.0	35.9 ± 6.3
	JW2-HT15	4.7 ± 3.5	1.7 ± 1.7	7.3 ± 6.7	4.7 ± 4.4	48.3 ± 14.6	0.4 ± 0.5	0.0 ± 0.0	32.9 ± 15.4

Table 6.27) Area analysis of the entire oxide layers and Ge-rich layers shown in EPMA maps for JW2 oxidised samples, values given in at.%.

		Nb	Si	Ti	Cr	Al	Ge	B	O
Total oxide layer:	JW2-AC	14.5 ± 9.5	7.1 ± 11.2	25.6 ± 13.8	5.5 ± 6.2	1.3 ± 4.2	0.2 ± 1.1	0.9 ± 1.6	44.9 ± 11.7
	JW2-HT13	17.8 ± 9.0	16.2 ± 14.1	15.7 ± 12.5	2.0 ± 3.1	1.0 ± 4.9	2.4 ± 4.8	1.7 ± 2.4	43.2 ± 15.1
	JW2-HT15	20.2 ± 9.9	14.4 ± 11.3	22.6 ± 16.1	2.2 ± 3.1	0.8 ± 0.9	3.8 ± 5.1	1.6 ± 4.6	34.2 ± 12.0
Ge-rich layer	JW2-AC	26.4 ± 9.8	18.5 ± 11.8	10.0 ± 12.6	0.3 ± 1.8	0.5 ± 0.8	13.6 ± 5.4	2.0 ± 3.8	28.8 ± 16.6
	JW2-HT13	19.6 ± 7.8	21.6 ± 11.3	10.5 ± 11.1	0.2 ± 0.3	0.5 ± 1.9	11.9 ± 5.1	1.3 ± 1.9	34.5 ± 13.7
	JW2-HT15	22.3 ± 11.1	15.8 ± 8.4	17.3 ± 15.7	0.2 ± 0.5	1.1 ± 1.1	13.1 ± 6.7	1.5 ± 2.4	28.7 ± 15.0

Table 6.28) Phase analysis of oxide phases in each JW2 oxidised sample from locations in the oxide scale, values given in at.%.

		Nb	Si	Ti	Cr	Al	Ge	B	O
Ge-rich phase	JW2-AC	50.0 ± 2.7	3.5 ± 2.0	2.8 ± 1.8	0.1 ± 0.2	0.2 ± 0.2	32.3 ± 1.2	3.8 ± 2.9	7.3 ± 3.5
	JW2-HT13	45.4 ± 3.0	3.3 ± 1.8	4.4 ± 7.0	0.5 ± 0.5	0.2 ± 0.2	30.6 ± 1.9	5.3 ± 2.0	10.3 ± 6.9
	JW2-HT15	50.8 ± 4.6	2.8 ± 2.1	1.9 ± 2.2	0.3 ± 0.3	0.3 ± 0.3	33.3 ± 2.3	5.6 ± 2.0	5.0 ± 4.5
Ti-rich oxide	JW2-AC	9.7 ± 2.9	0.7 ± 1.1	42.0 ± 6.3	3.1 ± 2.4	1.6 ± 0.4	0.2 ± 0.1	0.1 ± 0.3	42.7 ± 4.0
	JW2-HT13	10.1 ± 2.5	2.8 ± 4.1	39.7 ± 3.5	3.8 ± 1.5	1.1 ± 0.4	0.2 ± 0.2	0.2 ± 0.4	42.0 ± 9.1
	JW2-HT15	14.3 ± 2.3	0.4 ± 0.8	43.9 ± 4.7	4.5 ± 1.2	0.4 ± 0.3	0.1 ± 0.1	0.1 ± 0.4	36.4 ± 8.3
Nb-rich oxide	JW2-AC	35.8 ± 3.0	0.3 ± 0.4	16.2 ± 1.1	0.3 ± 0.3	0.3 ± 0.2	0.0 ± 0.0	3.7 ± 1.7	43.4 ± 4.3
	JW2-HT13	34.1 ± 2.2	2.2 ± 3.2	17.1 ± 1.0	0.3 ± 0.2	0.3 ± 0.2	0.0 ± 0.1	3.4 ± 1.5	42.6 ± 5.6
	JW2-HT15	41.9 ± 5.5	0.6 ± 1.5	18.2 ± 2.6	0.7 ± 1.5	0.2 ± 0.2	0.0 ± 0.1	2.1 ± 1.8	36.4 ± 5.9
Alternative Nb-rich oxide	JW2-AC	38.4 ± 3.3	2.6 ± 2.1	8.7 ± 1.0	0.4 ± 0.3	0.1 ± 0.1	0.1 ± 0.1	5.0 ± 1.5	44.7 ± 5.3
	JW2-HT13	40.7 ± 3.0	1.5 ± 2.0	8.6 ± 0.6	0.2 ± 0.2	0.1 ± 0.2	0.1 ± 0.2	5.8 ± 1.7	43.1 ± 5.2
	JW2-HT15	49.2 ± 3.2	1.0 ± 1.2	10.6 ± 0.9	0.6 ± 0.4	0.0 ± 0.1	0.0 ± 0.1	1.4 ± 0.9	37.2 ± 5.4
Si-rich oxide	JW2-AC	2.3 ± 1.3	38.2 ± 4.1	4.1 ± 1.5	0.5 ± 0.7	0.2 ± 0.2	0.5 ± 0.5	0.1 ± 0.2	54.1 ± 8.4
	JW2-HT13	0.9 ± 0.5	40.6 ± 1.3	1.5 ± 1.0	0.1 ± 0.1	0.1 ± 0.1	0.6 ± 0.3	0.2 ± 0.4	56.1 ± 4.2
	JW2-HT15	1.3 ± 1.1	40.7 ± 2.6	2.7 ± 1.8	0.6 ± 0.5	0.2 ± 0.1	0.4 ± 0.5	0.1 ± 0.2	53.9 ± 7.8
Cr-rich oxide	JW2-AC	1.9 ± 1.7	2.2 ± 2.0	1.9 ± 1.6	39.1 ± 4.0	0.1 ± 0.1	0.3 ± 0.5	0.1 ± 0.4	54.3 ± 7.3
NbB particles	JW2-AC	35.6 ± 4.5	0.4 ± 0.4	4.6 ± 4.7	0.4 ± 0.3	0.3 ± 0.4	0.9 ± 0.6	54.0 ± 11.5	3.9 ± 1.6
	JW2-HT13	30.9 ± 2.3	8.2 ± 5.1	8.2 ± 5.6	0.2 ± 0.2	0.1 ± 0.1	1.8 ± 1.3	42.5 ± 16.0	8.1 ± 4.7
	JW2-HT15	40.4 ± 3.2	7.9 ± 1.6	0.6 ± 0.5	0.1 ± 0.1	0.1 ± 0.2	2.2 ± 1.4	42.7 ± 5.4	6.0 ± 3.3

6.3.2.4 JW3

6.3.2.4.1 XRD

The XRD pattern of JW3-AC is shown in Figure 6.60. The phases that are identified are TiO_2, SiO_2, $TiNb_2O_7$. The XRD pattern of JW3-HT13 is shown in Figure 6.61. The phases that are identified are TiO_2, SiO_2, $TiNb_2O_7$. The XRD pattern of JW3-HT15 is shown in Figure 6.62. The phases that are identified are TiO_2, $TiNb_2O_7$, SiO_2.

Compared to the 1000°C samples of JW3, the main differences are that $Ti_2Nb_{10}O_{29}$ is absent from the XRD pattern of JW3-AC, JW3-HT13 and JW3-HT15, and SiO_2 is found in JW3-AC and JW3-HT13 1200°C samples. The underlying potential niobium-germanium phase seen in the 1000°C JW3-AC and JW3-HT15 samples were not found in any of the 1200°C samples.

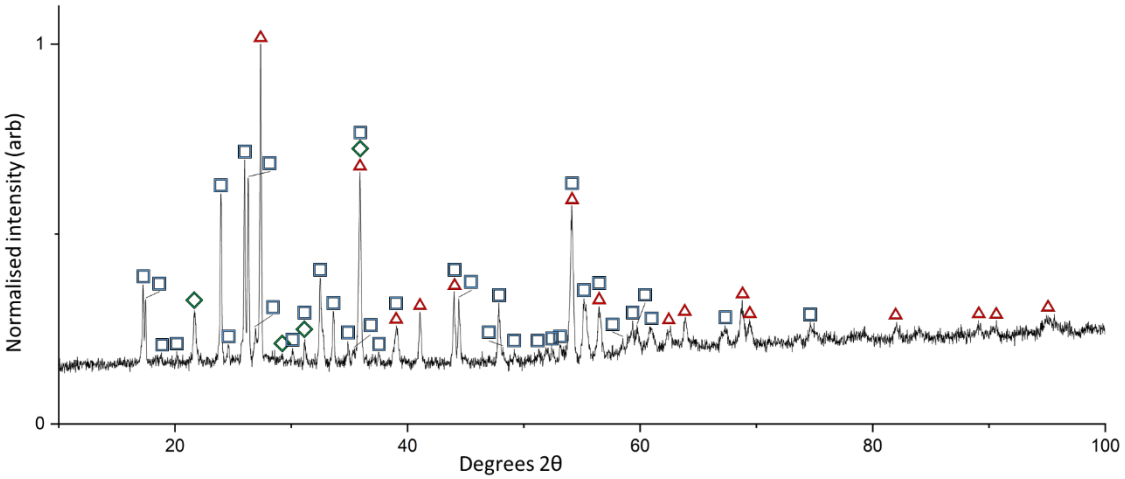

Figure 6.60) XRD pattern of oxidised at 1200°C JW3-AC. △ = TiO_2, □ =$TiNb_2O_7$ ◇ = SiO_2

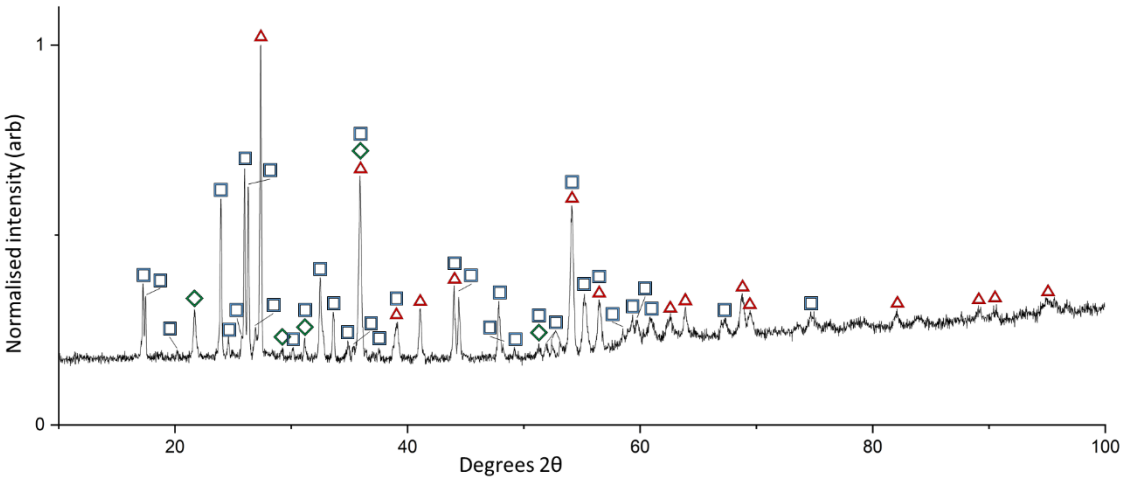

Figure 6.61) XRD pattern of oxidised at 1200°C JW3-HT13. △ = TiO_2, □ =$TiNb_2O_7$ ◇ = SiO_2

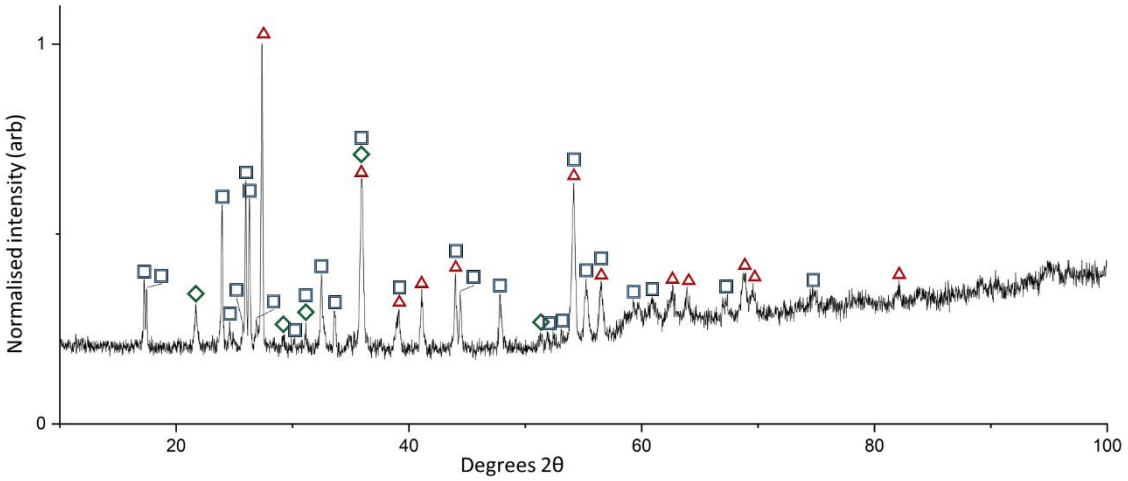

Figure 6.62) XRD pattern of oxidised at 1200°C JW3-HT15. △ *= TiO_2,* □ *=$TiNb_2O_7$* ◇ *= SiO_2*

6.3.2.4.2 EPMA

EPMA mapping of oxidised JW3 samples at 1200°C including elements Nb, Si, Ti, Cr, Al, Ge, B and O is presented in Figure 6.63, Figure 6.64 and Figure 6.65 for the as-cast state, heat-treated at 1300°C state, and heat-treated at 1500°C state, respectively. In the bulk of each oxidised sample, three phases were identified; $D8_8$, $NbCr_2$ and internal TiO_2. $D8_8$ and $NbCr_2$ are consistent with the unoxidised microstructures of each alloy; JW3-AC, JW3-HT13, JW3-HT15. T2 was identified in small and large particles in JW3-AC and JW3-HT15 respectively. T2 is not found in the unoxidised microstructure of JW3-AC so this is likely a result of the elevated temperature of the oxidation experiment causing the NbB -> T2 decay. NbB is found in the form of particles within the partially oxidised $D8_8$, as was seen in the case of JW2 oxidised at 1200°C alloys, and so is included in Table 6.31 relating to the oxide layers of JW3 alloys. In the particular location of JW3-HT13 examined, no high boron phase is found. No (Nb) was found in any alloy from these mapped locations, likely due to only existing in small quantities to begin with and then oxidation of this phase taking place. Whilst internal TiO_2 is found in all three alloys, it exists on the boundary of the bulk alloy and oxide layer in the case of the heat-treated alloys and in JW3-AC it extends from the bulk into the oxide scale. An Al-rich phase is present in each of the alloys, but only in JW3-AC is it coarse enough and in high enough quantity to measure. In the case of JW3-HT13 the same Al-rich phase is found within the oxide scale so this phase is reported in Table 6.29 as well. The Al-rich phase is a result of oxidation in each case, and is seen most clearly in the as-cast samples' bulk microstructure due to the higher volume fraction of the precursor phases in intergranular regions. The compositions of each of the phases in the oxidised samples are listed in Table 6.29.

Due to the thickness of the oxide scales in the particular locations chosen, limited area of the EPMA maps is devoted to the bulk material. As a result, it is difficult to comment on the full microstructure and how it has been effected by oxidation. $D8_8$ is the majority phase in each alloy, $NbCr_2$ exists as coarse grains in the heat-treated alloys and in more of a fine mixture with Ti-rich phase and Al-rich phase in the case of the as-cast alloy. The grain boundaries of $D8_8$ in the heat-treated alloys are rich in Ge and Low in Si content, suggesting Ge diffusion into the bulk of the sample from the high concentration of Ge in the Ge-rich layer at the oxide-bulk interface.

When considering the O contents of bulk phases in the microstructures of JW3 alloys, the silicide phases in each alloy, T2 and $D8_8$, and the $NbCr_2$ phase have similar O contents to each other and are within error of each other given that values of O content are reported as between 1.7 and 3.1 at.%

and standard errors are between 1.3 and 1.7 at.%. Most of the oxygen that has penetrated the oxide layer into the bulk of each sample exists in the internal TiO_2 and Al-rich phase. The Al-rich phase is assigned as a mixture of (Al) and Al_2O_3. Substitution of elements other than Al, Ti and O into these phases is low.

Area analysis was performed using this EPMA data in order to report average compositions of specific areas of the oxide scale, shown in Table 6.30. The layer of oxidised material of JW3-AC had an average composition of 16.8 at.% Nb, 12.7 at.% Si, 17.6 at.% Ti, 3.7 at.% Cr, 0.9 at.% Al, 3.4 at.% Ge, 1.2 at.% B, and 43.7 at.% O. The layer of oxidised material of JW3-HT13 had an average composition of 13.8 at.% Nb, 11.3 at.% Si, 13.0 at.% Ti, 2.1 at.% Cr, 5.4 at.% Al, 0.3 at.% Ge, 1.2 at.% B, and 52.9 at.% O. The layer of oxidised material of JW3-HT15 had an average composition of 14.4 at.% Nb, 16.0 at.% Si, 17.0 at.% Ti, 2.0 at.% Cr, 0.6 at.% Al, 1.3 at.% Ge, 1.1 at.% B, and 47.5 at.% O.

A layer that is rich in Ge can be seen between the oxide layer and the bulk alloy in each sample of JW3. It is unclear whether this layer is made up of a new phase or an existing phase has been enriched in Ge during the oxidation process. Area analysis of this layer was performed and considering the Ge content of these layers was at least 21.1 at.% in JW3-AC, which is greater than any $D8_8$ Ge composition found in the un-oxidised states of any JW series alloy despite this layer also containing a significant amount of O, it is suspected this is a distinct phase.

In the case of JW3-AC, the ratio of Nb + Ti to Ge + Si is 1.36, which is approaching the ratio expected of Nb_5Ge_3. The Nb + Ti to Ge + Si ratios of JW3-HT13 and JW3-HT15 are slightly closer to the Nb_5Ge_3 expected value, at 1.46 and 1.39, respectively. In each case the whole Ge-rich layer is likely Nb_5Ge_3.

Areas where Ge content is greater than the rest of the Ge-rich layer in EPMA maps for JW3-AC, JW3-HT13 and JW3-HT15 were examined. Points were taken from these high-Ge areas to calculate the compositions given in Table 6.31 for a Nb-Ge phase. Average Nb and Ge contents of this phase in JW3-AC were 47.2 at.% and 33.9 at.%. The ratio of Nb + Ti to Ge + Si is calculated as 1.50. Average Nb and Ge contents of this phase in JW3-HT13 were 38.3 at.% and 34.2 at.%. The ratio of Nb + Ti to Ge + Si is calculated as 1.33. Despite the higher Ge contents and lower Si contents, these ratios are similar to those calculated for the whole Ge-rich layers of JW3-AC and JW3-HT13, so it appears that these layers are a single phase of Nb_5Ge_3 with variable Si substitutions. In the case of JW3-HT15, there is a clear region of higher Ge content with the Ge-rich layer. Average Nb and Ge contents of this phase/region in JW3-HT15 were 27.4 at.% and 59.9 at.%. The ratio of Nb + Ti to Ge + Si is calculated as 0.44. This indicates the formation of $NbGe_2$ in the especially Ge-rich regions, with the rest of the layer likely Nb_5Ge_3.

Compositions of phases and regions within the oxide layer of each alloy are presented in Table 6.31. In each of the oxide scales four oxide phases are reported on and are designated based on their most notable element; Ti-rich oxide, Nb-rich oxide, an alternate Nb-rich oxide, and Si-rich oxide. As previously mentioned the internal TiO_2, usually identified in the bulk of the samples and that is exceptionally low in elements other than Ti and O, is also found in small amounts embedded in each of the oxide layers close to the bulk material. A Cr-rich oxide phase is present in JW3-AC and JW3-HT13, and a large region of coarse Al-rich phase usually seen in the bulk is present in the oxide layer of JW3-HT13. Additionally, small particles of a B-rich phase are found in the oxidised $D8_8$ of JW3-AC, which were previously assigned to NbB in the case of JW2 oxidised alloys.

In JW3-AC the Ti-rich oxide phase has titanium content of 26.9 at.% whilst Nb and Cr contents were 13.5 at.% and 10.1 at.%, respectively. As a result of having higher Ti content whilst containing significant amounts of Nb and Cr, this phase is considered to be rutile TiO_2 with substation of mainly

Nb and Cr onto Ti sites, (Ti,Nb,Cr)O_2. For alloys JW3-HT13 and JW3-HT15 the titanium contents of the Ti-rich phase were higher at 28.6 at.% and 34.7 at.%, and amounts of Nb and Cr still indicate a TiO_2 phase with Ti partially substituted for Cr and Nb.

The Nb-rich phase in JW3-AC had Nb content of 33.4 at.% and Ti content of 15.8 at.%, with the Nb/Ti ratio equal to 2.12. This ratio is close to the expected value of $TiNb_2O_7$ rather than $Ti_2Nb_{10}O_{29}$, so this phase is considered to be the $TiNb_2O_7$ oxide also identified through XRD. The alternate Nb-rich phase on the other hand has a Nb content of 37.1 at.% and a Ti content of 8.2 at.%, and therefore a Nb/Ti ratio of 4.54. This ratio is close to 5, and so can be considered $Ti_2Nb_{10}O_{29}$.

In JW3-HT13 the Nb-rich phase had Nb content of 31.0 at.% and Ti content of 14.5 at.%, with the Nb/Ti ratio equal to 2.14. This ratio is closer to the expected value of $TiNb_2O_7$ rather than $Ti_2Nb_{10}O_{29}$, so this phase is considered to be the $TiNb_2O_7$ oxide also identified through XRD. The alternate Nb-rich phase on the other hand has a Nb content of 34.8 at.% and a Ti content of 6.8 at.%, and therefore a Nb/Ti ratio of 5.08. This ratio is close to 5, and so can be considered $Ti_2Nb_{10}O_{29}$.

In JW3-HT15 the Nb-rich phase had Nb content of 29.6 at.% and Ti content of 15.4 at.%, with the Nb/Ti ratio equal to 1.92. This ratio is closer to the expected value of $TiNb_2O_7$ rather than $Ti_2Nb_{10}O_{29}$, so this phase is considered to be the $TiNb_2O_7$ oxide also identified through XRD. The alternate Nb-rich phase on the other hand has a Nb content of 41.4 at.% and a Ti content of 7.6 at.%, and therefore a Nb/Ti ratio of 5.44. This ratio is close to 5, and so can be considered $Ti_2Nb_{10}O_{29}$.

Si content in each Si-rich phase is 38.7 at.%, 33.5 at.% and 38.6 at.% for alloys JW3-AC, JW3-HT13 and JW3-HT15, respectively, whilst average Nb contents are only 0.6 at.%, 0.3 at.% and 1.0 at.%, respectively, and average Ti contents are only 1.5 at.%, 0.8 at.% and 2.0 at.%, respectively. This phase is identified as SiO_2, and according to XRD a cristobalite structure. The Si-rich phase is coarser in 1200°C samples compared to the 1000°C oxidised versions of JW3. As a result, the Nb and Ti contents, which are possibly a result of titanium-niobate oxide impurities or underlying phases, are lower in both the as-cast and heat-treated samples of JW3 oxidised at 1200°C. B and Ge contents in this SiO_2 phase are both very low, less than 1.0 at.% in all cases. A glassy layer containing Si, Ge and B is therefore not found in any case of JW3 and Ge and B substitution into this form of SiO_2 phase is extremely limited. Instead within the oxide layer, B is primarily found in titanium-niobate oxides and Ge is primarily found in the Ge-rich layer/Nb_5Ge_3. B is also found in the Ge-rich layers highest Ge points, but in the case of JW3-HT15 where this is believed to be $NbGe_2$ and not Nb_5Ge_3, B content is only 0.4 at.%.

The Cr-rich phase has Cr content of 39.7 at.% and 41.4 at.% for JW3-AC and JW3-HT13, respectively. Since Ti and Nb content in these phases is low, the majority elements of O and Cr suggest a Cr oxide. No Cr oxide phase was found in XRD, likely due to the small amounts of this phase in each oxide layer, but Cr_2O_3 is a possibility based on EPMA analysis of elemental contents. An Al-rich phase is found in the oxide scale of JW3-HT13 with major elements Al and O, but with an average weight percent of over 95 wt.%. Therefore, this phase cannot be considered Al_2O_3 as the ratio of elements does not agree with this and there is no missing wt% that could otherwise be assumed to be O. There is some uncertainty with this phase, as there is when it is found in other alloys, but it is assigned to a mixture of (Al) and Al_2O_3.

Small particles of a B and Nb phase are found in the partially oxidised $D8_8$ of JW3-AC. This speckling was seen in JW2 where this phase was assigned to NbB. In the case of JW3-AC there are elements present in concentrations that would be unexpected for this phase, such as 5.3 at.% Si and 5.6 at.% Ge. However given the high contents of Nb and B, 37.0 at.% and 42.9 at.% respectively, it seems

likely that the unexpected elements are a result of underlying phases because no other phase with such high B content is seen in any of the alloys in this study. A crucial difference that indicates this phase forms as a result of oxidation and is not from the original microstructure is the absence of Ti content, where in unoxidised samples where (Nb,Ti)B formed Ti content was at least 14.1 at.%.

The structure of the oxide layer of the as-cast sample consists of a fine mixture of SiO_2, $TiNb_2O_7$, $(Ti,Nb,Cr)O_2$, and $Ti_2Nb_{10}O_{29}$ where silicide grains previously existed in the unoxidised microstructure. Underneath this mixture is a coarser formation of $(Ti,Nb,Cr)O_2$ with small amounts of SiO_2 spread throughout. Cr_2O_3 exists at the edges of this $(Ti,Nb,Cr)O_2$ coarse layering. Then the Ge-rich layer is found below this, mixed with internal TiO_2. Below this Ge-rich layer is partially oxidised $D8_8$ with particles on NbB dispersed within.

JW3-HT13 has a similar fine mixture of SiO_2, $TiNb_2O_7$, $(Ti,Nb,Cr)O_2$, and $Ti_2Nb_{10}O_{29}$ on the outer surface followed by the Ge-rich layer and internal TiO_2. The coarse layering of $(Ti,Nb,Cr)O_2$ is less obvious in this location and sample. In the upper part of the scale it appears a pore in the oxide has been captured in this image, which has led to odd layering of low substitution TiO_2, then, moving into the sample, an Al-rich layer that is too fine to measure, and then a Cr_2O_3 layer. Underneath this odd layered area is a coarse region of Al-rich phase within the scale.

JW3-HT15 has a fine mixture of SiO_2, $TiNb_2O_7$, $(Ti,Nb,Cr)O_2$, and $Ti_2Nb_{10}O_{29}$ on the outer surface followed slightly coarser $(Ti,Nb,Cr)O_2$ as was the case with the as-cast sample. And then the Ge-rich layer and internal TiO_2 formation is seen, but in this case SiO_2 is found in large quantity in this location as well.

Generally, oxides are coarser in the 1200°C samples than the 1000°C samples, the high temperature titanium-niobate $TiNb_2O_7$ is found in 1200°C samples, and the silicide grains are oxidised to a greater degree and are less contiguous in the 1200°C samples.

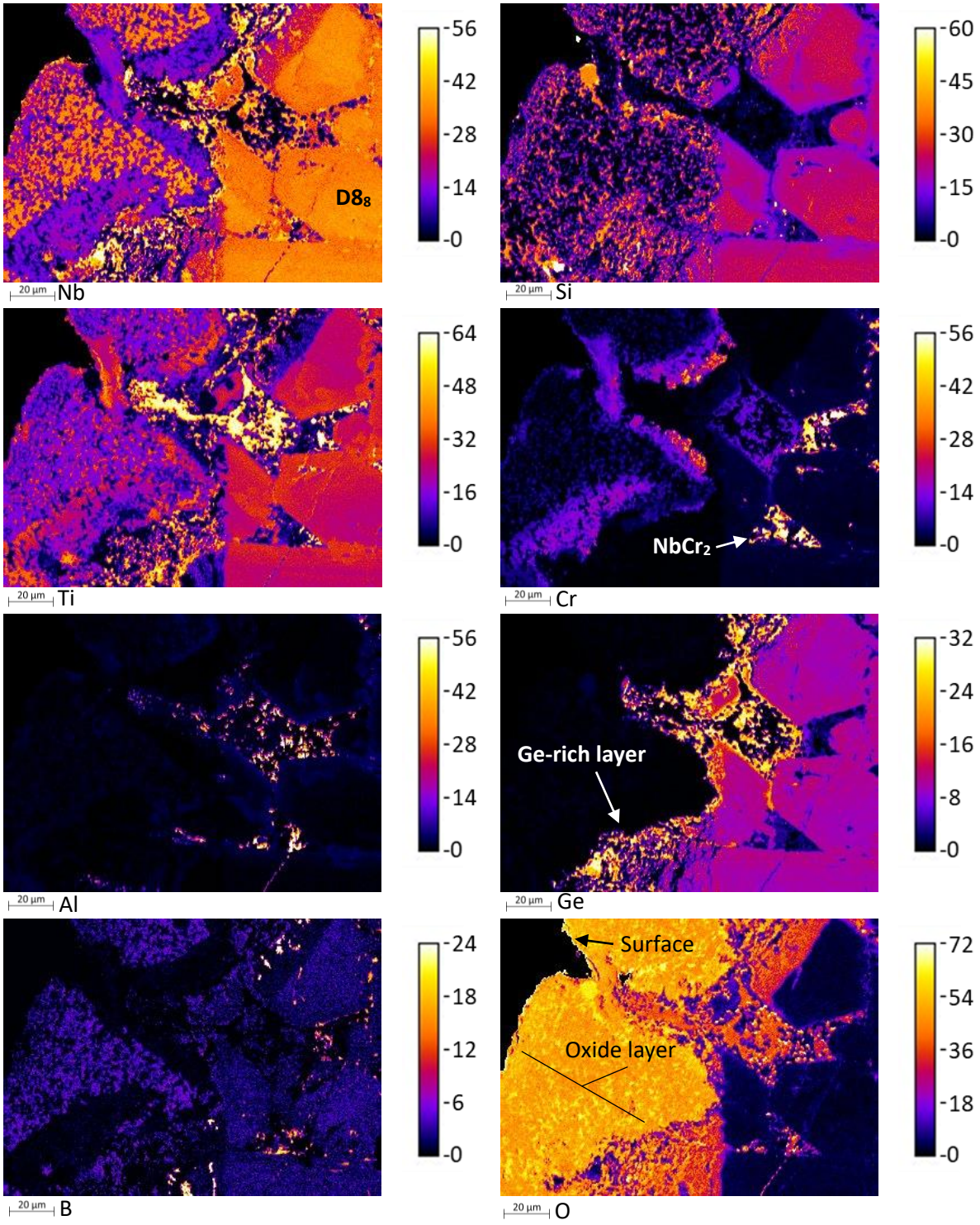

Figure 6.63a-h) EPMA maps of the oxide layer of JW3-AC in at.% of elements a) Nb, b) Si, c) Ti, d) Cr, e) Al, f) Ge, g) B h) O.

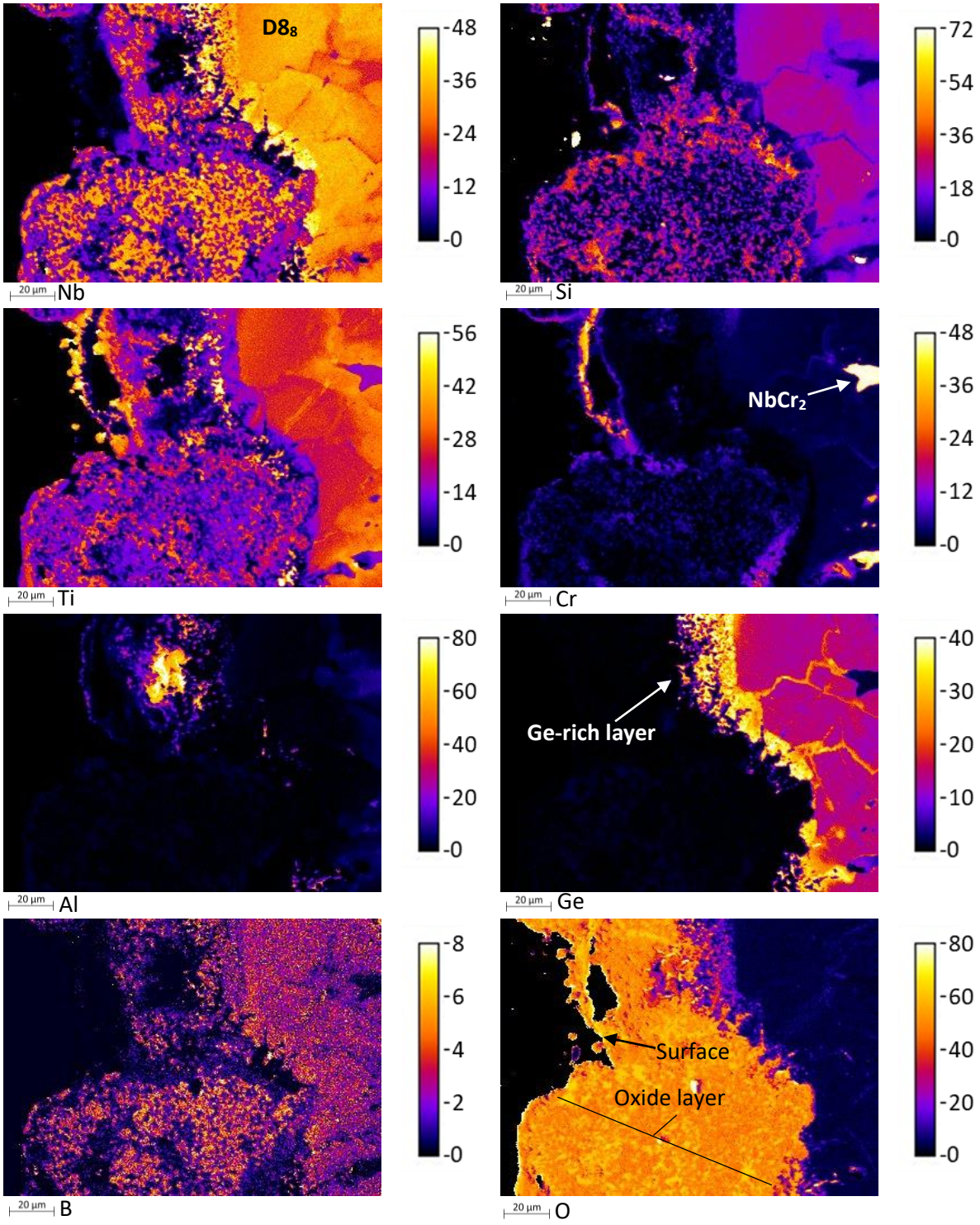

Figure 6.64a-h) EPMA maps of the oxide layer of JW3-HT13 in at.% of elements a) Nb, b) Si, c) Ti, d) Cr, e) Al, f) Ge, g) B h) O.

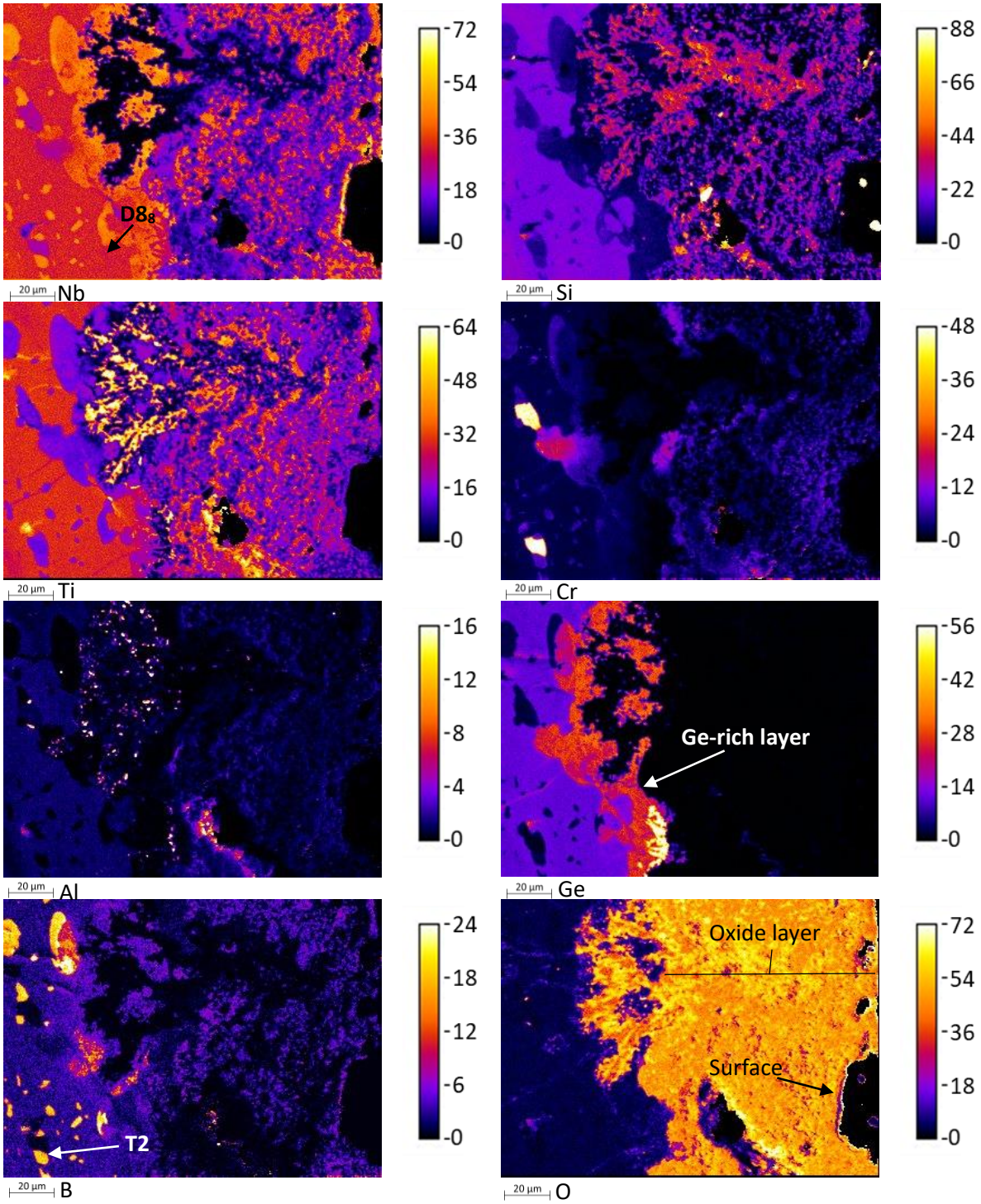

Figure 6.65a-h) EPMA maps of the oxide layer of JW3-HT15 in at.% of elements a) Nb, b) Si, c) Ti, d) Cr, e) Al, f) Ge, g) B h) O.

Table 6.29) Phase analysis of bulk phases present in each JW3 oxidised sample EPMA map, values given in at.%.

		Nb	Si	Ti	Cr	Al	Ge	B	O
$D8_8$	JW3-AC	33.7 ± 2.8	23.6 ± 2.8	26.0 ± 2.2	1.2 ± 1.2	0.5 ± 0.6	10.6 ± 1.1	2.2 ± 1.7	2.1 ± 1.4
	JW3-HT13	31.8 ± 2.5	22.0 ± 2.1	26.1 ± 1.7	1.7 ± 0.5	0.6 ± 0.4	12.4 ± 1.3	2.3 ± 1.3	3.0 ± 1.5
	JW3-HT15	30.8 ± 2.4	20.8 ± 2.1	28.6 ± 1.6	2.0 ± 0.7	1.1 ± 0.5	11.0 ± 1.1	2.6 ± 1.6	3.1 ± 1.5
T2	JW3-AC	42.6 ± 2.3	10.8 ± 1.9	11.7 ± 2.4	5.8 ± 1.4	0.2 ± 0.2	2.7 ± 0.6	24.4 ± 3.3	1.7 ± 1.3
	JW3-HT15	42.3 ± 2.8	10.9 ± 1.1	14.9 ± 1.4	6.9 ± 1.4	0.0 ± 0.1	2.4 ± 0.5	20.1 ± 2.4	2.4 ± 1.3
Ge-rich G.B.	JW3-HT13	20.5 ± 3.6	11.1 ± 2.8	29.1 ± 3.7	4.4 ± 1.5	0.5 ± 1.1	29.3 ± 2.4	0.5 ± 0.8	4.6 ± 2.7
Internal TiO_2	JW2-AC	0.2 ± 0.2	0.1 ± 0.1	63.2 ± 2.3	0.5 ± 0.2	0.9 ± 0.3	0.0 ± 0.1	0.0 ± 0.1	35.1 ± 4.4
	JW2-HT13	0.4 ± 0.5	1.4 ± 2.1	58.4 ± 2.7	0.1 ± 0.1	0.6 ± 0.4	0.2 ± 0.2	0.0 ± 0.0	38.9 ± 4.8
	JW2-HT15	0.2 ± 0.1	0.5 ± 0.7	62.6 ± 1.4	0.2 ± 0.2	0.5 ± 0.2	0.1 ± 0.1	0.0 ± 0.0	36.0 ± 3.2
$NbCr_2$	JW3-AC	27.8 ± 2.1	6.2 ± 2.3	4.5 ± 1.8	54.4 ± 4.0	0.1 ± 0.2	4.3 ± 2.1	0.3 ± 0.6	2.3 ± 1.7
	JW3-HT13	19.9 ± 1.8	4.2 ± 0.9	15.5 ± 1.5	48.7 ± 2.1	6.6 ± 1.9	2.4 ± 2.4	0.1 ± 0.3	2.4 ± 1.3
	JW3-HT15	22.3 ± 2.2	8.9 ± 1.2	13.0 ± 1.7	50.9 ± 2.1	1.1 ± 0.4	1.4 ± 0.6	0.3 ± 0.6	2.0 ± 1.3
Al-rich phase	JW3-AC	2.8 ± 2.7	1.0 ± 0.5	0.7 ± 0.4	0.5 ± 1.2	66.3 ± 2.5	0.3 ± 0.2	0.3 ± 0.9	28.1 ± 6.0
	JW3-HT13	0.1 ± 0.1	0.8 ± 0.8	0.3 ± 0.3	0.0 ± 0.0	60.2 ± 1.2	0.0 ± 0.0	0.0 ± 0.1	38.6 ± 5.6

Table 6.30) Area analysis of the entire oxide layers and Ge-rich layers shown in EPMA maps for JW3 oxidised samples, values given in at.%.

		Nb	Si	Ti	Cr	Al	Ge	B	O
Total oxide layer:	JW3-AC	16.8 ± 9.4	12.7 ± 14.3	17.6 ± 13.2	3.7 ± 5.6	0.9 ± 3.4	3.4 ± 6.2	1.2 ± 2.5	43.7 ± 17.7
	JW3-HT13	13.8 ± 8.2	11.3 ± 12.4	13.0 ± 8.3	2.1 ± 4.2	5.4 ± 21.0	0.3 ± 1.1	1.2 ± 1.4	52.9 ± 15.8
	JW3-HT15	14.4 ± 10.0	16.0 ± 15.7	17.0 ± 12.0	2.0 ± 2.5	0.6 ± 1.5	1.3 ± 4.6	1.1 ± 1.6	47.5 ± 19.0
Ge-rich layer	JW3-AC	32.9 ± 9.9	10.1 ± 12.4	9.5 ± 10.7	1.4 ± 2.5	1.7 ± 6.4	21.1 ± 6.7	2.0 ± 1.9	21.3 ± 20.0
	JW3-HT13	30.9 ± 6.6	6.5 ± 5.1	15.9 ± 7.8	1.7 ± 1.3	2.3 ± 6.4	25.6 ± 5.6	2.2 ± 1.6	14.9 ± 13.3
	JW3-HT15	35.2 ± 5.5	5.9 ± 2.9	15.0 ± 7.6	2.8 ± 3.7	0.5 ± 1.8	30.4 ± 10.1	4.5 ± 4.3	5.7 ± 5.5

Table 6.31) Phase analysis of oxide phases in each JW3 oxidised sample from locations in the oxide scale. , values given in at.%.

		Nb	Si	Ti	Cr	Al	Ge	B	O
Ge-rich phase	JW3-AC	47.2 ± 3.7	1.6 ± 1.4	6.1 ± 6.1	1.3 ± 2.1	0.3 ± 0.3	33.9 ± 1.2	3.6 ± 1.9	6.1 ± 3.7
	JW3-HT13	38.3 ± 1.8	3.3 ± 1.5	11.7 ± 1.8	1.4 ± 1.3	0.2 ± 0.4	34.2 ± 1.5	3.2 ± 1.4	7.5 ± 3.6
	JW3-HT15	27.4 ± 2.2	5.4 ± 0.7	1.6 ± 0.5	0.2 ± 0.2	0.2 ± 0.3	59.9 ± 2.4	0.4 ± 0.9	4.9 ± 2.3
Ti-rich oxide	JW3-AC	13.5 ± 2.1	0.9 ± 1.6	26.9 ± 4.6	10.1 ± 2.1	1.0 ± 0.5	0.1 ± 0.1	0.2 ± 0.5	47.3 ± 5.7
	JW3-HT13	11.4 ± 1.5	1.3 ± 2.1	28.6 ± 2.2	6.8 ± 2.1	1.0 ± 0.7	0.1 ± 0.1	0.7 ± 0.6	50.2 ± 3.0
	JW3-HT15	11.0 ± 1.6	0.6 ± 1.2	34.7 ± 2.7	4.9 ± 1.5	1.3 ± 0.4	0.1 ± 0.1	0.1 ± 0.2	47.4 ± 6.6
Nb-rich oxide	JW3-AC	33.4 ± 2.6	0.4 ± 0.9	15.8 ± 1.0	0.4 ± 0.3	0.3 ± 0.3	0.1 ± 0.1	4.3 ± 1.5	45.3 ± 5.3
	JW3-HT13	31.0 ± 3.4	1.3 ± 1.7	14.5 ± 1.4	0.4 ± 0.3	0.3 ± 0.2	0.1 ± 0.1	3.6 ± 1.6	48.9 ± 5.8
	JW3-HT15	29.6 ± 6.7	3.7 ± 6.1	15.4 ± 1.9	0.6 ± 0.6	0.4 ± 0.2	0.1 ± 0.3	2.6 ± 1.4	47.6 ± 7.4
Alternative Nb-rich oxide	JW3-AC	37.1 ± 3.0	3.0 ± 3.6	8.2 ± 1.0	0.2 ± 0.2	0.1 ± 0.1	0.0 ± 0.1	5.3 ± 1.6	46.0 ± 5.0
	JW3-HT13	34.8 ± 2.4	3.2 ± 2.2	6.8 ± 0.8	0.2 ± 0.2	0.2 ± 0.1	0.2 ± 0.3	3.8 ± 1.4	50.7 ± 5.3
	JW3-HT15	41.4 ± 2.3	0.8 ± 1.1	7.6 ± 0.7	0.3 ± 0.2	0.2 ± 0.1	0.1 ± 0.1	5.5 ± 1.4	44.1 ± 4.4
Si-rich oxide	JW3-AC	0.6 ± 0.3	38.7 ± 3.1	1.5 ± 1.8	0.1 ± 0.1	0.1 ± 0.1	0.5 ± 0.3	0.2 ± 0.3	58.3 ± 5.5
	JW3-HT13	0.3 ± 0.2	33.5 ± 2.4	0.8 ± 0.2	0.2 ± 0.3	0.1 ± 0.1	0.7 ± 0.3	0.3 ± 0.3	64.2 ± 3.2
	JW3-HT15	1.0 ± 0.7	38.6 ± 2.8	2.0 ± 1.0	0.2 ± 0.2	0.3 ± 0.4	0.0 ± 0.1	0.0 ± 0.1	57.8 ± 7.4
Cr-rich oxide	JW3-AC	1.9 ± 1.4	2.7 ± 2.1	1.6 ± 0.7	39.7 ± 2.6	0.1 ± 0.1	0.1 ± 0.1	0.0 ± 0.0	53.9 ± 5.1
	JW3-HT13	0.1 ± 0.2	0.3 ± 0.3	1.2 ± 0.2	41.4 ± 1.8	0.5 ± 0.4	0.1 ± 0.0	0.0 ± 0.0	56.5 ± 20.4
NbB particles	JW3-AC	37.0 ± 3.0	5.3 ± 1.7	0.7 ± 0.8	0.1 ± 0.1	0.1 ± 0.2	5.6 ± 1.1	42.9 ± 6.3	8.3 ± 4.0

6.3.3 Discussion

6.3.3.1 The effect of alloy composition on oxidation resistance

For oxidation at 1200°C, the general positive effect of B and Ge additions can be seen in Figure 6.39 where all experiments are plotted at this temperature. KZ5-AC and KZ5-HT have higher parabolic rates, higher linear rates and higher total mass gains when compared to any alloy in the JW series. In addition, the highest degree of linear behaviour is calculated for KZ5-AC, with an *n* value of 0.75. At this oxidation temperature, the heat-treatments seem to have less effect on the oxidation performance of the alloys compared to experiments performed at 1000°C. As a result, the composition can be considered more critically in regards to the impact B and Ge additions have on oxidation performance.

KZ5 has a total mass gain range of 15.37 to 16.18 mg.cm^{-2}, which is reduced by the addition 5 at.% B and 5 at.% Ge to a range of 10.06 to 10.77 mg.cm^{-2} in the case of JW1. The ranges of JW2 and JW3 then overlap with each other, at 8.38 to 9.20 mg.cm^{-2} and 8.03 to 9.10 mg.cm^{-2}, respectively. The additional 5 at.% B or 5 at.% Ge in JW2 and JW3 respectively has an overall positive effect on oxidation resistance at 1200°C when considering the stated total mass gain ranges, as well as the consistently lower linear rates of oxidation when compared to KZ5 and JW1 alloys. However, since the oxidation experiments produce similar TGA curves and oxidation parameters for JW2 and JW3 it is difficult to confirm which composition generally performs better. In the case of individual samples at different post-processing states, the best performing alloy over 100 hours was JW3-AC which displayed parabolic behaviour for the duration of the experiment. In the initial stages of oxidation JW2-HT13 and JW2-HT15 had lower total mass gain than JW3-AC up until it least 50 hours into the experiment. Therefore, B and Ge additions can be said to be equally as effective at reducing oxidation at 1200°C.

Several factors are identified to explain the effect of composition on oxidation resistance. Firstly, (Nb) volume fraction is generally reduced in higher B and Ge containing alloys. As this is considered the susceptible to oxidation phase, it follows that reducing the amount of (Nb) will lead to better oxidation performance. Although when the effects of processing conditions are discussed in the following section, it is clear that merely the elimination of this phase does not lead to superior oxidation performance. Another phase to consider is T2, which is found in JW1 and JW2 in the pre-oxidised states of each processing condition of the alloy. Additionally, since heat-treatment at 1300°C has been shown to develop T2, an assumption is made that in each B and Ge containing alloy some T2 will be present when oxidised at 1200°C. In the heat-treated at 1500°C versions of JW1 and JW2, the EPMA maps happen to include an area where T2 would have been in contact with the atmosphere during oxidation experiments. Where this occurs the Ge-rich layer is thinner and denser, and the T2 grain has less oxygen penetration than the adjacent $D8_8$, indicating T2 has inherently better oxidation resistance. This could be a reason as to why JW2 samples have consistently better oxidation resistance than JW1, as JW2 generally has a larger volume fraction of T2. This is not the case for the as-cast state of JW1 and JW2, with volume fractions of 4.29 ± 0.53 % and 0.66 ± 0.22 %, respectively. But it is plausible that T2 is developed in JW2-AC during the oxidation process. In fact, in the case of JW2-AC, the initial oxidation curve for approximately 50 hours is within the JW1 range of mass gain but then performs better over the final 50 hours after T2 potentially develops.

The SiO_2 phase identified in 1200°C oxidised samples is visually coarser, higher in Si content, and lower in Nb and Ti content than the equivalent phase identified in 1000°C oxidised samples. The purer composition is related to the coarseness of the SiO_2 regions, allowing measurements of a single phase to be obtained. This is a result of a greater degree of oxidation due to the higher temperature promoting SiO_2 formation and growth. SiO_2 is desirable in the oxide layer as it is

expected that O has a lower rate of diffusivity through this phase than titanium niobates [124] and can act as a protective phase. No complete layers of SiO_2 are formed despite the B and Ge additions into the JW series of alloys, as was the case with 1000°C oxidised samples. However, the SiO_2 phases in KZ5 oxidised at 1200°C were less developed than in the B and Ge containing alloys. The phase was visually finer and mixed with titanium niobates, and as a result the composition is reported as having higher levels of Nb and Ti; 6.7 at.% and 16.4 at.% Nb and 6.3 at.% and 9.7 at.% Ti in the as-cast sample and heat-treated sample, respectively. In the JW alloy series the highest Nb content in SiO_2 was 2.1 at.% and the highest Ti content was 3.4 at.%. Therefore, the B and Ge additions to KZ5 have promoted SiO_2 formation, likely a contributing factor to the improved oxidation resistances.

Although the NbB phase is thought to transition into T2 at elevated temperatures, NbB is believed to be forming in partially oxidised $D8_8$ during oxidation. This occurs in each processing state of JW2, but not in each case of JW1 or JW3, as this effect is likely linked to the boron content of the alloys. This NbB formation during oxidation does not occur at 1000°C. Where NbB is found in the bulk of specimens oxidised at 1000°C and 1200°C, it generally has one of the lowest oxygen contents compared to other bulk phases. NbB forming inside oxidising $D8_8$ as a result of a change in composition as Nb, Si, Ti, Cr and Al diffuse out of the phase could potentially provide a barrier to further oxidation in the same way as the Ge-rich layer is predicted to do. However, in these current alloys the NbB phase that forms due to oxidation is only found in discrete small particles and not a continuous layer, limiting the potential effectiveness. If these NbB particles were effective at reducing oxidisation of the samples then JW2 would have lower mass gains than both other alloys since this occurs to a greater degree in this alloy, but this is not the case.

In each alloy containing Ge, a Ge-rich layer forms on the bulk material and oxide scale interface. With alloys JW1 and JW2 the whole layer is difficult to assign to a distinct phase given the Nb, Ti, Si and Ge contents in each case of processing condition. In the case of JW3, Ge-rich layers were more likely to be Nb_5Ge_3 based on elemental ratios. Point analysis of the Ge-rich layers of each sample at high Ge content locations were found to be more likely Nb_5Ge_3 than other Nb-Ge phases, with elemental ratios of Nb,Ti:Ge,Si approaching 1.67. So for the most part this layer can be considered Nb_5Ge_3 if a single phase, or containing Nb_5Ge_3 if it is some mixture of partly oxidised silicide phases. For reference the Nb,Ti:Ge,Si ratio of $D8_8$ in unoxidised samples is between 1.90 and 2.28 and for $D8_8$ found in oxidised samples in the bulk material it is between 1.59 and 2.01. The differences pre and post oxidation, and the reason ratios above 1.67, are explained by Ti atoms residing in Si sites in some cases and an increased Si content found in $D8_8$ post oxidation. The maximum solubility of Ge in $D8_8$ is unknown in the ternary Nb-Si-Ge system as this is a metastable phase. However, the maximum Ge content found in $D8_8$ in this present study does not exceed 13 at.%. Point analysis of the Ge-rich layer had a minimum value of 29.3 at.% in 1200°C samples, hence why the higher Ge content of the Ge-rich layer is considered an indicator of a new phase that has formed due to oxidation. In each alloy no evidence of the $NbGe_2$ phase was found, as was the case in some samples oxidised at 1000°C, with the exception of JW3-HT15 where $NbGe_2$ is clearly identified based on elemental ratios. In 1000°C oxidation samples it is unclear whether $NbGe_2$ formation has a positive or negative effect on oxidation resistance, however the 1000°C oxidised version of JW3-HT15 had abnormal Ge-rich layer formation in the form of $NbGe_2$ particles instead of the complete layer. This was proposed to be a significant factor in the poor oxidation resistance of JW3-HT15 at 1000°C. Perhaps the $NbGe_2$ formation in JW3-HT15 that was oxidised at 1200°C is also a factor in the worse JW3 oxidation performance, although the difference between JW3 samples is to a much smaller degree as the Ge-rich layer has still formed in each case at 1200°C.

Also related to the Ge-rich layer is the internal TiO_2 that is believed to form from the (Ti) that exists as a result of oxygen diffusion into the (Nb) causing decomposition into (Ti) and a Nb-rich (Nb). The internal TiO_2 phase does not usually extend significant distance past the Ge-rich layer into the rest of the oxide layer. This indicates the formation of this oxide does occur internally due to O diffusion into the sample, rather than the regular growth of $(Ti,Nb,Cr)O_2$ which is found in the oxide scale.

Total average Ge contents of the entire Ge-rich layer is between 21.1 at.% and 30.4 at.% in JW3, 15.7 at.% and 19.0 at.% in JW1, and 11.9 at.% and 13.6 at.% in JW2. This shows the higher Ge content in JW3 encourages more Ge to concentrate at the oxide-bulk interface of the alloy, but also how B additions reduce the Ge enrichment of the oxide-bulk interface since in JW2 its generally poorer in Ge when compared to JW1. This trend is also seen to a lesser extend in samples oxidised at 1000°C. Visually the Ge-rich layer appears thicker in JW3 alloys. Also a phenomenon seen in each case of JW3 is the Ge-rich grain boundaries of $D8_8$. This implies that the high Ge concentration of the Ge-rich layer combined with outward diffusion of oxidising elements results in Ge not only being 'pushed back' from the oxide layer after not forming oxides but also driven into the bulk of the sample along grain boundaries acting as pathways for inwards diffusion. Since JW2 and JW3 have approximately the same oxidation performance at 1200°C, the increased Ge content of the Ge-rich layer may not be a relevant factor.

The Ge content of the $D8_8$ phase in post and pre-oxidation samples is generally similar for JW1 and JW2, at approximately 6 at.%, and almost double for JW3, at approximately 11 at.%. If an increased Ge content of the $D8_8$ was beneficial to oxidation resistance then JW3 would have lower mass gains than both other alloys, but this is not the case.

However, another consideration concerning higher Ge content of $D8_8$ in JW3, higher Ge content of the Ge-rich layer of JW3, and NbB formation in partially oxidised $D8_8$ in JW2 samples, is that these factors are generally beneficial to oxidation resistance, but to a comparable degree between JW2 and JW3. This results in generally better oxidation performance of JW2 and JW3 when compared to JW1 and KZ5, but is broadly equivalently when comparing alloys with compositions with higher B and higher Ge in JW2 and JW3, respectively. Therefore a conclusion can be drawn that additional B and Ge content greater than 5 at.% is equally effective at reducing oxidation resistance.

Little work is reported on the oxidation of NbB. Oxidation of NbB_2 is reported and can be used as a comparison. With oxidation of NbB_2, a niobium boron oxide forms, Nb_3BO_9, from B_2O_3 and Nb_2O_5 according to Equation (6). This reaction is also seen in Nb-Si-B systems containing (Nb) and T2 as a result of the boron present in T2 [205][206]. Nb_3BO_9 forms above 750°C in a study where a 85.8Nb-12.0Si-2.1B alloy is heated to 950°C as a result of the oxidation of $D8_8$ [207]. Therefore, there is a general consensus that Nb_3BO_9 forms in Nb and B (and Si) containing alloys at high temperature.

$$3Nb_2O_5 + B_2O_3 = 2Nb_3BO_9 \qquad (6)$$

The precursor phase, B_2O_3, forms when a boron containing phase is oxidised as one might expect [206][207]. B_2O_3 volatility in an air atmosphere can lead to mass loss in $NbB_2/NbSi_2$ coated Nb–Si–B alloys, and is notable at approximately 500°C to 1000°C in mass gain versus temperature graphs [206]. There exists the possibility B_2O_3 formed and volatilised in the JW alloy series as no amorphous borosilicate layer was found in the scales and B content in SiO_2 was low.

In a study investigating the initial stages (<30 minutes) of oxidation at 1100°C of Nb–Si–B ternary alloys, two alloys are of note; a T2 (Nb–25Si–12.5B) alloy and a T2 + (Nb) alloy (Nb–14Si–6B) [208]. In the T2 alloy, Nb_2O_5 was the only phase identified after 1 and 10 minutes oxidation in the oxide layer through XRD. In the T2 + (Nb) alloy, Nb_2O_5 and Nb_3BO_9 were identified at 1 and 10 minutes, despite

lower overall boron content in this alloy composition. In TGA experiments, the T2 alloy underwent mass loss after the first minute, i.e. B_2O_3 evaporation, and no B was found through EPMA analysis in the oxide layer. Whereas T2 + (Nb) alloy underwent mass gain as usual for niobium silicide-based alloys, and trace amounts of B were identified in the oxide layer. As a result of the (Nb) present in T2 + (Nb) alloy, Nb_2O_5 was formed in sufficient quantities, and rapidly enough, to retain boron in the form of Nb_3BO_9. After 30 minutes, the T2 alloy was found to contain Nb_2O_5 and Nb_3BO_9 in the oxide layer, indicating over time T2 oxidised and sufficient Nb_2O_5 is present for the reaction in Equation (6) to occur.

This is relevant to the current study as titanium is present in each alloy, which also reacts with Nb_2O_5 to form $Ti_2Nb_{10}O_{29}$ and $TiNb_2O_7$ according to Equation (4) and (5) [148] (repeated from Section 2.4.2). I.e. if B_2O_3 volatility is to be avoided through Nb_3BO_9 formation, B_2O_3 is in competition with TiO_2 for Nb_2O_5. From the XRD and EPMA results of each alloy assessed in this current work, Nb_2O_5 was absent from the oxide scales after 100 hours, i.e. it had been fully consumed through Equation (5). TiO_2 however was in abundance, meaning the mechanism for boron retention in the oxide scale was not able to occur as Nb_3BO_9 was also not found.

$$3TiO_2 + Ti_2Nb_{10}O_{29} = 5TiNb_2O_7 \quad (4)$$

$$5Nb_2O_5 + 2TiO_2 = Ti_2Nb_{10}O_{29} \quad (5)$$

However, it appears even with lack of Nb_3BO_9 formation, B is not available to react with SiO_2 or GeO_2 to form a glassy layer. Boron is found up to 7.3 at.% in oxides high in titanium and niobium identified as titanium niobates, $Ti_2Nb_{10}O_{29}$ and $TiNb_2O_7$, which suggest B is tied up in these phases. Therefore explanations may be that a) B_2O_3 does not interfere with reactions in Equation (4) and (5), and b) B_2O_3 either reacts with TiO_2 or Nb_2O_5 at some stage between Equations (4) and (5) to form some unknown $XB_2O_3.YTiO_2.ZNb_2O_5$, or c) B is able to enter the titanium niobate structures interstitially or as a substitute. Since $Ti_2Nb_{10}O_{29}$ and $TiNb_2O_7$ are identified through XRD in most 1200°C alloys and $Ti_2Nb_{10}O_{29}$ in most 1000°C, the latter explanation is applicable. In the Mo-Si-B system where successful formation of a borosilicate layer occurs after high temperature oxidation, MoO_3 is volatile and so Mo + B mixed oxides cannot form. In summary, lack of glassy layer formation may be related to a combination of volatilisation of B_2O_3 and substitution of B into titanium niobate oxide phases.

6.3.3.2 The effects of processing on oxidation resistance

The effect of heat treatment on these alloys has had mixed results. For alloys KZ5, JW1 and JW2, heat-treated samples at 1500°C have lower total mass gains than heat-treated samples at 1300°C, which in turn have lower total mass gains than samples in the as-cast state. The opposite is true for JW3 samples.

In the case of KZ5, the initial parabolic oxidation rate of KZ5-HT15 is greater than in the as-cast sample, and then the linear rate is lower for the remainder of the experiment. This is true for 1000°C experiments and 1200°C experiments alike. However, in the 1200°C experiment the difference in linear rates of oxidation is sufficient to allow the as-cast sample to overtake the heat-treated sample in terms of total mass gain. The KZ5-HT15 alloy also showed an *n* value closer to parabolic behaviour, 0.60, compared to the KZ5-AC, 0.75. This was the case at 1000°C also. In the initial stages of oxidation KZ5-AC performs better than KZ5-HT, but due to more parabolic oxidation kinetics KZ5-HT15 performs better in later stages of the experiment.

In the case of JW1, the initial portion of the oxidation graph of JW1-AC and JW1-HT15 begin similarly, but the heat-treated sample is more parabolic in nature and therefore performs slightly better over a longer period of time. The heat-treated at 1300°C has an initially lower parabolic rate of oxidation compared to the other JW1 samples, but then once linear oxidation behaviour becomes dominant at approximately 20 hours the higher rate of oxidation results in a total mass gain between that of JW1-AC and JW1-HT15. In the 1000°C experiments JW1 followed the opposite trend of increasing total mass gains, and was ordered AC, HT13, HT15. However, the best performing alloy at 1000°C, JW1-AC, and at 1200°C, JW1-HT15, were both modelled as completely parabolic based on *n* exponent values being close to 0.5. For the JW2 alloy, the heat-treated sample at 1500°C has lower total mass gains than heat-treated sample at 1300°C, which in turn has lower total mass gains than samples in the as-cast state. This trend was seen in 1000°C experiments as well, although generally differences were larger at this oxidation temperature. The initial parabolic rates of JW2-HT13 and JW2-HT15 were the lowest calculated at 1200°C, and the as-cast version was completely parabolic in nature according to the modelling method used.

In the case of JW3, the heat-treatments had a negative effect on oxidation resistance of this alloy. Total mass gain, initial parabolic rate and linear rate of oxidation were highest for the heat-treated at 1500°C sample and lowest for the as-cast sample. In the case of experiments at 1000°C, the heat-treated at 1500°C sample also performed the worse out of JW3 alloys. The as-cast sample oxidised at 1200°C was modelled as completely parabolic, and had the best overall oxidation performance of any alloy oxidised at 1200°C with the lowest total mass gain and lowest linear rate of oxidation. Conversely, the as-cast version of KZ5 performed the worst with the highest mass gain and highest linear rate of oxidation, 16.18 $mg.cm^{-2}$ and 3.96E-08 $mg.cm^{-2}.s^{-1}$, respectively.

The total mass gain of each oxidation experiment at 1200°C is plotted against the content of Si, Nb and Ti in $D8_8$ and βNb_5Si_3 in Figure 6.66, Figure 6.67 and Figure 6.68. A trend of increased total mass gain with decreasing Ti content and increasing Si and Nb content can be seen for B and Ge containing alloys and KZ5. With few data points it is not guaranteed that the content of these majority phases are a major factor regarding oxidation resistance. However, this figure is included as one potential reason heat-treatments have affected oxidation resistance. The same trend is presented in Figure 6.69 and Figure 6.70 for Nb and Ti content of the (Nb) phase, although this is less applicable given the drastically reduced volume fraction of (Nb) in high B+Ge content alloys.

The reasons for the effects of heat-treatments will now be considered. Initially the heat-treated version of KZ5 had a higher parabolic rate of oxidation than the as-cast version. This can be

attributed to the lack of eutectic silicide in KZ5-HT15 and coarsening of the microstructure [124][136][197], and potentially a lower Si content in the (Nb) phase, allowing oxygen penetration into the bulk of the alloy. Si content of (Nb) in KZ5-AC was 2.0 at.%, and in KZ5-HT15 it was 0.8 at.%. The superior performance after the initial parabolic behaviour is proposed to be linked to the major microstructural and phase difference between the two alloys; the development of αNb_5Si_3, as there are otherwise limited differences between the two processing states of KZ5. In the unoxidised version of αNb_5Si_3, Si content is greater than the retained βNb_5Si_3 (33.1 at.% vs 29.9 at.%). The reverse is true for the oxidised version of αNb_5Si_3 and βNb_5Si_3, perhaps suggesting that the Si content in αNb_5Si_3 is more available during oxidation to form beneficial oxides, e.g. SiO_2. Generally, there is more oxygen present in the oxide scale of KZ5-AC, whether that be the whole oxide layer from area analysis or individual oxide phases with higher O contents.

During heat-treatments of JW1 alloys, T2 volume fraction is increased from 4.3% in JW1-AC to 5.7 % in JW1-HT13 and to 6.4% in JW1-HT15. Where T2 is found on the surface of the samples, it is shown to have less O content than surrounding $D8_8$, implying superior oxidation resistance. Having a greater amount of this phase is proposed to improve the oxidation resistance of the heat-treated alloys. (Nb) volume fraction is reduced upon heat-treatment at 1500°C as well, so the best performing version of JW1 has less volume fraction of the susceptible to oxygen phase present. Additionally, the correlation between Nb, Ti, Si content of $D8_8$ and total mass gain is most clearly seen in JW1. The higher Ti content of $D8_8$ in JW1-HT15 pre-oxidation correlates well with a reduced overall total mass gain. Lastly, in the Ge map of JW1-AC, the Ge-rich layer appears incomplete. The interpretation of this is perhaps limited given the lack of repeat maps, but in the as-cast alloy this gap in Nb_5Ge_3 formation may be indicative of less prevalent Ge-rich layer formation, leading to less of a barrier to further oxidation. These factors combined are proposed to explain the improvement of oxidation performance upon heat-treatments of JW1. However, the difference of oxidation parameters and the oxidation curves shown in Figure 6.36 are relatively minor for this alloy. The removal of the eutectic $D8_8$ through heat-treatment was considered a significant factor in the 1000°C experiments to explain the better performance of the as-cast JW1 alloy. However, this is apparently less relevant at the higher temperature, possibly because at 1200°C the coarsening of eutectic $D8_8$ begins to take place in the as-cast sample, nullifying its benefit.

The main difference between JW2 samples at different processing states is the development of T2 in place of NbB in the heat-treated alloys. The T2 phase is thought to be beneficial for oxidation resistance as stated when considering JW1 samples. The reduction in solid solution volume from 8.12 to 5.4 to 0.5 % from JW2-AC, JW2-HT13 to JW2-HT15 is also likely a factor in the improved oxidation resistance of heat-treated samples. These factors are consistent with the oxidation results of the 1000°C experiments. In addition, a ‘gap’ in the Ge-rich layer is also seen in JW2-AC, the worst performing JW2 alloy, as was also noted in JW1-AC, which is circumstantial evidence of a less protective oxide layer interface. Overall the increase in T2 volume fraction and reduction in (Nb) volume fraction seem adequate factors to explain the improved oxidation resistance of heat-treated JW2 samples.

JW3 is the only alloy oxidised at 1200°C where heat-treated versions perform worse than the as-cast version. A number of factors that are given for other alloys are not applicable to JW3. This includes NbB decomposition into T2, as there is a low initial volume fraction of NbB in JW3-AC. Also a reduced amount of (Nb) after heat-treatment is likely less of a factor, as (Nb) volume fraction is effectively zero in JW3-HT15 and yet this alloy does not have the best oxidation resistance compared to other JW3 alloy processing states. In fact, the complete lack of (Nb) in heat-treated JW3 alloys might lead to a brittle alloy, which is susceptible to micro-cracking during oxidation. Anecdotally, the

JW3 alloys, especially the heat-treated versions were the most difficult to handle during sample preparation as cracking due to being held in a vice was common. Although no spallation of the oxide occurred in any of the oxidised JW3 samples. Lastly, a potential factor in the slight difference of JW3 oxidation results at different processing states is that the NbB formation within $D8_8$ due to oxidation was only observed in the best performing JW3 alloy; JW3-AC, and not in the heat-treated versions.

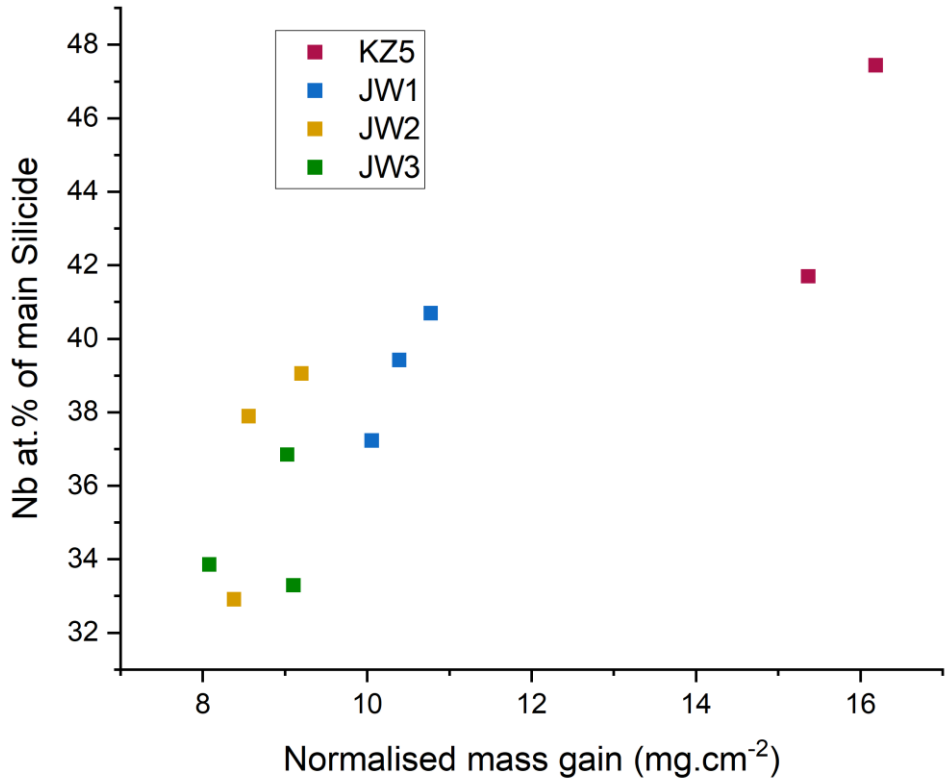

Figure 6.66) A graph to show correlation between Nb content of the main silicide phase and mass gain.

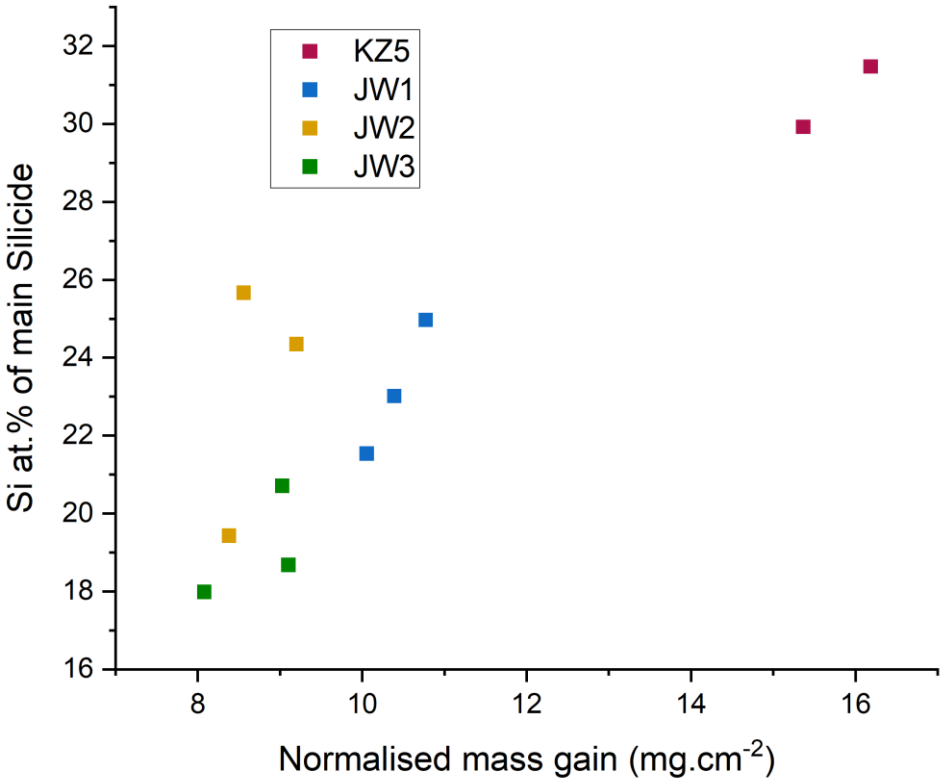

Figure 6.67) A graph to show correlation between Si content of the main silicide phase and mass gain.

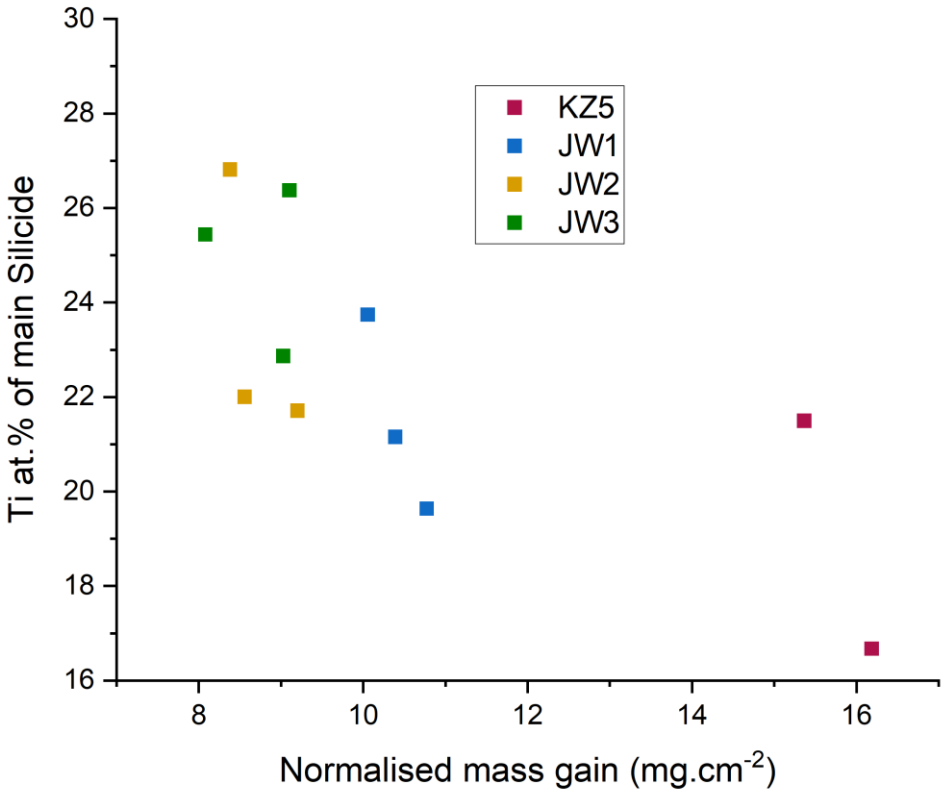

Figure 6.68) A graph to show correlation between Ti content of the main silicide phase and mass gain.

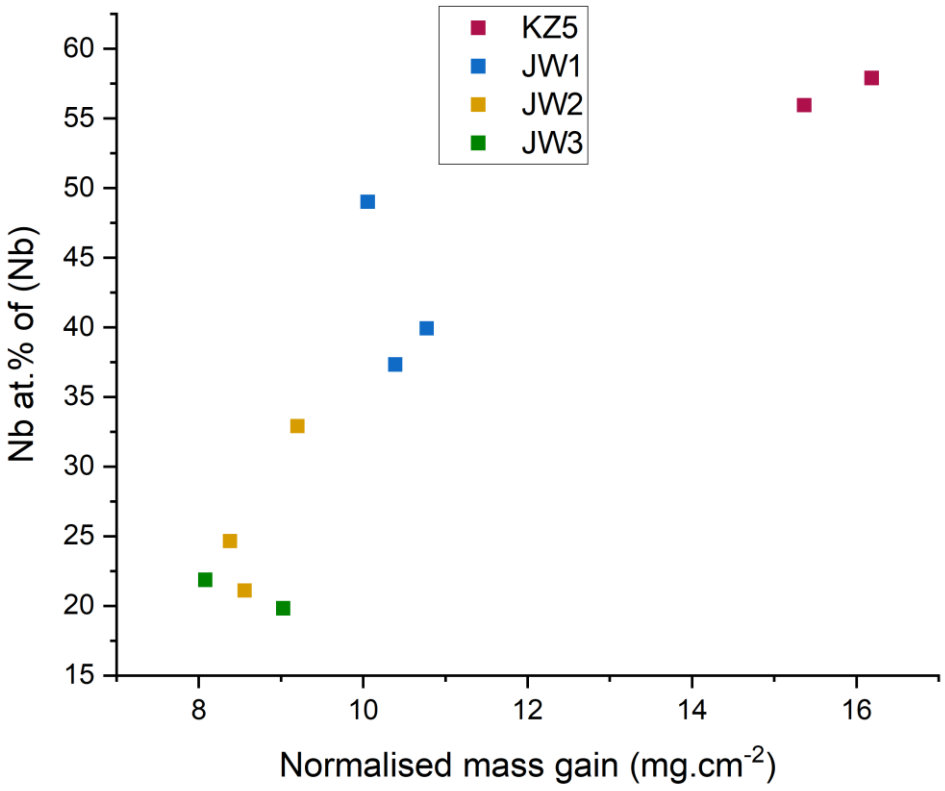

Figure 6.69) A graph to show correlation between Nb content of the (Nb) phase and mass gain.

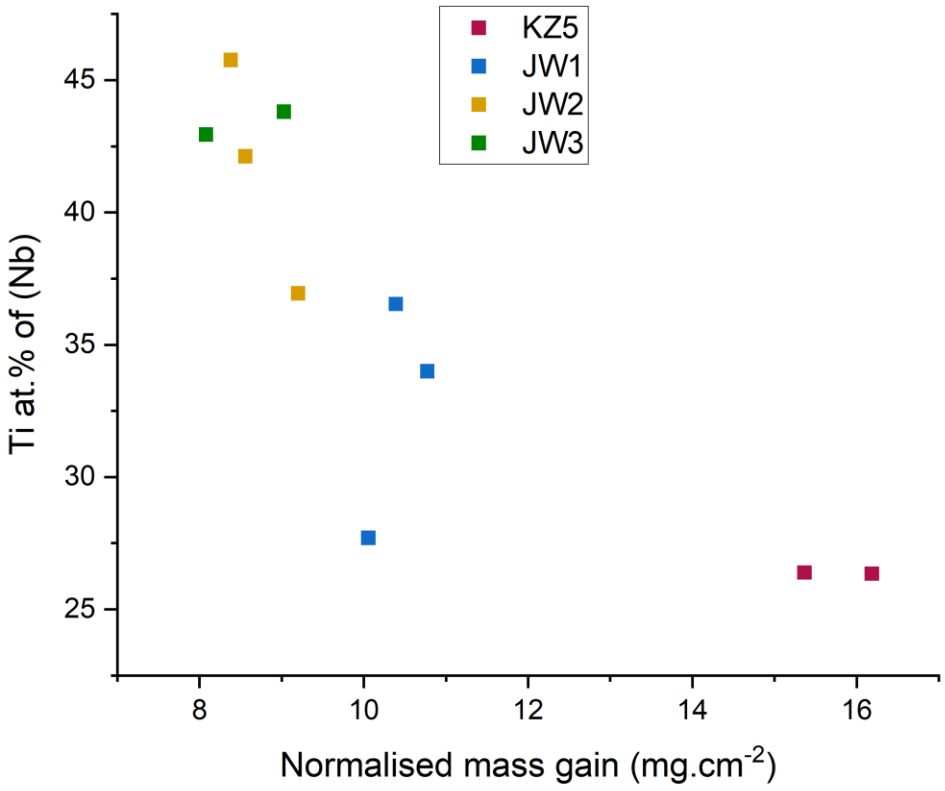

Figure 6.70) A graph to show correlation between Ti content of the (Nb) phase and mass gain.

6.3.4 Conclusion

- Initial addition of 5 at.% B and Ge to the base alloy results in significant reduction in total mass gain and improved oxidation kinetics. The SiO_2 phase was more developed in B and Ge containing alloys, indication these additions promote its growth.
- Alloys high in B and Ge, JW2 and JW3, respectively, offer further improvement to oxidation resistance. Both alloying additions are comparably effective from an oxidation resistance perspective.
- A Ge-rich layer was present in all Ge containing alloys after oxidation, located on the oxide-alloy interface. $Nb_5(Si,Ge)_3$ is suspected to partly make up this layer, but unlike samples oxidised at 1000^{o}C $NbGe_2$ was usually absent.
- The addition of 10 at.% B is proposed to be of benefit due to an increased volume fraction of T2, which has less diffusivity of oxygen than $D8_8$. The NbB phase is not of benefit to oxidation when in the bulk of the alloy, although formation of NbB just below the oxide-alloy interface was observed and is not fully understood.
- The addition of 10 at.% Ge is proposed to of benefit due to the increased Ge content of the $D8_8$ phase and enhanced Ge-rich layer formation.
- Generally, heat-treatment leads to improvement in oxidation resistance over longer periods of oxidation. JW3 is an exception to this, and it is proposed that the low volume of (Nb) leads to internal cracking exposing new surfaces to oxidise, as was potentially the case with JW3-HT15 when oxidised at 1000^{o}C.
- However, spallation of the scale does not occur in any B and Ge containing sample. Spallation of the faces and edges of KZ5 cubes does occur at 1200^{o}C

6.4 Oxidation at 800°C

TGA experiments were also performed at 800°C in order to assess whether the alloys experienced pest oxidation. The final normalised mass gains after 100 hours for alloys KZ5-AC, JW1-AC, JW2-AC, and JW3-AC were: 2.01 $mg.cm^{-2}$, 1.03 $mg.cm^{-2}$, 1.64 $mg.cm^{-2}$, 0.59 $mg.cm^{-2}$. Given these relatively small mass gains, as well as slightly smaller sample sizes compared to the 1000°C and 1200°C experiments, statistical noise caused by external airflows and daily cycles of the laboratory made assessment of the parabolic or linear nature of oxidation of the alloys at this temperature difficult. As a result, rates of oxidation could not be calculated, however the final mass gains reported by the internal balance of the Netzsch STA 449 F1 Jupiter were checked using an external balance post-experiment and the results were in agreement.

In general, pesting can be said not to have occurred as the reported mass gains are less than the corresponding as-cast results at 1000°C. This is in agreement with previous reports of KZ5-AC, which also did not pest at 800°C [152]. Additionally, visual inspection confirms the samples remained intact and did not degrade into a powder. The KZ5-AC alloy did not experience spallation at this temperature, as was the case for the 1000°C experiments. Zelenitsas [152] attributed the lack of pesting at 800°C to the presence of Cr and Al, which have higher affinity to oxygen compared to Si, so SiO_2 formation at grain boundaries is supressed compared to Al/Cr free alloys. B and Ge additions have not degraded intermediate-temperature oxidation performance in these alloys.

Chapter 7

7 Conclusions and suggestions for future work

7.1 Conclusions

7.1.1 Introduction

The research conducted in this thesis describes valuable new data on the microstructures, phase equilibria and oxidation resistance of three novel niobium silicide-based alloys, along with a base alloy for the purposes of comparison. Alloys were selected to assess the effect of boron and germanium additions together on microstructure, phase stability and resistance to oxidation, which has not been reported previously in detail. The amounts of boron and germanium were varied to further the understanding of phase equilibria regarding these elements in a complex niobium silicide-based alloy and search for a combination that results in the formation of a boria-germania-silica glassy layer to enhance oxidation resistance and achieve self-healing properties upon oxidation. This was not achieved for any boron and germanium containing alloy in this study, however insight was gained as to the factors resulting in the lack of such glassy layers. The non-volatility of Nb_2O_5 as a main factor in the lack of glassy layer formation is expanded upon with the proposed additional factor of boron having solubility in the titanium niobates that form during oxidation. Additionally, the germanium content in the oxide layer preferentially forms Nb-Ge intermetallic phases on the oxide-bulk interface rather than forming GeO_2 or interacting with SiO_2, limiting the intended effect of aiding SiO_2 glassy layer formation. Knowledge of these factors can be used to aid in alloy design when future work seeks to utilise boron and germanium additions to enhance oxidation resistance and possibly form the desired boria-germania-silica glassy layer. Alongside oxidation resistance and microstructure related aims, the investigation set out to assess the effect of heat-treatments on the four alloys and recommend direction for future alloy design research based on achieving a balance of mechanical properties and oxidation resistance.

7.1.2 KZ5 (Nb-18Si-24Ti-5Cr-5Al)

KZ5 (Nb-18Si-24Ti-5Cr-5Al): An alloy with previously studied microstructure was fabricated to facilitate direct comparison between boron and germanium containing alloys. The alloy consisted of βNb_5Si_3 and (Nb) in the as-cast and heat-treated state (1500°C), and additional αNb_5Si_3 was developed through heat-treatment. The equilibrium phases are suspected to be αNb_5Si_3 and (Nb), but longer heat-treatment would be required to eliminate βNb_5Si_3.

Oxidation experiments in the tested environment yielded mass gains of 7.29 $mg.cm^{-2}$ and 7.92 $mg.cm^{-2}$ at 1000°C and 16.18 $mg.cm^{-2}$ and 15.37 $mg.cm^{-2}$ at 1200°C for as-cast and heat-treated states, respectively. At both temperatures the linear rate of oxidation was reduced and the oxidation behaviour became more parabolic in nature after the heat-treatment and development of αNb_5Si_3. The initial oxidation of KZ5-HT is associated with a coarser microstructure and lower Si content in (Nb), and hence less resistance to initial oxygen diffusion. Whereas the reduced oxidation rates in the later stages of oxidation are assigned to the development of αNb_5Si_3 where Si is proposed to be more readily available to participate in oxidation reactions.

7.1.3 JW1 (Nb-18Si-24Ti-5Cr-5Al-5Ge-5B)

JW1 (Nb-18Si-24Ti-5Cr-5Al-5Ge-5B): A novel alloy with both boron and germanium additions was fabricated to assess their combined effect. The addition of 5 at.% B and 5 at.% Ge on the alloy KZ5 completely destabilised βNb_5Si_3 and enhanced the oxidation resistance at both 1000°C and 1200°C. The alloy consisted of $D8_8$, T2, (Nb), and $NbCr_2$ in the as-cast and heat-treated states (1300°C and 1500°C). Since these four phases persist through heat-treatments they are assumed to the equilibrium phases. T2 can be considered the same phase as αNb_5Si_3 in KZ5-HT15, which in the case of JW1 forms in lower volume fraction as a result of the B and Ge additions, but does form from the

initial melt in the as-cast sample where αNb_5Si_3 in KZ5-AC did not. $D8_8$ and $NbCr_2$ were stabilised by B and Ge additions. $D8_8$ is stabilised by the B addition primarily, as when considering similar alloys TT4 (Nb-24Ti-18Si-5Cr-5Al-8B) and ZF6 (Nb–24Ti–18Si–5Cr–5Al-5Ge) $D8_8$ is and is not present, respectively.

Oxidation experiments in the tested environment yielded mass gains between 2.37 $mg.cm^{-2}$ and 3.07 $mg.cm^{-2}$ at 1000°C and between 10.06 $mg.cm^{-2}$ and 10.77 $mg.cm^{-2}$ at 1200°C. The addition of B and Ge in this alloy has reduced mass gain by at least 58% at 1000°C and 30% at 1200°C. One sample at each temperature displayed oxidation behaviour that was able to be modelled as completely parabolic with *n* values of 0.47 and 0.54. The enhancement in oxidation resistance compared to KZ5 is attributed to the reduction in the susceptible phase (Nb), the development of silicides with superior oxidation resistance $D8_8$ and T2, and the formation of a Ge-rich layer upon oxidation. This Ge-rich layer is seen in all JW series alloys.

At 1000°C oxidation experiments, heat treatments resulted in marginally worse oxidation performance, whereas at 1200°C a higher degree of post processing results in marginal improvement. At 1000°C this was proposed to be a result of a more developed Ge-rich layer in the as-cast and heat-treated at 1300°C samples where $NbGe_2$ is formed, and the loss of the eutectic $D8_8$ in the heat-treated at 1500°C sample resulting in a coarser microstructure with less resistance to grain boundary diffusion of oxygen. At 1200°C this was attributed to the superior oxidation resistance of T2 compared to $D8_8$ at high temperature, as more T2 is present after heat-treatments, and the volume fraction of (Nb) is also reduced upon heat-treatment. Additionally, a broad correlation between lower Nb and Si and higher Ti content of the main silicide phase with lower total mass gain is noted. JW1 samples follow this trend well.

7.1.4 JW2 (Nb-18Si-24Ti-5Cr-5Al-5Ge-10B)

JW2 (Nb-18Si-24Ti-5Cr-5Al-5Ge-10B): A novel alloy with high boron content was fabricated to assess the effect of boron whilst in the presence of germanium. The alloy consisted of $D8_8$, (Nb), and $NbCr_2$ in the as-cast and heat-treated states (1300°C and 1500°C). In the as-cast state NbB was formed, and was partially converted to T2 after 1300°C heat-treatment and fully converted after 1500°C heat-treatment. The equilibrium phases were $D8_8$, $NbCr_2$, and T2, and likely not (Nb) as this was reduced to almost 0% volume fraction after heat-treatment at 1500°C for 100 hours. Generally, B additions have only a minor effect on the reduction of solid solution (Nb) volume fraction, so the near elimination of (Nb) is a results of the synergy of B with Ge to destabilised (Nb).

At 1000°C oxidation experiments, the boron and germanium additions have enhanced the oxidation resistance of the alloy compared to KZ5. The heat-treated JW2 alloys have superior oxidation resistance compared to JW1 alloys. However the as-cast version of JW2 has poor oxidation resistance compared to the JW1 alloys, as the 10 at.% boron content has been detrimental to oxidation resistance. At 1200°C the additional boron has certainly enhanced oxidation resistance compared to both KZ5 and JW1.

Oxidation experiments in the tested environment yielded mass gains between 1.66 $mg.cm^{-2}$ and 4.89 $mg.cm^{-2}$ at 1000°C and between 8.38 $mg.cm^{-2}$ and 9.20 $mg.cm^{-2}$ at 1200°C. The B and Ge additions to this alloy have reduced mass gain by at least 40% compared to KZ5 and 9% compared to JW1 at 1200°C, and if the poor oxidation resistance as-cast JW2 alloy is excluded, these additions have reduced mass gain by at least 69% and 6% at 1000°C. Two samples at 1000°C (JW2-HT13, JW2-HT15) and one sample at 1200°C (JW2-AC) displayed parabolic behaviour with *n* values of 0.51, 0.45, and 0.50, respectively.

The enhancement in oxidation resistance compared to KZ5 is attributed to the same factors as listed for JW1 having improved oxidation resistance over KZ5, i.e. a reduced (Nb) volume fraction, development of $D8_8$/T2 and Ge-rich layer formation. Oxidation rates are further reduced when comparing JW2 to JW1 as (Nb) volume fraction is lower in JW2, and in heat-treated JW2 alloys T2 volume fraction is further increased. The formation of metastable NbB is proposed to be detrimental to oxidation resistance as B is beneficial to oxidation resistance when in other phases and is 'locked away' in NbB in the as-cast state of JW2. At 1200°C particles of NbB form in partially oxidised $D8_8$ at the oxide-bulk interface which, since NbB in the bulk has low O solubility, are thought to be somewhat beneficial for oxidation resistance. These newly reported on NbB particles are found in as-cast JW3 as well.

In both 1000°C and 1200°C oxidation experiments JW2 samples heat-treated at 1500°C performed better than samples heat-treated at 1300°C which performed better than samples in the as-cast state. The increase in T2 volume fraction and reduction in (Nb) volume fraction are responsible for this. Spallation of the scale did not occur in any of the JW2 sample cubes at 1000°C or 1200°C. Oxides produced at 1000°C according to XRD were TiO_2, $Ti_2Nb_{10}O_{29}$ and $TiNb_2O_7$, as well as SiO_2 in the heat-treated alloys, and at 1200°C were TiO_2, $TiNb_2O_7$, and SiO_2 (with $Ti_2Nb_{10}O_{29}$ present in JW2-HT15). Generally, $Ti_2Nb_{10}O_{29}$ is detected less in 1200°C samples as expected, and ratios with $TiNb_2O_7$ can be confirmed more easily given the more developed and coarser oxide layer microstructure.

Macrosegregation was observed in the case of JW1, including 8.8 at.% *MACSi*. The additional boron has reduced macrosegregation of all elements including silicon to 4.9 at.% *MACSi*. This is true with the exception of boron itself which is concentrated in the centre of the alloy ingot owing to the formation of NbB here and less so at the top and bottom regions of the ingot. This is contrary to the expected trends based on alloy composition and respective parameters, and warrants further investigation of the effect of boron specifically.

7.1.5 JW3 (Nb-18Si-24Ti-5Cr-5Al-10Ge-5B)

JW3 (Nb-18Si-24Ti-5Cr-5Al-10Ge-5B): A novel alloy with high germanium content was fabricated to assess the effect of germanium whilst in the presence of boron. The alloy consisted of $D8_8$ and $NbCr_2$ in the as-cast and heat-treated states (1300°C and 1500°C). NbB was present in small amounts in the as-cast alloy and was removed after heat-treatment at 1300°C and 1500°C where T2 was developed, and (Nb) was removed only after heat-treatment at 1500°C. The equilibrium phases were $D8_8$, $NbCr_2$, and T2. The additional Ge content in synergy with the 5 at.% B present has resulted in the elimination of the (Nb) and shift towards a microstructure mostly composed of $D8_8$ (~90% volume fraction). This has resulted in a microstructure that is expected to be brittle, especially in the case of JW3-HT15. At 1000°C the boron and germanium additions have enhanced the oxidation resistance of the alloy compared to KZ5 and marginally improved upon JW1 by a small amount when the heat-treated at 1500°C sample is excluded from consideration. At 1200°C the additional germanium has certainly enhanced oxidation resistance compared to both KZ5 and JW1.

Oxidation experiments in the tested environment yielded mass gains between 2.27 $mg.cm^{-2}$ and 7.22 $mg.cm^{-2}$ at 1000°C and between 8.08 $mg.cm^{-2}$ and 9.10 $mg.cm^{-2}$ at 1200°C. The B and Ge additions to this alloy have reduced mass gain at 1200°C by at least 41% compared to KZ5 and 10% compared to JW1, and if the poor oxidation resistance heat-treated at 1500°C JW3 alloy is excluded, these additions have reduced mass gain by at least 69% and 4% at 1000°C. One sample at 1200°C (JW3-AC) displayed parabolic behaviour with an *n* value of 0.52.

The enhancement in oxidation resistance compared to KZ5 is attributed to the same factors as listed for JW1 and JW2 having improved oxidation resistance over KZ5, i.e. a reduced (Nb) volume fraction,

development of $D8_8$/T2 and Ge-rich layer formation. The oxidation performance of JW3 is similar to that of JW2, when considering the best performing processing condition of the alloys at 1000°C and 1200°C, despite differences in microstructure at each state (as-cast and heat-treated). Generally, in JW3 alloys the Ge-rich layer has higher concentration of Ge, is thicker and more obvious at 1200°C, and the $D8_8$ that is responsible for formation of said layer is approximately twice as rich in Ge compared to other alloy compositions. This is thought to be broadly equivalent to the increased T2 volume in the case of JW2 in terms of improvement in oxidation resistance compared to JW1.

The Ge-rich layer is found in each Ge containing alloy. The mechanism for its formation is proposed to be inwards diffusion of Ge as more reactive species, e.g. Nb and Ti, diffuse outwardly to participate in oxidation reactions. Ge is absent for the most part from the high Si areas of the oxide scale despite have significant concentration in the precursor $D8_8$ phase. This newly observed phenomena indicates it does not participate in said oxidation reactions and does not form oxides, and therefore concentration increases at the oxide-bulk interface to the point of phase formation of Nb_5Ge_3 and $NbGe_2$, which compared to (Nb) acts as a protective layer to further oxidation.

At both 1000°C and 1200°C heat-treatments have reduced the oxidation resistance of JW3 alloys. Whilst NbB is present in as-cast JW3 and T2 is developed thorough heat-treatments which in the case of JW2 was suspected to be a factor in improving oxidation resistance, the volume fractions concerned in JW3 are considerably smaller. Instead the reduction in (Nb) volume fraction and subsequent embrittlement of the microstructure, as well as the general coarsening of the microstructure as a result of heat treatments, is the attributed cause of this reduction in oxidation performance. Although it should be noted that at especially 1200°C alloy composition was the main factor in changes of oxidation rates and total mass gains.

7.1.6 Limitations

There are certain limitations with the methodologies and analysis covered in this work which will be addressed in this subsection. In regards to thermogravimetric experiments, two factors affect the repeatability of the results. Firstly, each alloy at each processing condition at each temperature was assessed once. Whilst this is in accordance with what is seen in the majority of the literature based on these types of alloys, it does open up the possibility of outliers being treated as reliable data. To cover a large quantity of samples for significant time periods of 100 hours, this was necessary, but future work in regards to one specific system, such as the promising JW1 alloy, could take repeated readings of TGA experiments to ensure more reliable rate values. Secondly, the airflow rate likely has a significant impact on the rate of oxidation, as a higher flow rate results in more oxygen at the surface of the sample. This was set at 20 ml/min for each experiment as there was concern the equipment could be damaged if significant high-temperature oxidation or pesting occurred. Therefore, the results are internally consistent, but may not be comparable to other experiments in the literature where airflow rates or not given, or where samples were oxidised in a furnace. In addition, the results are presented for isothermal oxidation. Application in engines will see cycling from low to high temperature throughout the lifetime of components, so how successful these alloys would be under those conditions is not known. This will be considered in the future work section.

The EPMA mapping of the oxide layer and underlying microstructure produced useful maps to identity features, such as the Ge-rich layer, and oxides that formed. However, this data was semi-quantitative due to the necessity to carbon coat the epoxy samples which lowered the received signal from mainly O that was present in bulk phases and especially the oxide phases. This was mitigated by using the ratio of elements other than oxygen to identify which oxides formed. This is

not ideal given the complex multicomponent mixed oxides that can form in this system, such as the titanium niobates and their variants. To improve the accuracy of this experimental technique future work could utilise hot mounting in conductive Bakelite, as was used for the non-oxidised samples, if elemental phase data is prioritised over structural information of the oxide layers.

The EPMA maps were also only taken of one small area, so comments on features such as the Ge-rich layer, and in some cases how it was not as fully formed as others, which was proposed to be the reason for inferior oxidation performance, may not be seen across the whole surface of the sample. For features such as these where light elements and oxygen are not of as much a concern, multiple repeat maps, perhaps utilising more rapid EDS, would be of use to definitively describe the layering behaviour and structure of the oxide layers. The decision was made that since the primary concern of this research was a borosilicate layer, that single, high-detail maps would be taken of each sample to search for this feature in particular. Compositional data in general would be improved by more phase specific standards for EPMA. For example, pure NbB and $\alpha/\beta Nb_5Si_3$ phases. This would allow more confidence to be placed in the results. However, obtaining these standards is challenging, not least because pure high temperature phases in the Nb-Si system are difficult to isolate through the manufacturing techniques available, such as arc-melting.

Further considering the manufacturing technique used in this work; non-consumable electrode arc-melting, inhomogeneity of the relatively small ingots of material was noted in SEM figures from the top, middle and bottom regions of the samples. The possibility of extra-ordinary regions of microstructure being present in TGA samples could not be completely ruled out without extensive SEM examination of each TGA sample before oxidation testing. A notable example of this in the post-oxidised samples was the apparent lack of αNb_5Si_3 in KZ5-HT15 oxidised at 1000°C, which through knowledge obtained through the other techniques utilised should have been present.

The modelling used as justification for proposed phase transitions, such as O additions resulting in the development of hexagonal (Ti) from Ti containing BCC (Nb), are limited by the lack of more complex database sets. A seven component system that would be capable of accurately modelling JW1 for example does not exist, and as such approximations must be made. In the above phase transition example Al and Cr were included from the relevant database to attempt to more closely match the (Nb) phase present in the alloys, but small additions of Si existing on interstitial sites could not be made, for example.

7.1.7 Summary

Generally, the boron and germanium additions to the base alloy KZ5 (Nb-18Si-24Ti-5Cr-5Al) improved the oxidation resistance, with either increased boron or germanium providing further improvement. The reasons proposed for this include the development of beneficial oxide resistant phases, formation of a Ge-rich layer at the oxide/bulk interface, and lowered diffusion of oxygen through the susceptible phases. These improvements to oxidation resistance and resultant lower mass gains were observed at 800°C, 1000°C and 1200°C. For the main two temperatures tested in this research, 1000°C and 1200°C, a larger percentage reduction compared to KZ5 in total normalised mass gain was generally found at the lower temperature of 1000°C. Therefore, the B and Ge additions in JW1, JW2, and JW3 can be said to be less effective at higher temperature.

The development of the T2 phase through heat-treatment is proposed to be beneficial for oxidation resistance, as is the removal of the NbB phase. The general coarsening of the microstructure upon heat-treatments is proposed to increase oxidation rates of these alloys. Reduction in (Nb) volume fraction expectably improves oxidation resistance up to a point, which is caused by both heat-treatments and elemental additions of B and Ge in synergy.

Four main oxides were identified across all the samples; TiO_2, $Ti_2Nb_{10}O_{29}$, $TiNb_2O_7$, and SiO_2. Generally, $Ti_2Nb_{10}O_{29}$ is detected less in 1200°C samples as expected, and ratios with $TiNb_2O_7$ can be confirmed more easily given the more developed and coarser oxide layer microstructure created at this temperature. There is evidence to suggest that the B and Ge additions to this alloy system promote the formation of $TiNb_2O_7$ at lower temperature given how this oxide was not found at 1000°C in the case of XRD results of the B and Ge free alloy, KZ5. In addition, in some 1200°C samples $Ti_2Nb_{10}O_{29}$ is not found in the oxide scale through XRD, perhaps as the transition to $TiNb_2O_7$ is more complete in JW1, JW2 and JW3. Spallation of the oxide scale occurred at the edges of the sample cubes of KZ5 at both 1000°C and 1200°C. Spallation of the oxide scale was eliminated by B and Ge additions to the base alloy KZ5, which is promising for future cyclic oxidation testing. Scale spallation was not simply a function of reduced oxidation as JW3-HT15 and JW2-AC had comparable oxidation parameters at 1000°C to KZ5 alloys, and spallation did not occur. Therefore, the boron and germanium additions in each case of JW1, JW2 and JW3 alloys has improved scale adhesion.

Macrosegregation was observed in the case of JW1, including 8.8 at.% *MACSi*. The additional boron present in JW2 has reduced macrosegregation of all elements including silicon to 4.9 at.% *MACSi*. This is true with the exception of boron itself which is concentrated in the centre of the alloy ingot owing to the formation of NbB here and less so at the top and bottom regions of the ingot. This is contrary to the expected trends based on alloy composition and respective parameters, and warrants further investigation of the effect of boron specifically. Macrosegregation was observed in the case of JW3. The additional germanium has increased macrosegregation of all elements including silicon to 9.7 at.% *MACSi*. This is true with the exception of titanium (*MACTi*) which is reduced. This is in agreement with the expected trends based on alloy composition and respective parameters, T_m, H_m/T_m, T_m^{sp} and T_m^{sd}/T_m^{sp} .

A summation of alloys with similar compositions to KZ5 is created by Tsakiropoulos [9] for oxidation experiments at 1200°C. These are KZ5+X, where X includes Mo, Mo+B, Mo+Hf+Sn, Mo+Ge+Sn, Hf, Hf+B, Hf+Ge, Ge, 2Sn/5Sn and Sn+B [136][209][210][211][127][212][213], as well as MASC alloy [214]. Comparing the JW series, or KZ5+Ge+B, to these alloys shows significant reductions in total mass gain after 100 hours. The only alloy that is comparable is KZ5+Hf+B with a mass gain of 11 $mg.cm^{-2}$. Each other alloy listed above has at least double the total mass gains of the JW alloys presented in this current work. Therefore, the goal of improving oxidation resistance in general by additions of Ge and B has been achieved. Ge additions can be said to be more beneficial than Mo and Sn when B is present, and B additions can be said to be more beneficial than Mo+Sn and Hf when Ge is present. Of course there is the possibility of non-similar methodologies in regards to the atmospheres these tests were conducted at. For the majority of these values the corresponding flow rate of air is not given. In the cases where it is given, i.e. KZ5+Ge+Sn, KZ5+Sn and MASC, flow rates of 20 – 25 ml/min were used. In which case the tests are broadly equivalent, and the direct comparison leading to the conclusions that B and Ge additions to KZ5 can be said to be successful at reducing the amount of oxidation taking place are supported.

It is difficult to compare the oxidation resistance of niobium silicide-based alloys at this stage in their development to nickel-based super alloys, as isothermal oxidation data in the literature is less common than the more extensive cyclic oxidation tests, with and without a coating system applied. In addition, the interest in niobium silicide-based alloys is due to the potential to be used at higher temperature than nickel-based superalloys, so the higher temperature of 1200°C is usually outside the scope of what is achievable for nickel-based superalloys. Considering the lower temperature covered in this research, 1000°C, the JW series had total mass gains after 100 hours of 1.66 to 4.89 $mg.cm^{-2}$ excluding the poor performing JW3-HT15. The well-known nickel-based superalloy, RR1000,

is reported to have mass gains between 0.2 and 0.3 mg.cm^{-2} at 800°C [215][216][217] and ~1.0 mg.cm^{-2} at 900°C [215] after 100 hours for isothermal experiments. Results at 1000°C are limited. Given the higher temperature applied to the JW series, the JW series could be said to be on par with RR1000, or at the least not significantly worse. This is confirmed by the mass gains reported for JW alloys at 800°C in this study, which were between 0.59 and 1.64 mg.cm^{-2}.

At 1200°C, the JW series had total mass gains after 100 hours of 8.08 to 10.77 mg.cm^{-2}. Super alloys in the CMSX series demonstrate mass changes of between 1 to 5 mg.cm^{-2} after 100 hours, however this is in fact mass loss from complete scale spallation which was not included in the mass measurements [218]. This study, where CMSX-2, CMSX-3, CMSX-4, CMSX-6 and SRR 99 are investigated over extended time scales, highlights the limitations with direct isothermal comparisons between systems. Although in the case of the JW series, it should be noted that no spallation takes place at this elevated temperature.

Generally, the isothermal oxidation tests performed on Mo-Si-B alloys result in an initial large mass loss followed by a greatly reduced rate of mass gain, explained by initial MoO_3 volatilisation and then formation of borosilicate glassy layer [161][158][154][6]. Comparison can still be made between the microstructures of niobium silicide-based and Mo-Si-B oxide scales. In Mo-Si-B SEM-BSE imaged cross sections, dense, continuous and homogenous borosilicate layers are clearly visible [158][159][161]. The scales produced in this current research lack these qualities in every instance where mapping was performed.

The reasons for failure of a borosilicate layer to form in the Nb-Si system have been expanded upon with regards to the boron and germanium additions. Adding to the understood concept of non-volatile, rapidly forming Nb_2O_5 preventing a continuous silica layer from forming is the location of the boron within the oxide scale. It is primarily found within the titanium niobate phases, and is believed to be in interstitial sites, rather than in the SiO_2 phase so it of less benefit to silica formation. Germanium on the other hand is rarely found in the oxide layer, and undergoes inward diffusion upon oxidation leading to the formation of niobium-germanium phases such as $NbGe_2$ and Nb_5Ge_3. Whilst this is proposed to be beneficial for reducing oxidation, it is not conducive to silica layer formation. Further work is required in order to generate a borosilicate glassy layer in these alloys.

7.2 Suggestions for future work

To complement the work described in this thesis, mechanical testing of hardness, fracture toughness and creep resistance of the JW series of alloy compositions should be performed. These properties are expected to be negatively affected by the alloying additions in comparison to alloys similar to KZ5, but the degree to which should be assessed. This is especially relevant to JW1 (Nb-24Ti-18Si-5Cr-5Al-5Ge-5B) where the microstructure is a desirable silicide + eutectic ((Nb) + silicide) structure. Samples for these mechanical tests would require larger ingots to be produced. Therefore, macrosegregation will need to be more crucially considered because test pieces, and as a result the relevant distances, would need to be an order of magnitude greater than the sections taken for oxidation testing in this current work. Casting of the liquid alloy post-arc melting may need to be incorporated into the production process, although the feasibility of this is unknown in the case of these alloys. The nano-hardness of the silicide phases would be of interest to compare to the αNb_5Si_3 and βNb_5Si_3 phases found in B and Ge free alloys and how the values are related to creep resistance.

The oxidation testing conducted in this research is limited in respect to how applicable it is to an in-service environment. Cyclic oxidation testing would be more applicable, and is the next step in alloy

development for these prospective alloys. Given most samples experienced linear oxidation kinetics in the later stages of isothermal testing, there is concern as to whether these alloys would be able to survive prolonged, cyclical oxidation testing for larger than 100-hour time scales. Close attention should be paid to the samples and their heat-treatment conditions that exhibited solely parabolic oxidation kinetics in order to assess the best case feasibility for the boron and germanium containing alloys under cyclic oxidation.

In addition, the oxidation testing was performed under an air atmosphere. This is representative of the in-service environment. However elemental nitrogen was not assessed in the EPMA mapping of the oxidised samples. In the future, this would especially be of interest regarding the Ti-rich phases that were assigned to (Ti), as a possibility of some Ti_xN_y phases forming could not be ruled out given the lack of nitrogen mapping.

In no alloy did a borosilicate layer form. To expand upon this current work, the constraints on the borosilicate layer formation should be considered. Titanium niobate oxides contained the majority of the boron in the oxide scales, and are therefore likely partly responsible for the lack of glassy layer formation. Suppression of these phases could be investigated by the removal of Ti from the composition to resemble an alloy such as Nb-18Si-5Cr-5Al-5Ge-5B. If glassy layer formation occurs, then Ti could be reintroduced at minimal content and increased in additional manufactured alloys until borosilicate layer formation no longer occurs. This would be the critical concentration of Ti, which could then be assessed in terms of a balance between mechanical properties and oxidation resistance.

Interestingly, this work highlighted that it may be possible to form a T2/(Nb) system with changes in the composition. $D8_8$ is not an ideal phase to form and the tetragonal, isomorphous with αNb_5Si_3, T2 phase would be the preferred main phase given the conclusion that it possesses inherently superior oxidation resistance as well as expectedly better mechanical properties. To achieve this whilst maintaining the boron content and Ge-rich layer formation mechanism, it is proposed that a reduction in Si content in a similar way to that proposed for Ti composition would result in a desirable T2 + (Nb) dominated microstructure. An example alloy of this research would be Nb-10Si-24Ti-5Cr-5Al-5Ge-5B. According to the Nb-Si-B phase diagram the T2 phase is located more towards the Nb rich corner where a (Nb)+T2 region exists.

To take this a step further, simplified systems could be studied to provide a baseline understanding to certain phenomena observed in this research. Originally Cr and Al were included to a) allow direct comparison to the microstructure of an existing base alloy KZ5, and b) to be a realistically complex system once the B and Ge additions are included. However, given that Ge-rich layers, an NbB to T2 phase transition, and the preferential formation of $D8_8$ instead of T2 were observed, the corresponding mechanisms and causes of these features could perhaps be better understood by reducing the variables to consider. As such future studies may benefit from investigations into more simple systems with fewer components, for example Nb-18Si-5Ge-5B.

Finally, in the case that further investigation proves unsuccessful at generating the desired borosilicate layer in these alloys upon oxidation, an alternative approach to reaching sufficient oxidation resistance is necessary. In this scenario the future of niobium silicide-based alloys likely lies with the identification of suitable coating system, much like nickel-based superalloys are successfully paired with yttria-stabilized zirconia to enhance high temperature oxidation resistance and resistance to high temperature. This coating could incorporate larger quantities of B and Ge, building on the foundation laid by this current work.

8 Appendix

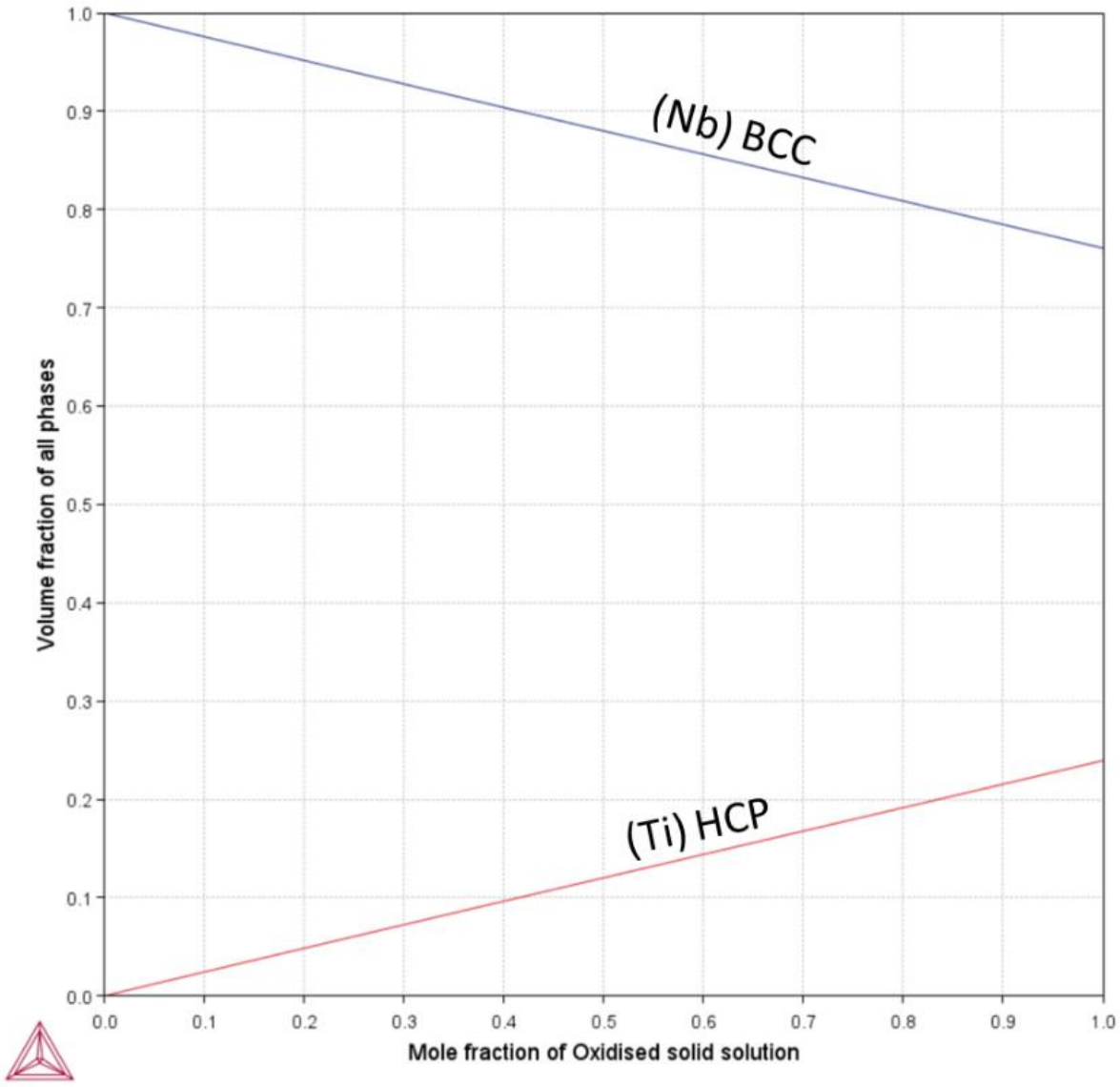

Figure 8.1) Thermocalc modelling of a niobium solid solution (Nb) of composition 43Nb-34Ti-15Cr-8Al that is an approximation of the (Nb) found in JW1-AC. A material to material plot with 38.7Nb-30.6Ti-13.5Cr-7.2Al-10O on the right-hand side (i.e. 10 at.% oxygen substitution, 0.1 "mole fraction of Oxidised solid solution" is equivalent to 1 at.% O addition). Each non-oxygen element is reduced proportionally to its original content to accommodate the substitution of 10 at.% O. Even small amounts of Oxygen results in separation of (Nb) into (Nb) + (Ti)

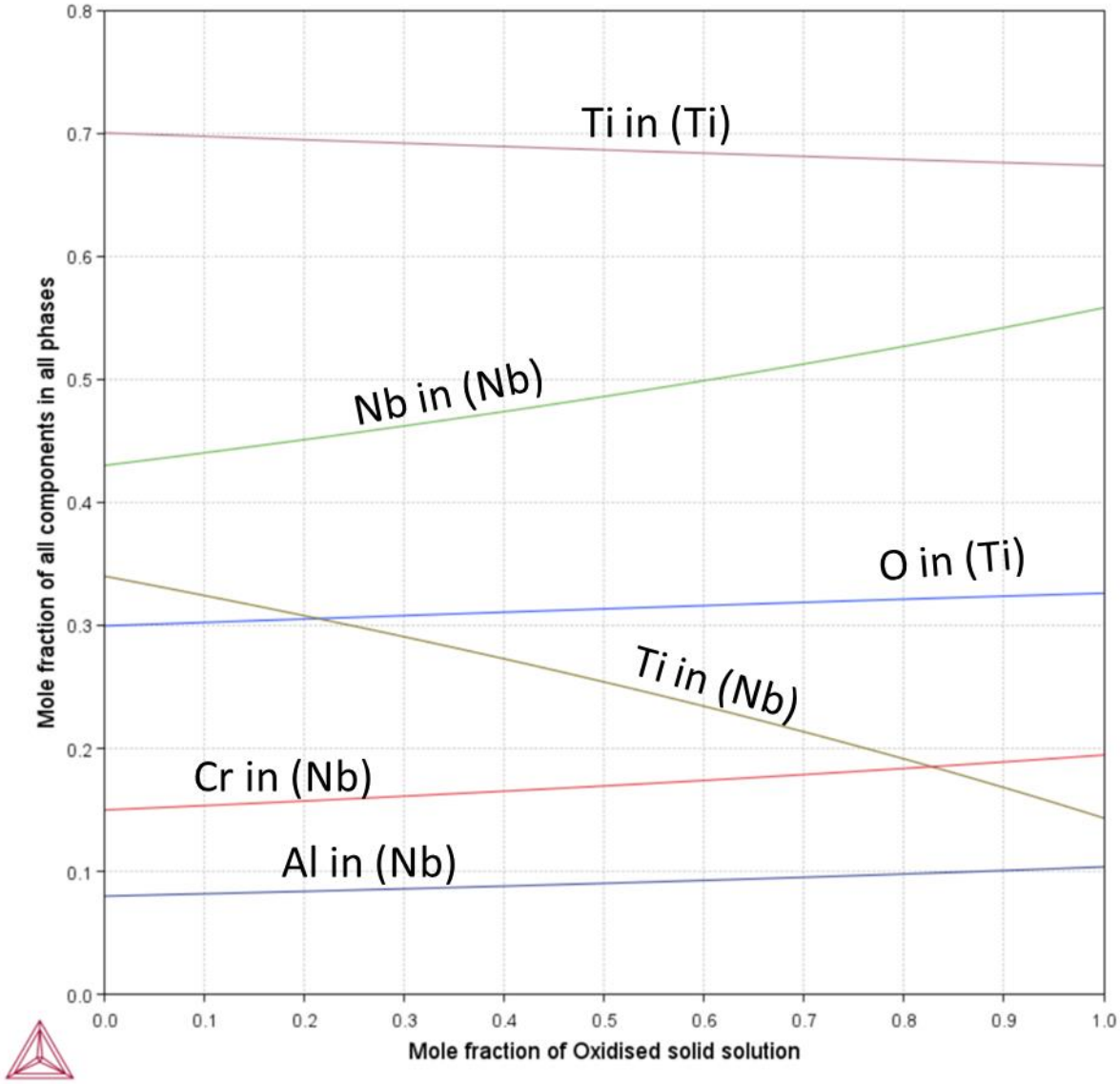

Figure 8.2) Thermocalc modelling of a niobium solid solution (Nb) of composition 43Nb-34Ti-15Cr-8Al in a material to material plot towards 38.7Nb-30.6Ti-13.5Cr-7.2Al-10O on the right-hand side. Each non-oxygen element is reduced proportionally to its original content to accommodate the substitution of 10 at.% O. The composition of phases shown in Figure 8.1 are plotted as oxygen content of the system is increased and (Ti) is stabilised. Nb content of (Nb) increases, Ti content of (Nb) decreases, O content is accommodated by (Ti).

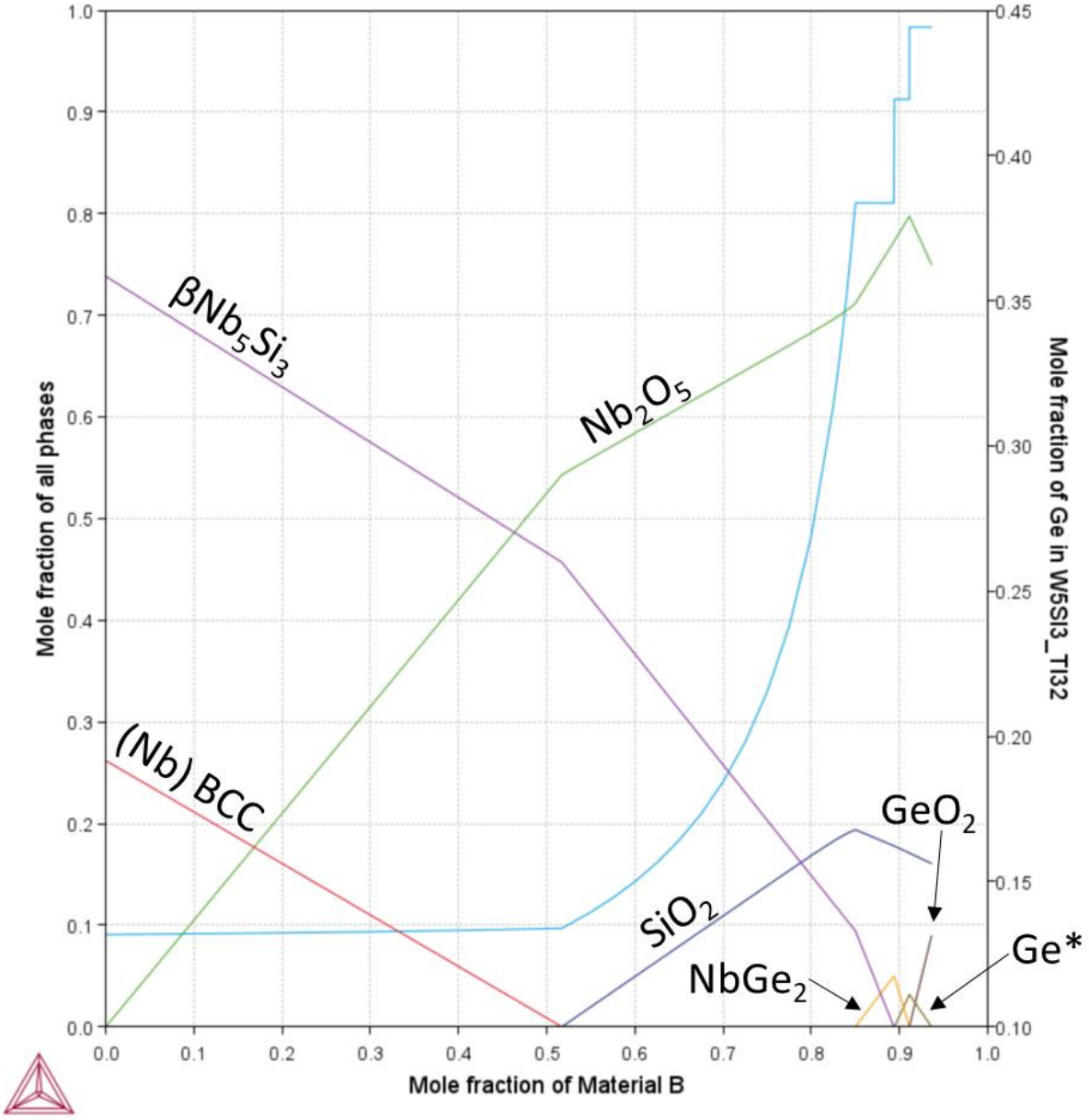

Figure 8.3) A material to material calculation of a Nb-Si-Ge system (72Nb-18Si-10Ge) as O content is increased to Material B (18Nb-4.5Si-2.5Ge-75O). Each non-oxygen element is reduced proportionally to its original content to accommodate the substitution of 75 at.% O. As Material B mole faction is increased oxides replace (Nb) and ϐNb_5Si_3 ($(Nb)_{0.5}(Nb,Si,Ge)_{0.12}(Va,Si,Ge)_{0.38}$), but in the later stages of ϐNb_5Si_3 destabilisation in favour of SiO_2, the $NbGe_2$ phase (Prototype $CrSi_2$, Pearson symbol hP9, $(Nb,Si,Ge)_{0.33}(Nb,Si,Ge)_{0.67}$) becomes an equilibrium phase and reaches its largest mole fraction (~0.05) before any GeO_2 oxide is stable. The Ge content of the ϐNb_5Si_3 increases, shown on the right hand axis and cyan upwards curve. The database produced by Utton et al. [76] is combined with the SSUB5: SGTE Substances v5.2 for the inclusion of oxide phases: Nb_2O_5, GeO_2, SiO_2 (cristobalite). αNb5Si3 and Nb_3Si were exclude from the Nb-Si-Ge database in order to produce the silicide ϐNb_5Si_3 in the starting equilibrium ($D8_8$ is not an equilibrium phase in the Nb-Si-Ge system so ϐNb_5Si_3 is an approximation). The appearance of Ge (Diamond structure) is an artefact of the phase having sub-lattices modelled as $(Nb,Si,Ge,)_1$ so it fills completely with Ge at this stage in O content.*

Table 8.1) Phases as they are referred to in the text and corresponding powder diffraction files (PDF) used to identify them from the PDF-4+ ICDD database.

Phase	PDF-4+ ICDD database entries
(Nb)	00-034-0370, 04-019-6430
αNb_5Si_3	00-030-0874
βNb_5Si_3	00-030-0875
$D8_8$ ($Nb_5Si_3B_{0.2}$)	04-001-6279
T2 ($Nb_5Si_{1.17}B_{1.83}$)	04-023-8213
NbB	00-032-0709, 04-019-6343
$NbCr_2$	00-047-1637
Nb_5Ge_3	01-072-9322, 04-003-4806
TiO_2	00-021-1276, 04-020-2381
$(Ti,Cr,Nb)O_2$	01-088-1982, 04-020-2381, 04-005-6493, 01-079-7560, 01-088-1984, 04-023-1478, 01-088-1985
SiO_2	00-039-1425, 04-002-8510
$Ti_2Nb_{10}O_{29}$	01-084-6449
$TiNb_2O_7$	01-091-2562, 01-084-8890

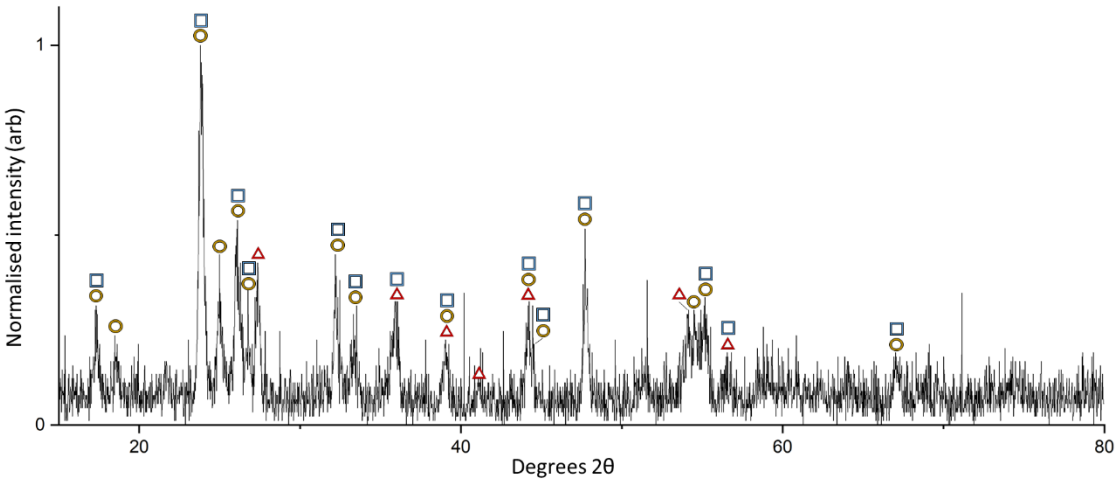

Figure 8.4) Grazing incident XRD pattern of oxidised at 1000°C JW1-AC. An omega angle of 2° was used. △ = TiO_2, ○ = $Ti_2Nb_{10}O_{29}$, □ = $TiNb_2O_7$

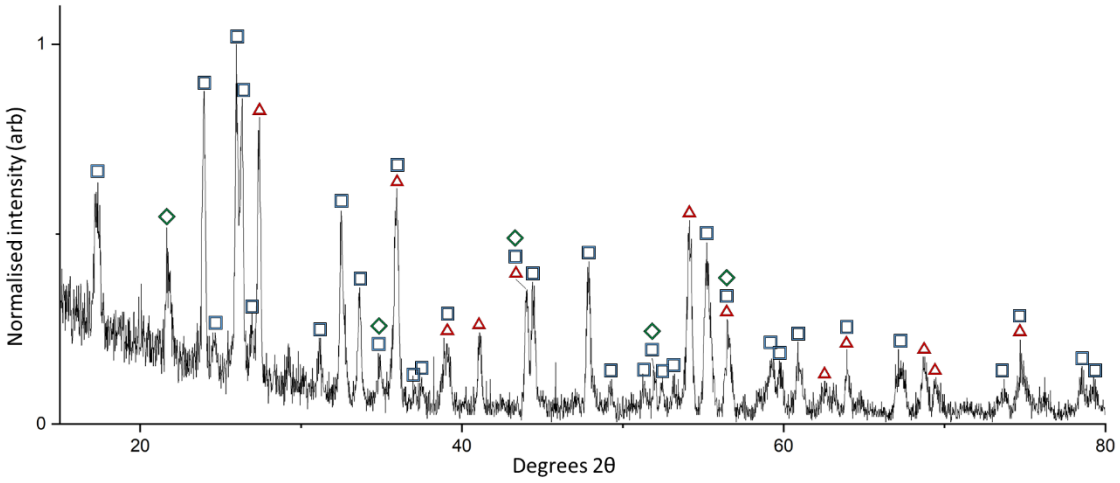

Figure 8.5) Grazing incident XRD pattern of oxidised at 1200°C JW1-AC. An omega angle of 2° was used. △ = TiO_2, □ = $TiNb_2O_7$, ◇ = SiO_2

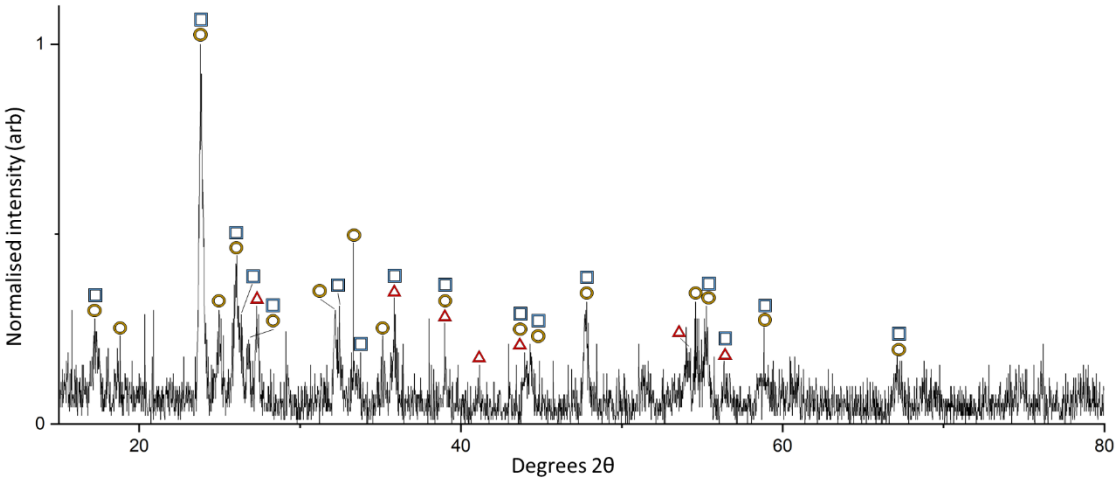

Figure 8.6) Grazing incident XRD pattern of oxidised at 1000°C JW2-AC. An omega angle of 2° was used. △ = TiO_2, ○ = $Ti_2Nb_{10}O_{29}$, □ = $TiNb_2O_7$

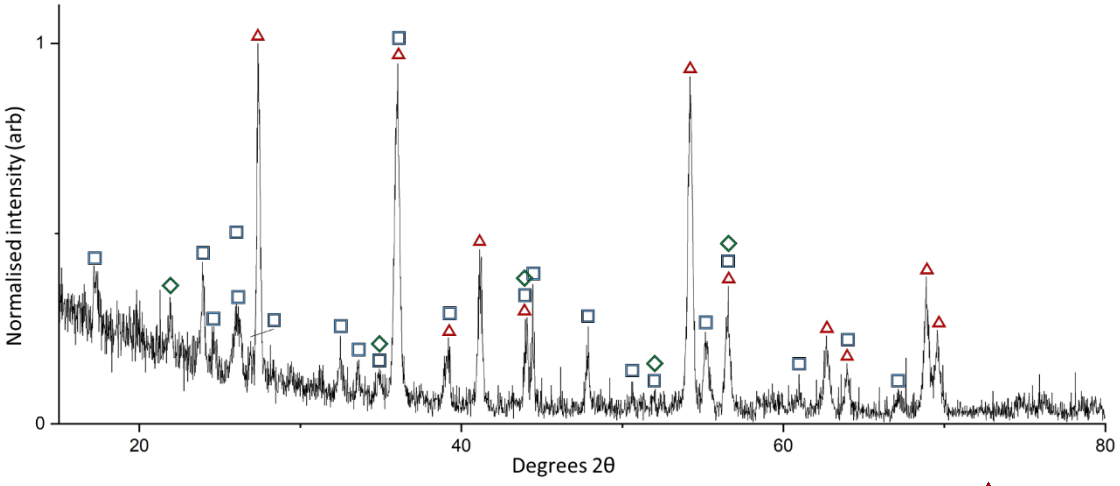

Figure 8.7) Grazing incident XRD pattern of oxidised at 1200°C JW2-AC. An omega angle of 2° was used. △ = TiO_2, □ = $TiNb_2O_7$, ◇ = SiO_2

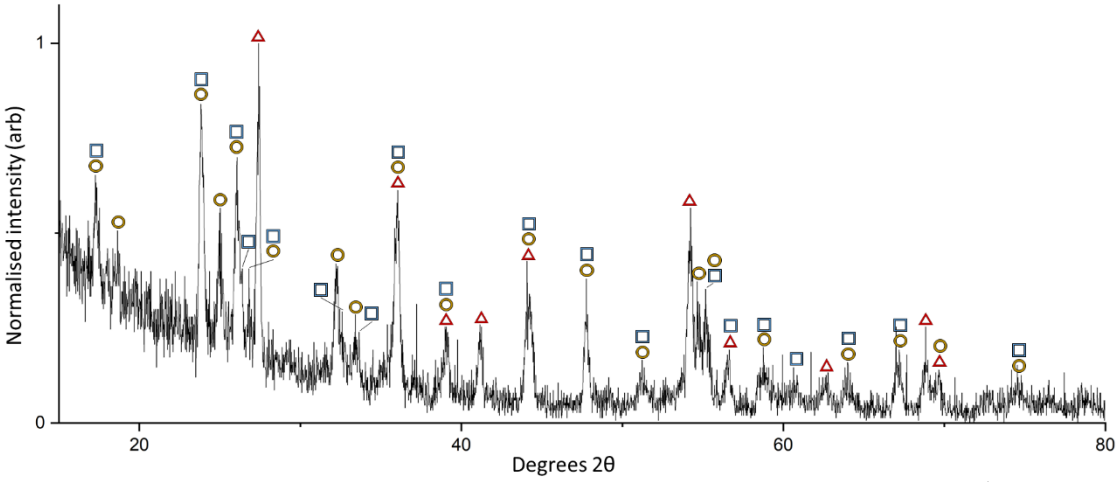

Figure 8.8) Grazing incident XRD pattern of oxidised at 1000°C JW2-AC. An omega angle of 2° was used. △ = TiO_2, ○ = $Ti_2Nb_{10}O_{29}$, □ = $TiNb_2O_7$

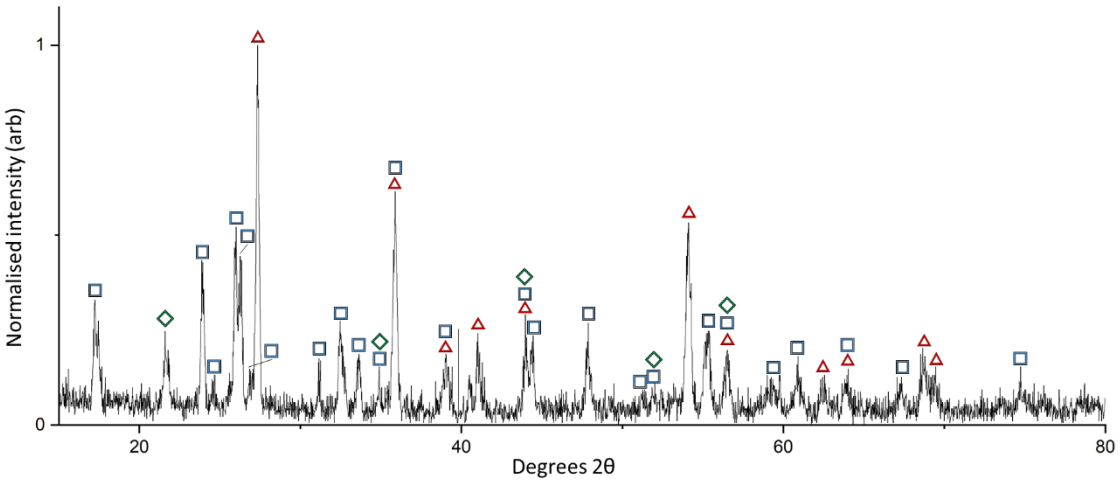

Figure 8.9) Grazing incident XRD pattern of oxidised at 1200°C JW2-AC. An omega angle of 2° was used. △ = TiO_2, □ = $TiNb_2O_7$, ◇ = SiO_2

References

[1] R. E. Sonntag, C. Borgnakke, and G. J. Van Wylen, *Fundamentals of thermodynamics*, 5th ed. New York: John Wiley & Sons, Inc, 1998.

[2] N. Cumpsty and A. Heyes, *Jet Propulsion: A Simple Guide to the Aerodynamics and Thermodynamic Design and Performance of Jet Engines*, 3rd ed. Cambridge : Cambridge University Press, 2015. doi: 10.1017/CBO9781316223116.

[3] R. C. Reed, "The Superalloys fundamentals and applications," *Superalloys Fundam. Appl.*, vol. 9780521859042, pp. 1–372, Jan. 2006, doi: 10.1017/CBO9780511541285.

[4] J. H. Horlock, D. T. Watson, and T. V. Jones, "Limitations of gas turbine performance imposed by large turbine cooling flows," *J. Eng. Gas Turbines Power*, vol. 123, no. 3, pp. 487–494, Jul. 2001, doi: 10.1115/1.1373398.

[5] M. R. Jackson, B. P. Bewlay, R. G. Rowe, D. W. Skelly, and H. A. Lipsitt, "High-temperature refractory metal-intermetallic composites," *JOM*, vol. 48, no. 1, pp. 39–44, 1996, doi: 10.1007/BF03221361/.

[6] M. K. Meyer and M. Akinc, "Oxidation behavior of boron-modified Mo5Si3 at 800°-1300°C," *J. Am. Ceram. Soc.*, vol. 79, no. 4, pp. 938–944, 1996, doi: 10.1111/j.1151-2916.1996.tb08528.x.

[7] The Nickel Institute, "HIGH-TEMPERATURE HIGH-STRENGTH NICKEL-BASE ALLOYS - A PRACTICAL GUIDE TO THE USE OF NICKEL-CONTAINING ALLOYS - NO 393," 2020. [Online]. Available: https://nickelinstitute.org

[8] R. A. Stevens and P. E. J. Flewitt, "The dependence of creep rate on microstructure in a γ' strengthened superalloy," *Acta Metall.*, vol. 29, no. 5, pp. 867–882, May 1981, doi: 10.1016/0001-6160(81)90129-2.

[9] P. Tsakiropoulos, "Alloys for application at ultra-high temperatures: Nb-silicide in situ composites: Challenges, breakthroughs and opportunities," *Progress in Materials Science*. Elsevier Ltd, pp. 1–42, Jul. 15, 2020. doi: 10.1016/j.pmatsci.2020.100714.

[10] Z. Yao, J. Stiglich, and T. S. Sudarshan, "Molybdenum silicide based materials and their properties," *J. Mater. Eng. Perform.*, vol. 8, no. 3, pp. 291–304, Jun. 1999, doi: 10.1361/105994999770346837/METRICS.

[11] L. Zhuo, Y. Xie, and B. Chen, "A review on recent progress of refractory high entropy alloys: From fundamental research to engineering applications," *J. Mater. Res. Technol.*, vol. 33, pp. 1097–1129, Nov. 2024, doi: 10.1016/J.JMRT.2024.09.131.

[12] R. Naslain, "Design, preparation and properties of non-oxide CMCs for application in engines and nuclear reactors: an overview," *Compos. Sci. Technol.*, vol. 64, no. 2, pp. 155–170, Feb. 2004, doi: 10.1016/S0266-3538(03)00230-6.

[13] A. M. Russell and K. L. Lee, *Structure-Property Relations in Nonferrous Metals*. John Wiley and Sons, 2005. doi: 10.1002/0471708542.

[14] B. Gorr, S. Schellert, F. Müller, H.-J. Christ, A. Kauffmann, and M. Heilmaier, "Current Status of Research on the Oxidation Behavior of Refractory High Entropy Alloys," *Adv. Eng. Mater.*, vol. 23, no. 5, pp. 1–14, May 2021, doi: 10.1002/adem.202001047.

[15] M. A. Adams, A. C. Roberts, and R. E. Smallman, "Yield and fracture in polycrystalline

niobium," *Acta Metall.*, vol. 8, no. 5, pp. 328–337, May 1960, doi: 10.1016/0001-6160(60)90118-8.

[16] A. S. Wronski, A. C. Chilton, and E. M. Capron, "The ductile-brittle transition in polycrystalline molybdenum," *Acta Metall.*, vol. 17, no. 6, pp. 751–755, Jun. 1969, doi: 10.1016/0001-6160(69)90081-9.

[17] M. E. Schlesinger, H. Okamoto, A. B. Gokhale, and R. Abbaschian, "The Nb-Si (Niobium-Silicon) system," *J. Phase Equilibria*, vol. 14, no. 4, pp. 502–509, 1993, doi: 10.1007/BF02671971.

[18] L. Haase and M. Kernforschungszentrum Karlsruhe, "HIGH TC PHASES IN THE Nb-Si, Nb-Ge, AND THE Nb-Ge-Si TERNARY SYSTEMS," *IEEE Trans. Magn.*, vol. 17, no. 1, pp. 541–544, 1981.

[19] W. K. Wang and F. Spaepen, "Face-centered-cubic Nb-Si solid solutions produced by picosecond pulsed laser quenching," *J. Appl. Phys*, vol. 58, pp. 4477–4479, 1985, doi: 10.1063/1.336260.

[20] J. M. Léger and H. T. Hall, "Pressure and temperature formation of A3B compounds I. Nb3Si and V3Al," *J. Less Common Met.*, vol. 32, no. 2, pp. 181–187, Aug. 1973, doi: 10.1016/0022-5088(73)90086-6.

[21] D. K. Deardorff, R. E. Siemens, P. A. Romans, and R. A. Mccune, "NEW* TETRAGONAL COMPOUNDS Nb3Si AND Ta3Si," *J. Less-Common Met.*, vol. 18, pp. 11–26, 1969.

[22] F. Galasso and J. Pyle, "Nb3Si, a superconductor with the ordered Cu3Au structure," *Acta Crystallogr.*, vol. 16, no. 3, pp. 228–229, Mar. 1963, doi: 10.1107/S0365110X63000554.

[23] H. Schachner, E. Cerwenka, and H. Nowotny, "Neue Silizide vom M5Si3-Typ mit D 88-Struktur," *Monatshefte für Chemie*, vol. 85, no. 1, pp. 245–254, Jan. 1954, doi: 10.1007/BF00900443.

[24] R. Kieffer and E. Cerwenka, "Beitrag zum System Molybdän-Silizium," *Int. J. Mater. Res.*, vol. 43, no. 4, pp. 101–105, 1952, doi: 10.1515/ijmr-1952-430401.

[25] G. Samsonov, V. Neshpor, and V. Yermakova, "ISSLEDOVANIE SVOISTV SPLAVOV SISTEMY NIOBII-KREMNII (Study of the properties of alloys of the columbium-silicon system)," *J. Inorg. Chem. USSR*, vol. 3, no. 3, pp. 868–878, 1958.

[26] A. G. Knapton, "The System Niobium-Silicon and the Effect of Carbon on the Structures of Certain Silicides," *Nature*, vol. 175, no. 4460, p. 730, 1955, doi: https://doi.org/10.1038/175730b0.

[27] M. Mendiratta and D. Dimiduk, "Phase relations and transformation kinetics in the high Nb region of the Nb-Si system," *Scr. Metall. Mater.*, vol. 25, no. 1, pp. 237–242, Jan. 1991, doi: 10.1016/0956-716X(91)90387-G.

[28] B. P. Bewlay, H. A. Lipsitt, M. R. Jackson, W. J. Reeder, and J. A. Sutliff, "Solidification processing of high temperature intermetallic eutectic-based alloys," *Mater. Sci. Eng. A*, vol. 192–193, no. PART 2, pp. 534–543, Feb. 1995, doi: 10.1016/0921-5093(95)03299-1.

[29] P. B. Fernandes, G. C. Coelho, F. Ferreira, C. A. Nunes, and B. Sundman, "Thermodynamic modeling of the Nb-Si system," *Intermetallics*, vol. 10, no. 10, pp. 993–999, 2002, doi: 10.1016/S0966-9795(02)00125-5.

[30] N. David, Y. Cartigny, T. Belmonte, J. M. Fiorani, and M. Vilasi, "Thermodynamic description of the Cr-Nb-Si isothermal section at 1473 K," *Intermetallics*, vol. 14, no. 4, pp. 464–473, 2006, doi: 10.1016/j.intermet.2005.08.013.

[31] H. L. Lukas, S. G. Fries, and B. Sundman, *Computational thermodynamics: The Calphad method*, vol. 9780521868. Cambridge University Press, 2007. doi: 10.1017/CBO9780511804137.

[32] T. Geng, C. Li, J. Bao, X. Zhao, Z. Du, and C. Guo, "Thermodynamic assessment of the Nb-Si-Ti system," *Intermetallics*, vol. 17, no. 5, pp. 343–357, 2009, doi: 10.1016/j.intermet.2008.11.011.

[33] P. Villars, *Pearson's handbook : crystallographic data for intermetallic phases*, Desk editi. ASM International, 1997.

[34] Y. Zhang, H. Liu, and Z. Jin, "Thermodynamic assessment of the Nb-Ti system," *Calphad Comput. Coupling Phase Diagrams Thermochem.*, vol. 25, no. 2, pp. 305–317, 2001, doi: 10.1016/S0364-5916(01)00051-7.

[35] E. Pontau and D. Lazarus, "Diffusion of titanium and niobium in bcc Ti-Nb alloys," *Phys. Rev. B*, vol. 19, no. 8, pp. 4027–4037, 1978.

[36] H. Okamoto, M. E. Schlesinger, and E. M. Mueller, *Alloy Phase Diagrams*, 3rd ed. ASM International, 2016. doi: https://doi.org/10.31399/asm.hb.v03.a0006187.

[37] J. C. Zhao, M. R. Jackson, and L. A. Peluso, "Mapping of the Nb–Ti–Si phase diagram using diffusion multiples," *Mater. Sci. Eng. A*, vol. 372, no. 1–2, pp. 21–27, May 2004, doi: 10.1016/J.MSEA.2003.08.008.

[38] H. Xu *et al.*, "Isothermal section at 1000 °C of the Nb–Ti–Si system," *J. Alloys Compd.*, vol. 394, no. 1–2, pp. 235–239, May 2005, doi: 10.1016/J.JALLCOM.2004.11.016.

[39] Y. Zhan, Z. Sun, J. Jiang, J. Ma, X. Zhang, and Y. Zhuang, "The 773 K isothermal section of the ternary phase diagram of the Nb–Ti–Si system," *J. Alloys Compd.*, vol. 468, no. 1–2, pp. 150–153, Jan. 2009, doi: 10.1016/J.JALLCOM.2008.01.009.

[40] B. P. Bewlay and M. R. Jackson, "The Nb-Ti-Si Ternary Phase Diagram: Evaluation of Liquid-Solid Phase Equilibria in Nb-and Ti-Rich Alloys," *J. Phase Equilibria*, vol. 18, no. 3, pp. 264–278, 1997.

[41] B. P. Bewlay, M. R. Jackson, and R. R. Bishop, "The Nb-Ti-Si ternary phase diagram: Determination of solid-state phase equilibria in Nb- and Ti-rich alloys," *J. Phase Equilibria*, vol. 19, no. 6, pp. 577–586, 1998, doi: 10.1361/105497198770341789.

[42] I. Papadimitriou, C. Utton, and P. Tsakiropoulos, "The impact of Ti and temperature on the stability of Nb5Si3 phases: a first-principles study," *Sci. Technol. Adv. Mater.*, vol. 18, no. 1, pp. 467–479, Dec. 2017, doi: 10.1080/14686996.2017.1341802.

[43] D. J. Thoma and J. H. Perepezko, "An experimental evaluation of the phase relationships and solubilities in the Nb□Cr system," *Mater. Sci. Eng. A*, vol. 156, no. 1, pp. 97–108, Aug. 1992, doi: 10.1016/0921-5093(92)90420-6.

[44] H. Okamoto, M. . Schlesinger, and E. M. Mueller, Eds., "Alloy Phase Diagrams," in *Alloy Phase Diagrams*, ASM International, 2016, pp. 281–297. doi: 10.31399/ASM.HB.V03.A0006157.

[45] B. S. Murty, J. W. Yeh, and S. Ranganathan, "Intermetallics, Interstitial Compounds and Metallic Glasses in High-Entropy Alloys," in *High Entropy Alloys*, Elsevier, 2014, pp. 119–131. doi: 10.1016/B978-0-12-800251-3.00007-9.

[46] M. Venkatraman and J. P. Neumann, "The Cr-Nb (Chromium-Niobium) system," *Bull. Alloy Phase Diagrams*, vol. 7, no. 5, pp. 462–466, Oct. 1986, doi: 10.1007/BF02867811.

[47] J. Aufrecht, A. Leineweber, A. Senyshyn, and E. J. Mittemeijer, “The absence of a stable hexagonal Laves phase modification (NbCr2) in the Nb–Cr system,” *Scr. Mater.*, vol. 62, no. 5, pp. 227–230, Mar. 2010, doi: 10.1016/J.SCRIPTAMAT.2009.11.002.

[48] F. Stein, C. He, and I. Wossack, “The liquidus surface of the Cr–Al–Nb system and re-investigation of the Cr–Nb and Al–Cr phase diagrams,” *J. Alloys Compd.*, vol. 598, pp. 253–265, Jun. 2014, doi: 10.1016/J.JALLCOM.2014.02.045.

[49] C. Schmetterer, A. Khvan, A. Jacob, B. Hallstedt, and T. Markus, “A new theoretical study of the Cr-Nb system,” *J. Phase Equilibria Diffus.*, vol. 35, no. 4, pp. 434–444, May 2014, doi: 10.1007/S11669-014-0313-Y/TABLES/7.

[50] H. J. Lu, W. B. Wang, N. Zou, J. Y. Shen, X. G. Lu, and Y. L. He, “Thermodynamic modeling of Cr–Nb and Zr–Cr with extension to the ternary Zr–Nb–Cr system,” *Calphad*, vol. 50, pp. 134–143, Sep. 2015, doi: 10.1016/J.CALPHAD.2015.06.002.

[51] Y. Jiang, S. Zomorodpoosh, I. Roslyakova, and L. Zhang, “Thermodynamic re-assessment of binary Cr-Nb system down to 0 K,” *Calphad*, vol. 62, pp. 109–118, Sep. 2018, doi: 10.1016/J.CALPHAD.2018.06.001.

[52] R. N. Hajra, C. Panwisawas, J. W. Park, W. Choo, B. J. Han, and J. H. Kim, “High-temperature phase stability and phase transformations of Niobium-Chromium Laves phase: Experimental and first-principles calculation studies,” *Mater. Des.*, vol. 236, p. 112483, Dec. 2023, doi: 10.1016/J.MATDES.2023.112483.

[53] B. Samanta *et al.*, “Experimental measurement and modeling of lattice thermal expansion and specific heat capacity of C15-Cr2Nb Laves phase intermetallic compound,” *J. Alloys Compd.*, vol. 976, p. 172960, Mar. 2024, doi: 10.1016/J.JALLCOM.2023.172960.

[54] X. W. Nie, “Comments on ‘The absence of a stable hexagonal Laves phase modification (NbCr2) in the Nb–Cr system,’” *Scr. Mater.*, vol. 64, no. 10, pp. 990–993, May 2011, doi: 10.1016/J.SCRIPTAMAT.2011.01.032.

[55] A. Leineweber, J. Aufrecht, A. Senyshyn, and E. J. Mittemeijer, “Reply to comments on the absence of a stable hexagonal Laves phase modification (NbCr2) in the Nb–Cr system,” *Scr. Mater.*, vol. 64, no. 10, pp. 994–997, May 2011, doi: 10.1016/J.SCRIPTAMAT.2011.01.035.

[56] H. J. Goldschmidt and J. A. Brand, “The constitution of the chromium-niobium-silicon system,” *J. Less Common Met.*, vol. 3, no. 1, pp. 34–43, Feb. 1961, doi: 10.1016/0022-5088(61)90041-8.

[57] J. C. Zhao, M. R. Jackson, and L. A. Peluso, “Determination of the Nb–Cr–Si phase diagram using diffusion multiples,” *Acta Mater.*, vol. 51, no. 20, pp. 6395–6405, Dec. 2003, doi: 10.1016/J.ACTAMAT.2003.08.007.

[58] G. Shao, “Thermodynamic modelling of the Cr–Nb–Si system,” *Intermetallics*, vol. 13, no. 1, pp. 69–78, Jan. 2005, doi: 10.1016/J.INTERMET.2004.06.003.

[59] N. David, Y. Cartigny, T. Belmonte, J. M. Fiorani, and M. Vilasi, “Thermodynamic description of the Cr–Nb–Si isothermal section at 1473 K,” *Intermetallics*, vol. 14, no. 4, pp. 464–473, Apr. 2006, doi: 10.1016/J.INTERMET.2005.08.013.

[60] J. Geng, G. Shao, and P. Tsakiropoulos, “Study of three-phase equilibrium in the Nb-rich corner of Nb–Si–Cr system,” *Intermetallics*, vol. 14, no. 7, pp. 832–837, Jul. 2006, doi: 10.1016/J.INTERMET.2005.12.004.

[61] B. P. Bewlay, Y. Yang, R. L. Casey, M. R. Jackson, and Y. A. Chang, “Experimental study of the

liquid–solid phase equilibria at the metal-rich region of the Nb–Cr–Si system," *Intermetallics*, vol. 17, no. 3, pp. 120–127, Mar. 2009, doi: 10.1016/J.INTERMET.2008.10.005.

[62] P. Maji, R. Mitra, and K. K. Ray, "Effect of Cr on the evolution of microstructures in as-cast ternary niobium-silicide-based composites," *Intermetallics*, vol. 85, pp. 34–47, Jun. 2017, doi: 10.1016/J.INTERMET.2017.01.012.

[63] O. Prymak and F. Stein, "The ternary Cr–Al–Nb phase diagram: Experimental investigations of isothermal sections at 1150, 1300 and 1450 °C," *J. Alloys Compd.*, vol. 513, pp. 378–386, Feb. 2012, doi: 10.1016/J.JALLCOM.2011.10.053.

[64] J.-C. Zhao, M. R. Jackson, and L. A. Peluso, "Mapping of the Nb–Cr–Ti phase diagram using diffusion multiples," *Int. J. Mater. Res.*, vol. 95, no. 3, pp. 142–146, Mar. 2004, doi: 10.3139/IJMR-2004-0031.

[65] H. Okamoto, "B-Nb (boron-niobium)," *J. Phase Equilibria Diffus.*, vol. 31, no. 2, pp. 208–209, Apr. 2010, doi: 10.1007/S11669-010-9657-0/TABLES/1.

[66] V. T. Witusiewicz, A. A. Bondar, U. Hecht, S. Rex, and T. Y. Velikanova, "The Al–B–Nb–Ti system: I. Re-assessment of the constituent binary systems B–Nb and B–Ti on the basis of new experimental data," *J. Alloys Compd.*, vol. 448, no. 1–2, pp. 185–194, Jan. 2008, doi: 10.1016/J.JALLCOM.2006.10.034.

[67] T. B. Massalski, H. Okamoto, P. R. Subramanian, and L. Kacprzak, *Binary alloy phase diagrams*, 2nd ed. Materials Park, OH: ASM International, 1990.

[68] E. Rudy and S. Windisch, "Ternary phase equilibria in transition metal–boron–carbon–silicon systems," Wright patterson AFB, OH, AFML-TR-65-2, Air Force Materials Lab., 1966.

[69] L. A. Borges, G. C. Coelho, C. A. Nunes, and P. A. Suzuki, "New data on phase equilibria in the Nb-rich region of the Nb-B system," *J. Phase Equilibria*, vol. 24, no. 2, pp. 140–146, Apr. 2003, doi: 10.1361/105497103770330758.

[70] R. M. Peçanha, F. Ferreira, G. C. Coelho, C. A. Nunes, and B. Sundman, "Thermodynamic modeling of the Nb–B system," *Intermetallics*, vol. 15, no. 8, pp. 999–1005, Aug. 2007, doi: 10.1016/J.INTERMET.2006.10.054.

[71] Z. Tang, M. J. Kramer, and M. Akinc, "Evaluation of phase equilibria in the Nb-rich portion of Nb–B system," *Intermetallics*, vol. 16, no. 2, pp. 255–261, Feb. 2008, doi: 10.1016/J.INTERMET.2007.10.004.

[72] H. Okamoto, "B-Nb (Boron-Niobium)," *J. Phase Equilibria Diffus. 2008 292*, vol. 29, no. 2, pp. 201–201, Feb. 2008, doi: 10.1007/S11669-008-9266-3.

[73] H. Bolmgren and T. Lundström, "A new binary boride, Nb5B6," *J. Less Common Met.*, vol. 159, no. C, pp. L25–L27, Apr. 1990, doi: 10.1016/0022-5088(90)90170-O.

[74] C. A. Nunes *et al.*, "The NbB2-phase revisited: Homogeneity range, defect structure, superconductivity," *Acta Mater.*, vol. 53, no. 13, pp. 3679–3687, Aug. 2005, doi: 10.1016/J.ACTAMAT.2005.04.020.

[75] S. Okada, K. Hamano, T. Lundström, I. Higashi, and T. Lundstr~m, "Crystal growth of the new compound Nb2B3, and the borides NbB, Nb5B6, Nb3B4, and NbB2, using the copper-flux method," *AIP Conf. Proc.*, vol. 231, no. 1, pp. 456–459, Jul. 1991, doi: 10.1063/1.40817.

[76] Y. B. Kuz'ma, "An X-ray structural investigation of the systems niobium-titanium-boron and niobium-molybdenum-boron," *Sov. Powder Metall. Met. Ceram.*, vol. 10, no. 4, pp. 298–300, Apr. 1971, doi: 10.1007/BF00795985.

[77] D. B. Borisov *et al.*, “Titanium-boride eutectic materials. Structure of the Ti-Nb-B alloys and phase equilibria,” *Powder Metall. Met. Ceram.*, vol. 46, no. 1–2, pp. 58–71, Jan. 2007, doi: 10.1007/S11106-007-0011-Y.

[78] Y. Nakama, H. Ohtani, and M. Hasebe, “Thermodynamic Analysis of the Nb–Ti–B Ternary Phase Diagram,” *Mater. Trans.*, vol. 50, no. 5, pp. 984–993, May 2009, doi: 10.2320/MATERTRANS.MC200820.

[79] V. T. Witusiewicz, A. A. Bondar, U. Hecht, S. Rex, and T. Y. Velikanova, “The Al–B–Nb–Ti system: II. Thermodynamic description of the constituent ternary system B–Nb–Ti,” *J. Alloys Compd.*, vol. 456, no. 1–2, pp. 143–150, May 2008, doi: 10.1016/J.JALLCOM.2007.02.030.

[80] H. Nowotny, F. Benesovsky, E. Rudy, and A. Wittmann, “Aufbau und Zunderverhalten von Niob-Bor-Silicium-Legierungen,” *Monatshefte für Chemie*, vol. 91, no. 5, pp. 975–990, Sep. 1960, doi: 10.1007/BF00929565.

[81] Z. Sun, Y. Yang, X. Guo, C. Zhang, and Y. A. Chang, “Thermodynamic modeling of the Nb-rich corner in the Nb–Si–B system,” *Intermetallics*, vol. 19, no. 1, pp. 26–34, Jan. 2011, doi: 10.1016/J.INTERMET.2010.09.003.

[82] S. V. N. Naidu, C. F. Mays, and C. R. Houska, “Integrated Intensities and Lattice Parameters for Mo5Si3,” *J. Am. Ceram. Soc.*, vol. 65, no. 4, pp. c58–c59, Apr. 1982, doi: 10.1111/J.1151-2916.1982.TB10419.X.

[83] G. Rodrigues, C. A. Nunes, P. A. Suzuki, and G. C. Coelho, “Lattice parameters and thermal expansion of the T2-phase of the Nb-Si-B system investigated by high-temperature X-ray diffraction,” *Intermetallics*, vol. 12, no. 2, pp. 181–188, Feb. 2004, doi: 10.1016/j.intermet.2003.09.015.

[84] C. A. Nunes, D. M. P. Júnior, G. C. Coelho, P. A. Suzuki, A. A. A. P. Da Silva, and R. B. Tomasiello, “Isothermal section of the Nb-Si-B system at 1700 °C in the Nb-NbSi 2-NbB 2 region,” *J. Phase Equilibria Diffus.*, vol. 32, no. 2, pp. 92–96, Apr. 2011, doi: 10.1007/S11669-010-9846-X/FIGURES/3.

[85] P. Dário Moreira, C. A. Nunes, G. C. Coelho, and F. Ferreira, “Liquidus projection of the Nb–Si–B system in the Nb-rich region,” *Intermetallics*, vol. 11, no. 3, pp. 251–255, Mar. 2003, doi: 10.1016/S0966-9795(02)00249-2.

[86] C. A. Utton, I. Papadimitriou, H. Kinoshita, and P. Tsakiropoulos, “Experimental and thermodynamic assessment of the Ge-Nb-Si ternary phase diagram,” *J. Alloys Compd.*, vol. 717, pp. 303–316, Sep. 2017, doi: 10.1016/J.JALLCOM.2017.04.279.

[87] V. M. Pan, V. I. Latysheva, and E. A. Shishkin, “Phase Diagram of the Nb—Ge System,” *Phys. Metall. Supercond.*, pp. 179–182, 1970, doi: 10.1007/978-1-4684-8220-1_31.

[88] H. Okamoto, “Ge-Nb (Germanium-Niobium),” *J. Phase Equilibria Diffus.*, vol. 33, no. 3, pp. 250–251, Jun. 2012, doi: 10.1007/S11669-012-0023-2.

[89] H. Nowotny, A. W. Searcy, and J. E. Orr, “Structures of some germanides of formula M5Ge3,” *J. Phys. Chem.*, vol. 60, no. 5, pp. 677–678, 1956, doi: 10.1021/j150539a042.

[90] J. L. Jorda, R. Flükiger, and J. Müller, “The phase diagram of the niobium-germanium system,” *J. Less Common Met.*, vol. 62, no. C, pp. 25–37, Nov. 1978, doi: 10.1016/0022-5088(78)90013-9.

[91] T. Geng, C. Li, Z. Du, C. Guo, X. Zhao, and H. Xu, “Thermodynamic assessment of the Nb–Ge system,” *J. Alloys Compd.*, vol. 509, no. 6, pp. 3080–3088, Feb. 2011, doi:

10.1016/J.JALLCOM.2010.12.005.

[92] I. Papadimitriou, C. Utton, and P. Tsakiropoulos, “On the Nb-Ge Binary System,” *Metall. Mater. Trans. A Phys. Metall. Mater. Sci.*, vol. 46, no. 12, pp. 5526–5536, Sep. 2015, doi: 10.1007/S11661-015-3149-0/TABLES/4.

[93] C. Colinet and J. C. Tedenac, “Enthalpies of formation of TM–X compounds (X=Al, Ga, Si, Ge, Sn). Comparison of ab-initio values and experimental data,” *Calphad*, vol. 54, pp. 16–34, Sep. 2016, doi: 10.1016/J.CALPHAD.2016.05.001.

[94] M. Kloska and E. L. Haase, “On the existence of the hexagonal Nb3Ge2 phase,” *J. Less Common Met.*, vol. 99, no. 2, pp. 241–248, Jun. 1984, doi: 10.1016/0022-5088(84)90221-2.

[95] K. W. Richter, H. Flandorfer, and H. F. Franzen, “On the stability of hexagonal Ge7Nb10,” *J. Alloys Compd.*, vol. 320, no. 1, pp. 87–92, May 2001, doi: 10.1016/S0925-8388(00)01499-7.

[96] L. I. Zifu and P. Tsakiropoulos, “Study of the effects of Ge addition on the microstructure of Nb–18Si in situ composites,” *Intermetallics*, vol. 18, no. 5, pp. 1072–1078, May 2010, doi: 10.1016/J.INTERMET.2010.02.012.

[97] V. M. Pan, V. I. Latysheva, O. G. Kulik, and A. G. Popov, “Effect of germanium and copper alloying on formation conditions of Nb3Si,” *Izv. Akad. Nauk SSSR, Met.*, vol. 3, pp. 191–195, 1982.

[98] V. M. Pan, V. I. Latysheva, D. G. Kulik, and A. G. Popov, “Influence of mutual alloying on formation of Nb3Ge and Nb3Si phases and on their superconductivity,” *Izv. Akad. Nauk SSSR, Met.*, vol. 4, pp. 184–187, 1982.

[99] R. M. Nekkanti and D. M. Dimiduk, “Ductile-Phase Toughening in Niobium-Niobium Silicide Powder Processed Composites,” *MRS Proc.*, vol. 194, no. 1, pp. 175–182, Oct. 1990, doi: 10.1557/PROC-194-175.

[100] I. Weiss, M. Thirukkonda, and R. Srinivasan, “Effect of deformation processing on mechanical properties of Nb-10 a/o Si IN-SITU composite,” in *High Temperature Silicides and Refractory Alloys*, 322nd ed., C. L. Briant, J. J. Petrovic, B. P. Bewlay, A. K. Vasudevan, and H. A. Lipsitt, Eds., Publ by Materials Research Society, 1994, pp. 377–386.

[101] B. P. Bewlay, M. R. Jackson, J. C. Zhao, P. R. Subramanian, M. G. Mendiratta, and J. J. Lewandowski, “Ultrahigh-temperature Nb-silicide-based composites,” *MRS Bull.*, vol. 28, no. 9, pp. 646–653, 2003, doi: 10.1557/mrs2003.192.

[102] M. G. Mendiratta, J. J. Lewandowski, and D. M. Dimiduk, “Strength and ductile-phase toughening in the two-phase Nb/Nb5Si3 alloys,” *Metall. Trans. A*, vol. 22, no. 7, pp. 1573–1583, Jul. 1991, doi: 10.1007/BF02667370.

[103] M. G. Mendiratta and D. M. Dimiduk, “Strength and toughness of a Nb/Nb5Si3 composite,” *Metall. Trans. A*, vol. 24, no. 2, pp. 501–504, Feb. 1993, doi: 10.1007/BF02657338.

[104] B. P. Bewlay, M. R. Jackson, and M. F. X. Gigliotti, “Niobium Silicide High Temperature In Situ Composites,” in *Intermetallic Compounds - Principles and Practice*, Chichester, UK: John Wiley & Sons, Ltd, 2002, pp. 541–560. doi: 10.1002/0470845856.ch26.

[105] B. P. Bewlay, M. R. Jackson, and C. L. Briant, “Creep Mechanisms in High-Temperature In-Situ Composites,” *Air Force Off. Sci. Res.*, pp. 1–31, 1999, Accessed: May 11, 2021. [Online]. Available: https://apps.dtic.mil/sti/tr/pdf/ADA369335.pdf

[106] B. Kong, L. Jia, L. Su, K. Guan, J. Weng, and H. Zhang, “Effects of minor Si on microstructures and room temperature fracture toughness of niobium solid solution alloys,” *Mater. Sci. Eng.*

A, vol. 639, pp. 114–121, Jul. 2015, doi: 10.1016/J.MSEA.2015.04.096.

[107] P. Tsakiropoulos, "On Nb Silicide Based Alloys: Alloy Design and Selection," *Materials (Basel).*, vol. 11, no. 5, p. 844, May 2018, doi: 10.3390/MA11050844.

[108] P. R. Subramanian, T. A. Parthasarathy, M. G. Mendiratta, and D. M. Dimiduk, "Compressive creep behavior of Nb5Si3," *Scr. Metall. Mater.*, vol. 32, no. 8, pp. 1227–1232, Apr. 1995, doi: 10.1016/0956-716X(95)00130-N.

[109] B. P. Bewlay, M. R. Jackson, P. R. Subramanian, and C. L. Briant, "Recent Advances in Nb-silicide in-situ composites," in *Powder Metallurgical High Performance Materials. Proceedings. Volume 1: high performance P/M metals*, G. Kneringer, P. Rödhammer, and H. Wildner, Eds., Reutte, Austira, May 2001, pp. 404–419.

[110] B. P. Bewlay, M. R. Jackson, W. J. Reeder, and H. A. Lipsitt, "Microstructure and properties of DS in-situ composites of Nb-Ti-Si alloys," *Mater. Res. Soc. Symp. - Proc.*, vol. 364, no. 2, pp. 943–948, Feb. 1995, doi: 10.1557/PROC-364-943.

[111] P. R. Subramanian, M. G. Mindiratta, and D. M. Dimiduk, "Microstructures and Mechanical Behavior of Nb-Ti Base Beta + Silicide Alloys," *MRS Proc.*, vol. 322, no. 1, pp. 491–502, Oct. 1993, doi: 10.1557/PROC-322-491.

[112] K. S. Chan and D. L. Davidson, "Improving the fracture toughness of constituent phases and Nb-based in-situ composites by a computational alloy design approach," *Metall. Mater. Trans. A Phys. Metall. Mater. Sci.*, vol. 34 A, no. 9, pp. 1833–1849, 2003, doi: 10.1007/S11661-003-0149-2/.

[113] K. S. Chan, "A computational approach to designing ductile Nb-Ti-Cr-Al solid-solution alloys," *Metall. Mater. Trans. A Phys. Metall. Mater. Sci.*, vol. 32, no. 10, pp. 2475–2487, 2001, doi: 10.1007/S11661-001-0037-6.

[114] B. P. Bewlay, M. R. Jackson, and H. A. Lipsitt, "The balance of mechanical and environmental properties of a multielement niobium-niobium silicide-based in situ composite," *Metall. Mater. Trans. A Phys. Metall. Mater. Sci.*, vol. 27, no. 12, pp. 3801–3808, 1996, doi: 10.1007/BF02595629.

[115] L. Cretegny, B. P. Bewlay, A. M. Ritter, and M. R. Jackson, "The effects of substitutional additions on tensile behavior of Nb-silicide based composites," *Mater. Res. Soc. Symp. Proc.*, vol. 842, no. 1, pp. 273–278, Feb. 2005, doi: 10.1557/PROC-842-S2.10/.

[116] B. P. Bewlay, P. W. Whiting, A. W. Davis, and C. L. Briant, "Creep mechanisms in niobium-suicide based in-situ composites," *Mater. Res. Soc. Symp. - Proc.*, vol. 552, 1999, doi: 10.1557/PROC-552-KK6.11.1.

[117] P. R. Subramanian, M. G. Mendiratta, D. M. Dimiduk, and M. A. Stucke, "Advanced intermetallic alloys-beyond gamma titanium aluminides," *Mater. Sci. Eng.*, vol. 239, pp. 1–13, 1997, doi: 10.1016/S0921-5093(97)00555-8.

[118] P. Tsakiropoulos, "On the Alloying and Properties of Tetragonal Nb5Si3 in Nb-Silicide Based Alloys," *Mater. 2018, Vol. 11, Page 69*, vol. 11, no. 1, p. 69, Jan. 2018, doi: 10.3390/MA11010069.

[119] Q. Huang, Y. Kang, J. Song, S. Qu, Y. Han, and X. Guo, "Effects of Ni, Co, B, and Ge on the microstructures and mechanical properties of Nb-Ti-Si ternary alloys," *Met. Mater. Int.*, vol. 20, no. 3, pp. 475–481, May 2014, doi: 10.1007/s12540-014-3010-9.

[120] C. S. Giggins and F. S. Pettit, "Oxidation of Ni-Cr-Al Alloys Between 1000° and 1200°C," *J.*

Electrochem. Soc., vol. 118, no. 11, p. 1782, Nov. 1971, doi: 10.1149/1.2407837.

[121] R. Mitra, "Oxidation Behavior of Silicides," *Diffus. Found.*, vol. 21, pp. 127–156, 2019, doi: 10.4028/www.scientific.net/df.21.127.

[122] K. S. Chan, "Cyclic-oxidation resistance of niobium-base in situ composites: Modeling and experimentation," *Oxid. Met.*, vol. 61, no. 3–4, pp. 165–194, Apr. 2004, doi: 10.1023/B:OXID.0000025330.65837.d1.

[123] R. A. Perkins and G. H. Meier, "The oxidation behavior and protection of niobium," *JOM*, vol. 42, no. 8, pp. 17–21, Aug. 1990, doi: 10.1007/BF03221046.

[124] K. Sala, S. K. Kashyap, and R. Mitra, "Effect of Ti addition on the kinetics and mechanism of non-isothermal and isothermal oxidation of Nb–Si–Mo alloys at 900 °C–1200 °C," *Intermetallics*, vol. 138, p. 107338, Nov. 2021, doi: 10.1016/J.INTERMET.2021.107338.

[125] J. Nelson, M. Ghadyani, C. Utton, and P. Tsakiropoulos, "A study of the effects of Al, Cr, Hf, and Ti additions on the microstructure and oxidation of Nb-24Ti-18Si silicide based alloys," *Materials (Basel).*, vol. 11, no. 9, Sep. 2018, doi: 10.3390/ma11091579.

[126] J. Geng and P. Tsakiropoulos, "A study of the microstructures and oxidation of Nb–Si–Cr–Al–Mo in situ composites alloyed with Ti, Hf and Sn," *Intermetallics*, vol. 15, no. 3, pp. 382–395, Mar. 2007, doi: 10.1016/J.INTERMET.2006.08.016.

[127] Z. Li and P. Tsakiropoulos, "The effect of Ge addition on the oxidation of Nb-24Ti-18Si Silicide Based Alloys," *Materials (Basel).*, vol. 12, no. 19, Oct. 2019, doi: 10.3390/ma12193120.

[128] K. Zelenitsas and P. Tsakiropoulos, "Effect of Al, Cr and Ta additions on the oxidation behaviour of Nb–Ti–Si in situ composites at 800 °C," *Mater. Sci. Eng. A*, vol. 416, no. 1–2, pp. 269–280, Jan. 2006, doi: 10.1016/J.MSEA.2005.10.017.

[129] Y. Wang, L. Jia, G. Sun, F. Zhang, C. Ye, and H. Zhang, "Synchronous improvement in room-temperature fracture toughness and high-temperature oxidation resistance of Nb–Si based alloys with Erbium addition," *Int. J. Refract. Met. Hard Mater.*, vol. 94, p. 105359, Jan. 2021, doi: 10.1016/j.ijrmhm.2020.105359.

[130] O. Hernández-Negrete and P. Tsakiropoulos, "On the Microstructure and Isothermal Oxidation at 800 and 1200 °C of the Nb-24Ti-18Si-5Al-5Cr-5Ge-5Sn (at.%) Silicide-Based Alloy," *Materials (Basel).*, vol. 13, no. 3, p. 722, Feb. 2020, doi: 10.3390/ma13030722.

[131] T. Thandorn and P. Tsakiropoulos, "The effect of boron on the microstructure and properties of refractory metal intermetallic composites (Rm(nb)ics) based on nb-24ti-xsi (x = 16, 17 or 18 at.%) with additions of al, cr or mo," *Materials (Basel).*, vol. 14, no. 20, p. 6101, Oct. 2021, doi: 10.3390/MA14206101/S1.

[132] P. Kofstad, "General Introduction," in *High Temperature Oxidation of Metals (Corrosion monographs)*, John Wiley & Sons, Ltd, 1966, pp. 1–20.

[133] P. Tsakiropoulos, "Alloys for application at ultra-high temperatures: Nb-silicide in situ composites: Challenges, breakthroughs and opportunities," *Prog. Mater. Sci.*, vol. 123, pp. 1–42, Jan. 2022, doi: 10.1016/J.PMATSCI.2020.100714.

[134] J. Zheng, X. Hou, X. Wang, Y. Meng, X. Zheng, and L. Zheng, "Isothermal oxidation mechanism of a newly developed Nb–Ti–V–Cr–Al–W–Mo–Hf alloy at 800–1200 °C," *Int. J. Refract. Met. Hard Mater.*, vol. 54, pp. 322–329, Jan. 2016, doi: 10.1016/J.IJRMHM.2015.08.012.

[135] E. Menon, M. Mendiratta, and D. Dimiduk, "High temperature oxidation mechanisms in Nb - Silicide bearing multicomponent alloys," in *Proceedings of the International Symposium*

Niobium 2001, Orlando, Florida, USA, 2001, pp. 121–145.

[136] J. Geng, P. Tsakiropoulos, and G. Shao, "Oxidation of Nb–Si–Cr–Al in situ composites with Mo, Ti and Hf additions," *Mater. Sci. Eng. A*, vol. 441, no. 1–2, pp. 26–38, Dec. 2006, doi: 10.1016/J.MSEA.2006.08.093.

[137] B. P. Bewlay, M. R. Jackson, J.-C. Zhao, P. R. Subramanian, and S. Metallurgists, "A Review of Very-High-Temperature Nb-Silicide-Based Composites under the auspices of the ASM and TMS Joint Committee on Mechanical Behavior of Materials," vol. 34, 2003.

[138] J. H. Westbrook and D. L. Wood, "'PEST' degradation in beryllides, silicides, aluminides, and related compounds," *J. Nucl. Mater.*, vol. 12, no. 2, pp. 208–215, Jul. 1964, doi: 10.1016/0022-3115(64)90142-4.

[139] K. Yanagihara, T. Maruyama, and K. Nagata, "Effect of third elements on the pesting suppression of Mo-Si-X intermetallics (X = Al, Ta, Ti, Zr and Y)," *Intermetallics*, vol. 4, no. SUPPL. 1, pp. S133–S139, Jan. 1996, doi: 10.1016/0966-9795(96)00019-2.

[140] M. R. Jackson, B. P. Bewlay, R. G. Rowe, D. W. Skelly, and H. A. Lipsitt, "High-temperature refractory metal-intermetallic composites," *J. Miner. Met. Mater. Soc.*, vol. 48, no. 1, pp. 39–44, 1996, doi: 10.1007/BF03221361.

[141] Y. Q. Liu, G. Shao, and P. Tsakiropoulos, "On the oxidation behaviour of MoSi2," *Intermetallics*, vol. 9, no. 2, pp. 125–136, Feb. 2001, doi: 10.1016/S0966-9795(00)00114-X.

[142] B. B. Argent and B. Phelps, "The oxidation of niobium-titanium and niobium-molybdenum alloys," *J. Less Common Met.*, vol. 2, no. 2–4, pp. 181–190, Apr. 1960, doi: 10.1016/0022-5088(60)90013-8.

[143] G. Ghosh and G. B. Olson, "Integrated design of Nb-based superalloys: Ab initio calculations, computational thermodynamics and kinetics, and experimental results," *Acta Mater.*, vol. 55, no. 10, pp. 3281–3303, Jun. 2007, doi: 10.1016/J.ACTAMAT.2007.01.036.

[144] A. Misra, "Noburnium: Systems design of niobium superalloys. - Northwestern University," NORTHWESTERN UNIVERSITY, 2005. Accessed: Sep. 02, 2024. [Online]. Available: https://ui.adsabs.harvard.edu/abs/2005PhDT.....92M/abstract

[145] J. H. Kim, T. Tabaru, M. Sakamoto, and S. Hanada, "Mechanical properties and fracture behavior of an NbSS/Nb5Si3 in-situ composite modified by Mo and Hf alloying," *Mater. Sci. Eng. A*, vol. 372, no. 1–2, pp. 137–144, May 2004, doi: 10.1016/J.MSEA.2003.12.010.

[146] P. Kofstad, "Oxidation of Group IVA and VA metals," in *High Temperature Oxidation of Metals (Corrosion monographs)*, 1st ed., John Wiley & Sons, Ltd, 1966, pp. 166–220.

[147] J. Geng and P. Tsakiropoulos, "A study of the microstructures and oxidation of Nb–Si–Cr–Al–Mo in situ composites alloyed with Ti, Hf and Sn," *Intermetallics*, vol. 15, no. 3, pp. 382–395, Mar. 2007, doi: 10.1016/J.INTERMET.2006.08.016.

[148] E. J. Felten, "The interaction of the alloy niobium-25Titanium with air, oxygen and nitrogen I. The unusual oxidation behavior of Nb-25Ti at 1000 ° C," *J. Less-Common Met.*, vol. 17, no. 2, pp. 185–197, Feb. 1969, doi: 10.1016/0022-5088(69)90052-6.

[149] Y. Li, X. Lin, Z. Zhao, W. Yan, J. Yu, and P. Bai, "Investigation on the composite effect of Zr and Cr on oxidation behavior and fracture toughness of Nb-Ti-Si-based alloys manufactured by directed energy deposition," *Mater. Charact.*, vol. 214, p. 114078, Aug. 2024, doi: 10.1016/J.MATCHAR.2024.114078.

[150] S. Zhang and X. Guo, "Effects of Cr and Hf additions on the microstructure and properties of

Nb silicide based ultrahigh temperature alloys," *Mater. Sci. Eng. A*, vol. 638, pp. 121–131, Jun. 2015, doi: 10.1016/J.MSEA.2015.04.003.

[151] L. Su, L. Jia, K. Jiang, and H. Zhang, "The oxidation behavior of high Cr and Al containing Nb-Si-Ti-Hf-Al-Cr alloys at 1200 and 1250 °C," *Int. J. Refract. Met. Hard Mater.*, vol. 69, pp. 131–137, Dec. 2017, doi: 10.1016/J.IJRMHM.2017.08.006.

[152] K. Zelenitsas, "Study of niobium silicide-based alloys for operational temperatures beyond 1150 degrees C. - University of Surrey," the University of Surrey, 2005. Accessed: Jul. 03, 2024. [Online]. Available: https://openresearch.surrey.ac.uk/esploro/outputs/99516848102346

[153] K. Zelenitsas and P. Tsakiropoulos, "Study of the role of Al and Cr additions in the microstructure of Nb-Ti-Si in situ composites," *Intermetallics*, vol. 13, no. 10, pp. 1079–1095, Jan. 2005, doi: 10.1016/j.intermet.2005.02.002.

[154] R. Mitra, "Mechanical behaviour and oxidation resistance of structural silicides," *International Materials Reviews*, vol. 51, no. 1. Taylor & Francis, pp. 13–64, Feb. 2006. doi: 10.1179/174328006X79454.

[155] R. Sakidja, G. Wilde, H. Sieber, and J. H. Perepezko, "Microstructural development of Mo(ss) + T2 two-phase alloys," *Mater. Res. Soc. Symp. - Proc.*, vol. 552, 1999, doi: 10.1557/proc-552-kk6.3.1.

[156] V. Supatarawanich, D. R. Johnson, and C. T. Liu, "Oxidation behavior of multiphase Mo-Si-B alloys," in *Intermetallics*, Elsevier, Jul. 2004, pp. 721–725. doi: 10.1016/j.intermet.2004.02.011.

[157] R. Sakidja, J. H. Perepezko, S. Kim, and N. Sekido, "Phase stability and structural defects in high-temperature Mo-Si-B alloys," *Acta Mater.*, vol. 56, no. 18, pp. 5223–5244, Oct. 2008, doi: 10.1016/j.actamat.2008.07.015.

[158] A. J. Thom, E. Summers, and M. Akinc, "Oxidation behavior of extruded Mo5Si3Bx-MoSi2-MoB intermetallics from 600°-1600 °C," *Intermetallics*, vol. 10, no. 6, pp. 555–570, Jun. 2002, doi: 10.1016/S0966-9795(02)00034-1.

[159] M. G. Mendiratta, T. A. Parthasarathy, and D. M. Dimiduk, "Oxidation behavior of αMo-Mo3Si-Mo5SiB2 (T2) three phase system," *Intermetallics*, vol. 10, no. 3, pp. 225–232, Mar. 2002, doi: 10.1016/S0966-9795(01)00118-2.

[160] S. Paswan, R. Mitra, and S. K. Roy, "Isothermal oxidation behaviour of Mo-Si-B and Mo-Si-B-Al alloys in the temperature range of 400-800 °C," *Mater. Sci. Eng. A*, vol. 424, no. 1–2, pp. 251–265, May 2006, doi: 10.1016/j.msea.2006.03.014.

[161] V. Behrani, A. J. Thom, M. J. Kramer, and M. Akinc, "Microstructure and oxidation behavior of Nb-Mo-Si-B alloys," *Intermetallics*, vol. 14, no. 1, pp. 24–32, Jan. 2006, doi: 10.1016/j.intermet.2005.03.007.

[162] Y. Liu, A. J. Thom, M. Kramer, and M. Akinc, "Processing and Oxidation Behavior of Nb-Si-B Intermetallics," Iowa State University, 2004. Accessed: Jan. 06, 2021. [Online]. Available: https://digital.library.unt.edu/ark:/67531/metadc779940/

[163] T. Murakami *et al.*, "Microstructure, mechanical properties and oxidation behavior of powder compacts of the Nb-Si-B system prepared by spark plasma sintering," *Intermetallics*, vol. 7, no. 9, pp. 1043–1048, Sep. 1999, doi: 10.1016/S0966-9795(99)00017-5.

[164] K. Kurokawa, A. Yamauchi, and S. Matsushita, "Improvement of Oxidation Resistance of NbSi2

by Addition of Boron," *Mater. Sci. Forum*, vol. 502, pp. 243–248, Dec. 2005, doi: 10.4028/www.scientific.net/msf.502.243.

[165] W. Jun, G. Xiping, and G. Jinming, "Effects of B on the Microstructure and Oxidation Resistance of Nb-Ti-Si-based Ultrahigh-temperature Alloy," *Chinese J. Aeronaut.*, vol. 22, no. 5, pp. 544–550, 2009.

[166] S. Zhang and X. Guo, "Alloying effects on the microstructure and properties of Nb-Si based ultrahigh temperature alloys," *Intermetallics*, vol. 70, pp. 33–44, Mar. 2016, doi: 10.1016/j.intermet.2015.12.002.

[167] L. Su, L. Jia, J. Weng, Z. Hong, C. Zhou, and H. Zhang, "Improvement in the oxidation resistance of Nb-Ti-Si-Cr-Al-Hf alloys containing alloyed Ge and B," *Corros. Sci.*, vol. 88, pp. 460–465, Nov. 2014, doi: 10.1016/j.corsci.2014.08.006.

[168] C. D. WirkuS and D. R. Wilder, "High-Temperature Oxidation of Molybdenum Disilicide," *J. Am. Ceram. Soc.*, vol. 49, no. 4, pp. 173–177, Apr. 1966, doi: 10.1111/j.1151-2916.1966.tb13227.x.

[169] D. A. Berztiss, R. R. Cerchiara, E. A. Gulbransen, F. S. Pettit, and G. H. Meier, "Oxidation of MoSi2 and comparison with other silicide materials," *Mater. Sci. Eng. A*, vol. 155, no. 1–2, pp. 165–181, Jun. 1992, doi: 10.1016/0921-5093(92)90324-T.

[170] A. Q. Liu, S. S. Li, L. Sun, and Y. F. Han, "Effect of B on the Microstructures and High Temperature Oxidation Resistance of a Nb-Si System In Situ Composite," *Mater. Sci. Forum*, vol. 546–549, pp. 1489–1494, May 2007, doi: 10.4028/www.scientific.net/msf.546-549.1489.

[171] L. Portebois, S. Mathieu, Y. Bouizi, M. Vilasi, and S. Mathieu, "Effect of boron addition on the oxidation resistance of silicide protective coatings: A focus on boron location in as-coated and oxidised coated niobium alloys," *Surf. Coatings Technol.*, vol. 253, pp. 292–299, Aug. 2014, doi: 10.1016/j.surfcoat.2014.05.058.

[172] S. Knittel, S. Mathieu, L. Portebois, S. Drawin, and M. Vilasi, "Development of silicide coatings to ensure the protection of Nb and silicide composites against high temperature oxidation," *Surf. Coatings Technol.*, vol. 235, pp. 401–406, Nov. 2013, doi: 10.1016/j.surfcoat.2013.07.053.

[173] A. Mueller, G. Wang, R. A. Rapp, E. L. Courtright, and T. A. Kircher, "Oxidation behavior of tungsten and germanium-alloyed molybdenum disilicide coatings," *Mater. Sci. Eng. A*, vol. 155, no. 1–2, pp. 199–207, Jun. 1992, doi: 10.1016/0921-5093(92)90326-V.

[174] C. Wang, W. Shao, W. Wang, and C. Zhou, "Oxidation behaviour of a Ge-modified silicide coating on an Nb-Si based alloy in the moderate temperature range," *Corros. Sci.*, vol. 163, p. 108249, Feb. 2020, doi: 10.1016/j.corsci.2019.108249.

[175] J. long Li, W. Wang, and C. gen Zhou, "Oxidation and interdiffusion behavior of a germanium-modified silicide coating on an Nb–Si-based alloy," *Int. J. Miner. Metall. Mater.*, vol. 24, no. 3, pp. 289–296, Mar. 2017, doi: 10.1007/s12613-017-1407-4.

[176] B. V. Cockeram, "Growth and oxidation resistance of boron-modified and germanium-doped silicide diffusion coatings formed by the halide-activated pack cementation method," *Surf. Coatings Technol.*, vol. 76–77, pp. 20–27, 1995, doi: 10.1016/0257-8972(95)02492-1.

[177] W. Wang, B. Yuan, and C. Zhou, "Formation and oxidation resistance of germanium modified silicide coating on Nb based in situ composites," *Corros. Sci.*, vol. 80, pp. 164–168, Mar. 2014, doi: 10.1016/j.corsci.2013.11.029.

[178] J. Schlichting and S. Neumann, “GeO2/SiO2-glasses from gels to increase the oxidation resistance of porous silicon containing ceramics,” *J. Non. Cryst. Solids*, vol. 48, no. 1, pp. 185–194, Mar. 1982, doi: 10.1016/0022-3093(82)90255-1.

[179] B. V. Cockeram and R. A. Rapp, “Oxidation-resistant boron- and germanium-doped silicide coatings for refractory metals at high temperature,” *Mater. Sci. Eng. A*, vol. 192–193, no. PART 2, pp. 980–986, Feb. 1995, doi: 10.1016/0921-5093(95)03342-4.

[180] The University of Edinburgh, “Vacuum pump test | GeoSciences.” Accessed: Oct. 04, 2023. [Online]. Available: https://geosciences.ed.ac.uk/about/facilities/all/ionprobe/technical/samples/epoxy-resins/results/pump-tests

[181] G. F. Bastin and H. J. M. Heijligers, *Quantitative Electron Probe Microanalysis of Ultra-Light Elements (Boron-Oxygen)*. Springer, Boston, MA, 1991. doi: 10.1007/978-1-4899-2617-3_8.

[182] N. Vellios and P. Tsakiropoulos, “Study of the role of Fe and Sn additions in the microstructure of Nb–24Ti–18Si–5Cr silicide based alloys,” *Intermetallics*, vol. 18, no. 9, pp. 1729–1736, Sep. 2010, doi: 10.1016/J.INTERMET.2010.05.012.

[183] I. Grammenos and P. Tsakiropoulos, “Study of the role of Mo and Ta additions in the microstructure of Nb–18Si–5Hf silicide based alloy,” *Intermetallics*, vol. 18, no. 8, pp. 1524–1530, Aug. 2010, doi: 10.1016/J.INTERMET.2010.04.004.

[184] P. Tsakiropoulos, “On the macrosegregation of silicon in niobium silicide based alloys,” *Intermetallics*, vol. 55, pp. 95–101, Dec. 2014, doi: 10.1016/J.INTERMET.2014.07.004.

[185] C. A. Schneider, W. S. Rasband, and K. W. Eliceiri, “NIH Image to ImageJ: 25 years of image analysis,” *Nat. Methods 2012 97*, vol. 9, no. 7, pp. 671–675, Jun. 2012, doi: 10.1038/nmeth.2089.

[186] K. Zelenitsas and P. Tsakiropoulos, “Study of the role of Al and Cr additions in the microstructure of Nb–Ti–Si in situ composites,” *Intermetallics*, vol. 13, no. 10, pp. 1079–1095, Jan. 2005, doi: 10.1016/J.INTERMET.2005.02.002.

[187] Z. Sun, Y. Yang, X. Guo, C. Zhang, and Y. A. Chang, “Experimental investigation on the phase equilibria of the nb-Ti-Si-B system at 1500 °c,” *J. Phase Equilibria Diffus.*, vol. 32, no. 5, pp. 407–411, Oct. 2011, doi: 10.1007/s11669-011-9928-4.

[188] D. L. Davidson, K. S. Chan, and D. L. Anton, “Effects on fracture toughness of ductile-phase composition and morphology in Nb-Cr-Ti and Nb-Si in situ composites,” *Metall. Mater. Trans. A Phys. Metall. Mater. Sci.*, vol. 27 A, no. 10, pp. 3007–3018, 1996, doi: 10.1007/BF02663850.

[189] C. Beckermann, “Modelling of macrosegregation: applications and future needs,” *Int. Mater. Rev.*, vol. 47, no. 5, pp. 243–262, 2002, doi: 10.1179/095066002225006557.

[190] D. U. Furrer and S. L. Semiatin, “Physical Constants and Physical Properties of the Elements,” in *ASM Handbook, Volume 22A: Fundamentals of Modeling for Metals Processing*, ASM International, 2009, pp. 588–598. doi: 10.31399/ASM.HB.V22A.A0005441.

[191] J.-C. Zhao, B. P. Bewlay, M. R. Jackson, and L. A. Peluso, “Alloying and phase stability in Niobium silicide in-situ composites,” in *Proceedings of the International Symposium on Structural Intermetallics*, 2001, pp. 483–491.

[192] B. P. Bewlay, M. R. Jackson, and R. R. Bishop, “The Nb-Ti-Si ternary phase diagram: Determination of solid-state phase equilibria in Nb- and Ti-rich alloys,” *J. Phase Equilibria*, vol. 19, no. 6, pp. 577–586, 1998, doi: 10.1361/105497198770341789.

[193] Z. Li and P. Tsakiropoulos, “Study of the effect of Cr and Ti additions in the microstructure of Nb–18Si–5Ge based in-situ composites,” *Intermetallics*, vol. 26, pp. 18–25, Jul. 2012, doi: 10.1016/J.INTERMET.2012.03.051.

[194] J. Zhao, C. Utton, and P. Tsakiropoulos, “On the Microstructure and Properties of Nb-12Ti-18Si-6Ta-5Al-5Cr-2.5W-1Hf (at.%) Silicide-Based Alloys with Ge and Sn Additions,” *Mater. 2020, Vol. 13, Page 3719*, vol. 13, no. 17, p. 3719, Aug. 2020, doi: 10.3390/MA13173719.

[195] J. Zhao, C. Utton, and P. Tsakiropoulos, “On the Microstructure and Properties of Nb-18Si-6Mo-5Al-5Cr-2.5W-1Hf Nb-Silicide Based Alloys with Ge, Sn and Ti Additions (at.%),” *Mater. 2020, Vol. 13, Page 4548*, vol. 13, no. 20, p. 4548, Oct. 2020, doi: 10.3390/MA13204548.

[196] C. McCaughey and P. Tsakiropoulos, “Type of Primary Nb5Si3 and Precipitation of Nbss in αNb5Si3 in a Nb-8.3Ti-21.1Si-5.4Mo-4W-0.7Hf (at.%) Near Eutectic Nb-Silicide-Based Alloy,” *Mater. 2018, Vol. 11, Page 967*, vol. 11, no. 6, p. 967, Jun. 2018, doi: 10.3390/MA11060967.

[197] J. Becker *et al.*, “Oxidation response of additively manufactured eutectic Mo-Si-B alloys,” *IOP Conf. Ser. Mater. Sci. Eng.*, vol. 882, no. 1, p. 012002, Jul. 2020, doi: 10.1088/1757-899X/882/1/012002.

[198] Z. Li and P. Tsakiropoulos, “Study of the effect of Ti and Ge in the microstructure of Nb–24Ti–18Si–5Ge in situ composite,” *Intermetallics*, vol. 19, no. 9, pp. 1291–1297, Sep. 2011, doi: 10.1016/J.INTERMET.2011.04.010.

[199] Z. Li and P. Tsakiropoulos, “The microstructures of Nb–18Si–5Ge–5Al and Nb–24Ti–18Si–5Ge–5Al in situ composites,” *J. Alloys Compd.*, vol. 550, pp. 553–560, Feb. 2013, doi: 10.1016/J.JALLCOM.2012.10.170.

[200] Z. Li and P. Tsakiropoulos, “On the microstructures and hardness of the Nb-24Ti-18Si-5Al-5Cr-5Ge and Nb-24Ti-18Si-5Al-5Cr-5Ge-5Hf (at.%) silicide based alloys,” *Materials (Basel).*, vol. 12, no. 7, 2019, doi: 10.3390/ma12172655.

[201] T. Thandorn and P. Tsakiropoulos, “Study of the role of B addition on the microstructure of the Nb-24Ti-18Si-8B alloy,” *Intermetallics*, vol. 18, no. 5, pp. 1033–1038, May 2010, doi: 10.1016/j.intermet.2010.01.033.

[202] S. Zhang, W. Liu, and J. Sha, “Microstructural evolution and mechanical properties of Nb-Si-Cr ternary alloys with a tri-phase Nb/Nb5Si3/Cr2Nb microstructure fabricated by spark plasma sintering,” *Prog. Nat. Sci. Mater. Int.*, vol. 28, no. 5, pp. 626–634, Oct. 2018, doi: 10.1016/j.pnsc.2018.09.001.

[203] H. A. Wriedt, “The Al-O (Aluminum-Oxygen) system,” *Bull. Alloy Phase Diagrams*, vol. 6, no. 6, pp. 548–553, Dec. 1985, doi: 10.1007/BF02887157.

[204] H. Okamoto, “O-Ti (Oxygen-Titanium),” *J. Phase Equilibria Diffus.*, vol. 32, no. 5, pp. 473–474, Oct. 2011, doi: 10.1007/S11669-011-9935-5/TABLES/1.

[205] I. Akin, B. C. Ocak, F. Sahin, and G. Goller, “Effects of SiC and SiC-GNP additions on the mechanical properties and oxidation behavior of NbB 2,” *J. Asian Ceram. Soc.*, vol. 7, no. 2, pp. 170–182, Apr. 2019, doi: 10.1080/21870764.2019.1595929.

[206] J. Cheng, S. Yi, and J. S. Park, “Simultaneous coating of Si and B on Nb–Si–B alloys by a halide activated pack cementation method and oxidation behaviors of the alloys with coatings at 1100 °C,” *J. Alloys Compd.*, vol. 644, pp. 975–981, Sep. 2015, doi: 10.1016/J.JALLCOM.2015.05.003.

[207] A. N. Mansurova, R. I. Gulyaeva, and V. M. Chumarev, “Kinetic analysis of the oxidation of

Nb–Si eutectic alloy doped with boron," *Inorg. Mater. Appl. Res.*, vol. 8, no. 2, pp. 318–326, Mar. 2017, doi: 10.1134/S2075113317020150.

[208] J. Cheng, S. Yi, and J. S. Park, "Oxidation behaviors of Nb-Si-B ternary alloys at 1100 °c under ambient atmosphere," *Intermetallics*, vol. 23, pp. 12–19, Apr. 2012, doi: 10.1016/j.intermet.2011.11.007.

[209] J. Geng, P. Tsakiropoulos, and G. Shao, "A thermo-gravimetric and microstructural study of the oxidation of Nbss/Nb5Si3-based in situ composites with Sn addition," *Intermetallics*, vol. 15, no. 3, pp. 270–281, Mar. 2007, doi: 10.1016/J.INTERMET.2006.06.003.

[210] O. Hernández-Negrete and P. Tsakiropoulos, "On the Microstructure and Isothermal Oxidation at 800 and 1200 °C of the Nb-24Ti-18Si-5Al-5Cr-5Ge-5Sn (at.%) Silicide-Based Alloy," *Materials (Basel).*, vol. 13, no. 3, p. 722, Feb. 2020, doi: 10.3390/MA13030722.

[211] J. Nelson, M. Ghadyani, C. Utton, and P. Tsakiropoulos, "A Study of the Effects of Al, Cr, Hf, and Ti Additions on the Microstructure and Oxidation of Nb-24Ti-18Si Silicide Based Alloys," *Materials (Basel).*, vol. 11, no. 9, p. 1579, Sep. 2018, doi: 10.3390/MA11091579.

[212] Z. Xu, C. Utton, and P. Tsakiropoulos, "A Study of the Effect of 2 at.% Sn on the Microstructure and Isothermal Oxidation at 800 and 1200 °C of Nb-24Ti-18Si-Based Alloys with Al and/or Cr Additions," *Mater. 2018, Vol. 11, Page 1826*, vol. 11, no. 10, p. 1826, Sep. 2018, doi: 10.3390/MA11101826.

[213] Z. Xu, C. Utton, and P. Tsakiropoulos, "A Study of the Effect of 5 at.% Sn on the Micro-Structure and Isothermal Oxidation at 800 and 1200 °C of Nb-24Ti-18Si Based Alloys with Al and/or Cr Additions," *Mater. 2020, Vol. 13, Page 245*, vol. 13, no. 1, p. 245, Jan. 2020, doi: 10.3390/MA13010245.

[214] S. Knittel, S. Mathieu, L. Portebois, and M. Vilasi, "Effect of tin addition on Nb–Si-based in situ composites. Part II: Oxidation behaviour," *Intermetallics*, vol. 47, pp. 43–52, Apr. 2014, doi: 10.1016/J.INTERMET.2013.12.010.

[215] S. Cruchley, M. P. Taylor, H. E. Evans, P. Bowen, M. C. Hardy, and S. Stekovic, "Microstructural Characterisation of High Temperature Oxidation of Nickel Base Superalloy RR1000 and the Effect of Shot-Peening," *Superalloys 2012*, pp. 751–758, Oct. 2012, doi: 10.1002/9781118516430.CH83.

[216] J. W. X. Wo, D. M. Collins, M. P. Taylor, M. C. Hardy, and H. J. Stone, "Delayed parabolic oxidation via transient thermal exposures on a polycrystalline nickel-based superalloy," *Corros. Sci.*, vol. 227, p. 111675, Feb. 2024, doi: 10.1016/J.CORSCI.2023.111675.

[217] A. Encinas-Oropesa, G. L. Drew, M. C. Hardy, A. J. Leggett, J. R. Nicholls, and N. J. Simms, "Effects of oxidation and hot corrosion in a nickel disc alloy," *Proc. Int. Symp. Superalloys*, pp. 609–618, 2008, doi: 10.7449/2008/SUPERALLOYS_2008_609_618.

[218] M. Göbel, A. Rahmel, and M. Schütze, "The isothermal-oxidation behavior of several nickel-base single-crystal superalloys with and without coatings," *Oxid. Met.*, vol. 39, no. 3–4, pp. 231–261, Apr. 1993, doi: 10.1007/BF00665614/METRICS.